(14) NSWC/TR-80-417

A102320 Phase II

LEVEL III

AD A103453

(1)

(6) SPACE SHUTTLE RANGE SAFETY COMMAND DESTRUCT SYSTEM ANALYSIS AND VERIFICATION.

PHASE I,– DESTRUCT SYSTEM ANALYSIS AND VERIFICATION

(10) W. M. /Hinckley D. L. /Lehto
N. L. /Coleburn A. J. /Gorechlad
J. M. /Ward

(11) MAR[redacted]81 (12) 359

PREPARED FOR THE
NATIONAL AERONAUTICS AND SPACE ADMINISTRATION
GEORGE C. MARSHALL SPACE FLIGHT CENTER, ALABAMA 35812

NASA DEFENSE PURCHASE REQUEST H–13047B, 15 MAY 1975

(9) Final rept.,

NSWC

NAVAL SURFACE WEAPONS CENTER

Dahlgren, Virginia 22448 • Silver Spring, Maryland 20910

81 8 13 048

411563

UNCLASSIFIED

SECURITY CLASSIFICATION OF THIS PAGE (When Data Entered)

REPORT DOCUMENTATION PAGE

READ INSTRUCTIONS BEFORE COMPLETING FORM

1. REPORT NUMBER NSWC TR 80-417	2. GOVT ACCESSION NO. AD-A103 453	3. RECIPIENT'S CATALOG NUMBER
4. TITLE (and Subtitle) PHASE I - SPACE SHUTTLE RANGE SAFETY COMMAND DESTRUCT SYSTEM ANALYSIS AND VERIFICATION		5. TYPE OF REPORT & PERIOD COVERED Final 6. PERFORMING ORG. REPORT NUMBER
7. AUTHOR(s) W. M. Hinckley, D. L. Lehto, N. L. Coleburn, A. J. Gorechlad, J. M. Ward, and J. Petes		8. CONTRACT OR GRANT NUMBER(s)
9. PERFORMING ORGANIZATION NAME AND ADDRESS Naval Surface Weapons Center White Oak Laboratory Silver Spring, MD 20910		10. PROGRAM ELEMENT, PROJECT, TASK AREA & WORK UNIT NUMBERS NASA 0,0,R15KA
11. CONTROLLING OFFICE NAME AND ADDRESS		12. REPORT DATE March 1981 13. NUMBER OF PAGES 364
14. MONITORING AGENCY NAME & ADDRESS(if different from Controlling Office)		15. SECURITY CLASS. (of this report) UNCLASSIFIED 15a. DECLASSIFICATION/DOWNGRADING SCHEDULE

16. DISTRIBUTION STATEMENT (of this Report)

Approved for public release; distribution unlimited.

17. DISTRIBUTION STATEMENT (of the abstract entered in Block 20, if different from Report)

18. SUPPLEMENTARY NOTES

19. KEY WORDS (Continue on reverse side if necessary and identify by block number)

space shuttle	solid rocket booster	finite elements	fragments
destruct system	structural response	flight dynamics	detonation
linear shaped charge	explosion	debris	
external tank	aerodynamic drag	hydrogen-oxygen-air	
orbiter	stress analysis	blast	

20. ABSTRACT (Continue on reverse side if necessary and identify by block number)

The planned Duplex Command Destruct System (one linear-shaped charge (LSC) on each solid rocket booster (SRB)) was analyzed for destruct effectiveness at all times of flight and for unintentional separation of one SRB of the Orbiter. The destruct system was found to be only marginally effective in destructing the external tank (ET) and dispersing the propellants for the first 50 seconds of flight. Further, inadvertent separation of one SRB results in cluster (SRB/ET/Orbiter) breakup within as little as 5 seconds, rendering the SRB mounted destruct system ineffective for destructing the ET.

DD FORM 1 JAN 73 1473 EDITION OF 1 NOV 65 IS OBSOLETE

S/N 0102-LF-014-6601

UNCLASSIFIED

SECURITY CLASSIFICATION OF THIS PAGE (When Data Entered)

FOREWORD

This report is submitted to the National Aeronautics and Space Administration (NASA), George C. Marshall Space Flight Center (MSFC), Alabama, in fulfillment of NASA Defense Purchase Request H-13047-B, dated May 1975. The report is an investigation of the Space Shuttle Command Destruct System. A later Phase II study analyzes ordnance options for a destruct system that will overcome the shortcomings of this system. A phase III study develops the breakup model of the Space Shuttle cluster at various times into flight.

The work accomplished in this task was under the technical cognizance of J. A. Roach, Code EL-42, MSFC. He very competently and expeditiously provided necessary and pertinent information and access to information through his co-workers at MSFC. His clear delineation of the problem and the tasks to be tackled was instrumental in enabling the work to proceed apace.

At the Naval Surface Weapons Center, White Oak Laboratory, many persons contributed their talents to the completion of the task. Principal investigators and authors of this report were:

D. L. Lehto and J. M. Ward - Chapter 2, Section I, on explosion effects.

N. L. Coleburn - Chapter 2, Section II, on conically shaped charge design and operation.

R. T. Hall and A. J. Gorechlad - Chapter 3, on aerodynamic effects and trajectories.

J. E. Goeller, W. M. Hinckley, J. C. S. Yang, E. P. Johnson, J. R. Renzi, W. T. Messick, J. J. O'Neill, and J. Berezow - Chapter 4, on stress analysis and delta times.

J. Petes served as project leader and wrote the background, objectives, and summary information in Chapter 1.

J. F. PROCTOR
By direction

CONTENTS

CONTENTS — Continued

CONTENTS — Continued

ILLUSTRATIONS

ILLUSTRATIONS — Continued

ILLUSTRATIONS — Continued

ILLUSTRATIONS — Continued

ILLUSTRATIONS -- Continued

ILLUSTRATIONS — Continued

TABLES

CHAPTER 1

BACKGROUND, OBJECTIVES, SUMMARY

EXECUTIVE SUMMARY

Two destructive mechanisms were investigated for destroying the LH_2 tank of the external tank (ET): (1) a clamshell-type of opening of the solid rocket boosters (SRB's), thereby generating a large lateral inboard thrust on the ET, and (2) a catastrophic and rapid rupture of the SRB's, generating blast and fragments. The two models are considered to be mutually exclusive, i.e., if one model is realized in actuality, the other is not. The blast model predicts that catastrophic buckling of the LH_2 tank will take place at all times of interest into flight. However, because the degree of rupture (tearing) of and the rate of LH_2 dispersal from the buckled LH_2 tank are difficult to quantify and because it is uncertain whether the blast model or the clamshell model is the one to be realized upon the destruct command, the clamshell model with its more modest destruct capabilities probably should be used in assessing the required functioning of the command destruct system. For the clamshell model, the LH_2 tank destruct is only assured as predicted at the later times into flight, e.g., 50 and 100 seconds; at the earlier times, destruct is marginal or unlikely. The destruct of the LOX tank by means of pairs of conically shaped charges located in the nose of the SRBs is predicted at all times of interest. These conditions prevail for both normal destruct and for destruct after the loss of the orbiter.

In the case of loss of one SRB, the blast effects are about the same, but the clamshell destruct mechanism is less effective. Furthermore, for this postulated situation, the time to initiate the Command Destruct System may be too short for effective action; at about 50 seconds into flight, only a few seconds are available between the time one SRB is separated and the remaining cluster breaks apart. Without SRB-ET design integrity, there is no command destruct mechanism for defeating the ET.

Tables 1-1 through 1-4 show the viability of the Command Destruct System aboard the Space Shuttle for the operational conditions of interest.

BACKGROUND. This report documents the work done and the conclusions reached by the Naval Surface Weapons Center, White Oak Laboratory, Silver Spring, Maryland, in response to NASA-Defense Purchase Request H-13047B of 15 May 1975 prepared by the National Aeronautics and Space Administration, George C. Marshall Space Flight Center (MSFC), Alabama, calling for a study of the Space Shuttle Command Destruct System.

TABLE 1-1 NORMAL DESTRUCT (TWO SRB'S ATTACHED TO ET)

Item	Model	Time Into Flight (sec)	Destruct Mechanism
LH_2 Tank	Clamshell	0	Marginal destruct
		10	Excessive ullage pressure
		50 } 100 }	Excessive deformation of LH_2 frames
	Blast	All	Buckling of LH_2 tank
	Fragments	All	No destruct
LOX Tank	Conically shaped charge (CSC)	All	Tear in tank plus hydraulic pressure

TABLE 1-2 NORMAL DESTRUCT FOLLOWING LOSS OF ORBITER

Item	Model	Time Into Flight (sec)	Destruct Mechanism
LH_2 Tank	Clamshell	0	Marginal destruct
		10	Excessive ullage pressure
		50 } 100 }	Excessive deformation of LH_2 frames
	Blast	All	Buckling of LH_2 tank
	Fragments	All	No destruct
LOX Tank	CSC	All	Tear in tank plus hydraulic pressure

TABLE 1-3 DESTRUCT FOLLOWING LOSS OF ONE SRB

Item	Model	Time Into Flight (sec)	Destruct Mechanism
LH_2 Tank	Clamshell	0	Destruct unlikely
		10	Marginal rupture of frames
		50	Rupture of LH_2 support frames
		100	Rupture of LH_2 support frames
	Blast	All	Buckling of LH_2 tank
	Fragments	All	No destruct
LOX Tank	CSC	All	Tear in tank and hydraulic pressure

TABLE 1-4 DELTA TIMES

Item	Time Into Flight (sec)	ΔT (sec)	Failure
Orbiter Loss	0	>30	
	10	>20	
	50	16.5	SRB/ET forward fitting and/or rear truss
	100	>20	
SRB Loss	0	15.75	Orbiter/ET forward joint
	10	>20	
	50	2	Orbiter/ET forward truss
	100	>20	

Prior to the purchase request and after several discussions between personnel of the MSFC and the White Oak Laboratory, the laboratory submitted a proposal to MSFC on 9 April 1975 outlining a two-phase program concerned with the viability of the command destruct system aboard the space shuttle configuration and the consequences of this destruct at the earth's surface. Phase I called for an analysis of the destruct system, as designed, for operation under normal and postulated abnormal conditions. Expecting that the analytical study would be based in part on broad assumptions, Phase II was proposed as a test program to provide experimental data to substantiate the assumptions and/or guide the subsequent updating analysis. This phase also proposed to determine the blast and fragment hazards on the ground, in case the destruct command was given. The purchase request called for the Phase I study only.

OBJECTIVES. The work statements for Phase I in the purchase request clearly state the technical objectives of the task and outline details of the study to be made.

1. Through analysis, the capability of the command destruct system to destruct the ET will be predicted for the following conditions:

a. Normal destruct operations, i.e., both SRB's attached to the ET.

b. Inadvertent separation of one SRB.

c. Inadvertent separation of the orbiter.

The above conditions will be analyzed for four times into flight: 0, 10, 50, and 100 seconds.

2. The destruct system to be analyzed consists of a linear-shaped charge (LSC) mounted outboard on the SRB and extending 70 percent over the length of the SRB, and a conically shaped charge mounted in the forward end of the SRB. Both SRB's are configured alike. The purpose of the linear-shaped charges is to assure destruction of the SRB's and through the SRB destructive effects, e.g., blast and fragments, assure destruction of the LH_2 portion of the ET. The purpose of the conically shaped charges is to assure destruction of the LO_2 portion of the ET. This destruction and dispersal of the solid and liquid propellant stages are required by the Air Force Eastern Test Range with the intent that impact area hazards of explosion be reduced to a minimum.

3. The Phase I effort will basically address three tasks:

a. The explosion phenomena, e.g., blast and fragments, initiated when the destruct command is given.

b. The aerodynamic and atmospheric flight mechanics of the cluster components upon inadvertent separation of one SRB or the orbiter.

c. The structural response of the SRB's and the ET to these explosion and aerodynamic loads.

4. The explosion effects study (Item 3a. above) will have the following objectives:

a. Determination of the blast and fragment fields generated by the action of the linear-shaped charges on the SRB's.

(1) Reactivity of the solid propellant.

(2) Breakup of the SRB case and propellant grain in terms of size and weight distribution and initial velocities of fragments.

(3) Airblast pressure field as a function of time of rupture and distance from SRB, and altitude of SRB at time of rupture.

b. Determination of the effects of a conically shaped charge producing holes 4 inches, 8 inches, and 12 inches in diameter in the LO_2 tank to further damage it through hydrodynamic loading.

(1) Reaction of conically shaped charge liner with LO_2.

(2) Hydrodynamic forces imposed on LO_2 tank by hydraulic ram effect.

5. The aerodynamic and atmospheric flight mechanics study task (Item 3b. above) will have the following objectives:

a. Provide aerodynamic loads data as a function of time on the remaining cluster components upon inadvertent separation of one SRB or the orbiter from the ET.

b. Provide separation data, i.e., trajectory data, for either the orbiter or an SRB which may have been inadvertently separated.

6. The structural response portion of the program (Item 3c. above) will have the following objectives:

a. Perform structural analysis of the ET during destruct of both attached SRB's to determine probability of rupture and extent of damage to the ET. The following principal damage modes will be investigated:

(1) Damage due to close-in fragments and overpressure generated by destruct command of the SRB's.

(2) Damage due to gross SRB body impact from venting of SRB rocket gases or subsequent impact of major fragments of SRB due to aerodynamic trajectory.

(3) Damage due to puncture at SRB support points and interaction of conically shaped charge with forward support points.

b. Analyze structural integrity of SRB, ET, orbiter configuration after inadvertent separation of a single SRB. Determine areas of critical stress based upon load-time data obtained from aerodynamic analysis.

c. Same as item above, except analysis is of two SRB's and ET after inadvertent separation of orbiter.

d. From the results obtained above plus the aerodynamic trajectory supplied for each case, establish delta time interval allowable before destruct command is given.

<u>SUMMARY</u>. The summary of the results of the study with a brief description of some assumptions and methodology follows. A detailed presentation of the work performed is given in the succeeding chapters and appendices.

<u>Normal Destruct Operations</u>. No data found were specifically concerned with the response of the Space Shuttle SRB to the effects of the LSC. Pertinent information on the several stages of the Minuteman and Titan missiles were used as a guide to

predict this response, along with general information on propellant vulnerability to detonation under the relatively mild excitation of the LSC's. On this basis, it is considered that the SRB propellant does not detonate. In the breakup process, however, the propellant may burn at a more rapid rate than in its normal motor operation because of the larger surface area presented. This will result in some early enhancement of the chamber pressure. This rapid burning and increased pressure will not occur as rapidly as the energy release associated with detonations, nor will the pressures be as high as those expected from detonations.

The structural response of the SRB to a long cut by the LSC is treated in two models, one at each end of the spectrum of possibilities. These models are used to predict the blast, fragment, and force fields generated by the SRB after rupture by the LSC.

In one model, it is assumed that the LSC cuts through the SRB steel skin, thus violating the hoop strength of the steel and resulting in a clamshell-like opening of the skin and subsequent longitudinal opening of the SRB grain. This produces, under the impetus of the operating pressure of about 800 psi contained within the chamber of the burning grain, a very large lateral thrust of the SRB. This, in turn, produces a large, lateral destructive force on the ET. In this clamshell model the blast field in the direction of the ET will be minimal and, hence, is not considered a destruct mechanism.

The other explosion model considered calls for the SRB case and contained propellant grain to break into many pieces with a wide range of fragment sizes. However, in the most conservative mode of breakup, i.e., without increased pressure being generated due to increased propellant surface available to burning, the velocity of most of the fragments under the initial 800 psi chamber pressure impetus is insufficient to cause penetration of the ET skin. The pressure of this cylindrical explosion model, however, is sufficiently large to cause buckling of the ET.

Breakup of the SRB in either of the two postulated models will probably result in destruct of the LH_2 tank. For the clamshell model, it appears that destruct will be by excessive deformation of the LH_2 frames for times 50 and 100 seconds into flight. For destruct at 10 seconds, catastrophic rupture of the LH_2 tank will result probably from excessive ullage pressure but rupture from excessive radial deformation is another possibility. For destruct at lift-off (T = 0 seconds), failure by excessive pressure is probable, but marginal.

For the blast and fragment model of SRB destruct, destruct of the ET is highly probable at all times into flight from lift-off to 100 seconds. The blast field is sufficiently large to cause severe buckling of the ET, but the degree of catastrophic rupturing of the tank is difficult to ascertain.

Fragments formed by the breakup of the SRB are not considered effective. For the most conservative model studied, the fragment impact energies are too low to produce much ET penetration.

In summary, calculations indicate that catastrophic rupture of the LH_2 tank is highly probable for normal operations, i.e., destruct by two SRB's at 10, 50, and 100 seconds into flight. Destruct is questionable at lift-off. The clamshell model provides marginal destruct. The blast model predicts gross buckling of the LH_2 tank, but the degree of fluid dispersal is uncertain.

The CSC's located in the forward end of the SRB have been designed in conceptual form to destruct the LOX tank in the ET. Two CSC's are designated for each SRB: one directed at the ogive or barrel of the aluminum skin of the LOX tank, the other at the dome. With two areas of attack, the probability of the jet hydrodynamic forces being transferred to the LOX itself for almost any altitude of the ET is greatly enhanced. The individual CSC's are expected to be in the 4 to 5 pounds explosive weight range. Both tandem and wide angle CSC's will be used to obtain the desired effects at the relatively long stand-off distances dictated by the ET-SRB configuration. Aluminum liners are recommended for the CSC's to minimize the chance of violent liner-LOX chemical reactions.

It is expected that with the oblique angles of attack required of the CSC jets, initial tears of at least 2 feet in length and 3 inches in width will be formed in the LOX tank. These tears, coupled with the hydraulic forces induced in the LOX, will result in catastrophic destruct of the LOX tank.

Destruct Following Loss of Orbiter. Although the orbiter may inadvertently separate from the Space Shuttle configuration, so long as the two SRB's are attached to the ET, destruct of the LH_2 and LOX tanks probably will occur upon command as in normal destruct operations. The time for giving this command is limited by the delta time available between the orbiter loss and the breakup of the remaining cluster (see "Delta Time to Destruct," below).

Destruct Following Loss of One SRB. The destruct mechanisms available for defeating the LH_2 and LOX tanks are essentially the same for the Space Shuttle configuration with one SRB attached as for the normal, two attached SRB's; however, the magnitudes of the forces on the ET are somewhat different, and usually less. This results in a lessened probability of destruct of the ET at times of interest. Using the clamshell model, catastrophic rupture of the SRB/ET/Orbiter cluster following the loss of one SRB is highly probable for times of 50 and 100 seconds into flight, is marginal for 10 seconds into flight, and is unlikely for time at lift-off (T = 0 seconds). Probable failure mode is rupture of LH_2 support frames due to excessive strain. Failure due to excessive ullage pressure buildup is not likely.

The blast-fragment model does predict LH_2 tank destruct at all times into flight, with blast overpressure being the mechanism causing ET buckling.

The CSC's in one SRB are expected to result in catastrophic destruct of the LOX tank in much the same manner as for normal destruct operations.

Delta Time To Destruct. Another important variable in the destruct analysis is delta time. It is the time internal between the loss of the orbiter or one SRB and the occurrence of the first subsequent structural failure in the remaining cluster which will cause separation of the remaining SRB (or SRB's, in case of orbiter separation). This time may govern, to a large extent, the time available for executing command destruct upon the inadvertent separation of the orbiter or SRB. With loss of both SRB's, there is no command destruct system to defeat the ET. The four times into flight (0, 10, 50, and 100 seconds) analyzed in this study correspond in general to the lift-off, roll maneuver, high dynamic pressure, and maximum acceleration conditions. The response of the cluster at these times will vary significantly due to the variance in aerodynamic forces and thrust vectors. The aerodynamic loads at 0, 10, and 100 seconds are small due to low dynamic pressure (low vehicle velocity or low air density). The resulting cluster motion is moderate, and the attach fitting loads remain within failure limits for many seconds. A separation at 50 seconds, however, occurs during a period of high aerodynamic loading. The resulting motion is violent and attach fitting loads approach failure limits more rapidly. (Note that although only four specified times into flight are analyzed in detail, these times and the results predicted at these times represent a relatively broad time period. For example, 50 seconds is referred to as the time of high dynamic pressure q; yet, in reality, maximum q occurs at about 66 seconds into flight, with high q's lasting from about 40 to 75 seconds.)

Given an inadvertent orbiter separation, subsequent structural failure of the remaining cluster will not occur for at least 30 seconds following a separation at lift-off or for at least 20 seconds following a separation at 10 or 100 seconds into flight. Loss of the orbiter at 50 seconds, however, will result in failure of either or both the left SRB/ET forward fitting or rear truss at 16.5 ± 1.0 seconds following separation.

In the event of an inadvertent separation of the right SRB at lift-off, possible failure of the forward orbiter/ET joint occurs at 15.75 seconds. No failures are expected for at least 20 seconds following separation of the SRB at 10 or 100 seconds into flight. However, failure of the forward orbiter/ET truss will occur just 2 seconds after separation of the right SRB at 50 seconds into flight.

For the situation concerned with the loss of one SRB, the calculations were made to determine first probable failure of the remaining cluster and that it is the forward orbiter/ET joint that fails before SRB/ET attach points. This initial orbiter/ET joint separation leaves the rear joint still attached (even if momentarily), putting the cluster in a very unstable aerodynamic condition. It is impracticable to calculate this condition; however, it is fully expected that this instability will lead to a highly erratic trajectory and high aerodynamic forces on the crippled cluster, resulting in full orbiter separation and SRB/ET separation. The SRB/ET separation should occur in considerably less time than that given for the inadvertent orbiter separation.

CHAPTER 2

EXPLOSION EFFECTS

Section I. BLAST AND FRAGMENT EFFECTS FROM SRB BREAKUP

INTRODUCTION

The NASA Space Shuttle has a linear-shaped charge (LSC) mounted outboard on the solid rocket booster (SRB) and extending 70 percent over the length of the propellant grain as part of the Space Shuttle Range Safety Command Destruct System. The Space Shuttle vehicle, which includes the orbiter and two SRB's mounted to the external tank (ET), is shown in Figure 2-1.[1] The location of the LSC is shown schematically in this figure.

The function of the LSC is to break up each SRB. The assumed stages in the SRB breakup model are illustrated in Figure 2-2.

1. The LSC makes a segmented cut along the side of the SRB case, leaving the strengthened segment joints partly intact.

2. The cut segments increase in length since the full load goes into the remaining parts of the joints, which then fail in tension, producing a single long cut.

3. The SRB case begins to open like a clamshell. The chamber gases vent through the LSC cut and produce a lateral thrust on the SRB. Computation with the clamshell model begins here.

4. The unburned propellant grain cracks and breaks into fragments. The surfaces of the fragments burn and drive up the chamber pressure.

5. The increased pressure in the chamber ruptures the remaining portion of the case beyond the confines of the LSC. This produces the explosions seen on films of missile destructs with LSC destruct systems.

---

[1] Warden, W.R., "Shuttle Vehicle Mold Lines and Protuberances," ICD No. 2-00001, Space Shuttle Interface Control Document Level II, National Aeronautics and Space Administration, Johnson Space Center, Houston, Texas, 19 Feb 1975.

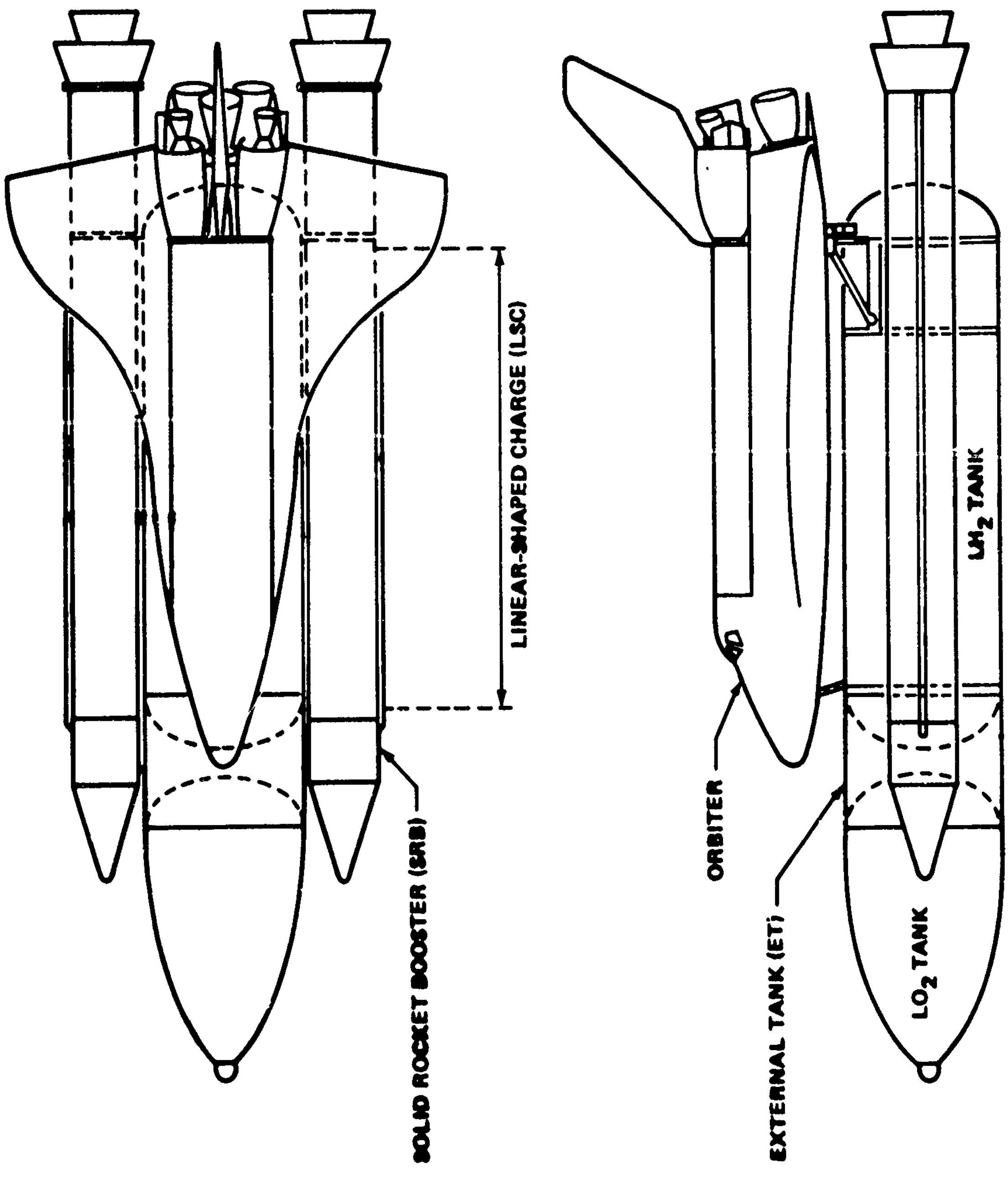

FIGURE 2-1 SPACE SHUTTLE CONFIGURATION

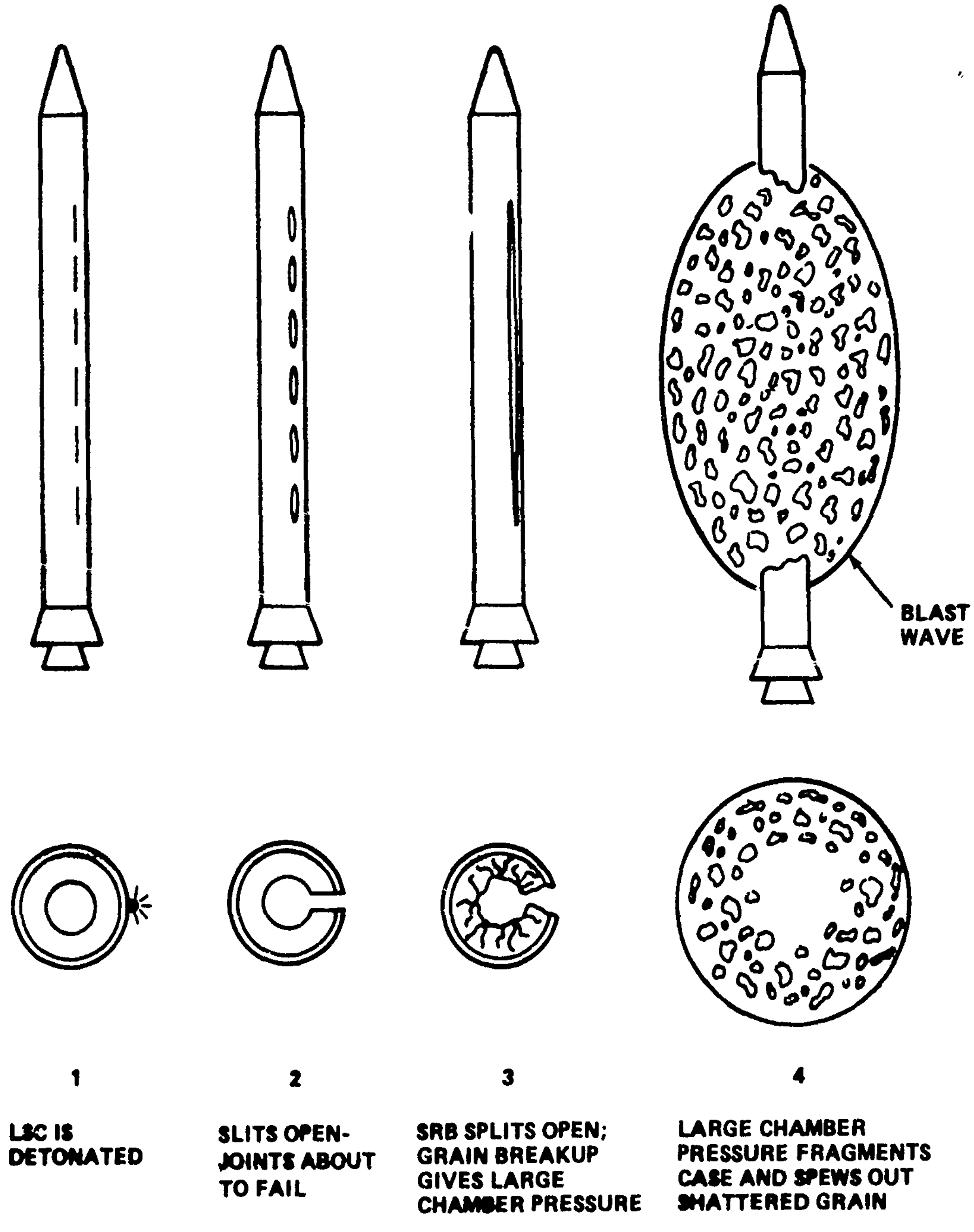

FIGURE 2-2 BREAKUP OF SRB

The destructive effects of the SRB airblast and fragments are to assure the destruction of the LH_2 tank in the ET. Three ET destruct mechanisms are considered:

a. Airblast loads on the ET from the SRB breakup.

b. SRB propellant grain fragments impact with the ET driven by the SRB breakup pressures.

c. SRB impact against the ET produced by the lateral thrust of the SRB propellant gas jet from the slit opened by the LSC.

The analysis discussed in this part of the final report provides the following results:

1. Chamber pressure, LSC slit width, and forward/side thrust time histories following the LSC cut.

2. Propellant grain fragment size distribution and fragment velocities following SRB breakup.

3. Airblast overpressures following SRB destruct.

The actual manner of rocket breakup following the destruct command is not known (an assumed breakup model is described above).* The mechanism of breakup may very well depend upon the time into flight because of the tremendous variation in mass of the onboard solid propellant as the burn progresses. The application of the present results depends upon the true breakup model. Some examples are presented below.

If the SRB case disintegrates upon detonation of the LSC, then airblast loads on the ET can be determined by releasing the normal chamber operating pressure to drive a cylindrical shock wave (one-dimensional hydrocode calculation). Information derived from the clamshell model is not applicable. Results from the propellant fragment models are useful to give propellant fragment size distribution with a separate estimate of early-time fragment velocity history.

If, on the other hand, the SRB case were to open as a clamshell upon detonation of the LSC, then the clamshell model provides lateral thrust information. Also, the angular displacement of the clamshell and chamber conditions obtained from the present analysis can be used as boundary conditions (time dependent) for a two-dimensional hydrocode calculation to give airblast loads on the ET.

The analytic models for the combustion chamber operation, nozzle, flow, clamshell motion, propellant fragment size distribution, propellant fragment motion, and the airblast model are described in the following paragraphs. Results of calculations are presented for four times into the Space Shuttle flight: 1, 10, 50, and 100 seconds.

---

*A discussion of the possibility of propellant detonation during destruct is given in Appendix A.

ROCKET MODEL

The early stages of SRB breakup are calculated by integrating the angular acceleration of the halves of the clamshell formed after the case has been cut by the LSC. The propellant grain burn rate and the flow rates through the thrust nozzle and the LSC slit are used to determine the change in chamber conditions. The model considers formation of grain cracks or fragments as separate options which can greatly affect the grain burn rate. This, in turn, has a large influence on the forces exerted by the chamber pressure on the SRB clamshell halves.

The data used to define the model are given in Tables 2-1 through 2-3 which specify pertinent SRB dimensions, solid rocket motor (SRM) propellant gas properties, and propellant grain mass/ballistic properties, respectively. Sutton's Rocket Propulsion Elements was used extensively as a general source of information for expressions dealing with propellant grain burning phenomena and nozzle theory.[2]

The standard assumptions for an ideal rocket analysis are used. The propellant grain is homogeneous with a uniform burning rate. The propellant gas products (with no condensed phase) are homogeneous throughout the chamber and nozzle. Chemical equilibrium is attained in the chamber and does not shift in the nozzle or in the LSC slit. Flow through the nozzle and the LSC slit is one-dimensional. The exhaust gases have only an axially directed velocity and the gas velocity, pressure, and density are uniform at any cross-section location. The propellant flow is steady and isentropic. There are no shocks, and friction/heat transfer effects are neglected. The propellant gas products obey the laws for a calorically perfect gas.

A correction (~ ± 5%) is applied to the thrust nozzle mass flow rate to obtain better chamber-pressure versus time agreement between the "ideal" calculation and the data in Table 2-3 for normal SRM chamber operation.

COMBUSTION CHAMBER OPERATION. The propellant grain is in the shape of a hollow cylinder with an 11-point star-shaped perforation in the cap at the head end. The cylindrical grain portion consists of four sections. Each of these sections has a constant outside diameter with an initial perforation radius of 30 inches at the head end and 32 inches at the aft end. For the chamber model in this analysis, a constant perforation radius is assumed for the entire grain length.* The length of the LSC is estimated to be 70 percent of the grain length.

Table 2-4 relates the grain burn area and chamber volume to the perforation (burn) radius during normal burn operation. This information was derived from the data given in Table 2-3 for propellant weight and burning area versus flight time. The model for burn area and chamber volume does include contributions from the star-shaped perforation at the head end.

[2] Sutton, G.P., Rocket Propulsion Elements, 3rd Edition (New York: John Wiley & Sons, Inc., 1964).

*The presence of a small gap between grain segments (~1 in) is ignored. The propellant is, for the most part, bonded with inhibitor on these nearly joined surfaces.

TABLE 2-1 SPACE SHUTTLE PARAMETERS

Propellant grain burn area, at 1 sec (in^2)*	461336.0
Initial burn area for the 11-point star-shaped perforation in the propellant grain nose cap (in^2)†	171585.0
Initial Chamber Volume†	4365466.0
Solid rocket booster inert weight (lbf)‡	174753.0
Solid rocket booster propellant weight, at 1 sec (lbf)*	1108355.0
Thrust nozzle exit area (in^2)‡	16660.0
Thrust nozzle throat area (in^2)‡	2326.85
Solid rocket booster case inside radius (in)†	72.52
Solid rocket booster case outside radius (in)‡	73.00
Propellant grain weight density (lbf/in^3)‡	0.0635
Solid rocket booster D6AC steel case weight density (lbf/in^3)‡	0.283
Solid propellant grain length (in)†	1374.0
Linear-shaped charge length (in)	1032.6
Internal energy of gas products from burning propellant grain (cal/gm)	1200.0
Ratio of specific heats for chamber gas	1.2
Molecular weight for chamber gas (lbf/lbf-mole)	28.38

*Data taken from memo from J. A. Roach (MSFC/NASA-EL-42), Huntsville, Alabama, to J. Petes (NSWC/WOL-WR-14), Silver Spring, Maryland; title: "Closing of Action Items Resulting from NSWC and MSFC Mtg. of 17 July 1975.

†Data taken from notes of phone conversation between D. Lehto (NSWC/WOL-WR-14) and E. Jacobs (MSFC/NASA) on 10 July 1975.

‡Taken from "Solid Rocket Booster Mass Properties Status Report No. 21," Design Integration Branch, Systems Analysis and Integration Laboratory, NASA/MSFC, Huntsville, Alabama, 15 July 1975.

TABLE 2-2 SPACE SHUTTLE SRM PROPELLANT GAS PROPERTIES*

Chamber Pressure (psia)	Chamber Gas Temperature (°K)	Chamber Gas Density (RHO, g/cc)
5	2911	3.8226-5
50	3154	3.6239-4
100	3226	7.1434-4
150	3267	1.0629-3
200	3295	1.4094-3
250	3317	1.7545-3
300	3334	2.0985-3
350	3349	2.4416-3
400	3361	2.7840-3
450	3372	3.1257-3
500	3382	3.4669-3
550	3390	3.8076-3
600	3398	4.1479-3
650	3405	4.4878-3
700	3411	4.8274-3
750	3417	5.1667-3
800	3423	5.5056-3
850	3428	5.8443-3
900	3433	6.1828-3
950	3437	6.5211-3
1000	3442	6.8591-3
15	3027	1.1170-4
25	3081	1.8399-4

*Table taken from memorandum from J. A. Roach (MSFC/NASA-EL-42, Huntsville, AL) to J. Petes (NSWC/WOL-WR-15, Silver Spring, MD) with subject title: "Closing of Action Items Resulting from NSWC and MSFC Meeting of July 17 1975."

TABLE 2-3 SPACE SHUTTLE SRM TC-273B-75 GRAIN MASS AND BALLISTIC HISTORIES*

Time (sec)	Propellant Weight (lb)	Burning Area (in^2)	Chamber Pressure (psia)	
			Head	Aft End
1	1,108,355	461,336	831.5	759.5
6	1,051,639	477,994	848.2	794.4
12	981,275	487,578	850.1	809.3
18	909,343	495,370	852.4	820.0
24	840,987	469,380	771.9	747.5
30	781,382	440,032	700.5	681.6
36	726,201	419,440	644.7	629.7
42	673,831	400,537	591.4	579.5
48	624,044	385,567	556.9	547.2
54	575,407	382,237	541.7	533.5
60	526,297	390,886	548.1	540.7
66	476,384	396,986	561.1	554.3
72	424,727	409,223	577.6	571.5
78	370,760	421,554	588.4	582.9
84	314,736	424,782	597.6	592.7
90	258,294	432,464	606.2	601.7
96	200,243	440,387	615.3	611.2
102	143,571	425,016	597.9	594.3
108	89,025	408,811	564.5	561.4
110	71,584	400,355	551.6	548.7
112	54,717	386,063	537.1	534.3
114	39,054	383,733	473.0	470.6
116	24,366	333,787	382.8	380.9
118	13,310	262,552	252.7	251.4
120	5,975	186,429	149.0	148.3
122	2,383	69,990	32.9	32.7
124	2,246	9,093	6.7	6.6

*Table taken from memorandum from J. A. Roach (MSFC/NASA-EL-42, Huntsville, AL) to J. Petes (NSWC/WOL-WR-15, Silver Spring, MD) with subject title: "Closing of Action Items Resulting from NSWC and MSFC Meeting of July 17 1975."

TABLE 2-4 CHAMBER PARAMETERS VS. BURN RADIUS

Flight Time (sec)	Burn Radius (in)	Propellant Burn Area (in^2)	Chamber Volume (in^3)
0	30.398	434013.9	4365466.0
1	30.698	461336.0	4365466.0
6	32.605	477994.0	5258631.4
12	34.911	487578.0	6366725.8
18	37.224	495370.0	7499513.2
24	39.503	469380.0	8575985.7
30	41.707	440032.0	9514647.1
36	43.844	419440.0	10383639.2
42	45.919	400537.0	11208363.6
48	47.943	385567.0	11992410.9
54	49.937	382237.0	12758347.9
60	51.926	390886.0	13531733.7
66	53.928	396986.0	14317765.2
72	55.948	409223.0	15131261.3
78	57.986	421554.0	15981135.3
84	60.037	424782.0	16863403.0
90	62.099	432464.0	17752253.4
96	64.171	440387.0	18666442.4
102	66.239	425016.0	19558914.8
108	68.331	408811.0	20417906.9
110	69.019	400355.0	20692568.4
112	69.682	386063.0	20958190.4
114	70.329	383733.0	21204851.8
116	70.939	333787.0	21436158.9
118	71.489	262552.0	21610269.1
120	71.957	186429.0	21725781.0
122	72.312	69990.0	21782347.9
124	72.520	9093.0	21784505.4

The grain burn area is determined according to the breakup model option:

1. If there are no grain cracks or fragments, then the new burn area is interpolated from Table 2-4 corresponding to the appropriate radius determined by the elapsed burning time and burn rate. This area is termed $A_b = (A_b)c$.

2. If the SRB is cut by the LSC, but there are no additional cracks or fragments, then the total burn area is:

$$A_B = (AB)_c + 2L\ (R_o - R_i)\ (in^2)$$

where

L = LSC cut length (in)

R_o = Propellant grain outside radius (in)

R_i = Propellant grain perforation radius (in)

The area contributed by one radial crack through the grain at the clamshell hinge point is included (Fig. 2-3).

3. If the SRB is cut by the LSC and there are additional cracks, then the burn area is:

$$A_B = (AB)_c + 2L\ (R_o - R_i)\ (1 + N)\ (in^2)$$

where

N = Number of cracks in propellant grain

4. If the SRB is cut by the LSC and the propellant is broken into fragments, then the burn area is defined to be the surface area of the fragments, $A_B = (A_B)_F$. The expression for this area is given with the discussion for the fragment size distribution (p. 2-19).

The chamber volume shown in Figure 2-3 is composed of two contributions:

a. The original chamber volume plus the volume added by expending solid propellant. This contribution of volume V_{BURN} is interpolated from Table 2-4 corresponding to the appropriate burn radius.

b. The wedge-shaped volume V_{WEDGE} swept out by the open clamshell.

$$V_{WEDGE} = L\ (R_o + R_i)^2 \sin\left(\frac{\Theta}{2}\right) \cos\left(\frac{\Theta}{2}\right)\ (in^3)$$

The wedge angle, Θ, is defined in Figure 2-3. The total chamber volume is formed by the sum

$$V_c = V_{BURN} + V_{WEDGE}\ (in^3)$$

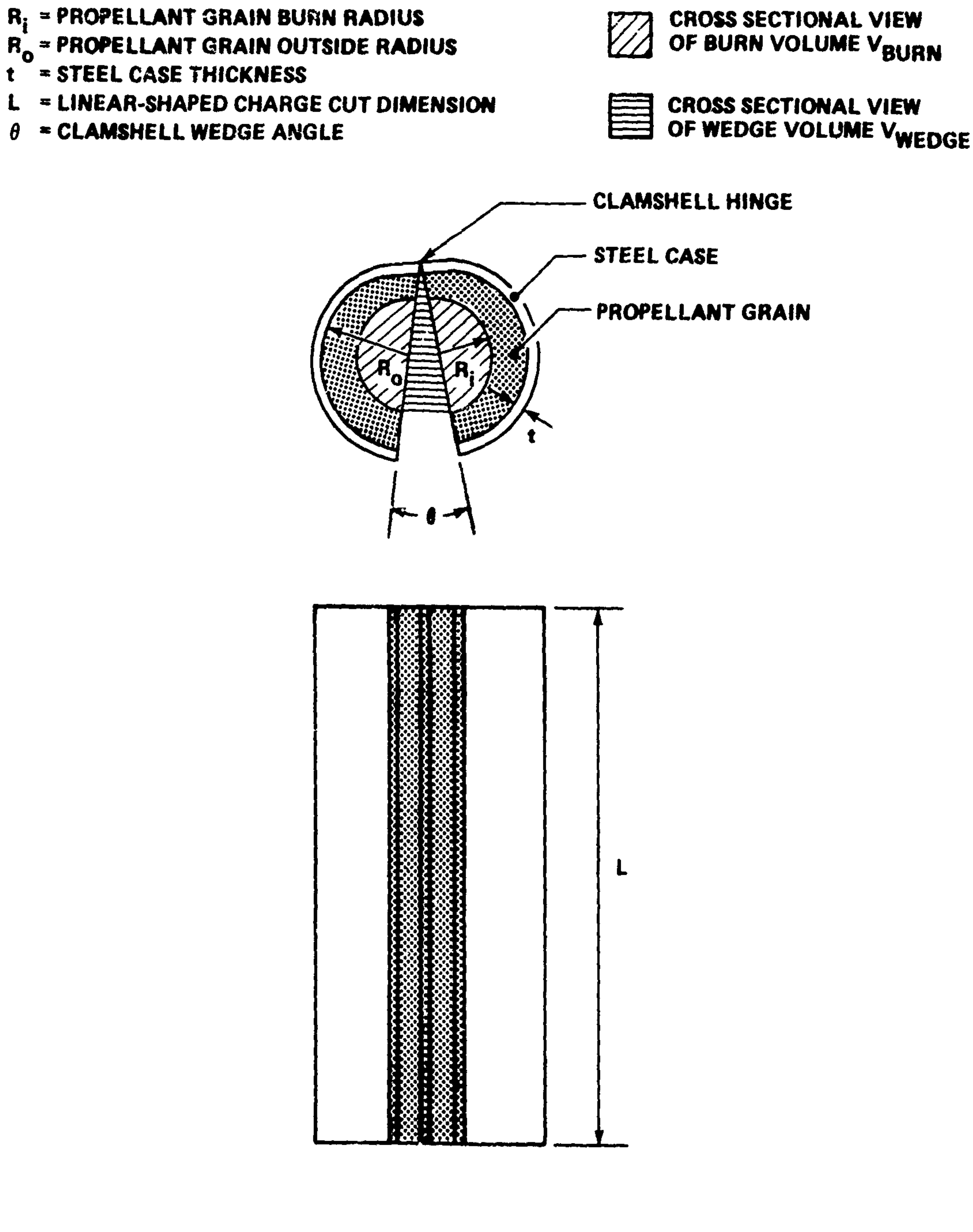

FIGURE 2-3 CLAMSHELL GEOMETRY

The propellant grain burn rate is given by

$$r = a\, p_c^n \text{ (in/sec)}$$

where

$$p_c = \text{chamber pressure (psi)}$$

The burn rate parameters are specified in Table 2-5 along with other SRB propellant properties. The propellant weight burned per unit time is given by

$$\dot{W}_B = A_B r\, \rho_B \text{ (lbf/sec)}$$

where

$$\rho_B = \text{Solid propellant weight density (lbf/in}^3\text{)}$$

The weight of propellant gas in the chamber W_c is determined from a flow balance as follows. Gas is introduced into the chamber from the burning propellant $\dot{W}_B$ and leaves the chamber through the thrust nozzle $\dot{W}_N$ and the LSC cut $\dot{W}_c$. During a time step Δt, the change in weight of the propellant gas in the chamber is

$$\Delta W_c = (\dot{W}_B - \dot{W}_N - \dot{W}_c)\, \Delta t \text{ (lbf)}$$

An expression for nozzle flow rates such as $\dot{W}_N$ and $\dot{W}_c$ is included in the nozzle flow discussion (p. 2-14).

TABLE 2-5 PROPELLANT DATA *

Composition:	Ammonium perchlorate	69.6% by weight
	Aluminum	16.0
	PBAN polymer†	12.04
	Iron oxide catalyst	0.4
	Epoxy curing agent	1.96
Burning Rate:	$r = 0.3663\ (p_c)^{0.35}$ (in/sec) (p_c = chamber pressure in psi)	

*Data taken from notes of phone conversation between D. Lehto (NSWC/WOL-WR-14) and E. Jacobs (MSFC/NASA) on 10 July 1975.

† Polybutadiene acrylonitrile terpolymer

The change in internal energy of the propellant gas in the chamber during time step Δt is obtained employing the same flow balance used above (for weight balance) plus the pV work term.

$$\Delta E = p_c\,(\Delta V_c) + \dot{W}_B\,(\Delta t)\,E_{SOLID} - (\dot{W}_N + \dot{W}_c)\,(\Delta t)\,E_c \quad \text{(in-lbf)}$$

where

ΔV_c = Change in chamber volume during time step (in^3)

E_{SOLID} = Specific internal energy of solid propellant gas (new burn products) (in-lbf/lbf)

ΔE_c = Specific internal energy of chamber gas (in-lbf/lbf)

The propellant gas (properties given in Table 2-2) can be considered a perfect gas to a good approximation, with the molecular weight M_w = 28.38 lbf/mole and the ratio of specific heats $\gamma = 1.2$. With this approximation, the state variables for the propellant gas are given by

$$\rho_c = \frac{W_c}{V_c} \quad (\text{lbf/in}^3)$$

$$p_c = (\gamma - 1)\,\rho_c\,E_c \quad (\text{lbf/in}^2)$$

$$T_c = (\gamma - 1)\,M_w\,E_c/R \quad (^\circ R)$$

where

R = universal gas constant = 18528 (in-lbf/mole °R)

<u>NOZZLE FLOW</u>. Isentropic nozzle flow is assumed for both the motor thrust nozzle and the linear slit produced by the LSC.* The nozzle area ratio (nozzle thrust area A_t to local nozzle area A_x) is a function of the pressure ratio (local pressure p_x to nozzle inlet pressure p_c).

$$\frac{A_t}{A_x} = \left(\frac{\gamma + 1}{2}\right)^{1/(\gamma - 1)} \left(\frac{p_x}{p_c}\right) \left(\frac{\gamma + 1}{\gamma - 1}\right)^{1/2} \left(1 - \left(\frac{p_x}{p_c}\right)^{(\gamma - 1)/\gamma}\right)^{1/2}$$

Two pressure ratios satisfy the above expression per area ratio: the subsonic and supersonic flow solutions. The supersonic solution is of interest here. In the above expression the local area ratio is usually known and the local pressure ratio is computed by an iteration scheme, such as the Newton-Raphson method.

*Effects of burning propellant along the surface of the LSC slit "nozzle" are ignored.

An expression similar in form to that for area ratio is used to determine the velocity ratio as a function of pressure ratio.

$$\frac{v_x}{v_t} = \left(\frac{\gamma + 1}{\gamma - 1}\right)^{1/2} \left(1 - \left(\frac{p_x}{p_c}\right)^{(\gamma - 1)/\gamma}\right)^{1/2}$$

where

v_t = Flow velocity at nozzle throat location (in/sec)

$$= \left(\frac{2\gamma G\ RT_c}{(\gamma + 1)\ M_w}\right)^{1/2}$$

G = Acceleration of gravity = 386.0892 in/sec^2

T_c = Chamber temperature (°R)

The flow rate through a real nozzle can be expressed as

$$\dot{W} = A_t\ P_c\ (G_1/T_c)^{1/2}\ N_d\ \text{(lbf/sec)}$$

with

$$G_1 = (G/R)\ M_w\ \gamma \left(\frac{\gamma}{\gamma + 1}\right)^{(\gamma + 1)/(\gamma - 1)}$$

The discharge correction factor N_d is defined as the ratio of the flow rate through a real nozzle to that through an ideal nozzle. For the LSC cut, no real nozzle corrections are made since the model is very crude (N_d = 1.0 for LSC cut). However, for the thrust motor nozzle the correction factor $N_d = \dot{W}_B/\dot{W}_N$ is used which sets the nozzle flow rate equal to the burn flow rate (normal operation) initially. When the correction parameter is determined in this manner, good chamber pressure/time comparisons are obtained between the calculations made with the model and the data presented in Table 2-3 for normal chamber operations.

To determine the external force on the rocket, whether in the side (LSC cut) or in the forward (motor thrust nozzle) directions, two contributions must be considered.

$$T = \frac{\dot{W}}{G} v_{ex} + (p_{ex} - p_a)\ A_{ex}\ \text{(lbf)}$$

The first term on the right hand side is the momentum thrust which is the product of the nozzle flow rate and the exhaust velocity v_{ex} relative to the vehicle. The second term is the pressure thrust which is the product of the nozzle exit area A_{ex} (assuming no separation between the exhausting flow and the nozzle) and the difference in pressure between exhaust flow p_{ex} and the local atmospheric pressure p_a. The total thrust T is the sum of the momentum and pressure thrusts.

Table 2-1 gives the motor thrust nozzle throat and exit area values. The geometry for the LSC cut configuration is given in Figure 2-3. The expressions for the throat area $(A_t)_{cut}$ and exit area $(A_{ex})_{cut}$ are given below.

$$(A_t)_{cut} = 2L\ (R_o + R_i + t)\ \sin\left(\frac{\Theta}{2}\right)\ (in^2)$$

$$(A_{ex})_{cut} = 4L\ R_o\ \sin\left(\frac{\Theta}{2}\right)\ (in^2)$$

CLAMSHELL MOTION

In this model for SRB breakup, the rocket case begins to open like a clamshell after the segmented cuts created by the LSC have merged into one single longitudinal cut.* The computational model for the clamshell begins at this time (stage 3 of the SRB breakup model outlined in the introduction, p. 2-1).

The force on each half clamshell is given by the product of the projected internal area and the chamber pressure.

$$F = 2\ (R_o + t)\ L\ p_c\ (lbf)$$

The chamber pressure is a sensitive function of the propellant grain burn area which is dependent on the method of rocket breakup (options 1 through 4 contained in the discussion of combustion chamber operation, p. 2-10).

The moment produced by the above force about the clamshell hinge axis determines the angular acceleration of each half clamshell

$$\alpha = F(R_o + t)/I\ (sec^{-2})$$

where t is the metal case thickness (negligible). I is the moment of inertia of the half clamshell which is a composite structure consisting of solid propellant grain and steel case, both of which are in the shape of hollow cylindrical half shells. Liner materials such as inhibitors and insulation are not considered. Using the notation given in Figure 2-4, the moment of inertia is given by

$$I = I_1 + \frac{M_1}{2G}\ (X_1^2 + R^2) + I_2 + \frac{M_2}{2G}\ (X_2^2 + R^2)\ (lbf\text{-}sec^2\text{-}in)$$

*Interaction between the boundary layer flow around the SRB with the clamshell motion is not considered in this model.

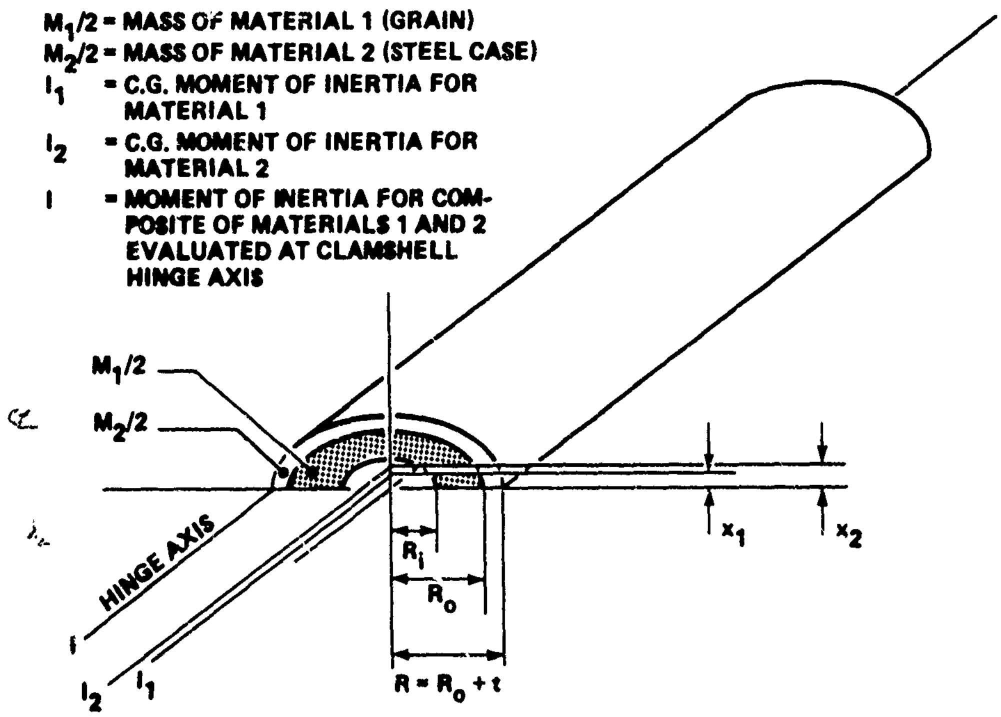

FIGURE 2-4 HALF CLAMSHELL GEOMETRY

with

$$I_1 = \frac{\pi\rho_B L}{8G}(R_o^4 - R_i^4) - \frac{8\rho_B L}{9\pi G}\frac{(R_o^3 - R_i^3)^2}{(R_o^2 - R_i^2)} \quad \text{(in-lbf)}$$

$$I_2 = \frac{\pi\rho_S L}{8G}(R^4 - R_o^4) - \frac{8\rho_S L}{9\pi G}\frac{(R^3 - R_i^3)^2}{(R^2 - R_i^2)} \quad \text{(in-lbf)}$$

$$M_1 = \rho_B\pi\,(R_o^2 - R_i^2)L \quad \text{(lbf)}$$

$$M_2 = \rho_s\pi\,(R^2 - R_o^2)L \quad \text{(lbf)}$$

$$X_1 = \frac{4}{3\pi} \frac{(R_o^3 - R_i^3)}{(R_o^2 - R_i^2)} \qquad \text{(in)}$$

$$X_2 = \frac{4}{3\pi} \frac{(R^3 - R_o^3)}{(R^2 - R_o^2)} \qquad \text{(in)}$$

ρ_B = Solid propellant weight density (lbf/in^3)

ρ_S = Metal case density (lbf/in^3)

For density data refer to Table 2-1. Hudson discusses the area moment of inertia for a hollow half-circle from which I_1 and I_2 were derived.[3] The above properties (subscript 1) which pertain to the propellant grain vary as burning progresses, whereas the properties (subscript 2) which correspond to the steel case remain constant.

The total angular displacement between the two half clamshells is given by

$$\Theta = 2\int_0^t \int_0^t \alpha \, dt \, dt$$

The integral is computed numerically using a quadratic fit for two time steps.

PROPELLANT GRAIN FRAGMENTS

One of the models for SRB breakup, listed as option 4 in the discussion of the combustion chamber operation (p. 2-10), includes the formation of propellant grain fragments. This section presents the method used to evaluate the fragment size distribution and separately to determine the early-time fragment velocity and position versus time history for rocket case rupture.

The case rupture in the fragment motion model is concerned with radially outward motion only, no clamshell motion is considered. Velocity/position results from this model are to be used to assess fragment damage to the ET. These determinations are reported in a separate part of this report. In each of the fragment models, propellant fragmentation is assumed to occur at the time of LSC detonation.

FRAGMENT SIZE DISTRIBUTION. The development of the fragment distribution function is a modification of one used for and checked out against bomb fragmentation distribution.* The modification attempts to account for the differences between the relatively thin case fragmentation of the bomb and the breakup of the thick propellant grain.

[3]Hudson, R.G., The Engineers' Manual (New York: John Wiley & Sons, Inc., 1917).

*Private communication from F. B. Porzel, Naval Surface Weapons Center, White Oak, Maryland.

The distribution function in differential form is

$$\frac{dN_L}{N_L} = -\frac{dL}{L_o}$$

where

L_o = Characteristic fragment dimension

L = Fragment dimension

N_L = Number of fragments with dimension greater than L

Integrating the above expression and defining boundary conditions gives

$$N_L = N_o\, e^{-(L - L_{min})/L_o}$$

where

N_o = Total number of fragments

L_{min} = Minimum fragment dimension, $N_L = N_o$ for $L = L_{min}$

To determine N_o and L_o for a specific propellant grain geometry, the following assumptions are made:

1. There is a maximum fragment dimension L_{MAX} determined by the geometry of the propellant grain. This dimension is taken to be $L_{MAX} = R_o - R_i$, the thickness of the hollow cylindrical propellant grain.

2. At $L = L_{MAX}$ set $N_L = N_{LMAX} = 1$. This assumes there is only one largest fragment. The relation $Ln\ (N_o) = L_{MAX}/L_o$ follows from this assumption.

3. Set $L_{MIN} = 0$ to simplify the evaluation of the boundary conditions. After N_o and L_o are determined, L_{MIN} can be calculated and then retained in the distribution function.

4. Grain fragment volume and surface area are given by $V_F = L^3$ and $A_F = 6L^2$, respectively. The fragments are assumed to be shaped like cubes.

With these assumptions, the expressions for total fragment weight and surface area become

$$(W_B)_F = \int_0^{N_o} \rho_B \, V_F \, dN_L$$

$$= \rho_B \, N_o L_o^3 \, e^{L_{MIN}/L_o} \left[({}^L/Lo)^3 + 3\,({}^L/Lo)^2 + 6\,({}^L/Lo) + 6 \right] e^{-L/Lo} \Bigg|_{L_{MAX}}^{L} \quad \text{(lbf)}$$

$$(A_B)_F = \int_0^{N_o} A_F \, dN_L$$

$$= 6N_o L_o^2 \, e^{L_{MIN}/L_o} \left[({}^L/Lo)^2 + 2\,({}^L/Lo) + 2 \right] e^{-L/Lo} \Bigg|_{L_{MAX}}^{L} \quad (\text{in}^2)$$

where

$$e^{L_{MIN}/L_o} \equiv 1 \text{ by assumption.}$$

The equation for $(W_B)_F$ must satisfy mass conservation. $(W_B)_F$ equals the total weight of the solid propellant at the specific flight time. The unknowns in the equation are N_o and L_o which are related in the manner specified by Assumption 2 above. The expression for mass conservation may be transformed to produce the equation

$$f(Z) = \frac{(W_B)_F}{\rho_B \, L_{MAX}^3} - \frac{e^y}{y^3} \left[6 - (y^3 + 3y^2 + 6y + 6) \, e^{-y} \right] = 0$$

where

$$Z = L_{MAX}/L_o.$$

This expression can be solved (to determine L_o and then N_o) by iteration, using a method such as that of Newton-Raphson. An estimate of $L_{MIN} \doteq L'$ is obtained by evaluating $(N_o - 1) = N_o \exp(-L'/L_o)$.

<u>FRAGMENT MOTION</u>. The fragment motion model was developed in an internal memorandum. Lorenz compared computational and experimental results and used the model to predict fragment velocity/position histories for a series of high pressure tank rupture experiments.[4] The velocity predictions were found to be on the order of 40 percent below experimental values for cylindrical tank ruptures.

---

[4] Pittman, J.F., "Blast and Fragment Hazards from Bursting High Pressure Tanks," Naval Ordnance Laboratory, NOLTR 72-102, Appendix B, Lorenz R. A., "A Short Computer Code to Estimate the Early-Time Fragment Velocity and Position vs Time for a High Pressure Spherical or Cylind.ical Tank Rupture, 17 May 1972.

A detailed description of the fragment motion model is not presented here; only a brief outline of the important assumptions will be discussed. Modifications to the original model to include propellant burning and thrust nozzle outflow are also listed.

The original model considers the following factors most important in determining fragment motion:

1. Driving pressure immediately behind each fragment.

2. Jetting of compressed gas between the fragments which results in reduced driving pressure.

3. Accumulation of compressed gas ahead of the fragments and in the jets which absorb energy and tend to slow fragments down.

The following simplifying assumptions are made in constructing the model:

1. Constant total projected fragment area for pressure loading.

2. Fragment volume neglected.

3. Fragment tumbling forbidden.

4. Fragment aerodynamic drag loads neglected.

5. Compressed gas is uniform (pressure, internal energy, and density) throughout gas volume at each instant.

6. Tank and ambient gas satisfy one caloric equation of state.

7. Cylindrical end effects are not included.

Two pie-shaped flow regions (cylindrical geometry) are defined, one containing driving gas subtended by the fragment projected area, and the other filled with jetting gas (Fig. 2-5, taken from footnote 4). As fragment motion progresses, a larger fraction of the total solid angle becomes available for jetting since the total projected fragment area is held constant. System motion is constrained to radially outward flow with three separate velocities considered: fragment velocity, fragment region outer boundary, and jetting region outer boundary. The mass of ambient air swept into the flow as the boundaries move outward is added to the system.

Modifications to the original model for the present analysis include:

1. Production and loss of chamber gas mass and internal energy from propellant burning and thrust nozzle flow.

2. Separate caloric equations of state for chamber gas and ambient air.

These modifications correspond to the analysis discussed earlier in the sections on combustion chamber operation (p.2-5) and nozzle flow (p. 2-13).

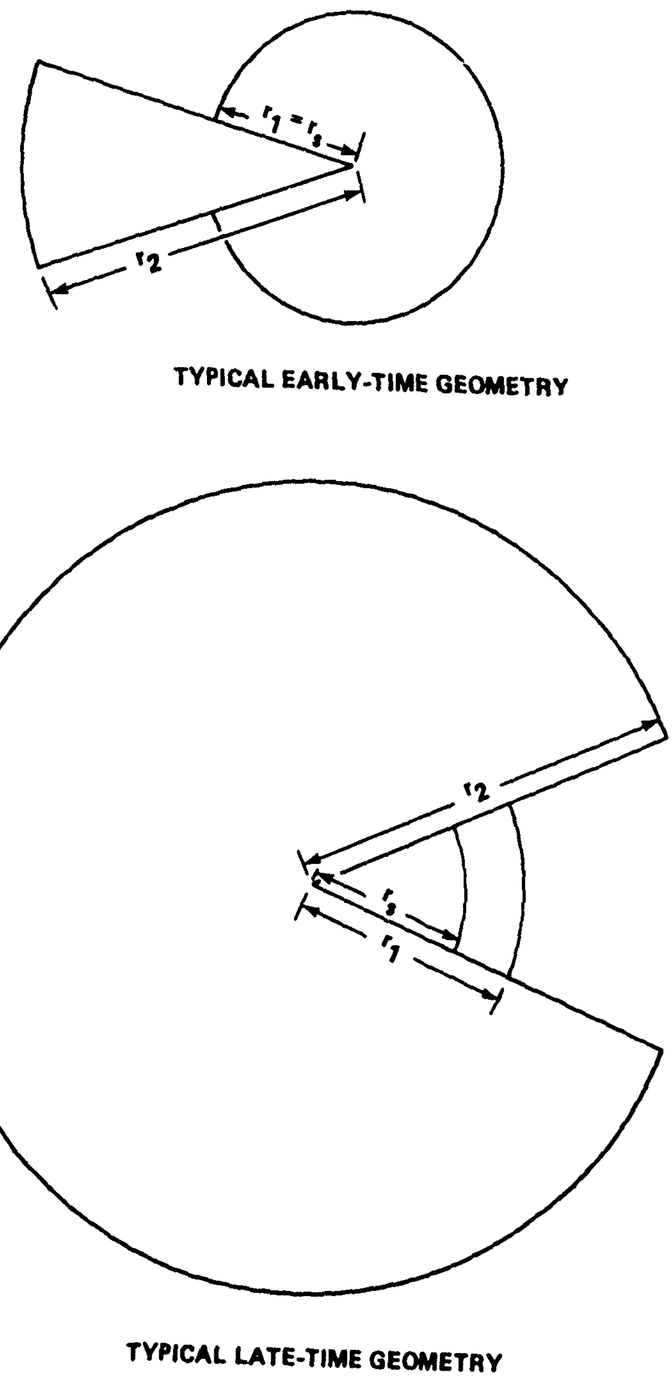

r_s = RADIUS OF TANK FRAGMENTS
r_1 = RADIUS OF COMPRESSED GAS AHEAD OF FRAGMENTS
r_2 = RADIUS OF JETTING GAS

FIGURE 2-5 FRAGMENT MOTION GEOMETRY

RESULTS

ROCKET MODEL. Pressure-time histories for normal chamber operations calculated by the present model are given in Figure 2-6. The average of the head and aft chamber pressures was used as the initial pressure for each calculation. Initial conditions for four flight times (1, 10, 50, and 100 seconds) are given in Table 2-6. The discharge correction factor N_d given in Table 2-6 was determined by setting the nozzle flow rates equal to the normal operating propellant burn (gas generation) rates initially. The rates do not remain equal as the calculation progresses. The shape of the computed pressure-time history is very sensitive to this parameter. Determining the correction factor in this manner provides a fairly good fit, as shown in Figure 2-6, between model calculations (the dashed curves) and the computed data taken from Table 2-3. Agreement is not as good at the two early flight times, t = 1 and t = 10 sec, after about three seconds; better agreement for time durations longer than three seconds at these two flight times can be obtained by varying the discharge coefficient. However, this was not done. In order to simplify the analysis, only one method was used for calculating the discharge coefficient for the entire flight time range.

The time of interest during destruct is on the order of milliseconds (~40 milliseconds; by this time the side thrust has already peaked and the decay rate is defined. See Figs. 2-7 through 2-10). Figure 2-7, case (c), indicates that the chamber pressure is essentially constant under normal operating conditions for a time scale of such short duration. The results displayed in Figures 2-6 and 2-7 show that the rocket model developed is adequate to represent the computed SRB flight condition. Additional initial conditions (or normal operating conditions) for the rocket model at the four flight times of interest are given in Table 2-7.

CLAMSHELL MODEL. Results for the clamshell model for flight times equal to 1, 10, 50, and 100 seconds are presented in Figures 2-7 through 2-10, respectively. Two solutions for chamber pressure, angular displacement, forward thrust, and lateral thrust as functions of time (given in milliseconds) following the detonation of the LSC are displayed.* One solution (a) does not include any effects from formation of propellant cracks or fragments, whereas the other solution (b) considers complete grain fragmentation. The two solutions represent bounds for the clamshell model calculations. The real situation is closer to case (a) than to case (b). In an actual destruct, there will be some propellant cracks and fragments formed at the time of LSC detonation followed by a period of crack propagation and increased fragmentation. Case (b) represents an upper bound (a high one) for this process in which complete fragmentation of the propellant grain is assumed to occur simultaneously with LSC detonation.

Significant trends exhibited by the results presented in Figures 2-7 through 2-10 are discussed on the following pages.

*Figure 2-7 also includes the solution for normal operation, case (c) given in the graphs for chamber pressure and forward thrust. There is no clamshell angular acceleration or lateral thrust for normal operation.

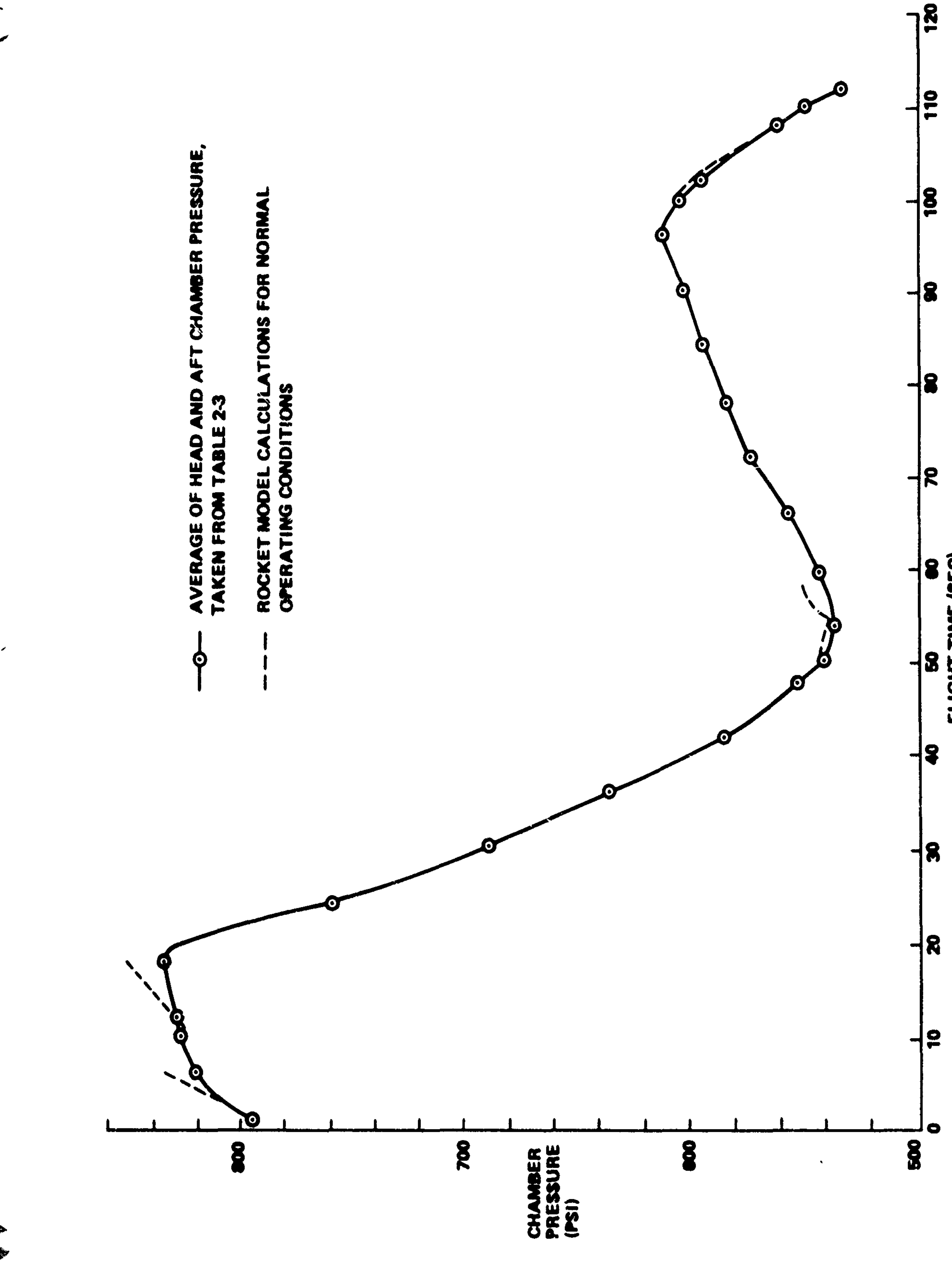

FIGURE 2-6 CHAMBER PRESSURE FLIGHT TIME HISTORY

TABLE 2-6 INITIAL CONDITIONS

Flight Time (sec)	Chamber Pressure (psi)	Chamber Temperature (°R)	Chamber Gas Density (lbf/in^3)	Grain Burn Radius (in)	Atmospheric Pressure (psi)	Discharge Correction Factor
1.0	795.5	6161	1.978E-4	30.698	14.7	0.945
10.0	827.4	6166	2.056E-4	34.138	14.22	0.967
50.0	542.4	6100	1.357E-4	48.608	5.086	1.0052
100.0	605.6	6118	1.512E-4	65.548	0.1876	1.0483

Chamber Pressure. The chamber venting shown in Figures 2-7 through 2-10 chamber pressure, case (a), is very similar for three of the four flight times considered: 1, 10, and 100 seconds. The chamber pressure decays at a comparatively slower rate if flight time equals 50 seconds. Actually, however, there is a dependence of the pressure decay rate on the initial chamber operating pressure. For flight times 1, 10, and 50 seconds, the amount of initial pressure is directly related to pressure decay, i.e., the lower the initial pressure, the less rapid the pressure decay. Pressure decay for flight time equals 100 seconds does not follow this trend; the decay rate at this flight time (initial pressure p_c = 605.6 psi) is even somewhat faster than if flight time equals 10 seconds (initial pressure p_c = 827.4 psi).

Folded into the dependence of the pressure decay on the magnitude of the initial pressure is the effect of the faster clamshell opening rate for later flight times. (See clamshell angular displacement profiles in Figs. 2-7 through 2-10). If flight time equals 100 seconds, the mass of propellant remaining onboard has been reduced to about 25 percent of the propellant mass onboard at 10 seconds = flight time. For this initial flight condition (flight time equal to 100 seconds), the clamshell opens quite rapidly (compared to the other three flight conditions) after being cut by the LSC. This produces a pressure decay rate characteristic of a higher initial chamber pressure with a more massive clamshell (such as flight times equal to 1 and 10 seconds).

Chamber venting calculations have been made with this model for a different solid rocket motor configuration. The chamber venting results have been compared with experimental data. The motor is described in Table 2-8. The unclassified experimental data were obtained from a test series with small plugged motors. The rocket model was modified in the following manner to simulate the small plugged motor test.

1. The plugged motor characteristics given in Table 2-8 were incorporated into the rocket model; however, the SRB propellant properties were used.

2. The mass flow through the thrust nozzle was set to zero by using N_d = 0.0.

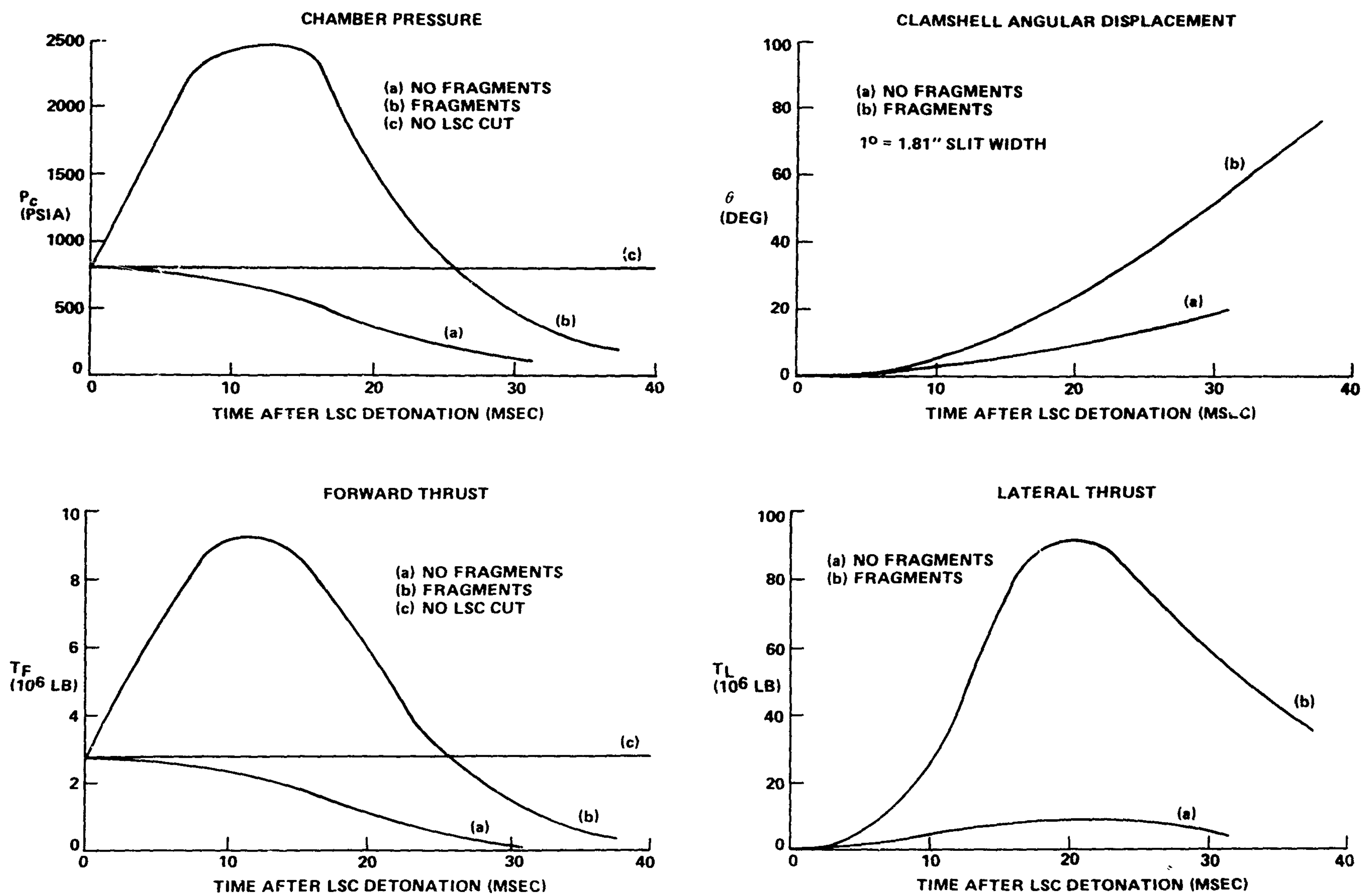

FIGURE 2-7 CLAMSHELL RESULTS FOR FLIGHT TIME = 1 SECOND

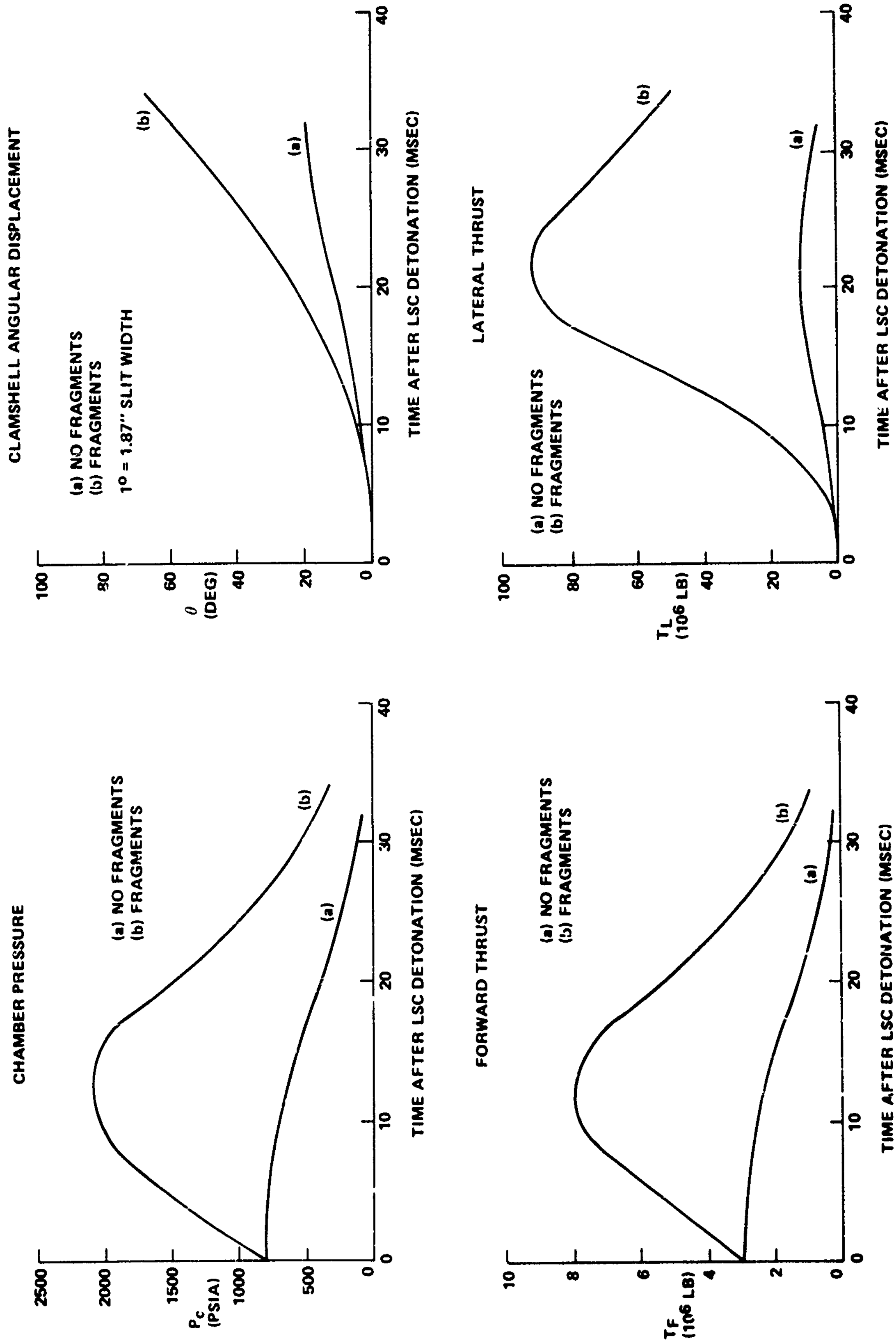

FIGURE 2-8 CLAMSHELL RESULTS FOR FLIGHT TIME = 10 SECONDS

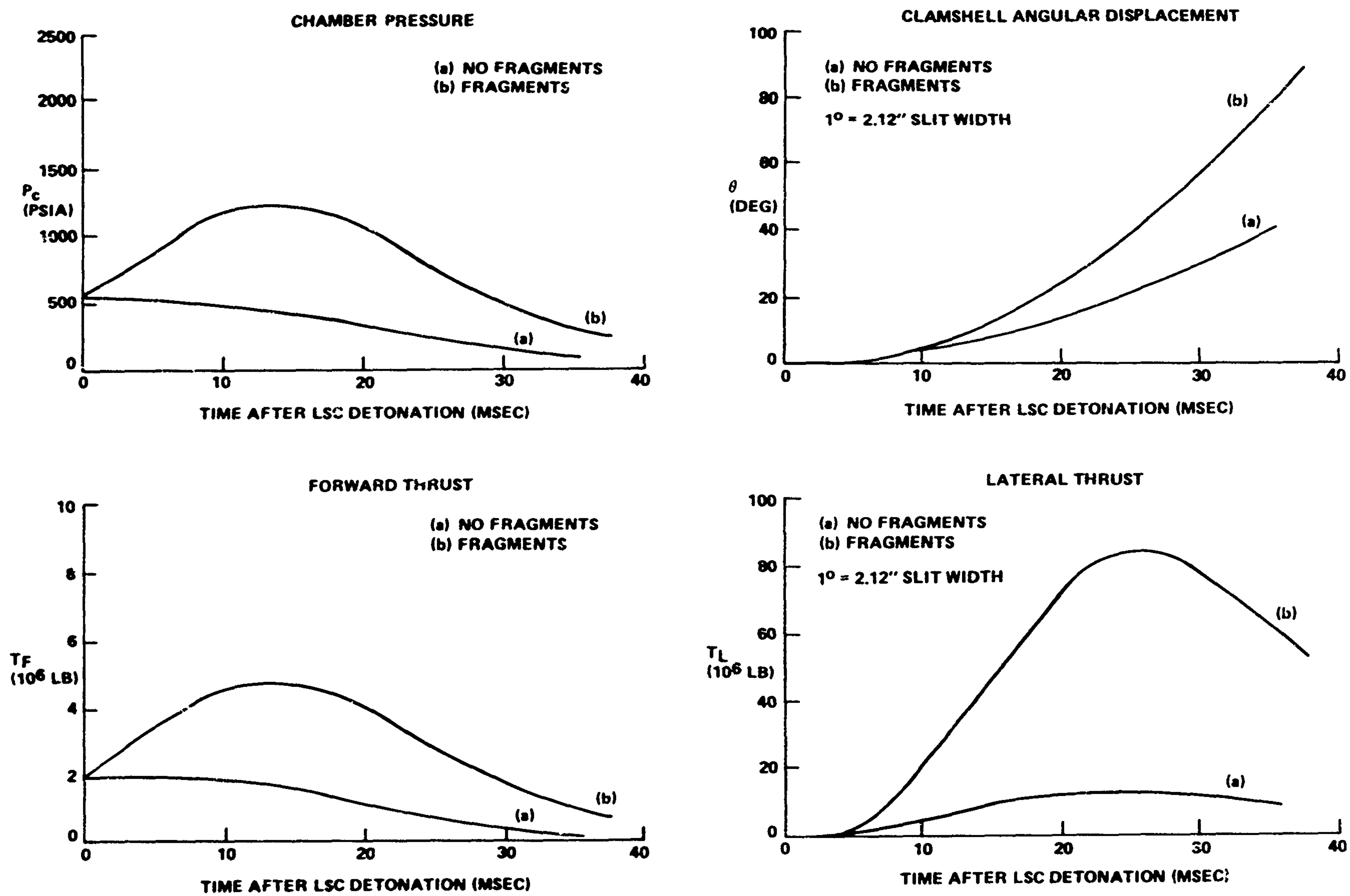

FIGURE 2-9 CLAMSHELL RESULTS FOR FLIGHT TIME = 50 SECONDS

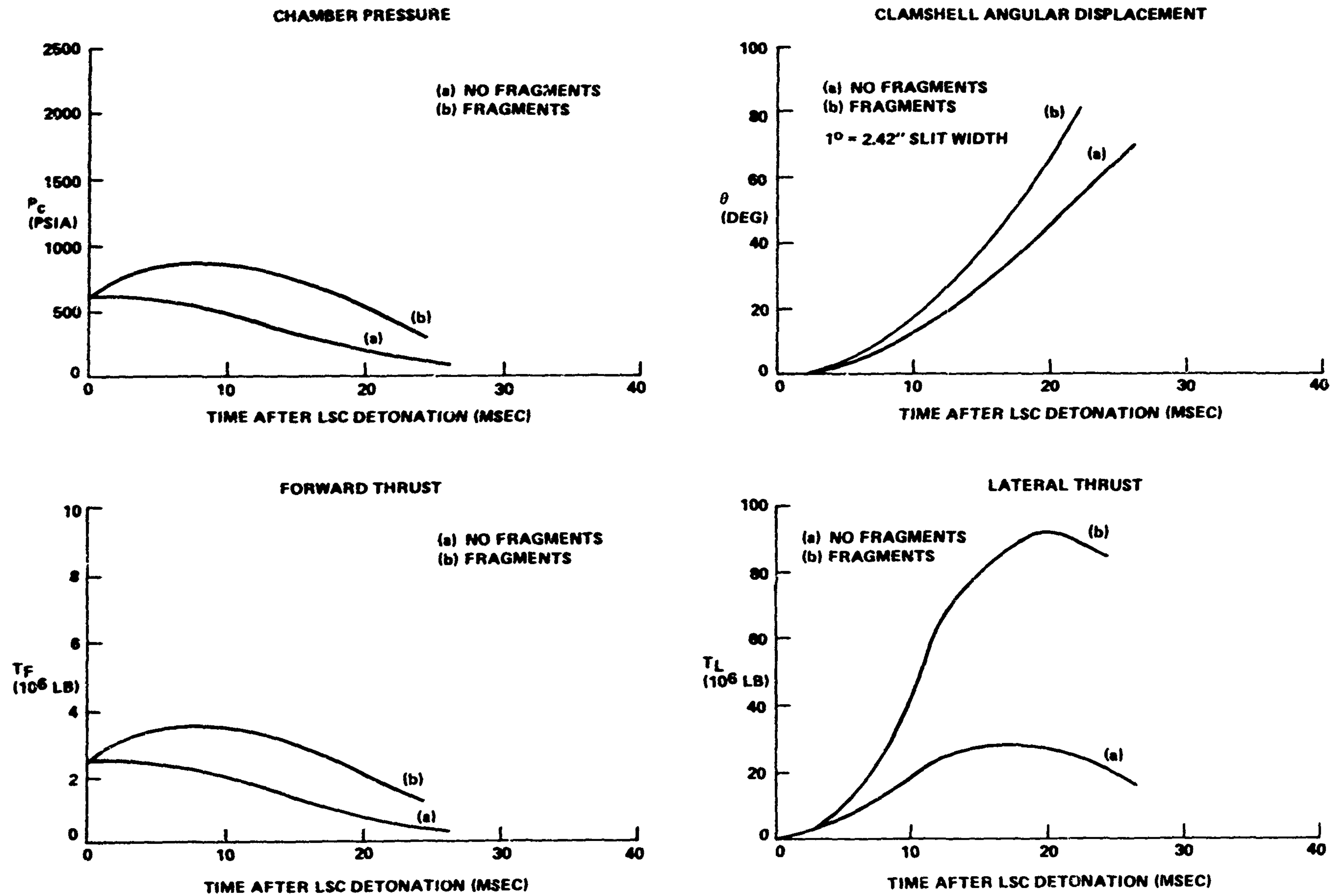

FIGURE 2-10 CLAMSHELL RESULTS FOR FLIGHT TIME = 100 SECONDS

TABLE 2-7 ROCKET OPERATING CONDITIONS

Flight Time (sec)	Nozzle Thrust (lbf)	Nozzle Thrust (Momentum) (lbf)	Nozzle Thrust (Pressure) (lbf)	Nozzle Exhaust Pressure (psia)	Nozzle Exhaust Velocity (ft/sec)	Vehicle Total Weight (lbf)	Half Clamshell Propellant Weight (lbf)	Chamber Volume (in^3)	Initial Burn Area (in^2)
1.0	2.740E6	2.725E6	0.0145E6	15.57	7889	1.283E6	0.4446E6	4.365E6	0.4613E6
10.0	2.933E6	2.900E6	0.0329E6	16.20	7892	1.179E6	0.4216E6	5.997E6	0.5636E6
50.0	2.069E6	1.976E6	0.0922E6	10.62	7849	0.7826E6	0.2983E6	12.25E6	0.3845E6
100.0	2.496E6	2.301E6	0.1944E6	11.85	7861	0.3372E6	0.0992E6	19.26E6	0.4301E6

TABLE 2-8 SMALL PLUGGED MOTOR PARAMETERS

Initial propellant grain burn area (in^2)	184.0
Initial chamber volume (in^3)*	227.0
Nozzle discharge correction factor†	0.0
Initial burn radius	1.5
Solid propellant grain length (in)	19.5
Linear-shaped charge length (in)‡	11.5
Rocket case inside radius (in)	5.0
Rocket case outside radius (in)	5.09375
Rocket case density (lbf/in^3)	0.0903
Propellant grain weight density (lbf/in^3)	0.0969
Internal energy of gas products from burning propellant grain (cal/gm)	1200.0
Ratio of specific heats for chamber gas	1.2
Molecular weight (lbf/lbf-mole)	28.38
Propellant burning rate (in/sec) (p_c = chamber pressure in psi)	$0.3663\ (p_c)^{0.35}$
Initial chamber pressure (psi)	400.0
Chamber pressure at rupture (psi)	3140.0
Atmospheric pressure (psi)	14.7

*Chamber volume includes volume of a 16 inch (1.5 inch ID) pipe extension.

†N_d = 0.0 sets the nozzle flow to zero (plugged motor).

‡The LSC cut was set equal to the length of the thinnest section of the plugged motor case.

3. Initial chamber conditions for the confined propellant burn correspond to 400 psi (see Table 2-2) because a rapid rise in chamber pressure prior to rupture began around 400 psi for the plugged motor tests.

4. Clamshell motion was initiated after the chamber pressure built up to 3140 psi because the plugged motor ruptured at this pressure.

This auxiliary calculation was performed in order to compare the pressure decay time computed by the clamshell model with experimental venting time for the plugged motor chamber rupture. The plugged motor pressure dropped from the rupture pressure (3140 psi) to atmospheric pressure in ~2 msec, whereas the clamshell model predicted that the venting time was ~3 msec. The breakup mode for the plugged motor was not a clamshell as considered in the rocket model developed here (the plugged motor appeared to rupture uniformly around the periphery); however, the experimental and analytical venting times are comparable. The clamshell model does appear to predict reasonable venting time for chamber rupture.

The following trends are observed for the chamber pressure profiles in Figures 2-7 through 2-10 for case (b):

1. The peak values decrease as flight time increases.

2. The delay for attainment of peak values increases as flight time increases for calculations 1, 10, and 50 seconds. This trend reverses for flight time equals 100 seconds. In that case, the chamber pressure peak occurs even before that for the 1-second flight time. These trends are produced primarily by the competing processes listed below.

a. The clamshell mass decreases as flight time increases.

b. The normal operating chamber pressure varies, as shown in Figure 2-6.

c. For normal operation, the burn area variation with flight time is very similar to the chamber pressure profile (Fig. 2-6). This is not true for case (b) which includes complete grain fragmentation. For case (b), as the flight time increases the characteristic dimension for the grain fragments formed decreases in magnitude since it is controlled by the thickness of the remaining solid propellant grain which also decreases. The net effect of having a smaller characteristic fragment size, even for less available propellant to form fragments, is to have increasing burn area for flight times 1, 10, 50, and 100 seconds (see "Size Distribution," p. 2-32).

Clamshell Angular Displacement. The corresponding profiles for (a) and (b) are essentially the same for 1- and 10-second flight times, although the angular displacement rate is slightly higher for the 10-second case.* The increase in angular displacement rate with increase in flight time is more evident for results at 50- and 100-second flight times.

*There is an increase in magnitude of conversion factors between angular and linear dimensions for the four flight times displayed in Figures 2-7 through 2-10.

As flight time progresses, there is less unburned solid propellant grain onboard. Therefore, even if the chamber pressure were constant throughout the flight (which it is not, as shown in Fig. 2-6), the half clamshells would experience higher acceleration at later flight times for the same pressure loading because of the reduced half clamshell mass. The reduction in propellant mass along with the change in chamber pressure conditions produces the trend described above for the angular displacement of the clamshell. The variation of chamber pressure has less of an effect on the angular displacement behavior than the variation in the solid propellant mass because the grain mass varies dramatically during the flight, whereas the variation of the chamber pressure is much smaller (Tables 2-6 and 2-7). The clamshell opens at a considerably faster rate for 100-second flight time (Fig. 2-10). The solid propellant is almost depleted by this time.

Forward Thrust. All of the total forward thrust profiles follow very closely the corresponding profiles for chamber pressure. All profile maximums for forward thrust occur at the same time as do the corresponding chamber pressure profile peaks. The forward thrust dependence on chamber pressure is quite evident. The forward thrust can increase threefold over normal operation for peak values because of the increased chamber pressure, case (b).

Lateral Thrust. The lateral thrust profiles for both cases (a) and (b) follow the same trends exhibited by the chamber pressure profiles for case (b). The peaks for lateral thrust for both cases (a) and (b) lag the corresponding chamber pressure peaks, case (b), by approximately 8 msec.

The lateral thrust peaks later than the forward thrust, because the clamshell continues to open wider beyond the point where the chamber pressure and the forward thrust have peaked. The peak does occur, however, when the effect of the chamber pressure decay on the lateral thrust overtakes that for the clamshell opening. The peak values for lateral thrust, case (b), attain extremely high values because of the large "nozzle" area obtained with the LSC slit and the increased chamber pressures.

FRAGMENT MODELS The fragment models have been divided into size distribution and fragment velocity which are described in detail in the following paragraphs.

Size Distribution. Table 2-9 presents the fragment size distribution parameters determined for the four flight times. Figure 2-11 indicates the distribution profiles. Each point in the flight has a different fragment size distribution function determined by the geometry of the solid propellant remaining onboard. There are several methods of establishing the boundary conditions for the function, in order to determine the distribution parameters. The method used in this analysis and discussed earlier (p. 2-17) depends on the assumption that there is only one largest fragment.

TABLE 2-9 FRAGMENT DISTRIBUTION PARAMETERS

Flight Time (sec)	Total Number of Fragments N_o	Minimum Fragment Dimension L_{MIN} (in)	Maximum Fragment Dimension L_{MAX} (in)	Characteristic Fragment Dimension L_o (in)	Largest Fragment Weight (lbf)	Characteristic Fragment Weight (lbf)	Fragment Burn Area $(A_B)_F$ (in^2)
1	50,952	0.3794E-4	41.82	3.859	4640.0	3.65	9.091E6
10	63,503	0.3846E-4	38.38	3.471	3590.0	2.66	9.169E6
50	217,171	0.3318E-4	23.91	1.946	868.0	0.47	9.864E6
100	4,539,277	0.3448E-4	6.972	0.4548	21.5	0.006	11.27E6

$N_L = N_o e^{-(L - L_{MIN})/L_o}$ = Number of fragments with dimension greater than or equal to L

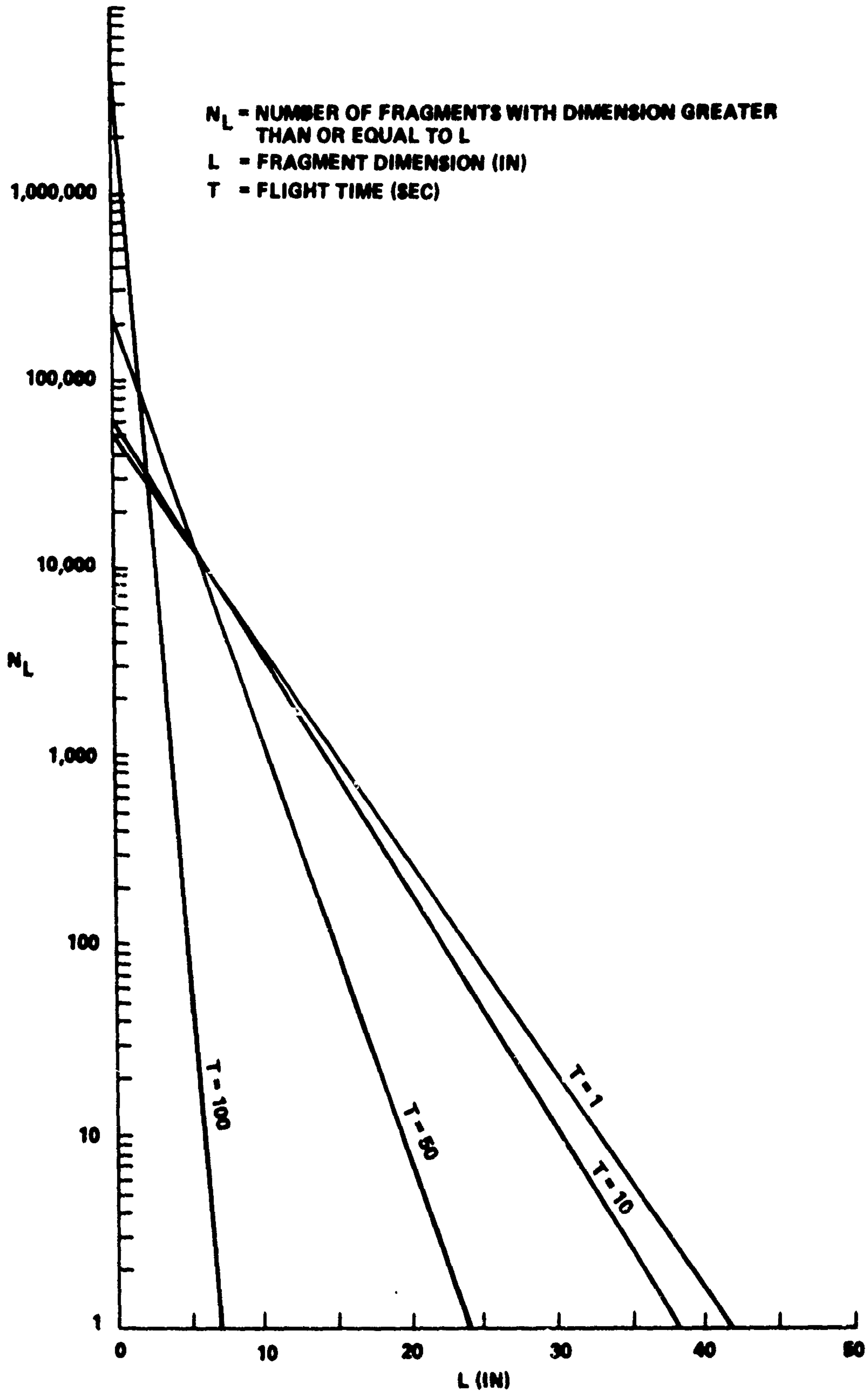

FIGURE 2-11 FRAGMENT SIZE DISTRIBUTION FUNCTION FOR PROPELLANT

The amount of solid propellant onboard the rocket decreases for increasing flight time. The grain has the geometry of a hollow cylinder (neglecting the star-shaped head); therefore, as the propellant is depleted, the thickness of the hollow cylinder decreases. The decrease in grain shell thickness with flight time produces the same trend with the maximum fragment size L_{MAX} (which in this model is assumed to be equal to the shell thickness) and the characteristic fragment dimension L_0. The total number of propellant fragments and the burn surface area increases with flight time, despite less available propellant, because the characteristic fragment size decreases with flight time. These trends are indicated in Table 2-9 and Figure 2-11.

Fragment Velocity. Four fragment velocity/position profiles are given in Figure 2-12. Each calculation is terminated when the driving pressure decays to the local atmospheric pressure. At this point in the fragment trajectory all fragment driving forces have ceased. The final fragment velocity attained is considered to be the fragment impact velocity at the ET location. The initial and final conditions are listed in Table 2-10.

The final velocities indicated are low estimates. A comparison between the original fragment motion model results and experimental data for cylindrical tank rupture indicates that the theoretical predictions are on the order of 40 percent lower than the experimental values (see footnote 4.)

The fragment velocity at the surface of the ET, where the damage is to be assessed in another part of this final report (p. 4-48), is assumed to be equal to the final velocity indicated by Figure 2-11 and listed in Table 2-10. The final fragment velocity does not consider the effect of aerodynamic drag loads since the model does predict lower than expected velocities. The fragment velocities are low, and the fragment traverse distance to the ET surface is short.

The final fragment velocity increases as flight time increases because (1) the total mass of the fragments decreases, (2) the total mass of the compressed gas increases,* (3) the duration of the action of the driving force (chamber overpressure) increases, and (4) the magnitude of the local atmospheric pressure decreases.

AIRBLAST MODEL

The SRB is a long cylinder whose distance from the cylindrical ET is small compared to the length of either. Therefore, we may assume in calculating the blast that both are of infinite length. We further assume that the SRB steel case and propellant are not there, i.e., they are fragmented to such an extent that the chamber gases escape easily in all directions. We take the high-pressure chamber as an infinite cylinder of gas initially at rest at the normal operating conditions. We neglect the chamber pressure boost due to grain breakup. The relatively small amount of energy lost from the shockwave to fragment acceleration should be more than compensated by the extra energy added from the new burn area opened up during fragmentation.

---

*For the four flight times of interest, the initial chamber pressure only varies from 800 to 600 psi (for increasing flight time). However, the chamber volume increases by a factor of 4.

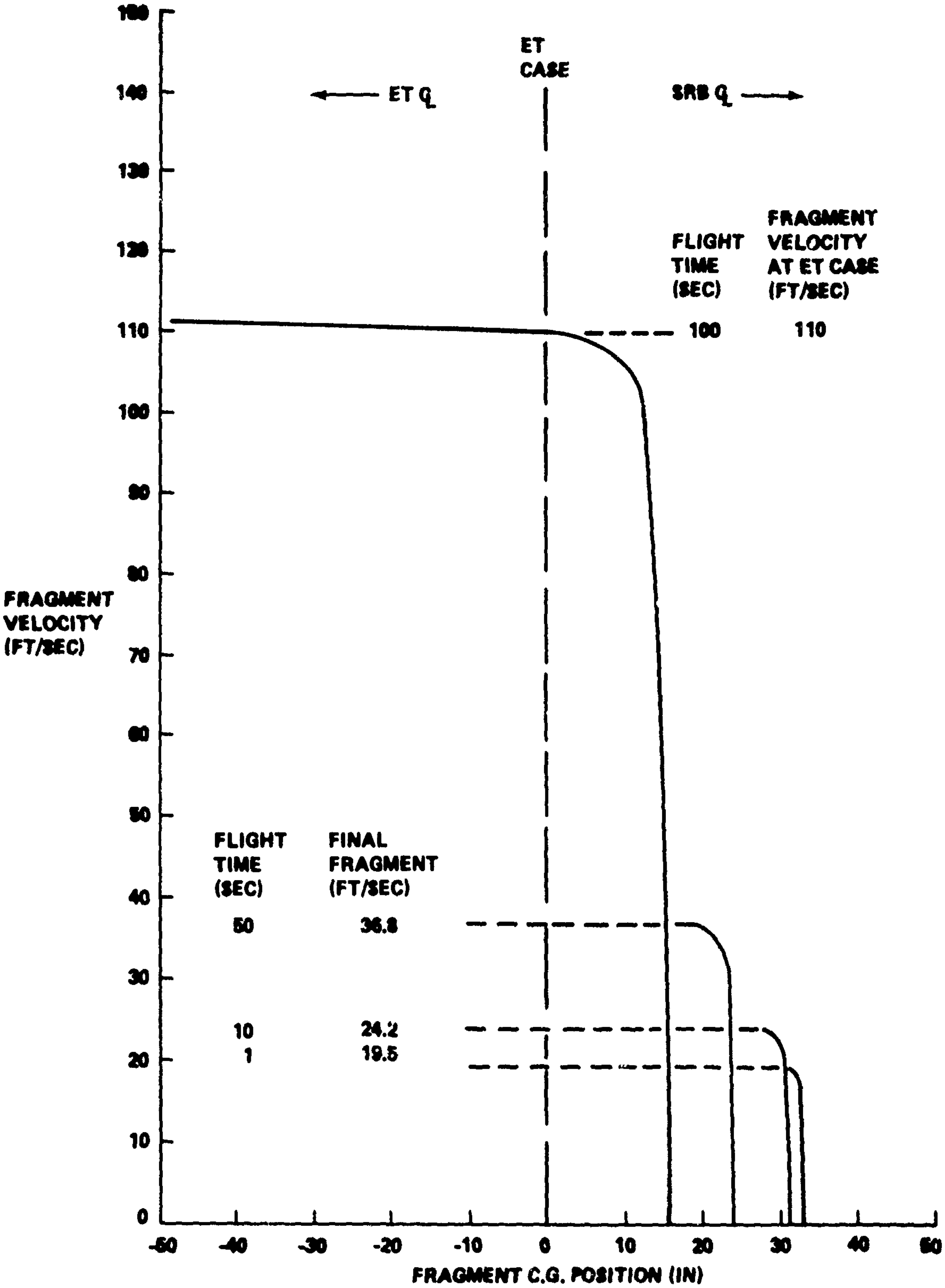

FIGURE 2-12 PROPELLANT FRAGMENT VELOCITY VS. POSITION

TABLE 2-10 FRAGMENT MOTION RESULTS

Flight Times (sec)	1	10	50	100
Initial Chamber Pressure (psi)	795.5	827.4	542.4	605.5
Final Chamber Pressure (psi)* (Local Atmospheric Pressure)	14.70	14.22	5.09	0.19
Initial Distance between Fragment C.G. and ET Case (in)†	33.15	31.45	24.2	15.73
Final Distance between Fragment C.G. and ET Case (in)*†	30.40	27.88	16.2	-47.77§
Fragment ET Impact Velocity (ft/sec)‡	19.5	24.2	36.8	110.0‖

*Final values occur at termination of the driving force. The chamber pressure has reached local atmospheric pressure.

†Fragment Center of Gravity (C.G.) is the half-thickness location for the propellant grain.

‡Fragment ET impact velocity is equal to the final fragment velocity indicated in Figure 2-11.

§Negative distance indicates that the fragments are beyond the ET case location.

‖Fragment C.G. velocity at ET case location.

In assuming that the chamber is a cylinder, we neglect the effect of the grain star and of the small gaps between the casting sections. The star is at the end and will not influence the flow at the ET during the times of interest. The gaps contain very little energy.

The chamber and ambient conditions for the times of interest are listed in Table 2-11. The equivalent TNT energies are only presented to give a rough idea of the blast energy available from the chamber. These TNT values are not used anywhere in this work and are not intended for predicting blast effects.

The model problem is the formation of a shockwave from the infinite SRB chamber cylinder and the diffraction of this wave over the ET cylinder. First, the free-air cylindrical shockwave with the WUNDY one-dimensional hydrocode was generated.[5] Figure 2-13 shows the results. The T = 1 second case was not calculated because the results were expected to lie just below the T = 10 curve. The T = 10 and T = 100 cases were selected for complete ET loading calculations because they bound all other T values of interest. Partial results will be given for T = 50. The decay rate of the reflected shock is assumed to be the same as for the free-air shock (Figs. 2-14 and 2-15).

[5] Lehto, D. and Lutzky, M., "One-Dimensional Hydrodynamic Code for Nuclear-Explosion Calculations," Naval Ordnance Laboratory, NOLTR 62-168, DASA-1518, AD-615801, Mar 1965.

TABLE 2-11 CHAMBER AND AMBIENT CONDITIONS AT VARIOUS TIMES

Time (sec)	1	10	50	100
Chamber Conditions				
Radius (in)	30.70	34.14	48.61	65.55
Radius (m)	0.780	0.867	1.235	1.665
Pressure (psia)	795.5	827.4	542.4	605.6
Pressure (bar)	54.8	57.0	37.9	41.4
Density (g/cc)	5.472-3	5.689-3	3.808-3	4.148-3
Temp (k)	3423.0	3425.0	3390.0	3398.0
Sound Speed (km/s)	1.096	1.097	1.093	1.094
TNT Energy (lb)	490.0	700.0	1040.0	2490.0
Ambient Conditions				
Altitude (ft)	0.0	904.0	26624.0	96721.0
Pressure (psia)	14.70	14.22	5.086	0.1876
Pressure (bar)	1.013	0.9804	0.3507	0.0129
Density (g/cc)	1.225-3	1.193-3	5.188-4	1.994-5
Temp (c)	15.0	13.2	-37.7	-47.1
Sound Speed (km/s)	0.3403	0.3391	0.3076	0.3012
	gamma	mol wt		
Propellant Gas	1.200	28.38		
Air	1.400	28.96		

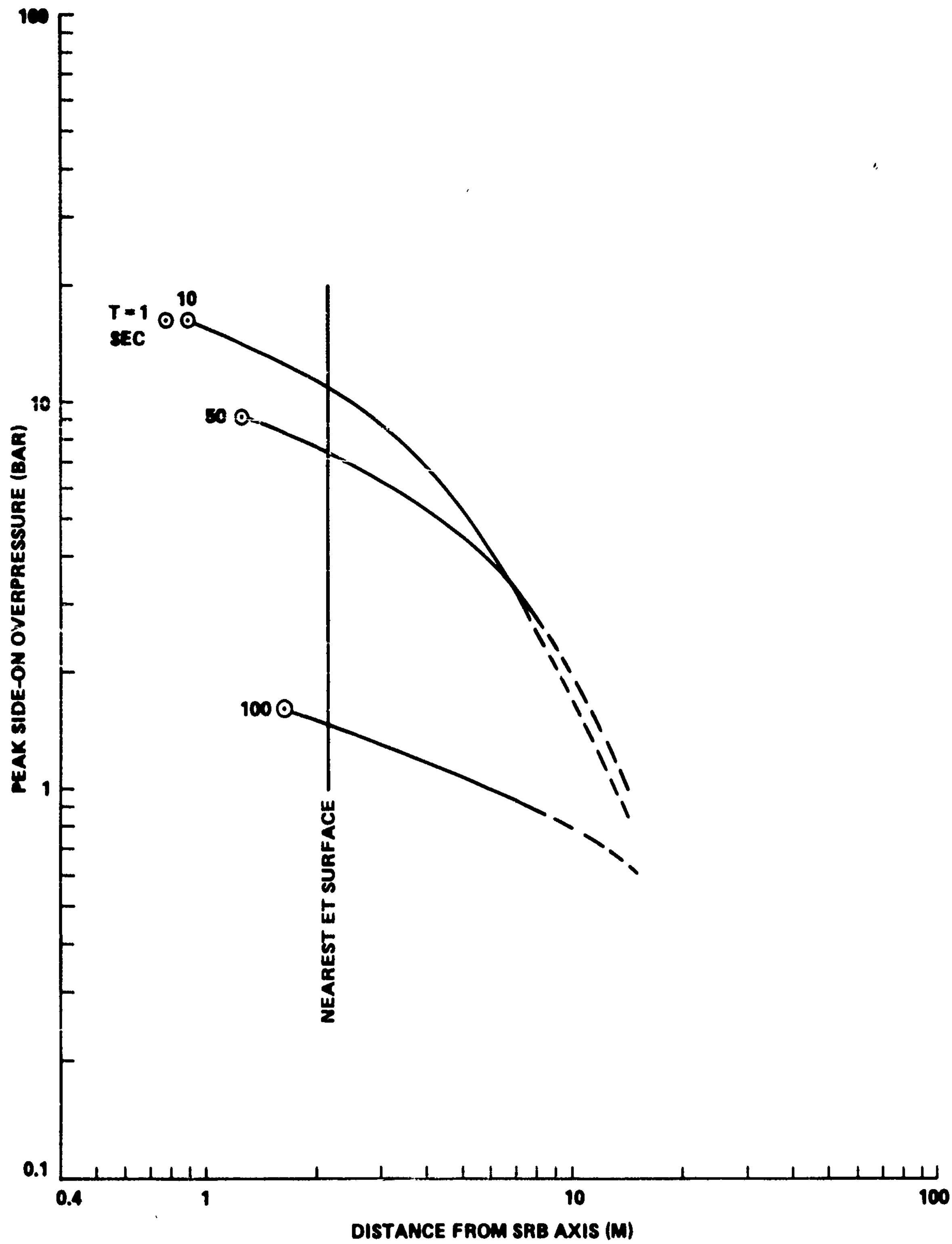

FIGURE 2-13 FREE-AIR SHOCK PRESSURE VS. DISTANCE FOR EXPLOSION OF BARE SRB CHAMBER AT NORMAL OPERATING CONDITIONS

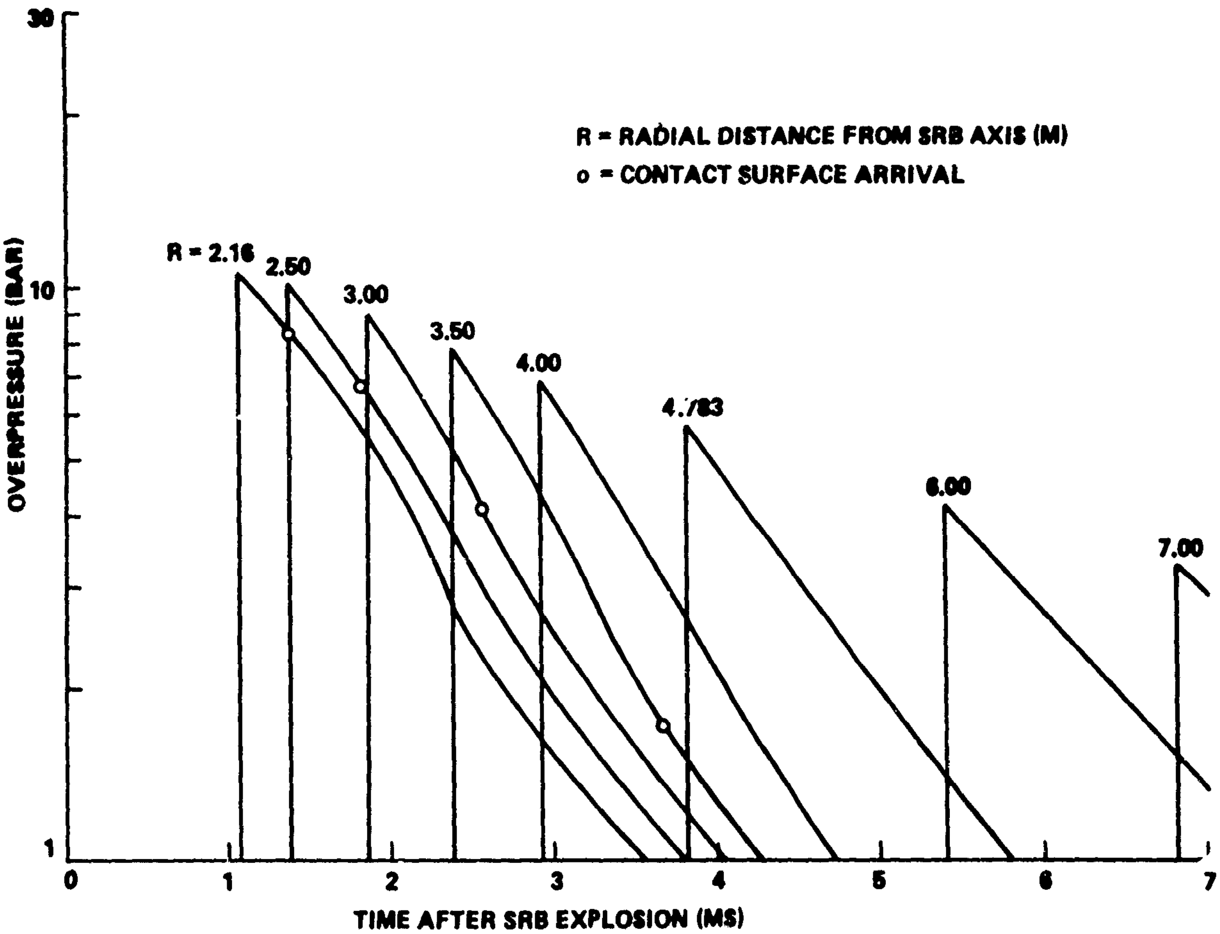

FIGURE 2-14 FREE-AIR PRESSURE VS. TIME AT VARIOUS DISTANCES FROM AXIS OF BARE 827 PSIA SRB CHAMBER EXPLODED AT T = 10 SECONDS

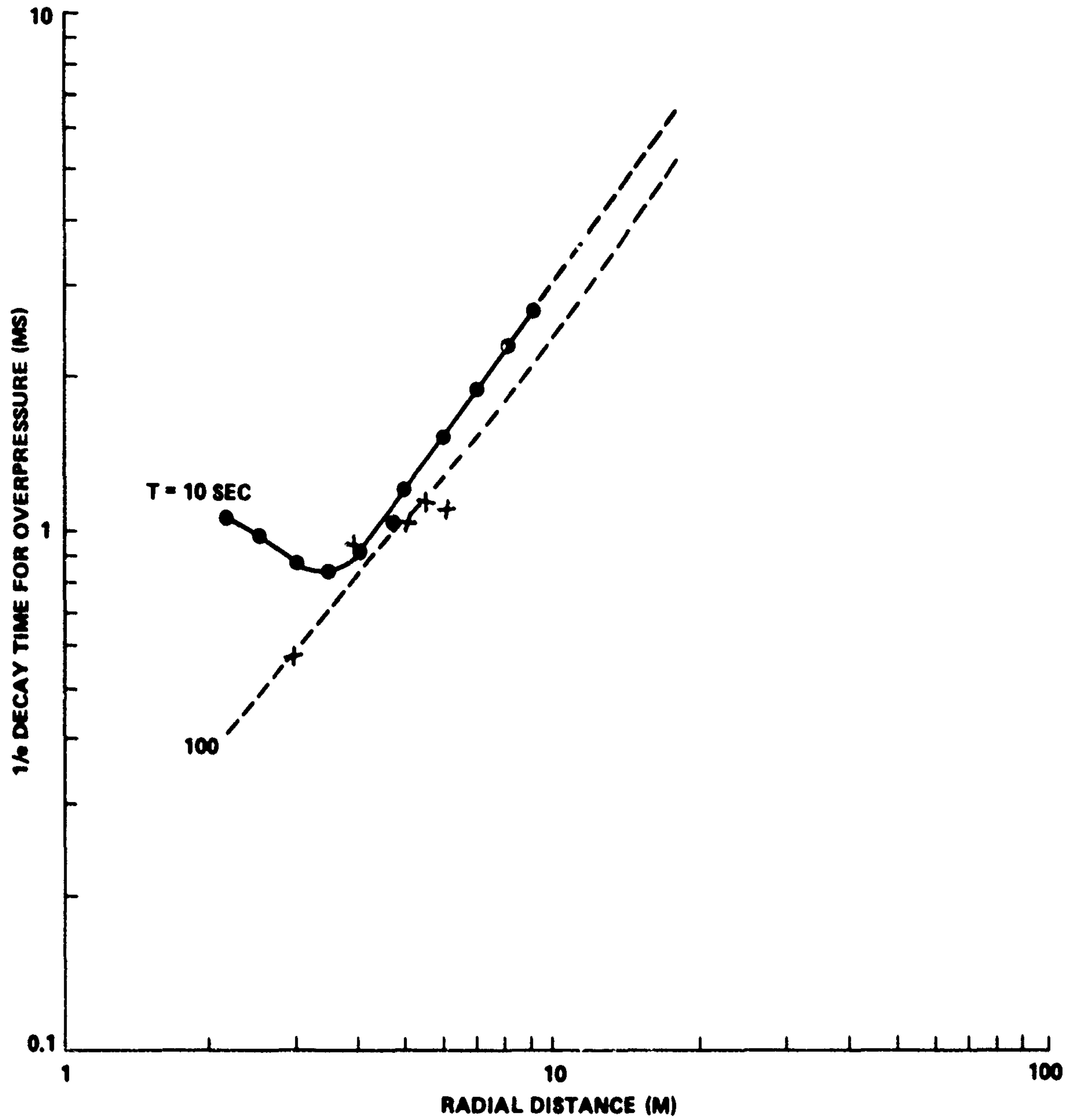

FIGURE 2-15 1/e DECAY TIME FOR FREE-AIR OVERPRESSURE VS. RADIAL DISTANCE FROM SRB AXIS

When the shock passes over some point on the ET, the incident shock overpressure is enhanced by a reflection factor. The reflection factor is a function of the incident shock strength, the angle of incidence, and the equation of state of the gas. Here a combination of the curves[6] and results calculated from ideal-reflection theory[7] was used. The geometry of the shock interaction is shown in Figure 2-16.

The peak reflected overpressures along the ET surface, obtained by multiplying the ' dent free-air overpressures by reflection factors, are shown in Figure 2-17 and es 2-12, 2-13, and 2-14. The pressure peak near 15 degrees is due to Mach stem rmation. For points on the ET beyond the flow-tangency point at alpha of 90 degrees, the pressures are small and are arbitrarily generated by taking the free-air overpressure at a slant range equal to the distance around to the back of the ET (14.44 m), dividing by two to allow for reduction of pressure by diffraction, and drawing a smooth curve to join this point at 180 degrees with the results for theta between 0 and 48.6 degrees.

The overpressures decay exponentially from their peak values. The decay constants are taken from Figure 2-14 for Table 2-12 and from similar calculations for T = 100. The decay constants are shown in Figure 2-15 and in the last column of Tables 2-12 and 2-14. For T = 10, Table 2-12 contains enough data to define the pressure-time history on the ET. For T = 100 seconds, the exponential decay does not last long before the product gases arrive and boost the pressure. The product-gas impact was calculated for T = 100 with the TUULI* two-dimensional hydrocode and the air shock, which was poorly resolved in the TUULI results, was filled in from the one-dimensional results with reflection factors as shown in Table 2-14. Figure 2-18 shows the resulting pressure loading on the ET for T = 100.

*The two dimensional hydrocode TUULI (formerly named TUTTI) was developed at NSWC, White Oak Laboratory by D. L. Lehto.

[6]Glasstone, S., The Effects of Nuclear Weapons, USAEC, GPO, 1962.

[7]Bleakney, W., and Taub, A.H., "Interaction of Shock Waves," Reviews of Modern Physics, Vol. 21, No. 6, 1949, p. 584.

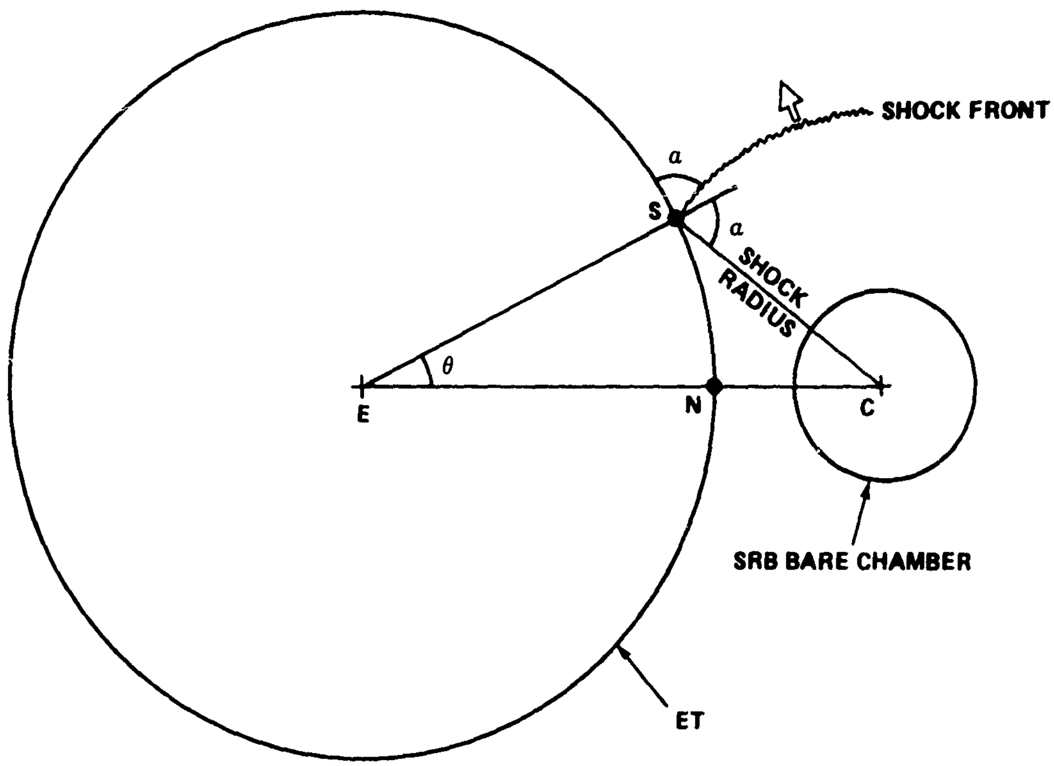

$\overline{EN}$ = RADIUS OF ET = 4.22 M (166 IN)
$\overline{CN}$ = DISTANCE TO NEAREST POINT OF ET = 2.16 M (85 IN)
$\overline{CS}$ = RADIUS OF SHOCK FRONT; LET t = 0 WHEN $\overline{CS}$ = $\overline{CN}$
$\overline{CE}$ = AXIS-TO-AXIS DISTANCE = 6.38 M (251 IN)

FIGURE 2-16 GEOMETRY OF SHOCK IMPACT ON EXTERNAL TANK

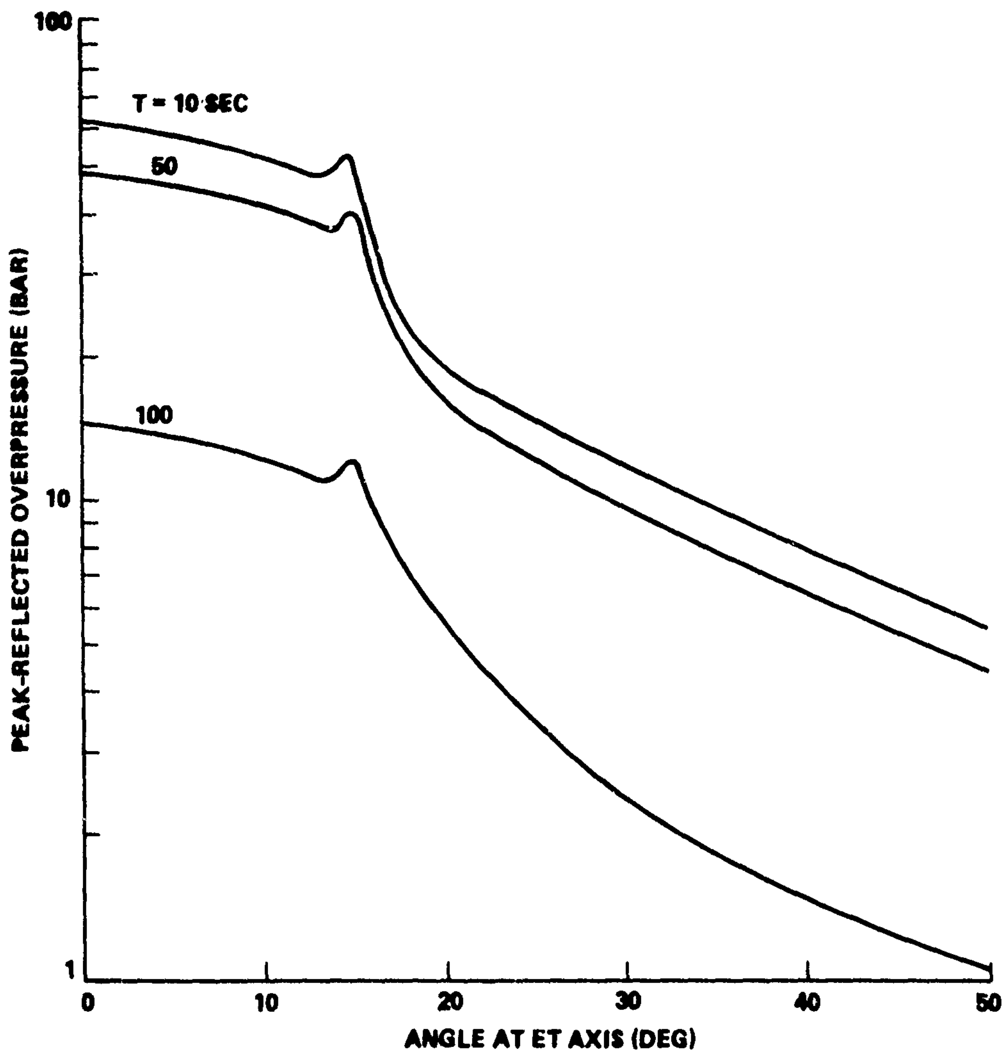

FIGURE 2-17 PEAK REFLECTED OVERPRESSURE ALONG SURFACE OF ET DUE TO EXPLOSION OF BARE SRB CHAMBER AT NORMAL OPERATING PRESSURE

TABLE 2-12 BLAST IMPACT ON ET AT FLIGHT TIME OF 10 SECONDS FOR SRB CHAMBER PRESSURE OF 827 PSIA

AMBIENT PRESSURE(BAR)= 0.980 SOUND SPEED(M/MSEC)= .3391

SHOCK P VS R FROM WUNDY 7597--

RADIUS(M)=	.867	1.200	1.500	2.000	2.439
	2.846	3.252	4.065	4.878	5.691
	6.504	8.130	9.756	13.010	14.450
PBAR =	16.470	14.500	13.000	11.400	10.200
	9.300	8.400	6.900	5.600	4.500
	3.600	2.550	1.850	1.060	0.880

THETA	ALPHA	DIST	OVPI	Q	MI	UI	TIME	REFL	OVPR	TE
.1	.3	2.159	10.92	11.14	3.25	1.102	0.000	5.63	61.5	1.08
5.0	14.6	2.205	10.79	11.01	3.23	1.095	.043	5.42	58.5	1.07
8.0	22.9	2.276	10.60	10.81	3.20	1.087	.108	5.17	54.8	1.04
10.0	28.2	2.339	10.44	10.65	3.18	1.080	.167	4.95	51.2	1.02
11.0	30.8	2.377	10.35	10.56	3.17	1.074	.200	4.86	50.3	1.01
12.0	33.3	2.416	10.25	10.46	3.16	1.069	.237	4.80	49.3	1.00
13.0	35.7	2.459	10.15	10.36	3.14	1.067	.276	4.76	48.3	1.00
14.0	38.1	[illegible]	10.05	10.25	3.13	1.062	.317	4.85	48.6	.99
15.0	40.4	2.548	9.94	10.13	3.11	1.054	.361	5.32	52.9	.98
20.0	50.9	2.812	9.37	9.56	3.03	1.029	.614	2.05	19.2	.91
25.0	59.9	3.114	8.68	8.86	2.93	.993	.913	1.72	14.9	.85
30.0	67.7	3.444	7.98	8.14	2.83	.958	1.252	1.49	11.9	.85
35.0	74.6	3.792	7.34	7.48	2.72	.922	1.622	1.31	9.58	.89
40.0	80.7	4.153	6.73	6.87	2.62	.889	2.018	1.19	8.00	.97
45.0	86.3	4.519	6.11	6.24	2.52	.853	2.437	1.07	6.55	1.08
48.6	90.0	4.783	5.73	5.84	2.45	.831	2.752	1.00	5.72	1.15
60.0		*5.621		4.22	2.30	.782	3.825		4.14	1.42
80.0		*7.092		2.64	1.98	.673	6.01		2.59	1.93
100.0		*8.562		1.77	1.70	.577	8.56		1.74	2.49
120.0		*10.03		1.23	1.51	.513	11.43		1.21	3.1
140.0		*11.50		0.92	1.39	.470	14.56		.83	3.7
160.0		*12.97		0.62	1.29	.437	17.92		.61	4.4
180.0		*14.44		0.45	1.21	.409	21.52		.44	5.0

THETA=ANGLE AT ET AXIS.
ALPHA=ANGLE OF SHOCK INCIDENCE.
DIST =DISTANCE (M) SRB AXIS TO SHOCK FRONT ON ET (CS ON FIG. 2-2).
*MEASURED ALONG ET SURFACE BEYOND DIST=4.783 M.
OVPI =INCIDENT OVERPRESSURE(BAR).
Q =INCIDENT SHOCK STRENGTH=OVPI/PAMB.
MI =INCIDENT SHOCK MACH NUMBER.
UI =INCIDENT SHOCK VELOCITY (M/MSEC).
TIME =TIME SINCE FIRST SHOCK IMPACT ON ET (MSEC).
REFL =SHOCK REFLECTION FACTOR.
OVPR =REFLECTED SHOCK OVERPRESSURE(BAR).
TE =1/E DECAY TIME OF OVERPRESSURE (MSEC).

TABLE 2-13 BLAST IMPACT ON ET AT FLIGHT TIME OF 50 SECONDS FOR SRB CHAMBER PRESSURE OF 550 PSIA

AMBIENT PRESSURE(BAR)= 0.351 SOUND SPEED(M/MSEC)= .3076

SHOCK P VS R FROM WUNDY 7582--

RADIUS(M)=	1.230	2.490	3.120	3.740	4.980
	6.230	7.480	8.720	9.970	12.500
	14.450				
PBAR =	9.144	7.000	6.200	5.550	4.550
	3.750	3.050	2.500	2.000	1.350
	1.000				

THETA	ALPHA	DIST	OVPI	Q	MI	UI	TIME	REFL	OVPR
.1	.3	2.159	7.39	21.07	4.37	1.344	0.000	6.51	48.1
5.0	14.6	2.205	7.33	20.90	4.35	1.339	.035	6.25	45.8
8.0	22.9	2.276	7.24	20.65	4.32	1.331	.088	5.90	42.7
10.0	28.2	2.339	7.16	20.44	4.30	1.323	.136	5.65	40.5
11.0	30.8	2.377	7.12	20.32	4.29	1.321	.164	5.50	39.2
12.0	33.3	2.416	7.08	20.19	4.28	1.316	.193	5.40	38.3
13.0	35.7	2.459	7.03	20.06	4.27	1.313	.225	5.34	37.6
14.0	38.1	2.502	6.98	19.91	4.25	1.308	.259	5.36	37.5
15.0	40.4	2.548	6.92	19.72	4.23	1.300	.294	5.92	40.9
20.0	50.9	2.812	6.56	18.70	4.13	1.270	.499	2.63	17.2
25.0	59.9	3.114	6.21	17.70	4.02	1.237	.741	2.00	12.4
30.0	67.7	3.444	5.83	16.64	3.91	1.201	1.012	1.68	9.79
35.0	74.6	3.792	5.50	15.67	3.80	1.168	1.305	1.43	7.86
40.0	80.7	4.153	5.16	14.72	3.69	1.135	1.617	1.27	6.55
45.0	86.3	4.519	4.87	13.88	3.59	1.105	1.944	1.12	5.45
48.6	90.0	4.783	4.68	13.35	3.53	1.085	2.186	1.00	4.68
60.0		*5.621		9.82	3.31	1.016	3.01		3.45
80.0		*7.092		6.48	3.08	.947	4.70		2.28
100.0		*8.562		4.52	2.94	.904	6.70		1.59
120.0		*10.03		3.30	2.85	.876	8.99		1.16
140.0		*11.50		2.46	2.79	.859	11.56		.86
160.0		*12.97		1.87	2.74	.843	14.39		.66
180.0		*14.44		1.41	2.71	.833	17.47		.50

THETA=ANGLE AT ET AXIS.
ALPHA=ANGLE OF SHOCK INCIDENCE.
DIST =DISTANCE (M) SRB AXIS TO SHOCK FRONT ON ET (CS ON FIG. 2-2).
*MEASURED ALONG ET SURFACE BEYOND DIST=4.783 M.
OVPI =INCIDENT OVERPRESSURE(BAR).
Q =INCIDENT SHOCK STRENGTH=OVPI/PAMB.
MI =INCIDENT SHOCK MACH NUMBER.
UI =INCIDENT SHOCK VELOCITY (M/MSEC).
TIME =TIME SINCE FIRST SHOCK IMPACT ON ET (MSEC).
REFL =SHOCK REFLECTION FACTOR.
OVPR =REFLECTED SHOCK OVERPRESSURE(BAR).

PRECURSOR JET – 45 DEGREE APEX, 0.03-INCH THICK WALL
SECOND JET – 75 DEGREE APEX, 0.08-INCH THICK WALL
EXPLOSIVE WEIGHT – 4 LB OF HNS/TEFLON (90/10)

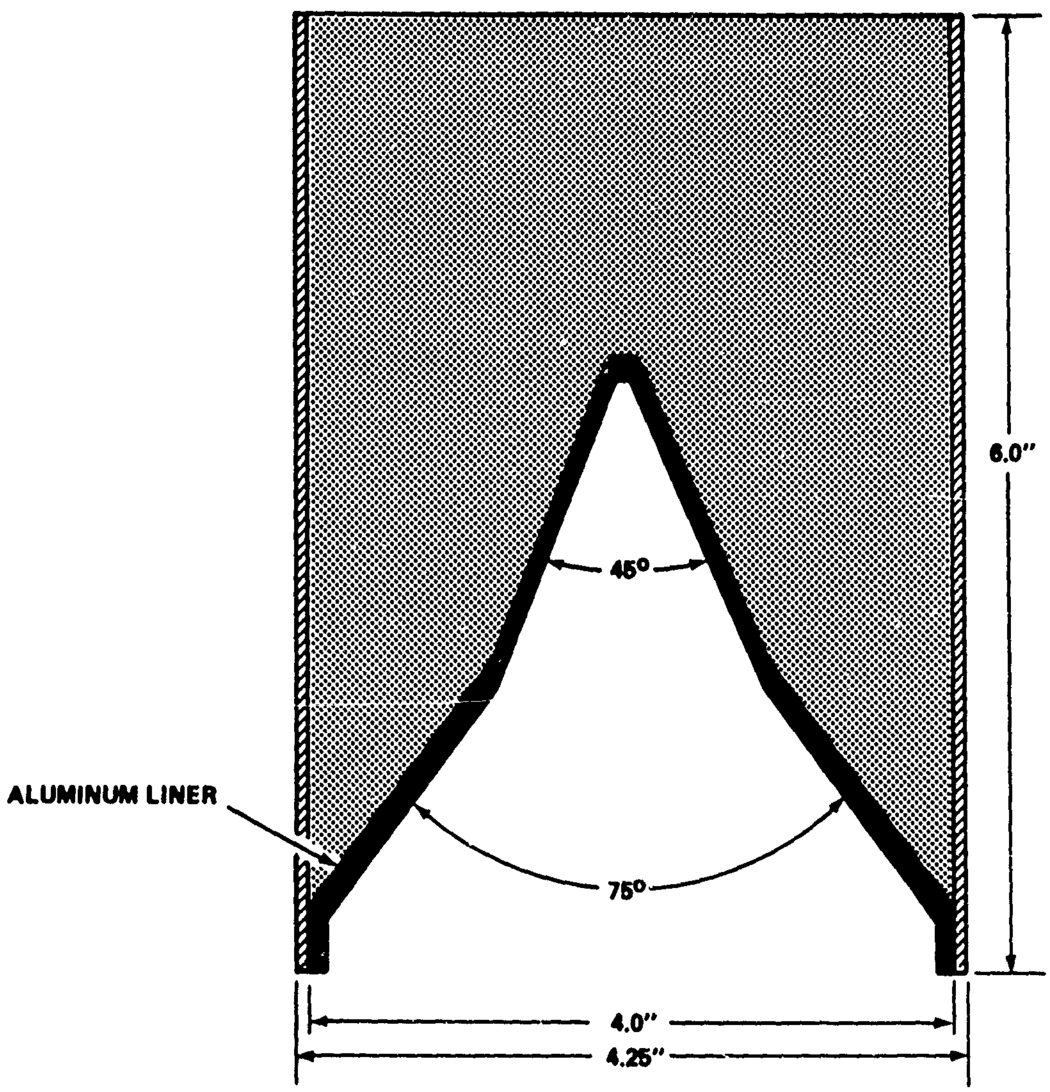

FIGURE 2-19 TANDEM LINER

SECTION II. LOX TANK DESTRUCT

REQUIREMENTS

The dispersal problem and requirements have been investigated. An analysis was made of the destruct configuration promising the maximum possible dispersion of the LOX compatible with safety and short time requirements. Since it is necessary to make the largest size hole or rupture compatible with prompt propellant dispersal and charge size limitation, a configuration must be designed which produces the maximum effect over a wide area of the LOX tank and advantageously utilizes the possibility of shock-loading the liquid oxygen to abet tank rupture.

DESIGN CONSIDERATIONS

The above requirement has led to the selection of a destruct configuration that will employ shaped charges for maximum tank perforation. A detailed analysis has been made of data and semi-empirical equations treating the projectile impact of liquid-filled tanks fabricated from 2219-T87 aluminum.[8-13] The analysis, which includes predicted shock effects derived from NSWC work and shock pressure-particle velocity data for liquid oxygen, has led to the estimate that a 0.60-inch diameter hold produced by a shaped charge jet traveling at about 6000 m/sec will produce catastrophic rupture of the LOX tank. This size perforation is considered a minimum requirement; the proposed destruct configurations are intended to substantially exceed this requirement.

---

[8] Stepka, F.S., and Morse, C.R., "Preliminary Investigation of Catastrophic Fracture of Liquid-Filled Tanks Impacted by High-Velocity Particles," NASA TN D-1537, May 1963.

[9] Stepka, F.S., Morse, C.R., and Dengler, R.P., "Investigation of Characteristics of Pressure Waves Generated in Water-Filled Tanks Impacted by High-Velocity Projectiles," NASA TN D-3143, Dec 1965.

[10] Morse, C.R., and Stepka, F.S., "Effect of Projectile Size and Material on Impact Fracture of Walls of Liquid-Filled Tanks," NASA TN D-362, Sep 1966.

[11] Ferguson, C.W., "Hypervelocity Impact Effects on Liquid Hydrogen Tanks," NASA CR-54852, Douglas Report SM-52027, Mar 1966.

[12] Cosner, L. H., Sewell, R. G. S., Wedan, H. W., "A Semiquantitative Analysis of Shaped Charge Vaporific Damage," NAVORD Report 6398, NOSTP-2093, Sep 1958.

[13] Kilmer, E.E., "Plastic Bonded, Thermally Stable Explosive for an Apollo Experiment," Journal of Spacecraft and Rockets, Vol. 10, No. 7, 1973, p. 463.

SECTION II. LOX TANK DESTRUCT

REQUIREMENTS

The dispersal problem and requirements have been investigated. An analysis was made of the destruct configuration promising the maximum possible dispersion of the LOX compatible with safety and short time requirements. Since it is necessary to make the largest size hole or rupture compatible with prompt propellant dispersal and charge size limitation, a configuration must be designed which produces the maximum effect over a wide area of the LOX tank and advantageously utilizes the possibility of shock-loading the liquid oxygen to abet tank rupture.

DESIGN CONSIDERATIONS

The above requirement has led to the selection of a destruct configuration that will employ shaped charges for maximum tank perforation. A detailed analysis has been made of data and semi-empirical equations treating the projectile impact of liquid-filled tanks fabricated from 2219-T87 aluminum.[8-13] The analysis, which includes predicted shock effects derived from NSWC work and shock pressure-particle velocity data for liquid oxygen, has led to the estimate that a 0.60-inch diameter hold produced by a shaped charge jet traveling at about 6000 m/sec will produce catastrophic rupture of the LOX tank. This size perforation is considered a minimum requirement; the proposed destruct configurations are intended to substantially exceed this requirement.

---

[8] Stepka, F.S., and Morse, C.R., "Preliminary Investigation of Catastrophic Fracture of Liquid-Filled Tanks Impacted by High-Velocity Particles," NASA TN D-1537, May 1963.

[9] Stepka, F.S., Morse, C.R., and Dengler, R.P., "Investigation of Characteristics of Pressure Waves Generated in Water-Filled Tanks Impacted by High-Velocity Projectiles," NASA TN D-3143, Dec 1965.

[10] Morse, C.R., and Stepka, F.S., "Effect of Projectile Size and Material on Impact Fracture of Walls of Liquid-Filled Tanks," NASA TN D-362, Sep 1966.

[11] Ferguson, C.W., "Hypervelocity Impact Effects on Liquid Hydrogen Tanks," NASA CR-54852, Douglas Report SM-52027, Mar 1966.

[12] Cosner, L. H., Sewell, R. G. S., Wedan, H. W., "A Semiquantitative Analysis of Shaped Charge Vaporific Damage," NAVORD Report 6398, NOSTP-2093, Sep 1958.

[13] Kilmer, E.E., "Plastic Bonded, Thermally Stable Explosive for an Apollo Experiment," Journal of Spacecraft and Rockets, Vol. 10, No. 7, 1973, p. 463.

Three basic considerations have been utilized in the analysis to support the shaped charge design. (1) A shaped charge jet of suitable design, e.g., a tandem liner or wide-angle cone (Figs. 2-19 and 2-20) fabricated from aluminum or copper, will satisfy penetration depth and rupture size requirements. (2) Increasing the angle of attack on the LOX tank to an oblique angle of about 60 degrees from the normal will increase the rupture action of the jet over a wide area of the tank (footnote 12, p. 2-49). (3) Spalled fragments from the intervening material in the path of the jet and the associated jet action in the LOX will produce shock waves which will enhance the rupture.

Prospective configurations employing conically shaped charges have been analyzed using empirical equations to predict probable depth of penetration and hole size, the effects of penetrating attenuating material, stand-off distance of the charge to the LOX tank, and the location within the SRB for the most efficient rupture action.

DESTRUCT CONFIGURATION LOCATION: OPTIONS, CONSTRAINTS, AND TRADE-OFFS

The following four general requirements underlie the selection of sites in the SRB and target areas in the ET for the destruct system:

1. Oblique Impact. This technique is essential, particularly since maximum disruption of the thin-skinned LOX tank is required and penetration depth by the shaped charge jet is not a significant factor. There is a significant difference between jet impacts at normal incidence and at oblique angles. When a shaped charge jet strikes a target at normal incidence, only the lead particles in the jet make contact with the target surface. As the angle of incidence is increased, e.g., 60 degrees from the normal, the total area of contact between the fragments is increased. More than the lead jet fragments make contact. Refer to footnote 13 on page 2-49 for data showing that catastrophic rupture and extensive damage to airplane fuselages can be achieved by shaped charge jets impacting at 60-degree obliquity, while normal impact produced only a comparatively small perforation.

2. Dual Destruct Configurations to Ensure Impacting a Liquid-Backed Target Area. Two shaped charges would be used at each of the optional locations 1, 2, and 3 discussed below. This requirement is based on NASA tests with hypervelocity pellets (footnote 8, p. 2-49). The requirement is intended to utilize hydrodynamic shock loading of the LOX to ensure fracture of the tank over a large area independent of any other damage mechanism. Location of the LOX is not specified during the flight, and this requirement will increase the probability of shock-loading.

3. Minimizing LOX Mixing with Hydrogen After Firing of the Destruct Charges. Destructive rupture of the ET LOX tank dome would vent oxygen directly into the liquid hydrogen ruptured tank area. Rupture of the ogive area of the LOX tank would appear to be preferable.

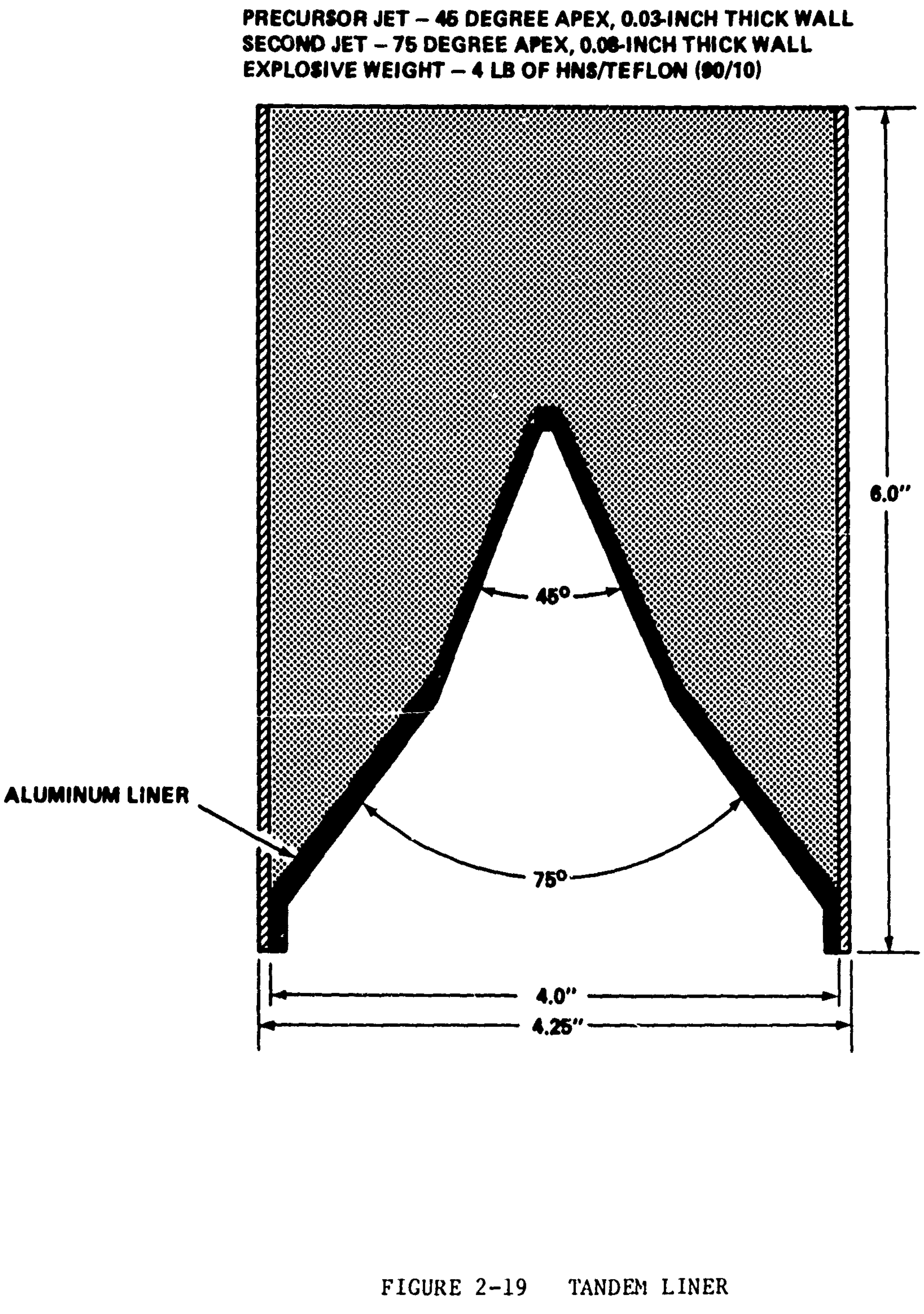

FIGURE 2-19 TANDEM LINER

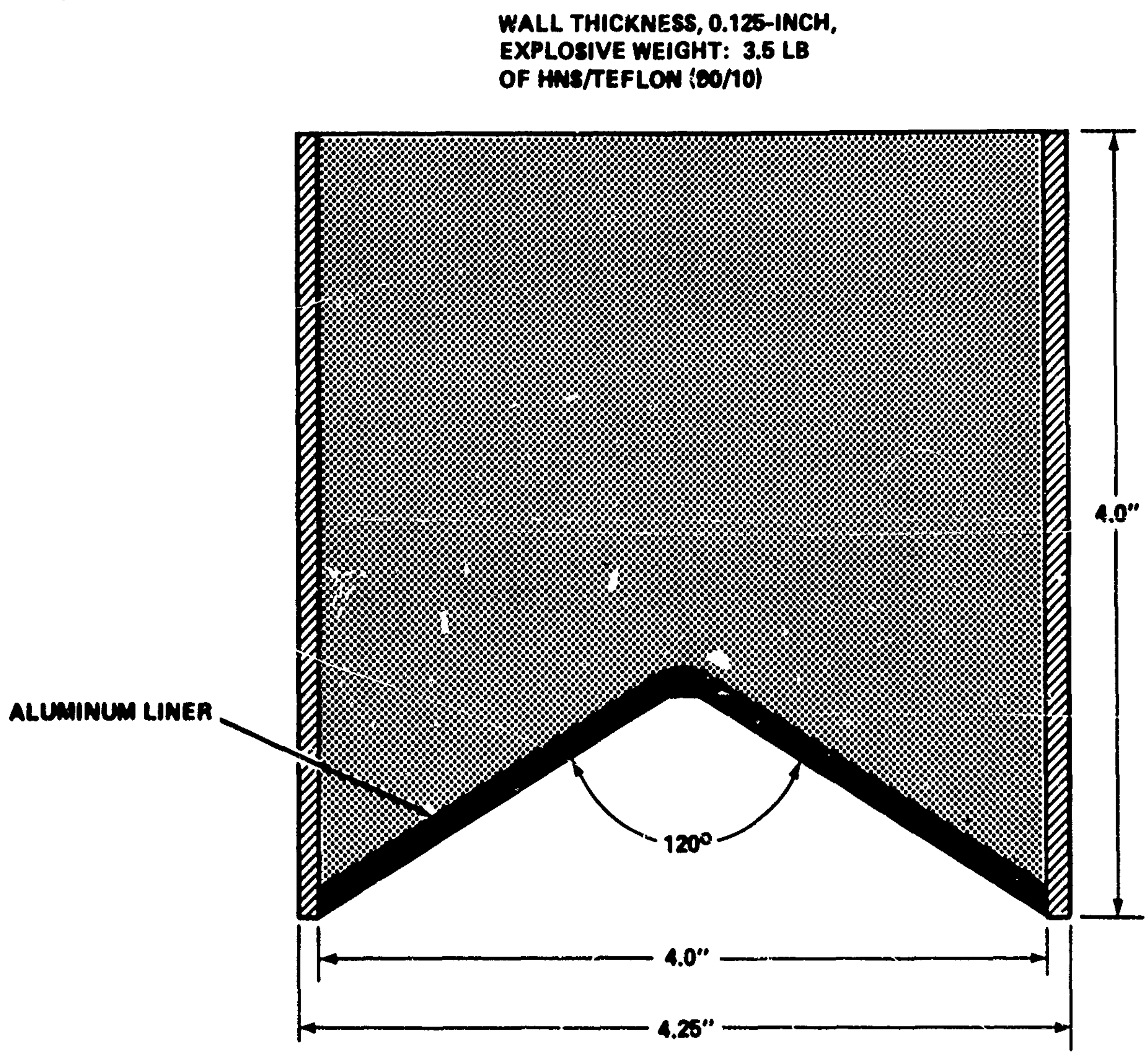

FIGURE 2-20 120-DEGREE CONICAL LINER

4. Impact Membrane Areas of the Gores. These are the thinnest areas of the ET, extending over substantial areas and, therefore, readily lending themselves to extensive rupture propagation.

Optional locations of the shaped charge destruct system are listed below and were analyzed with respect to the possibility of satisfying the above requirements. See Figure 2-21 for the optional locations.

Option 1. One arrangement which would satisfy the above requirements would be to locate a shaped charge in the SRB nose frustum; for example, locations X_B275 and X_B318 shown in Figure 2-21. The charge would be aimed at an angle up from the horizontal so that the charge center line intercepts the ET-LOX aft ogive just above the barrel weld stiffened area (760). A drawback for this location exists in that it is outside the pressurized space in the SRB and, therefore, requires that initiation leads pass through the pressurized boundary (401).

Option 2. This arrangement would avoid passing leads through the pressurized boundary of the SRB by locating the shaped charge beneath the SRB dome (401 to 371). The charge would be aimed at the same points as in Option 1. The jet would pass through more material in the SRB. Final choice of the location, e.g., stand-off would be designed to minimize penetration through solid obstacles.

Option 3. In this arrangement the shaped charge is located in the area originally designated (below X_B 401) but is aimed to impact the barrel of the ET. As in Option 2, this configuration avoids the need to pass leads through the pressurized boundary of the SRB. The option reduces the amount of solid material the shaped charge jet must penetrate. Among its less desirable features are the slope of the glancing impact angle and the ~30 percent greater thickness of the barrel membrane for jet penetration as compared to the thickness of the aft ogive wall.

Option 4. In order to increase the likelihood of impacting a liquid-backed area and thus assuring LOX tank skin fracture, one of two shaped charges positioned at each of the three optional locations noted above may be aimed at the dome and one at the aft ogive or barrel.

The charge site options in the SRB and the jet impact points on the ET are shown in Figure 2-21. These options and impact points are intended as a general guide only. When the selection of preferred trajectory is made, detailed specifications of the sites may reflect other SRB requirements and possible optimization of the shaped charge performance by reducing the amount of material to be penetrated and adjusting the angles of impact.

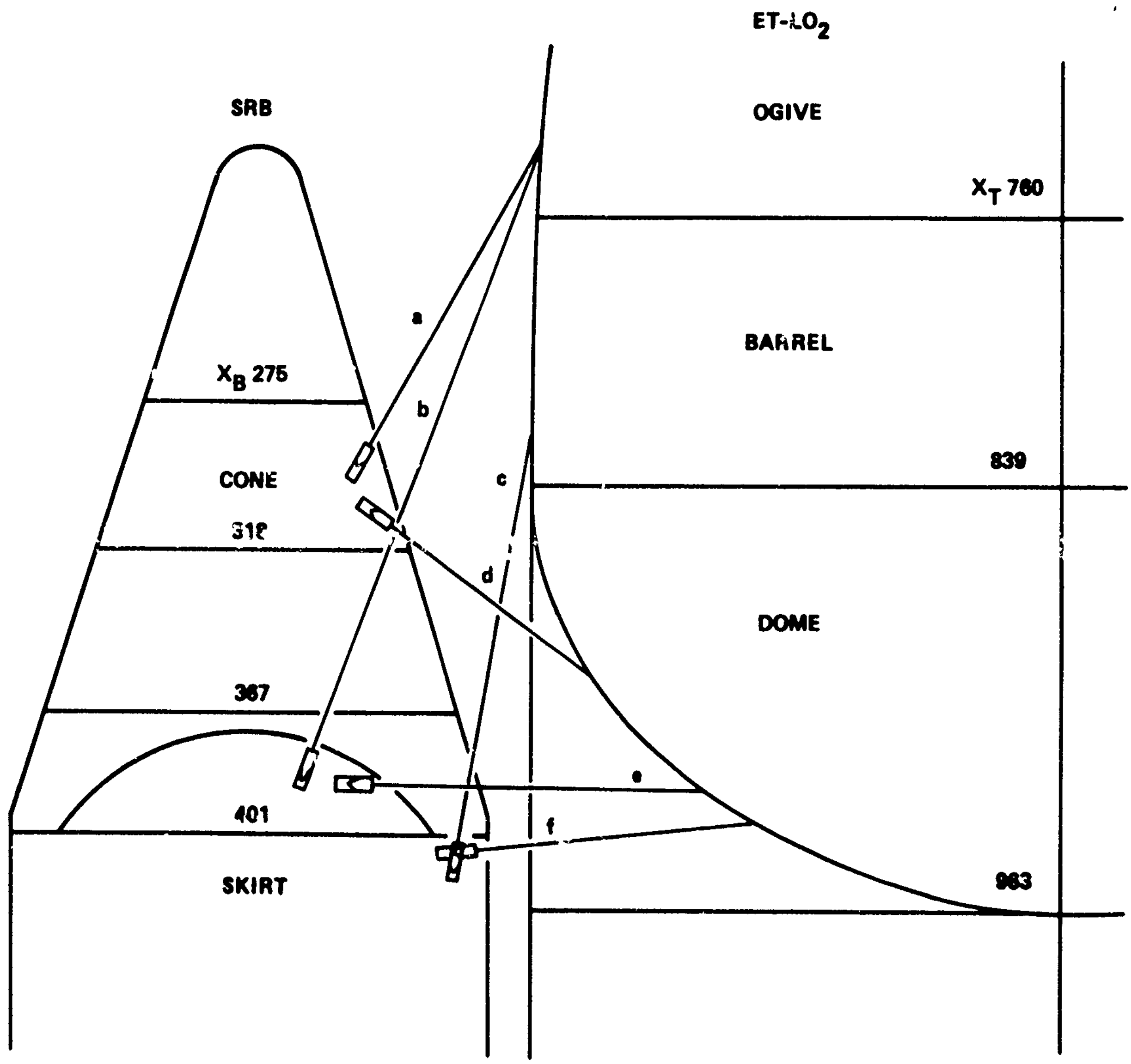

FIGURE 2-21 ET-LO_2 DESTRUCT TRAJECTORY OPTIONS FOR SHAPED CHARGE JETS

Table 2-15 summarizes the trajectory locations, giving the corresponding angles of impact, coordinates of the shaped charge sites in the SRB, coordinates of the jet impact sites, and the path lengths that the jet must travel to impact each site. It is noted that Trajectory b produces the longest jet path, i.e., 195 inches. The jet path length, i.e., the stand-off from charge site to impact site, will affect the number of significant holes produced in the ET. Three major factors will contribute to the number of extent of the perforations or ET rupture.

1. After an optimum air stand-off is reached, the velocity spectrum of the jet causes it to elongate to a point where the jet breaks into comparatively long fragments.

2. As the jet moves further out, the jet fragments break into smaller ones, owing both to high velocity passage through the intervening material and the air.

3. Resistance of the intervening material will cause the jet fragments to slow down, decreasing their hole-producing ability. The perforations will only be small holes, i.e., 0.125-inch to 0.25-inch diameter, if the jet impacts the ET normally. NSWC has shown that for normal impacts a conically shaped charge consisting of a 4-inch long pentolite (50/50 PETN/TNT) cylinder, 1.63-inch diameter cast over a 0.05-inch thick steel liner of 45-degree apex angle, will produce about 30 small holes through a 0.40-inch thick mild steel plate within an area covered by a 5-inch circle at a stand-off of 20 feet.[14] The damage can be expected to increase with increasing charge diameter.

In the case of the destruct system operating at the trajectory paths of Table 2-15, however, the affected area of perforation would be actually a large rip or extensive rupture due to oblique impact. Moreover, since the 4-inch diameter destruct system charges are larger than the charges fired in the above cited work, the ruptured area would be considerably larger. At about 195-inches (Trajectory b, Table 2-15) stand-off, optimum dispersion of the jet fragments would occur. Jet fragments penetrating the ET at smaller distances from the SRB would make larger but fewer perforations and the area covered would be smaller than the stand-off for Trajectory b.

For a given angle of impact, the choice of the conically shaped charge configuration would affect the jet action, producing the most extensive damage to the ET. As the apex angle of the conically shaped charge is increased, the extent of damage would, for near normal impact, occur over a greater area and at a greater distance. A 120-degree cone would produce ~70 percent greater structural damage to the ET impacting the dome at Trajectories e and f, than a tandem liner or 45-degree cone, in accordance with the data of footnote 12 on page 2-49. Table 2-15 lists the recommended shaped charge type for each trajectory.

---

[14] Drimmer, B.E., "Penetration of Steel Targets at Long Stand-Offs by Steel-Cone-Lined Shaped Charges," NOLR 1145, Aug 1950.

TABLE 2-15 DESTRUCT SYSTEM OPTIONAL TRAJECTORY LOCATIONS ET-IMPACT SITES AND JET PATHS

Trajectory	Shaped Charge Type	Shaped Charge Site	ET-Impact Site, Angle*	Jet Path Length (in)
a (Option 1)	Tandem Liner	X_B 300, 60° Adjacent to Cone Wall	X_T 780, 60° AFT Ogive	100
b (Option 2)	Tandem Liner	X_B 390, 79° Adjacent to Interior of Pressurized Dome	X_T 780, 70° AFT Cgive	195
c (Option 3)	Tandem Liner	X_B 410, 80° Adjacent to Interior of Pressurized Boundary	X_T 820, 80° Barrel	130
d (Option 4-1)	120° Cone, Tandem Liner	X_B 300, 35° Adjacent to Cone Wall	X_T 895, 70° Dome	73
e (Option 4-2)	120° Cone, Tandem Liner	X_B 390, 0° Adjacent to Interior of Pressurized Dome	X_T 930, 57°† Dome	100
f (Option 4-3)	120° Cone, Tandem Liner	X_B 405, 7° Adjacent to Skirt	X_T 937, 59°† Dome	80

*All angles measured from the horizontal except as noted.

†Angles measured from the normal to tank surface.

Jet penetrations equivalent to 8 inches of mild steel can be expected at optimum air stand-off (~3-charge diameters) for 120-degree conical charges of 4-inch diameter lined with copper. This penetration would be reduced because of jet velocity degradation over the longer stand-off distances required for the trajectory path lengths of Table 2-15. To avoid retardation effects of the insulating material and other materials in the SRB on the jet propagation velocity, the tandem liner would produce more effective penetration if utilized in the destruct system array, Option 4 impacting along the Trajectories a, b, and c. This configuration takes advantage of the difference in jet velocities from conical liners of widely different apex angles. A 45-degree copper liner produces a jet which will propagate at a velocity ~30 percent faster than a wide-angle cone of 75-degree angle. This precursor jet will penetrate through the attenuating materials and provide a largely uninhibited path for the second jet. Increased penetration (~50 percent greater than 120-degree cone) and more extensive shock effects will result in the liquid oxygen. However, if either of the designated shaped charge configurations is fired along the trajectory paths shown in Table 2-15, it is conservatively estimated that LOX tank rips ranging over 2-feet long and 3-inches wide should occur. Shock loading of the LOX by the jet penetration will exceed 50 kilobars (50,000 atmospheres) within 2 to 3 inches of penetration. As a consequence, even greater destruction is probable.

OTHER CONSIDERATIONS

EFFECT OF SLOSH BAFFLE. A metal slosh baffle grid extends over a large area of the tank shell, including some of the proposed shaped charge impact points. However, since the baffle mean mesh size is large, ~3-feet by 3-feet, it is not considered a serious impediment to other damage mechanisms, e.g., shock-loading of the LOX tank, or damage produced by spallation of SRB material impacted by the jet fragments.

CHOICE OF METAL LINER AND REACTION EFFECTS. The choice of aluminum or copper for the liner material in the shaped charge destruct system will not appreciably affect the performance. Copper liners produce jets with greater penetrating power than aluminum at minimum stand-offs. When the air stand-off is increased beyond an optimum, ~2 charge diameter (CD) for copper liners, a subsequent decrease in penetration occurs. Aluminum, which forms a more coherent, rod-like jet, is favored by increased stand-off (optimum ~4.5 CD). There remains, however, a need to consider the possibility of reaction effects with the LOX on penetration of the liquid oxygen tank by an aluminum jet.

Explosive reaction of metal from a shaped charge jet with the liquid oxygen would provide a powerful additional mechanism for rupturing the LOX tank in a massive way. It has been established that a metal pellet moving at a velocity as low as 1100 ft/sec, on impacting and penetrating a LOX-backed titanium plate, caused the titanium to react with the liquid oxygen in a self-propagating manner.[15,16] The result was a violent explosion. Such behavior, however, was not obtained in tests with aluminum plates; consequently, a violent explosion is not expected in penetration of the ET by either an aluminum or copper jet.

FRAGMENTATION EFFECTS. Spalled material will be generated from the outer surface of the SRB by jet particles from a shaped charge positioned at any of the optional locations. The jet will easily penetrate the SRB skin and other material. However, the jet is not a continuous body, but a stream of fragments with each succeeding fragment of lower velocity. These fragments will be diverted on passage and produce additional spalled fragments which will be projected over a much larger area than the jet cross-section. This effect will be enhanced by the oblique impact of jet particles. Figure 2-22 shows a typical region of dispersion for fragments impacting the LOX tank at an oblique angle. Some work on fragmentation effects from shaped charge jets impacting targets has been done. Further analysis can help determine the potentiality of spall impacts for producing structural damage to the ET. However, experimental tests of the recommended shaped charge configurations fired against scaled target prototypes are recommended to verify the effectiveness of the destruct system design.

---

[15] Dengler, R.P., "An Experimental Investigation of Chemical Reaction between Propellant Tank Materials and Rocket Fuels as Oxidizer When Impacted by Small High-Velocity Projectiles," NASA TN D-1882, Aug 1963.

[16] Riehl, W.A., Key, C.F., and Gayle, J.B., "Reactivity of Titanium with Oxygen," NASA TR-R-180, 1963.

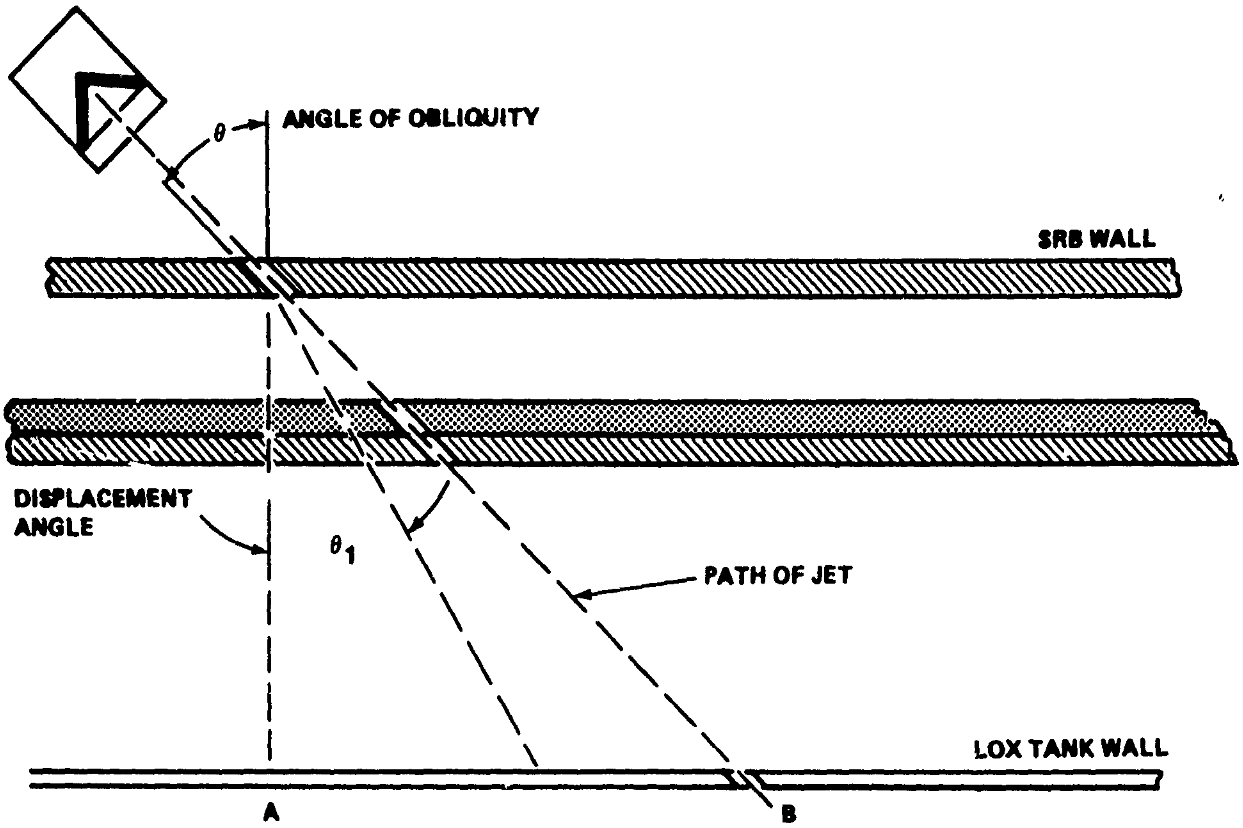

FIGURE 2-22 REGION OF DISPERSION FOR SPALLED FRAGMENTS IMPACTING THE LOX TANK WALL

EXPLOSIVE SELECTION

NSWC has developed a number of explosives of high thermal stability in recent years. In particular, the thermal stability and other desirable properties of the plastic-bonded explosive composition,* HNS/Teflon, 90/10, makes it a suitable choice for use in the shaped charge destruct configurations. Explosive charges of HNS/Teflon were used by NASA in its Apollo program to generate a source of seismic energy by detonation in lunar explorations (see footnote 13, p. 2-49).

Table 2-16 compares the properties of HNS/Teflon, 90/10, with the properties of TNT. Note the large differences in the melting points, vacuum thermal stability, and maximum theoretical densities. HNS/Teflon, 90/10, is more sensitive, e.g., its 50 percent initiation pressure is 21.9 kilobars at a loading density of 1.70 gram per cubic centimeter as compared to 46 kilobars for cast TNT.

*HNS is 2, 2', 4, 4', 6, 6' Hexanitrostilibene.

TABLE 2-16 PROPERTIES OF HNS/TEFLON, 90/10, COMPARED TO TNT

Property	HNS/Teflon 90/10	TNT
Melting Point (°C)	318	81
Theoretical Maximum Density (g/cc)	1.78	1.651
Vacuum Thermal Stability (cc/g/hr)	At 250°C 0.52	At 100°C 0.10
Detonation Velocity (m/sec) at Density (g/cc)	6900 (1.68)	6940 (1.60)
50% Initiation Pressure (Kbar) at Density (g/cc)	21.9 (1.70)	46 (1.62)
Steel Dent Output (mils)	43	46.5
Specification	NOLS1015	MIL-T-2481T

The detonation velocity and higher loading density of HNS/Teflon, 90/10, indicates that its performance in shaped charge applications will be slightly better than TNT. It should give penetrations about 30 percent less than the more common shaped charge explosives, e.g., Cyclotol (60/40 RDX/TNT) or Octol (65/35 HMX/TNT). However, the penetration and rupturing capability of jets from shaped charges of HNS/Teflon, 90/10, are more than sufficient to achieve the destruct system objectives.

SUMMARY

An analysis was made of the problems encountered in dispersing the liquid oxygen in the LOX tank. A destruct system was designed employing the thermally stable explosive, HNS/Teflon, 90/10, in four-pound conically shaped charges with 120-degree and tandem liners.

The charges were located at suitable stand-offs from the SRB wall so that extensive structural damage to the LOX tank would result from the oblique impact of a stream of jet fragments. Four options in locating the destruct system were discussed. The trajectory paths of the jet fragments, coordinates of the destruct system in the SRB, and the impact sites on the LOX tank were specified for the options. Three of the optional locations for the destruct system consider impact sites on the aft ogive and barrel of the ET. The fourth option positions a second charge at either of the above locations so that its jet trajectory would provide an additional impact site on the ET-dome. This option which uses both liner types provides the most effective destruct system.

CHAPTER 3

AERODYNAMICS AND ATMOSPHERIC FLIGHT MECHANICS

INTRODUCTION

The aerodynamic and atmospheric flight mechanics of the Space Shuttle configuration in normal operation are well documented. This chapter deals primarily with the flight mechanics of the cluster upon inadvertent separation of one solid rocket booster (SRB) or the orbiter at four specified times into flight, i.e., 0 (lift-off), 10, 50, and 100 seconds.* Sketches of the full and partial clusters are shown in Figure 3-1, Views A through C.

The following discussion describes the methods used to determine the flight mechanics for these partial configurations and presents the results of the study in graphical form.

AERODYNAMICS

A general approach was adopted with respect to determining the aerodynamic input data required by the study. In considering the time allotted for completing the study, the number of configurations and parameters being considered and the fact that much of the work to be done in the study is sequential in nature, it was decided that experimental aerodynamic data obtained on the Space Shuttle would be used to the extent that it was available. Essentially, all of the experimental aerodynamic data provided for use in this study are contained in footnotes 1 and 2. To provide a consistent data base, recent updates of portions of the space shuttle aerodynamic data files were not considered. In addition, "missing" data were qualitatively evaluated with respect to their effect on the overall vehicle flight before attempts were made to analytically predict the "missing" data. It is estimated that more than 95 percent of the aerodynamic data provided for use in the White Oak Laboratory (WO trajectory studies (discussed on the following page) was obtained or derived from the data in footnotes 1 and 2, below.

*NASA Defense Purchase Request, H-13047B, 15 May 1975.

[1]"Orbiter Vehicle," Rockwell International Report No. SD72-SH-0060-1I, Aerodynamic Design Data Book, Vol. 1, Jun 1975.

[2]"Mated Vehicle," Rockwell International Report No. SD72-SH-0060-2H, Aerodynamic Design Data Book, Vol. 2, Feb 1975.

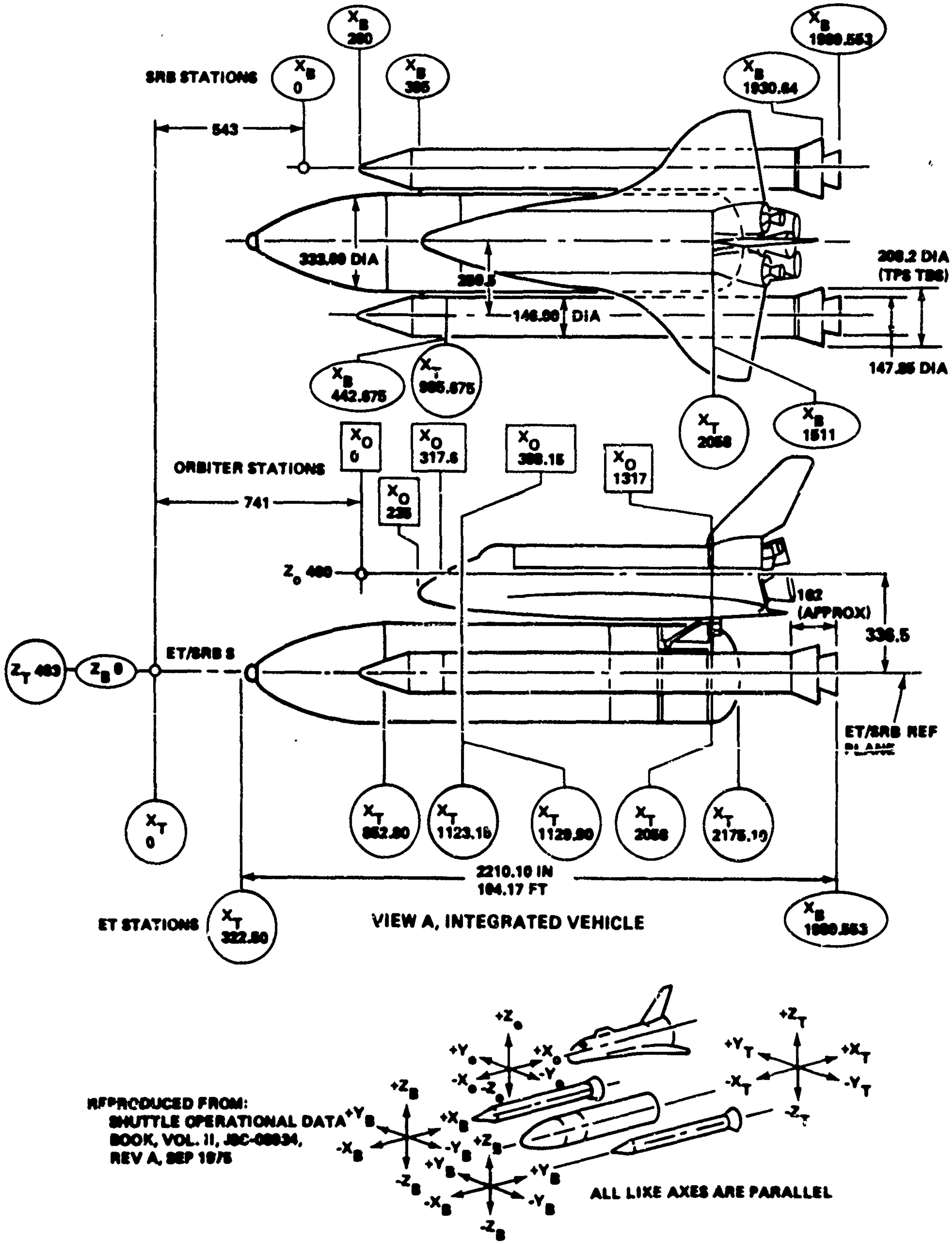

FIGURE 3-1 SHUTTLE STUDY CONFIGURATIONS (Sheet 1 of 2)

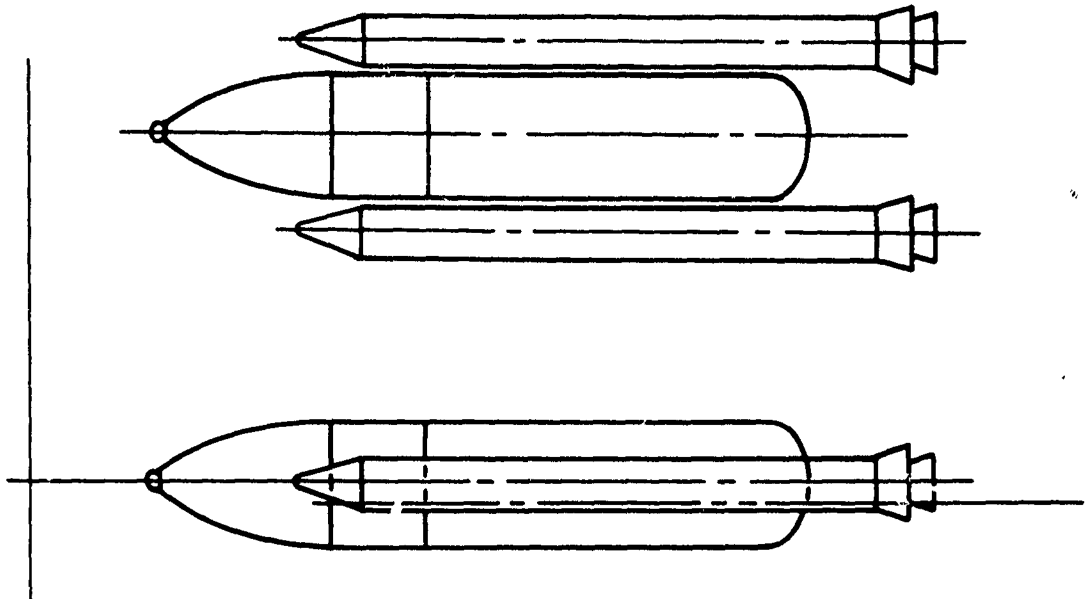

VIEW B, ORBITER SEPARATED

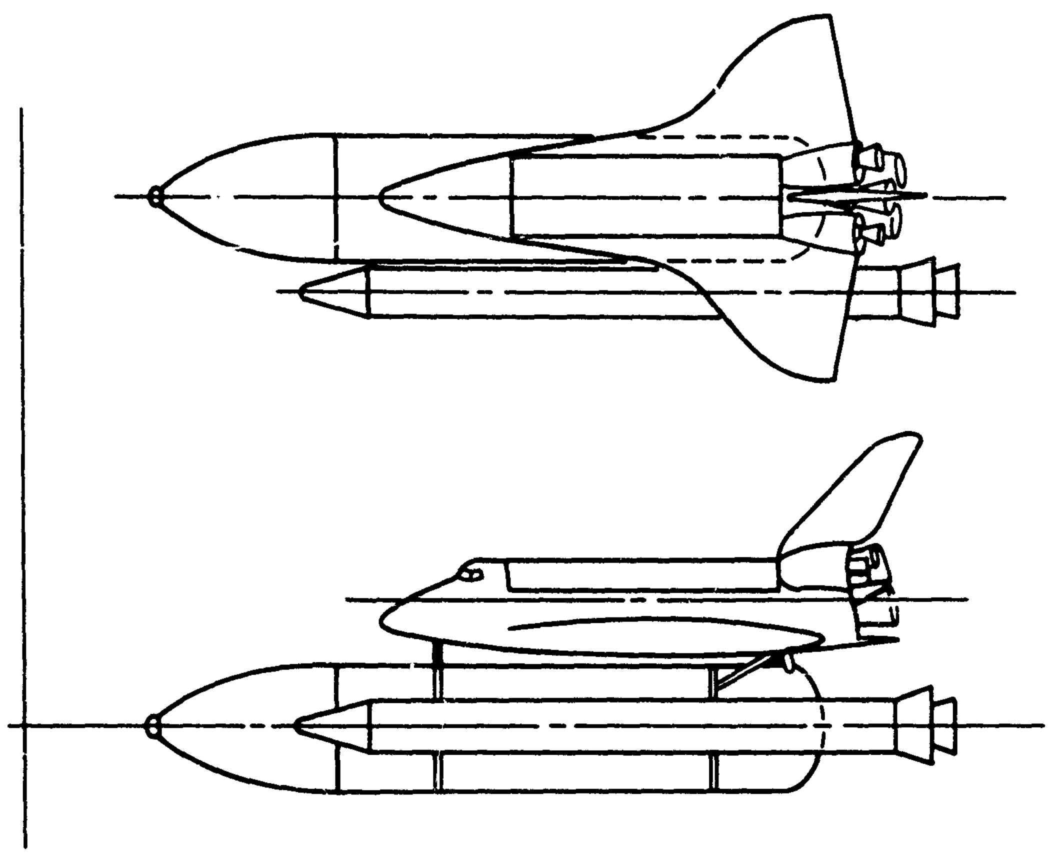

VIEW C, RH SRB SEPARATED

FIGURE 3-1 SHUTTLE STUDY CONFIGURATIONS (Sheet 2 of 2)

Since there are many shuttle flights in the planning stage, Marshall Space Flight Center (MSFC) specified that Mission 1, to be launched from the Eastern Test Range (ETR), was to be the flight of interest. MSFC provided Naval Surface Weapons Center (NSWC) with a 3-D flight trajectory output for reference purposes which described a nominal ascent phase of flight up to SRB separation (~120 seconds after liftoff). Selected portions of these data were plotted to obtain the range of flight parameters and environment to be considered in the study. A presentation of Mach number, M; dynamic pressure, q; altitude, h; and static pressure, P_∞, plotted as a function of time is shown in Figure 3-2. These same parameters, at the four times considered in this study, are presented in Table 3-1.

In general, the major static longitudinal, lateral, and directional stability data were presented for the configurations being studied. Because a review of the experimental data revealed that many of the configurations exhibited nonlinear aerodynamic characteristics, the various aerodynamic coefficients were presented in tabular form at discreet Mach numbers over a range of M = 0 to M = 5, and for discreet angles-of-attack (yaw) over a range of -10 degrees to +10 degrees. Dynamic data were also listed when available. All data were presented in the body axis system, using the moment reference center (MRC) and reference dimensions given on each set of data. Coefficients to be reduced about different MRC's or referenced to different reference dimensions were recalculated in the trajectory program. The sign conventions used in data presentation are those given in Section 2 of footnote 2, p. 3-1.

The only major assumptions made with respect to the data was that longitudinal forces and moments were independent of the sideslip angle, β, and that yawing forces and moments were independent of the angle of attack, α. A review of the 6 × 6 matrix data plots presented in footnote 2 show that these assumptions are well within reason.

INTEGRATED VEHICLE DATA. These data were primarily provided to check the results from the WOL 6-D trajectory program against the 3-D trajectory output provided by MSFC. For all practical purposes, the experimental aerodynamic data given in footnote 2 were readily available and reasonably complete. It was only necessary to convert the data into the format required by the WOL 6-D program. One problem arose with these data in that the configuration was tested with the inboard and outboard elevons set at 0 degrees. However, the ascent flight schedule calls for "programmed" elevon deflection up to SRB staging. Information from MSFC indicated that these elevon deflections were not being used to trim the flight path but were to alleviate certain loading conditions. Since data were neither available for the elevon deflection schedule provided by MSFC nor for interpolation or extrapolation, aerodynamic force and moment corrections were not applied to the basic data. The assumption that these corrections were not needed to provide a reasonable check of the vehicle flight path and attitudes was justified in that the trajectory comparisons were good. However, late in the study, the structural analysis showed that, for the case of inadvertent separation of one SRB, the limit load of the front ORB/ET attach joint was exceeded almost simultaneously with the event at 50 seconds into the flight. Time and funding did not permit correcting the data to see if the elevon deflection would, indeed, "unload" the front ORB/ET attach joint. It is recommended that any future studies include this data correction.

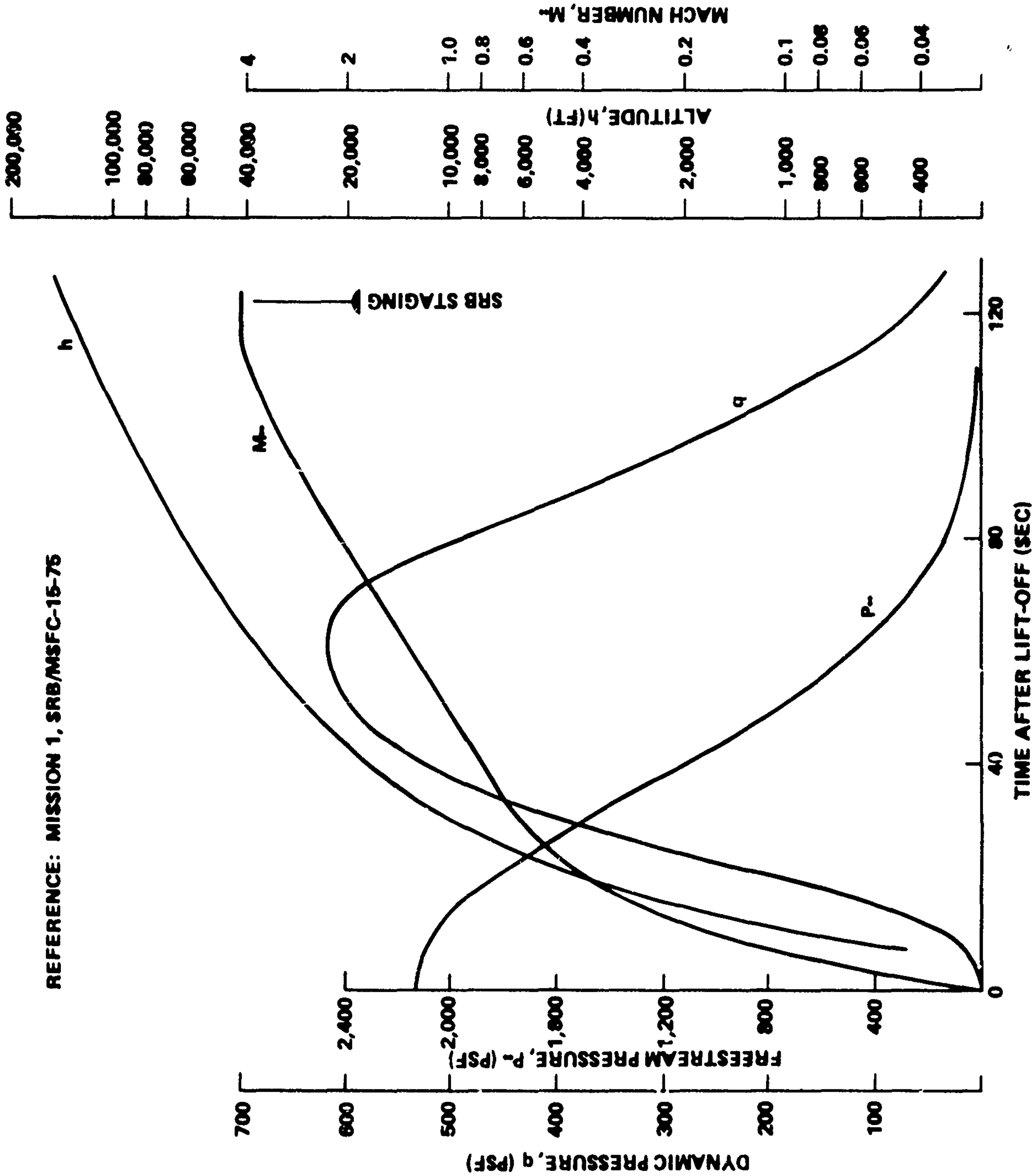

FIGURE 3-2 TRAJECTORY PARAMETERS, MISSION 1

TABLE 3-1 FLIGHT PARAMETERS

t sec	M	h (ft)	q (psf)	P_∞ (psf)
0	0	0	0	2116
10	0.16	900	37	2060
50	1.0	26,000	590	775
100	3.3	94,000	242	40

INADVERTENT ORBITER SEPARATION. This event results in a configuration consisting of the ET and SRB's. Again, experimental static aerodynamic data were readily available (footnote 2, p. 3-1) with the exception of rolling moment and dynamics data. With regard to the rolling moment data, it was assumed that because of symmetrical configuration there would be no induced rolling moment for small angles of attack. It is recognized, however, that, at a large angle of attack, induced roll will start to build up and it is further recognized that, due to the quasi-elliptical cross-section of the configuration, a dihedral effect due to sideslip, Cl_β, will be introduced into the overall vehicle aerodynamics. Presently, however, satisfactory analytical methods for predicting these rolling moments are unavailable.

INADVERTENT SEPARATION OF ONE SRB. This separation results in a configuration which is completely nonsymmetric. No experimental data for this specific configuration were available. However, data for the integrated vehicle and the configuration resulting after SRB separation (ORB + ET) were available and these data were used to estimate the aerodynamics of the configuration of interest. Fortunately, sufficient aerodynamic data were available to cross-check the estimated aerodynamics. The initial approach was to compare "like" data for the integrated vehicle and the ORB + ET. By splitting the difference between the two sets of data (effectively adding back in the aerodynamics of one SRB), an estimate of the aerodynamics for this configuration was obtained. A check of this method was available by taking the data for the integrated vehicle and subtracting from this the data for one SRB. Both approaches provided resulting data which checked reasonably well. The latter approach was the one used to obtain the data input required by the WOL trajectory program.

When one SRB is separated from the integrated vehicle configuration, one wing panel of the orbiter is exposed to the freestream. It was felt that such a condition would result in large aerodynamic rolling movements which could significantly affect the resulting motion of the vehicle. Therefore, using isolated wing panel data (see footnote 2, p. 3-1), an estimate of the panel normal force and center of pressure was included as a part of the aerodynamic data package for this event.

To simplify the overall calculations and to reduce computer time and costs, an aerodynamic loading subroutine was added to the trajectory program. This subroutine calculates the reaction loads at the ORB/ET and SRB/ET attach joints at each integration time step. In order to do this, it was necessary to estimate the portion of the total load of any given configuration being carried by individual components comprising that configuration. This was accomplished as follows:

1. "Like" force coefficients for the individual components comprising the integrated vehicle were summed to give a "total" load. These "total" loads were

determined as a function of Mach number and angle of attack (yaw). It is to be noted that this calculation results in a fictitious "total" load since no aerodynamic interference effects are included.

2. The ratio of the individual component load to the "total" load is computed. This provides the percentage of the "total" load being carried by that component.

3. The above percentage is then applied to the actual total load estimated for the configuration to determine the portion of the actual load being carried by the individual component. From this load and an estimate of the component center of pressure, the reaction forces and moments at the attach joints may be estimated.

The implied assumption in the above approach is that, regardless of the configuration under consideration, the percentage of the actual total load being carried by an individual component is constant.

The estimated confidence level of the aerodynamics where experimental data are available is greater than 95 percent. Where data had to be "derived" from experimental data, such as the event for inadvertent separation of one SRB and the estimation of component loading, the confidence level decreases to the order of 75 percent. The confidence level for the over-all aerodynamic portion of the study is on the order of 85 percent.

ATMOSPHERIC FLIGHT MECHANICS

Six degree-of-freedom rigid-body Space Shuttle trajectories were generated to determine the aerodynamic and inertial loadings needed for the structural calculations. Verification of the ascent vehicle math model being used was accomplished by computing nominal trajectories and then comparing these with NASA printouts for Mission 1.[3] A trajectory consisted of a nominal flight to the time of separation, when an instantaneous configurational change was programmed to simulate the occurrence of an inadvertent separation. The possibility of further breakup of the ascent vehicle after the inadvertent separation was ignored and a trajectory was calculated assuming that the components still joined together underwent no additional breakup.

Two cases of unintentional separation were evaluated. The first case was that of separation of the orbiter; the second case was separation of a solid rocket booster. For the purposes of this study, the right SRB was arbitrarily selected. In all cases, the separation was assumed to be extremely clean, as if the component of interest had instantaneously vanished. No attempt was made to hypothesize either the case or the mode of the separation. Interference effects between the wayward component and the surviving cluster were ignored, as were any separation impulses or reactions. The flight path of the separated component was not determined. Thus, the possibility of a physical collision after the moment of separation was not weighed.

---

[3]Computer Printout, Mission 1 (due east), MSN-1/DRAG + BASE FRCE UPDAT/SRB-MSFC-15-75/LO TO AOA MECO, Marshall Space Flight Center, NASA.

The trajectories were computed by using a version of the six-degree-of-freedom computer program.[4] The modified version features more input flexibility than the original. It also uses a nearly complete form of the equations of motion; only the $\overline{\omega}(d/dt)$ I terms are deleted from the rotational equations. A rotating spherical earth model and a 1959 standard atmosphere model were used for the computations.

Modifications to the computer program were required primarily to permit instantaneous changes in the ascent vehicle characteristics (simulation of separation), and to allow the simultaneous calculation of the internal reactions at the SRB and orbiter attachment locations. The use of an existent NASA computer program was considered, but rejected since modifications would have also been necessary. Furthermore, unfamiliarity with the programming logic presented the possibility of unforeseen difficulties in adapting the code.

The major objective of the trajectory matching with NASA flight profiles was to obtain reasonable agreement with respect to the accelerations and rates and the attitude of the first stage during the first 120 seconds after liftoff. Precise matching of the spatial coordinates contained in NASA trajectories was not judged to be critical, since estimating the dispersion of the fragments resulting from a destruct event or the impact location of any separated components was not an objective of this study.

Relatively minor discrepancies with the nominal NASA trajectories exist because updating of the available data causes slight variations in the math models being used for the computations. These discrepancies are most marked during the period between 30 and 70 seconds after lift-off, when the influence of aerodynamic pressures is greatest. These differences are attributed primarily to the exclusion of aerodynamic data which reflect the effects of elevon and flap deflections. Thus, the trajectories are representative of an ascent vehicle with the aerodynamic control surfaces nulled.

The guidance and control system was modeled using the candidate control scheme.[5,6] Additional information on the guidance and control system, the schedule of the control system gains, and the modeling for the engine nozzle actuators was taken from footnote 7. A block diagram of the guidance and control system model is

---

[4]Degrafft, W.E., A Powered Six-Degree-of-Freedom Trajectory Program for an IBM 7090 Computer, U.S. Naval Ordnance Laboratory, NOLTR 66-199, Mar 1967.

[5]Documentation of the Shuttle Trajectories for Analysis and Research in Three Degrees-of-Freedom (STAR3D) Program, Northrop Corporation, TR-244-984, Jul 1971.

[6]A Six-Degree-of-Freedom Addition to the STAR3D Program, Northrop Corporation, TR-240-1375, Apr 1975.

[7]Space Shuttle Flight Control System Data Book/Volume I — Integrated Vehicle, Space Division, Rockwell International Corporation, SD73-SH-0097-1D, Mar 1975 (2 Jun 75 revision).

presented in Figure 3-3, Views A through C. The SRB gimbal commands, the vehicle attitude commands, and the vehicle acceleration references were taken from tables presented in footnote 8 for reference Mission 1, IVBC No. 1 configuration. These data have been reproduced in Table 3-2. The pitch rate table is an interpretation of the values in the pitch attitude table. The roll attitude and roll rate commands were slightly revised for the roll maneuver which starts 6 seconds after lift-off. Steering commands are not transmitted to the SRB thrust-vectored nozzles upon separation of the orbiter.

It was assumed that no special guidance and control mode for inadvertent separations exists. Therefore, the guidance and control equations and commands for the nominal ascent were used for all trajectories calculated in this analysis.

Because of the time limitations imposed on this investigation, no effort was made to include allowance for the effects of either aeroelasticity or the movement and sloshing of the propellants in the math model. Neither of these considerations is absolutely vital to the results of this analysis, and the extent to which their inclusion would have improved the analysis is probably not significant. The mass distribution of the liquid propellants after an unintentional separation was assumed to be the same as for the ascent vehicle during a nominal flight. The effect of the acceleration and orientation of the vehicle after a separation upon the distribution of the liquid propellants was neglected.

The results of the trajectory computations are presented in Appendix B, which contains plots of the flight variables for each case studied for approximately 18 seconds after the occurrence of separation. For the case of accidental SRB separation, the resultant motion is rather violent, and control of the ascent vehicle could not be maintained (Figs. B-2 through B-25). The motion arising as a result of orbiter separation was a more benign aerodynamic angle divergence with times on the order of 10 seconds being required before catastrophic attitudes were attained (Figs. B-26 to B-41). It should be noted that this analysis was made without consideration of SRB nozzle misalignments or a SRB thrust mismatch. Thus, in reality, the divergence should occur more rapidly than this study indicates.

[8] Space Shuttle Flight Systems Performance Data Book/Volume I -- Ascent, Space Division, Rockwell International Corporation, SD73-SH-0178-1B, Dec 1974.

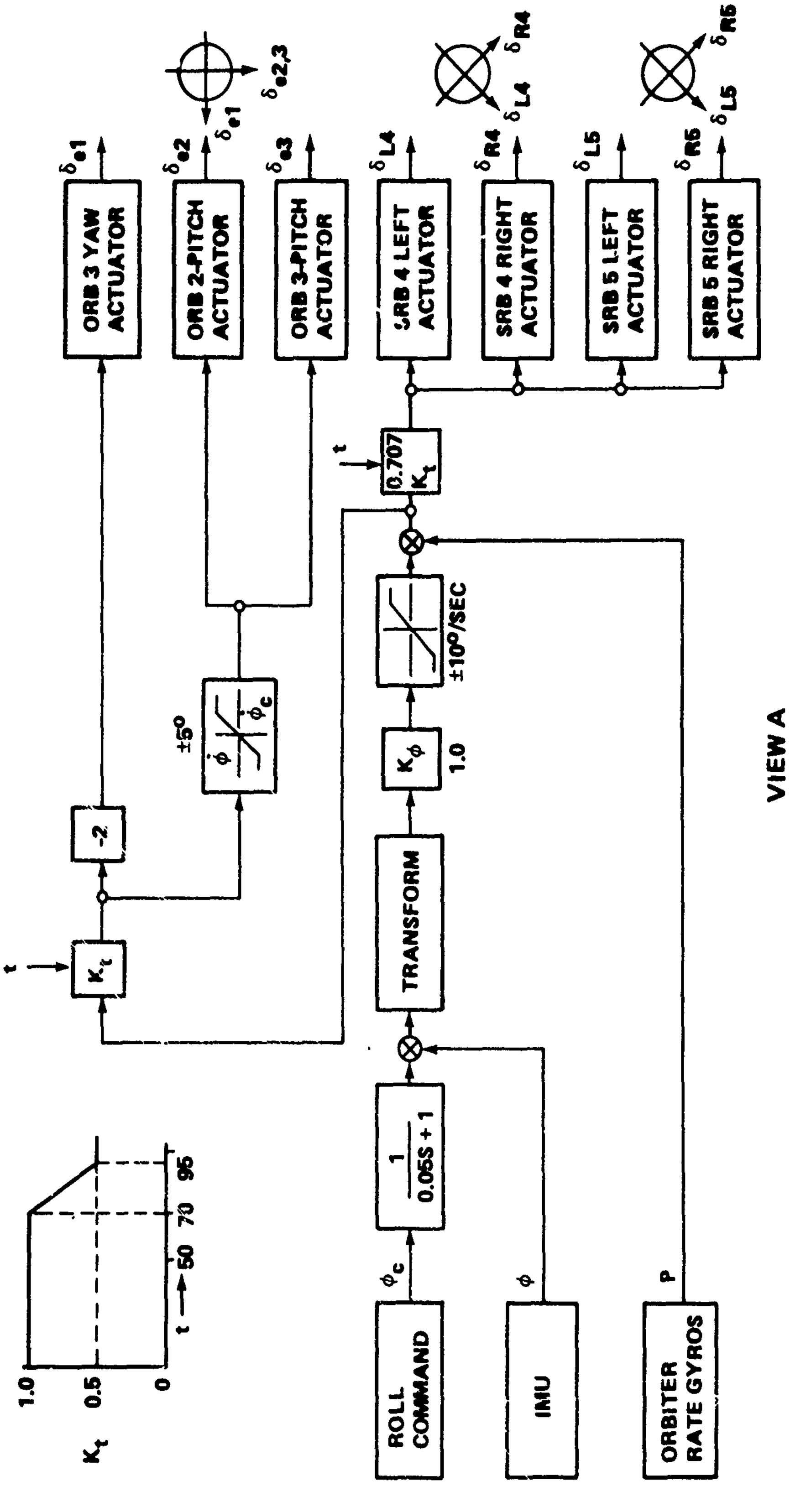

FIGURE 3-3 MATED ASCENT ROLL AXIS CONTROL (Sheet 1 of 3)

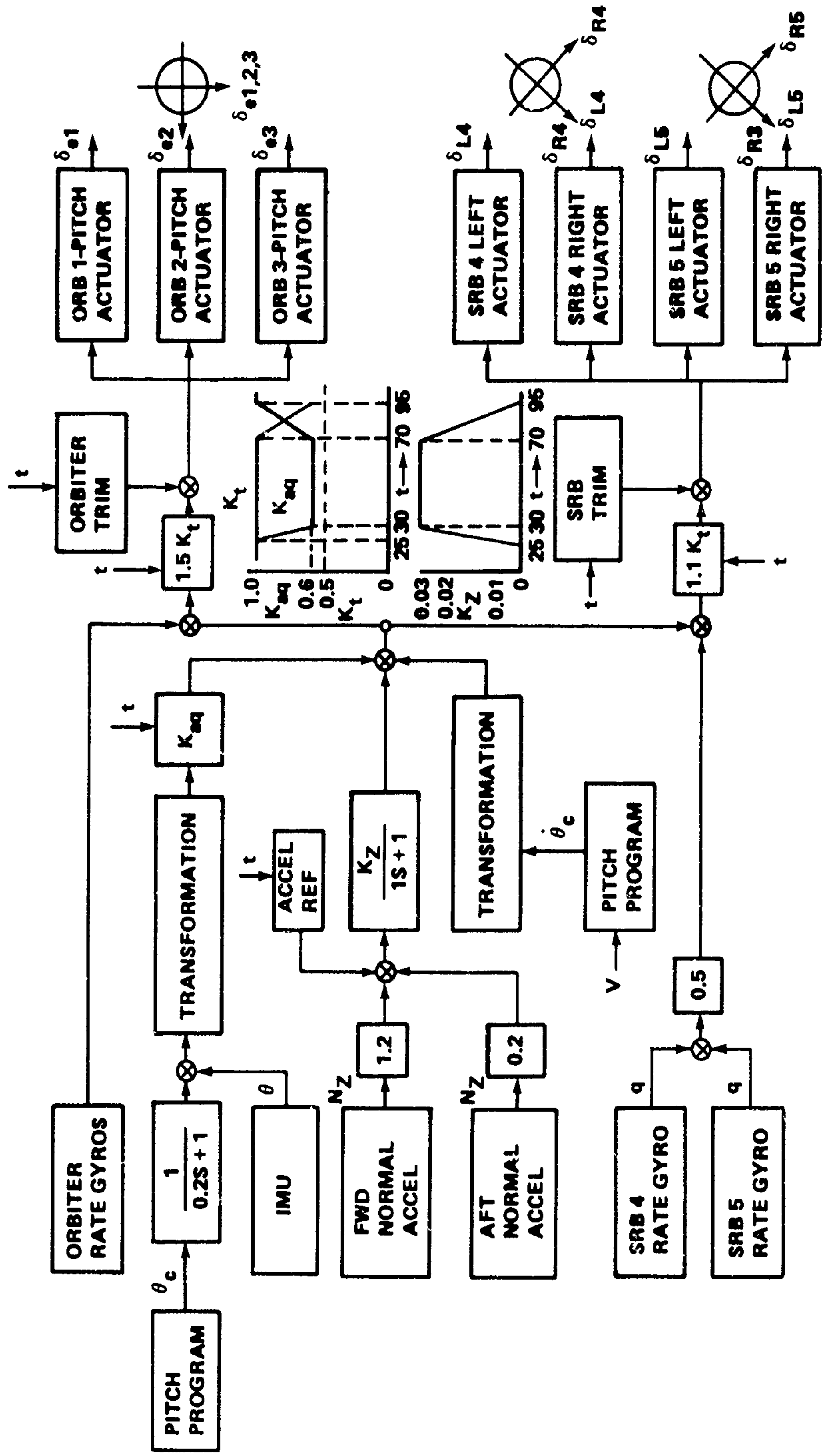

VIEW B

FIGURE 3-3 MATED ASCENT PITCH AXIS CONTROL (Sheet 2 of 3)

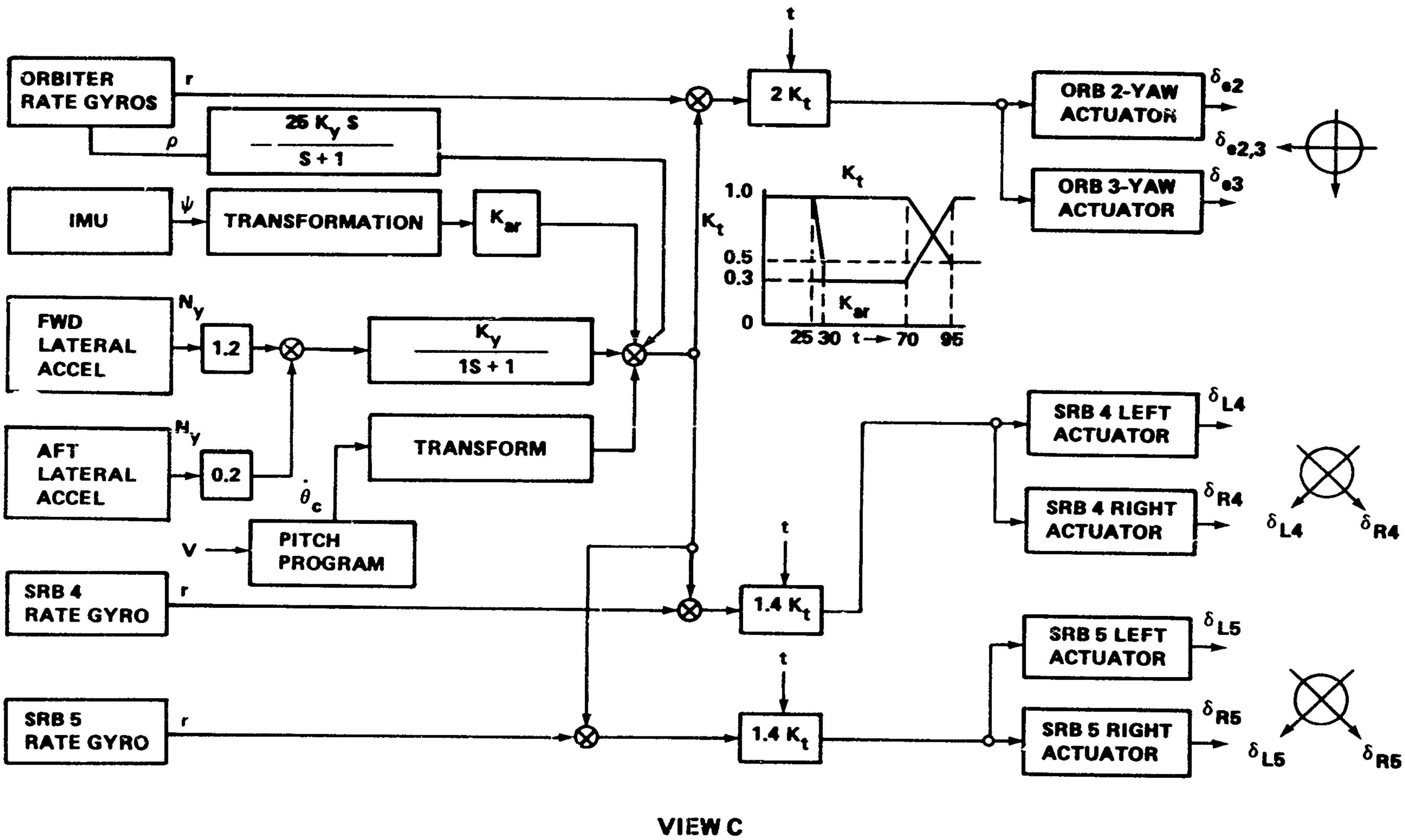

FIGURE 3-3 MATED ASCENT YAW AXIS CONTROL (Sheet 3 of 3)

TABLE 3-2 SRB GIMBAL AND VEHICLE ATTITUDE COMMANDS, MISSION 1
IVBC NO. 1 CONFIGURATION

Time (sec)	SRB Pitch Gimbal (deg)	Time (sec)	Roll Attitude (deg)	Roll Rate (deg/sec)
0.0	-1.3090	0.0	90.00	0.0
2.0	-0.4847	6.0	90.00	0.0
10.0	-0.4241	8.0	97.50	7.5
20.0	-0.5302	10.0	120.00	15.0
30.0	-1.0052	12.0	150.00	15.0
36.0	-1.1017	14.0	172.50	7.5
44.0	-1.6524	16.0	180.00	0.0
52.0	-0.4014	20.0	180.00	0.0
58.0	-1.1802	30.0	180.00	0.0
78.0	-0.0428	40.0	180.00	0.0
96.0	0.5345	56.0	180.00	0.0
110.0	0.7278	60.0	180.00	0.0
112.0	0.6755	62.0	180.00	0.0
116.0	0.0	70.0	180.00	0.0
130.0	0.0	105.0	180.00	0.0
		115.0	180.00	0.0
		117.0	180.00	0.0
		120.0	180.00	0.0
		150.0	180.00	0.0

TABLE 3-2 SRB GIMBAL AND VEHICLE ATTITUDE COMMANDS, MISSION 1
IVBC NO. 1 CONFIGURATION — Continued

Relative Velocity (fps)	Pitch Attitude (deg)	Vehicle Heading (deg)	Pitch Rate (deg/sec)	Time (sec)	Normal Load Factor (g's)	Side Load Factor (g's)
0.0	90.0000	-90.0000	0.0	0.0	0.0690	0.0006
100.447	90.0000	90.0120	0.0	20.0	0.0677	-0.0111
183.790	84.1213	90.0200	1.369	24.0	0.0791	-0.0117
324.734	75.5453	90.0323	1.369	30.0	0.1090	-0.0120
430.447	73.6010	90.0408	0.475	36.0	0.1356	-0.0123
533.611	70.8694	90.0496	0.475	40.0	0.1631	-0.0112
629.792	68.6142	90.0588	0.475	44.0	0.1918	-0.0068
925.516	62.8789	90.0942	0.475	50.0	0.2103	-0.0093
1230.564	57.7617	90.1404	0.475	54.0	0.2296	-0.0112
1442.417	53.6101	90.1662	0.475	56.0	0.2470	-0.0069
1731.019	48.7288	90.1946	0.475	58.0	0.2530	-0.0059
2094.415	44.0816	90.2265	0.475	60.0	0.2454	-0.0036
2539.578	39.3671	90.2630	0.475	64.0	0.2499	-0.0016
3073.764	34.7397	90.3052	0.475	70.0	0.2237	0.0021
3669.917	30.5038	90.3542	0.475	74.0	0.1944	0.0030
4133.099	28.5373	90.3957	0.475	80.0	0.1733	0.0031
4269.988	27.9630	90.4104	0.475	90.0	0.1354	0.0016
4454.594	26.8114	90.4410	0.475	96.0	0.1240	0.0008
4529.420	26.1538	90.4733	0.475	100.0	0.1226	0.0010
5350.000	20.0000	90.7722	0.475	122.0	0.2241	0.0009

CHAPTER 4

STRESS ANALYSIS OF SPACE SHUTTLE DURING DESTRUCT

This chapter contains dynamic response calculations and supporting stress analyses of the Space Shuttle during the following conditions:

1. Destruct by linear-shaped charges on two solid rocket boosters (SRB's).

2. Destruct following loss of orbiter.

3. Destruct following loss of one SRB.

4. Delta time to initiate destruct following loss of orbiter or SRB.

The stress calculations indicate that for clamshell opening of SRB

- Catastrophic rupture of the LH_2 tank is highly probable for destruct by two SRB's at 10, 50, and 100 seconds into flight. Destruct is questionable at lift-off.

- Destruct following loss of orbiter is the same as above.

- Catastrophic rupture of the LH_2 tank is highly probable for destruct by one SRB at 50 and 100 seconds into flight. Destruct is marginal at 10 seconds and improbable at lift-off.

for fragmentation of the SRB

- Fragmentation damage to LH_2 tank is negligible.

- Blast pressure will buckle the LH_2 tank in all cases, but the degree of fluid dispersal is difficult to predict.

for inadvertent separations

- Breakup of the cluster is likely to occur two seconds after loss of one SRB or 16.5 seconds after loss of the orbiter at 50 seconds into flight. Longer survival times are predicted for inadvertent separations at lift-off, 10, and 100 seconds.

Section I. DYNAMIC ANALYSIS OF ET DURING NORMAL DESTRUCT AND DESTRUCT FOLLOWING LOSS OF ORBITER

INTRODUCTION

During destruct, the linear-shaped charge on the outboard side causes the SRB's to open up in a clamshell manner, thereby generating a large lateral thrust load as illustrated in Figure 4-1. The SRB's are connected to the external tank (ET) at stations X_T 985 and X_T 2058. An elastic dynamic response analysis, discussed in the following, indicates that the joints and frames will clearly be overloaded. The purpose of this analysis is to estimate large deformation of the ET using simplified dynamic plasticity models so that judgments of most probable failure modes can be made. An assessment is then made of the probability of destruct to the LH_2 tank. In Figure 4-1, the inboard side of an SRB has a standoff distance of about 12 inches from the outboard side of the ET. Thus, during the early part of the impulse, the thrust load is reacted at joints X_T 985 and X_T 2058, as illustrated in Figure 4-2.

During destruct, the SRB's should be propelled into the LH_2 tank and crush it inward until it ruptures as a result of excessive deformation or excessive internal pressure buildup. Line contact of the SRB's with the ET would be desirable since the ring frames in the LH_2 tank between stations X_T 985 and X_T 2058 are rather weak (Fig. 4-3). Since the SRB is made in several spool piece sections with pinned circumferential joints, breakup of the SRB into large sections, as illustrated in Figure 4-3, View B, is another possibility. A third possibility is puncture of the LH_2 tank by the concentrated loads at the aft joint struts. Hence, the destruct mechanism depends on the probable mode of failure of the SRB and ET structures, particularly the joints.

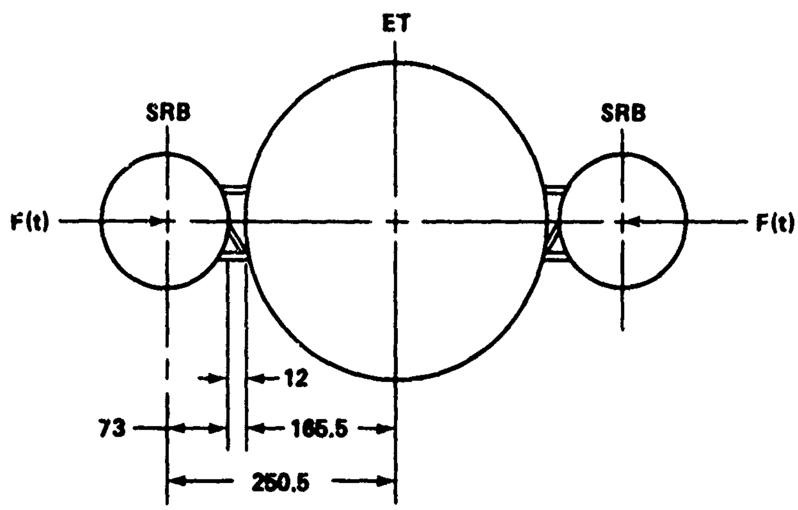

FIGURE 4-1 ET/SRB GEOMETRY

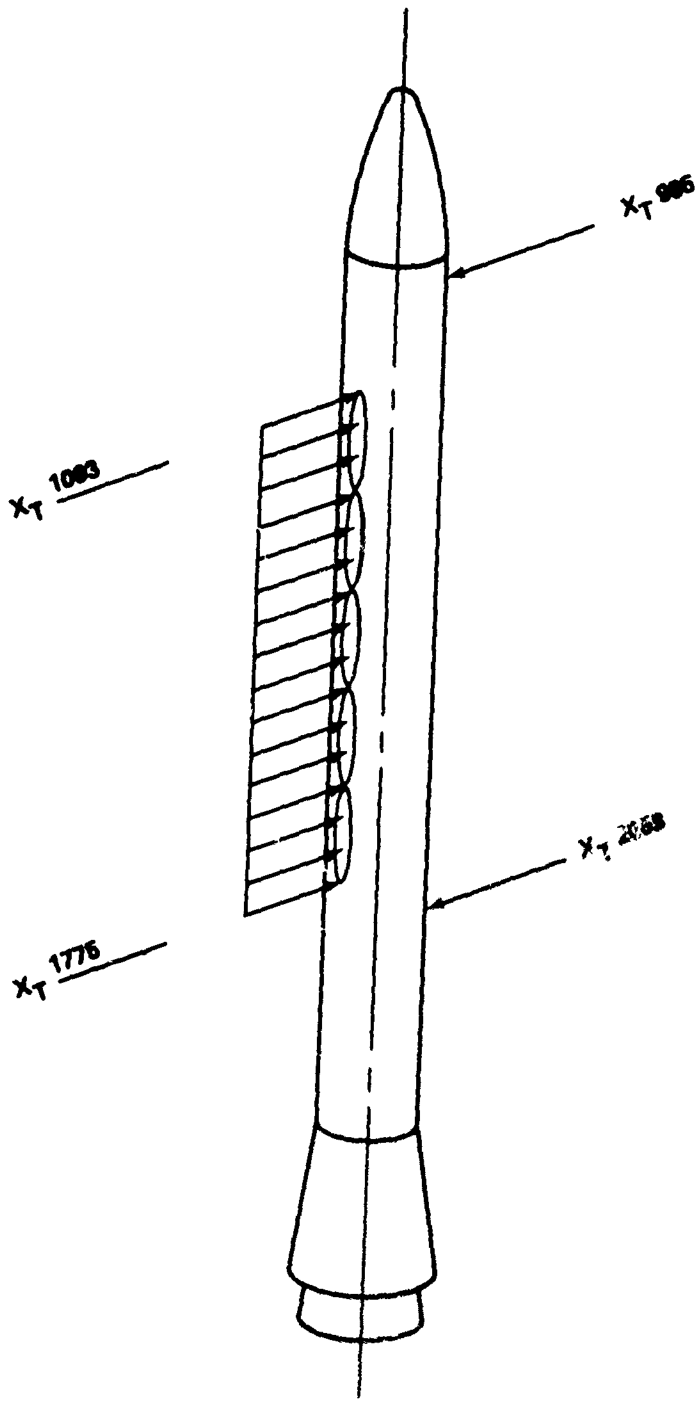

FIGURE 4-2 THRUST FROM CLAMSHELL RUPTURE

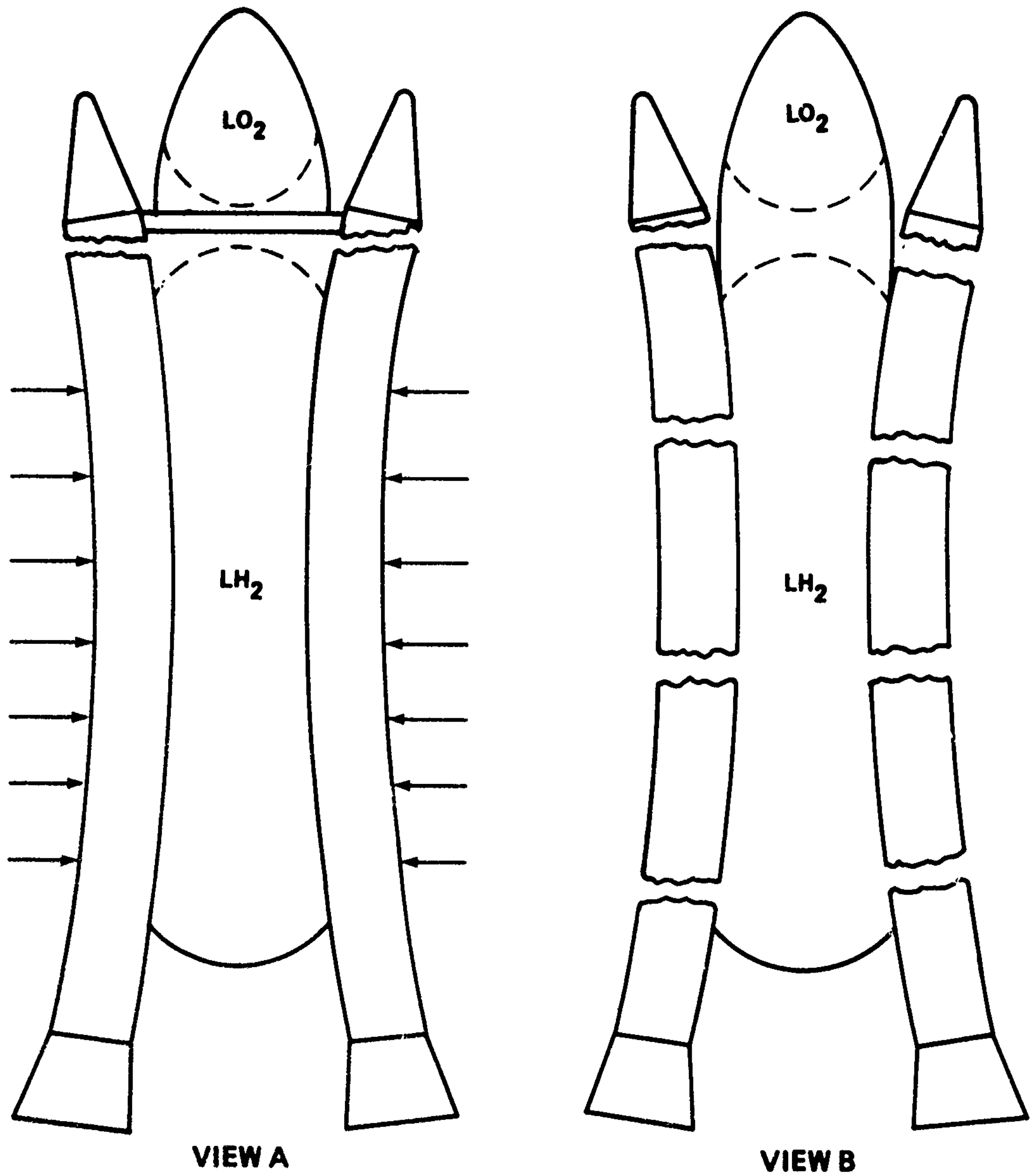

FIGURE 4-3 VARIOUS DESTRUCT MODES

DYNAMIC ELASTIC RESPONSE OF SRB'S TO LATERAL THRUST

A dynamic response analysis was made considering the SRB's as beams elastically supported at stations X_T 985 and X_T 2058 (Fig. 4-4). The forces at the joints and bending stresses in the SRB's were estimated for the thrust generated by a clamshell-type rupture. The SRB shell was modeled using beam-type finite elements. Detailed finite-element models, using 2-D plate and 3-D isoparametric finite elements, of the ET and SRB structures were made in the vicinity of the joints to estimate the local stiffness and deduce equivalent spring constants. See Appendices C, D, E, and F. Scalar springs were then used at the joints to reduce the number of degrees of freedom and hence reduce the computer running time to tolerable limits. Sufficient accuracy of the results was imperative for this study since the response was dictated by the fundamental mode. In order to estimate the spring constants, two diametrically opposed radial loads were applied to the ET frame X_T 985, as described in Appendix E. The resulting radial deflection was used to compute the spring constant of 2.016×10^6 lb/in. A single equal and opposite radial load applied to the SRB forward joint produced a deflection corresponding to a spring constant of 0.819×10^6 lb/in. The equivalent spring constant at the joint was deduced by considering two springs in series. This resulted in an equivalent spring constant of 0.582×10^6 lb/in. Similarly, the spring constant for the aft joint was computed to be 0.585×10^6 lb/in.

The SRB design is shown in Figure 4-5. The aft part of the SRB shell is D6AC steel with a nominal thickness of 0.52 inch and is essentially a pressure vessel designed to carry internal pressure as well as structural loads. There are nine circumferential joints holding the SRB together. A typical joint is shown in Figure 4-6. The linear-shaped charge used for destruct runs on the outboard side between stations X_T 1093 and X_T 1775. The forward skirt section is 2219 aluminum.

The lateral thrust-time curves for destruct at T = 0, 10, 50, and 100 seconds into flight are shown in Figure 4-7. The peak values of thrust range from 8.6×10^6 lb to 27.5×10^6 lb. The pulse duration is on the order of 40 to 50 msec. Figure 4-8 shows the predicted forces (F1 and F2) at the forward and aft joints (X_T 985 and X_T 2058) and the velocity at the joints (V_1 and V_2) as a function of time during and after the impulsive thrust that occurs during destruct at T = 0. The actual force felt by the forward and aft support joints is small in comparison to the peak thrust load. This is due to the fact that the pulse duration τ_{max} is small in comparison to the fundamental period T_N (first mode) of the SRB and its support system. Ratios of τ_{max}/T_N are on the order of one-third. However, since the retardation forces at the joints are small (in comparison to the total lateral thrust), the SRB's are accelerated rather easily, and the velocity builds up as illustrated. The force and velocity are highest at the forward joint since the centroid of the lateral thrust force is forward of the SRB center of gravity. Figure 4-9 shows a similar plot for destruct at T = 100 seconds. Similar calculations were made for destruct at 10 and 50 seconds. The purpose of these calculations was to determine expected joint failure, as well as corresponding SRB velocity at the joints (V_{R1} and V_{R2}) at the time of failure. The kinetic energy associated with these velocities was available for destruct of the LH_2 tank. In addition, bending stresses were calculated in the SRB to assess the probability of SRB failure. Typical plots of maximum bending stress versus time are shown in Figure 4-10. The question to be answered was, "What is the most probable failure mode of the ET and SRB's from this load environment?" Static analyses of the frames and attachment joints in the ET and SRB were made to provide some guidance.

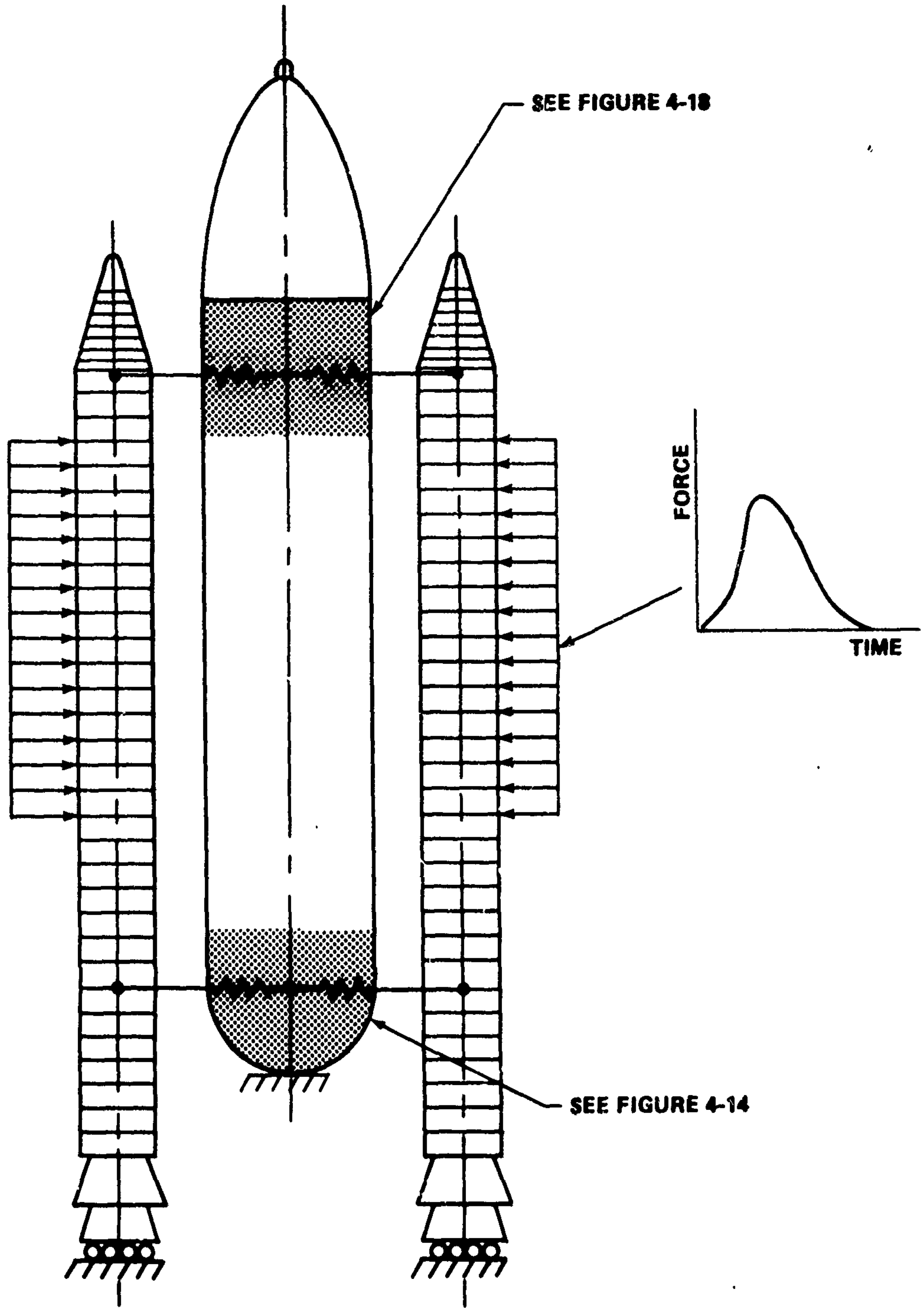

FIGURE 4-4 FINITE ELEMENT MODEL FOR RESPONSE DUE TO LATERAL THRUST

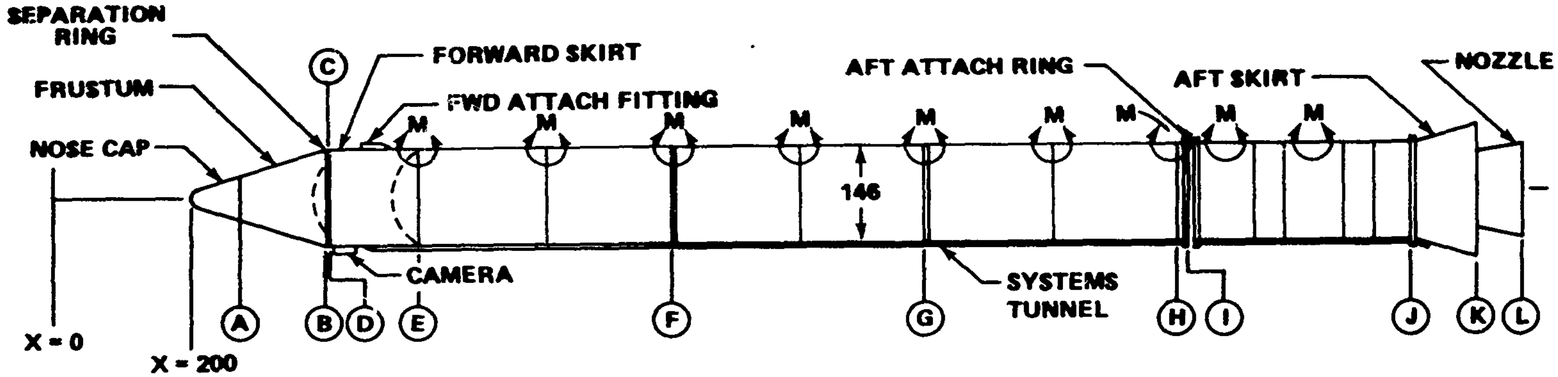

LOC.	DESCRIPTION	STATION
A	NOSE CAP/FRUSTUM SEPARATION PLANE	275.00
B	FRUSTUM/SEPARATION RING INTERFACE	394.875
C	SEPARATION RING SEPARATION PLANE	398.00
D	SEPARATION RING/FORWARD SKIRT INTERFACE	401.00
E	FORWARD SKIRT/SRM INTERFACE (℄ HOLES)	523.83
F	SRM FORWARD/CENTER 1 SEGMENT JOINT	851.48
G	SRM CENTER 1/CENTER 2 SEGMENT JOINT	1171.48
H	SRM CENTER 2/AFT SEGMENT JOINT	1491.48
I	SRB/EXTERNAL TANK ATTACH STATION	1511.00
J	SRM/AFT SKIRT INTERFACE (℄ HOLES)	1837.087
K	SRB AFT SKIRT AFT FACE	1930.637
L	SRM NOZZLE EXIT PLANE	
M	JOINT	

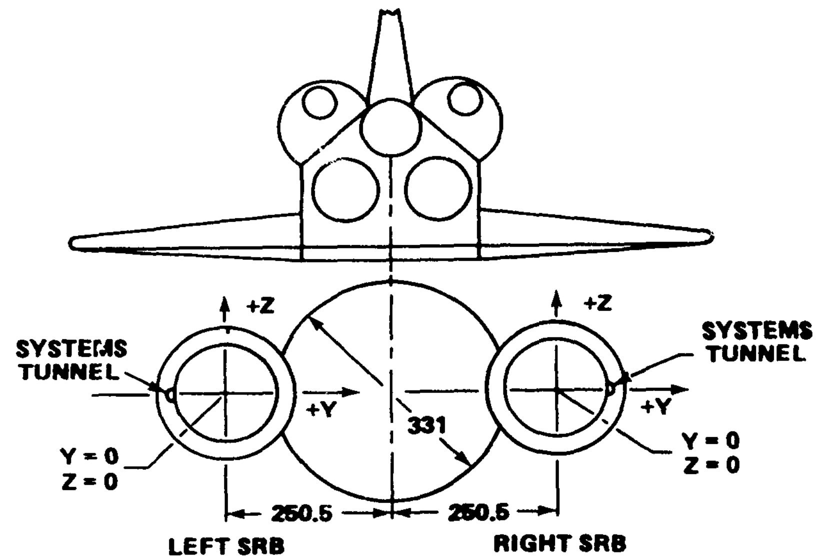

FIGURE 4-5 SRB DESIGN

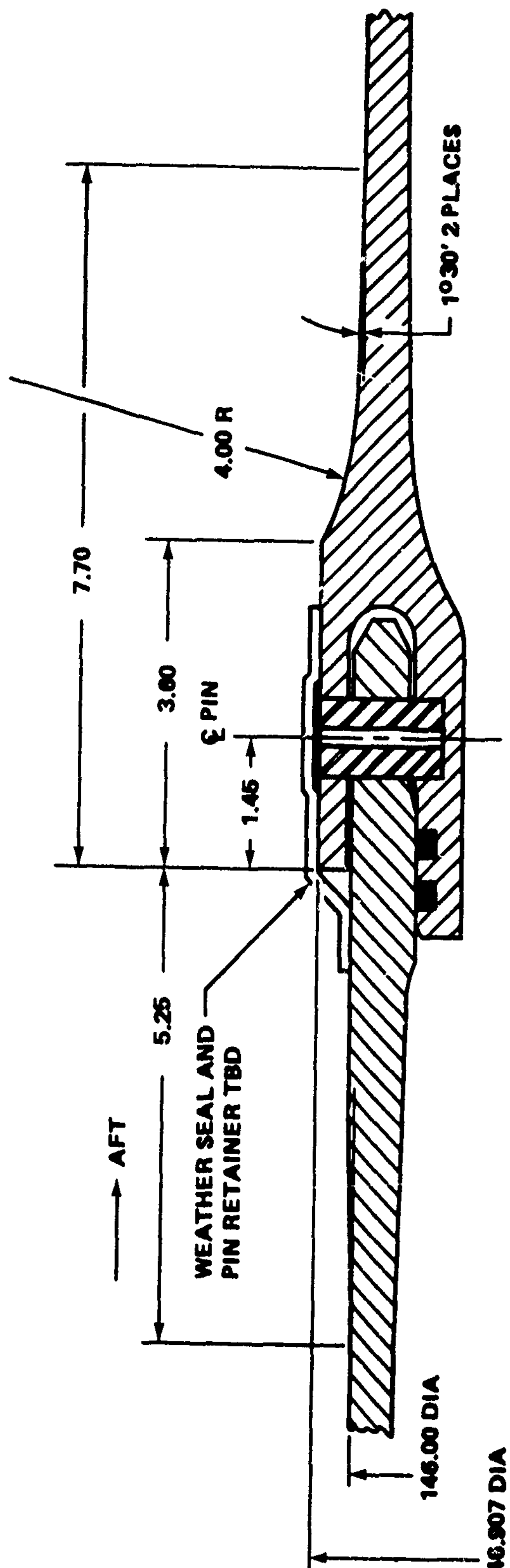

FIGURE 4-6 TYPICAL CIRCUMFERENTIAL JOINT

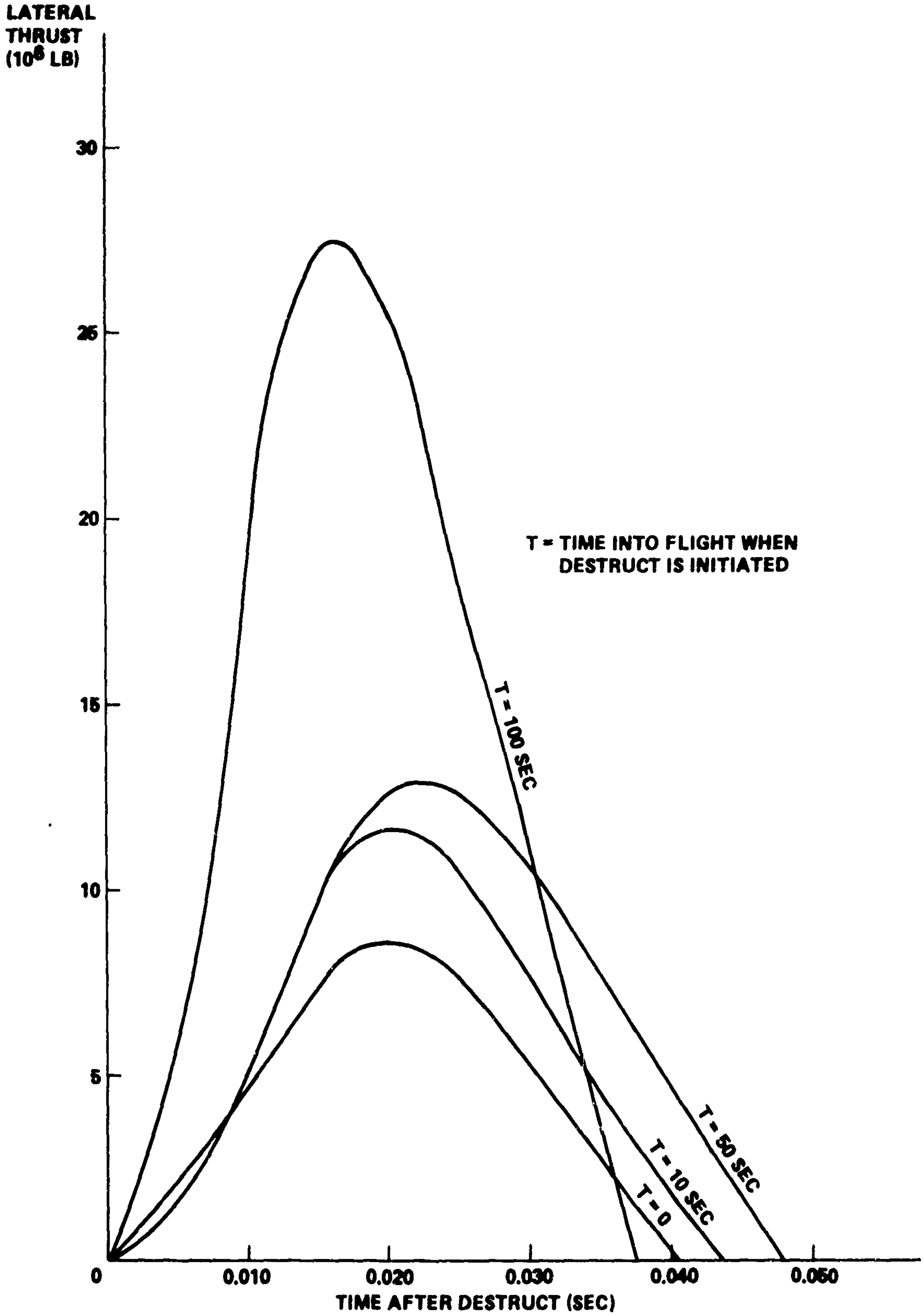

FIGURE 4-7 LATERAL THRUST VS. TIME DUE TO CLAMSHELL RUPTURE OF SRB

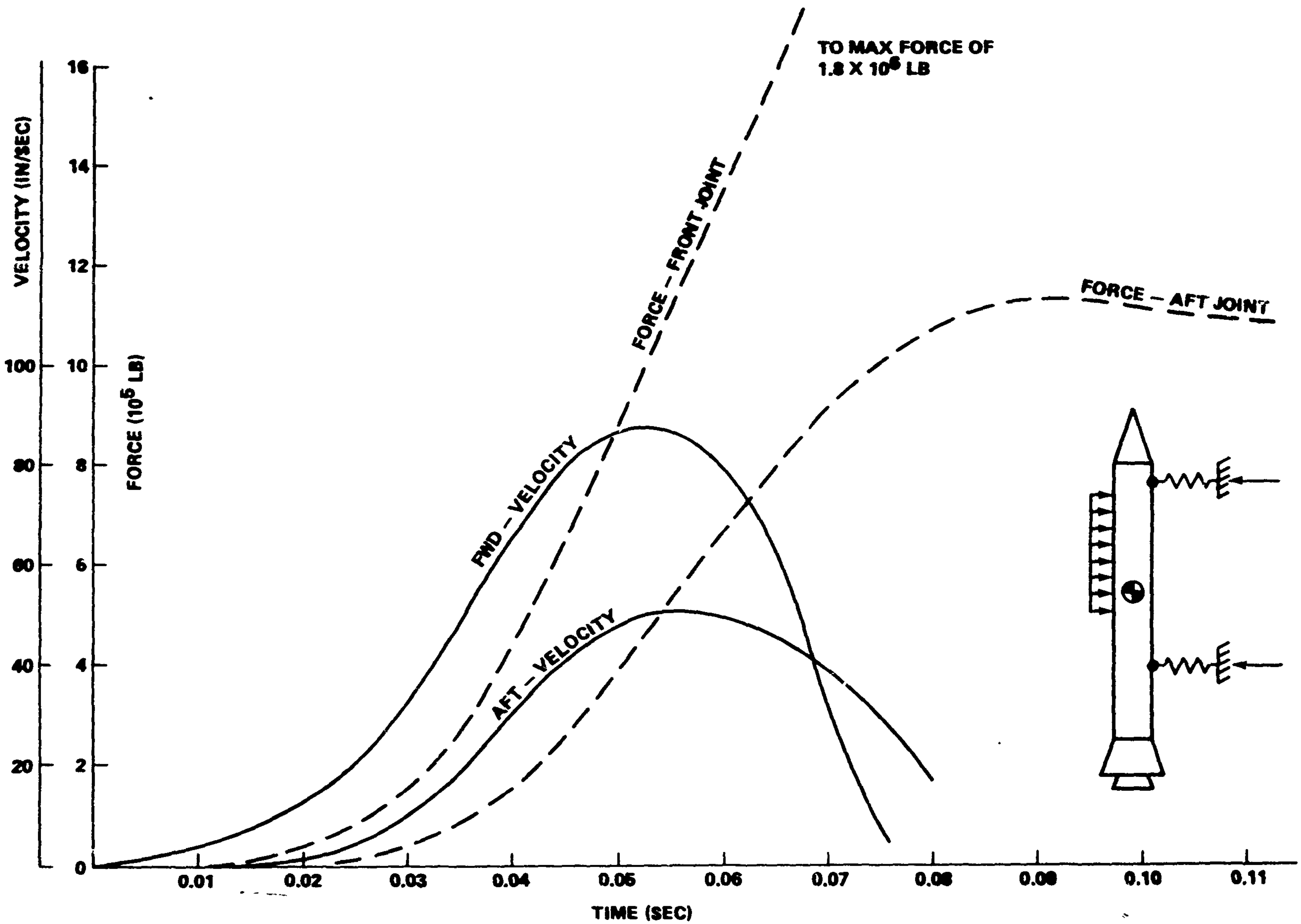

FIGURE 4-8 FORCE AND VELOCITY AT FORWARD AND AFT JOINT VS. TIME AFTER DESTRUCT AT LIFT-OFF (T = 0)

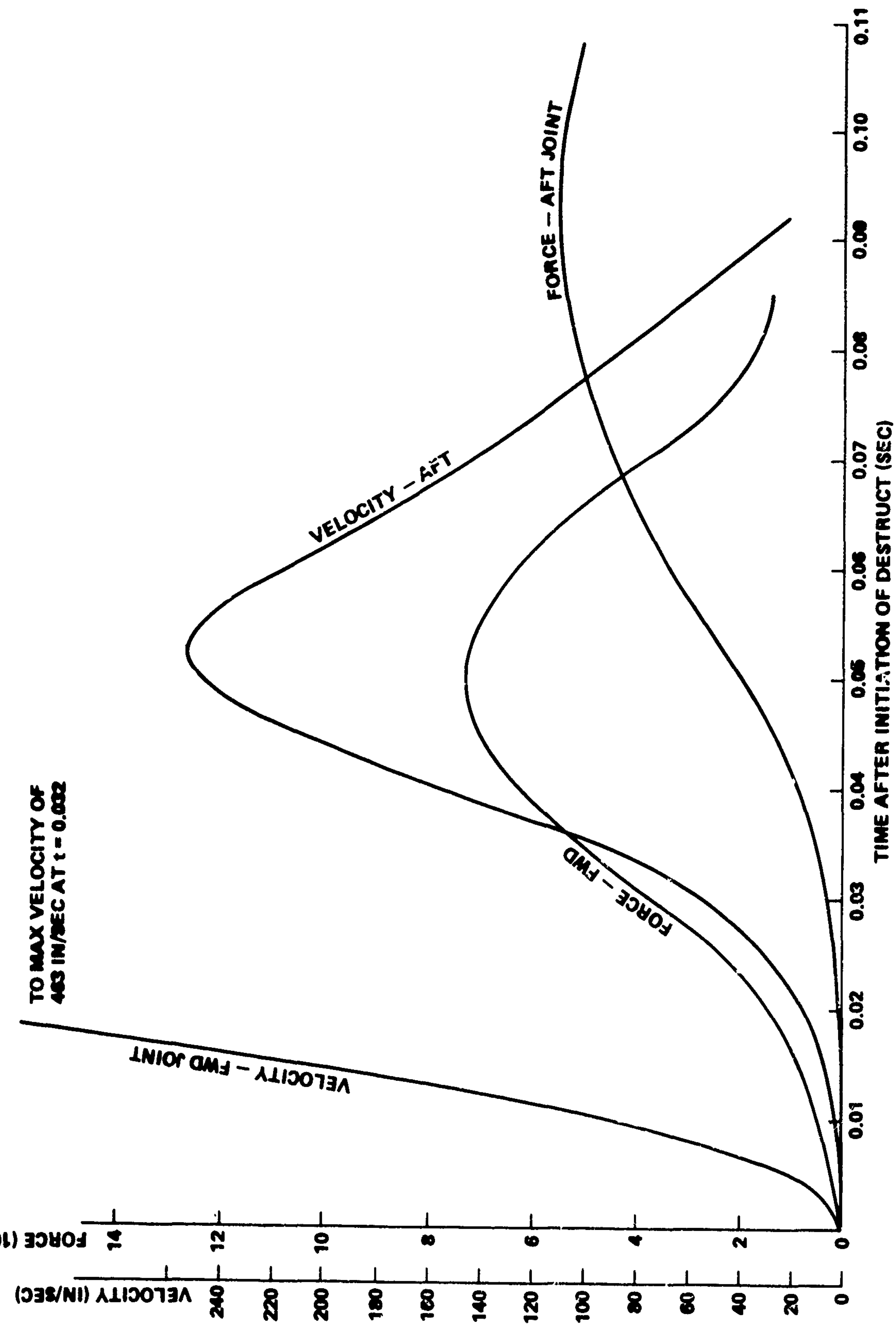

FIGURE 4-9 FORCE AND VELOCITY AT FORWARD AND AFT JOINT VS. TIME AFTER DESTRUCT (T = 100 SEC)

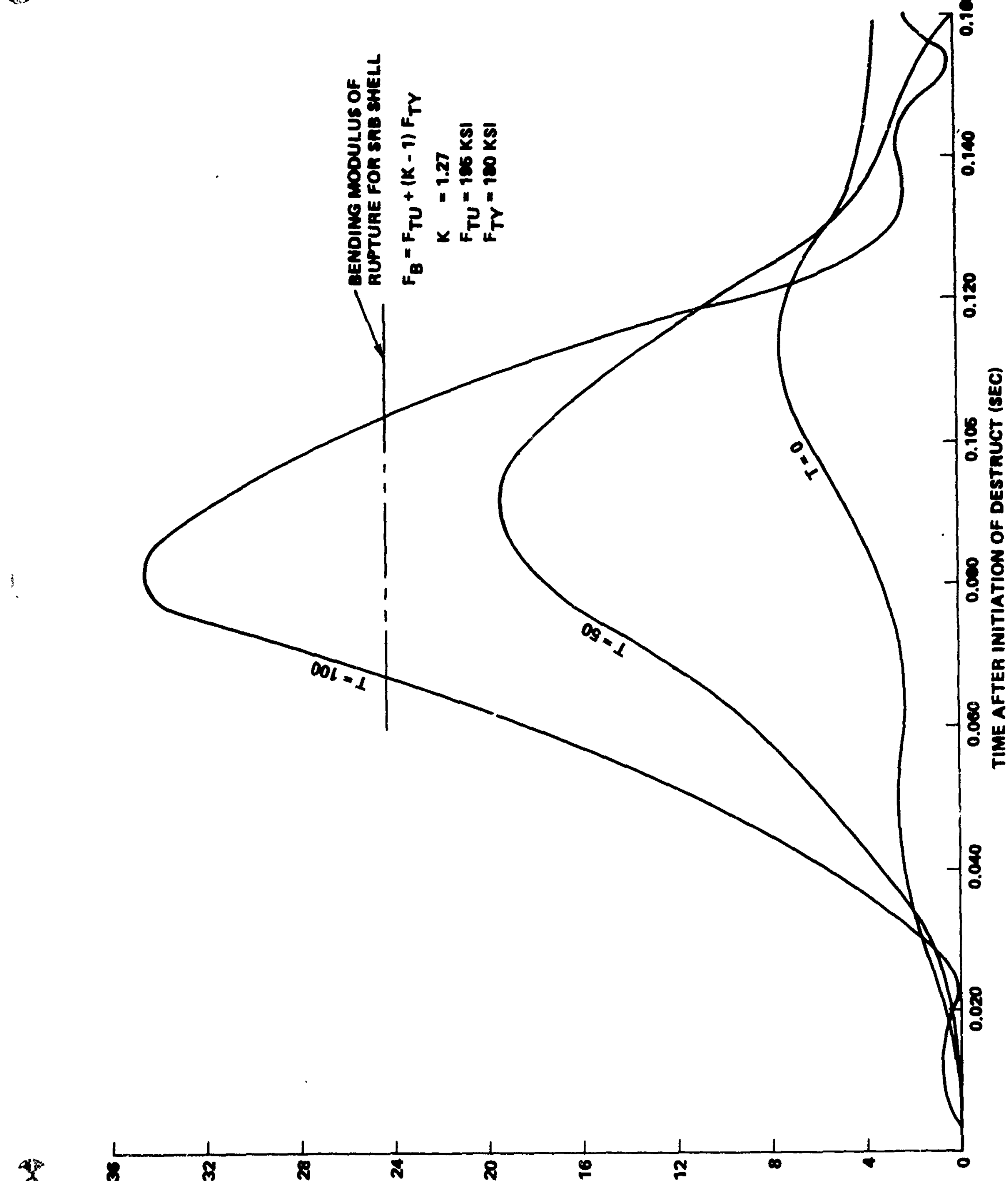

FIGURE 4-10 MAXIMUM BENDING STRESS IN SRB VS. TIME FOLLOWING INITIATION OF DESTRUCT

STATIC ANALYSIS OF AFT JOINT

A finite element model was developed (Appendix C) to predict the elastic stresses in the frame at X_T 2058 and the surrounding skin in the LH_2 tank. The analysis was made for lateral loads directed inboard from the lateral thrust as illustrated in Figure 4-11. The analysis is conservative from a destruct viewpoint since the loads on the frame from the orbiter were not considered. Hence, the load required to collapse the frame will be overestimated.

The details of the joint design are shown in Figure 4-12. The ET frame is a massive built-up beam constructed of 2024T8511 and 2219T8511 aluminum with cross section dimensions as shown in Figure 4-13. The degree of sophistication in the finite-element model is shown in Figure 4-14 which illustrates the deformation for equal and opposite lateral loads as shown in Figure 4-11. The analysis indicates that yielding in the frame will occur for a total lateral load $P = 1.42 \times 10^6$ lb. The corresponding inward deflection is 2.13 inches which gives an equivalent spring constant of $K = 0.666 \times 10^6$ lb/in. If we assume rigid-plastic stress-strain behavior, the collapse load is estimated to be on the order of 1.8×10^6 lb. Collapse load in this sense is defined by limit analysis as the load required to cause instability by the formation of plastic hinges. Hence, it appears that this frame collapse load is very large in comparison to the limit design load of 290,000 pounds indicated in the loads manual for the HE258R(2) condition.

The stress analysis of the aft SRB ring frame from the destruct load reactions in the attachment truss was done using the BOSOR4 model described in Appendix D. The total aft attachment truss reaction load of P was divided equally into loads of P/2 in each of the parallel struts, as shown in Figure 4-11. In addition, an internal pressure of 885 psig was applied to the rocket motor casing, representing a nominal pressure over the first 25 seconds of flight.

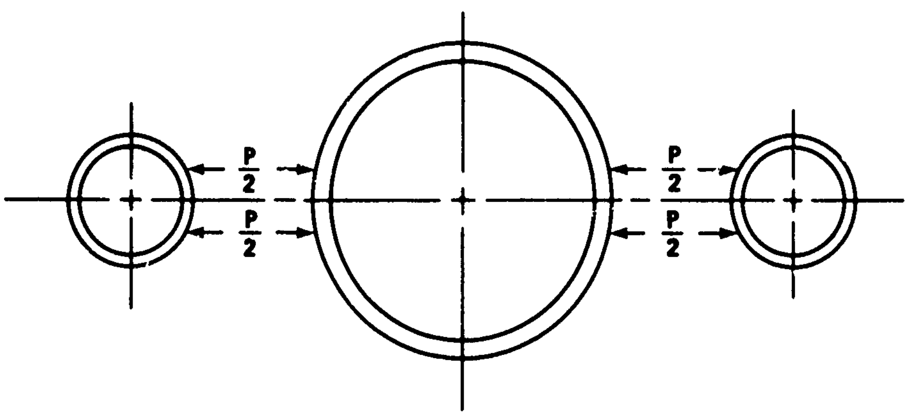

FIGURE 4-11 LATERAL LOADS DIRECTED INBOARD FROM LATERAL THRUST

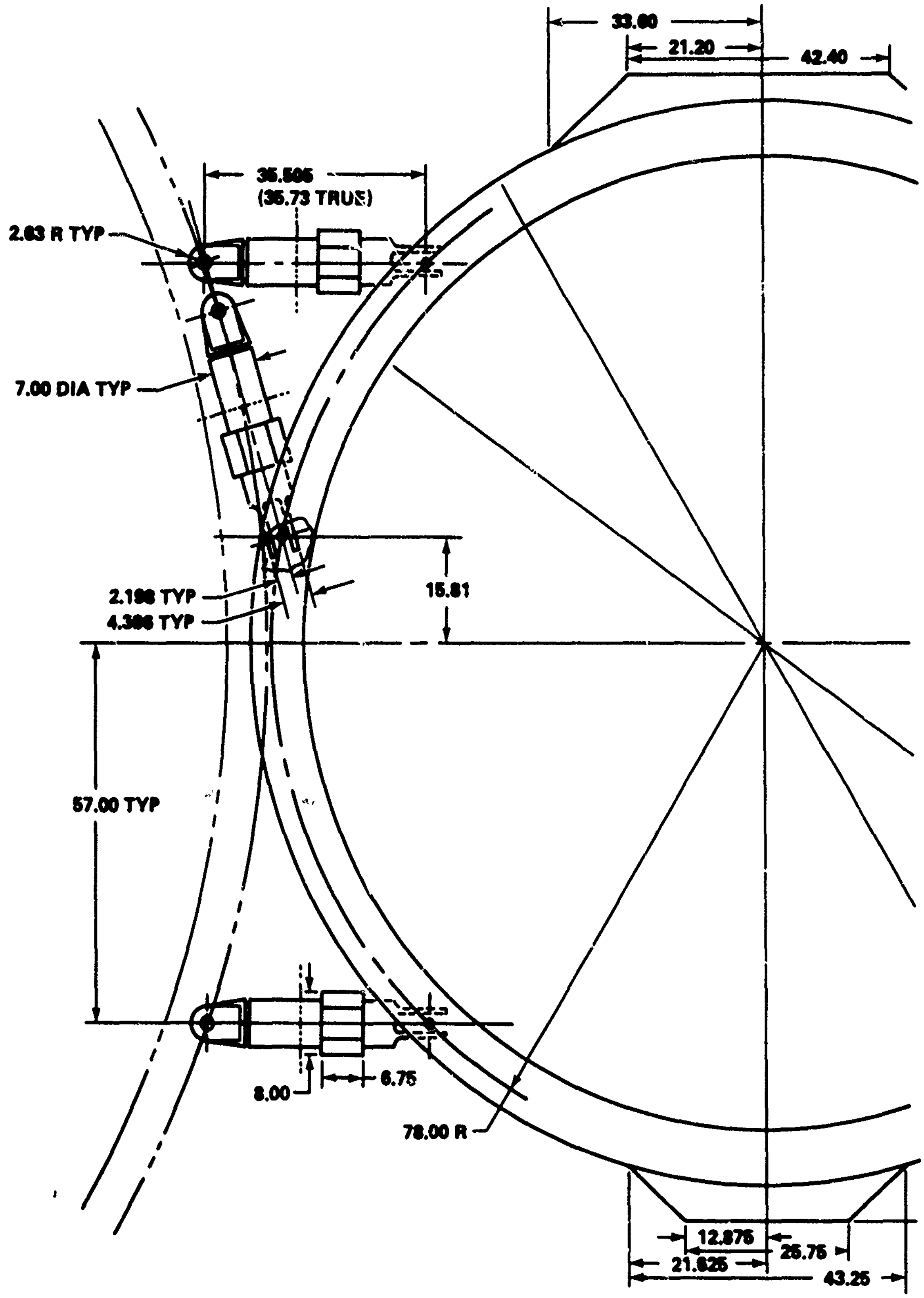

FIGURE 4-12 JOINT DESIGN

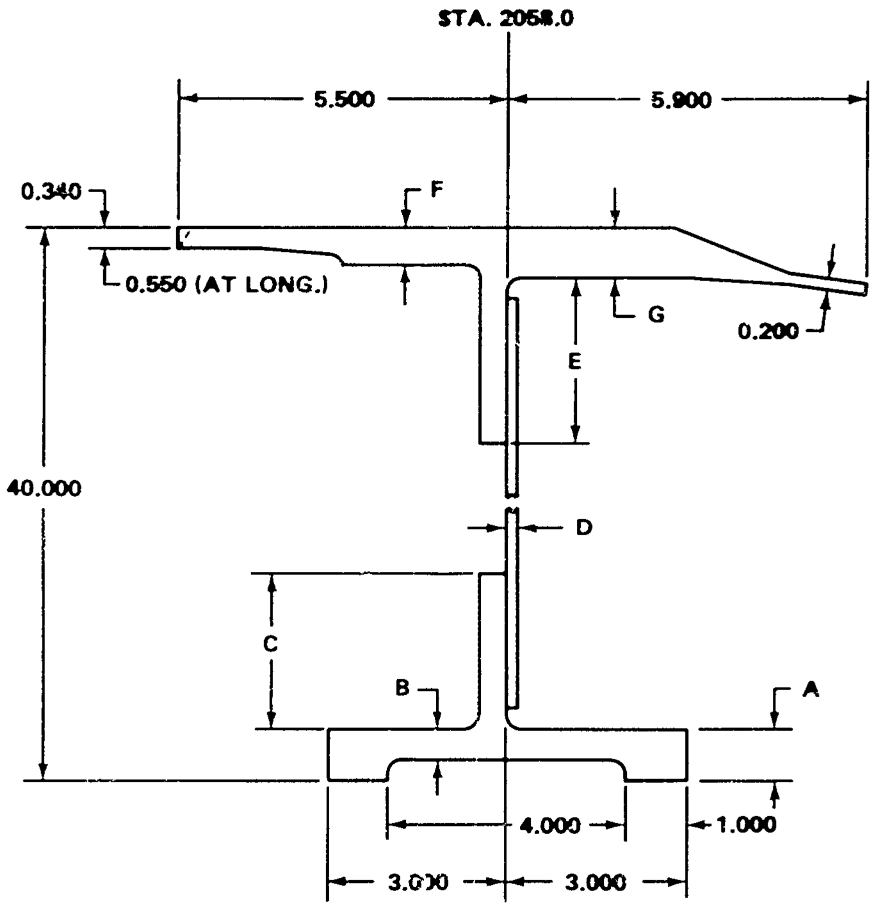

STA NO.	DIM. A	DIM. B	DIM. C	DIM. D	DIM. E	DIM. F	DIM. G
1	0.900	0.530	2.77	0.157	2.94	0.630	0.870
2	1.200	0.530	2.94	0.125	2.94	0.630	0.870
3	1.200	0.530	2.77	0.125	2.61	0.630	1.086
4	1.200	0.530	2.94	0.280	2.94	1.575	1.575
5	1.200	0.700	2.94	0.310	3.44	1.700	1.700
6	1.200	0.900	2.94	0.286	3.40	1.583	1.583
7	1.200	0.900	2.94	0.286	3.44	1.350	1.350
8	1.300	1.200	2.810	0.125	2.94	0.925	0.925
9	1.200	1.200	2.810	0.125	2.94	0.630	0.870
10	1.200	0.900	2.94	0.262	3.190	1.350	1.350
11	1.200	0.836	2.94	0.267	2.94	1.110	1.190
12	1.200	0.530	2.94	0.250	2.94	0.630	0.870
13	1.200	0.530	2.81	0.177	2.61	0.630	0.870
14	1.200	0.530	2.94	0.140	2.94	0.630	0.870
15	1.200	0.530	2.94	0.110	2.94	0.630	0.870
16	0.900	0.900	2.81	0.085	2.94	0.630	0.870
17	0.900	0.900	2.81	0.085	2.94	0.630	0.870
18	1.200	0.530	2.94	0.110	2.94	0.630	0.870
19	1.200	0.530	2.94	0.140	2.94	0.630	0.870
20	1.200	0.530	2.61	0.177	2.61	0.630	0.870
21	1.200	0.530	2.94	0.250	2.94	0.630	0.870
22	1.200	0.836	2.94	0.267	2.94	1.110	1.190
23	1.200	0.900	2.94	0.262	3.19	1.350	1.350
24	1.200	1.200	2.81	0.125	2.94	0.630	0.870
25	1.200	1.200	2.81	0.125	2.94	0.925	0.925
26	1.200	0.900	2.94	0.286	3.44	1.350	1.350
27	1.200	0.900	2.94	0.286	3.40	1.583	1.583
28	1.200	0.700	2.94	0.310	3.44	1.700	1.700
29	1.200	0.530	2.94	0.280	2.94	1.575	1.675
30	1.200	0.530	2.44	0.220	2.44	1.110	1.110
31	1.200	0.530	2.44	0.220	2.44	0.630	0.870
32	1.060	0.715	2.56	0.220	2.88	1.165	1.285

FIGURE 4-13   RING FRAME CROSS SECTION – X_T 2058

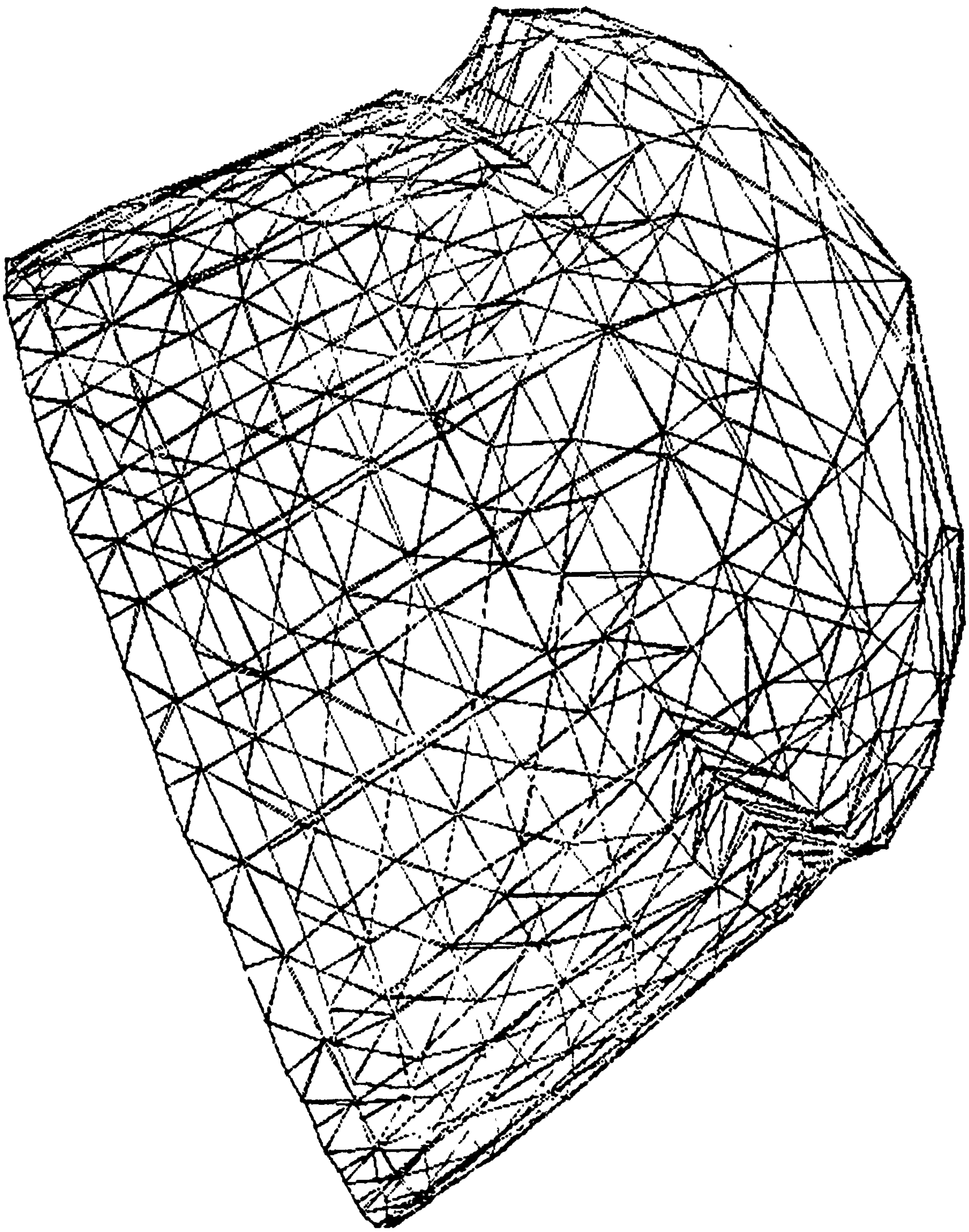

FIGURE 4-14 STATIC ANALYSIS OF ET RING FRAME LOCATED AT STATION X_T 2058 DESTRUCT OF TWO SRB'S CLAMSHELL OPENING

In order to find the side thrust load necessary to cause yielding in the ring frame, four cases were run as follows. The first three cases were for lateral loads of P = 290,000; 500,000;and 2.5 × 10^6 lb with an internal pressure of 885 psi superimposed. The fourth case was for internal pressure only. The resulting maximum effective stress in the ring frame is plotted versus total lateral load P in Figure 4-15. The rings and skin are made of D6AC steel with the following properties:

F_{tu} = 195,000 psi

F_{ty} = 180,000 psi

F_{su} ≈ 117,000 psi

ε_{ult} = 0.10 in/in

From Figure 4-15, it appears that yielding will occur at about P = 680,000 pounds. The corresponding lateral deflection at the point of load is 0.14 which yields an equivalent spring constant of K = 4.86 × 10^6 lb/in. The collapse load is estimated to be about 850,000 pounds.

Hence, finite-element models of the aft SRB frame and aft ET frame indicate that the SRB is the weaker of the two for lateral thrust loads during destruct. Pin failure in the struts connecting the SRB's to the ET must also be considered. Figure 4-12 shows the method of attachment between the SRB and ET. The 2.25-inch diameter pin has an estimated pin bending capability of about 575,000 pounds. Since there are two pins, the failure load is on the order of 1,150,000 pounds. Hence, it appears that collapse of the aft SRB is the probable failure mode. Compression failure of the struts is also another possibility, but design data for this were not available. The struts must have an ultimate strength of at least 1.4 × 290,000 or 406,000 lb.

STATIC ANALYSIS OF FORWARD JOINT

Static analyses were also made of the forward joint for thrust loads, as indicated in Figure 4-16. Analysis of the ET frame (X_T 985) is given in Appendix E. Figure 4-17 shows a schematic of the frame at X_T 985 with surrounding skin and intermediate frames in the intertank region. The frame is a built-up I beam with chords fabricated from 7075 - T73517 aluminum. The SRB cross beam is designed to carry the radial loads from the SRB's during boost. The finite element model of the intertank region showing deformation of the frame and skin resulting from equal and opposite radial loads is shown in Figure 4-18. The analysis indicates that the bulk of the radial load is carried by the cross beam in compression. An approximate analysis indicates that elastic buckling of the cross beam occurs for a radial load of 550,000 pounds.

Once the cross beam buckles, the surrounding frame can only support a radial load P of about 200,000 pounds. For a conservative analysis, it is assumed that the collapse load (with cross beam) is the same as the elastic buckling load, namely 550,000 pounds. The corresponding radial deflection is 0.273 inch, giving an equivalent spring constant of 2.016 × 10^6 lb/in.

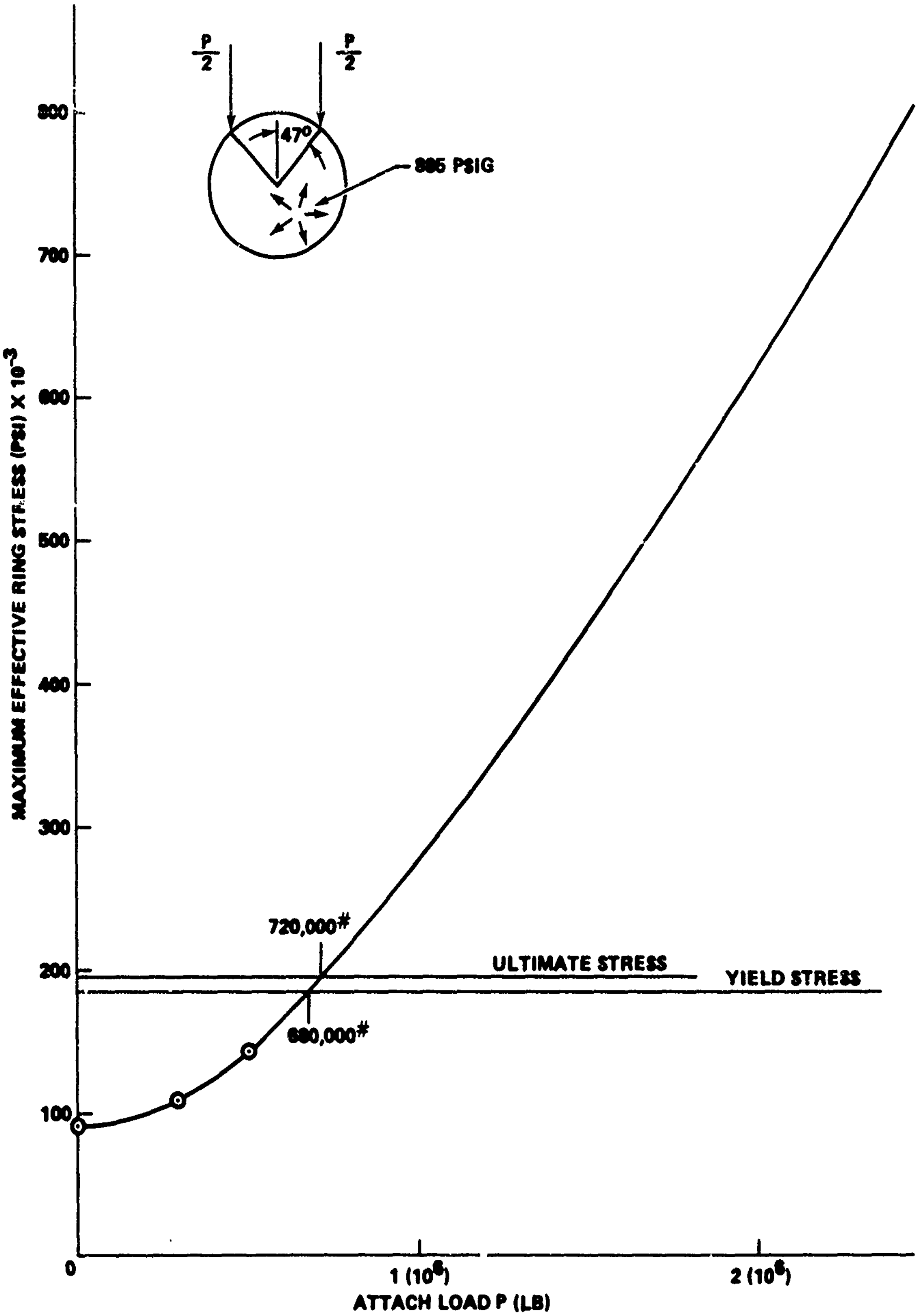

FIGURE 4-15 MAXIMUM EFFECTIVE STRESS IN REAR SRB ATTACH RINGS VS. ATTACH LOAD

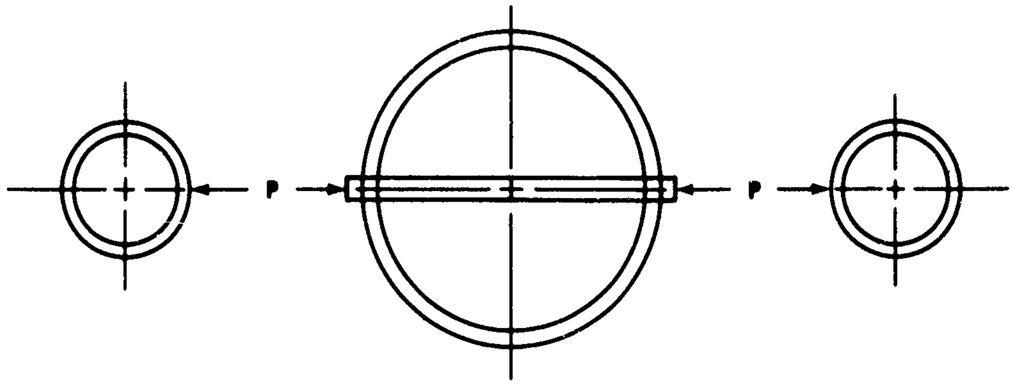

FIGURE 4-16 STATIC ANALYSIS OF FORWARD JOINT

Appendix F makes an analysis of the SRB forward skirt for the loading condition shown in Figure 4-16. This 2219 aluminum structure is somewhat complicated, as shown in Figure 4-19. The radial load P is distributed to several frames by a beam-type box structure. Figure 4-20 shows the finite element model deformed by a radial load and thrust load during destruct. Our analysis indicates that the collapse load is on the order of 400,000 pounds. This could be pessimistic, however, since rather coarse elements were used where the load was applied. For a conservative analysis (from a destruct viewpoint), it is assumed that the collapse load is at least as high as that of the forward ET frame structure, namely 550,000 pounds. The elastic deflection for a radial load of 400,000 pounds is 0.488, yielding an equivalent spring constant of 0.819×10^6 lb.

The forward joint between the SRB and ET is shown in Figure 4-21. The problem was to determine if either the forward or aft joints will fail in lateral shear before the frame collapse load of 550,000 pounds is reached. If the joints fail before collapse, the SRB's will be released at the velocity V_R which exists at the time of failure. On the other hand, if the joints do not fail in shear, the SRB will encounter a resistance at each joint approximately equal to the collapse load, as illustrated in Figure 4-22, assuming rigid-plastic stress-strain behavior. The resistances will exist until the frames deform a distance X_{MAX} corresponding to the ultimate strain in bending on the tension side. The resistances will, of course, slow down the SRB's and, hence, reduce the kinetic energy available for destruct. In order to bracket the problem, two cases were investigated:

In Case 1 it was assumed that when the radial load reaches a certain magnitude, the SRB is suddenly released due to catastrophic failure. This may be caused by failure of the pins or struts, rupture of a frame due to exceeding the ultimate strain, or rupture of the SRB shell at the joint. After the failure, there is no resistance to the SRB inertia until it travels the 12-inch standoff distance and impacts the LH_2 tank. The velocity at impact will be essentially the same as the velocity at failure. As will be discussed, it may be beneficial to purposely cause failure of the joint by the destruct system.

INTERTANK SUMMARY

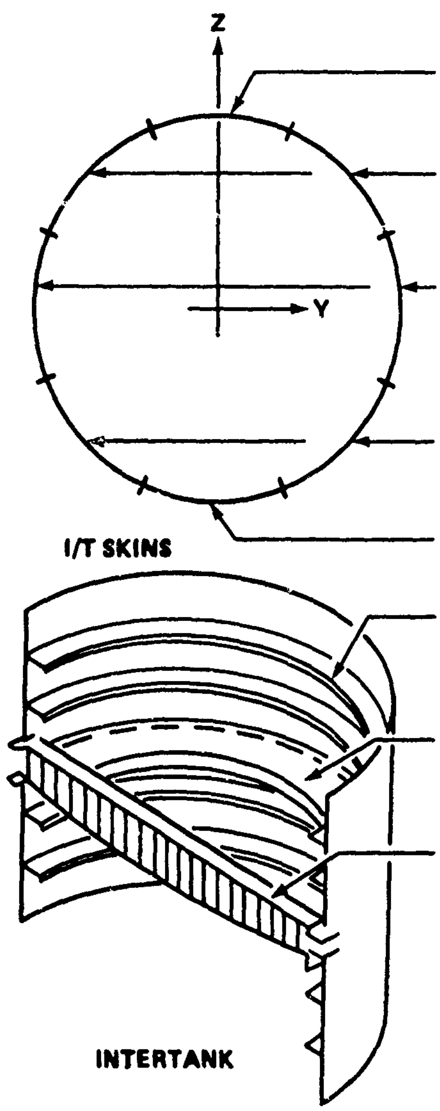

COMPONENT	DESIGN CONDITION
PANEL 1	LIFT-OFF
PANELS 2 AND 3	MAX SRB
PANELS 4 AND 5	MAX SRB (FWD) POST STAGING (AFT)
PANELS 6 AND 7	MAX SRB
PANEL 8	LIFT-OFF
INTERMEDIATE FRAMES	MAX SRB
985 RING	LIFT-OFF
SRB BEAM	1) MAX SRB 2) STIFFNESS CRITERIA – CLEARANCE WITH TANK BULKHEADS REQ'D

FIGURE 4-17 SCHEMATIC OF FRAME AT X_T 985

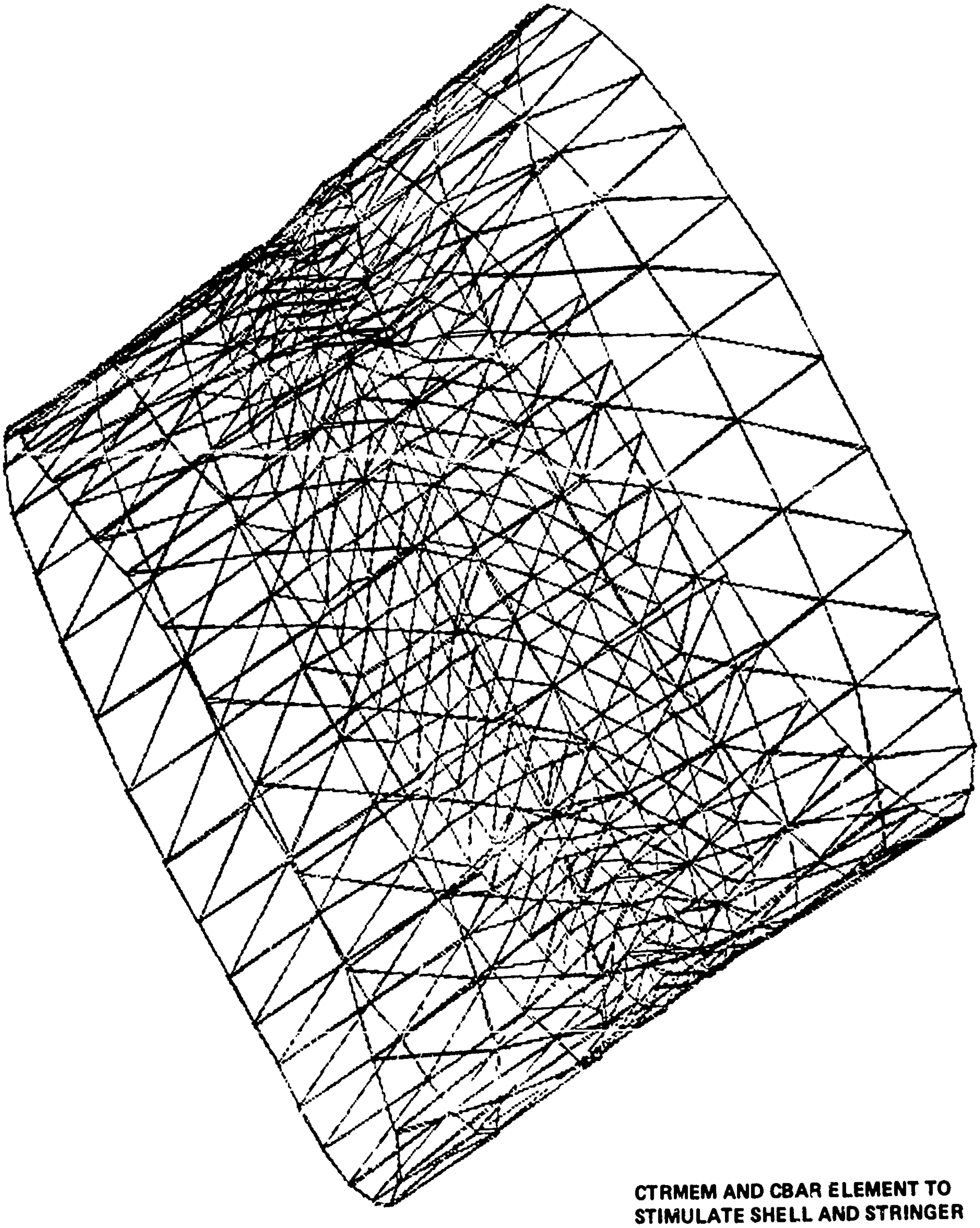

FIGURE 4-18 FINITE ELEMENT MODEL OF ET INTERTANK

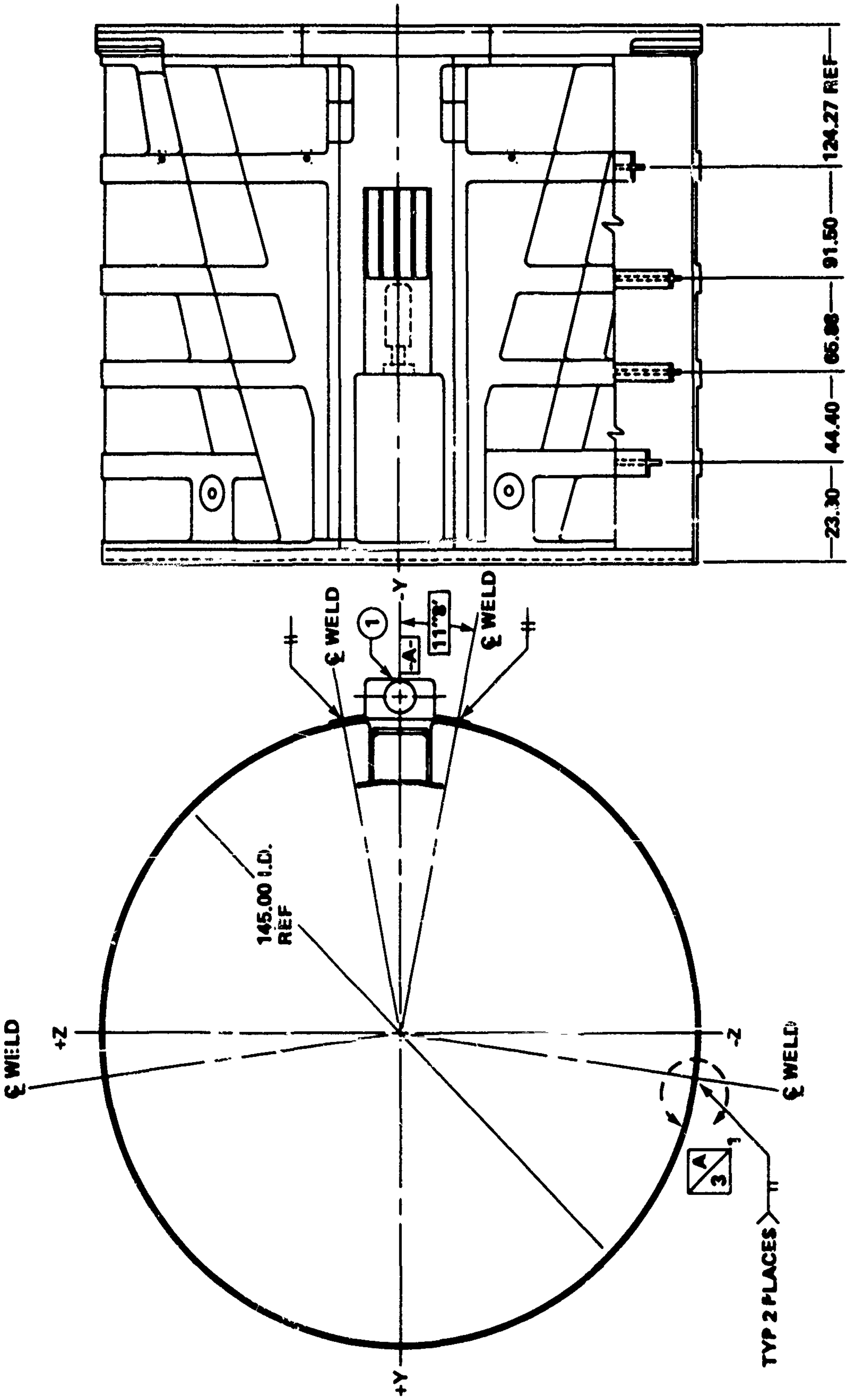

FIGURE 4-19 SRB FORWARD SKIRT

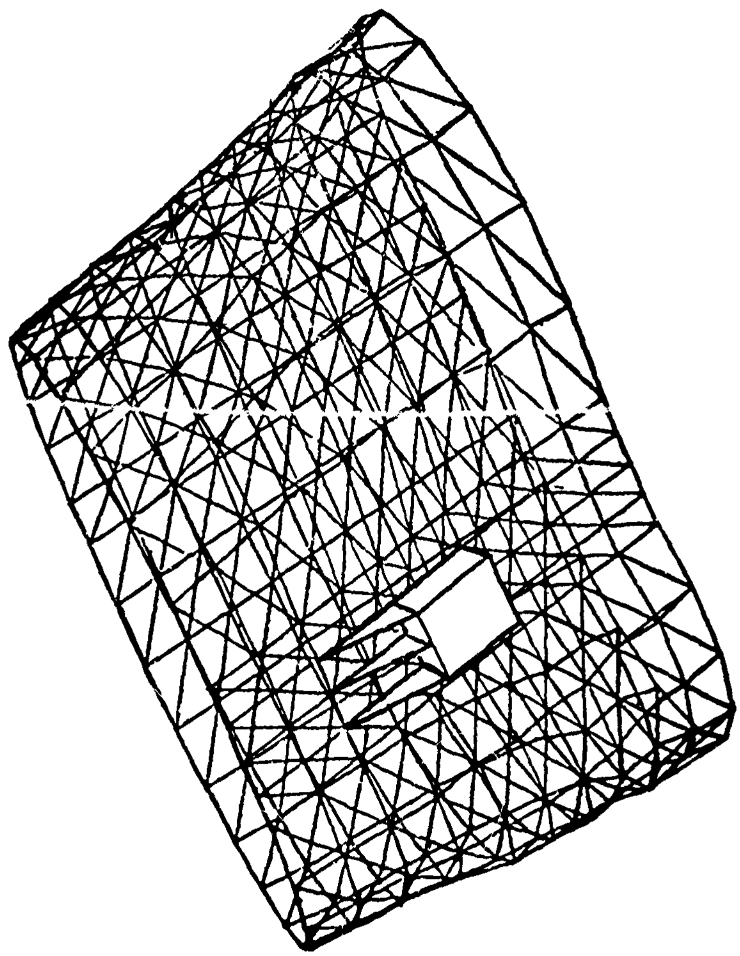

FIGURE 4-20 FINITE ELEMENT MODEL OF SRB FORWARD SKIRT

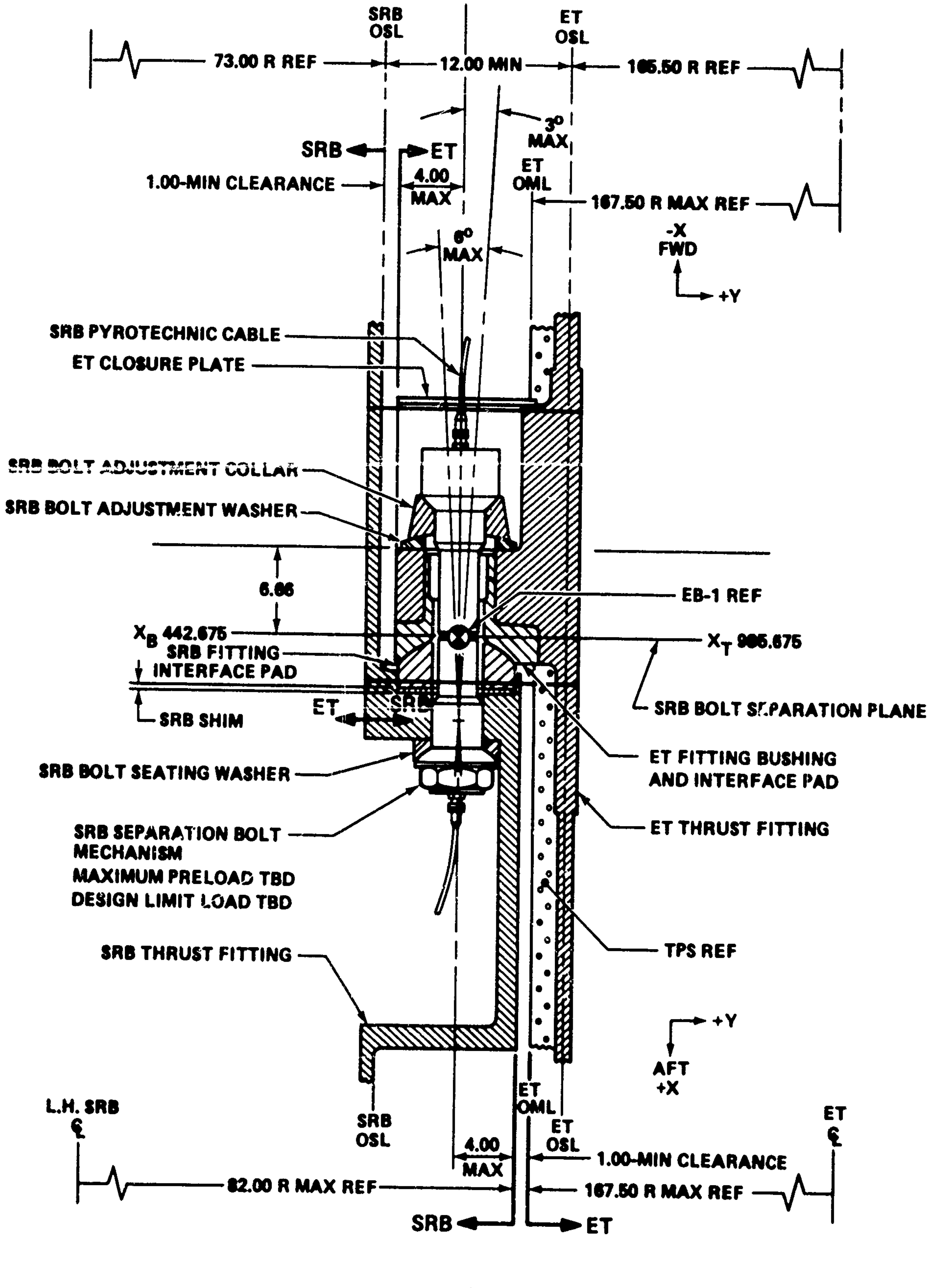

FIGURE 4-21 SRB/ET FORWARD JOINT

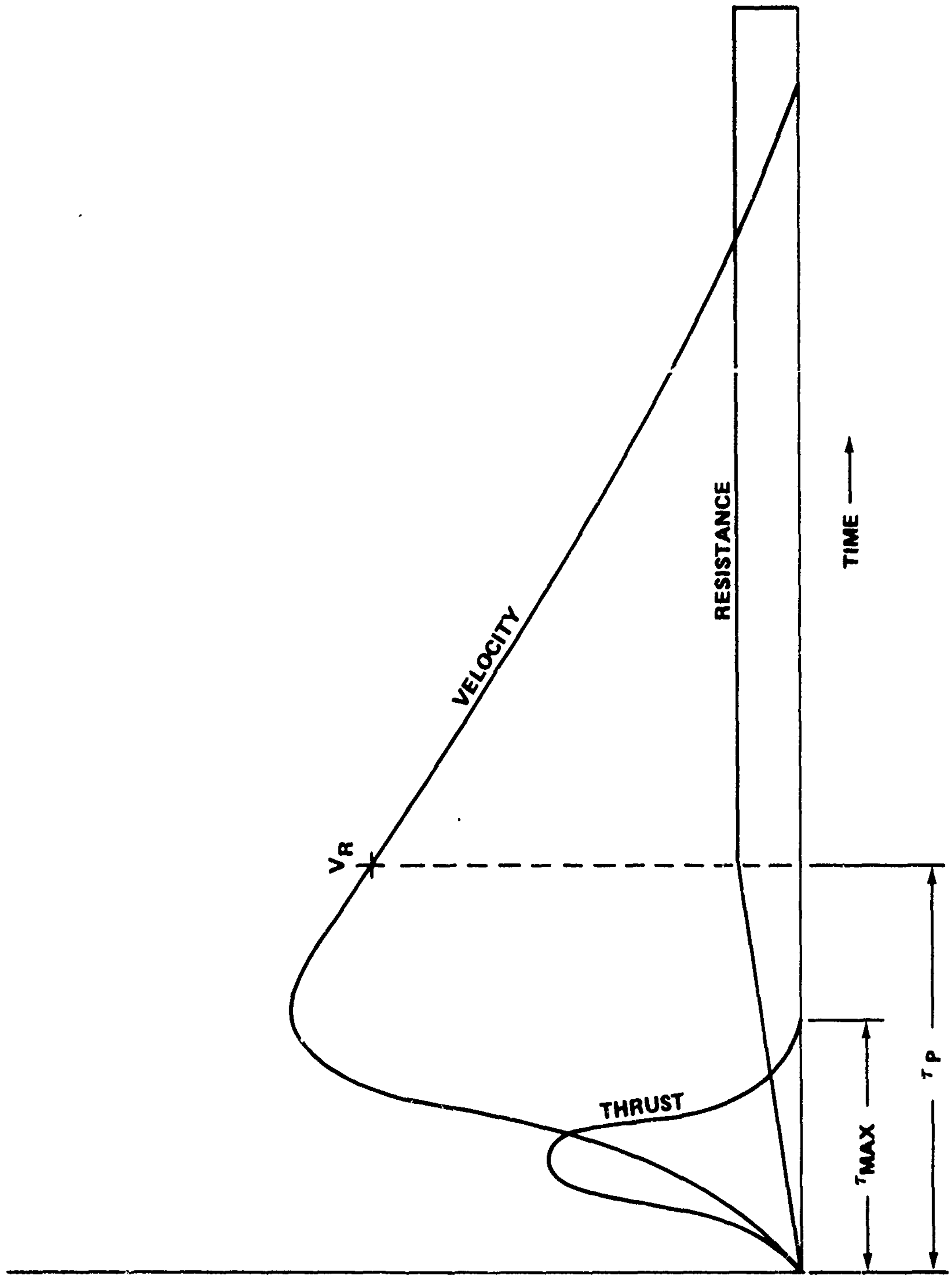

FIGURE 4-22 FRAME RESISTANCE – RIGID PLASTIC BEHAVIOR

In Case 2 it was assumed that the aft SRB frame (X_T 2058) collapses at a force of 850,000 pounds. Correspondingly, the collapse load of the forward ET and SRB frames is 550,000 pounds. Assuming rigid plastic stress-strain behavior, the frames will provide a net resistance of 1,400,000 pounds to the inertia generated by the lateral thrust load. The SRB will either stop over the 12-inch standoff, or it will impact the ET at some unknown velocity which will be estimated later. In the latter case, severe damage (destruct) may result in the LH_2 tank.

CASE 1: MOTION OF THE SRB WITH NO RESISTANCE AT ET/SRB JOINTS

In this case, it was assumed that the forward and aft joints would fail during the early part of the impulsive lateral thrust from clamshell-type rupture of the SRB. The velocity of the SRB's at joint failure would then go into available kinetic energy for gross deformation and potential destruct of the LH_2 tank during impact. For a worst case, it was assumed that the ultimate strength of the forward and aft pin joints was the same as the estimated collapse loads of 550,000 pounds at the forward joint and 850,000 pounds at the aft joint. The results of the dynamic analysis of the SRB's discussed in Section II were used. First, destruct at T = 0 (lift-off) was considered. Figure 4-8 shows the forces at the joints from the lateral impulse given in Figure 4-7. As shown in Figure 4-8, failure can be expected at the forward joint at t = 0.042 seconds after initiation of destruct. The corresponding velocity V_{R1} in 75 in/sec. The radial deflection of the forward joint frames at failure is about 1 inch. The aft joint will fail at t = 0.068 sec, and the corresponding velocity V_{R2} is about 40 in/sec. The radial deflection of the frames at failure is about 1.5 inches. The average impact velocity is 57.5 in/sec. The maximum bending stress in the SRB shell is 75,000 psi (Fig. 4-10), and the maximum deflection at the center span is about 5 inches. It was difficult to say whether or not the SRB shell would fail in bending. The linear-shaped charge will destroy structural integrity of the shell and, the shell may buckle on the compression side due to the opening caused by the shaped charge.

Similar calculations were made for destruct at times 10, 50, and 100 seconds. Table 4-1 shows a summary of pertinent results. Failure of the SRB shell at T = 50 and 100 seconds is highly possible. Failure of the shell at T = 10 seconds is at best marginal.

Based on the data in this table, it is obvious that the probability of destruct increases significantly at increasing times into the flight. The average impact velocity and SRB bending stress are the critical parameters. The effect of these parameters on LH_2 destruct will be discussed later. It should be noted that if the pins dictate the strength of the aft joint, failure is predicted at 1,150,000 pounds. Note that in Figure 4-8, the expected force at the aft joint for T = 0 (lift-off) is of about the same magnitude. Failure of this joint for T = 0 is marginal. Destruct could be effected by purposely making the struts fail at some value like 850,000 pounds.

TABLE 4-1 SUMMARY OF FORCES, VELOCITIES, DEFLECTIONS, AND BENDING STRESS DURING DESTRUCT

Time of Destruct (sec)	Force at Failure		V_R Velocity at Failure		X_R Deflection at Failure		Average Impact Velocity (in/sec)	SRB MAX Bending (psi)
	FWD (lb)	AFT (lb)	FWD (in/sec)	AFT (in/sec)	FWD (in)	AFT (in)		
0	550,000	850,000	75	40	1.0	1.5	57.5	74,000
10	550,000	850,000	110	65	1.0	1.5	87.5	90,000
50	550,000	850,000	240	120	1.0	1.5	180.0	190,000
100	550,000	850,000	463	145	1.0	1.5	304.0	342,000

CASE 2: MOTION OF SRB WITH RESISTANCE AT ET/SRB FRAMES (X_T 985 AND X_T 2058)

For this case, it was assumed that the frames at stations X_T 985 and X_T 2058 would provide a resistance to the motion of the SRB during initiation of destruct. Elastic-perfectly plastic behavior was assumed for the force displacement, as illustrated in Figure 4-23.

The resistance of each frame was assumed to be equal to the static collapse load in accordance with limit analysis theory. The elastic dynamic response analysis was used to predict time of collapse. The corresponding displacement and velocity were used as initial conditions in this analysis. Instead of the joint force dropping to zero at failure, as in Case 1, the joint force remained constant at the collapse load until rupture of the frames by excessive strain or until the SRB's impact the LH_2 tank.

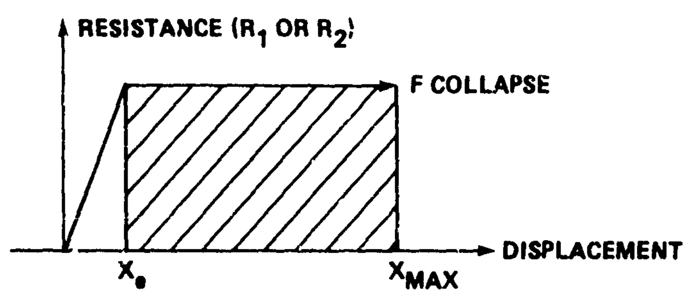

FIGURE 4-23 FORCE DISPLACEMENT

The equations of motion of the SRB for the forces shown in Figure 4-24 are as follows:

$$M_{SRB}\frac{d^2x}{dt^2} + R_1 + R_2 = 0 \tag{4-1}$$

$$I\frac{d^2\theta}{dt^2} = R_2 b - R_1 a \tag{4-2}$$

$$V_1 = \frac{dx}{dt} + a\frac{d\theta}{dt} \tag{4-3}$$

$$V_2 = \frac{dx}{dt} - b\frac{d\theta}{dt} \tag{4-4}$$

$$X_1 = X + a\theta \tag{4-5}$$

$$X_2 = X - b\theta \tag{4-6}$$

The boundary conditions are:

$V_1(0) = V_{R1}$ (velocity at failure)

$V_2(0) = V_{R2}$ (velocity at failure)

$X_1(0) = X_{R1}$ (displacement at failure)

$X_2(0) = X_{R2}$ (displacement at failure)

$\theta(0) = W_R$ (angular velocity at failure)

$\theta(0) = \theta_R$ (rotation at failure)

where t is conveniently measured from time of failure.

The equations were solved using the initial conditions shown in Table 4-1. Table 4-2 shows the velocity at the forward and aft supports after the SRB has traveled the 12-inch standoff distance. The results show that the 1.4×10^6 lb resistance from the support frames at X_T 985 and X_T 2058 is sufficient to stop the SRB before it travels the 12-inch standoff distance for destruct at T = 0. For destruct at T = 0 seconds, the SRB velocity at impact into the ET is quite small and destruct at T = 10 seconds, the SRB velocity at impact into the ET is quite small and quite high. It will be shown later that the SRB's will destruct the LH_2 tank.

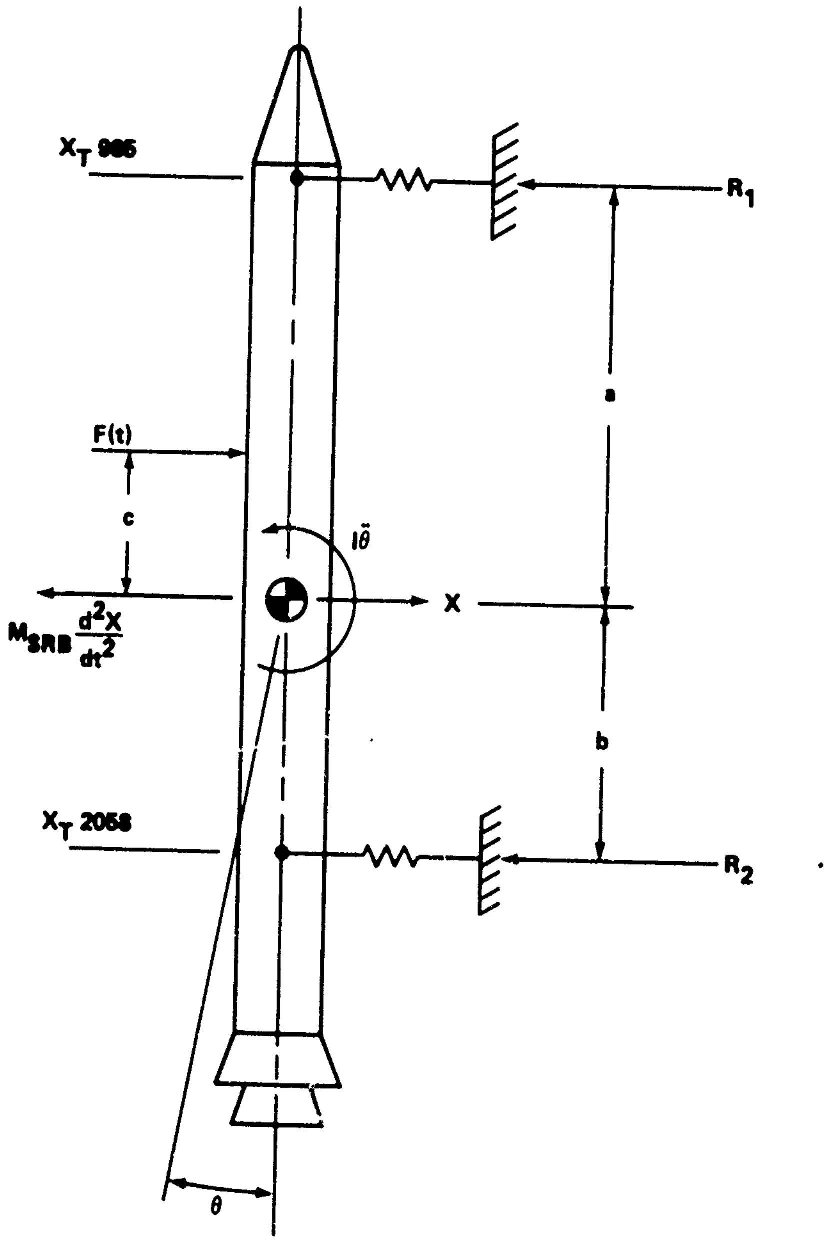

FIGURE 4-24 FORCES ACTING ON SRB DURING DESTRUCT

TABLE 4-2 SRB IMPACT VELOCITIES FOR CASE 2, ACCOUNTING FOR RESISTANCE FROM FRAMES AT X_T 985 AND X_T 2058

Time of Destruct (sec)	Total Impulse (lb/sec)	Weight of SRB (lb)	Net Resistance (lb)	Velocity After Moving 12-in Standoff		Average Velocity (in/sec)
				Fwd (in/sec)	Aft (in/sec)	
0	0.18×10^6	1.288×10^6	1.4×10^6	0*	0.0	0
10	0.26×10^6	1.177×10^6	1.4×10^6	2	6.0	4
50	0.32×10^6	0.767×10^6	1.4×10^6	176	94.5	135
100	0.55×10^6	0.323×10^6	1.4×10^6	399	111.2	255

*Aft joint travels 3.8 inches and forward joint travels 5.8 inches before SRB stops.

A question to be addressed was, "Can the frames at stations X_T 985 and X_T 2058 deform radially through a distance of 12 inches without prior failure caused by excessive strain?" If rigid-plastic stress-strain behavior is assumed, a crude estimate of the displacement X_{MAX} in terms of the ultimate plastic strain is (from Appendix D):

$$X_{max} = \frac{\zeta h \varepsilon_{ult} R}{C_{max}} \tag{4-7}$$

where C_{max} is the distance from the plastic neutral axis, R is the initial radius of the frame, and ζ is the average plastic hinge length factor. For D6AC steel, if we assume the ultimate strain to failure to be 0.10 in/in, $\zeta = 6$, $h = 8.6$ inches, $C_{max} = 4.3$ inches and $R = 73$ inches, then $X_{max} = 8.8$ inches. Hence, it is possible that the frame could rupture before it travels the 12-inch standoff distance. This would alleviate the situation. A more expedient solution would be to design the joint so that the pins or struts fail at a load of about 600,000 pounds.

Qualitative behavior of the SRB motion can be examined by neglecting rotational effects as being small. Since the frame resistance is generally small in comparison to the lateral thrust generated, a good approximation of the SRB lateral velocity at frame collapse is given by

$$V_R = \frac{\int F dt}{M_{SRB}} = \frac{I_o}{M_{SRB}} \tag{4-8}$$

Since the duration of the impulse is so small, on the order of 0.040 seconds, the maximum displacement can be estimated by the following simple energy balance: kinetic energy is equal to the work due to the resistances. The kinetic energy is

$$KE = \frac{1}{2} MV_R^2 = \frac{1}{2} \frac{I_o^2}{M} \tag{4-9}$$

where I_o is impulse.

The energy balance is

$$\frac{1}{2} \frac{I_o^2}{M_{SRB}} = (R_1 + R_2) X_{MAX} \tag{4-10a}$$

or the maximum displacement of the ring frames is:

$$X_{MAX} = \frac{1}{2} \frac{I_o^2}{M_{SRB} (R_1 + R_2)} \tag{4-10b}$$

Hence, it can be seen that the deformation of the frames is directly dependent on impulse squared and is inversely dependent on mass of the SRB's. This explains why the deformation is so small at early destruct times where the impulse is small and the SRB mass is large. If the impact velocities from Table 4-2 are compared with those of Table 4-1, it becomes evident that the resistance given by the frames during plastic deformation can be appreciable. Next, the extent of destruct when the SRB's impact the LH_2 tank at the predicted impact velocities must be determined.

DYNAMIC PLASTIC DEFORMATION OF LH_2 TANK

In the following analysis it is assumed that the SRB's are propelled into the LH_2 tank by the lateral thrust developed during SRB rupture. The impact velocity V_i is assumed to be uniform along the length. A schematic drawing of the LH_2 tank is shown in Figure 4-25. Internal support frames exist at stations X_T 1130, X_T 1377, X_T 1624, X_T 1871, and X_T 2058. As previously stated, the frame at X_T 2058 is extremely rugged. The frames at stations X_T 1377 and X_T 1624 are somewhat less stiff and are quite vulnerable to collapse during impact. These frames are nominally 6 inches deep and fabricated from 2219T8511 (outer chord), 2024T81 (webs), and 2024T8511 (inner chords), aluminum. The LH_2 tank is 2219-T87 aluminum and is nominally 0.137 inch thick.

There are various possible modes of failure. The following are the principal modes to be investigated:

1. Mode 1 — Excessive Strain. If the SRB breaks into segments as previously illustrated in Figure 4-3, View B, rupture of the skin by sharp corner impacts is possible but not certian. If the SRB impacts the LH_2 tank in one piece or in large sections, a conservative approach (from a destruct viewpoint) would be to assume that the frames must crush until they rupture because of excessive strain.

2. Mode 2 — Excessive Pressure Buildup. This mode of failure is illustrated in Figure 4-26. During destruct, the wall of the LH_2 tank could be crushed, thereby forcing the LH_2 into the ullage volume. If this is likened to a piston, the pressure in the ullage volume will increase due to adiabatic compression of the trapped vapor. If the pressure exceeds the burst pressure of the tank, a longitudinal seam, caused by excessive hoop stress, will result.

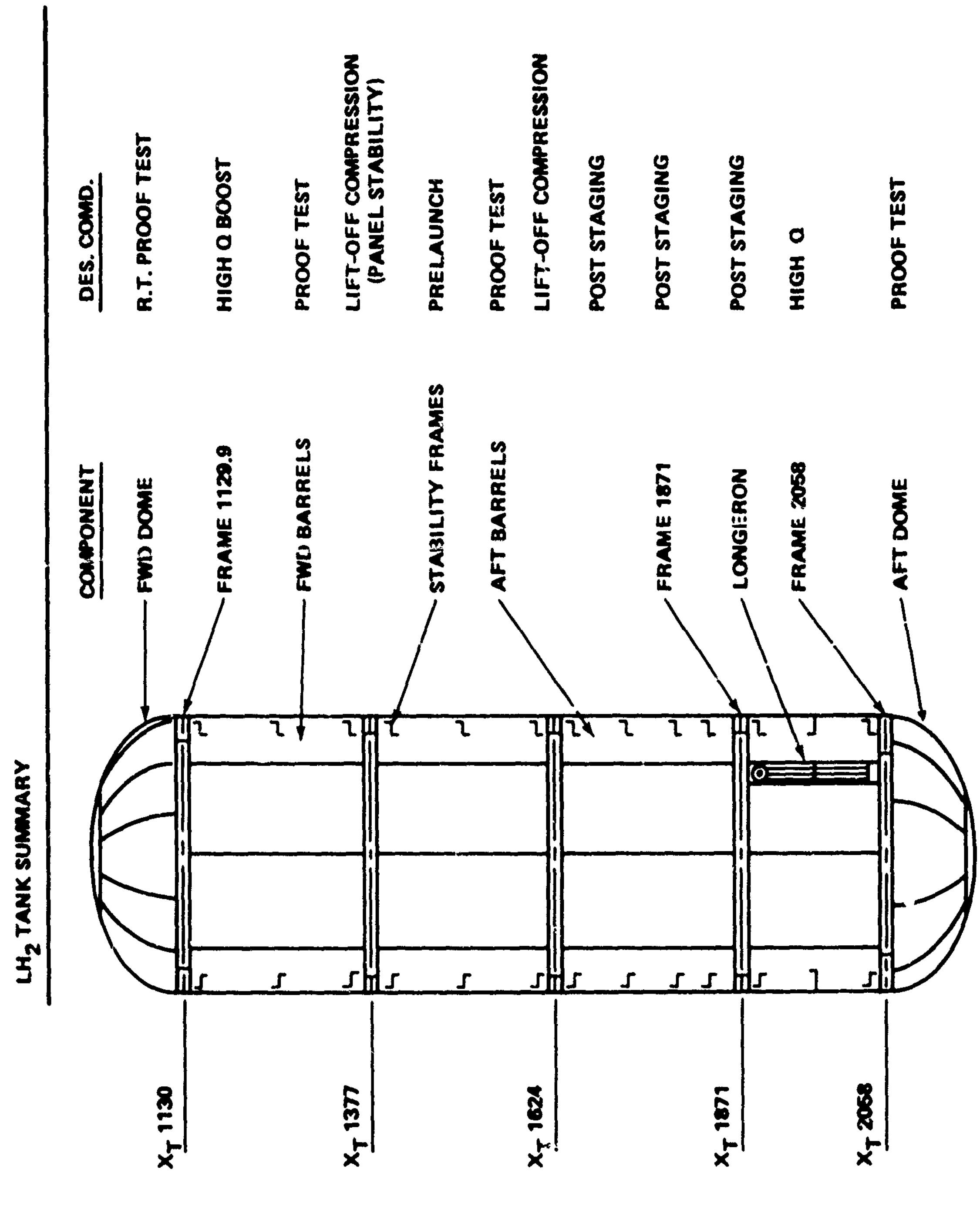

FIGURE 4-25 LH_2 TANK

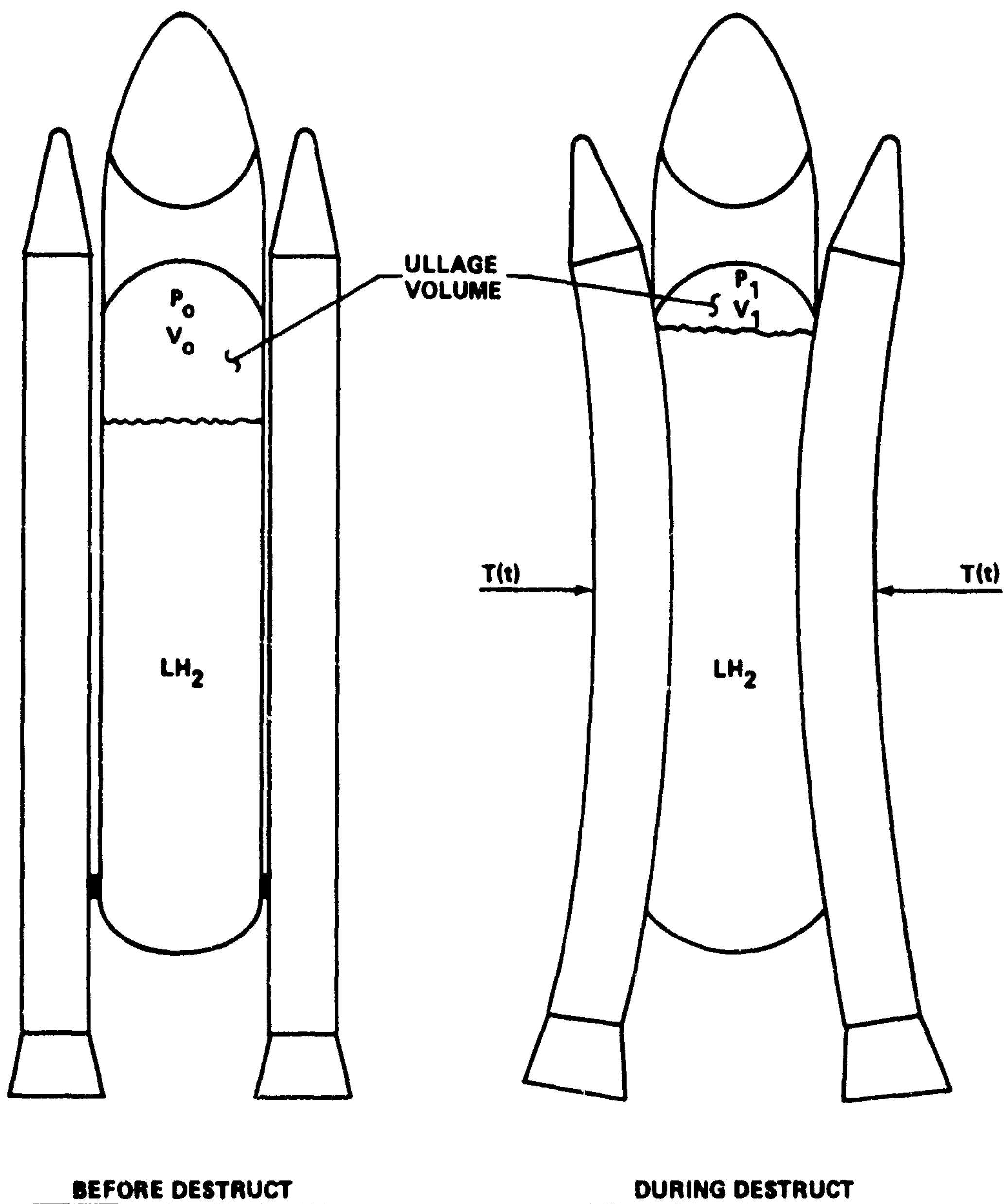

FIGURE 4-26 COMPRESSION OF ULLAGE VOLUME DURING DESTRUCT

CRUSHING OF LH_2 TANK. Consider a section of the SRB of length ℓ, impacting a section of LH_2 tank supported by an internal ring frame as shown in Figure 4-27. It is extremely difficult to predict the plastically deformed shape of a supporting ring frame in the LH_2 tank and the corresponding deformation of the SRB. Hence, the following simplifying assumptions are made:

1. The SRB remains essentially circular in cross section and absorbs very little of the impacting energy. This is based on the relatively thick (0.52 inch) steel casing backed up by the solid propellant grain.

2. To compute the resistance of the LH_2 tank frames at X_T 1377, X_T 1624, and X_T 1871, we will assume rigid plastic dynamic behavior as previously illustrated. The elastic energy is small in comparison to the plastic work and will, therefore, be neglected. The resistance is therefore constant at a value R_i for each frame and corresponds to the collapse load in limit analysis.

3. The hydroelastic effect of the LH_2 will be evaluated in an approximate manner, considering only its added mass effect.

4. The deformed shape of the LH_2 tank frames will be bounded by two extremes, as shown in Figure 4-28. The deformed shape is only important in estimating the volume change caused by piston action in Mode 2 type failure. In the "local crushing" deformation, it is assumed the frame crushes in locally in a circular pattern. In the elliptical deformation, the frame deforms into an ellipse. The actual deformed shape should be somewhere in between. The equation of motion of the SRB can now be written as:

$$(M_{SRB}) \frac{dV}{dt} + \frac{d}{dt} (M_F V) + R_i = 0$$

or (4-11)

$$M_{SRB} \frac{d^2X}{dt^2} + \frac{d}{dt} (M_F V) + R_i = 0$$

where

M_{SRB} = Mass of SRB over length ℓ

M_F = Added mass of fluid which must be accelerated

R_i = Resistance of frame impacted by the SRB

V = Instantaneous SRB velocity

X = Displacement of SRB

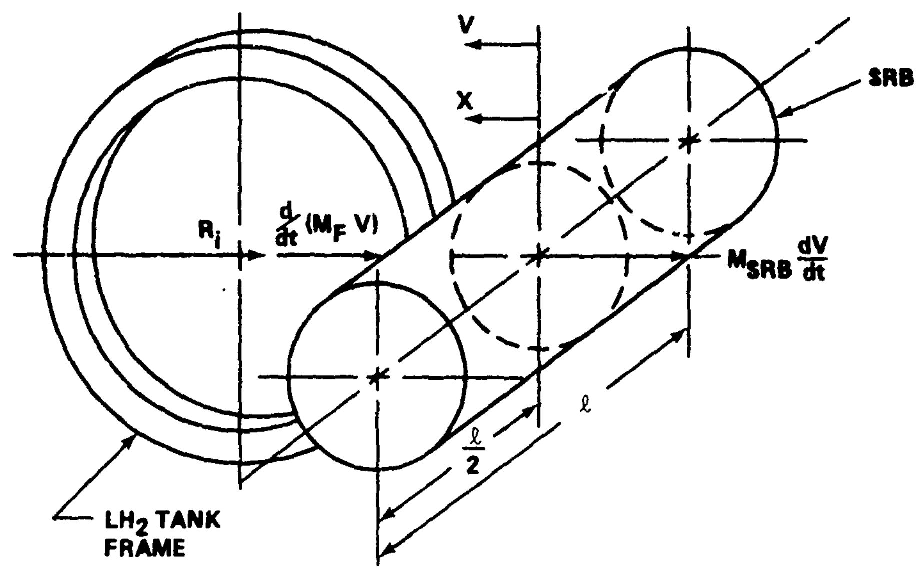

FIGURE 4-27 SECTION OF SRB IMPACTING A SECTION OF LH_2 TANK SUPPORTED BY AN INTERNAL RING FRAME

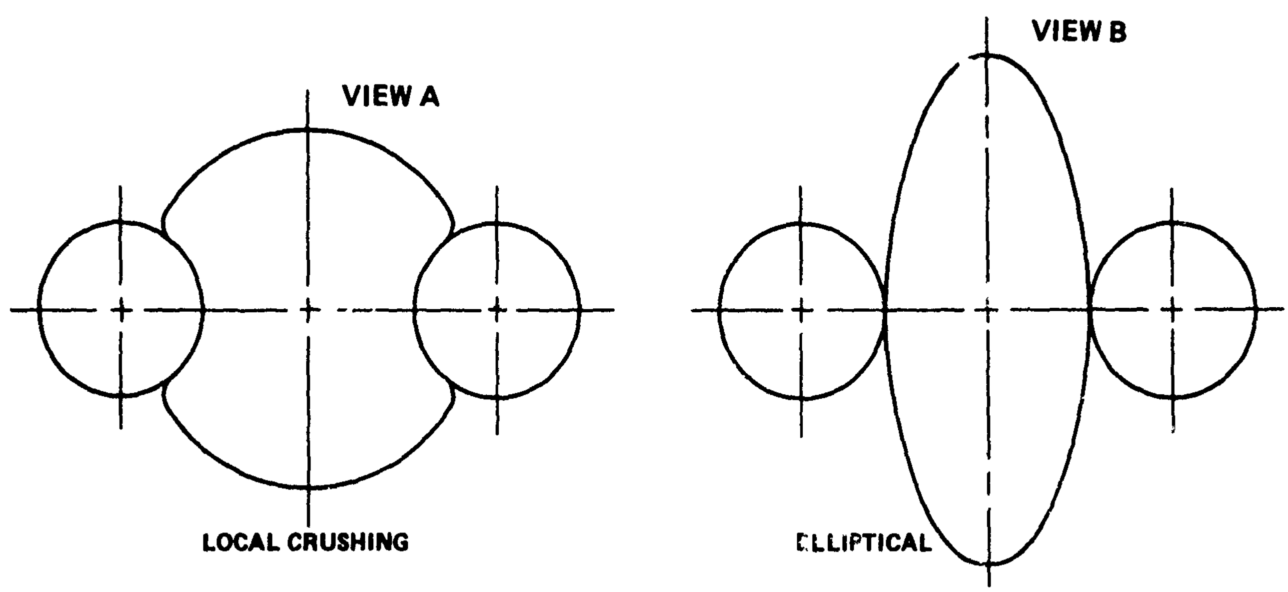

FIGURE 4-28 DEFORMED SHAPE OF LH_2 TANK FRAMES BOUNDED BY TWO EXTREMES

Let us, for example, consider frame X_T 1624. The effective mass of SRB impacting this frame is assumed to be that extending 1/2 the bay length on each side. From Figure 4-25, the effective length ℓ is 470 inches at frame X_T 1624. The resistance R_i can be computed using the results of Appendix H which estimate the maximum bending moment for the ring loaded by two radial loads, as shown in Figure 4-29. The maximum bending moment occurs at $\Phi = 0$ and is

$$M_\Phi = 0.16\, P_o R \tag{4-12}$$

The frame cross section at $\phi = 0°$ is shown in Figure 4-30. The bending moment to initiate yielding is

$$M_{yield} = F_{ty} \frac{I}{c_{max}} \tag{4-13}$$

Assuming rigid-plastic stress strain behavior. the moment to cause yielding of the entire cross section is:

$$M_{plastic} = \Sigma F_{ty} A \bar{v} \tag{4-14}$$

where $\bar{v}$ is the distance from the plastic neutral axis. The tensile force on the area inboard of the neutral axis is equal to the compressive force on the area outboard of the neutral axis, as shown in Figure 4-31. For Frame X_T 1624

$$K_b = \frac{M_{plastic}}{M_{yield}} = \frac{\Sigma A\bar{v}}{I/c} = \frac{3.09\ (2.675 + 0.325)}{32.58/3.986}$$

$$K_b = 1.134 \tag{4-15}$$

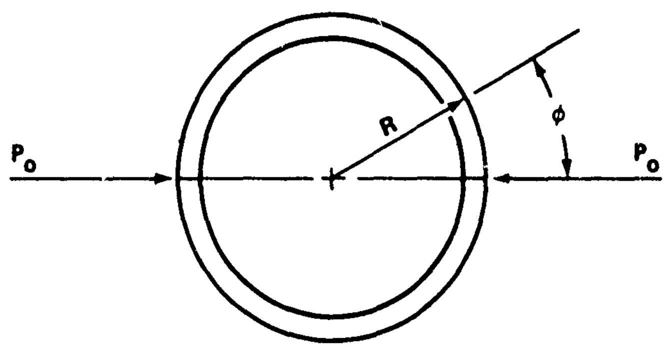

FIGURE 4-29 RESISTANCE FOR RING LOADED BY TWO RADIAL LOADS

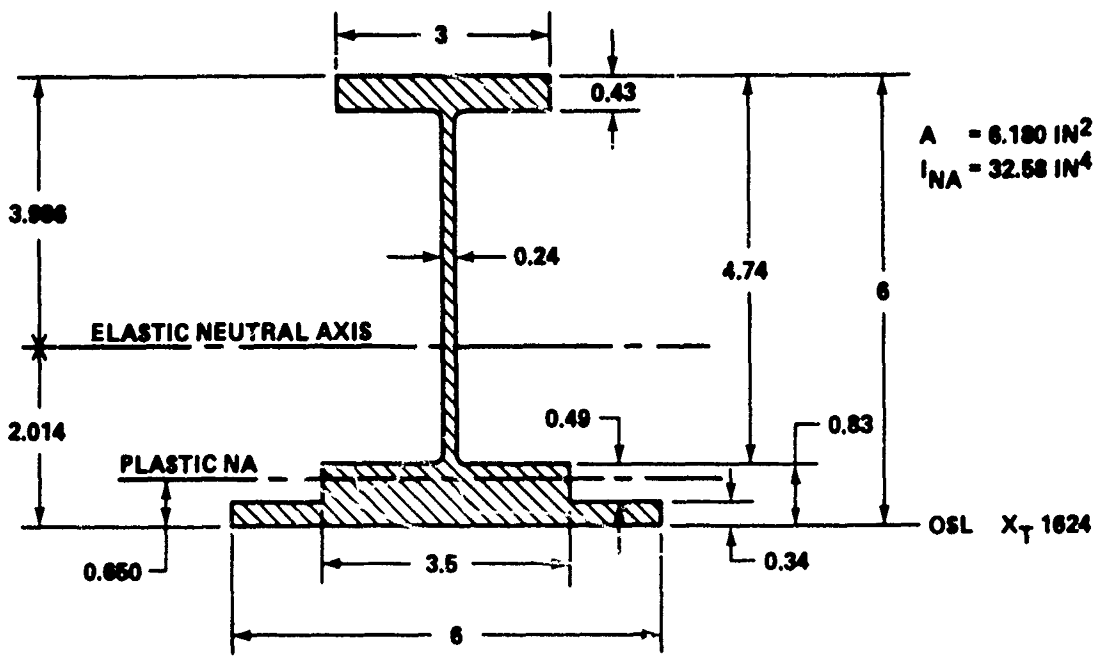

FIGURE 4-30 FRAME CROSS SECTION AT $\phi = 0^{\circ}$

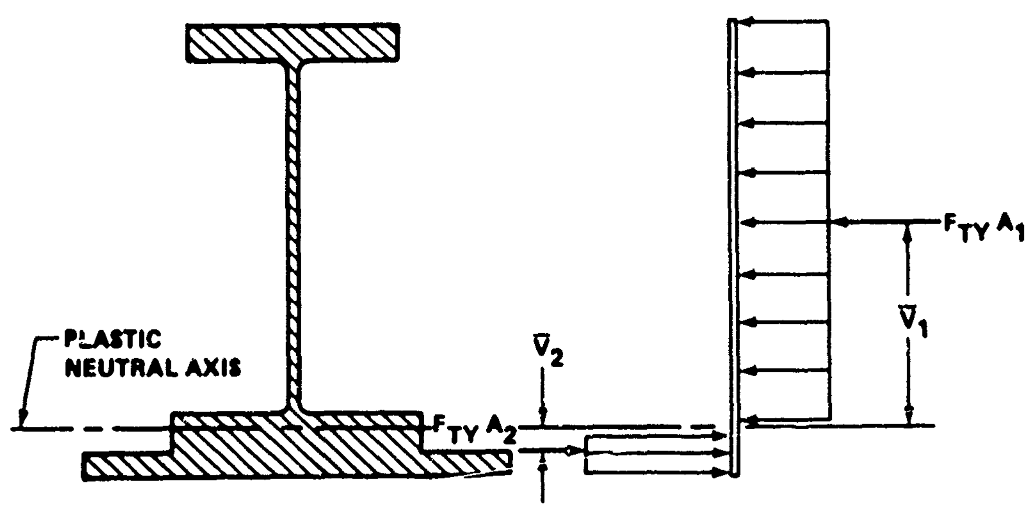

FIGURE 4-31 FORCE BALANCE FOR FRAME CROSS SECTION AT $\phi = 0^{\circ}$

Since the frame is made up of different aluminum alloys with different properties, average values will be used. Assuming a temperature of -320°F, a conservative upper limit of yield strength is 85,000 psi. Hence, from Equations 4-13 and 4-15, the plastic moment is:

$$M_{plastic} = 1.134 \times 85{,}000 \times \frac{32.58}{3.986} = 788{,}000 \text{ in/lb}$$

The force required to form a plastic hinge is estimated using Equation 4-12. Hence

$$P_o = \frac{M_{plastic}}{0.16\ R_o} = \frac{788{,}000}{(0.16)\ (165.5)} = 29{,}800 \text{ lb}$$

In terms of limit analysis, the load required to form another plastic hinge 90 degrees away from the point of load is estimated (Appendix G) to be

$$P_{collapse} = \frac{4}{\pi}\, p = \frac{4}{\pi}\,(29{,}800) = 37{,}900 \text{ lb}$$

For a conservative analysis (from a destruct viewpoint) the collapse load must be increased by 10 percent to cover strain hardening and strain rate effects. Hence, the resistance for rigid plastic behavior is

$$R = 1.10 \times 37{,}900 = 41{,}700 \text{ lb}$$

Next, the effect of the liquid hydrogen in providing resistance to deformation must be evaluated. First, consider deformation as shown in Figure 4-32. The LH_2 within the distance a on either side of the centerline will be accelerated. If the tank wall is assumed to behave like a flat plate of width 2a pushing against a fluid, the added mass (according to von Karman's approach in analyzing seaplane floats)[1] is:

$$M_{FL} = \frac{\pi}{2}\, a^2 \rho \ell \tag{4-16}$$

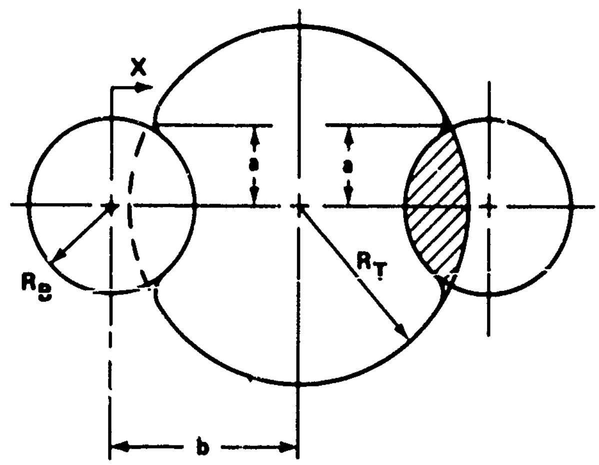

FIGURE 4-32 DEFORMATION-LOCAL CRUSHING MODE

[1] Von Karman, T., "The Impact of Seaplane Floats During Landing," NACA TN 321, 1929.

Hence, Equation 4-11 can be rewritten as:

$$M_{SRB} \frac{dV}{dt} + \frac{\pi}{2} \ell\rho \frac{d}{dt} (a^2V) + R_i = 0 \tag{4-17a}$$

or

$$\left(M_{SRB} + \frac{\pi}{2} \ell\rho a^2\right) \frac{dV}{dt} + \frac{\pi}{2} \ell\rho V \frac{da^2}{dt} + R_i = 0 \tag{4-17b}$$

Assuming that the ET and SRB remain circular (except where crushing occurs), the change in the dimension a^2 is given by

$$\frac{da^2}{dt} = 2 \left[\frac{b^2 + R_B^2 - R_T^2}{2b}\right] \left[1 - \frac{1}{b} \frac{b^2 + R_B^2 - R_T^2}{2b}\right] V \tag{4-18}$$

where

$b = R_T + R_B - X$

R_T = Radius of the LH_2 tank

R_B = Radius of the SRB

Equations 4-17a, b and 4-18 were solved numerically to obtain the displacement X at frames X_T 1377, X_T 1624, and X_T 1871 for impact of an SRB mass increment M_{SRB} at initial velocity V_R. It was assumed that the frames at X_T 1130 and X_T 2058 did not deform nearly as much because of their greater stiffness and strength. Hence, the deformed shape of the LH_2 tank is illustrated in Figure 4-33 showing appropriate geometrical dimensions. This model assumes that the SRB loses a great deal of its structural integrity due to destruct and is free to deform as illustrated or breaks up into large pieces. The SRB mass M_{SRB} assumed to act on each frame is shown in Figure 4-34 at various times of destruct.

The volume change for the assumed deformed shape of Figure 4-33 is as follows. For local crushing deformation (Fig. 4-28) we get:

$$\Delta V = \left[a\sqrt{R_T^2 - a^2} + R_T^2 \sin^{-1} \frac{a}{R_T} - ba + a\sqrt{R_B^2 - a^2} + R_B^2 \sin^{-1} \frac{a}{R_B}\right] \ell_{eff} \tag{4-19}$$

For the elliptical deformation we get:

$$\Delta V = \left[\pi R_T^2 - \pi (R_T - X) \sqrt{2R_T^2 - (R_T - X)^2}\right] \ell_{eff} \tag{4-20}$$

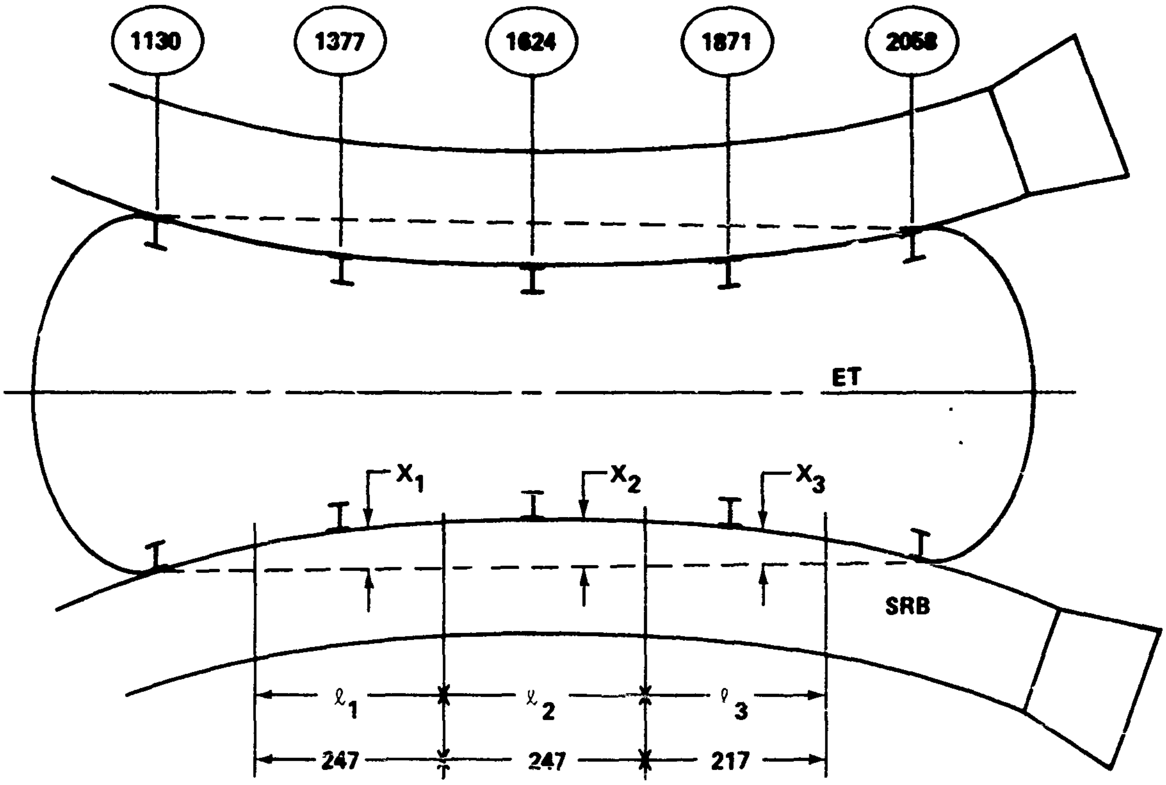

FIGURE 4-33 DEFORMED SHAPE OF LH_2 TANK

where ℓ_{eff} is the average length of deformed structure. A reasonable approximation is:

$$\ell_{eff} = (\ell_1 + \ell_2 + \ell_3) \tag{4-21}$$

Assuming adiabatic compression, the pressure in the ullage volume is given by:

$$P = P_o \left(\frac{V_o}{V_o - \Delta V}\right)^{\lambda} \tag{4-22}$$

where P_o and V_o are the initial pressure and volume in the ullage space. Typical pressures in the LH_2 tank at various times into flight prior to destruct are shown in Figure 4-35.

Typical computer results of displacement at frame X_T 1624 as a function of time for destruct at T = 0, 10, 50, and 100 seconds are shown in Figure 4-36. These results are for the initial velocities shown in Table 4-1 corresponding to Case 1 (motion of SRB with no resistance at joints following joint failure). Figure 4-37 shows the corresponding velocity of SRB during crushing of the ET. Figure 4-38 shows the pressure buildup in the ullage volume for "local crushing" which turned out to predict lower pressures than for the elliptical deformation.

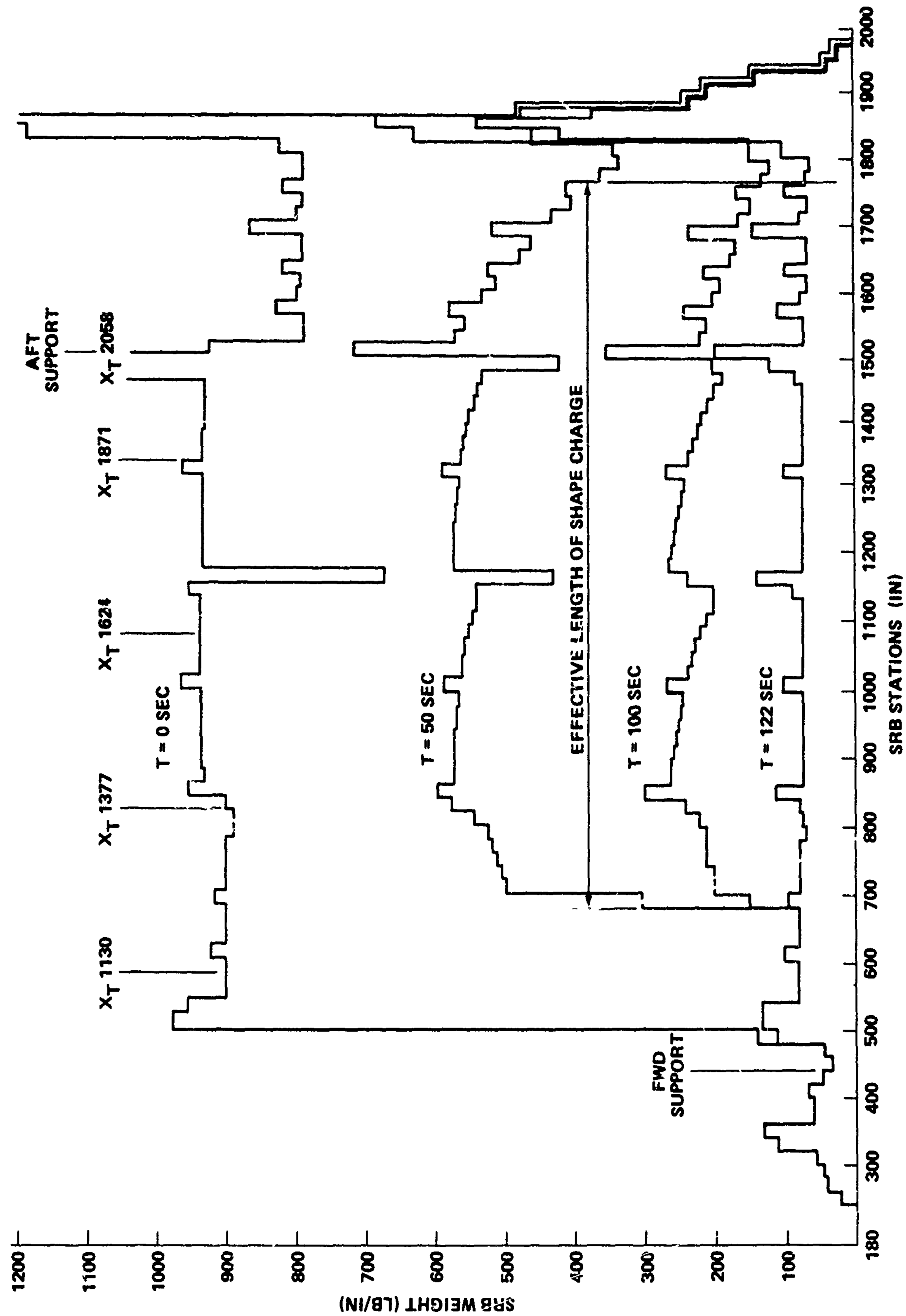

FIGURE 4-34 SRB WEIGHT VS. STATION

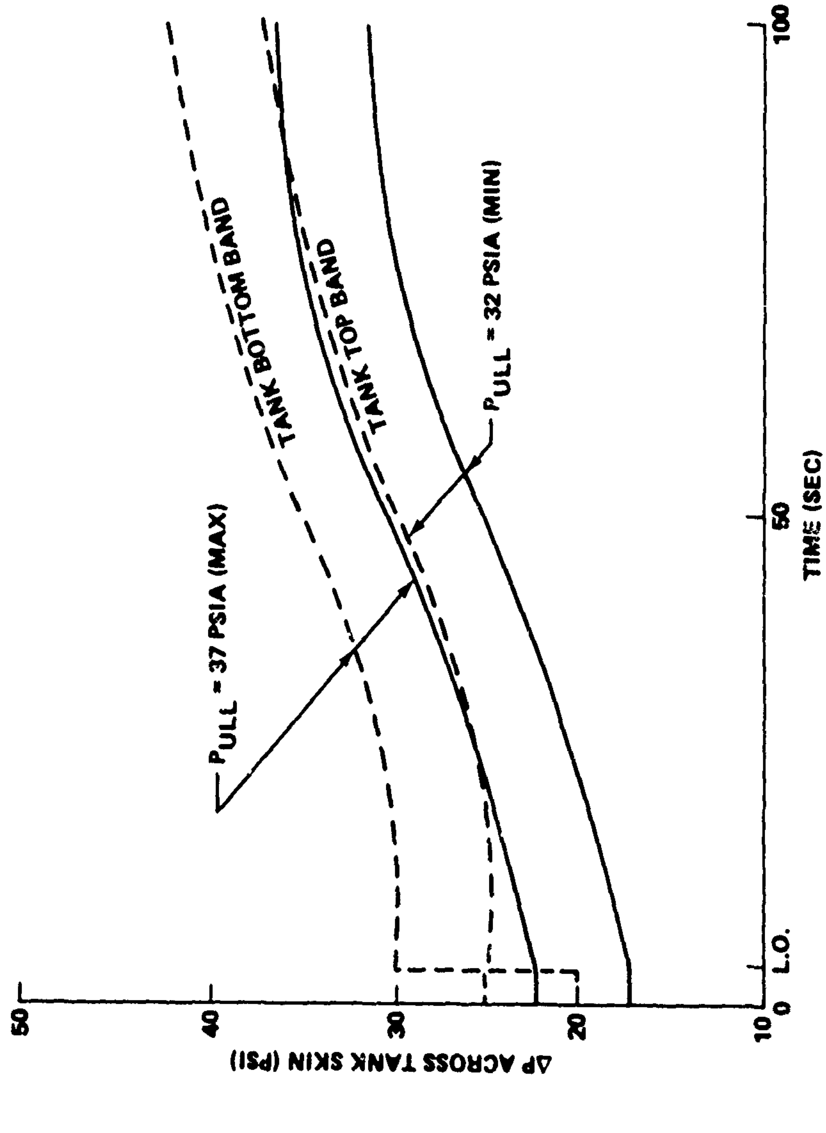

FIGURE 4-35 LH_2 — ΔP VS. FLIGHT TIME

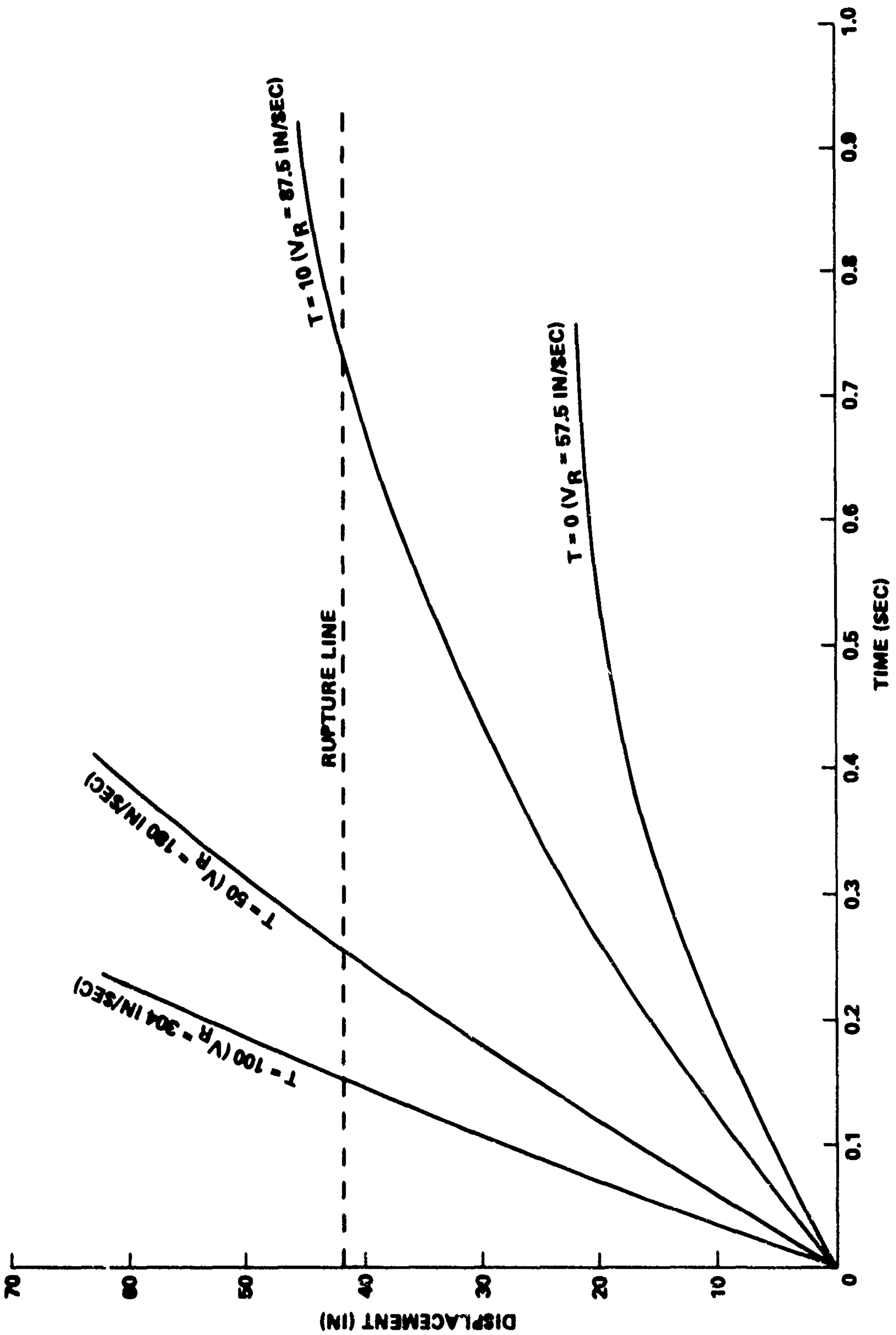

FIGURE 4-36 LH_2 TANK FRAME DISPLACEMENT VS. TIME FOR DESTRUCT AT T = 0, 10, 50, 100 SECONDS

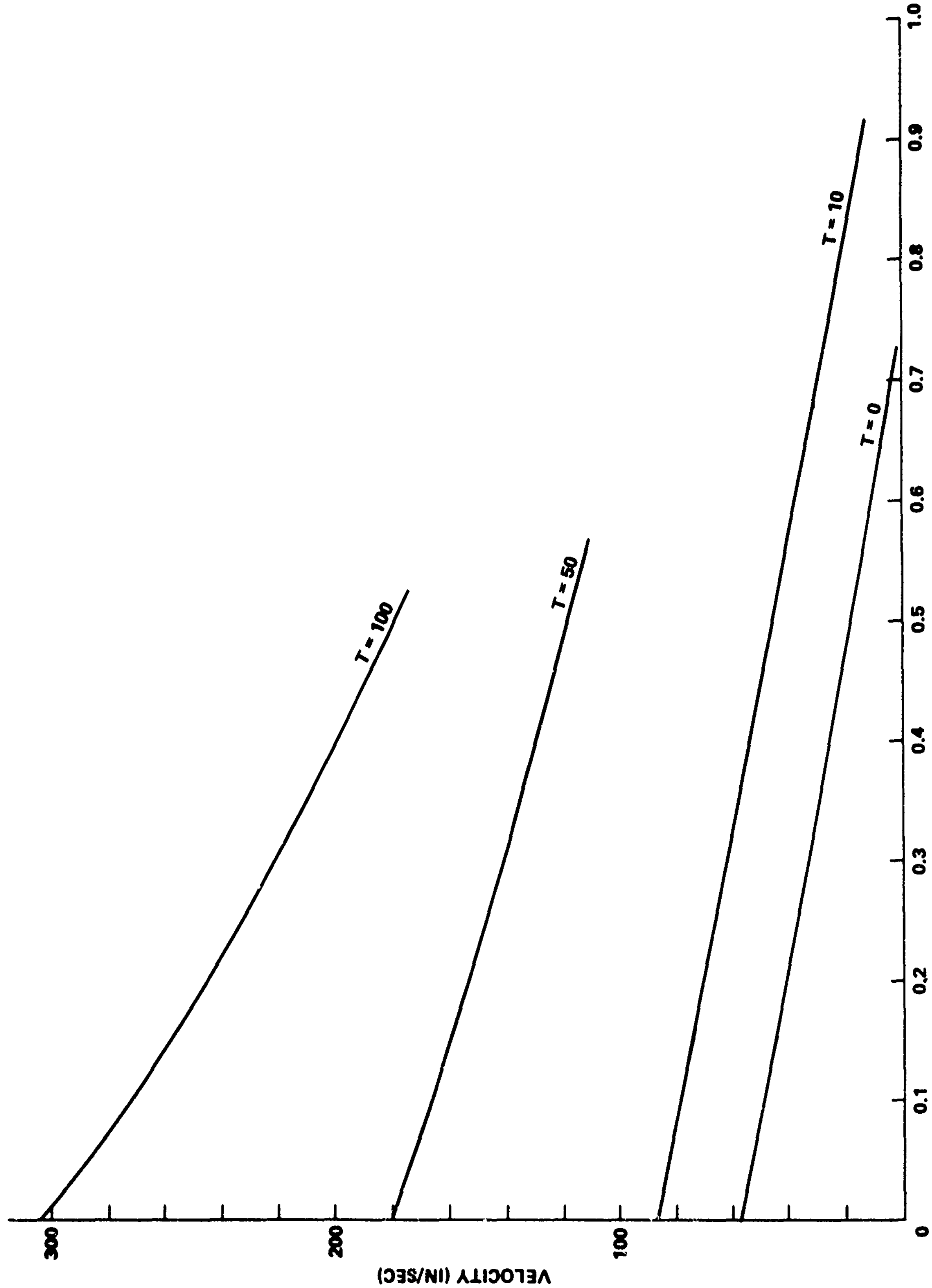

FIGURE 4-37 SRB LATERAL VELOCITY VS. TIME

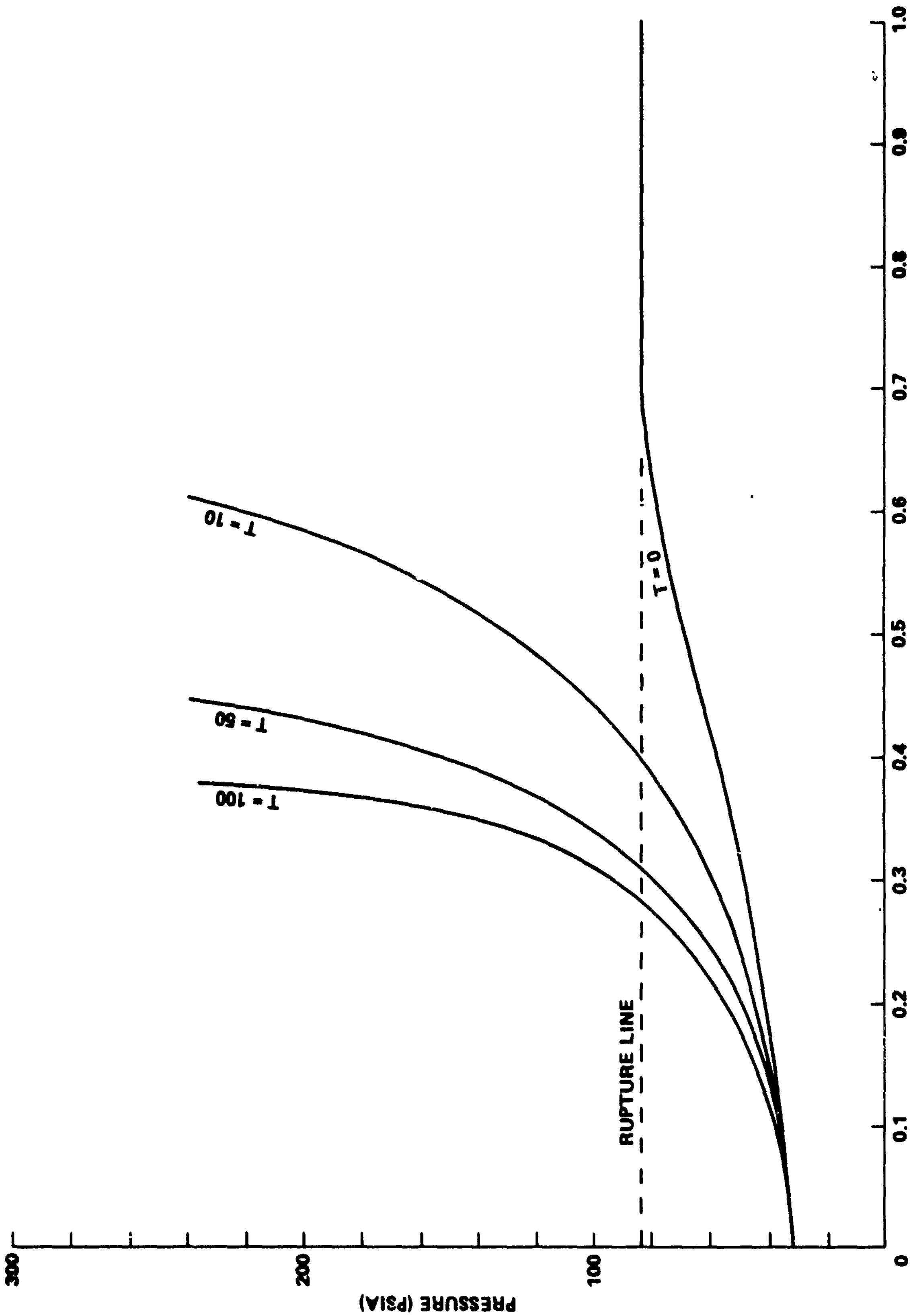

FIGURE 4-38 PRESSURE IN ULLAGE VOLUME VS. TIME

FAILURE MODES OF LH_2 TANK. An assessment of the failure mode is as follows. Again, using the simplified model for maximum strain during plastic deformation, the strain to failure can be estimated from Equation 4-7.

For the ET frame X_T 1624, take $\varepsilon_{ult} = 0.08$, $R = 165.5$, $C_{max} = 5.36$, $h = 6$, and $\zeta = 3$. Then

$$X_{max} = \frac{3 \times 6 \times 0.08 \times 165.5}{5.36} = 44 \text{ in.}$$

This estimate indicates that the frames could possibly deform 44 inches before rupture. Hence, for this analysis it is assumed that $X_{max} = 44$ inches. If this is plotted on Figure 4-36, it becomes obvious that catastrophic failure of the LH_2 tank is probable for destruct at times 10, 50, and 100 seconds. For destruct at T = 0, catastrophic rupture of the LH_2 tank is at best marginal.

Another possible mode of failure is burst of the tank due to pressure buildup during deformation. A crude estimate of the burst strength can be obtained by considering the hoop stress.

$$\sigma = \frac{pr}{t} \tag{4-23}$$

The effect of restraint from the frames can be neglected if

$$\frac{L}{\sqrt{Rt}} > 10 \tag{4-24}$$

as shown by Augusti and d'Agostino.[2] In our case L = 247, R = 165.5, t = 0.137. Hence

$$\frac{L}{\sqrt{Rt}} = 51.8$$

Therefore, end effects can be neglected and the burst pressure can be estimated by limit theory using a rigid plastic material. For 2219 T87 aluminum at -320F, a reasonable value of F_{tu} is 100,000 psi. The nominal skin thickness is 0.137 inches. Hence

$$P_{burst} = \frac{100{,}000 \times 0.137}{165.5} = 82.7 \text{ psi}$$

If we take this as a threshold value and plot it on Figure 4-38, we see that rupture of the LH_2 tank is highly probable at T = 10, 50, and 100 and marginal at lift-off (T = 0).

---

[2] Augusti, G. and d'Agostino, S., "Experiments on the Plastic Behavior of Short Steel Cylindrical Shells Subject to Internal Pressure," First International Conference on Pressure Vessel Technology, Part 1 – Design and Analysis, p. 45.

CONCLUSIONS. Destruct at times 10, 50, and 100 seconds into flight is highly probable. It appears that destruct will be by gross deformation of the LH_2 tank frames at 50 and 100 seconds. For destruct at 10 seconds, catastrophic rupture will probably result from excessive pressure. However, catastrophic rupture from excessive radial deformation is another possibility. There will, no doubt, be a coupling effect to enhance destruct. Once the frames do fail, the skin will be no match for the remaining SRB inertia.

For destruct at T = 0, catastrophic failure by excessive pressure buildup is probable but marginal. The crucial aspect in the analysis is the degree of deformation before the ultimate strain is exceeded. This can best be obtained by tests, possibly on small-scale models.

The only marginal aspect of the analyses occurs for Case 2 at lift-off. This is the case where the frames at X_T 985 and X_T 2058 provide a resistance during the time the SRB must travel the 12-inch standoff distance. This problem could easily be solved by purposely designing the forward and aft joints to fail at a load of about 500,000 pounds, which would still be well above the ultimate design load. Another possibility would be to effect failure of the SRB shell by a circumferential shape charge.

BLAST AND FRAGMENT ANALYSIS

Another possible mechanism for destruct of the LH_2 tank is the combined effects of blast and fragments from catastrophic rupture of the SRB's. The details of the blast calculations, estimates of fragment velocity, and mass distribution are given in the explosives section. The following analysis was made to assess the probability of LH_2 tank destruct from the predicted blast and fragment environment.

FRAGMENT DAMAGE. Let us first consider the effect of the fragments. Figure 4-39 contains the predicted size L of cubical fragments versus N_L, the number of fragments with dimensions greater than or equal to L. The four curves shown are for destruct at 1, 10, 50, and 100 seconds into flight. Fragment velocities at the various times and the chamber pressure during breakup are as follows:

T = 1 sec	V = 20 fps	p = 759 psi
T = 10 sec	V = 24 fps	p = 827 psi
T = 50 sec	V = 35 fps	p = 542 psi
T = 100 sec	V = 100 fps	p = 605 psi

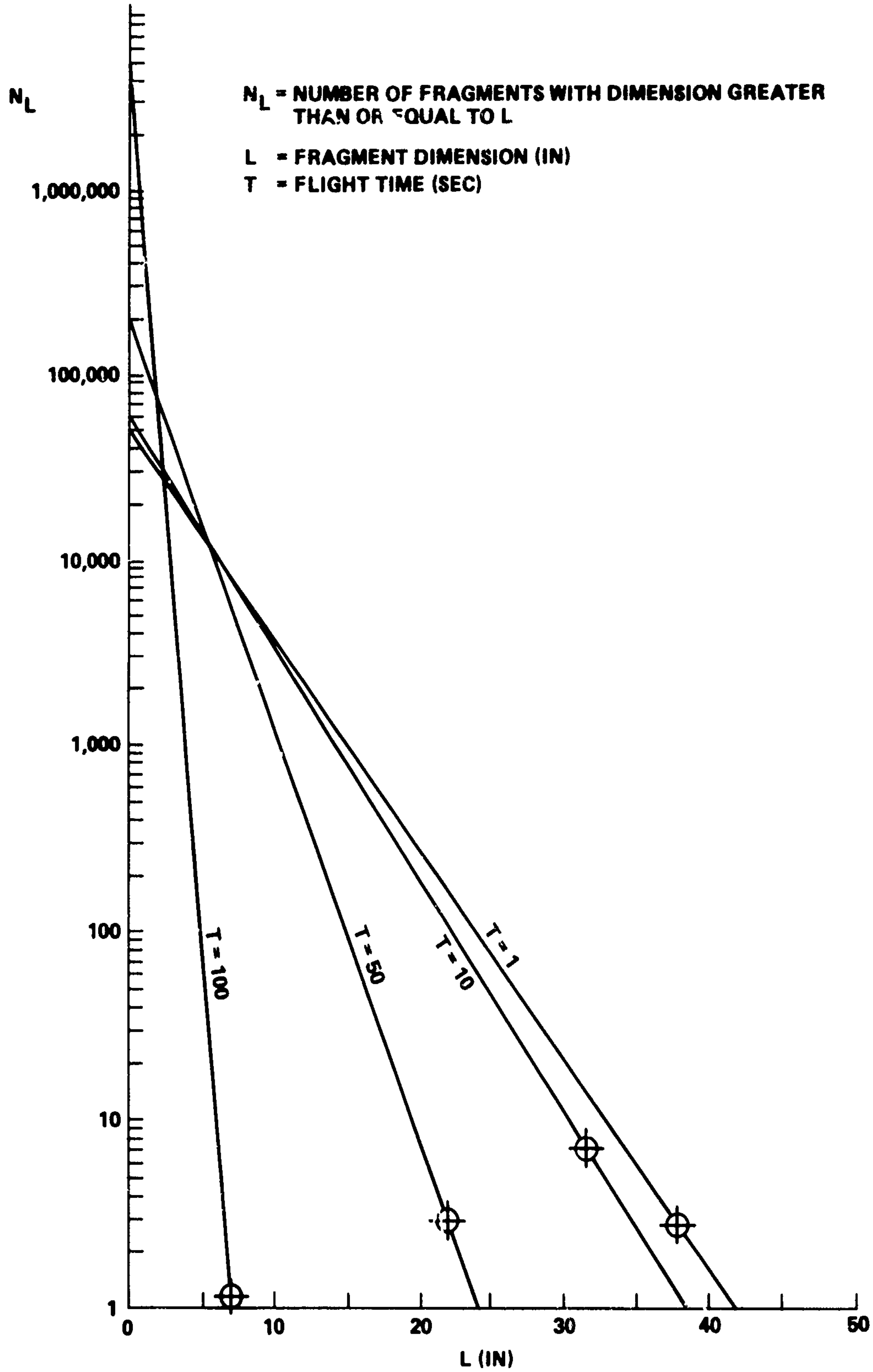

FIGURE 4-39 FRAGMENT SIZE DISTRIBUTION FUNCTION FOR PROPELLANT

The lethal size of fragments, L_E, is defined as the minimum size required to puncture the skin of the LH_2 tank which is 2219-T87 aluminum with a nominal thickness of 0.137. The fragments are propellant grain with a nominal density of 0.0635 lb/in^3. In order to estimate the size of fragment required to puncture the skin at the previously estimated velocities, the penetration data from Project THOR were used.[3] The empirical equation for the residual velocity after penetrating the skin is:

$$V_r = V_s - 10^c \, (eA)^\alpha \, m_s^{\,\beta} \, (\sec\theta)^\gamma \, V_s^{\,\lambda} \tag{4-25}$$

where

V_r = Residual velocity fps

V_s = Striking velocity fps

e = Skin thickness (in)

A = Area of projectile (in^2)

m_s = Projectile weight (grains)

θ = Obliquity angle with respect to the nominal to the target

The constants c, α, β, γ, λ depend on the skin material. Although no data were found specifically for 2219-T87 aluminum, data were obtained for 2024-T3 aluminum. The penetration characteristics should be quite similar, hence,

$$c = 7.047, \ \alpha = 1.029, \ \beta = -1.072, \ \gamma = 1.251, \ \lambda = -0.139$$

Since just puncturing the skin is of interest here, the residual velocity V_r can be set equal to zero. Hence,

$$V_s = \left[10^{7.047} \, (eA)^{1.029} \, m_s^{\,-1.072} \, \sec\theta^{1.251}\right]^{\frac{1}{1 + 0.139}} \tag{4-26}$$

For a cubical fragment

$$A = L^2$$

$$m_s = \rho L^3 = 0.0635L^3 \times 7000 = 444.5L^3 \text{ (grains)}$$

Equation 4-26 can be solved for the lethal size L_E for the predicted fragment velocities. The results are shown in Table 4-3.

---

[3] "The Resistance of Various Metallic Materials to Perforation by Steel Fragments; Empirical Relationships for Fragment Residual Velocity and Residual Weight," Project THOR, Technical Report No. 47, Ballistic Analysis Laboratory Institute for Cooperative Research, Johns Hopkins University, Apr 1961.

TABLE 4-3 SIZE AND NUMBER OF LETHAL FRAGMENTS AS FUNCTION OF VELOCITY

Time (sec)	Velocity (fps)	Lethal Size (in)	Lethal Mass (lb)	Number of Lethal Fragments
1	20	38.6	3650.0	2
10	24	32.2	2131.0	6
50	35	22.3	700.0	3
100	100	7.92	31.6	1

The lethal size was plotted on Figure 4-39 to obtain the number of fragments having a mass greater than the lethal mass. The results are given in the last column of Table 4-3. The results are somewhat discouraging from a destruct viewpoint. For example, only a maximum of six lethal fragments for destruct at 10 seconds into flight are obtained. Considering the azimuth effect shown in Figure 4-40, the probability of a hit into the LH_2 tank is about 0.2 or 1 fragment. The situation is worse at T = 100 seconds since there is only one lethal fragment.

The effect of fragment shape on penetration was also investigated. Figure 4-41 shows a plot of fragment mass versus striking velocity for a cylindrical fragment (with length to diameter ratio of one) compared to cubical fragments. There is no significant difference.

Table 4-3 indicates that the lethal fragment size required is quite large at the early destruct times. The applicability of the fragment penetration (Equation 4-25) becomes very questionable for large fragments. It cannot be doubted that corner impact of such large fragments on the skin would puncture it. However, should the large fragment hit flat against the skin, it is likely to hit an internal frame. For a conservative analysis, it is assumed that a cubical fragment of 38.6 inches on a side (at lift-off) hits a frame at 20 ft/sec. Consider frames at X_T 1377 and X_T 1624. Again, based on conservation of energy and assuming rigid-plastic behavior of the frame, the maximum displacement of the frame is:

$$X_{max} = \frac{1}{2}\frac{MV^2}{R} = \frac{1}{2} \times \frac{3650 \times 20^2}{32 \times 41{,}700} = 0.547 \text{ ft}$$

$$X_{max} = 6.5 \text{ inches}$$

This is not sufficient to rupture the frame. Hence, it is concluded that there is enough uncertainty as to the damaging effect of the fragments that they should not be considered as a primary destruct mechanism.

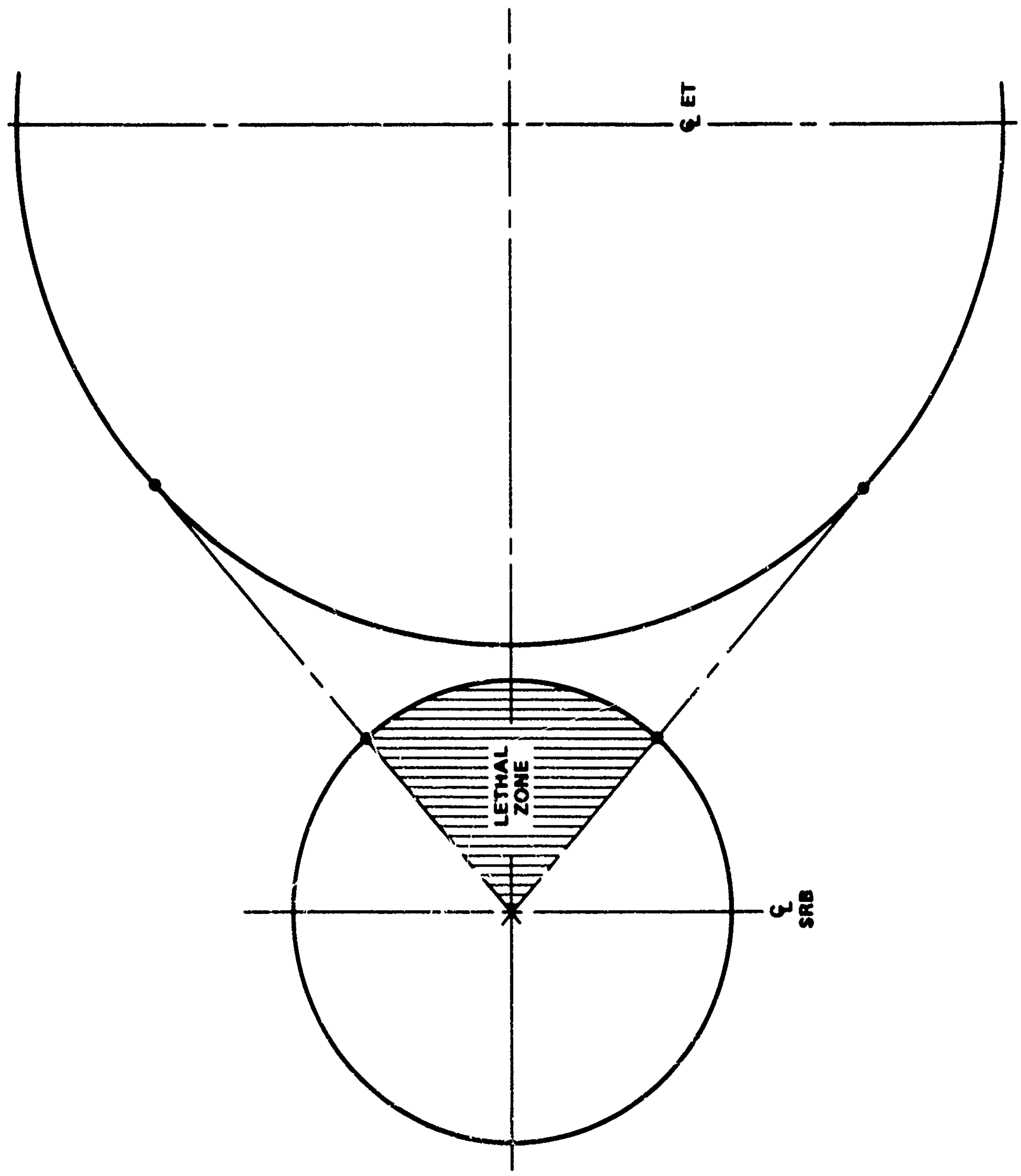

FIGURE 4-40 LETHAL ZONE FOR FRAGMENTS

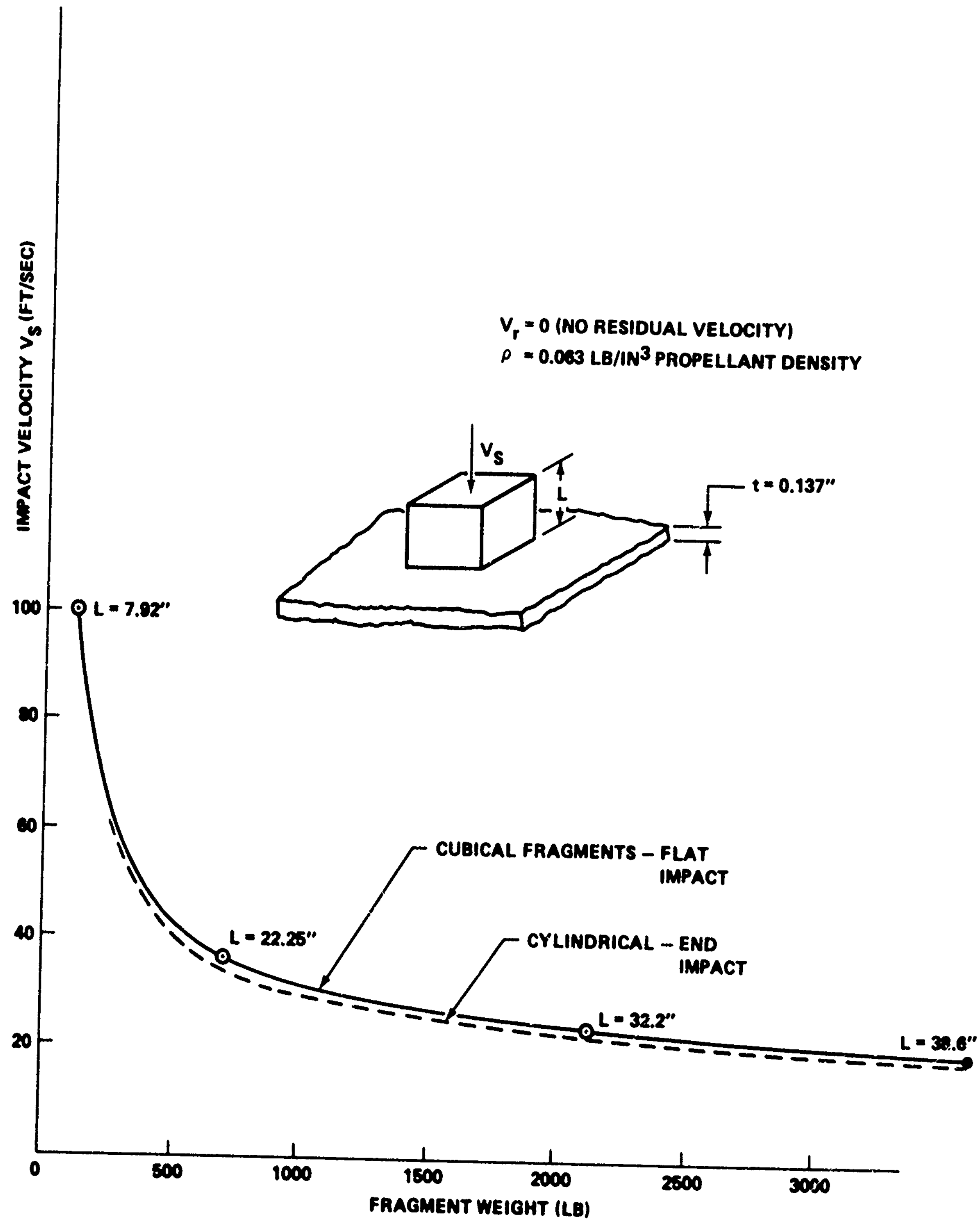

FIGURE 4-41 FRAGMENT WEIGHT VS. IMPACT VELOCITY

BLAST ON LH_2 TANK. The LH_2 tank could also experience blast loads due to breakup of the SRB during destruct. The primary destruct mechanism would be collapse of the tank shell until rupture due to excessive deformation of skin and frames or excessive pressure buildup in the ullage volume during gross deformation. See "Dynamic Plastic Deformation of LH_2 Tank," p. 4-32.

The area of highest blast load is near the upper portion of the LH_2 in the vicinity of frame X_T 1624. This is also the area most vulnerable to gross deformation since the frames at X_T 1624 and X_T 1377 are rather weak in comparison to frames at X_T 985 and X_T 2058. Hence, a buckling analysis was made of the LH_2 tank as illustrated in Figure 4-42. Basically, the BOSOR computer program was used to perform a static analysis. The structural model included frames at X_T 1377 and X_T 1624 and the smaller intermediate stability frames. The effect of longitudinal stiffeners was included by a smearing technique internal to BOSOR which computes effective orthotropic properties. The effect of internal pressure was also included.

The external pressure on the shell varies in magnitude and distribution as the blast wave engulfs the cylindrical structure. An examination of the circumferential distribution resulted in the selection of the distribution shown in Figure 4-43 as the most damaging for destruct at 10 seconds into flight. Also shown in Figure 4-43 is the estimated internal pressure accounting for ullage pressure and hydrostatic pressure at 10 seconds into flight. The results of the BOSOR calculations indicated gross deformation. In fact, the pressure differential required to buckle the skin is on the order of 0.2 psi. The maximum applied pressure differential is on the order of 644 psi. Hence, it is obvious that based on a static analysis the skin and frames will buckle and experience gross deformation.

An analysis was also made for destruct at T = 100 seconds into flight. The external and internal pressure distribution is shown in Figure 4-44. The BOSOR results again indicated buckling of the skin and frames and gross deformation.

DYNAMIC BUCKLING ENHANCEMENT. The blast causes a transient pressure rather than a static pressure as previously analyzed. The critical buckling pressure, therefore, depends on the impulse as described by Anderson.[4] The details in constructing the familiar pressure-impulse (P-I) curve are given in footnote 3 on page 4-50. Basically, the P-I curve is calculated in the elastic and inelastic ranges. In the elastic range, the asymptotes are given by:

$$P_E = 0.92E \left(\frac{a}{L}\right) \left(\frac{h}{a}\right)^{5/2} \tag{4-27}$$

$$L_E = 5\, \rho c a \left(\frac{h}{a}\right)^2 \tag{4-28}$$

[4] Anderson, D.L., and Lindberg, H.E., "Dynamic Pulse Buckling of Cylindrical Shells under Transient Lateral Pressures," AIAA Journal, Vol. 6, No. 4, Apr 1968.

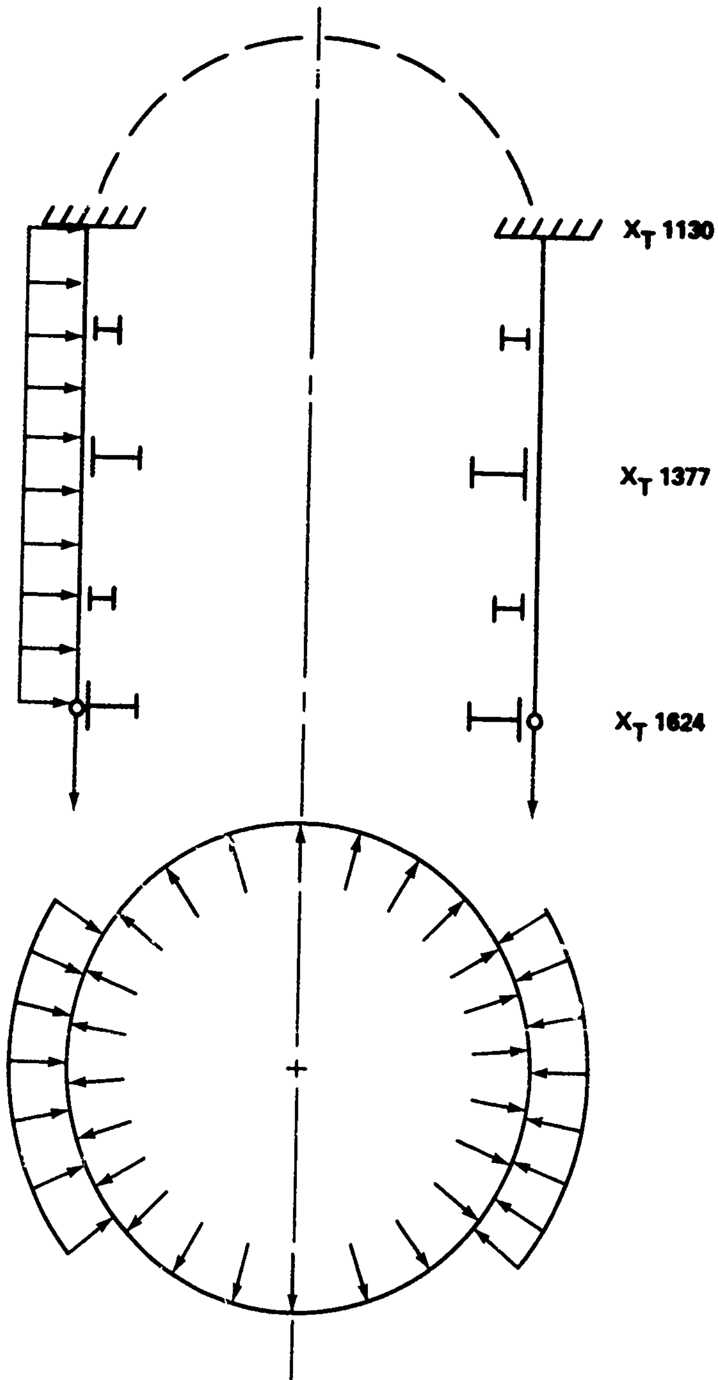

FIGURE 4-42 SCHEMATIC OF BOSOR MODEL

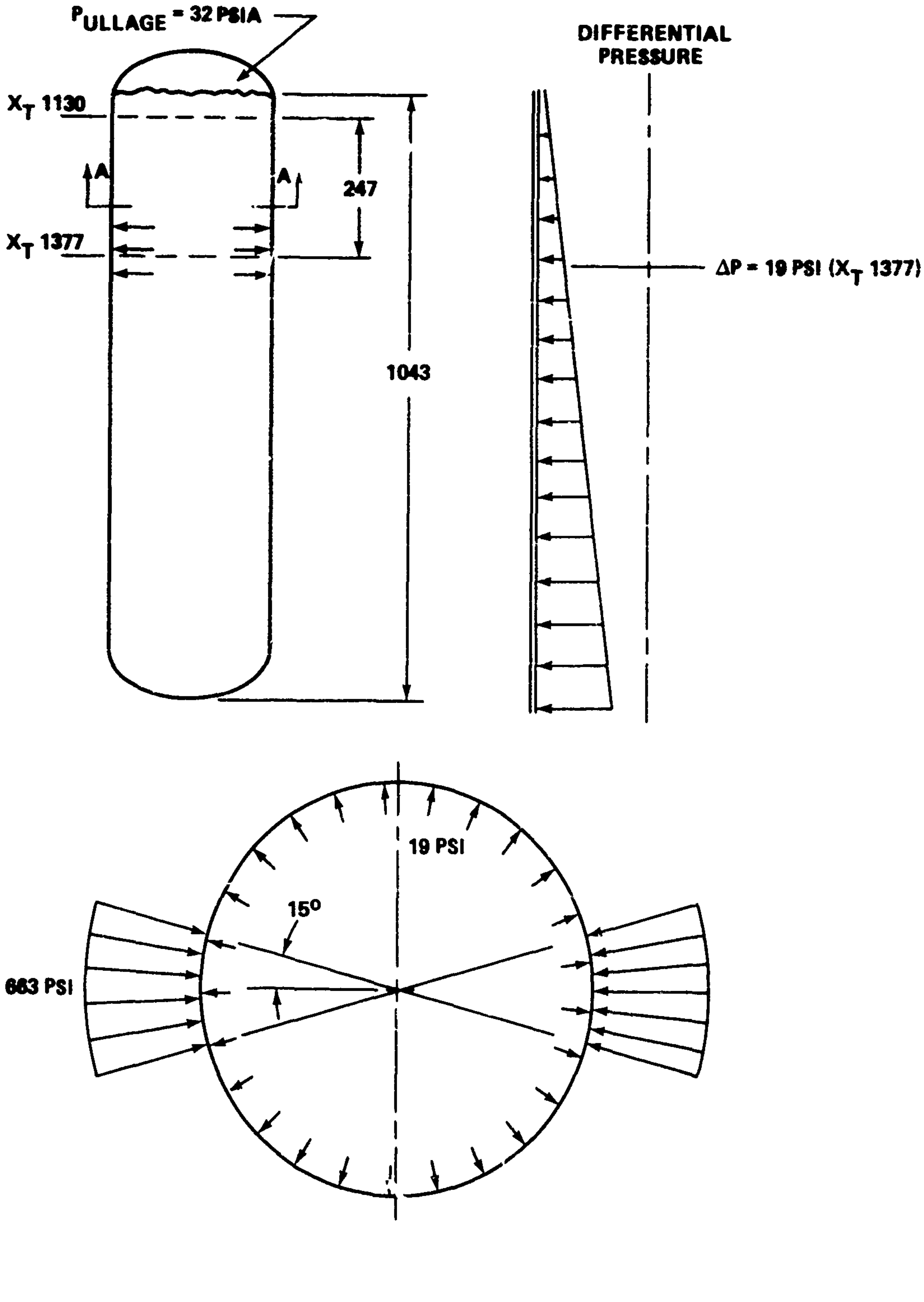

FIGURE 4-43 EXTERNAL BLAST PRESSURE AND INTERNAL PRESSURE AT T = 10 SECONDS

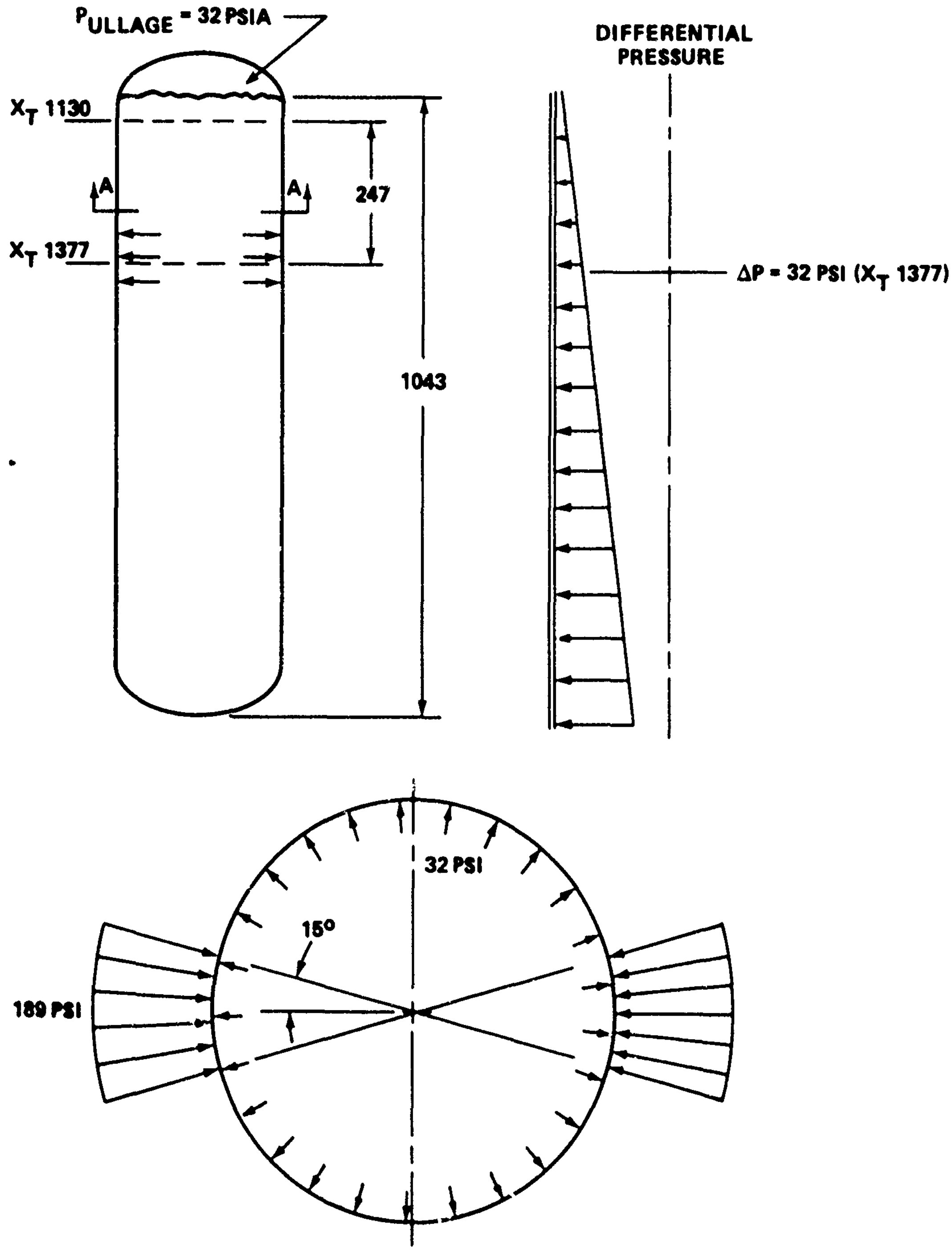

FIGURE 4-44 EXTERNAL BLAST PRESSURE AND INTERNAL PRESSURE AT T = 100 SECONDS

In the inelastic range, buckling is based on the tangent modulus. In this range

$$P_T = \frac{3}{4}\sigma_y\, h/a \tag{4-29}$$

$$I_T = \left(\frac{96}{K}\right)^{1/4} a(\rho\sigma_y)^{1/2}\,(h/a)^{3/2} \tag{4-30}$$

where

L = Length of span = 247 in

h = Thickness of skin = 0.137 in

a = Radius = 165.5 in

ρ = Density = 0.1 $\mathrm{lb/in^2}$

c = Wave speed = 200,000 in/sec

K = Slope beyond yield of a plot of σ/E_T versus compressive hoop strain = 35

For a span of 247 inches, the elastic buckling pressure is 0.12 psi. Assuming that the intermediate stability frames stabilize the skin, the buckling pressure is still only 0.24 psi. The distribution between the asymptotes is approximated by simple hyperbolas of the form:

$$\left[\left(\frac{P}{PA}\right) - 1\right]\left[\frac{I}{I_A} - 1\right] = 1 \tag{4-31}$$

Figure 4-45 shows a plot of the P-I curve for 2219T87 aluminum. The results as developed are for a uniform external pressure but, as discussed by Anderson (footnote 4, p. 4-54), the results can be used to estimate the buckling pressure for a cosine loading. The buckling pressure should be increased by about a factor of 2. The impulse can be estimated by assuming an exponential decay.

$$I = \int_o^\infty P dt = P_o \int e^{\frac{-t}{T}}\, dt$$

$$I = P_o T \tag{4-32}$$

where

T = Time constant

Hence, for the case of destruct at 10 sec, T = 1 msec, P_O = 644 psi, making I = 644 psi-msec. From Figure 4-45 the buckling pressure is 0.13 psi for a span of 247 inches. For a cosine distribution, the buckling pressure is on the order of 0.26 psi.

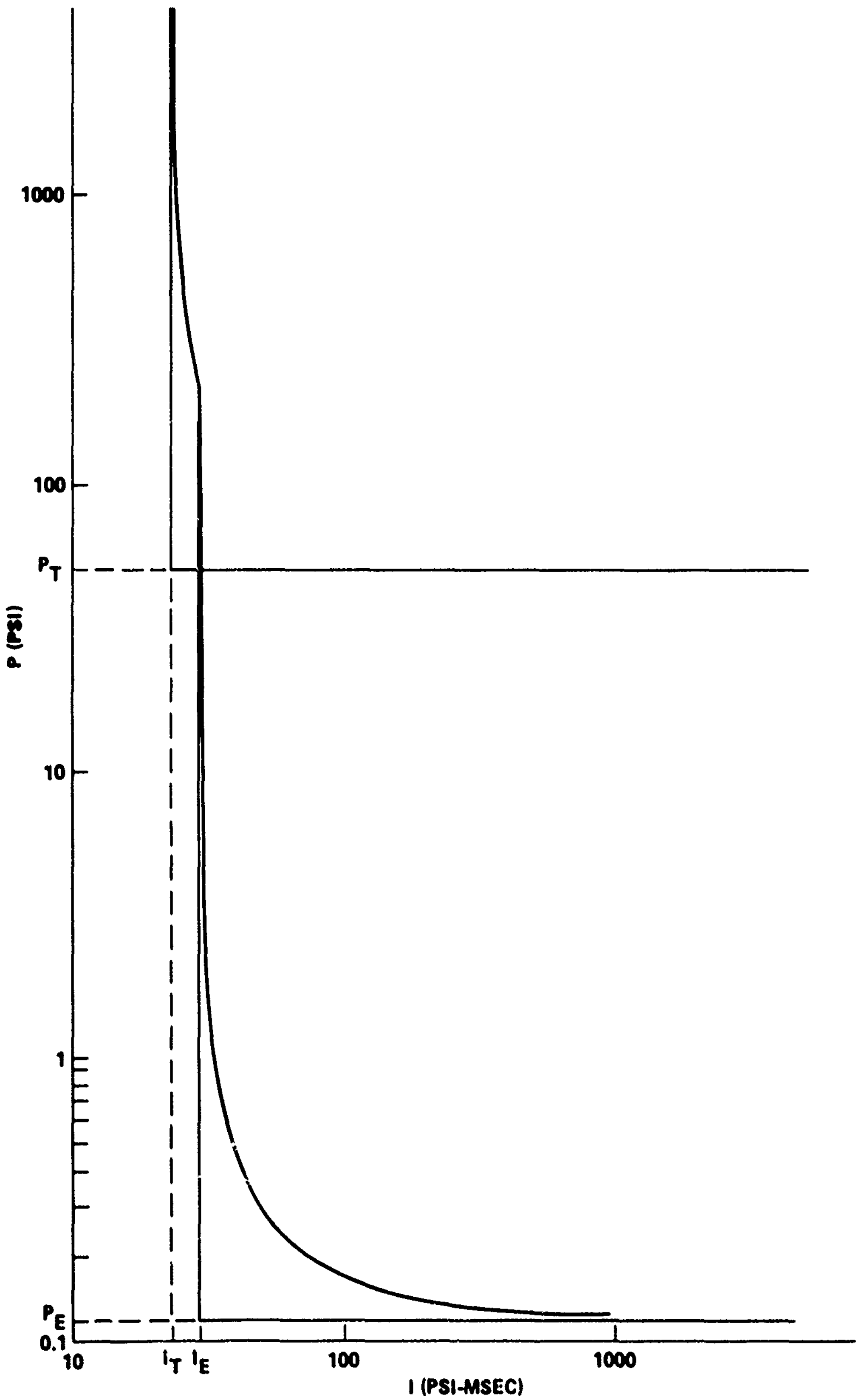

FIGURE 4-45 P-I CURVE - h = 0.137 IN

The previous calculations did not account for the longitudinal stiffeners. An estimate was made using an effective skin thickness based on equality of stiffness. For example, there are 96 longitudinal stiffeners as shown in Figure 4-46. The spacing is about 10.83 inches. The cross section of the stiffener is shown in Figure 4-46. The width of effective skin in axial compression can be estimated from:

$$W_1 = 0.60t \sqrt{\frac{E}{F_c}} \qquad (4\text{-}33)$$

$$W_1 = 0.60 \times 0.137 \sqrt{\frac{10 \times 10^6}{75,000}} = 0.95$$

Using the effective width, the moment of inertia about the neutral axis is 0.138 in^4. Equating this to the moment of inertia of skin of uniform thickness t_e yields:

$$t_e = \sqrt[3]{\frac{12I}{B}} = 0.535 \text{ inch}$$

The P-I curve for this effective skin thickness for a frame spacing of 123 inches is shown in Figure 4-47. This represents an upper bound for the dynamic buckling pressure. For an impulse of 644 psi-msec, the buckling pressure is still only 22 psi. Hence, even though there is some dynamic enhancement, the shell is still completely overmatched by the applied external pressure. Hence, it is concluded that during destruct, the LH_2 tank will experience severe buckling. Catastrophic rupture is probable, although it is difficult to predict the degree of destruct. This was found to be the case for destruct at 1 and 50 seconds.

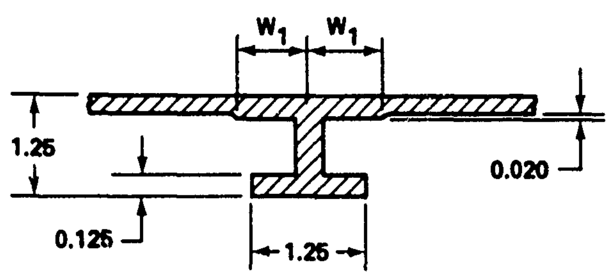

FIGURE 4-46 STIFFENER CROSS SECTION

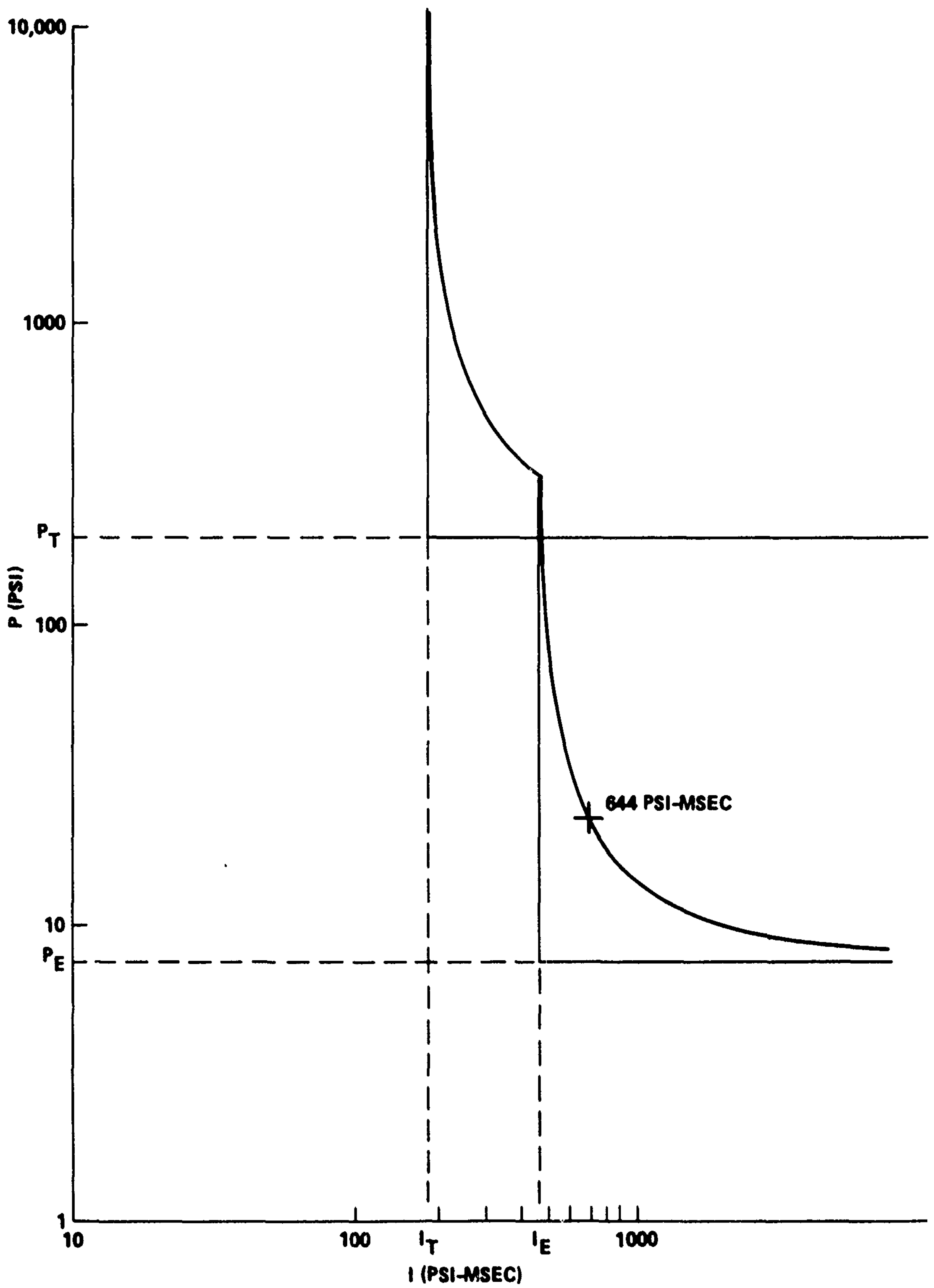

FIGURE 4-47 P-I CURVE - h = 0.535 IN

Section II. DESTRUCT FOLLOWING LOSS OF ONE SRB

INTRODUCTION

The purpose of this analysis was to investigate the feasibility of destructing the ET following the loss of one SRB at times of 0, 10, 50, and 100 seconds into flight. The methodology used was basically the same as for destruct from two SRB's. A linear-shaped charge was used on the outboard side of the SRB. The lateral thrust generated was still the same as that presented in Figure 4-7. The primary difference was that the ET was only loaded by the thrust on one side.

DYNAMIC RESPONSE OF SRB/ET TO LATERAL THRUST

An elastic dynamic response analysis was made of the SRB/ET cluster as shown in Figure 4-48. Finite element beam elements used in the SRB were identical to those used in the analysis previously described for two SRB's. The ET was rather coarsely modeled. Of primary interest was simulating its mass since it provides lateral inertia to the lateral thrust. The inertia of the orbiter was conservatively neglected.

The local stiffness of the structure in the ET and SRB at the forward and aft joint was calculated using finite element models described in Appendices C, D, E, and F. Equivalent spring constants were then calculated so that scalar springs could be used to simulate local deformation of the ET and SRB at the joints. For the forward joint, a single radial load produced a deflection corresponding to a spring constant of 0.4×10^6 lb/in. The spring constant was lower than in the previous case (p. 4-6). In this case, the bulk of the load was carried by frame bending, whereas in the previous case, the load was primarily carried by compression in the cross beam. An equal and opposite radial load on the SRB forward joint produced a deflection corresponding to a spring constant of 0.819×10^6 lb/in. The equivalent spring constant for the two springs in series was 0.27×10^6 lb/in. Similarly, the spring constant for the aft SRB/ET support structure was 0.52×10^6 lb/in.

The lateral thrust generated at T = 0 by clamshell rupture (Fig. 4-7) was used as an input to the finite element model. The resulting response is shown in Figure 4-49. The loads at the joints are lower than in the previous case because the effective springs are softer. The collapse load of the forward frame (X_T 985) is estimated to be on the order of 550,000 pounds. This load is developed at a time of 54 msec after initiation of destruct. Assuming the joint fails at 550,000 pounds, the velocity of the SRB joint at failure is about 112 in/sec. The velocity of the ET forward joint at the same time is about 5 in/sec. This yields a net velocity of the SRB relative to the ET of 107 in/sec. This is only slightly lower than for the case of destruct by two SRB's. However, the force at the aft joint never reaches the estimated 850,000 pounds collapse load of the aft SRB frame. The maximum load at the aft joint is about 550,000 pounds. One possible solution to this is relocation of the linear-shaped charge to a more central location between the forward and aft joints, thereby distributing the thrust load more evenly. Another solution is to purposely design the aft joint for failure below 600,000 pounds. Even though the aft joint does not fail theoretically, the SRB could still rotate about the aft joint and impact the ET at fairly high velocity near the front joint. Based on this analysis, it appears that destruct at lift-off following loss of one SRB is very marginal.

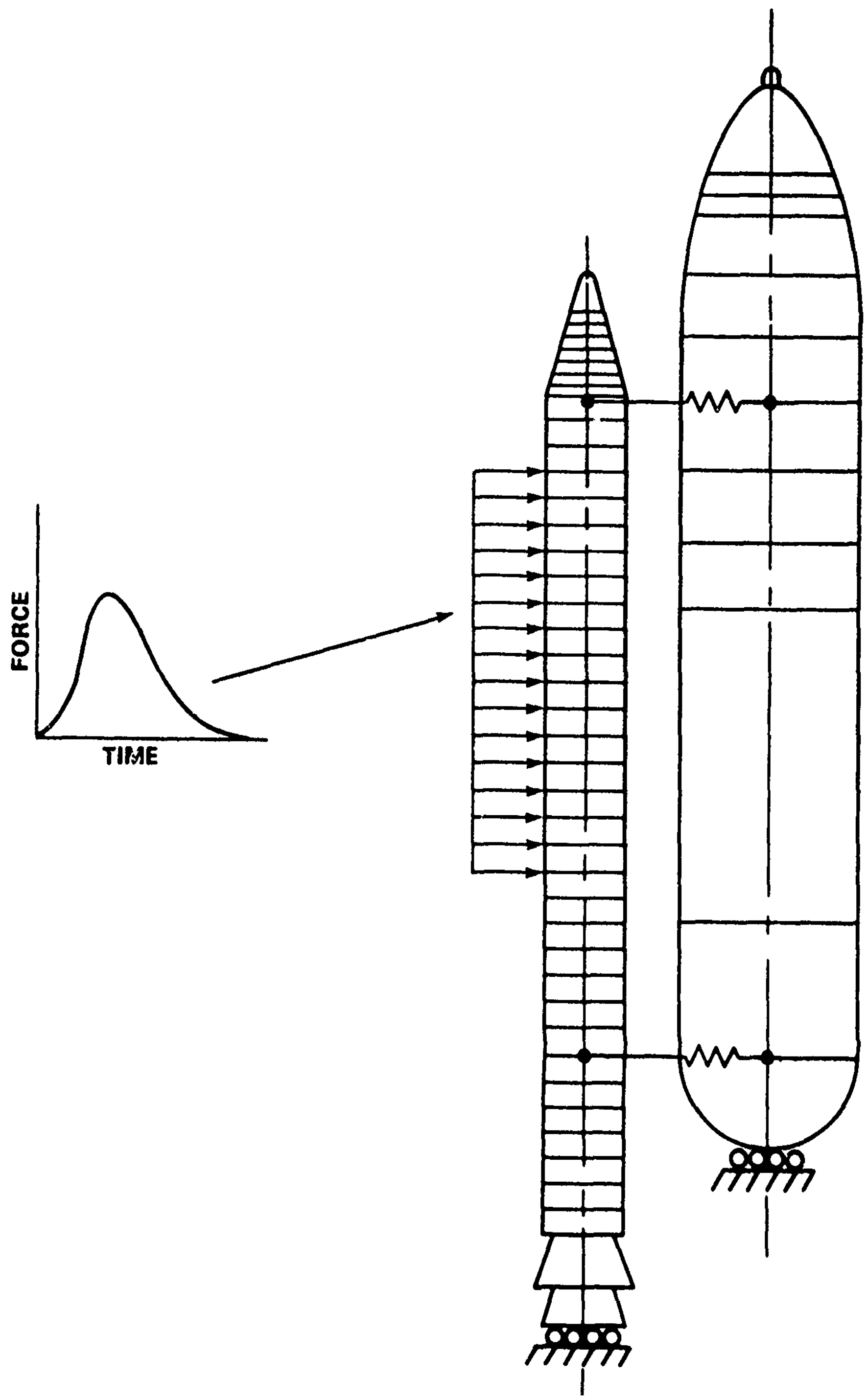

FIGURE 4-48 FINITE ELEMENT MODEL FOR RESPONSE DUE TO LATERAL THRUST OF ONE SRB

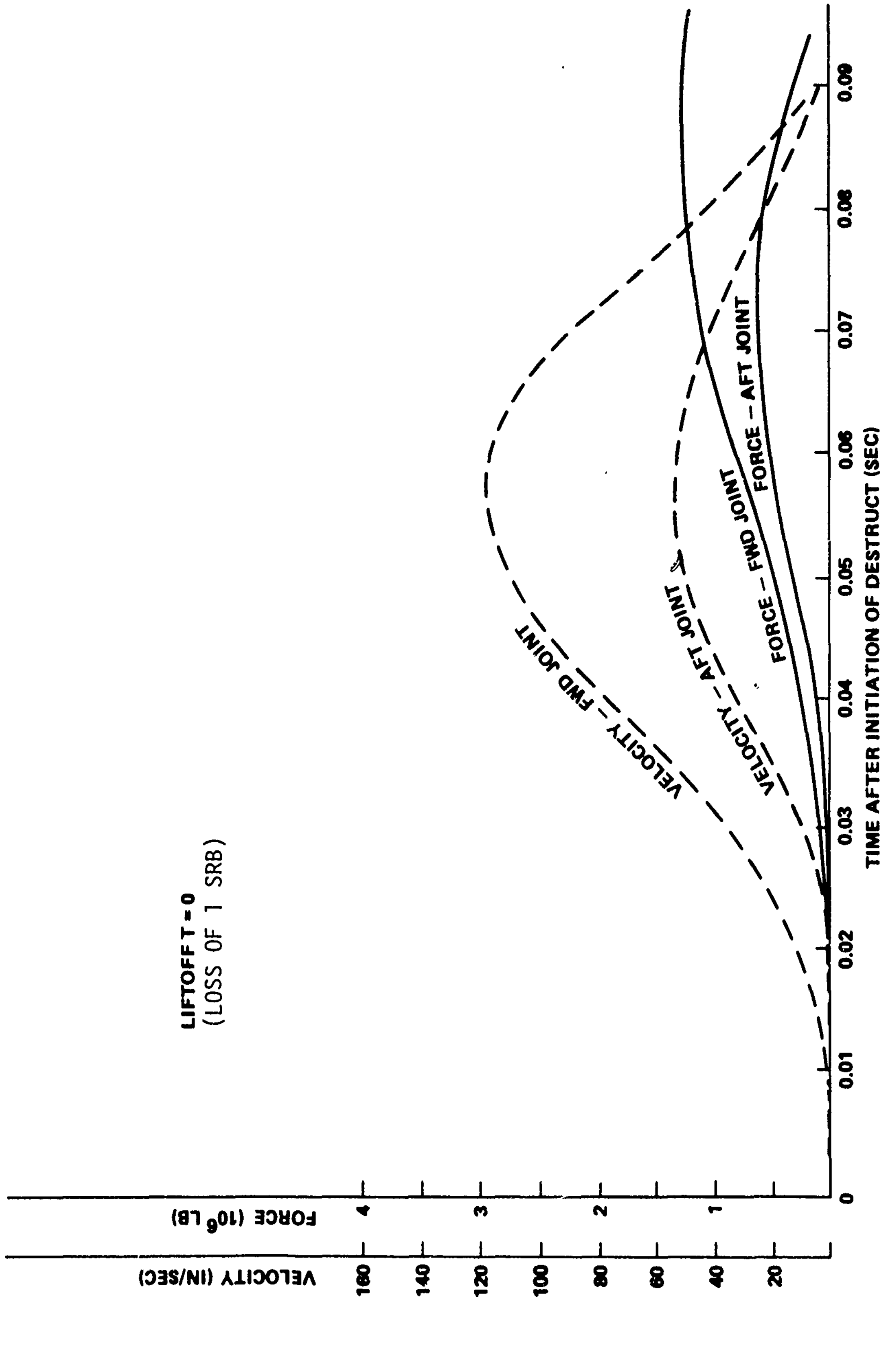

FIGURE 4-49 FORCE AND VELOCITY AT FORWARD AND AFT JOINTS DURING DESTRUCT

The response for destruct at T = 50 seconds is much more encouraging, as shown in Figure 4-50. The force at the forward joint builds up to the collapse load of 550,000 pounds in about 27 msec. The corresponding velocity of the SRB forward joint is about 220 in/sec. However, the remaining impulse from the lateral thrust increases the velocity to about 366 in/sec. The corresponding velocity of the ET forward joint is 4 in/sec, yielding a relative velocity of 362 in/sec. The aft joint reaches the 850,000-pound collapse load after 54 msec. The velocity of the SRB at the aft joint is 120 in/sec. The ET velocity is 30 in/sec, yielding a relative velocity of 90 in/sec. The average velocity of the SRB relative to the ET is 153 in/sec, using the 216 in/sec relative velocity at the front joint rather than 362 in/sec. As will be shown later, this is more than sufficient to cause catastrophic rupture of the LH_2 tank. Table 4-4 shows a summary of impact velocities. Compared with those in Table 4-2 (Destruct by two SRB's), they are slightly lower.

FAILURE MODES

Static analyses were made of the forward and aft joints to determine equivalent spring constants and investigate failure modes during destruct. The results for the forward and aft SRB joint substructure were previously discussed. In summary, it was estimated that the SRB forward joint substructure would collapse at a load of about 550,000 pounds. The aft SRB collapse load was estimated to be 850,000 pounds. The spring constants for the joints were found to be 0.819×10^6 lb/in and 4.83×10^6 lb/in, respectively.

The forward and aft joints of the ET are only loaded on one side. A finite element model of the ET frame (Appendix E) indicates that the 550,000-pound load used in Section I will produce an elastic stress of 79,500 psi in the frame and 9,950 psi in the cross beam. Hence, a 550,000-pound load is a reasonable estimate of the ultimate or collapse strength of the frame under loading on one side only. The deformed shape of the frame is shown in Figure 4-51. Deflection caused by the 550,000-pound force is 1.39, yielding a spring constant of 0.4×10^6 lb/in.

An analysis of the aft ET frame X_T 2058 shows that the force to initiate yielding is about 12 percent higher than in the case of two SRB's simultaneously loading the ring (Appendix C). The net lateral load P (P/2 at the two strut locations) to initiate yielding is about 1.6×10^6 lb. Hence, the strength of this frame is no issue. The SRB aft frame is clearly the weaker of the two. The question of the strength of the struts and pins is the same as in the case for normal destruct. Failure is assumed to occur at 850,000 pounds. The spring constant of the aft ET frame is 0.58×10^6 lb/in for radial loads on one side.

DYNAMIC PLASTIC DEFORMATION OF LH_2 DURING IMPACT OF ONE SRB

This analysis is quite similar to that in Section I, p. 4-32. The collapse load of the frames at X_T 1377 and X_T 1624 is slightly different due to the type of loading, as illustrated in Figure 4-52. The maximum bending movement in the frame under the loading is slightly different than in the case of two radial loads. In the case of destruct by one SRB, the load P_o is resisted primarily by the inertia of the fluid. In this case

$$M_{max} = 0.238 \, P_o R$$

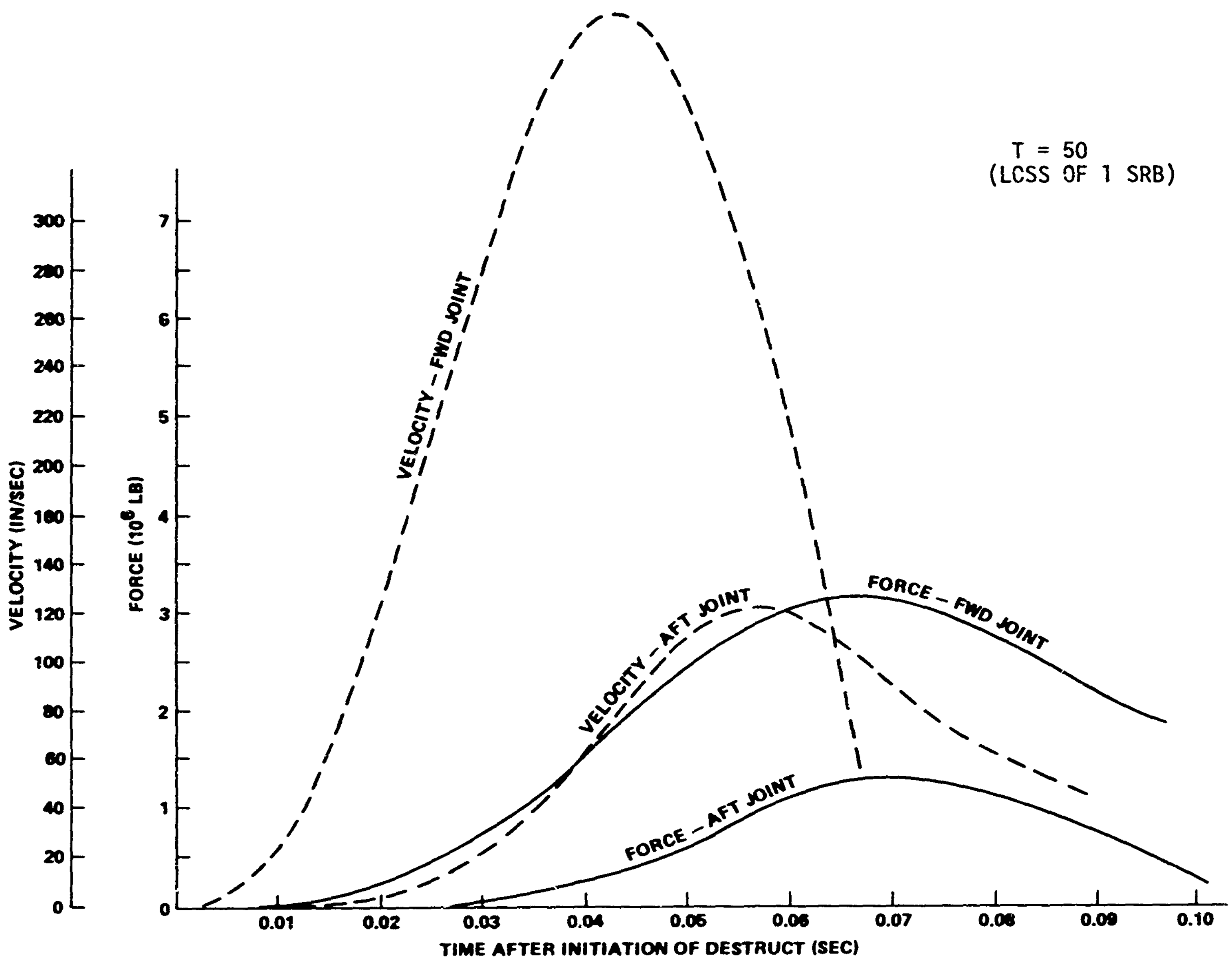

FIGURE 4-50 FORCE AND VELOCITY AT FORWARD AND AFT JOINTS

TABLE 4-4 SUMMARY OF SRB IMPACT VELOCITIES FOR DESTRUCT FOLLOWING LOSS OF ONE SRB

Time of Destruct (sec)	Impulse (lb/sec)	Weight of SRB (lb)	Weight of Orbiter Plus SRB (lb)	Velocities Fwd (in/sec)	Velocities Aft (in/sec)	Average Velocity (in/sec)
0	0.18×10^6	1.28×10^6	1.895×10^6	107	0	53.5
10	0.26×10^6	1.177×10^6	1.861×10^6	100	50	75.0
50	0.32×10^6	0.767×10^6	1.733×10^6	216	90	153.0
100	0.55×10^6	0.323×10^6	1.57×10^6	400	125	262.0

In the case of two radial loads (neglecting the restraint of skin and adjacent frames) the maximum moment is

$$M_{max} = 0.318\ P_o R$$

As discussed in Appendix G, the skin and adjacent frames reduce this to

$$M_{max} = 0.16\ P_o R$$

If it is conservatively assumed that the skin has the same effect in the case of one SRB, then the collapse load given in Section I, p. 4-32 can be ratioed as follows:

$$P_{collapse} = \left(\frac{0.318}{0.238}\right)(41{,}700) = 55{,}700\ \text{lb}$$

Thus, the collapse load for impact of one SRB is higher than expected.

The equation of motion (Equation 4-11) must be expanded to include the motion of the ET (no longer stationary, as in the case of normal destruct with two SRB's). Again, assuming rigid plastic stress strain behavior, the resistance R_i at the ET frames is transferred to the ET, causing it to move. The equation of motion of the ET is shown in Figure 4-53.

$$M_{ET} \frac{d^2X_2}{dt^2} = R_i \qquad (4\text{-}34)$$

This equation was solved along with Equation 4-11 to estimate the deformation of the LH_2 frames. The net deformation of the frame is then

$$X = X_1 - X_2 \qquad (4\text{-}35)$$

and the velocity of the SRB relative to the ET is

$$V = V_1 - V_2 \qquad (4\text{-}36)$$

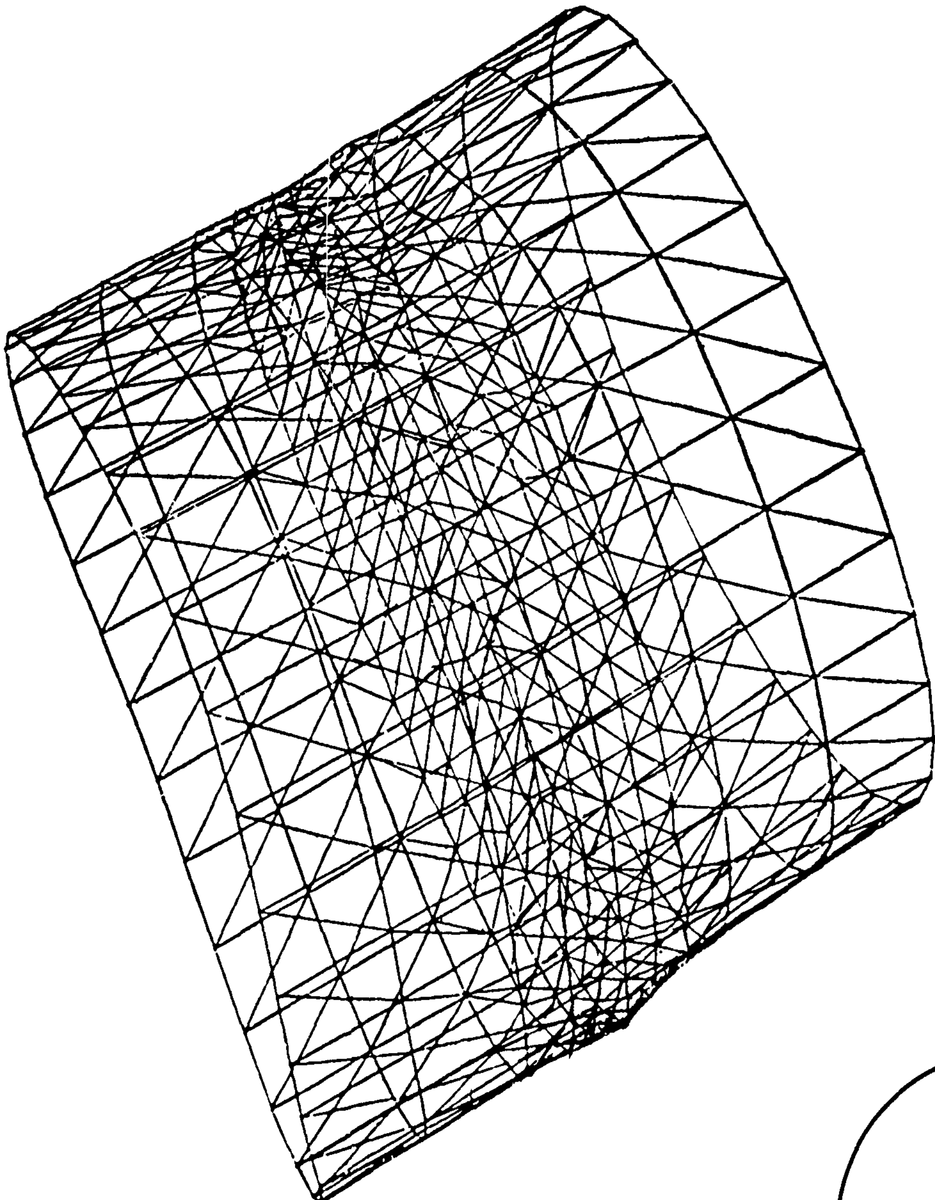

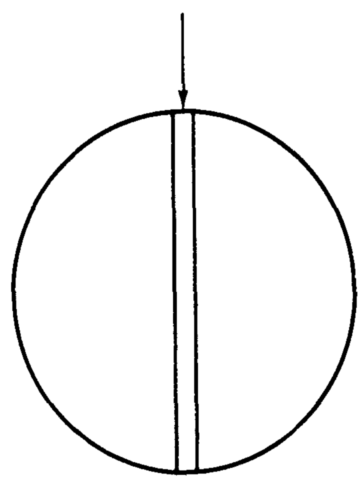

FIGURE 4-51 FINITE ELEMENT MODEL OF ET INTERTANK STRUCTURE DEFORMED SHAPE DUE TO 1 RADIAL LOAD

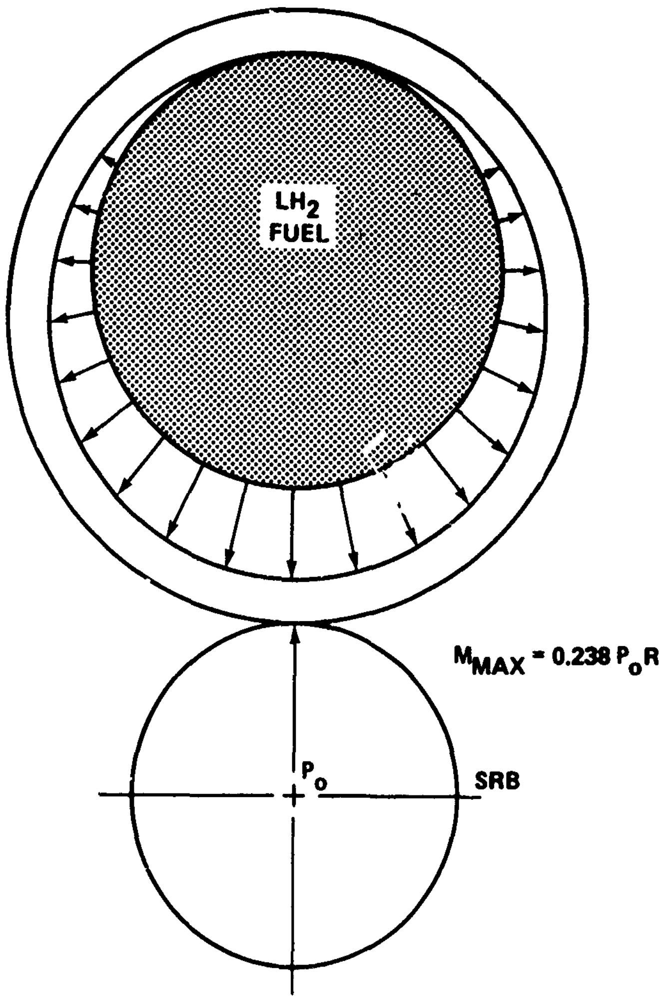

FIGURE 4-52 LOADING ON ET FRAMES DURING DESTRUCT (LOSS OF 1 SRB)

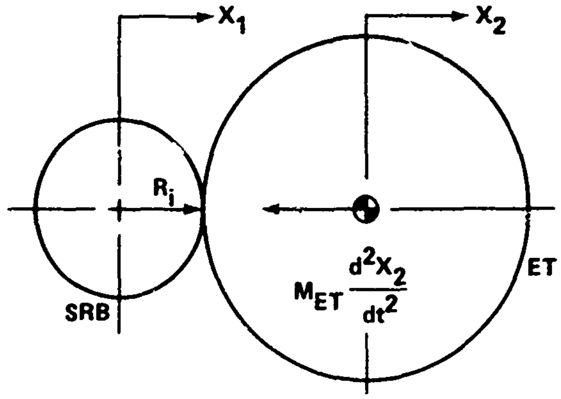

FIGURE 4-53 MOTION OF ET

The only other difference is the volume change due to local crushing of the LH_2 tank for estimating the pressure buildup for Mode 2 failure described in Section I. For this case, only one side of the LH_2 tank is crushed in.

Figure 4-54 shows the estimated displacement of frames X_T 1377 and X_T 1624 for destruct at 10, 50, and 100 seconds. If it is again assumed that 42 inches in the threshold deflection causes failure by excessive strain (Section I, p. 4-47), then destruct will occur at T = 50 and 100 seconds. Destruct at T = 10 seconds might occur since the 42-inch threshold value could be high. Destruct at T = 0 is unlikely. The primary difference between destruct by two SRB's and destruct by one SRB is that in the latter case, the ET/orbiter cluster moves away as the SRB is propelled toward the cluster.

Figure 4-55 shows the estimated pressure buildup caused by local crushing of the LH_2 tank. The estimated threshold value of 82 psi is not exceeded at T = 0, 10, 50, or 100 seconds. The pressure is lower than in Section I because only one side of the LH_2 tank is crushed in and displacement X is smaller.

BLAST AND FRAGMENT ANALYSIS

The combined effects of blast and fragments from catastrophic rupture of one SRB are expected to be essentially the same as those given in Section I, p. 4-48. The probability of fragment damage is again negligible. The pressure from the blast wave completely overmatches the buckling strength of the shell for pressure on one side or on both sides.

CONCLUSIONS

Catastrophic rupture of the ET following loss of one SRB is highly probable for times of 50 and 100 seconds, is marginal for T = 10 seconds, and unlikely for T = 0 (lift-off). The probable failure mode is rupture of LH_2 tank support frames due to excessive strain. Failure due to excessive pressure buildup is not likely.

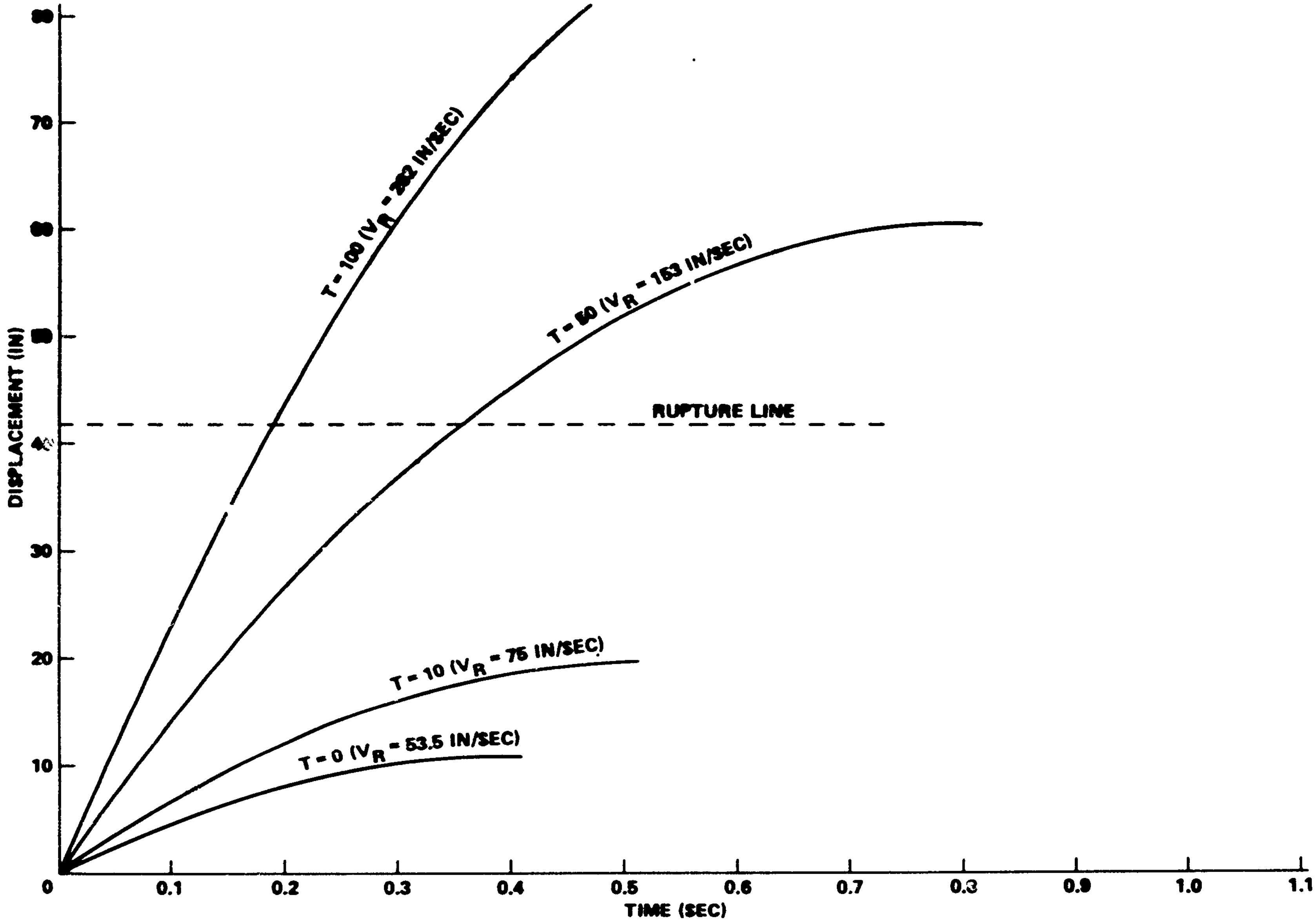

FIGURE 4-54 LH_2 TANK FRAME DISPLACEMENT VS. TIME FOR DESTRUCT BY 1 SRB AT T = 0, 10, 50, 100 SECONDS

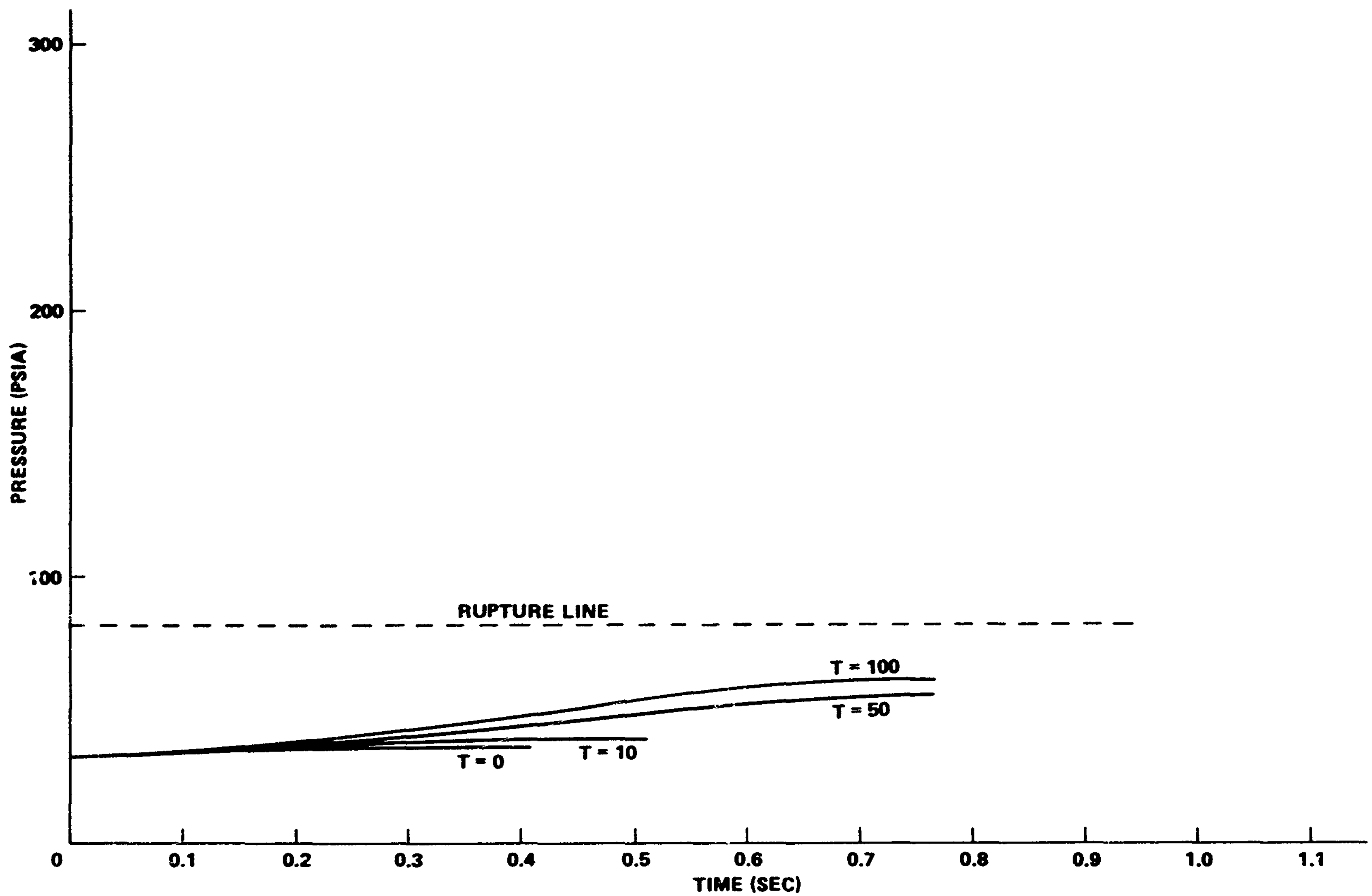

FIGURE 4-55 PRESSURE IN ULLAGE TANK VS. TIME FOR DESTRUCT BY 1 SRB AT T = 0, 10, 50, 100 SECONDS

The inability to destruct is probably of little consequence since the analysis of Section IV indicates that the cluster will break up 2 seconds after loss of one SRB. This does not leave sufficient time to initiate destruct from a range safety viewpoint.

RECOMMENDATIONS

The following three recommendations are made:

1. Forward and aft joint should be designed so that pins/struts fail before collapse of the support frames.

2. Model tests should be conducted to determine threshold value for frame deflection at failure.

3. The linear-shaped charge should be centrally located to evenly load the forward and aft joint.

FURTHER RESEARCH

A reassessment of the destruct mechanism for the clamshell-type SRB breakup based on the actual LSC length and placement (Fig. 4-1) is presented in Appendix H.

Section III. CATASTROPHIC RUPTURE OF LOX TANK

INTRODUCTION

As illustrated in Figure 4-56, the LOX tank is located forward of the solid rocket motors (SRM). No direct contact between the SRM and the LOX tank will occur in case of a clamshell-type SRM destruct, and little blast or fragment damage can be expected because of the distance from the source. Therefore, conically shaped charges, mounted in the forward frustum or skirt of each SRB, have been proposed to puncture the LOX tank and initiate a catastrophic failure. A critical puncture size, dependent upon material properties, is required to generate a flaw that will propagate under a given state of stress.

In this case, the LOX tank material, 2219-T87 aluminum, has been chosen for its fracture toughness. The tank has been designed to leak before burst. The minimum flaw size to guarantee rupture, based on the normal operating stress, is very large. However, when puncturing a liquid-filled tank, the required flaw size is dramatically reduced due to the additional stress generated by the shock pressure in the fluid.

Much of the lower dome is stiffened to carry a compressive hoop stress or local fitting load (Fig. 4-57). In order to avoid these supported areas, the annular section located between R = 80 in and R = 130 in was selected for puncturing. It carries tensile membrane stresses in both the hoop and meridian directions. It also provides a location subject to oblique impact by the shaped charge jet. Experience has shown oblique impact to be more effective in damaging shell-type structures.

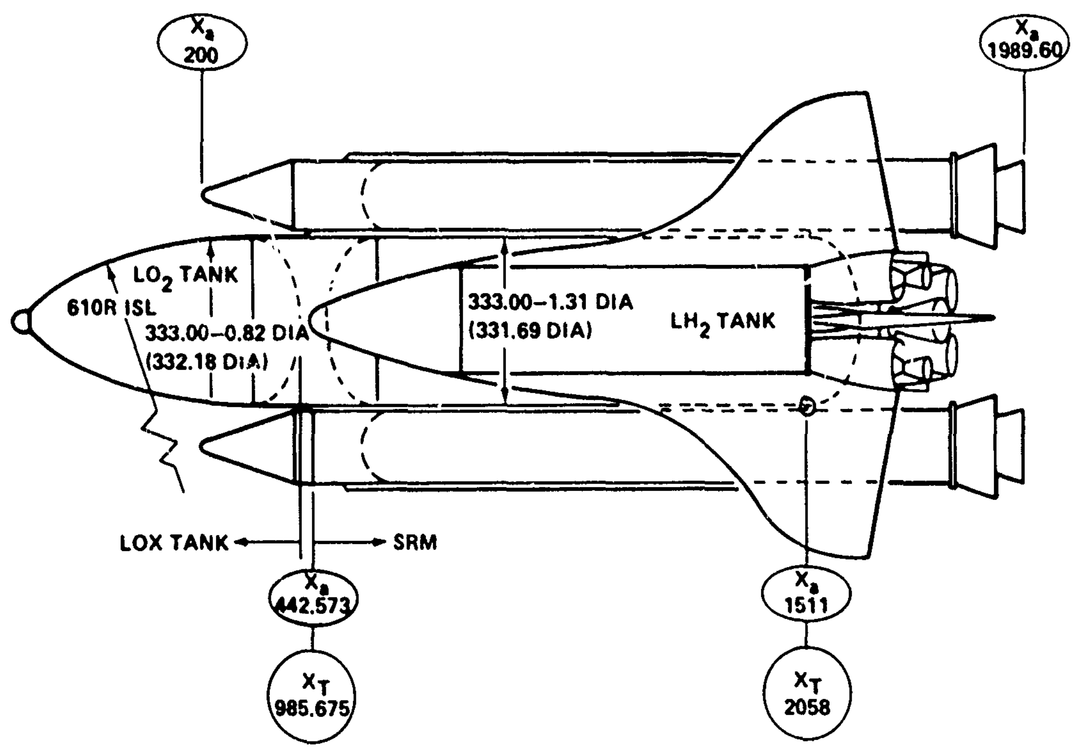

FIGURE 4-56 RELATIVE LOCATION OF LOX TANK TO SRM

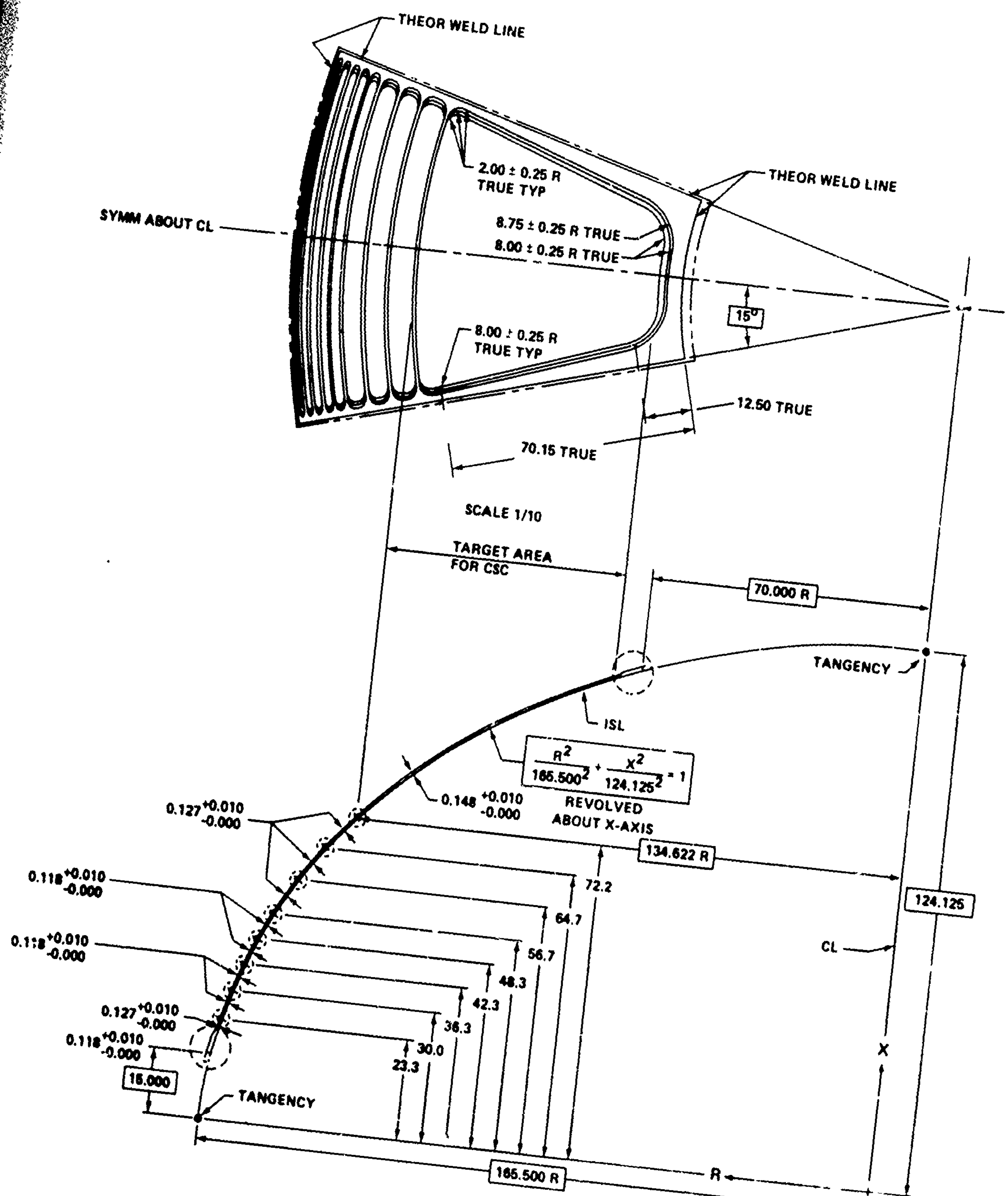

FIGURE 4-57 SKIN PANEL LOX TANK DOME

MEMBRANE STRESSES IN DOME

Consider only axial loading, as occurs at lift-off (Fig. 4-58). The pressure on an element of the lower dome at radius R is given by

$$P\ (R) = P_{ull} + \rho_{LOX}\ N_x\ [h - 124.125 + x] \tag{4-37}$$

where

ρ_{LOX} = 0.40945 lb/in^3 (density of LOX)

N_x = Load factor

h = Height of LOX

$$x = 124.125 \left[1 - \frac{R^2}{165.5^2}\right]^{1/2}$$

The stress on that element in the meridian direction is given by

$$f_\phi = \frac{P_{ull}\ \pi R^2 + \int_0^R P(R) 2\pi r dr}{2\pi R t_w \sin\phi} \tag{4-38}$$

where

t_w = Skin thickness

$$\phi = \tan^{-1} \left|\frac{dX}{dR}\right| = \tan^{-1} \left[0.75 \frac{R}{\left(165.5^2 - R^2\right)}\ 1/2\right]$$

Integrating yields

$$f_\phi = \frac{\left[P_{ull} + \rho_{LOX} N_x (h-124.125)\right]\ R^2 - 0.5\,\rho_{LOX} N_x \left[\left(165.5^2 - R^2\right)^{3/2} - 165.5^3\right]}{2\ R\ t_w\ \sin\ \phi} \tag{4-39}$$

The stress in the hoop direction is then given by

$$f_\theta = \left[48{,}690 - 0.7778\ R^2\right]^{1/2} \frac{P(R)}{t_w} - \left[\frac{f_\phi}{1 - 1.597 \cdot 10^{-5}\ R^2}\right] \tag{4-40}$$

Since the critical flaw size is inversely proportional to the magnitude of the stress, the minimum ullage pressure (Fig. 4-59) is used 'ere to compute stresses. In addition, the intertank is assumed to be vented to the free stream.

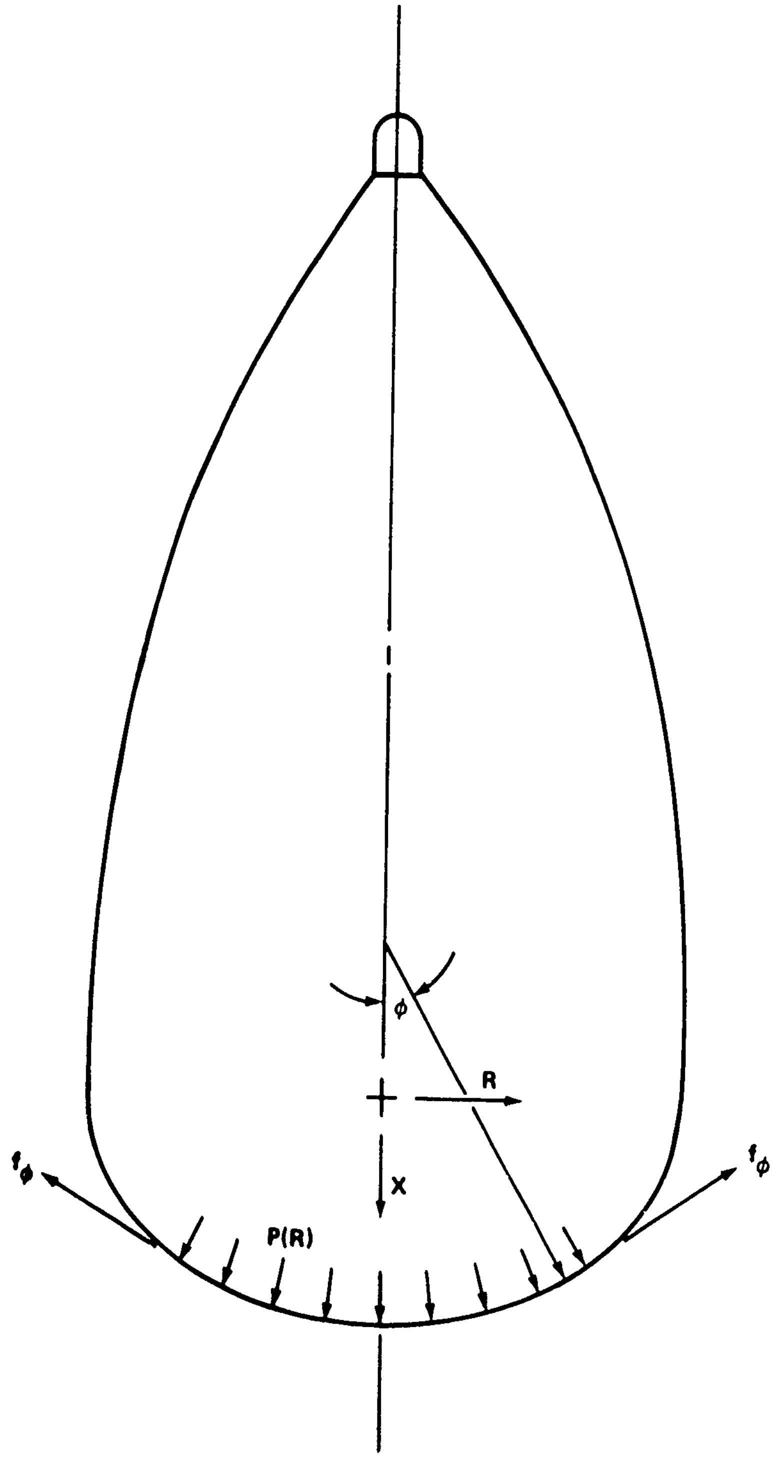

FIGURE 4-58 LOADING ON LOX TANK DOME

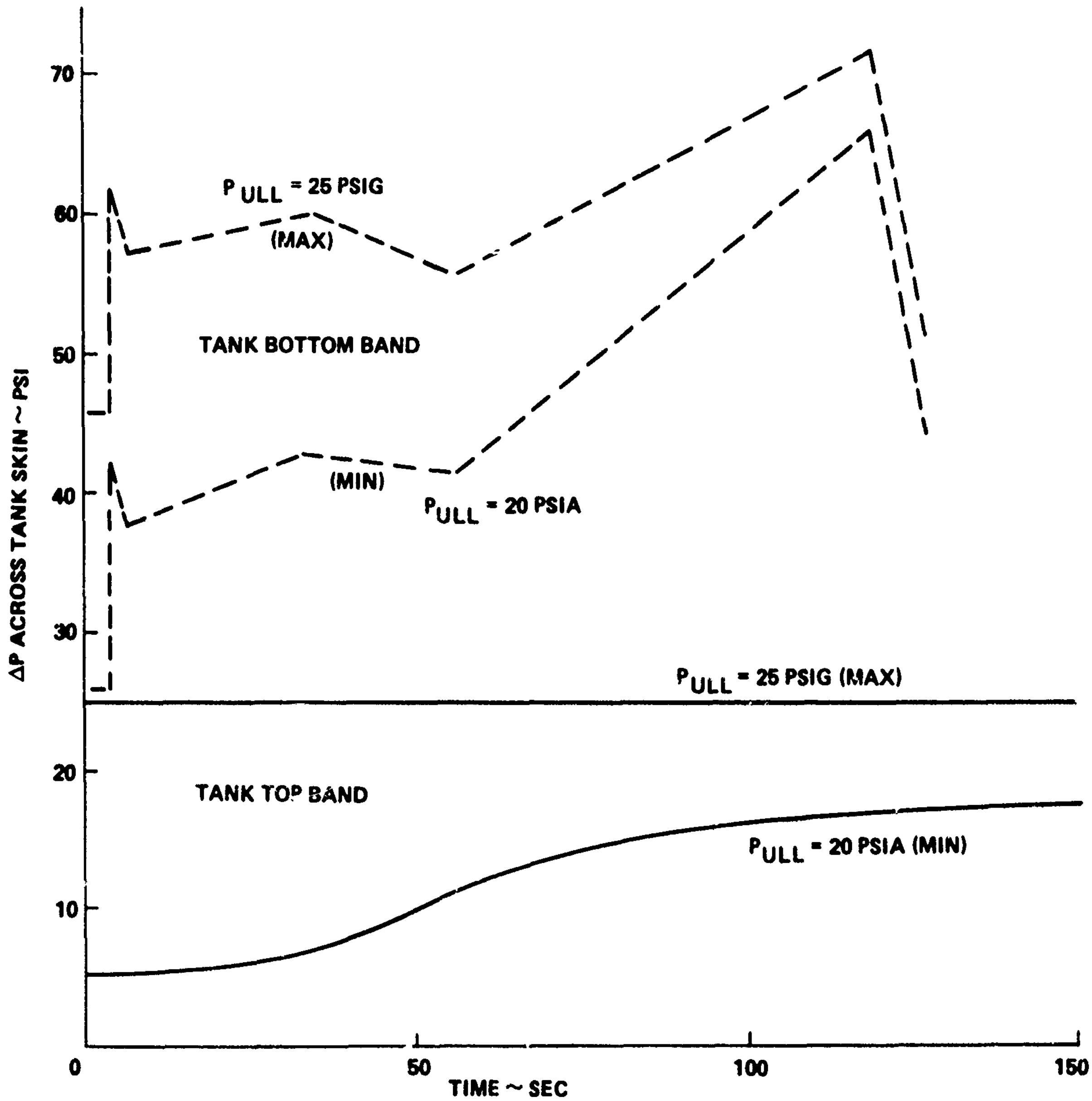

FIGURE 4-59 LOX – ΔP VS. FLIGHT TIME

In Figure 4-60, f_ϕ and f_θ are shown as functions of flight time for a representative element at R = 100 in. The minimum stresses occur at lift-off.

DYNAMIC FRACTURE OF DOME

Ferguson presents an empirical correlation that delineates the dynamic fracture boundary between simple penetration and catastrophic failure for liquid-filled tanks impacted by hypervelocity projectiles.[5] The fracture behavior is expressed as a function of the projectile kinetic energy, KE; material strength, F_{tu}; fracture toughness, K_c; tank wall thickness, t_w; projectile radius, R_o; and the bulk modulus of the contained fluid, E_b. The correlation is given as

$$\frac{f_m}{F_{tu}} = 1 - 0.180 \left[\frac{E_b \; R_o^{1/4} \; KE^{1/2}}{K_c^{3/2} \; t_w} \right]^{2.25} \tag{4-41}$$

where f_m is the critical membrane stress for the onset of catastrophic failure (Fig. 4-61). The exponents and coefficients are derived from physical analyses, dimensional analysis, and correlation of test data on materials including 2219-T87 aluminum, the LOX tank material.

In order to apply the correlation developed for spherical projectiles to the study of a shaped charge jet, some understanding of the phenomena is necessary. Ferguson states that the fluid shock overpressure is the dominant factor influencing the fracture behavior and that the critical loading is a function of the maximum pressure at the shock front (see footnote 5 below). The correlation, however, is expressed in terms of $KE^{1/2}$. For a given projectile and given fluid, the shock pressure generated is nearly proportional to the impact velocity to the first power (or $KE^{1/2}$). If the shaped charge jet is assumed to act as a projectile in producing a shock front in the fluid, then the proper KE to use in the correlation becomes that of a sphere of the same velocity, V_j; material, ρ_j; and radius, R_{oj} as the jet.

$$KE = \frac{2}{3} \pi \rho_j R_{oj}^3 V_j^2 \tag{4-42}$$

The total kinetic energy of the jet far exceeds this value and should render the analysis conservative.

For an aluminum jet

$$KE = 5.426 \times 10^{-4} \; R_{oj}^3 \; V_j^2 \; \text{(in/lb)} \tag{4-43}$$

[5] Ferguson, C.W., "Hypervelocity Impact Effects on Liquid Hydrogen Tanks," NASA CR-54852, Douglas Report SM-52027, Mar 1966.

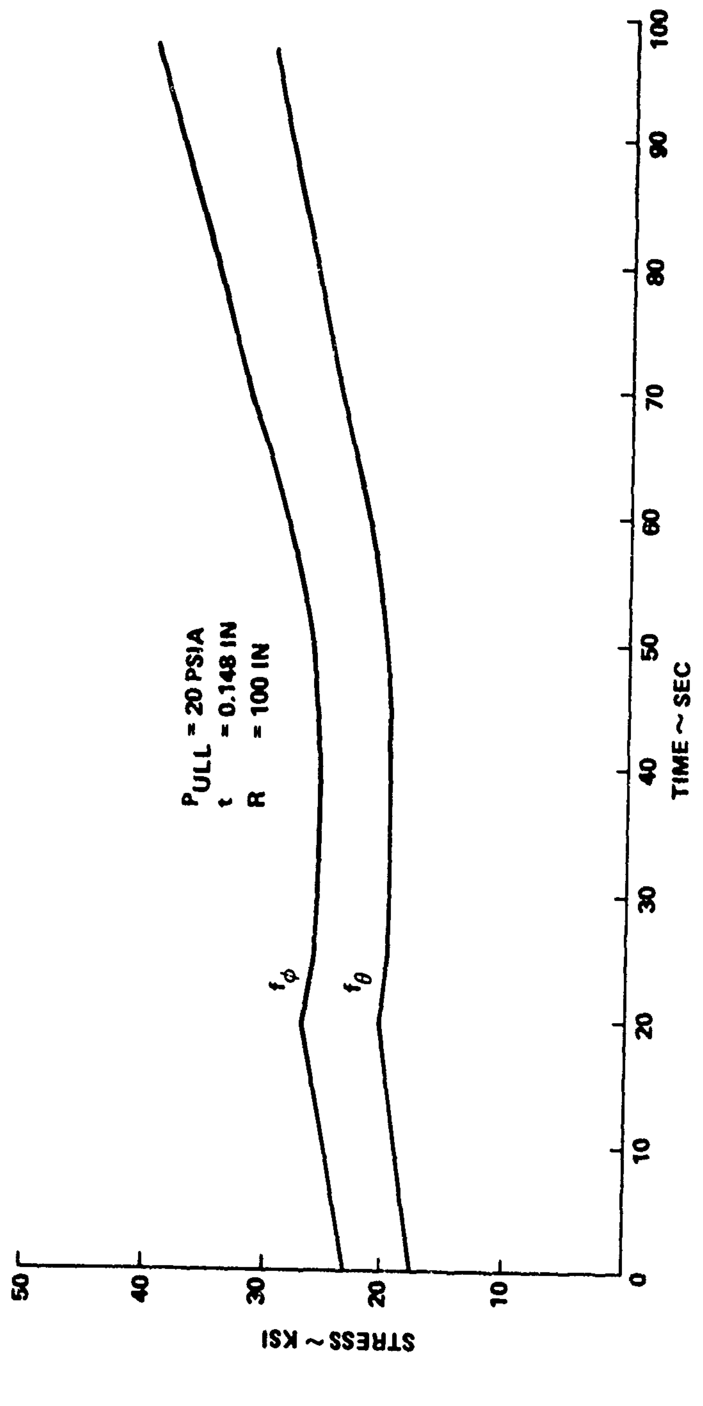

FIGURE 4-60 LOX TANK – MEMBRANE STRESS VS. TIME

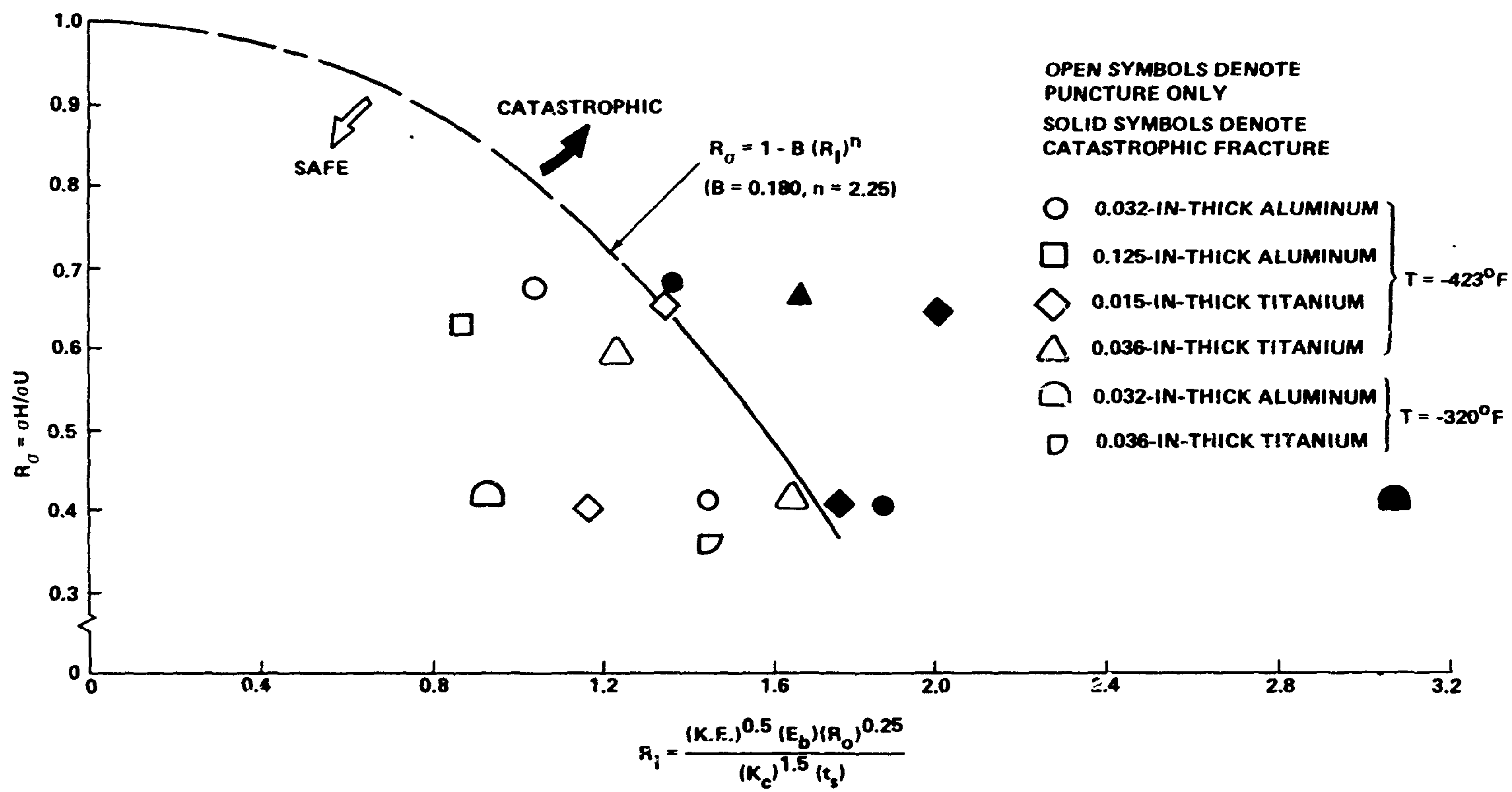

FIGURE 4-6J MASTER CURVE RESULTS OF BIAXIAL PANEL POINT LOAD TESTS (BEHAVIOR OF 2219-T87 ALUMINUM AND 5A1-2.5 SN (ELI) TITANIUM AT LH_2 AND LN_2 TEMPERATURES)

Substituting Equation 4-43 in Equation 4-41 and rearranging terms yields the critical jet radius

$$R_{oj} = 13.25 \left[\frac{\left(1 - f_m/F_{tu}\right)^{\frac{1}{2.25}} K_c^{3/2} \; t_w}{E_b \; V_j} \right]^{4/7} \quad \text{(in)} \tag{4-44}$$

Consider the following characteristics for the LOX tank material, 2219-T87 Al; the contained fluid, LOX; and the shaped charge jet.

F_{tu} = 85,000 psi at -296°F (Fig. 4-62)

K_c = 110,000 psi $\sqrt{in}$ at -296°F[6]

t_w = 0.148 in (Fig. 4-57)

E_b = 135,000 psi at -296°F[7]

V_j = 20,000 ft/sec = 240,000 in/sec

The required jet radius then becomes

$$R_{oj} = 0.0919 \left[1 - \frac{f_m}{85,000} \right]^{0.254} \quad \text{(in)} \tag{4-45}$$

For even the minimum membrane stress encountered (Fig. 4-60), the required jet radius is only 0.0866 in (Fig. 4-63).

CRITICAL HOLE SIZE

A relation that defines hypervelocity puncture size in thin shields gives the ratio of the hole diameter D to the penetrator diameter d as

$$D/d_j = (1.37 \times 10^{-4}) V_j \; (t_w/d)^{2/3} + 0.90 \tag{4-46}$$

where V_j is in ft/sec (see footnote 5, p. 4-80). For this case, the minimum required hole diameter becomes 0.583 in.

---

6 Liebowitz, H., Fracture -- An Advanced Treatise, Vol. VI, Fracture of Metals, Academic Press, New York, 1969, p. 338.

7 Gorter, C. J., Progress in Low Temperature Physics, Vol. 1, North-Holland Publishing Co., Amsterdam, 1957.

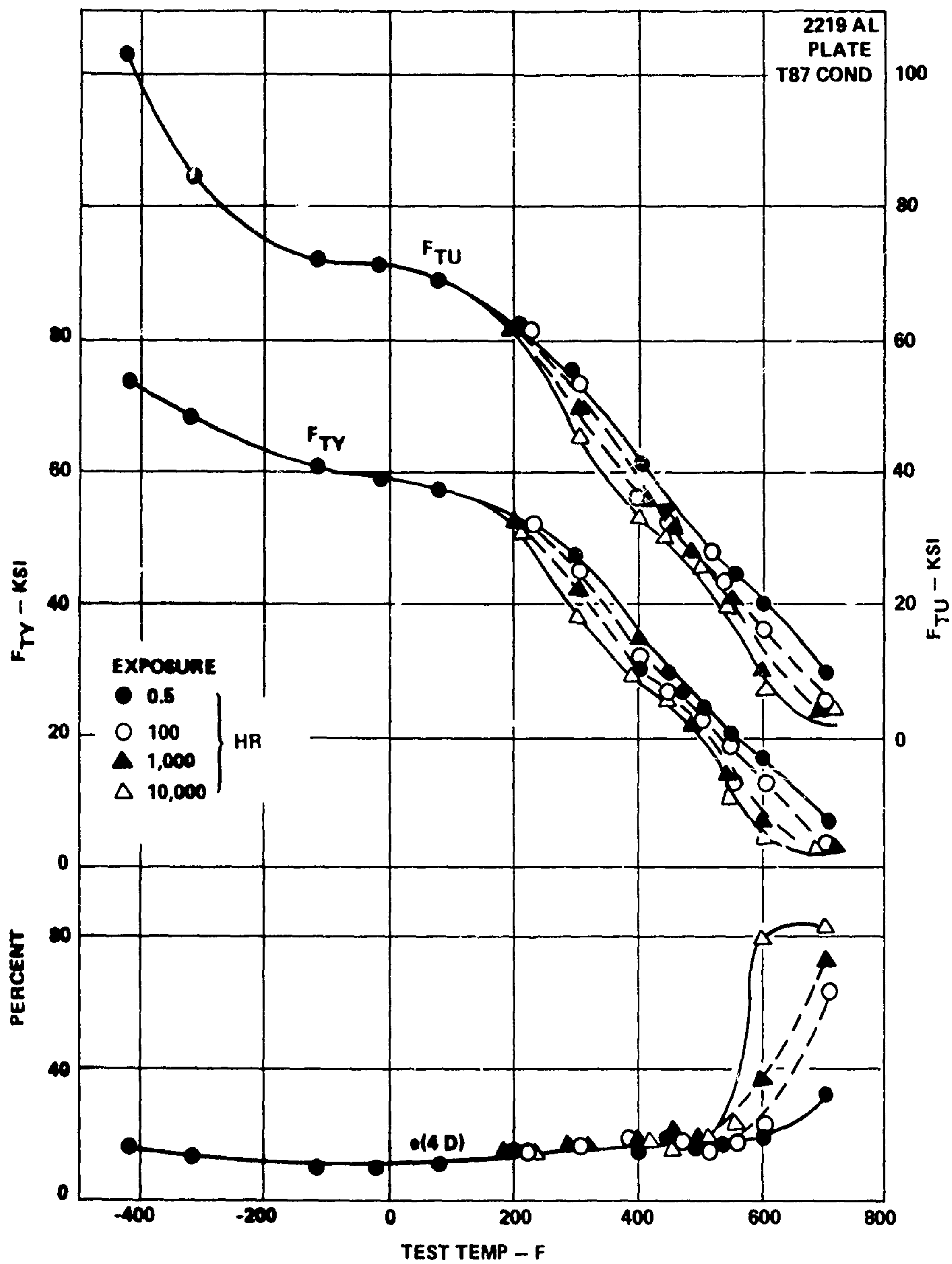

FIGURE 4-62 EFFECT OF TEST TEMPERATURE AND EXPOSURE TIME ON TENSILE PROPERTIES OF PLATE IN T87 CONDITION

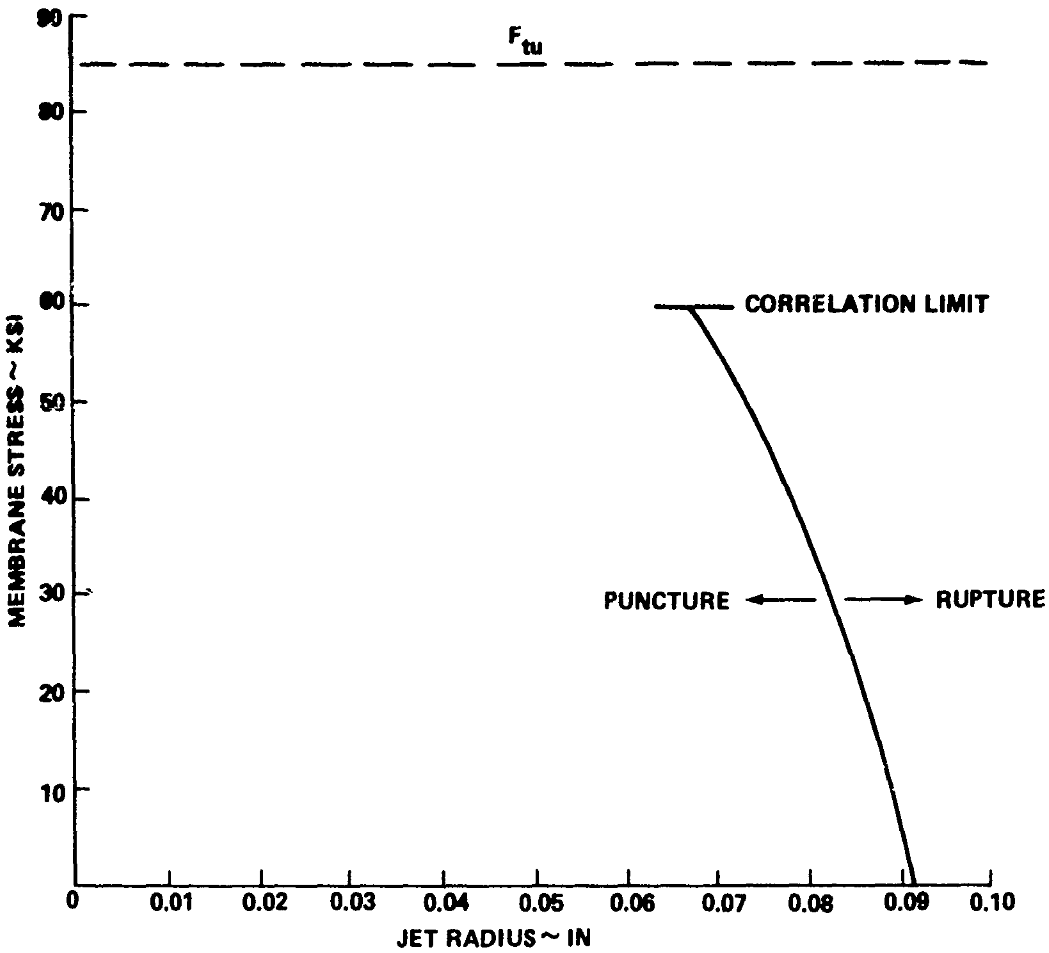

FIGURE 4-63 MINIMUM JET RADIUS TO RUPTURE LOX TANK

FAILURE OF DOME UNDER STATIC STRESS

To illustrate the necessity of puncturing the tank in a region backed by fluid, consider the required hole size to rupture without the benefit of the fluid shock pressure. Ferguson suggests that under static plane stress conditions, the critical flaw size for a ragged hole formed by a projectile is near that for a fatigue crack (see footnote 5, p. 4-80). The analysis presented in Chapter 2 indicates that the oblique impact will generate a hole 3 inches wide by 24 inches long, oriented with the maximum dimension in the meridian direction. The critical flaw dimension is given by

$$2a = \frac{2}{\pi}\left[\frac{K_c^2}{f_\theta^2} - 0.5\,\frac{K_c^2}{Ft_y^2}\right] \tag{4-47}$$

where

$2a$ = Total flaw length

K_c = 110,000 psi $\sqrt{in}$ at -296°F (see footnote 6, p. 4-83)

f_θ = Hoop stress

F_{ty} = 70,000 psi at -296°F (Fig. 4-62)

This expression is obtained for the Irwin-Anderson equation describing the fracture behavior of biaxially stressed panels (see footnote 5, p. 4-80).

$$f_\theta = \frac{K_c}{\left[\pi a + \frac{K_c^2}{2F_{ty}^2}\right]^{1/2} \left(1 + C\frac{a}{R}\right)} \qquad (4\text{-}48)$$

where C is a bulge coefficient. The term C(a/R) was assumed to be negligible in determining Equation 4-47.

A reasonable stress state for this analysis is that produced by the minimum ullage pressure, 20 psia. This could pertain to a situation in which the fluid has moved to the forward end of the LOX tank. The membrane stress can be obtained from Equations 4-38 and 4-40 where P(R) equals the differential pressure between P_{ull} and P_{atm}. f_ϕ and f_θ equal only 13,700 psi and 11,100 psi respectively at 100 seconds, the time of near maximum differential pressure. From Equation 4-47, the critical flaw length becomes 62 inches. Clearly, this results in a gross extrapolation of the data forming the basis of the analysis and is, therefore, subject to considerable error. However, it suggests a hole size requirement many times greater than that attainable by the shaped charge jet. Without fluid backing, a puncture of the LOX tank wall by the jet may not propagate.

CONCLUSIONS

1. The conically shaped charge is capable of rupturing the LOX tank when penetrating a region backed by fluid.

2 Without fluid backing, a puncture of a size attainable with the conically shaped charge may not propagate.

Section IV. DELTA TIME TO DESTRUCT

INTRODUCTION

A critical issue in range safety pertains to the time available to command destruct in the event of an inadvertent separation of the orbiter or an SRB during the first 120 seconds of flight. The analysis of the performance of this destruct system is predicated on the assumption that the SRB is attached to the ET. Subsequent loss of the remaining SRB is assumed to render the destruct system ineffective in destructing the ET. Therefore, the time available for executing command destruct (delta time) is taken to be the interval between the loss of the orbiter or one SRB and the occurrence of the first subsequent structural failure in the remaining cluster. For this study, an inadvertent separation is assumed to be clean with no contact or damage sustained by the remaining cluster.

The maximum loads identified in the Structural Design Loads Data Book for failure and no failure, Table 4-5, were assumed to be indicative of the limit loads of the attach fittings.[8] Loads above the limit loads suggest possible failure. A subroutine was inserted into the trajectory program to compute the attach fitting loads at selected integration intervals following inadvertent separation. These loads were determined as the rigid body reactions required to place an SRB or the orbiter in equilibrium when given the aerodynamic, thrust, body, and inertia loads on that component and the velocities and accelerations of the cluster. Finite element models of the ET and SRB structures in the neighborhood of the forward and aft attachment points were generated for analysis using NASTRAN (Appendices C, D, E, and F). Starting with the earliest occurrence, overload conditions were analyzed for joint or ET/SRB structural failures until the first probable failure was encountered. This then established the time interval available to execute destruct. In addition, overall bending of the ET structure was checked for local shell failure elsewhere in the structure.

Inadvertent separations were postulated at four times into flight (0, 10, 50, and 100 seconds). Generally, these corresponded to the lift-off roll maneuver, high dynamic pressure and maximum acceleration conditions. The response of the cluster at these times can be expected to vary significantly due to the variance in aerodynamic forces and thrust vectors. The aerodynamic loads at 0, 10, and 100 seconds are small due to low dynamic pressure (low vehicle velocity or low air density). The resulting cluster motion is moderate, and the attach fitting loads remain within failure limits for many seconds. A separation at 50 seconds, however, occurs during a period of high aerodynamic loading. The resulting motion is violent. Attach fitting loads approach failure limits more rapidly.

In the event of an inadvertent separation of the orbiter, the minimum delta time to destruct is 16.5 seconds. For the loss of the right SRB, the minimum delta time to destruct is 2 seconds. More detailed results of each situation are given in the following sections.

---

[8] Structural Design Loads Data Book, Vol. 2B SD73-SH-0069-2B, Vol. 3B SD73-SH-0069-3B, Vol. 4B SD73-SH-0069-4B, Space Division, Rockwell International, Oct 1974.

TABLE 4-5 ATTACH FITTING LOADS, FAILURE AND NO FAILURE

Fitting	Max + Load × 10^{-3} (lb)	Condition	Time	Max - Load × 10^{-3} (lb)	Condition	Time
F01	128.68	L0335	4.620	-103.43	HQ773	56.00
F02	63.82	HD271	58.000	- 63.82	HD271R(2)	58.00
F03	438.60	HE113R(2)	50.000	-301.30	HD223R(2)	58.00
F04	438.60	HE113	50.000	-301.30	HD223	58.00
F05	—	—	—	—	—	—
F06	107.47	HQ808	42.000	-107.47	HQ808R(2)	42.00
F07	689.45	P0303	122.500	-151.87	FRF331	6.035
F08	689.45	P0303R(2)	122.500	-151.87	FRF331	6.035
FB1	199.46	FRF331	6.245	-184.86	L0323	4.675
FB2	199.46	FRF331	6.245	-184.86	L0323R(2)	4.675
FB3	107.34	L0329	5.107	-260.29	L0329	5.287
FB4	260.29	L0329R(2)	5.287	-107.34	L0329R(2)	5.107
FB5	1653.67	BA309	113.300	-181.38	PR318R(2)	120.500
FB6	1653.67	BA309R(2)	113.300	-181.38	PR318	120.500
FB7	187.22	HQ854R(2)	42.000	-279.97	HE171R(2)	50.000
FB8	187.22	HQ854	42.000	-279.97	HE171	50.000
FB9	290.94	HE258R(2)	44.000	-132.90	HQ885	49.600
FB0	132.90	HQ885R(2)	49.600	-290.94	HE258	44.000
MB1	19.40(1)	HE114R(2)	50.000	- 11.38(1)	HQ821R(2)	56.000
MB2	11.38(1)	HQ821	56.000	- 19.40(1)	HE114	50.000

(1) Moment × 10^{-6} in-lb

(2) Mirror image of an existing case

LOSS OF ORBITER

First, consider loss of the orbiter. The remaining cluster is relatively symmetric but lacks control. The SRB nozzles null to zero at a finite rate. The thrust is not terminated. Given an inadvertent separation at lift-off, all attach fitting loads remain within limit loads for at least 30 seconds into flight. Similarly, given a separation at 10 or 100 seconds, all attach fitting loads remain within limit loads for at least 20 seconds. In these cases, the aerodynamic loads are small due to low dynamic pressure (low vehicle velocity or low air density).

However, a separation at 50 seconds occurs at a time when the aerodynamic loads are not small. The attach fitting loads (Figs. 4-64 through 4-66) begin to increase and oscillate as the flight time approaches 66 seconds (nominal max q). The first overload occurs in FB1 at 65.25 seconds (Fig. 4-66, View C), 15.25 seconds after separation. This overload, -229,600 pounds, is only slightly above the limit load, -184,900 pounds, and no failure is expected. FB1 is the tangential load at the left SRB/ET forward joint. The shear capability of the joint, at least 1.4 times the limit load, is not exceeded. The contributions to the SRB/ET ring frame bending moments are small (Fig. 4-67). From Figure 4-68, using $A = 2 \times 10^6$ and $A/B = 5 \times 10^3$, the skin shear flow is

$$q_\phi = C_{qt_o} \frac{T_o}{R} + C_{qr_o} \frac{P_o}{R} \tag{4-49}$$

Neglecting the radial contribution which is small, the maximum skin shear flow is

$$q_{\phi_o} = 1260 \text{ lb/in}$$

$$f_s = q_{\phi_o}/t_w = 14{,}000 \text{ psi} \tag{4-50}$$

The shear flow in the ET skin is within failure limit. The shear load in the skin of the SRB should not present a failure problem since the thrust post fitting and beam spread the load over several frames.

The next overload arises in FB10 at 66 seconds. FB10, FB8, and MB2 radial load at the right SRB/ET aft joint equal -428,100 lb, -13,300 lb, and -1,138,000 in-lb, respectively. The aft truss is illustrated in Figure 4-69. Resolving the attach fitting loads into component member loads yields

$$P10 = FB8/\cos 16°45' = 1.044FB8 = -13{,}900 \text{ lb} \tag{4-51}$$

$$P8 = -0.5FB10 - 0.2195FB8 + 0.00877M_B2 = 207{,}000 \text{ lb} \tag{4-52}$$

$$P9 = -0.5FB10 - 0.08285FB8 - 0.00877MB2 = 225{,}100 \text{ lb} \tag{4-53}$$

where tension loads are positive. The three truss members are of a common design. The limit load in tension for all truss members is 274,000 lb (Table 4-6). None are loaded above the limit load.

Appendix C presents an analysis of the aft ring frame in the ET. Scaling the radial load to 428,100 lb results in a maximum stress of 21,000 psi which is below yield. Figure 4-15 shows the failure limit of the SRB ring frame at the aft attachment point. Again, the radial load is below that required to yield the ring. Hence, no failures are expected.

ALL LOADS ARE APPLIED TO SRB'S.
POSITIVE DIRECTIONS ARE SHOWN.
SECTIONS ARE LOOKING FORWARD.
DIMENSIONS ARE IN INCHES.

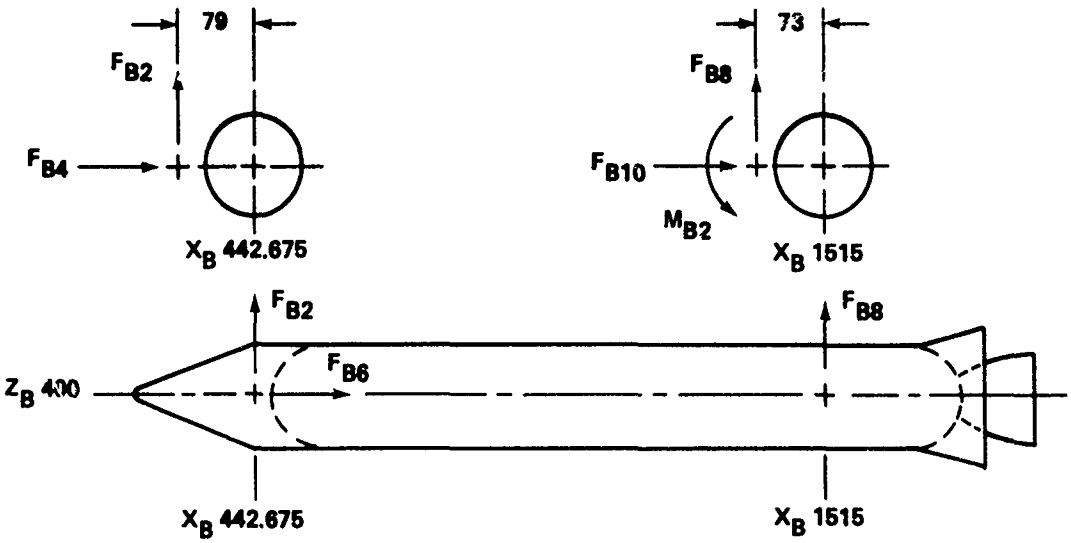

RIGHT SIDE SRB
LOOKING RIGHT

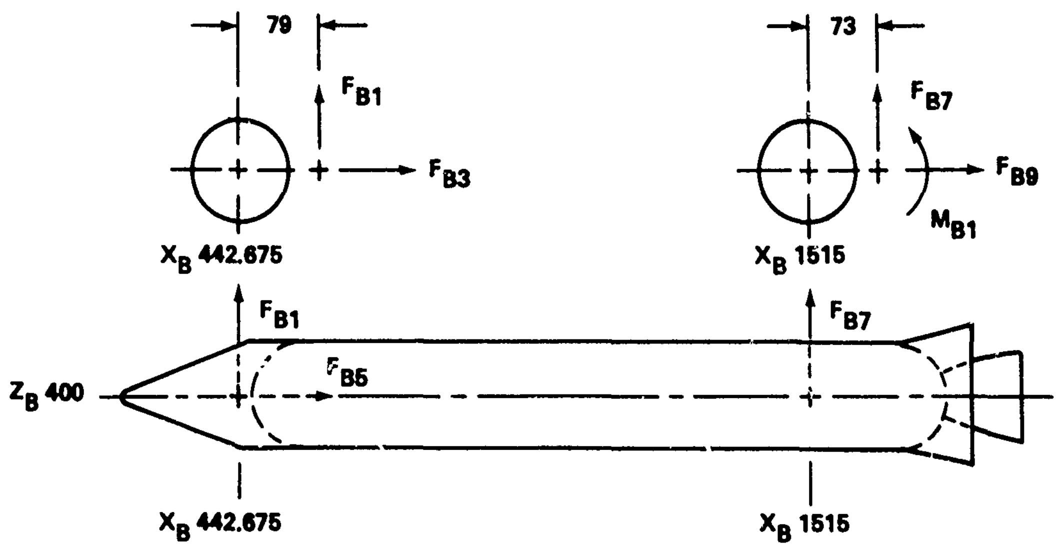

LEFT SIDE SRB
LOOKING RIGHT

FIGURF 4-64 SRB ATTACHMENT FITTING LOAD LOCATIONS

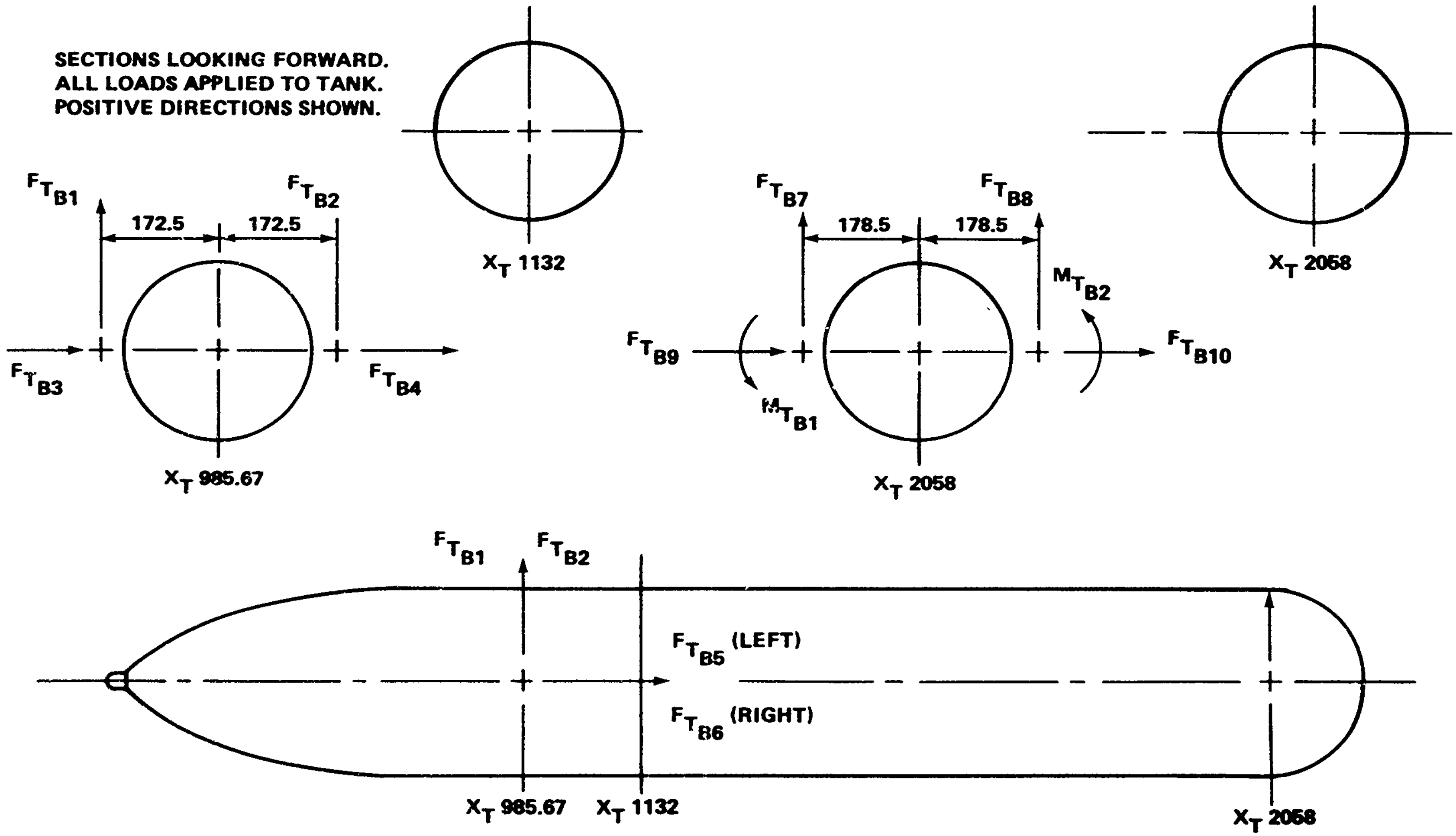

FIGURE 4-65 EXTERNAL TANK ATTACH LOADS AND DIRECTIONS

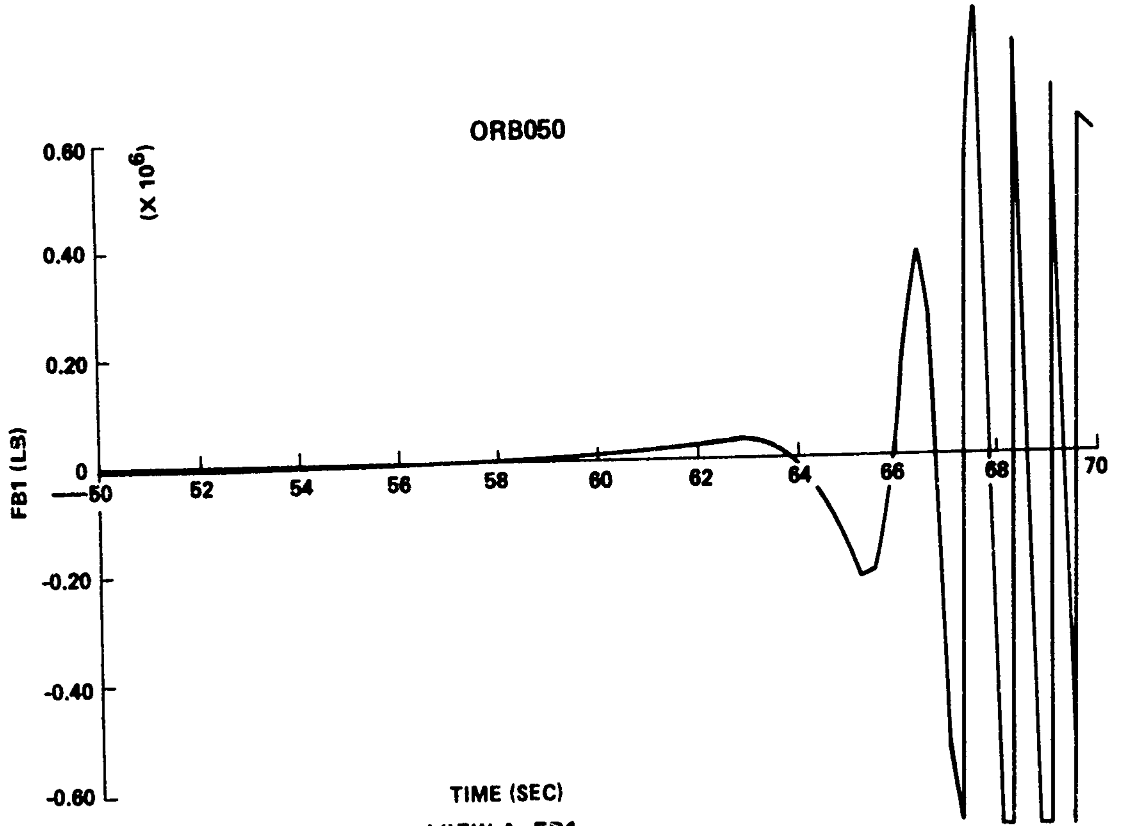

VIEW A, FB1

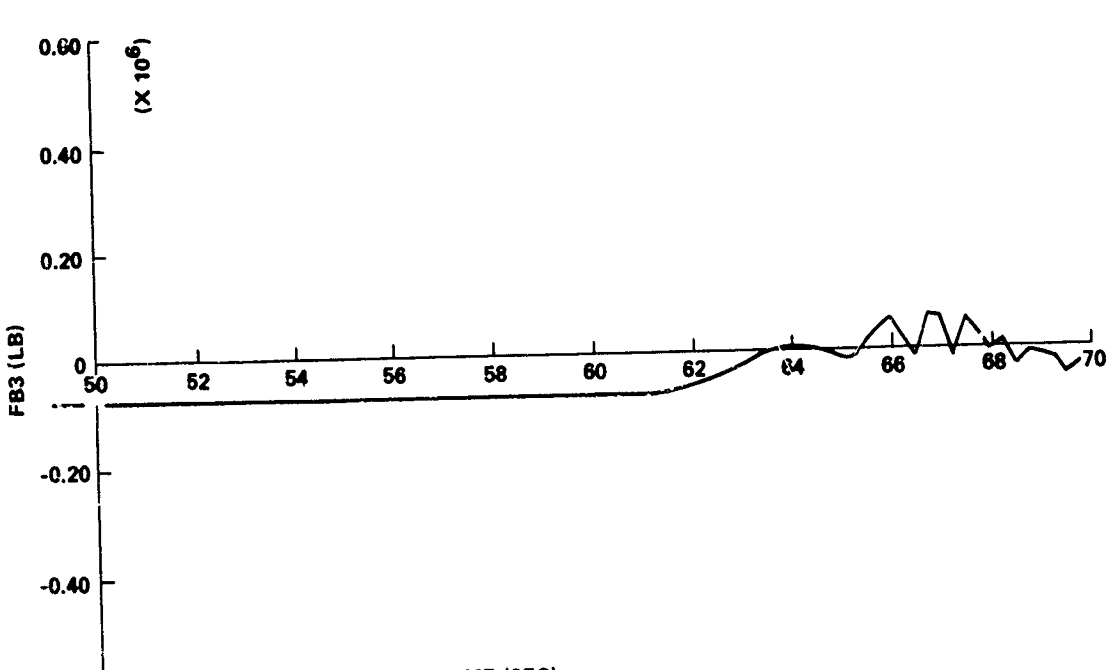

VIEW B, FB3

FIGURE 4-66 ATTACH FITTING LOADS -- LOSS OF ORBITER AT 50 SECONDS (Sheet 1 of 6)

ORB050

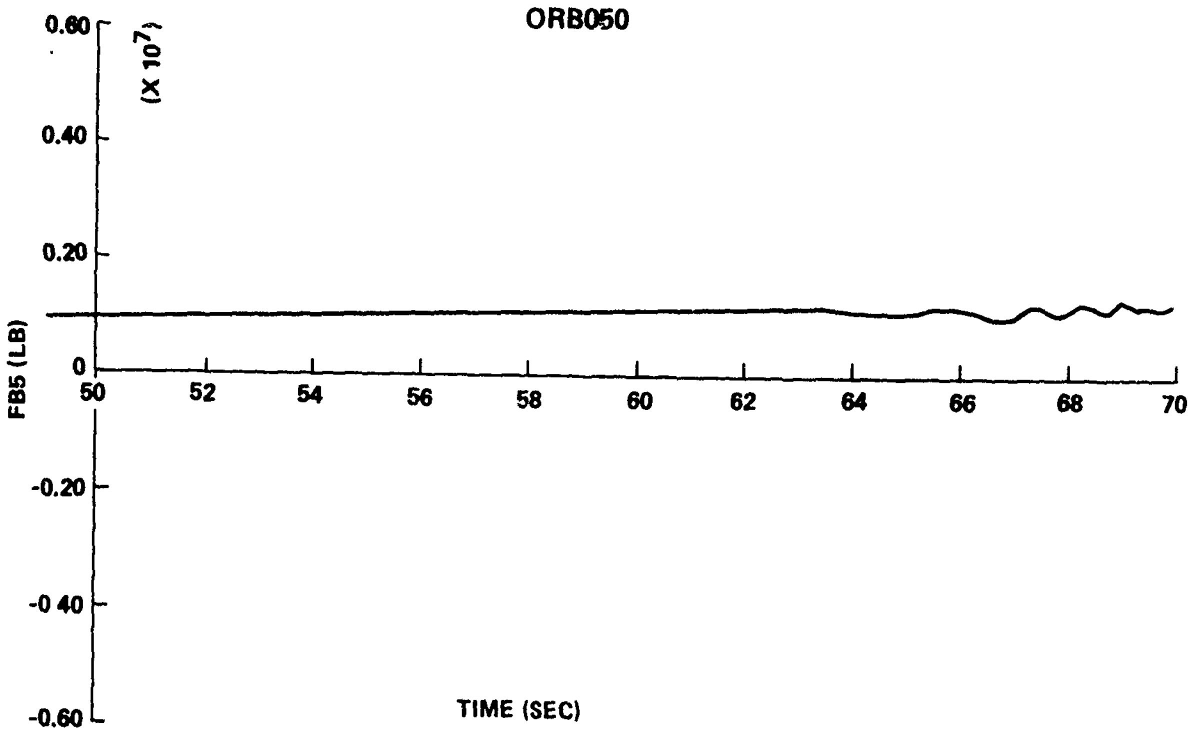

VIEW C, FB5

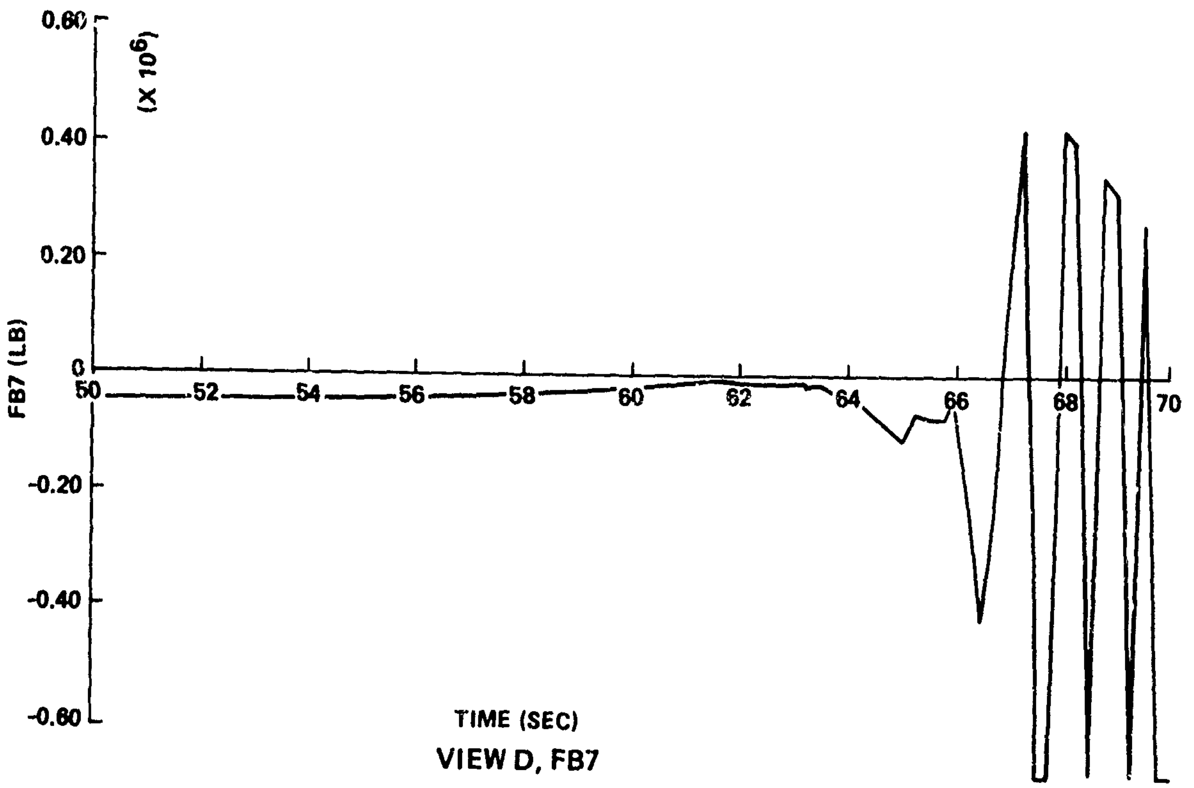

VIEW D, FB7

FIGURE 4-66 ATTACH FITTING LOADS — LOSS OF ORBITER AT 50 SECONDS (Sheet 2 of 6)

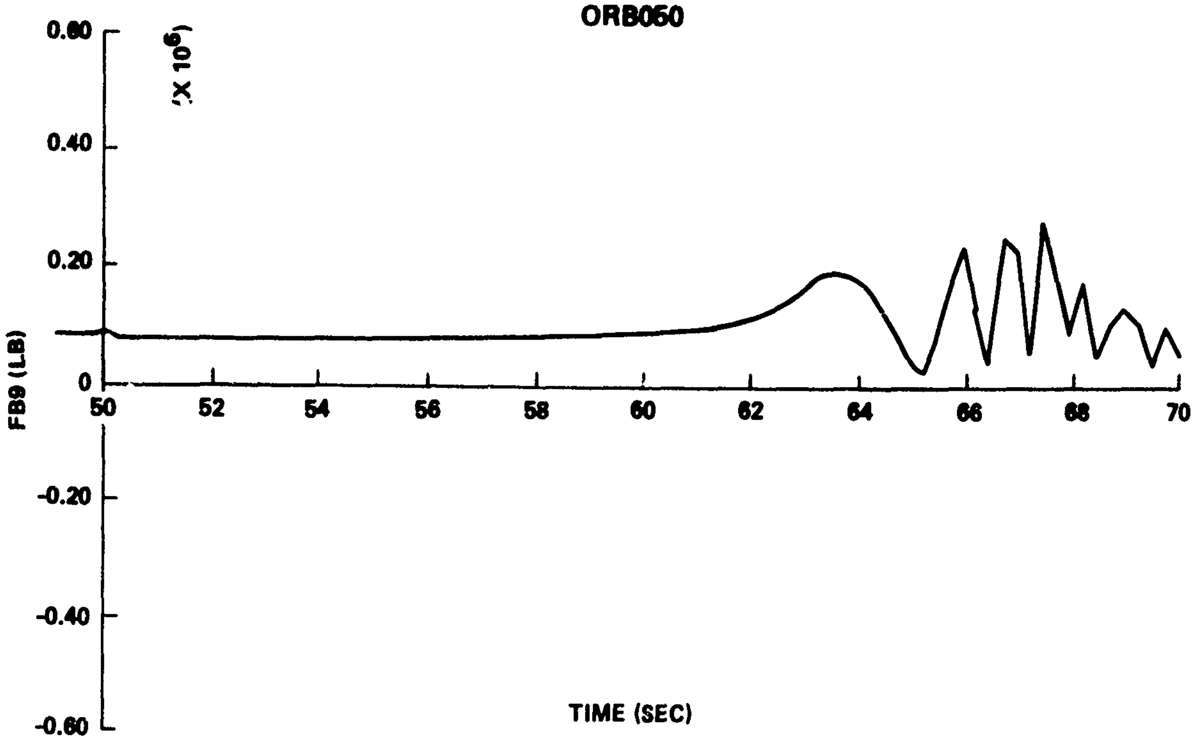

VIEW E, FB9

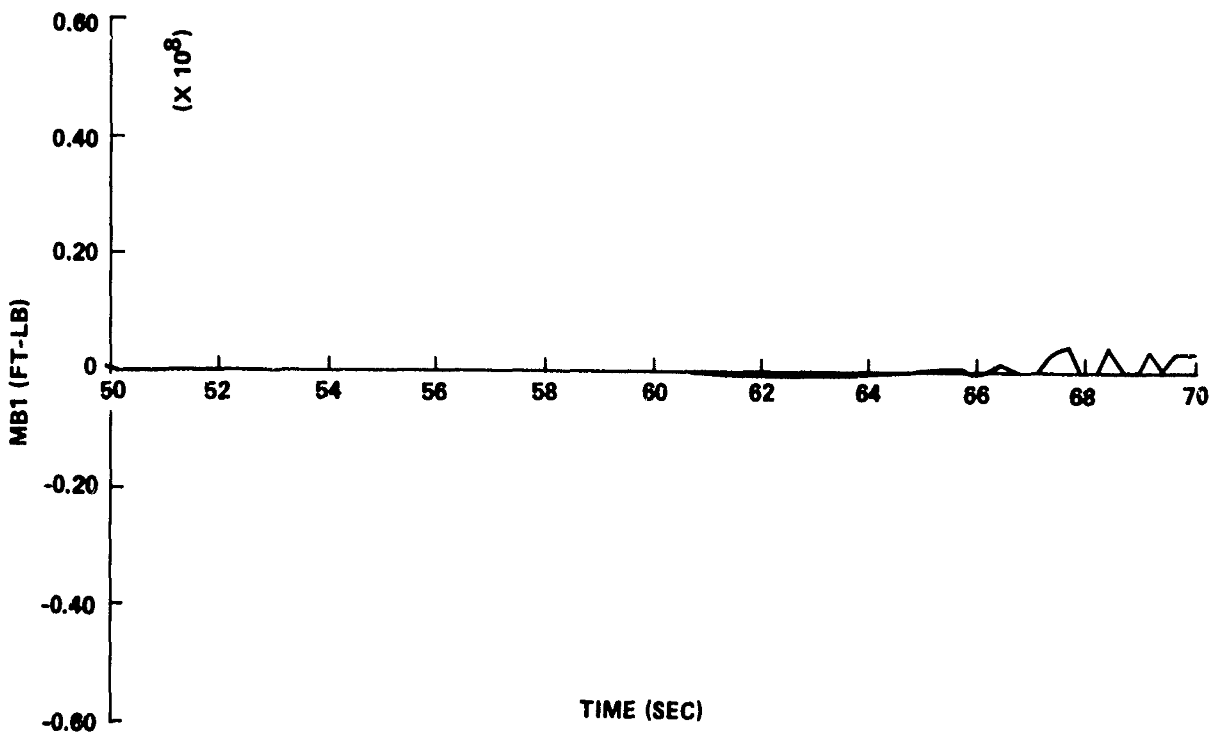

VIEW F, MB1

FIGURE 4-66 ATTACH FITTING LOADS — LOSS OF ORBITER AT 50 SECONDS (Sheet 3 of 6)

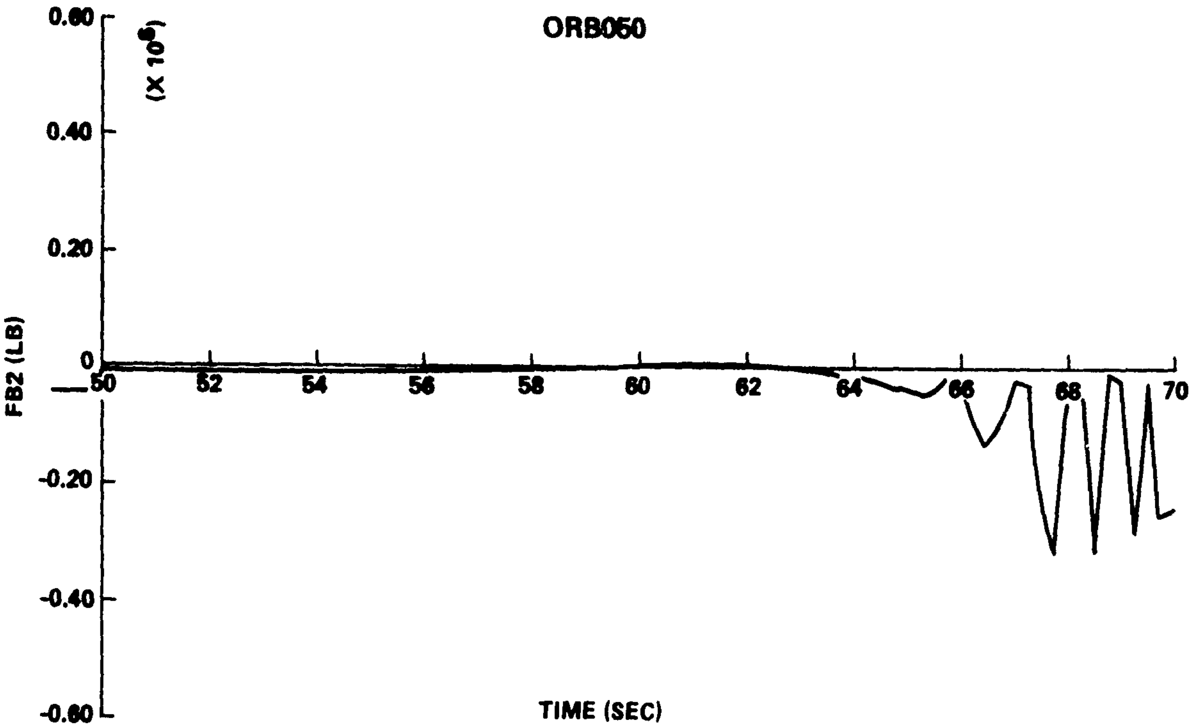

VIEW G, FB2

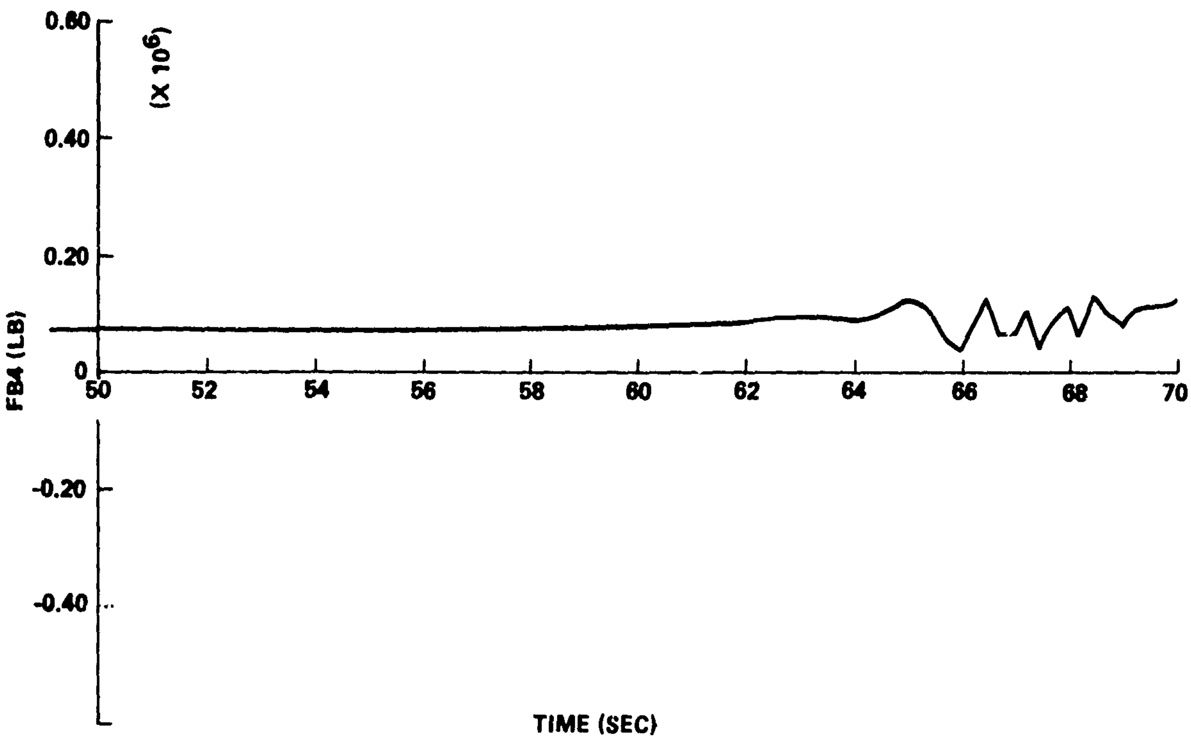

VIEW H, FB4

FIGURE 4-66 ATTACH FITTING LOADS – LOSS OF ORBITER AT 50 SECONDS (Sheet 4 of 6)

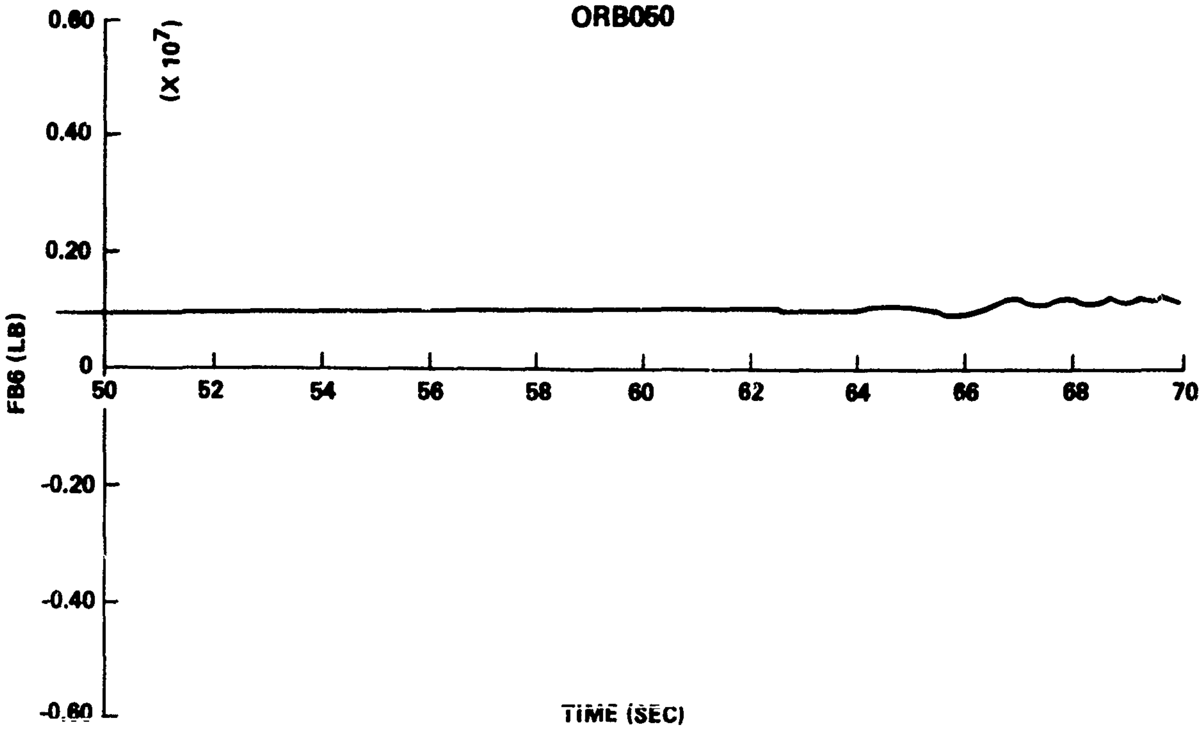

VIEW I, FB6

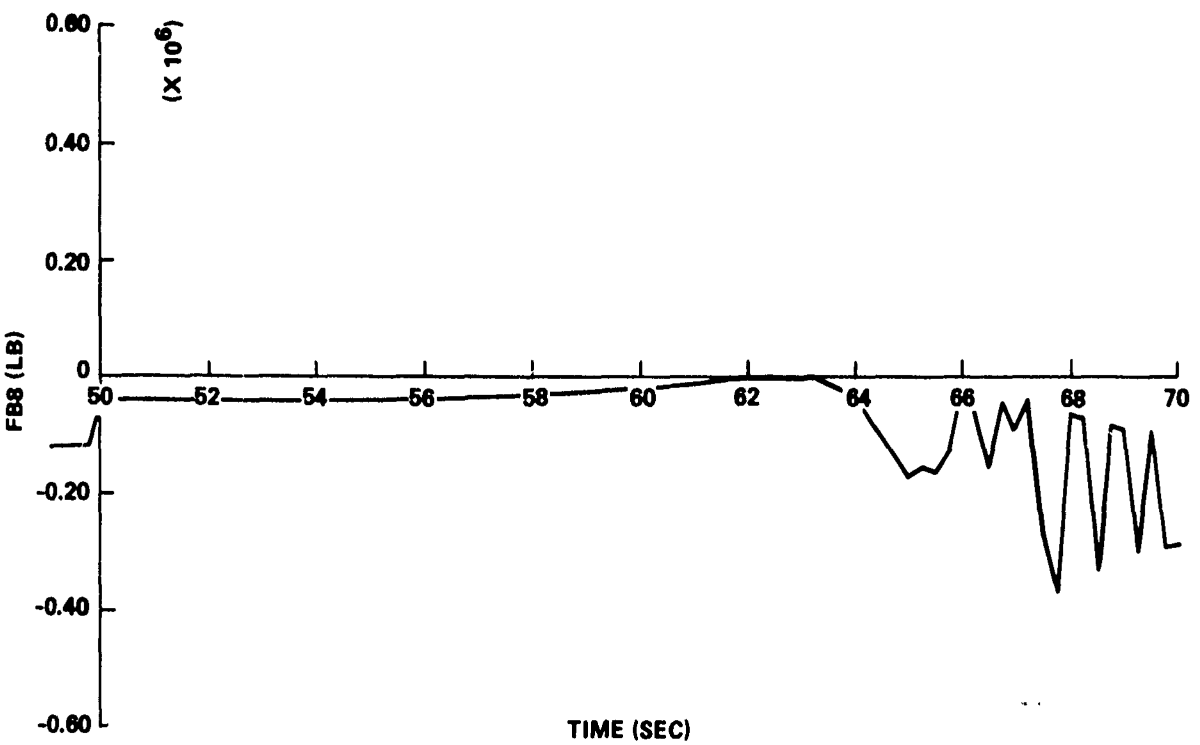

V'EW J, FB8

FIGURE 4-66 ATTACH FITTING LOADS – LOSS OF ORBITER AT 50 SECONDS (Sheet 5 of 6)

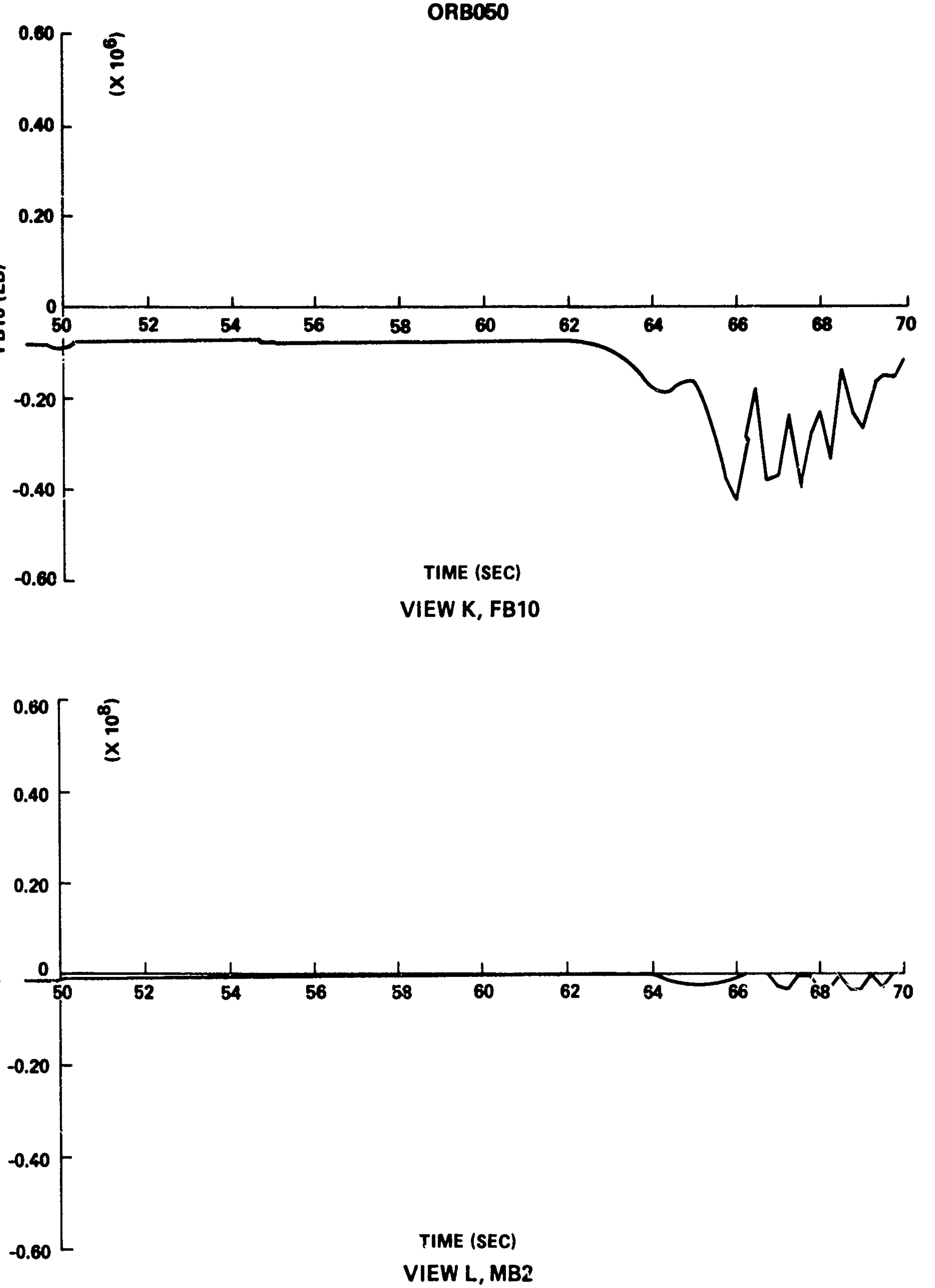

FIGURE 4-66 ATTACH FITTING LOADS — LOSS OF ORBITER AT 50 SECONDS (Sheet 6 of 6)

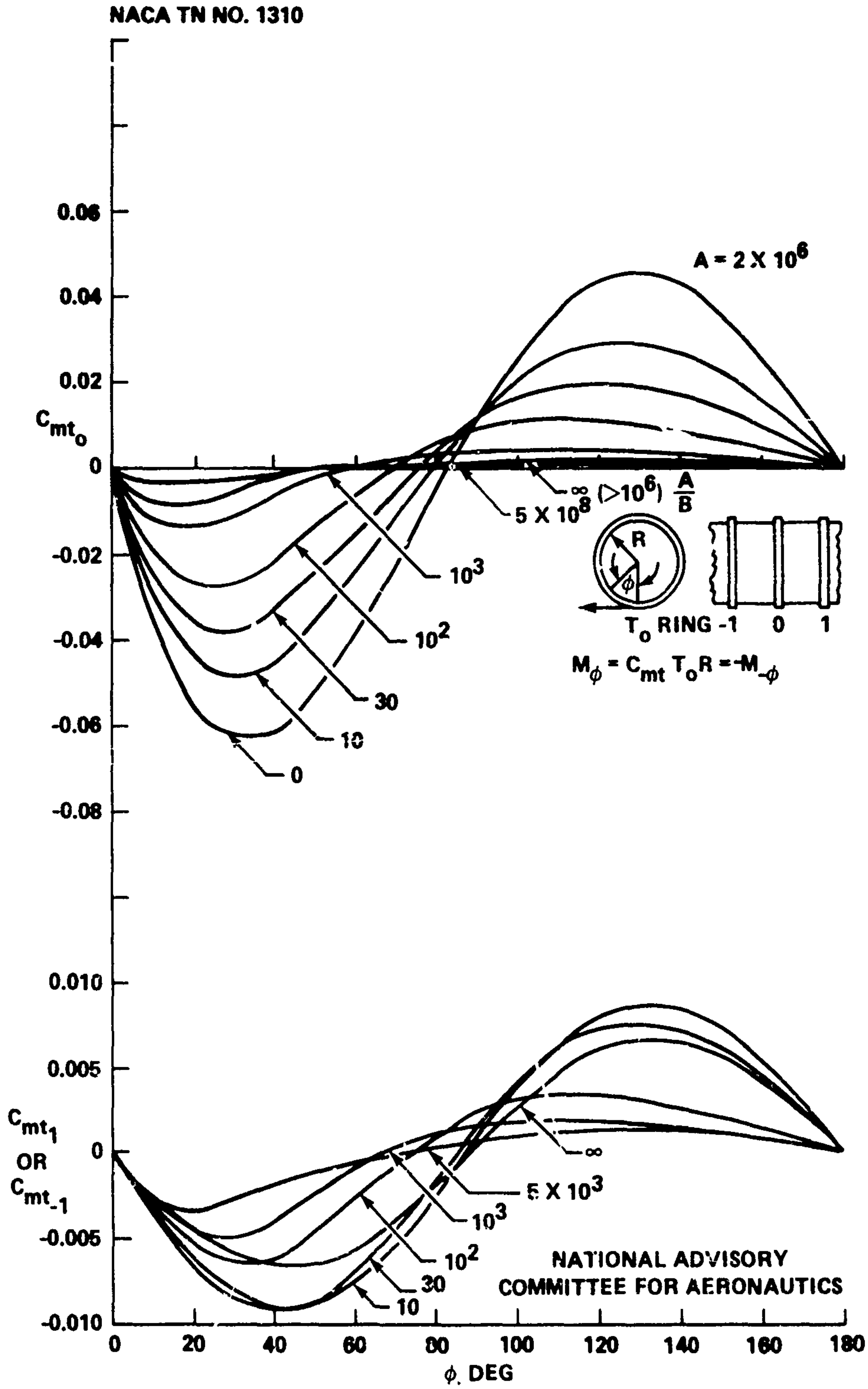

FIGURE 4-67 RING BENDING-MOMENT COEFFICIENTS FOR TANGENTIAL LOAD
($A = 2 \times 10^6$)

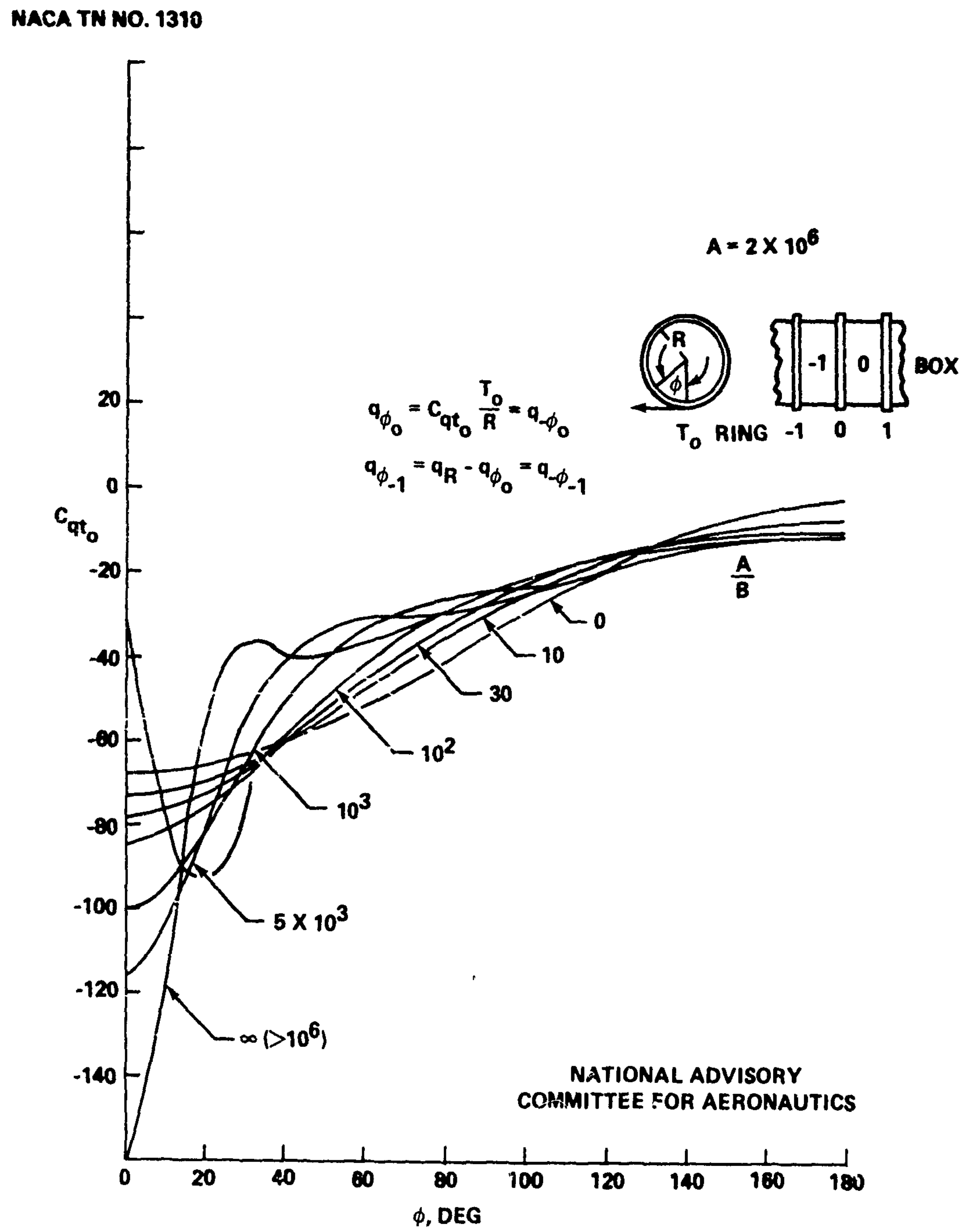

FIGURE 4-68 SKIN SHEAR-FLOW COEFFICIENTS FOR TANGENTIAL LOAD
($A = 2 \times 10^6$)

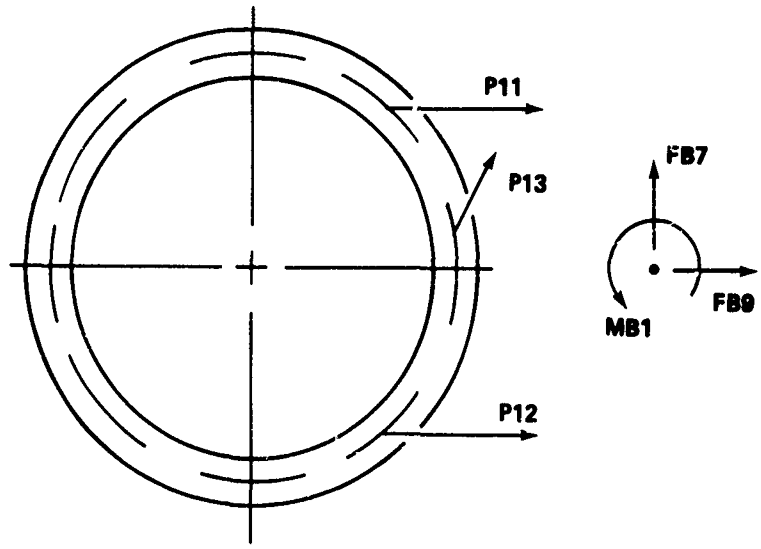

LEFT-HAND SRB LOOKING FORWARD

P11 = 0.5FB9 - 0.22FB7 - 0.0088MB1

P12 = 0.5FB9 -0.063FB7 + 0.0068MB1

P13 = 1.044FB7

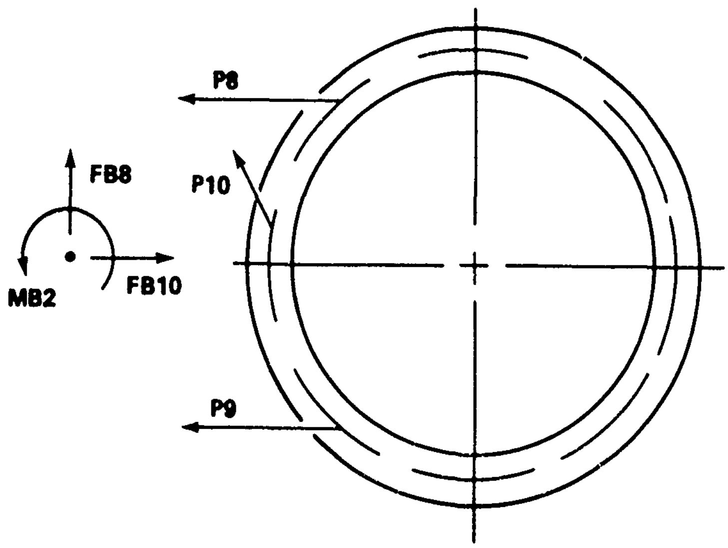

RIGHT-HAND SRB LOOKING FORWARD

P8 = -0.5FB10 - 0.22FB8 + 0.0068MB2

P9 = -0.5FB10 - 0.063FB8 - 0.0068MB2

P10 = 1.044FB8

FIGURE 4-69 COMPONENT AND ATTACH FITTING LOADS — AFT SRB JOINTS

TABLE 4-6 ATTACH MEMBER LOADS, FAILURE AND NO FAILURE

Member	Max (+) Load × 10^{-3} (lb)	Condition	Time	Max (-) Load × 10^{-3} (lb)	Condition	Time
P1	56.20	HQ757	—	- 89.85	LO341	5.024
P2	106.70	HQ774	—	- 89.90	LO341	5.024
P8	179.63	HE257	44.000	- 147.33	HE113	50.000
P9	273.97	HE266R(1)	50.000	- 97.05	HQ774R(1)	56.000
P10	195.46	HQ854	42.000	- 292.29	HE171	50.000
P11	179.63	HE257R(1)	44.000	- 147.33	HE113R(1)	50.000
P12	273.97	HE266	50.000	- 97.05	HQ774	56.000
P13	195.46	HQ854R(1)	42.000	- 292.29	HE171R(1)	50.000
P14	181.38	PR318	120.500	-1653.67	BA309R(1)	113.370
P15	107.34	LO329R(1)	5.107	- 260.29	LO329R(1)	5.287
P16	184.86	LO323R(1)	4.675	- 199.46	FRF331	6.245
P17	181.38	PR318R(1)	120.500	-1653.67	BA309R(1)	113.300
P18	260.29	LO329	5.287	- 107.34	LO329	5.107
P19	184.86	LO323	4.675	- 199.46	FRF331	6.245

(1) Mirror image of an existing case.

The major overloads occur in FB1 and FB7, the tangential loads at the left SRB/ET forward and aft attachment points, after 66 seconds. These tangential loads do not severely stress the SRB/ET structures as shown before. The expected failure, therefore, is in the forward fitting or the aft truss. The tangential load in the forward fitting is equal to the attach fitting load FB1.

$$P19 = FB1 \tag{4-54}$$

The entire tangential load at the aft joint is carried by component member 13 (Fig. 4-69). The load in that member is given as

$$P13 = FB7/\cos\,(16°45') = 1.044\ FB7 \tag{4-55}$$

The histories of P19 and P13 are given in Figure 4-70, starting at 65 seconds. No overloads occur before 65 seconds. The initial overload in P19 has been discussed above. A second overload in P19 and an initial overload in P13 occur nearly simultaneously around 66.5 seconds.

$$P19 = 378{,}700\ \text{lb} = 1.9 \times \text{limit load}$$

$$P13 = -436{,}000\ \text{lb} = 1.5 \times \text{limit load}$$

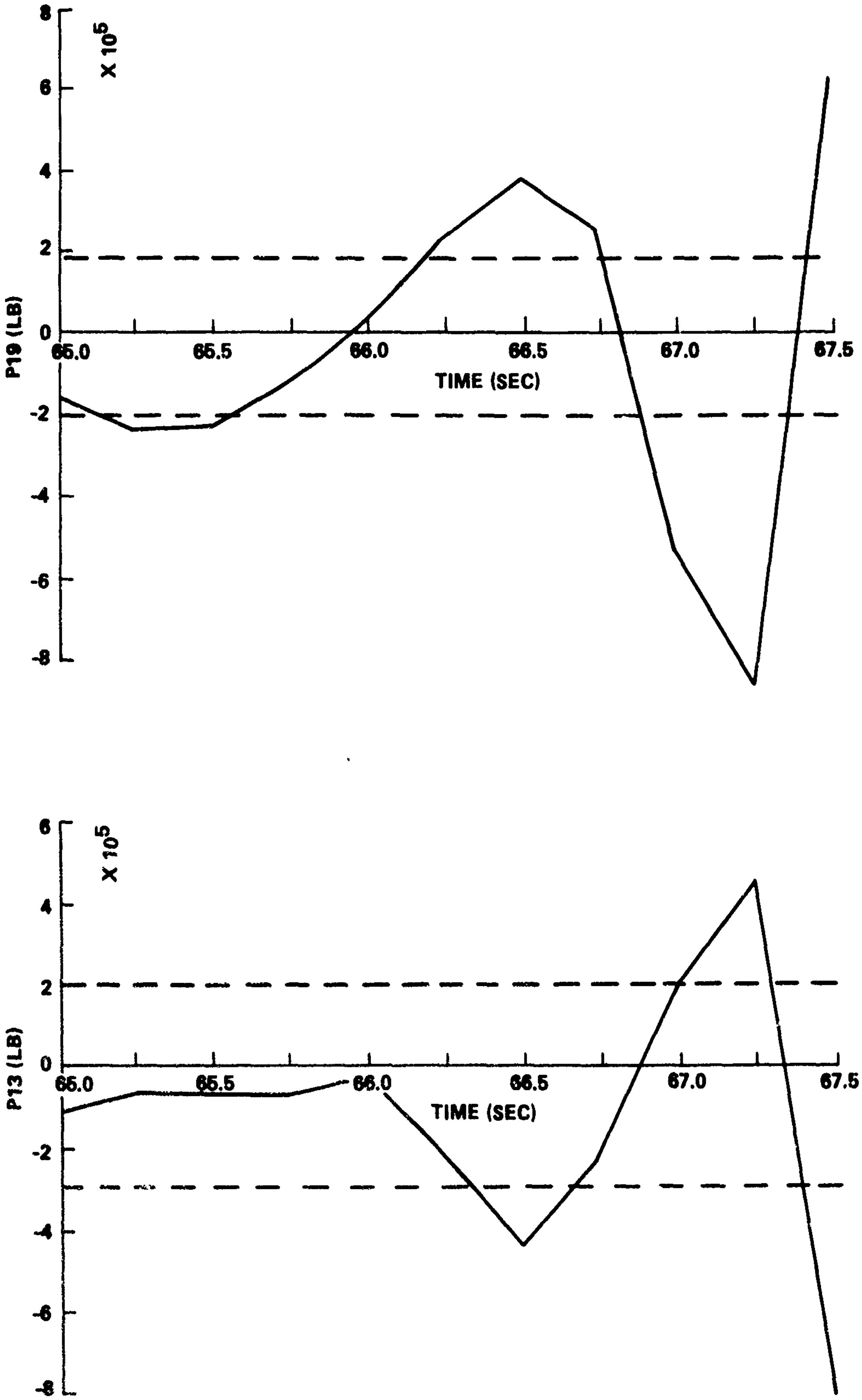

FIGURE 4-70 COMPONENT LOADS (P19, P13) VS. TIME – LOSS OF ORBITER AT 50 SECONDS

Both component members are marginal. If failure does not occur at 66.5 seconds, both members become severely overloaded (>2 × limit load) within another second (Fig. 4-70). Therefore, failure of either or both the left SRB/ET forward joint or rear truss member 13 is expected $16.5^{+1.0}_{-0.0}$ seconds following separation of the orbiter at 50 seconds into flight.

Assuming that bending of the clevis pin (Fig. 4-71), is the failure mode for strut 13, the ultimate modulus of rupture becomes

$$F_o = F_{t_u} + F_{ty}\,(k - 1) \tag{4-56}$$

where

$k = 1.7$ for a solid circular pin

For Inconel 718 (AMS - 5664)

$F_{t_u} = 180{,}000$ psi

$F_{ty} = 150{,}000$ psi

$F_b = 180{,}000 + 0.7\,(150{,}000) = 285{,}000$ psi

The bending moment on the pin is found to be

$$M_b = 0.5Pb \tag{4-57}$$

where

P = load on strut

$$b = 0.5t_1 + 0.25t_2 + q = 1.104 \text{ (Fig. 4-71)} \tag{4-58}$$

The stress at the outer fiber is

$$f_b = M_b r/I = 10.19\ M_b/D^3 \tag{4-59}$$

or for $D = 2.25$ in

$$f_b = 0.89M_b = 0.494P \tag{4-60}$$

The failure load for pin bending becomes

$$P = 2.024\ f_b = 2.024\ F_b = 577{,}000 \text{ lb} \tag{4-61}$$

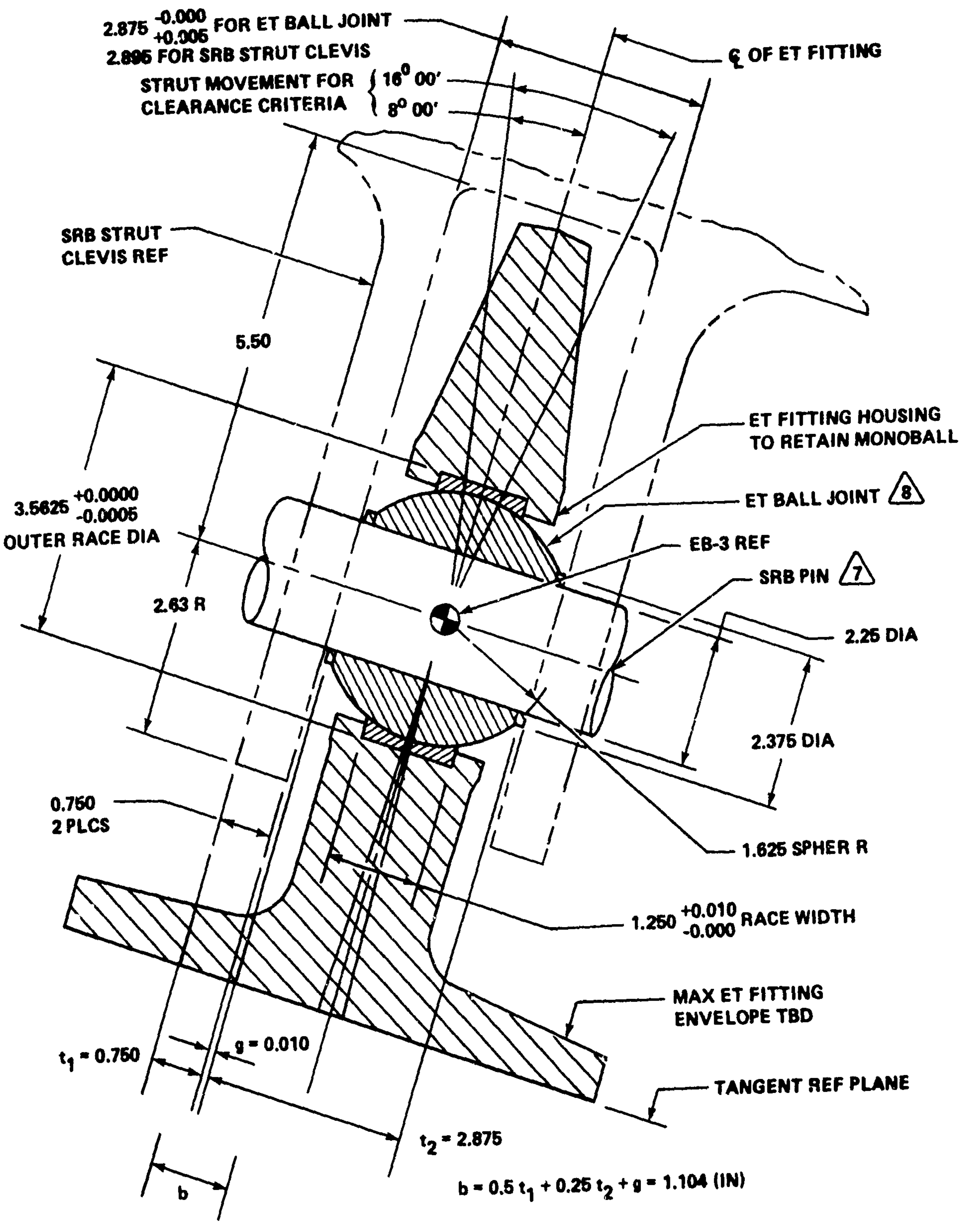

FIGURE 4-71 CLEVIS JOINT – SRB/ET AFT STRUT

Taking the ultimate shear strength as 65 percent of the ultimate tensile strength gives

$$F_{su} = 0.65\ (F_{tu}) = 117{,}000 \text{ psi} \tag{4-62}$$

The double shear capability of the pin becomes

$$P = 2AF_{su} = 930{,}000 \text{ lb} \tag{4-63}$$

which is greater than that for pin bending. From Figure 4-70 it can be seen that the pin in truss member 13 will fail at about 67.5 seconds.

Bending moment, shear, and end load curves were constructed for the ET for three times following separation: T = 64.25 sec, 66 sec, and 67.5 sec (Fig. 4-72). The time of 64.25 seconds was chosen because of the high aerodynamic load applied in the Y-direction and the high acceleration in the Z-direction. None of the parameters exceeded the limits established in Appendix J. The second time, 66 seconds, was selected because of a higher acceleration in the Z-direction. Figure 4-73 illustrates the bending moment curves for this case. The moment in the X-Y plane exceeds the 1.2×10^7 ft-lb limit presented in Appendix J. All of the other parameters remain within the allowable limits. This suggests that it is the high aerodynamic load and not the high acceleration which produces the excessive bending moment.

The concentrated aerodynamic load, -6.78×10^5 lb, is applied near the mid-point of the ET, X_T 1260, in the Y-direction. The reactions at the forward and aft SRB/ET joints generated by the aerodynamic load only are:

$$R_{FY} = -5.04 \times 10^5 \text{ lb}$$

$$R_{RY} = -1.74 \times 10^5 \text{ lb}$$

These loads cause a bending moment of -1.16×10^7 ft-lb at X_T 1260 in the X-Y plane.

A more reasonable approximation of the actual load is given by a uniform running load centered about the point of application of the concentrated load and ranging over about 1600 inches. The reactions remain as above, but a bending moment of 1.13×10^7 ft-lb at X_T 1260 in the X-Y plane added to the result shown in Figure 4-73. The bending moment at X_T 1260 becomes -6.60×10^6 ft-lb, which is well within the capability of the shell.

It can be surmised that a similar situation exists at 65.25 seconds, although no analysis has been done here for that time.

The third time investigated was 67.5 seconds. Both the aerodynamic load and acceleration in the Z-direction are high at that time. The end load and shear curves are within the limits set in Appendix J. However, the bending moment curves, Figure 4-74, exceed the 1.2×10^7 ft-lb limit in both the X-Y and X-Z planes. The maximum moment in the X-Y plane exceeds the limit by only a small amount and can be reconciled in the same manner as above.

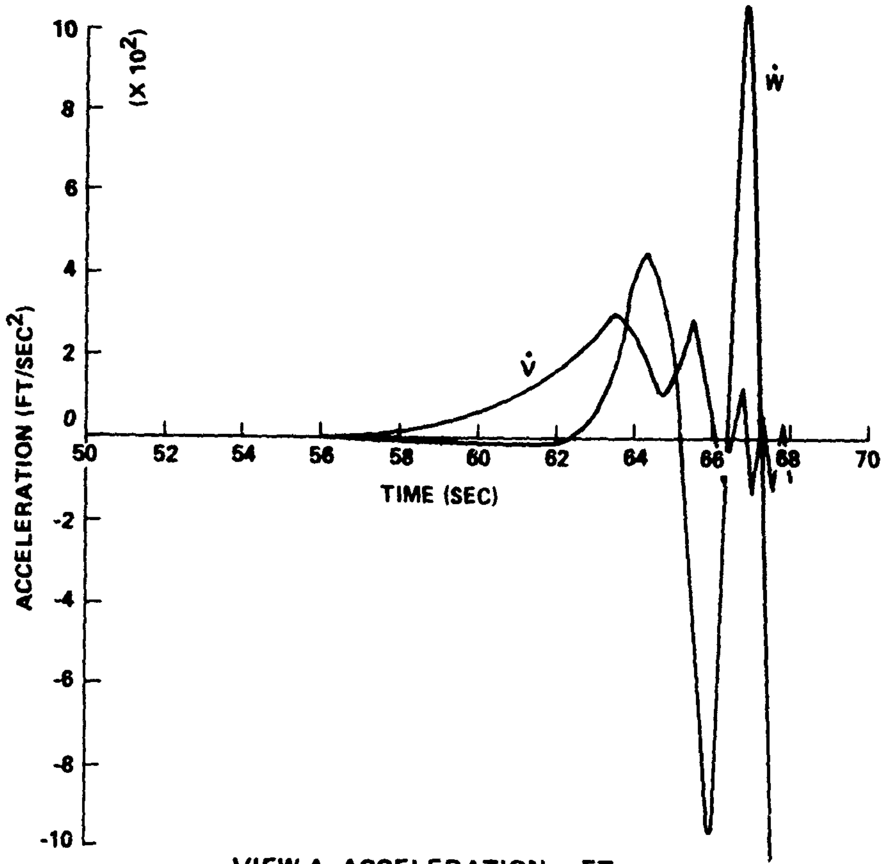

VIEW A, ACCELERATION – ET

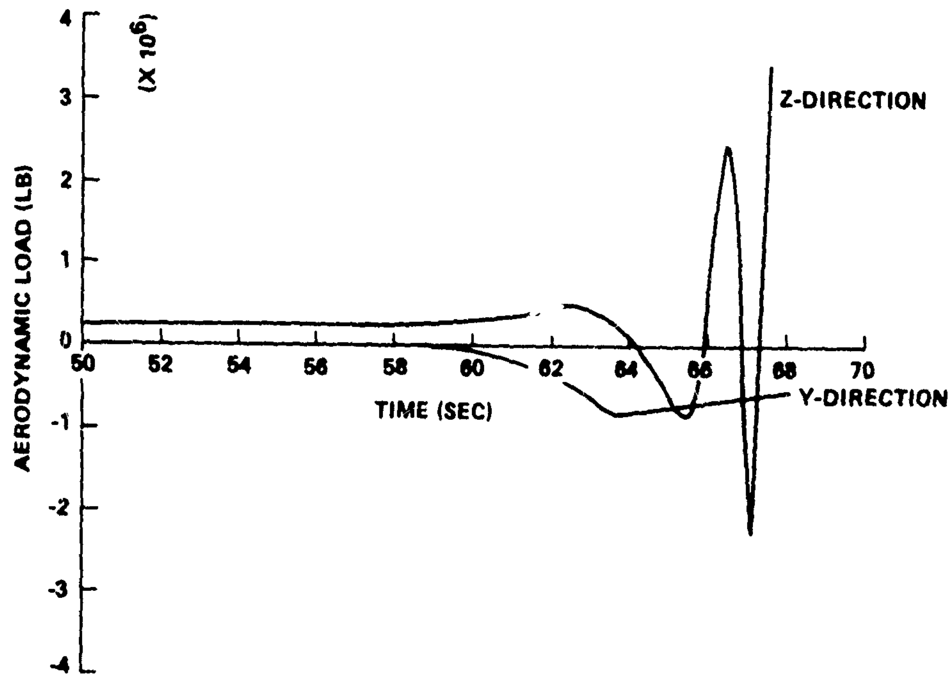

VIEW B, AERODYNAMIC LOAD – ET

FIGURE 4-72 LOAD HISTORY OF ET FOLLOWING LOSS OF ORBITER AT 50 SECONDS

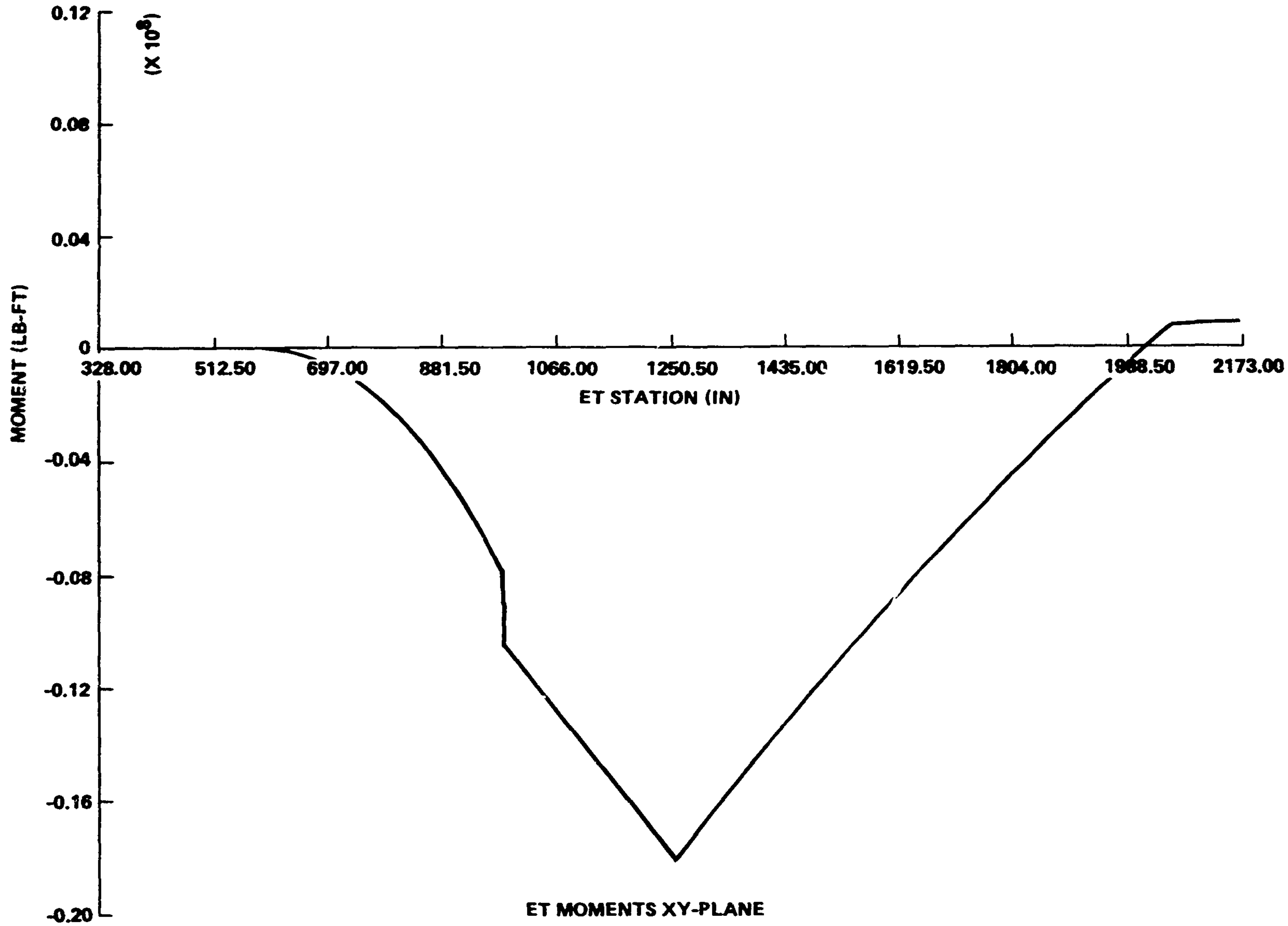

FIGURE 4-73 ET BENDING MOMENT (T = 66 SEC) FOLLOWING LOSS OF ORBITER AT 50 SECONDS

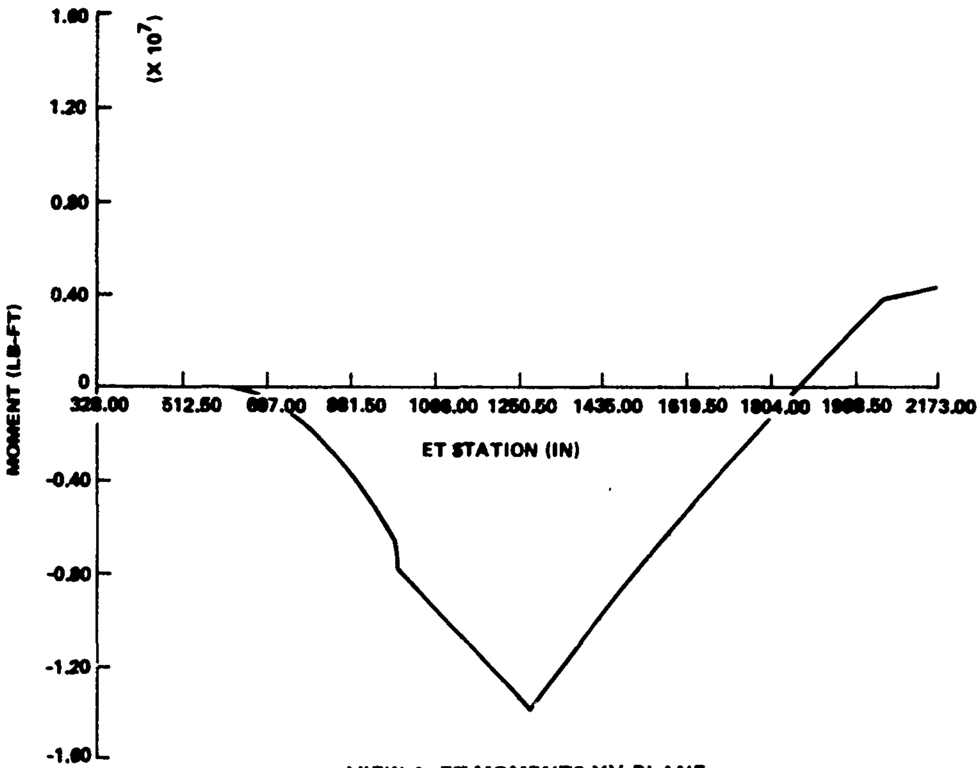

VIEW A, ET MOMENTS XY-PLANE

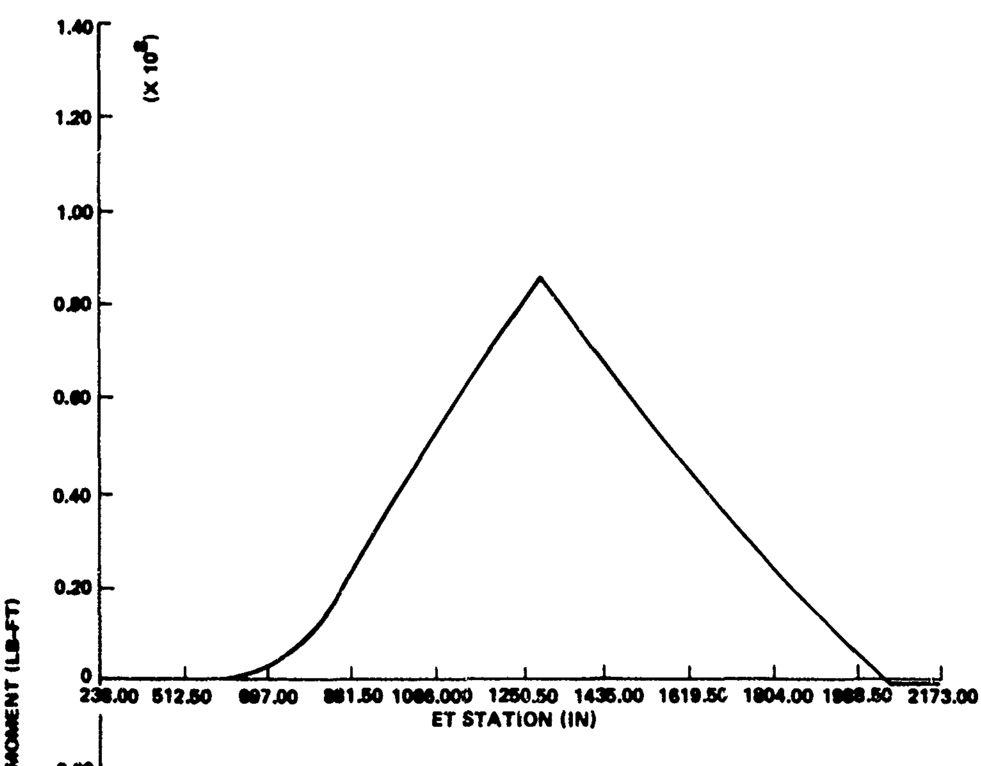

VIEW B, ET MOMENTS XZ-PLANE

FIGURE 4-74 ET BENDING MOMENT (T = 67.5 SEC) FOLLOWING LOSS OF ORBITER AT 50 SECONDS

The maximum bending moment in the X-Z plane, 8.59×10^7 ft-lb, however, exceeds the limit by a factor of 7. Following the approach presented above yields a reduced bending moment of 3.09×10^7 ft-lb at X_T 1290. This still exceeds the limit by a factor of more than 2. Failure of the ET structure due to buckling of the shell's compression side can be expected. In fact, if the high aerodynamic load is the major contributing factor, shell failure could be encountered as early as T = 66.5 seconds.

The mode of failure remains failure of the left SRB/ET forward or aft joint and/or buckling of the ET shell. Thus, for orbiter separation at the four times specified (0, 10, 50, and 100 seconds), the remaining cluster should stay intact for at least 16.5 seconds.

LOSS OF SRB

Now consider the loss of one SRB (in this case, the right one). The remaining cluster is no longer symmetric but retains thrust vector control on the orbiter and left SRB. The attach fitting loads are, therefore, a function of the control mode. It is assumed here that the control mode remains the same as before separation, i.e., the control system attempts to maintain the nominal trajectory rather than vehicle stability.

If the right SRB separates at lift-off, all SRB/ET attach fitting loads remain with limit load for 30 seconds. An exception to this is FB9, the aft radial load (Figs. 4-64, 4-75, 4-76, 4-77, View E). The maximum FB9 of 201,969 lb occurs at 9.25 seconds. At that time, FB7 and MB_1 equal -21,709 lb and 2,300,000 in.-lb, respectively. These loads translate into the following component loads (Fig. 4-69):

$$P13 = FB7/16.75° = -22{,}670 \text{ lb} \qquad (4\text{-}64)$$

$$P11 = 0.5FB9 - 0.220FB7 - 0.00877MB1 = 85{,}600 \text{ lb} \qquad (4\text{-}65)$$

$$P12 = 0.5FB - 0.0829FB7 + 0.00877MB1 = 123{,}000 \text{ lb} \qquad (4\text{-}66)$$

Since all members have a compressive limit load of 292,300 lb, none of the members are overloaded.

However, at 14 seconds into flight, the forward orbiter joint becomes overloaded in the radial direction. At 15.75 seconds, FO1 peaks at -227,830 lb, while FO2 remains at -57,410 lb. Resolving these loads into component loads, Figure 4-78 yields

$$P1 = -0.64FO1 + 0.81FO2 = 99{,}300 \text{ lb} \qquad (4\text{-}67)$$

$$P2 = -0.64FO1 - 0.81FO2 = 192{,}300 \text{ lb} \qquad (4\text{-}68)$$

P2 exceeds the limit load of 106,700 lb (Table 4-6) by a factor of 1.8. While no analysis has been made here on the clevis pins of the forward orbiter truss (no dimensions were obtained), the analysis of those of the rear SRB truss revealed a failure load of 2 times the limit load. Component 2 is marginal, and failure may occur.

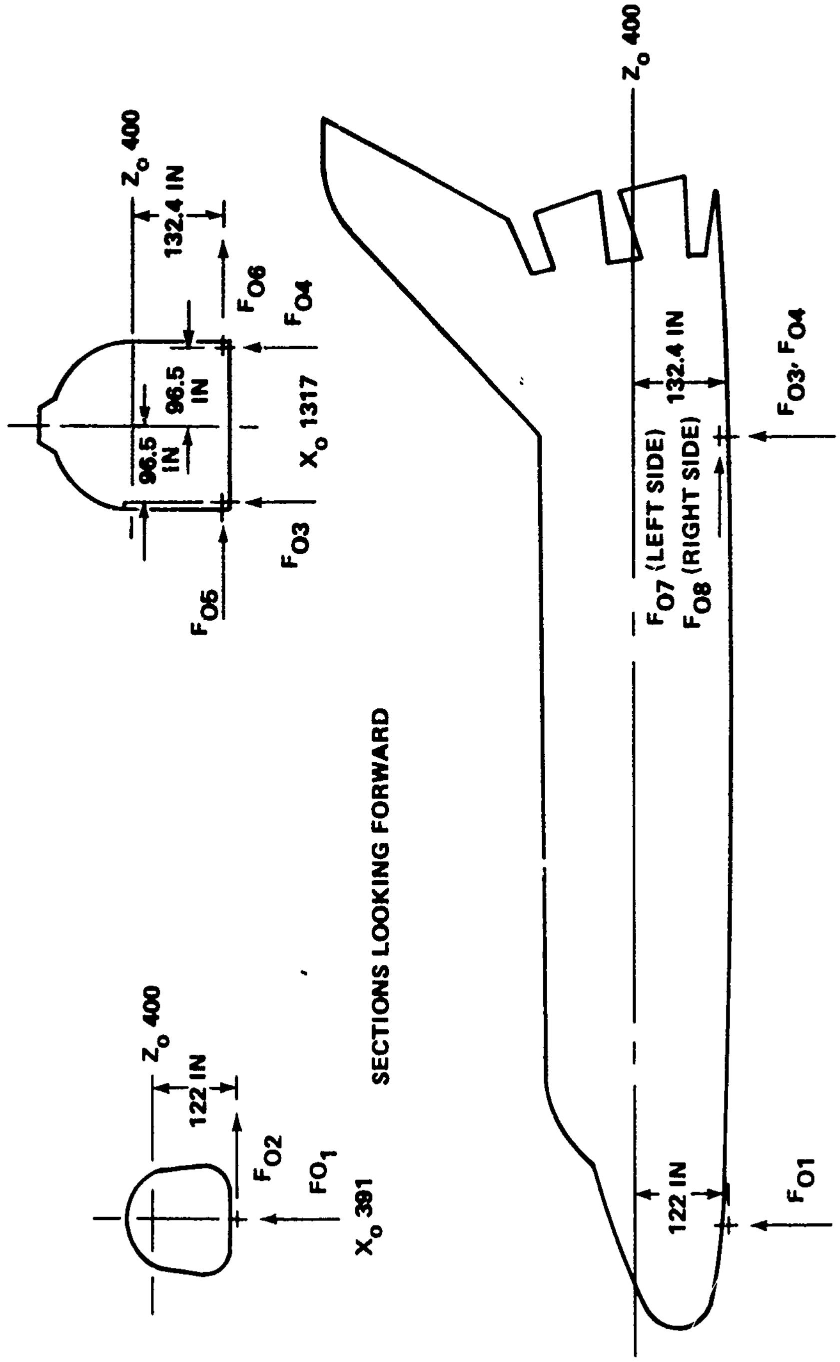

FIGURE 4-75 ORBITER FITTING LOAD LOCATIONS AND DIRECTIONS

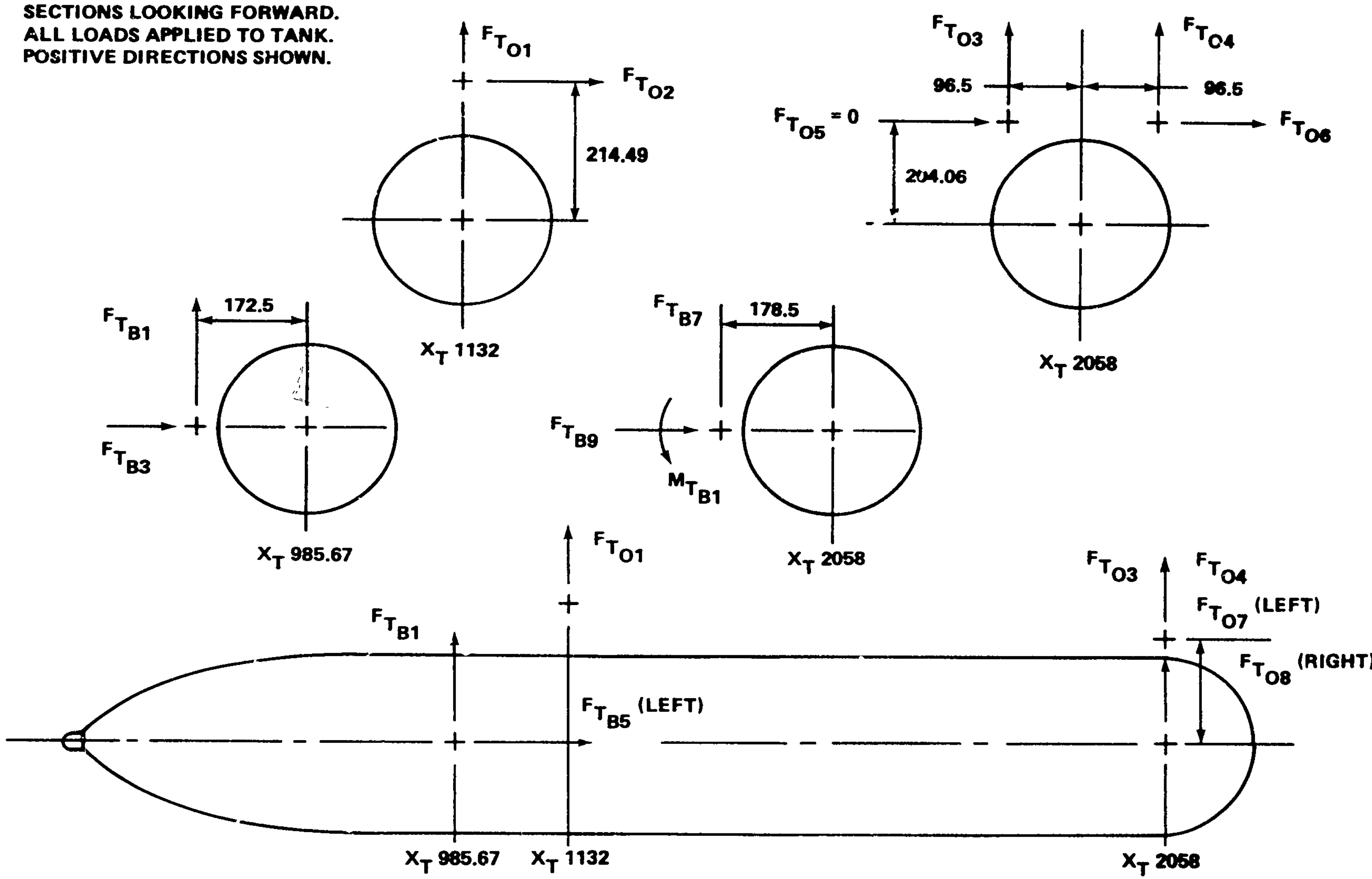

FIGURE 4-76 EXTERNAL TANK ATTACH LOADS AND DIRECTIONS

SRB000

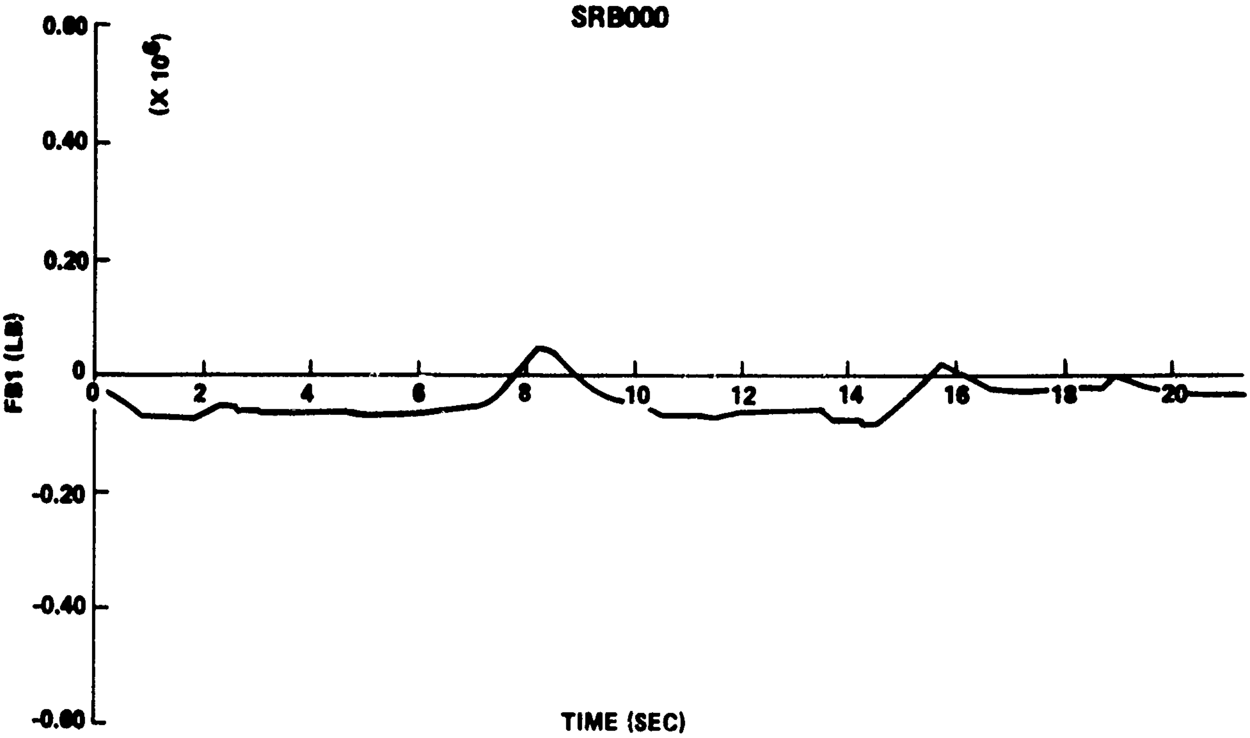

VIEW A, FB1

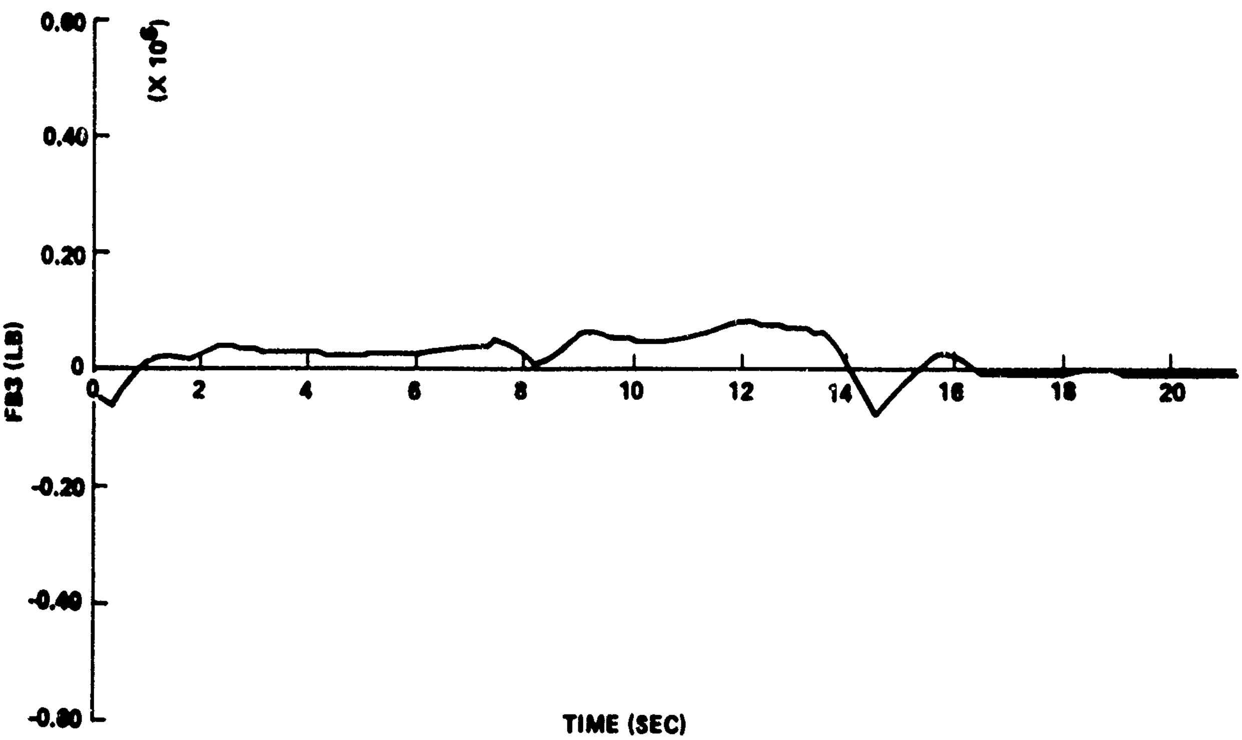

VIEW B, FB3

FIGURE 4-77 ATTACH FITTING LOADS — LOSS OF SRB AT LIFT-OFF (Sheet 1 of 6)

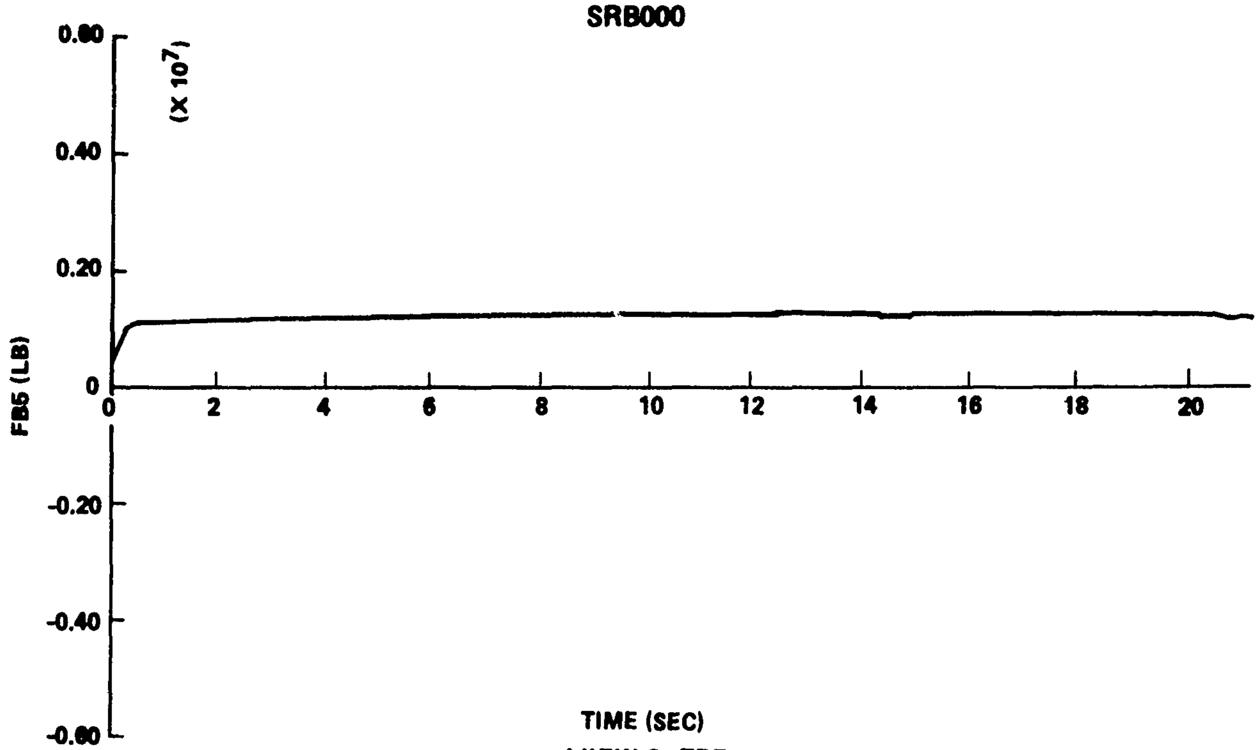

VIEW C, FB5

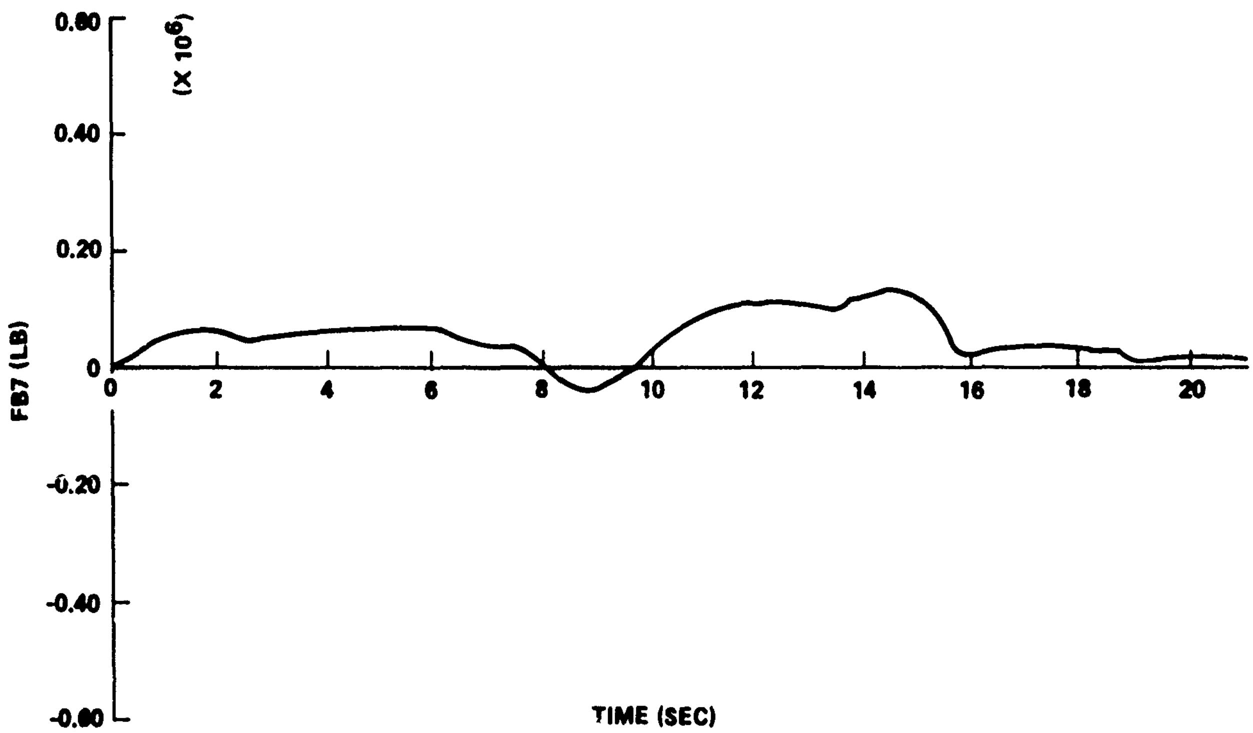

VIEW D, FB7

FIGURE 4-77 ATTACH FITTING LOADS – LOSS OF SRB AT LIFT-OFF (Sheet 2 of 6)

SRB000

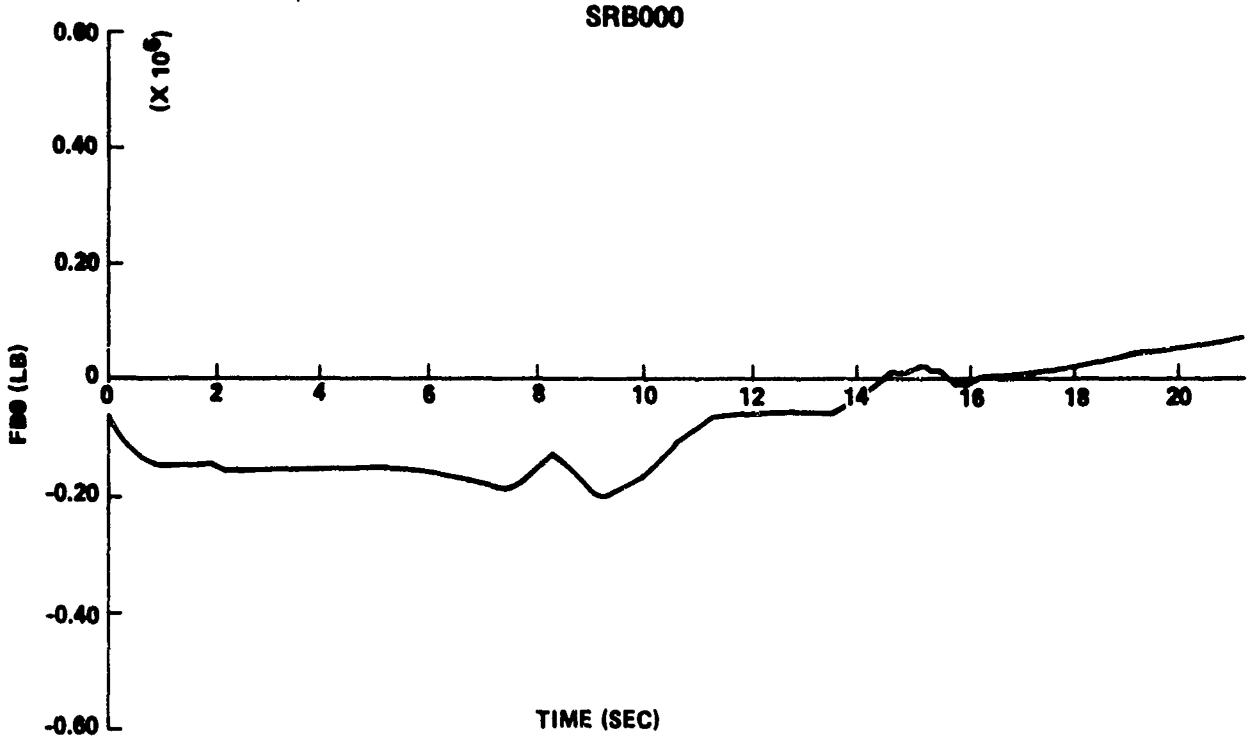

VIEW E, FB9

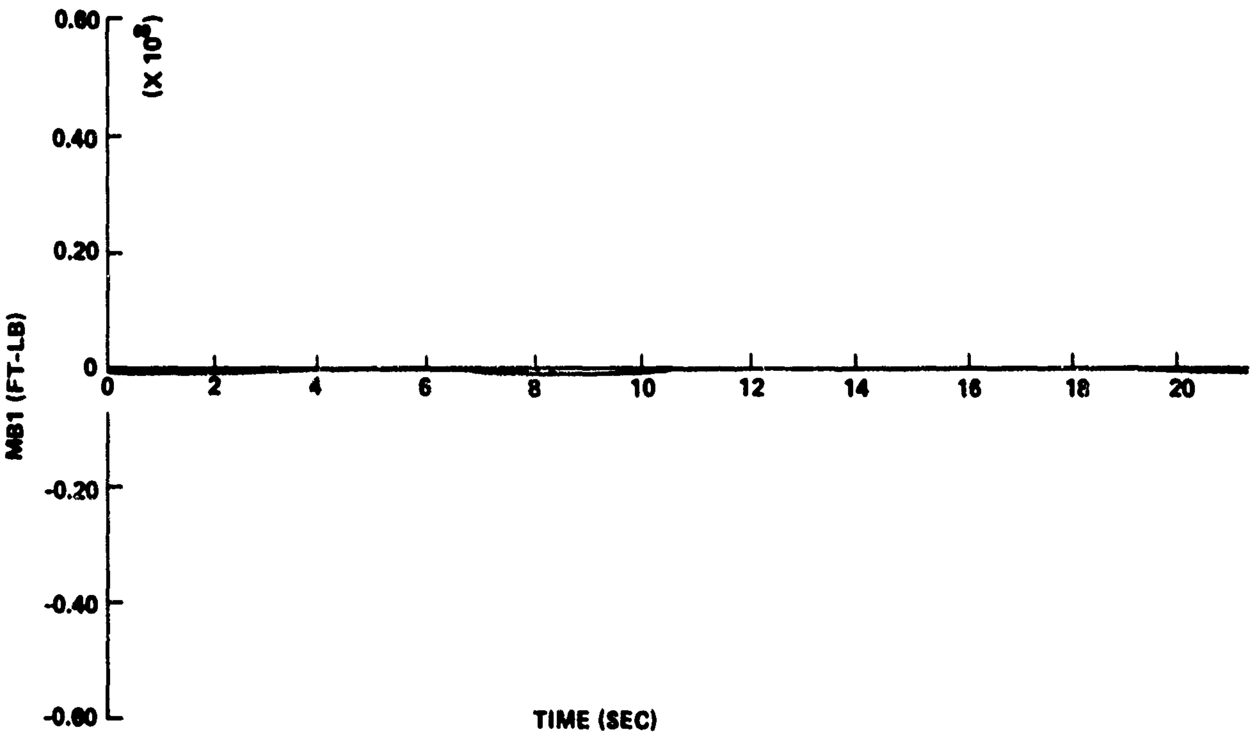

VIEW F, MB1

FIGURE 4-77 ATTACH FITTING LOADS – LOSS OF SRB AT LIFT-OFF (Sheet 3 of 6)

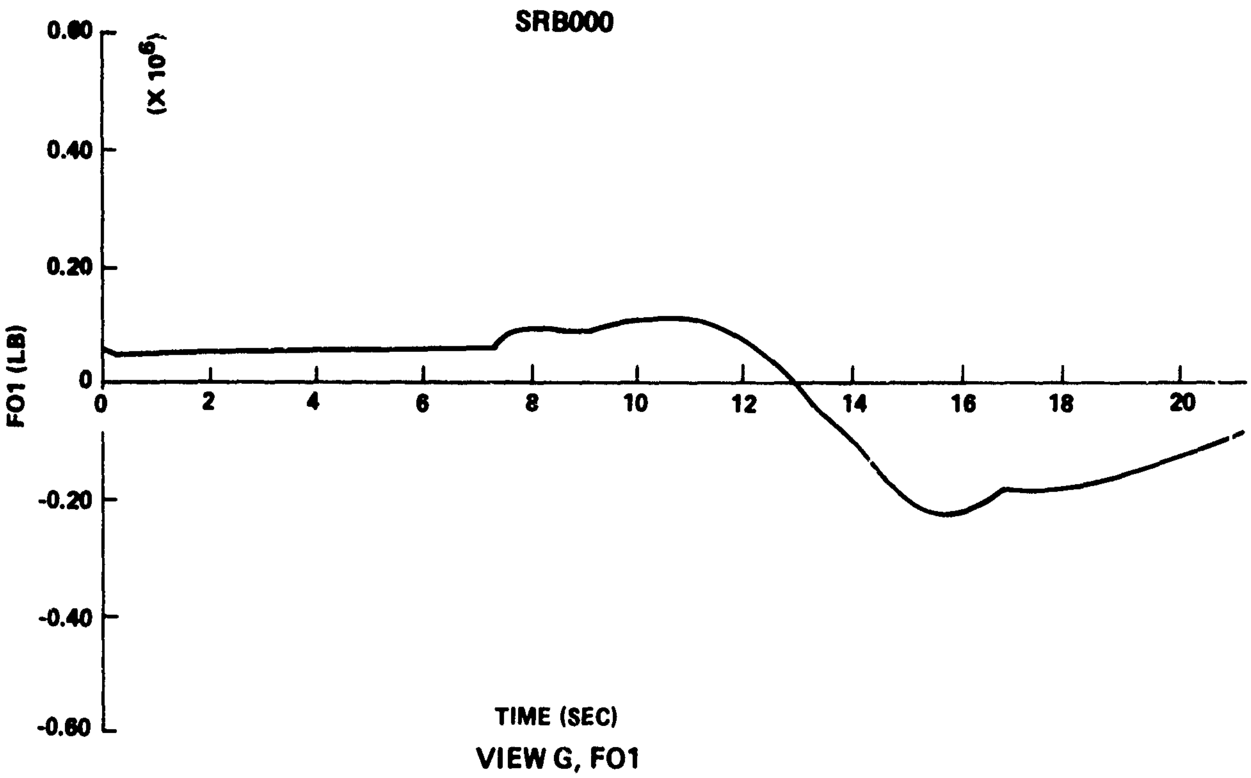

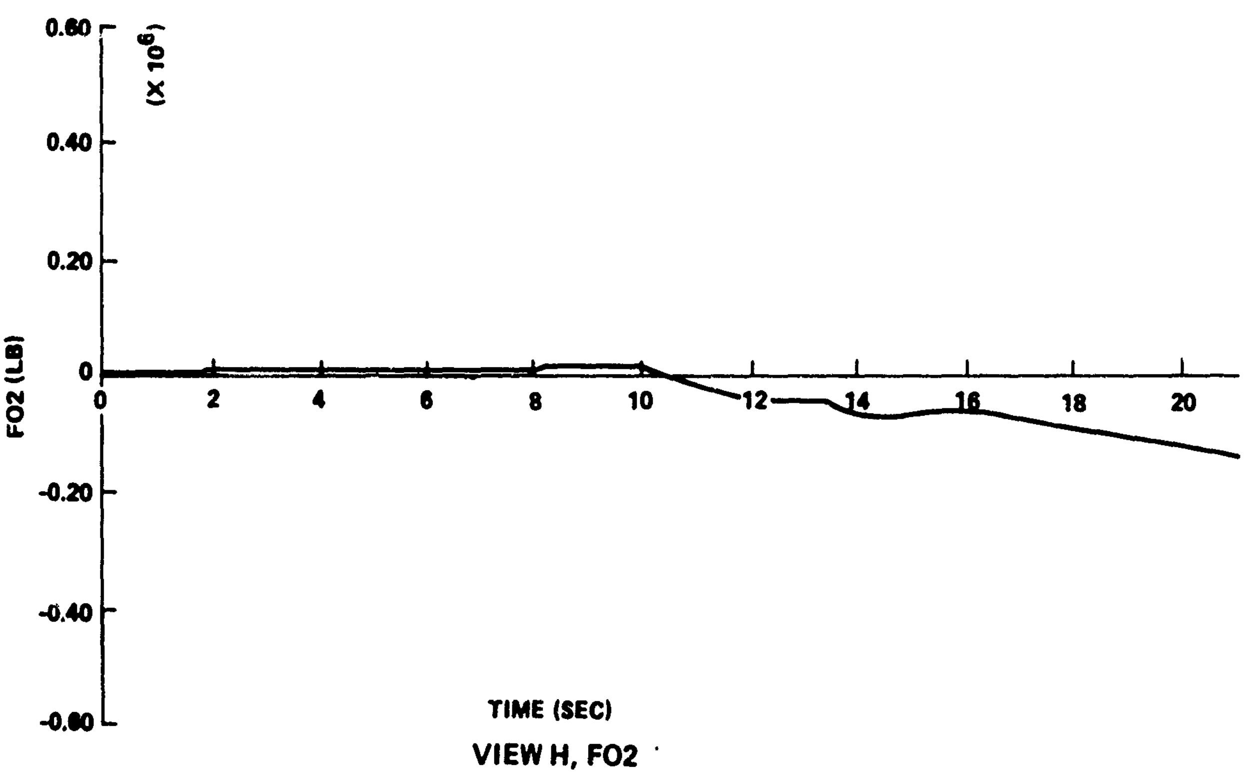

FIGURE 4-77 ATTACH FITTING LOADS — LOSS OF SRB AT LIFT-OFF (Sheet 4 of 6)

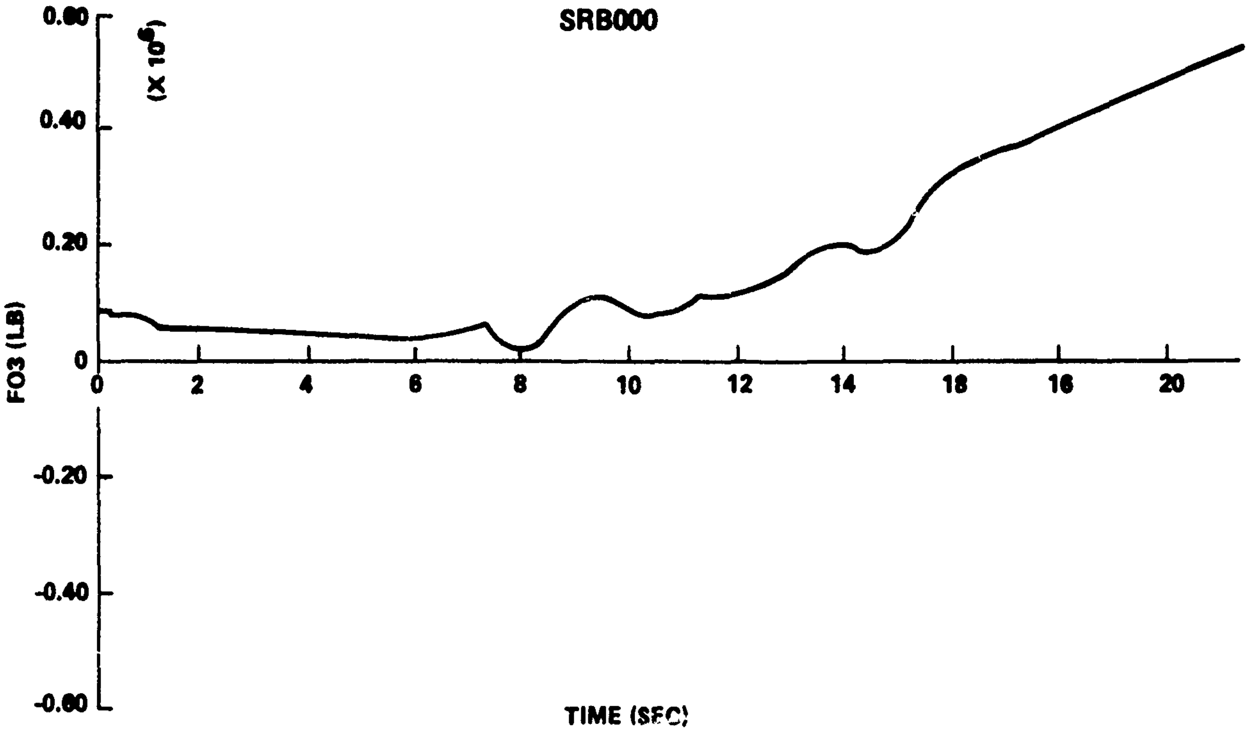

VIEW I, FO3

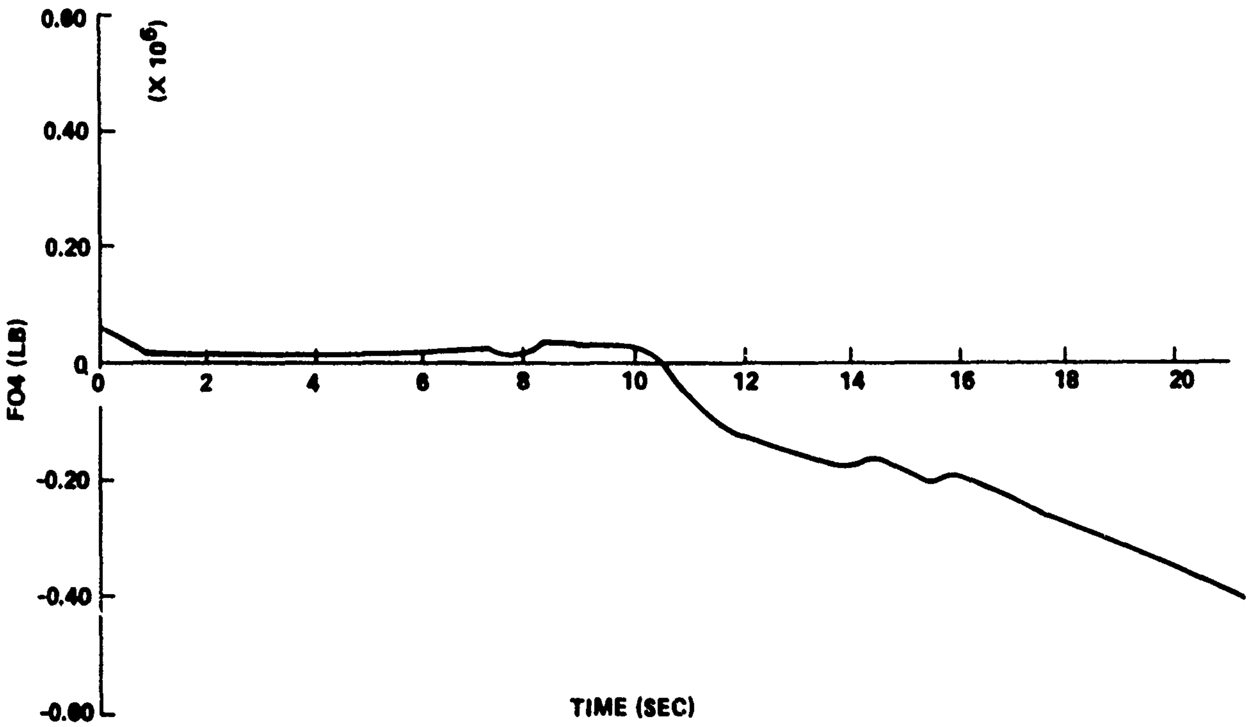

VIEW J, FO4

FIGURE 4-77 ATTACH FITTING LOADS — LOSS OF SRB AT LIFT-OFF (Sheet 5 of 6)

SRB000

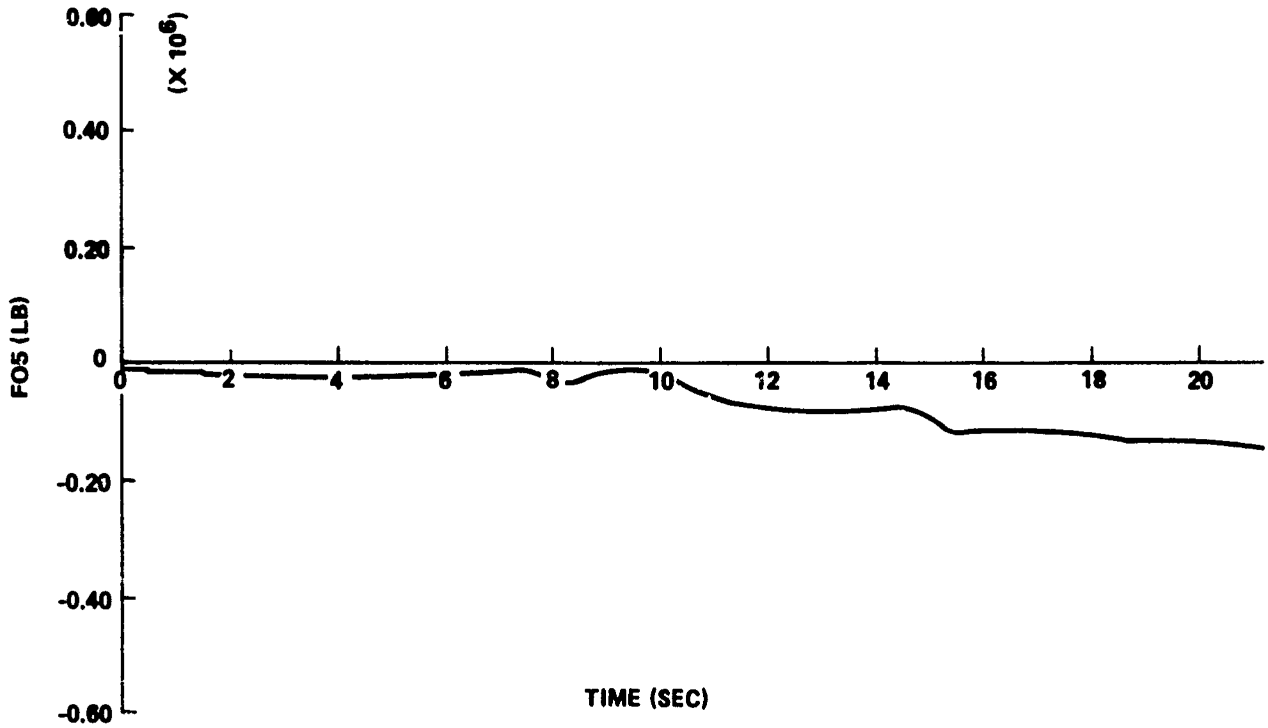

VIEW K, FO5

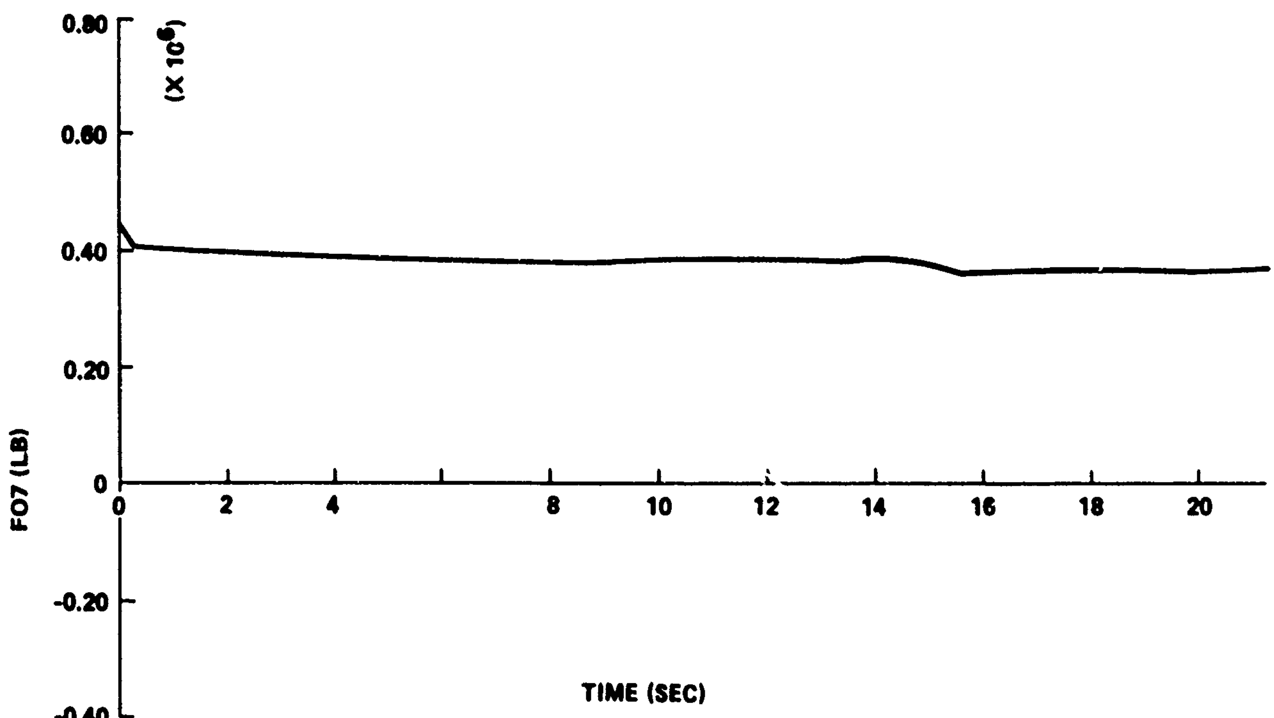

VIEW L, FO7

FIGURE 4-77 ATTACH FITTING LOADS — LOSS OF SRB AT LIFT-OFF (Sheet 6 of 6)

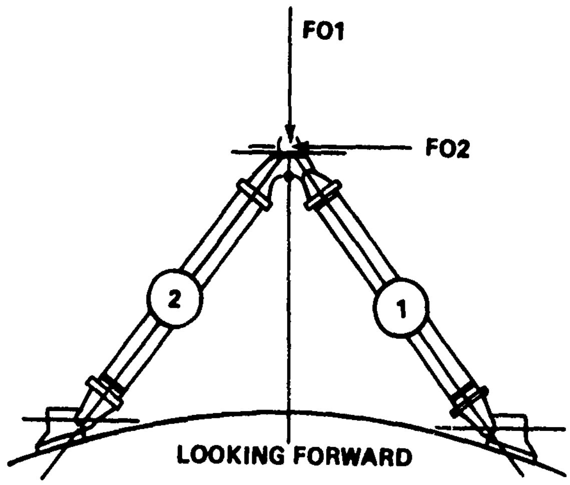

FIGURE 4-78 FORWARD ORBITER JOINT COMPONENT AND ATTACH FITTING LOADS

A more probable mode of failure existing at the same time is tensile failure of the forward orbiter separation bolt (Fig. 4-79). The existing load is 2.2 times the limit load. In either case, possible failure of the forward orbiter attachment is expected about 15.75 seconds after a separation at lift-off. Similar situations do not exist for separations at 10 and 100 seconds into flight. No failures are expected for 20 seconds following separations at these times.

As with the loss of the orbiter, loss of the right SRB at 50 seconds results in a violent response to aerodynamic loading. Attach fitting loads at the aft SRB joint and the forward orbiter joint exceed limit loads within a few seconds (Fig. 4-80). Resolving FO1 (193,800 lb) and FO2 (19,800 lb) into component loads yields

$$P1 = -108,000 \text{ lb}$$

$$P2 = -140,100 \text{ lb}$$

The limit load in compression is given as 106,700 lb (Table 4-6). Hence, the overload is only 1.3 times the limit load. A check of the separation bolt reveals an overload in compression of only 1.5 times the limit load. Appendix K indicates no failure is encountered in frame X_T 1129.9 of the ET. Failure of the forward orbiter joint at separation is not probable. However, 2 seconds later the loads on the separation bolt and struts become tensile and reach sufficient magnitudes for failure.

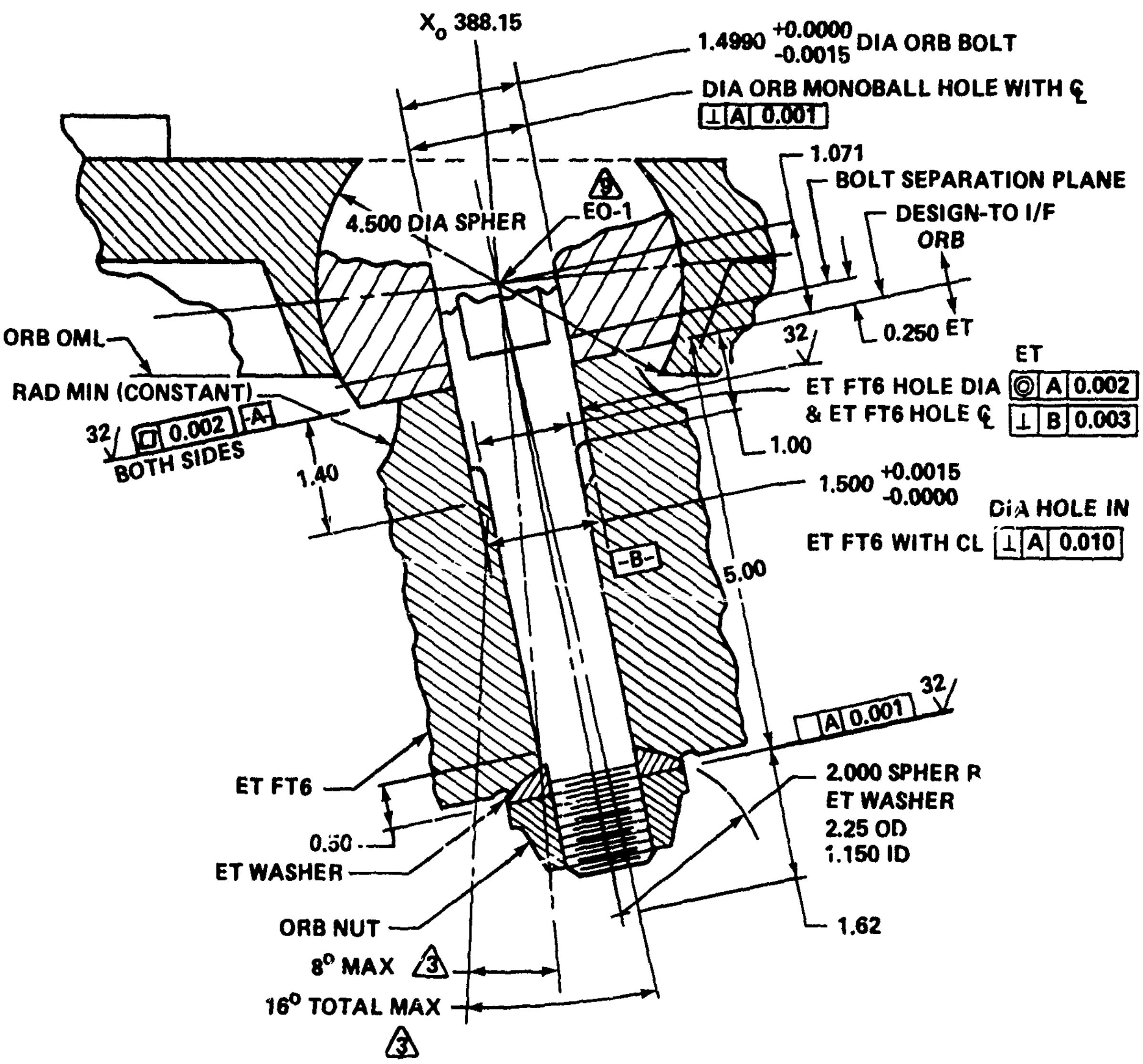

FIGURE 4-79 ORBITER SEPARATION BOLT

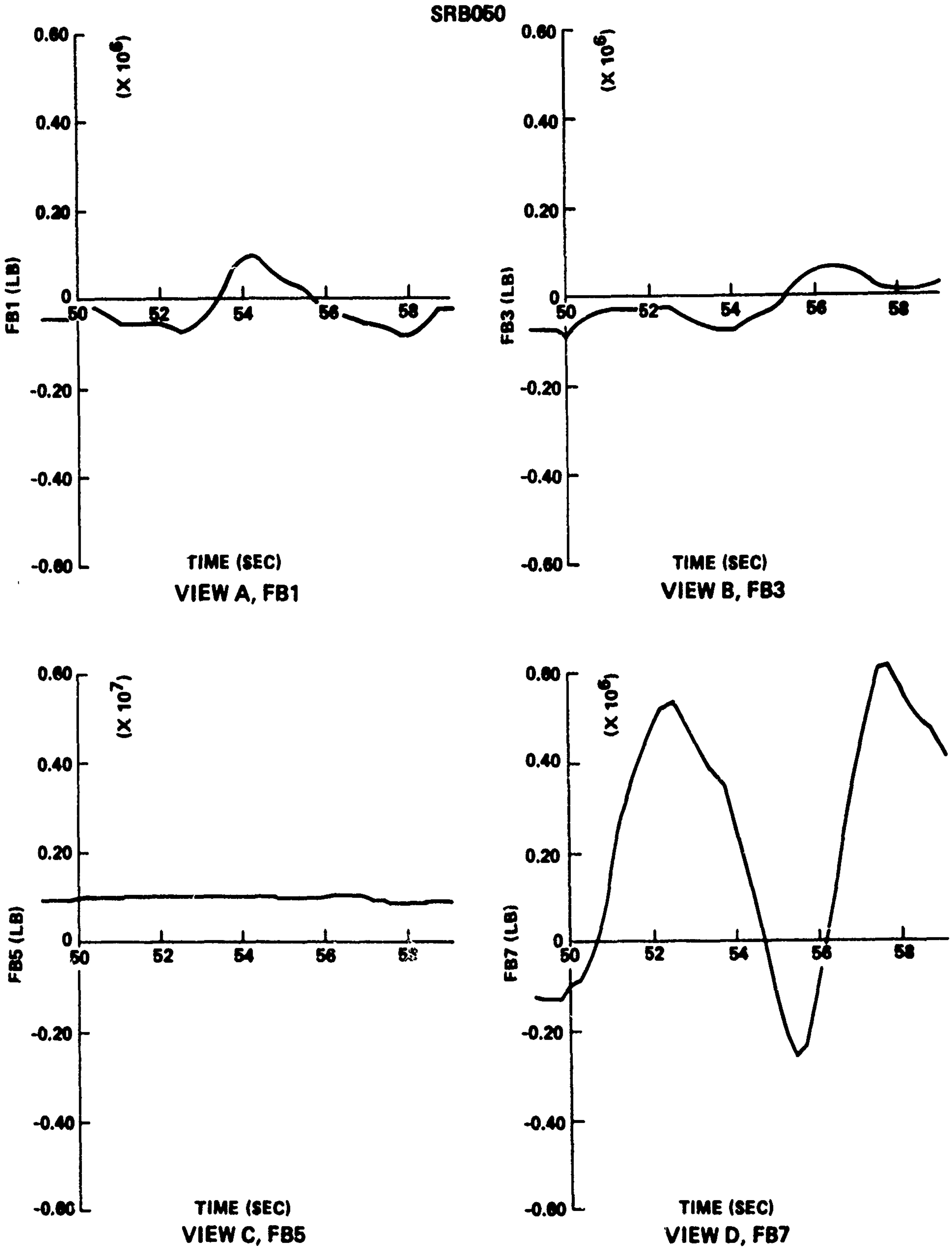

FIGURE 4-80 ATTACH FITTING LOADS — LOSS OF SRB AT 50 SECONDS (Sheet 1 of 3)

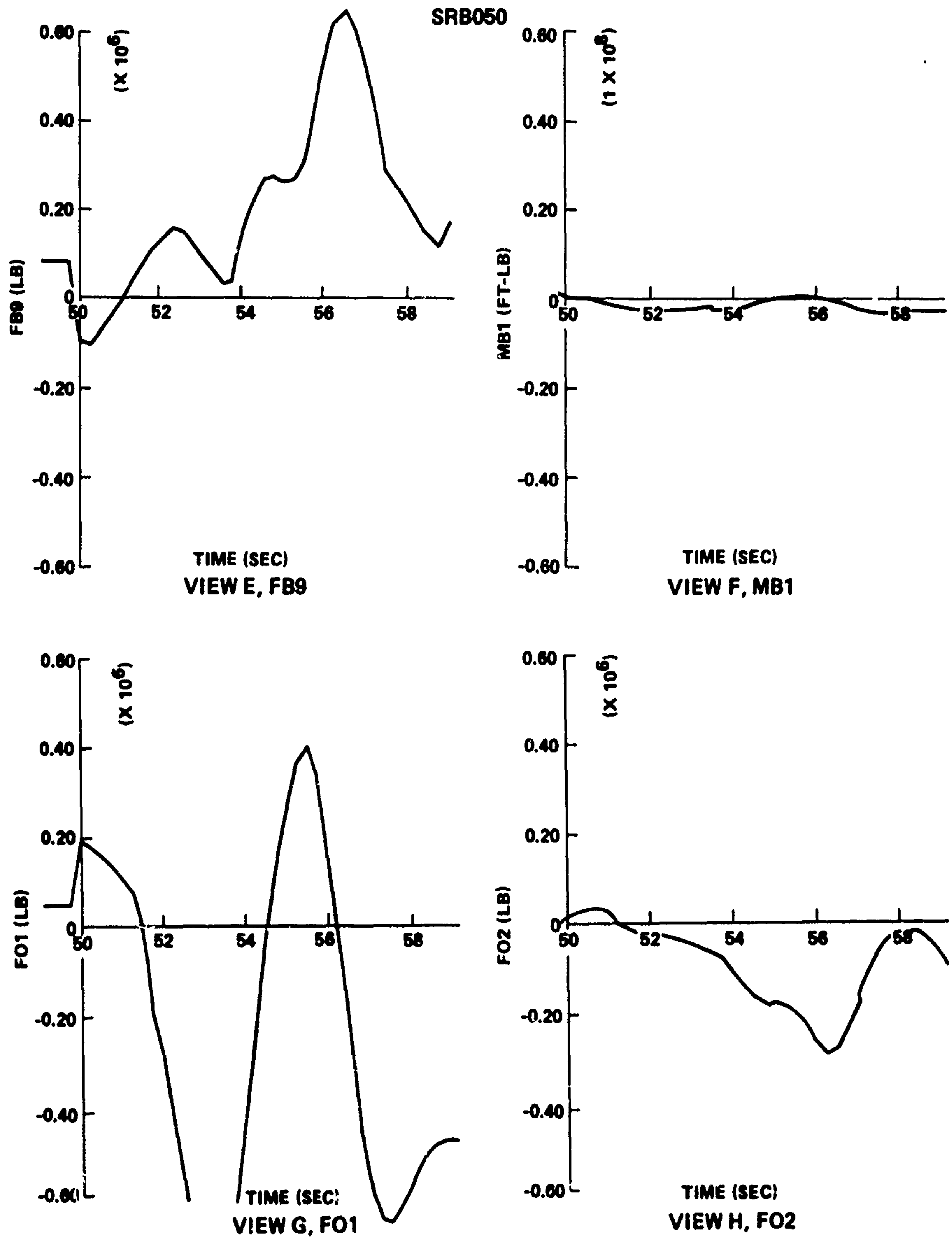

FIGURE 4-80 ATTACH FITTING LOADS — LOSS OF SRB AT 50 SECONDS (Sheet 2 of 3)

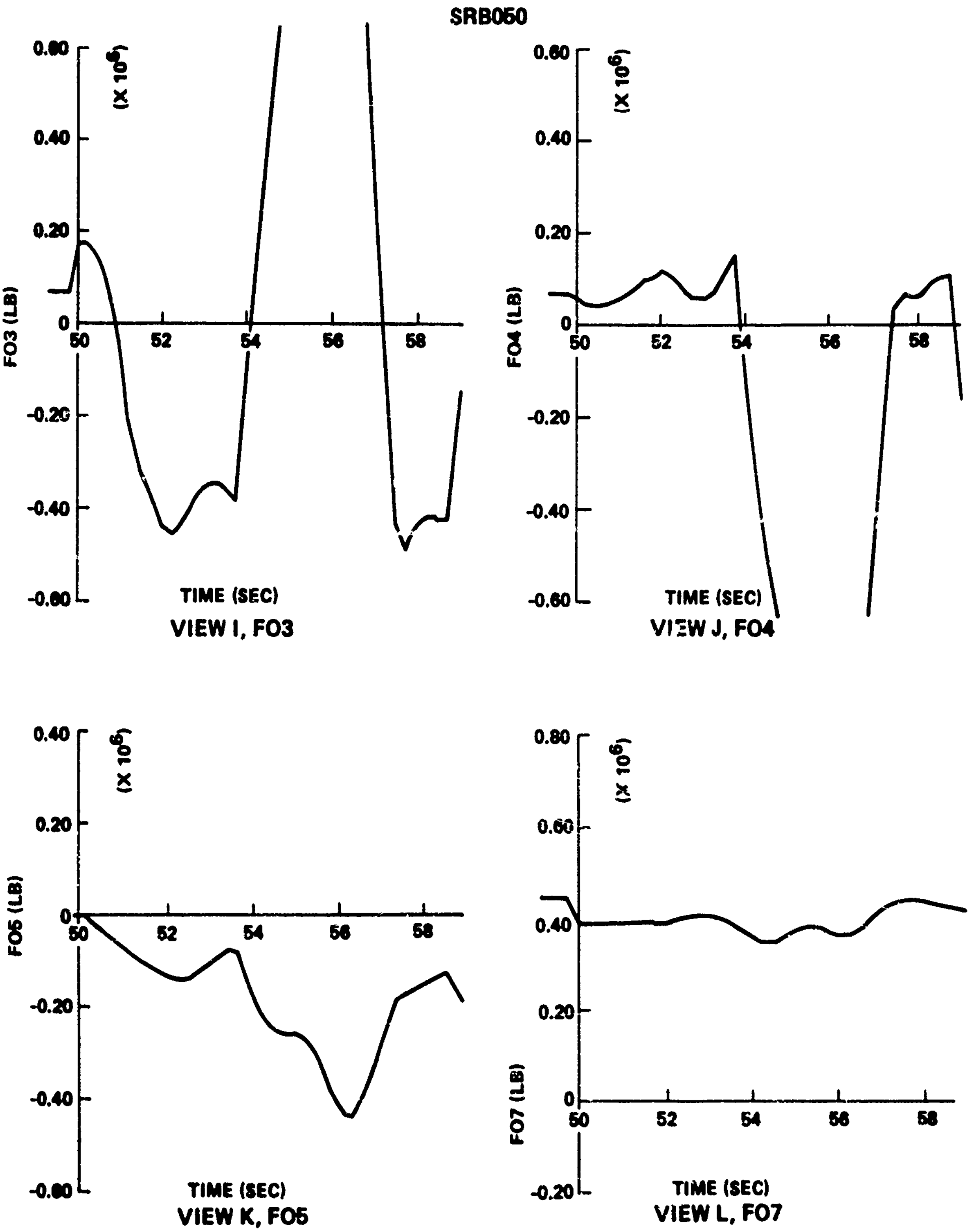

FIGURE 4-80 ATTACH FITTING LOADS – LOSS OF SRB AT 50 SECONDS (Sheet 3 of 3)

While failure of the forward orbiter joint does not preclude the ability to destruct for some additional delta time, the analysis undertaken in this study was not designed to handle the dynamics of cluster components following a joint failure. As previously stated, the postulated separations were assumed to be instantaneous and clean. Therefore, the attach fitting loads calculated are only valid up to the time of first failure. No firm prediction can be made for the first SRB joint failure. However, because of the violent motion, it can be expected to occur within a few seconds.

Again, a check of the bending moment, shear and end load distributions at 51.75 seconds, reveals no indication of overall shell failure (Figs. 4-81 through 4-83). The mode of failure remains failure of the forward orbiter/ET joint.

CONCLUSIONS

1. Given an inadvertent separation of the orbiter, subsequent structural failure of the remaining cluster will not occur for at least 30 seconds following a separation at lift-off, or for at least 20 seconds following a separation at 10 or 100 seconds into flight.

2. Loss of the orbiter at 50 seconds will result in failure of either or both the left SRB/ET forward fitting(s) or rear truss at $16.5^{+1.0}_{-0.0}$ seconds following separation.

3. In the event of an inadvertent separation of the right SRB at lift-off, possible failure of the forward orbiter/ET joint occurs at 15.75 seconds.

4. No failures are expected for at least 20 seconds following separation of the SRB at 10 or 100 seconds into flight.

5. Failure of the forward orbiter/ET truss will occur just 2 seconds after separation of the right SRB at 50 seconds into flight.

6. The minimum delta time to destruct occurs near the max q portion of the flight. These conditions can be expected to exist over a significant portion of the boost phase.

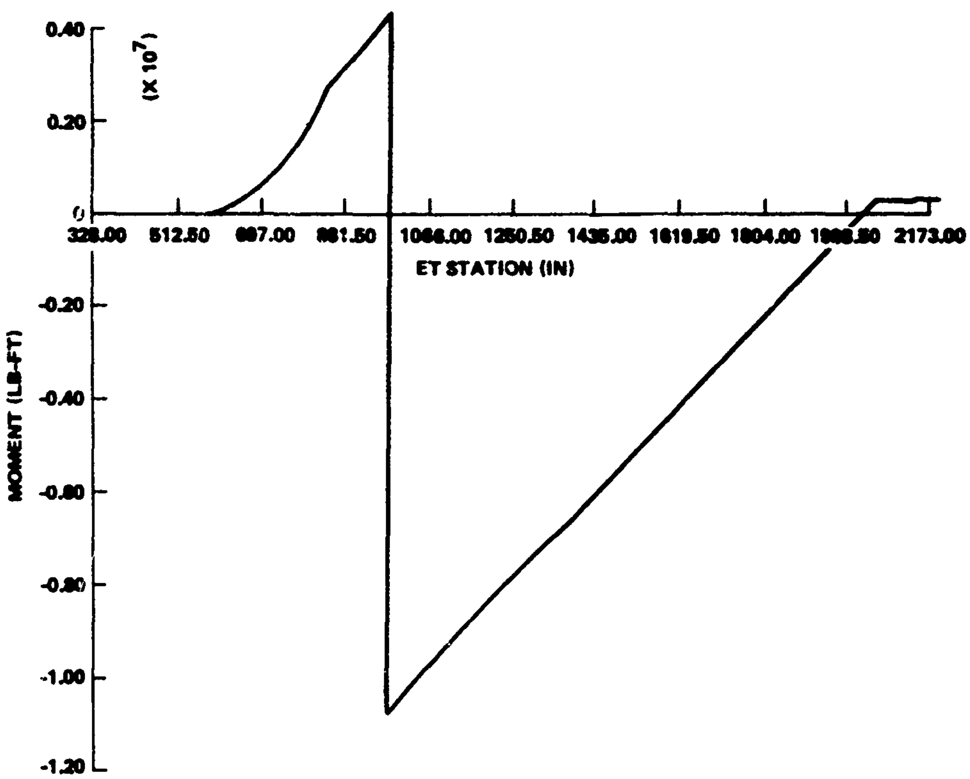

VIEW A, ET MOMENTS XY-PLANE

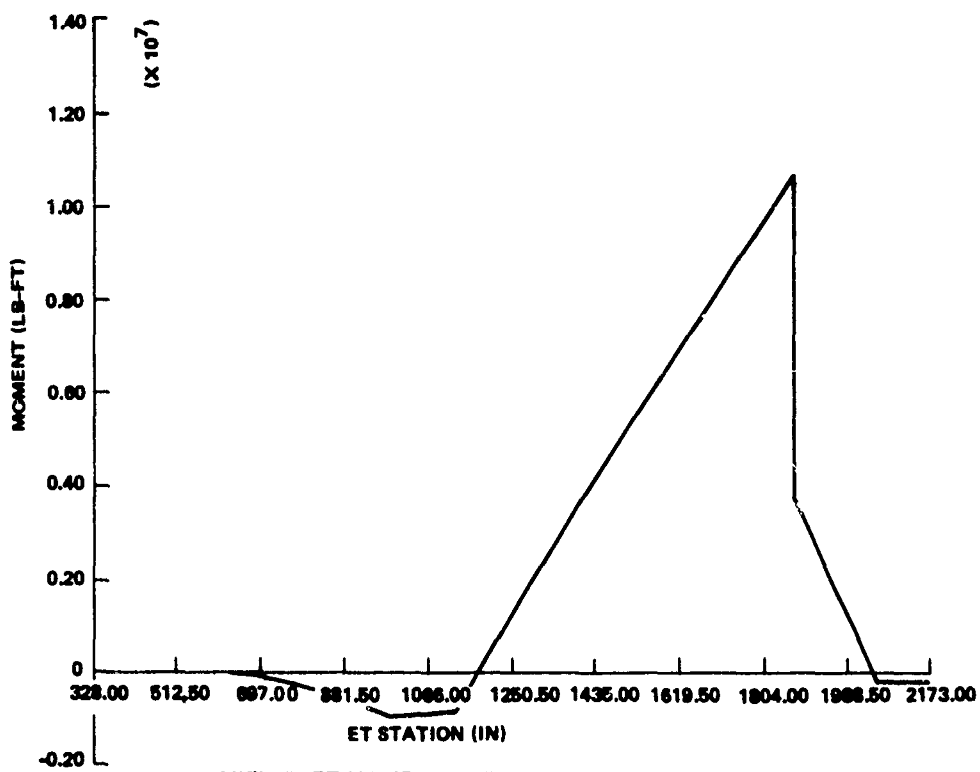

VIEW B, ET MOMENTS XZ-PLANE

FIGURE 4-81 ET BENDING MOMENT (T = 51.75 SEC) FOLLOWING LOSS OF SRB AT 50 SECONDS

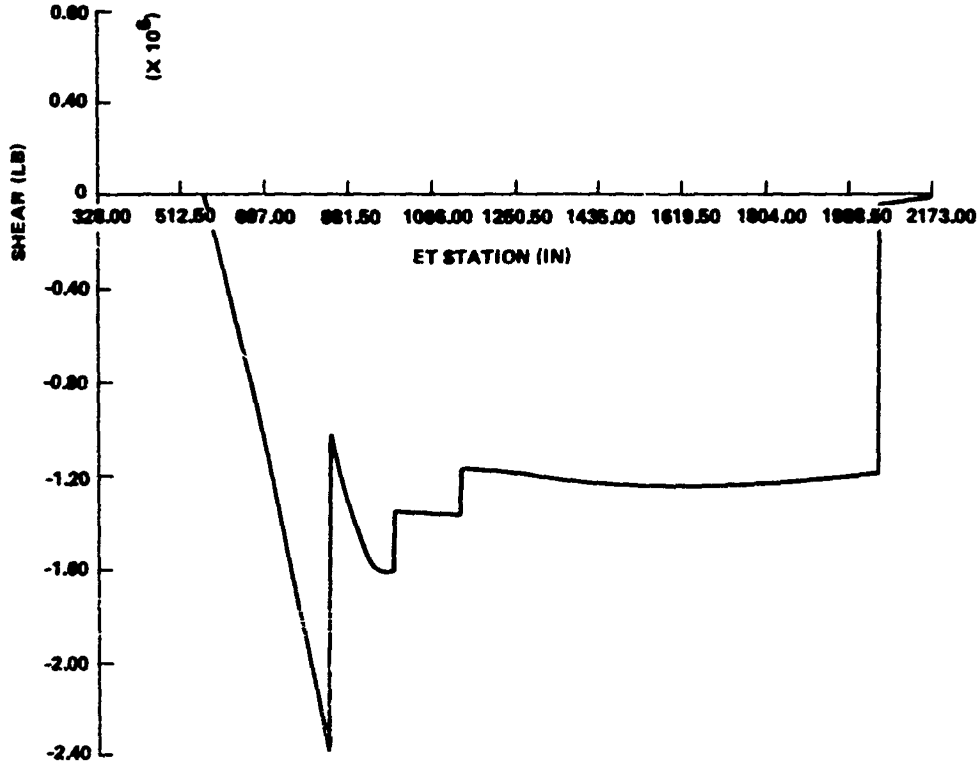

VIEW A, ET SHEAR, Y-DIRECTION

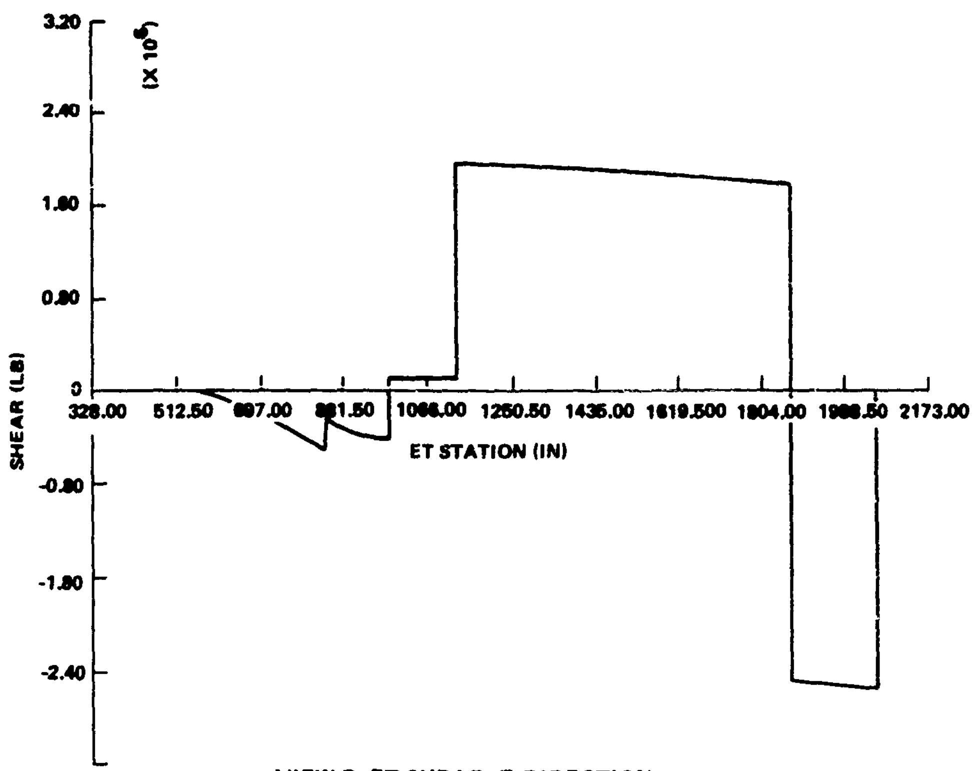

VIEW B, ET SHEAR, Z-DIRECTION

FIGURE 4-82 ET SHEAR (T = 51.75 SEC) FOLLOWING LOSS OF SRB AT 50 SECONDS

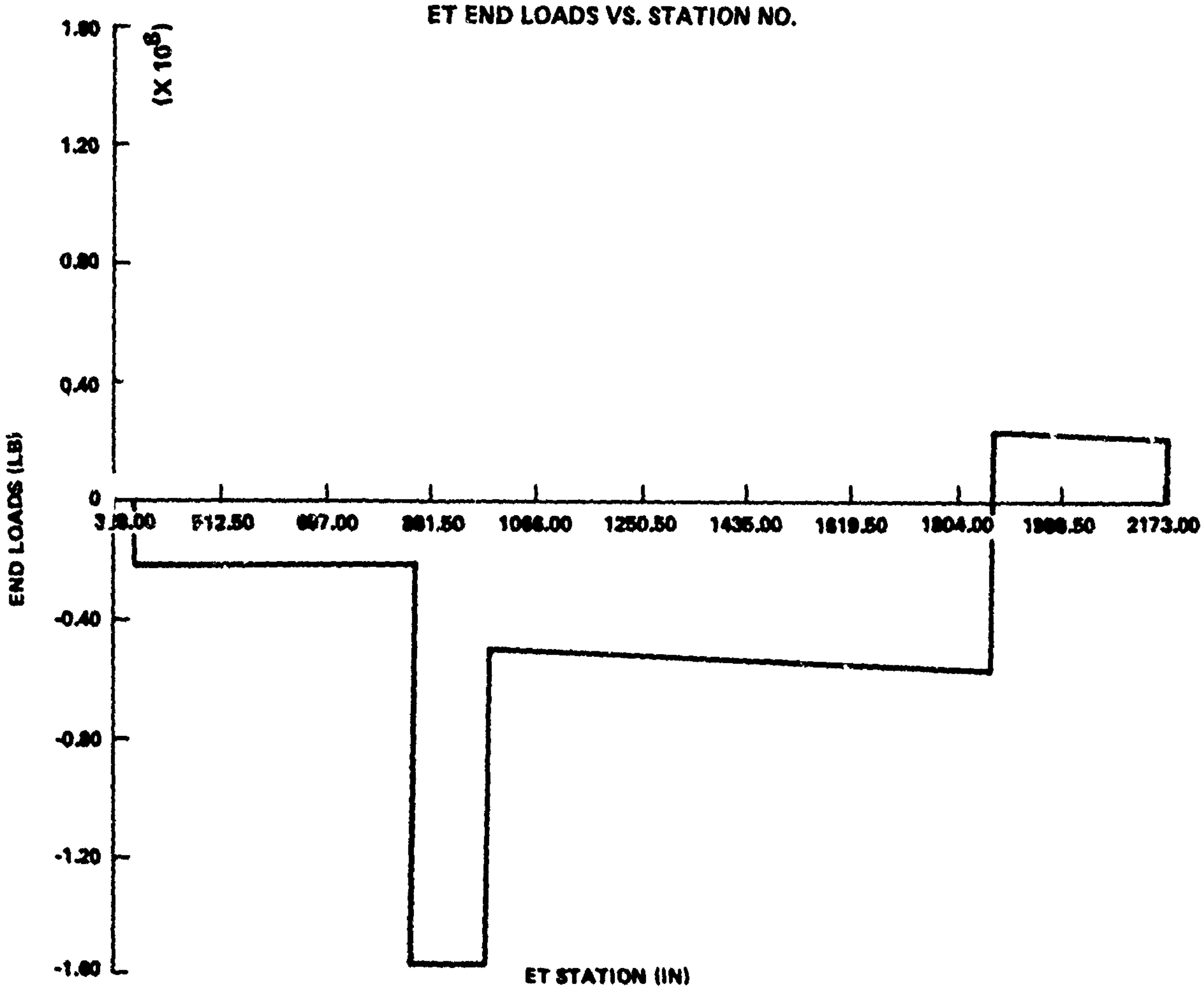

FIGURE 4-83 ET END LOAD (T = 51.75 SEC) FOLLOWING LOSS OF SRB AT 50 SECONDS

BIBLIOGRAPHY

A Six-Degree-of-Freedom Addition to the STAR3D Program, Northrop Corporation, TR-240-1375, Apr 1975.

Anderson, D. L., and Lindberg, H. E., "Dynamic Pulse Buckling of Cylindrical Shells under Transient Lateral Pressures," AIAA Journal, Vol. 6, No. 4, p. 589, Apr 1968.

Augusti, G., and d'Agostino, S., "Experiments on the Plastic Behavior of Short Steel Cylindrical Shells Subject to Internal Pressure," First International Conference on Pressure Vessel Technology, Part 1 - Design and Analysis, p. 45.

Bleakney, W., and Taub, A.H., "Interaction of Shock Waves," Reviews of Modern Physics, Vol. 21, No. 6, 1949, p. 584.

Computer Printout, Mission 1 (due east), MSN-1/DRAG + BASE FRCE UPDAT/SRB-MSFC-15-75/LO TO AOA MECO, Marshall Space Flight Center, NASA.

Cosner, L. H., Sewell, R. G. S., Wedan, H. W., "A Semiquantitative Analysis of Shaped Charge Vaporific Damage," NAVORD Report 6398, NOSTP-2093, Sep 1958.

Degrafft, W.E., A Powered Six-Degree-of-Freedom Trajectory Program for an IBM 7090 Computer, U.S. Naval Ordnance Laboratory, NOLTR 66-199, Mar 1967.

Dengler, R.P., "An Experimental Investigation of Chemical Reaction between Propellant Tank Materials and Rocket Fuels as Oxidizers When Impacted by Small High-Velocity Projectiles," NASA TN D-1882, Aug 1963.

Documentation of the Shuttle Trajectories for Analysis and Research in Three Degrees-of-Freedom (STAR3D) Program, Northrop Corporation, TR-244-984, Jul 1971.

Drimmer, B.E., "Penetration of Steel Targets at Long Stand-Offs by Steel-Cone-Lined Shaped Charges," NOLR 1145, Aug 1950.

Ferguson, C.W., "Hypervelocity Impact Effects on Liquid Hydrogen Tanks," NASA CR-54852, Douglas Report SM-52027, Mar 1966.

Glasstone, S., The Effects of Nuclear Weapons, USAEC, GPO, 1962.

Gorter, C. J., Progress in Low Temperature Physics, Vol. I, North-Holland Publishing Co., Amsterdam, 1957.

Hudson, R.G., The Engineers' Manual (New York: John Wiley & Sons, Inc., 1917).

Kilmer, E.E., "Plastic Bonded, Thermally Stable Explosive for an Apollo Experiment," Journal of Spacecraft and Rockets, Vol. 10, No. 7, 1973, p. 463.

Lehto, D., and Lutzky, M., "One-Dimensional Hydrodynamic Code for Nuclear-Explosion Calculations," Naval Ordnance Laboratory, NOLTR 62-168, DASA-1518, AD-615801, Mar 1965.

Liebowitz, H., Fracture -- An Advanced Treatise, Vol. VI, Fracture of Metals, Academic Press, New York, 1969, p. 338.

"Mated Vehicle," Rockwell International Report No. SD72-SH-0060-2H, Aerodynamic Design Data Book, Vol. 2, Feb 1975.

Minimum Hamiltonian Ascent Shuttle Trajectory Program (MASTRE)/Users Manual, Northrop Corporation, TR-240-1360, Jan 1975.

Morse, C.R., and Stepka, F.S., "Effect of Projectile Size and Material on Impact Fracture of Walls of Liquid-Filled Tanks," NASA TN D-362, Sep 1966.

"Orbiter Vehicle," Rockwell International Report No. SD72-SH-0060-1I, Aerodynamic Design Data Book, Vol. 1, Jun 1975.

Pittman, J.F., "Blast and Fragment Hazards from Bursting High Pressure Tanks," Naval Ordnance Laboratory, NOLTR 72-102, 17 May 1972.

Riehl, W.A., Key, C.F., and Gayle, J.B., "Reactivity of Titanium with Oxygen," NASA TR-R-180, 1963.

Shuttle Operational Data Book/Volume II — Mission Mass Properties, Johnson Space Center, NASA, JSC-08934, Vol. 2, Feb 1975.

Space Shuttle Flight Control System Data Book/Volume I — Integrated Vehicle, Space Division, Rockwell International Corporation, SD73-SH-0097-1D, Mar 1975 (2 Jun 75 revision).

Space Shuttle Flight Systems Performance Data Book/Volume I — Ascent, Space Division, Rockwell International Corporation, SD73-SH-0178-1B, Dec 1974.

Space Shuttle Orbiter Vehicle/Main Engine Interface Control Document, Space Division, Rockwell International Corporation, 13M15000F, Feb 1973.

SRB Performance Data Book, Systems Performance Branch, Marshall Space Flight Center, NASA, Aug 1975.

Stepka, F.S., Morse, C.R., and Dengler, R.P., "Investigation of Characteristics of Pressure Waves Generated in Water-Filled Tanks Impacted by High-Velocity Projectiles," NASA TN D-3143, Dec 1965.

Stepka, F.S., and Morse, C.R., "Preliminary Investigation of Catastrophic Fracture of Liquid-Filled Tanks Impacted by High-Velocity Particles," NASA TN D-1537, May 1963.

Structural Design Loads Data Book, Vol. 2B SD73-SH-0069-2B, Vol. 3B SD73-SH-0069-3B, Vol. 4B SD73-SH-0069-4B, Space Division, Rockwell International, Oct 1974.

Sutton, G.P., Rocket Propulsion Elements, 3rd Edition (New York: John Wiley & Sons, Inc., 1964).

"The Resistance of Various Metallic Materials to Perforation by Steel Fragments; Empirical Relationships for Fragment Residual Velocity and Residual Weight," Project THOR, Technical Report No. 47, Ballistic Analysis Laboratory Institute for Cooperative Research, Johns Hopkins University, Apr 1961.

Von Karman, T., "The Impact of Seaplane Floats During Landing," NACA TN 321, 1929.

Warden, W.R., "Shuttle Vehicle Mold Lines and Protuberances," ICD No. 2-00001, Space Shuttle Interface Control Document Level II, National Aeronautics and Space Administration, Johnson Space Center, Houston, Texas, 19 Feb 1975.

APPENDIX A

PROPELLANT SENSITIVITY TO DETONATION DURING LSC DESTRUCT

A destruct breakup mode for the solid rocket booster (SRB) during linear-shaped charges (LSC) detonation which is not discussed in the text of this report is the possibility of propellant detonation during detonation of the LSC. The available evidence indicates that this is not the case; that is, the propellant does not detonate upon detonation of the LSC. The purpose of this appendix is to document the data upon which this conclusion is based.

A full-scale, stage I flight-weight Minuteman development motor hot destruct test was performed in July 1962.[A-1]

> "The test was conducted to demonstrate that the LSC destruct subsystem would terminate stage I motor operation, but would not detonate the propellant."

The objective of the test was successfully met:

> "Camera coverage and visual observation of the test verified that operation of the LSC destruct subsystem did not detonate the propellant but opened the motor case, causing a complete rupture of the case with expulsion of burned and unburned propellant. This was further verified by the fact that unburned propellant was found at several locations around the test area."

The results quoted above show that an LSC destruct system was able to rupture a pressurized Minuteman stage I motor case during normal burn operation without detonating the propellant. These results are applicable to the SRB LSC destruct system analysis for the following reasons:

1. The propellants are very similar for the SRB and the Minuteman stage I. The major components for the stage I propellant are given on the following page.[A-1] The SRB propellant composition is given in Table 2-5 of the text.

[A-1] Gould, T.W., "Final Test Results TU-122-1570.307, Full-Scale Stage I Flight-Weight Minuteman Development Motor Hot Destruct Test," TW-327-9-62, Thiokol Chemical Corp., Wasatch Division, Brigham City, Utah, 29 Nov 1962.

Case Propellant — Minuteman Stage I (TP-H-1011)

$NH_4\ ClO_4$........................	70% by weight
PBAA............................	12.26
Aluminum........................	16.0
DER.............................	1.74

The main difference between the SRB propellant and the Minuteman stage I propellant described above was in the type of fuel binder used (PBAN — SRB and PBAA — Minuteman stage I). In the development of the solid propellant for the Minuteman stage I, both fuel binders PBAA and PBAN (also called HB) have been used. PBAN is presently being used for Minuteman stage I.

2. The case material for the SRB and the Minuteman stage I is D6AC steel.[A-2]

3. The explosive used in the LSC for the Minuteman state I hot destruct test was RDX with an explosive weight of 200 grains per foot.[A-1] The LSC for the SRB is said to be RDX Type B class G.

Additional Minuteman stage I data are contained in the Thiokol Report, where many detonation tests are documented. The results of several key tests in this reference indicating that the Minuteman stage I propellant does not detonate in the full-scale configuration or in any other configuration tested are summarized below.[A-3]

1. Propellant sample detonation test — Sixty samples of cured TP-H-1001 propellant (diameter = 3.5 inches, length = 6 inches) did not detonate using a 10-gm tetryl booster. Samples were confined and unconfined and tests were conducted at 100°, 80°, and 60°F.

2. Subscale engine detonation tests — Cured TP-H-1001 propellant (quantity = 300 pounds) contained in a case (diameter = 15 inches, length = 32 inches) did not detonate. Two tests were conducted with 4.7- to 4.9-pound cast comp. B booster charges.

3. First-stage subscale engine detonation test — Test results indicated that the propellant TP-H-1002 (quantity = 10,095 pounds) in a subscale engine configuration did not sustain a detonation when subjected to the explosive energy from a 100-pound comp. B booster charge attached externally to the engine case.

4. First-stage engine detonation test — The propellant TRX-H609 (quantity = 42,381 pounds) did not detonate in a first-stage configuration when subjected to explosive energy from a 100-pound comp. B booster charge attached externally to the case.

[A-2] Kapp, J.R., Daines, J.V., and Anderson, E., "Stress Analysis Report for the Structural Elements of the SRM," Thiokol Chemical Corporation, Wasatch Division, Brigham City, Utah, TWR-10435, 18 Mar 1975.

[A-3] "Thiokol Chemical Corporation Propulsion System for Weapon System 133A (Minuteman) Explosive Classification Tests Final Report," TW-543-5-61, Thiokol Chemical Corporation, Utah Division, Brigham City, Utah, 15 May 1961.

The available data indicate that the SRB propellant will not detonate upon detonation of the LSC.

The experimental work to date has been with the Minuteman configuration.

APPENDIX B

TRAJECTORIES

This appendix is an illustration of the ascent vehicle axis system (Fig. B-1) and contains plots of the flight variables for each inadvertent separation condition (Figs. B-2 through B-41). The variables are plotted for an arbitrary 18-second period after the separation occurs. Rocket engine deflections are not shown for the separated component, nor are they shown if the nozzle is nulled. The body axes form a right-handed system, and all rotations are positive, according to the right-handed rule. The conventional psi, theta, and phi euler angles are used to define the orientation of the body axes.

Dashed lines in Figures B-2 thru B-41 are used to indicate locations of calculated points. Densely packed calculated points are represented by solid lines.

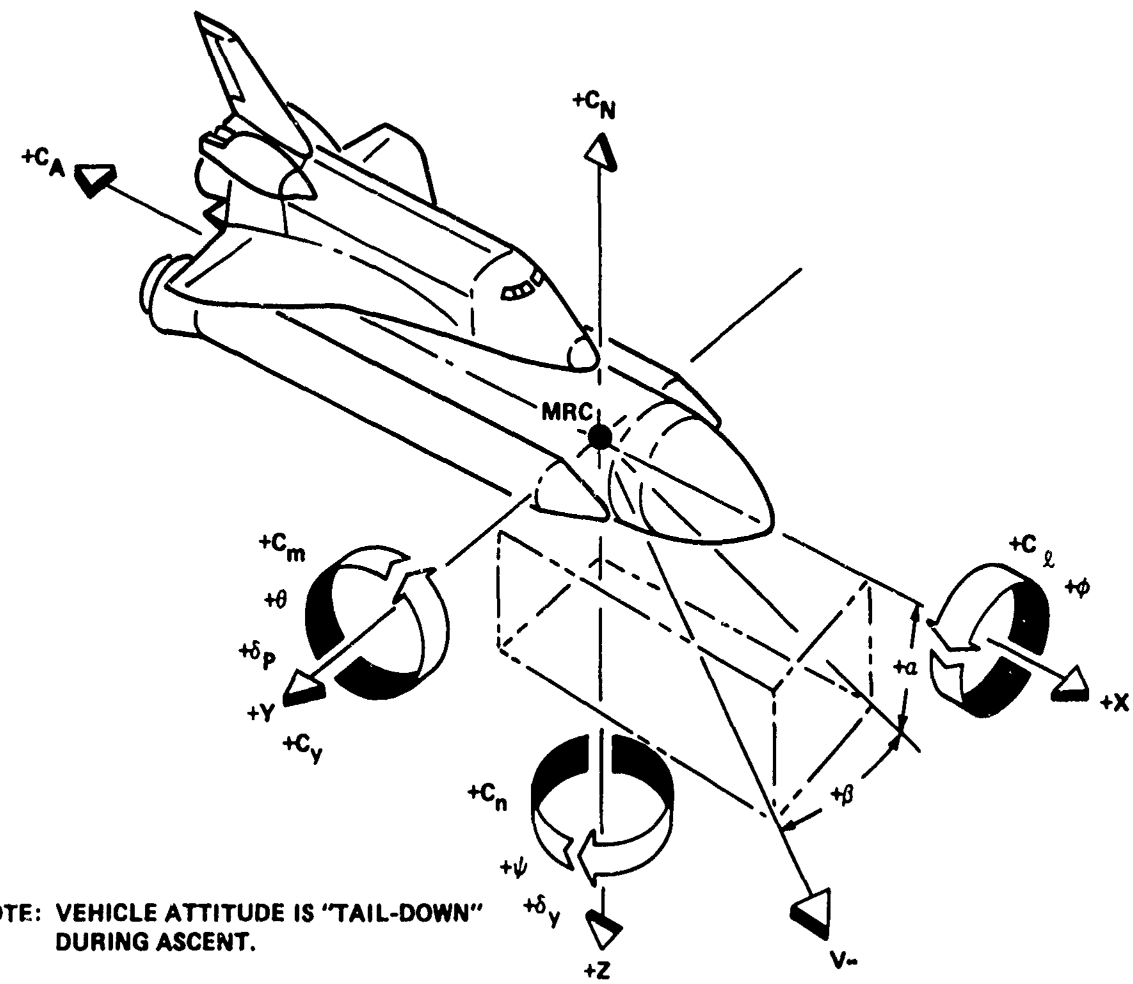

NOTE: VEHICLE ATTITUDE IS "TAIL-DOWN" DURING ASCENT.

FIGURE B-1 ASCENT VEHICLE AXIS SYSTEM

AXIS LABELS

TIME (SEC)	Time from Lift-off (seconds)
PHI (DEG)	Roll Orientation Angle (degrees)
THETA (DEG)	Angle of Elevation (degrees)
PSI (DEG)	Heading or Azimuth (degrees)
P (DEG/SEC)	Rolling Velocity (degrees/second)
Q (DEG/SEC)	Pitching Velocity (degrees/second)
R (DEG/SEC)	Yawing Velocity (degrees/second)
PDOT (D/S2)	Rolling Acceleration (degrees/second^2)
QDOT (D/S2)	Pitching Acceleration (degrees/second^2)
RDOT (D/S2)	Yawing Acceleration (degrees/second^2)
AX (FT/S2)	Axial Acceleration (feet/second^2)
AY (FT/S2)	Side Transverse Acceleration (feet/second^2)
AZ (FT/S2)	Normal Transverse Acceleration (feet/second^2)
ALPHA (DEG)	Angle of Attack (degrees)
BETA (DEG)	Angle of Sideslip (degrees)
UORBP (DEG)	Pitch Deflection of Upper SSME (degrees)
UORBY (DEG)	Yaw Deflection of Upper SSME (degrees)
LORBP (DEG)	Pitch Deflection of Lower Left SSME (degrees)
LORBY (DEG)	Yaw Deflection of Lower Left SSME (degrees)
RORBP (DEG)	Pitch Deflection of Lower Right SSME (degrees)
RORBY (DEG)	Yaw Deflection of Lower Right SSME (degrees)
LSRBP (DEG)	Pitch Deflection of Left SRB Engine (degrees)
LSRBY (DEG)	Yaw Deflection of Left SRB Engine (degrees)
RSRBP (DEG)	Pitch Deflection of Right SRB Engine (degrees)
RSRBY (DEG)	Yaw Deflection of Right SRB Engine (degrees)

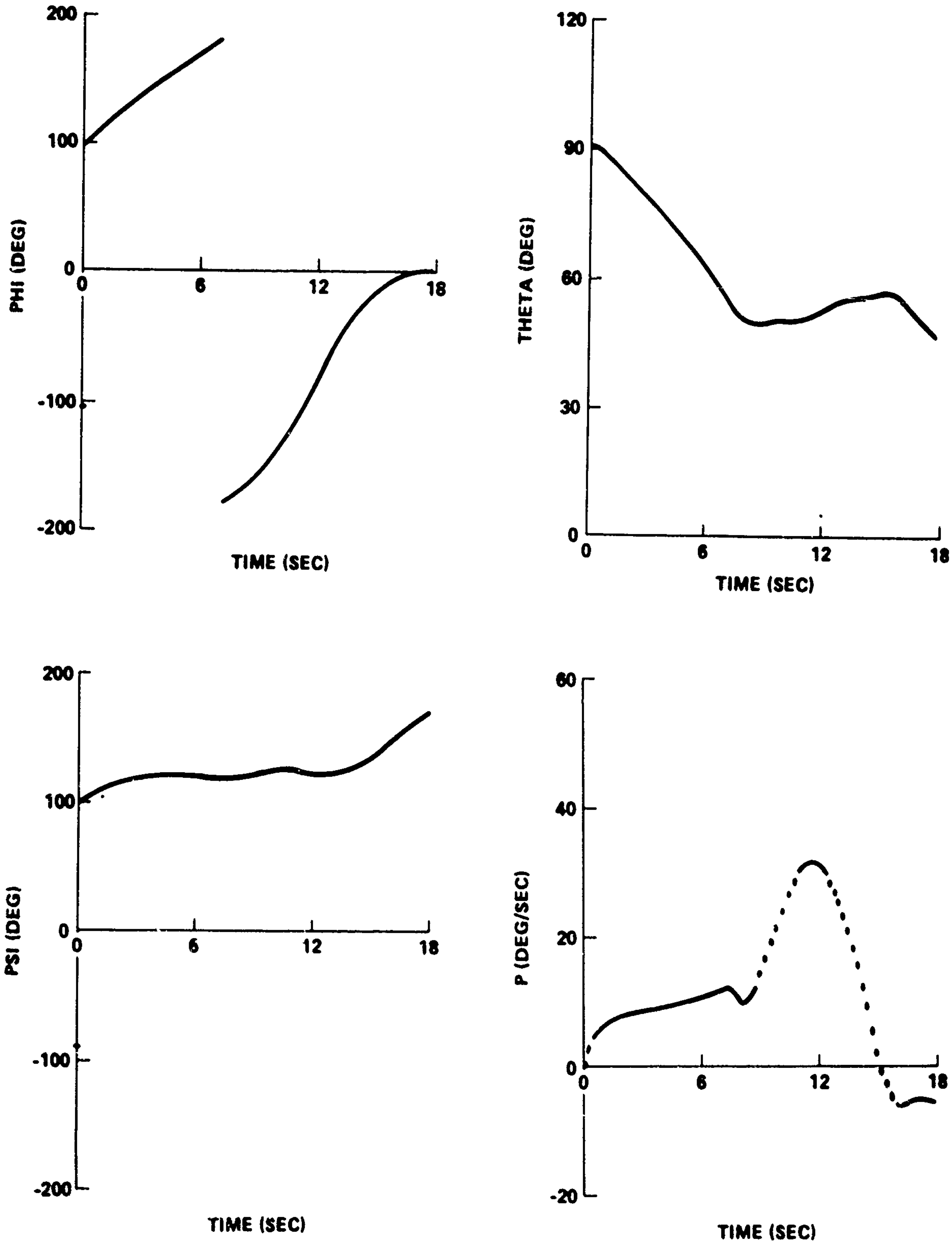

FIGURE B-2 ASCENT TRAJECTORY PARAMETERS FOR INTEGRATED VEHICLE WITH INADVERTENT RIGHT SRB SEPARATION AT LIFT-OFF

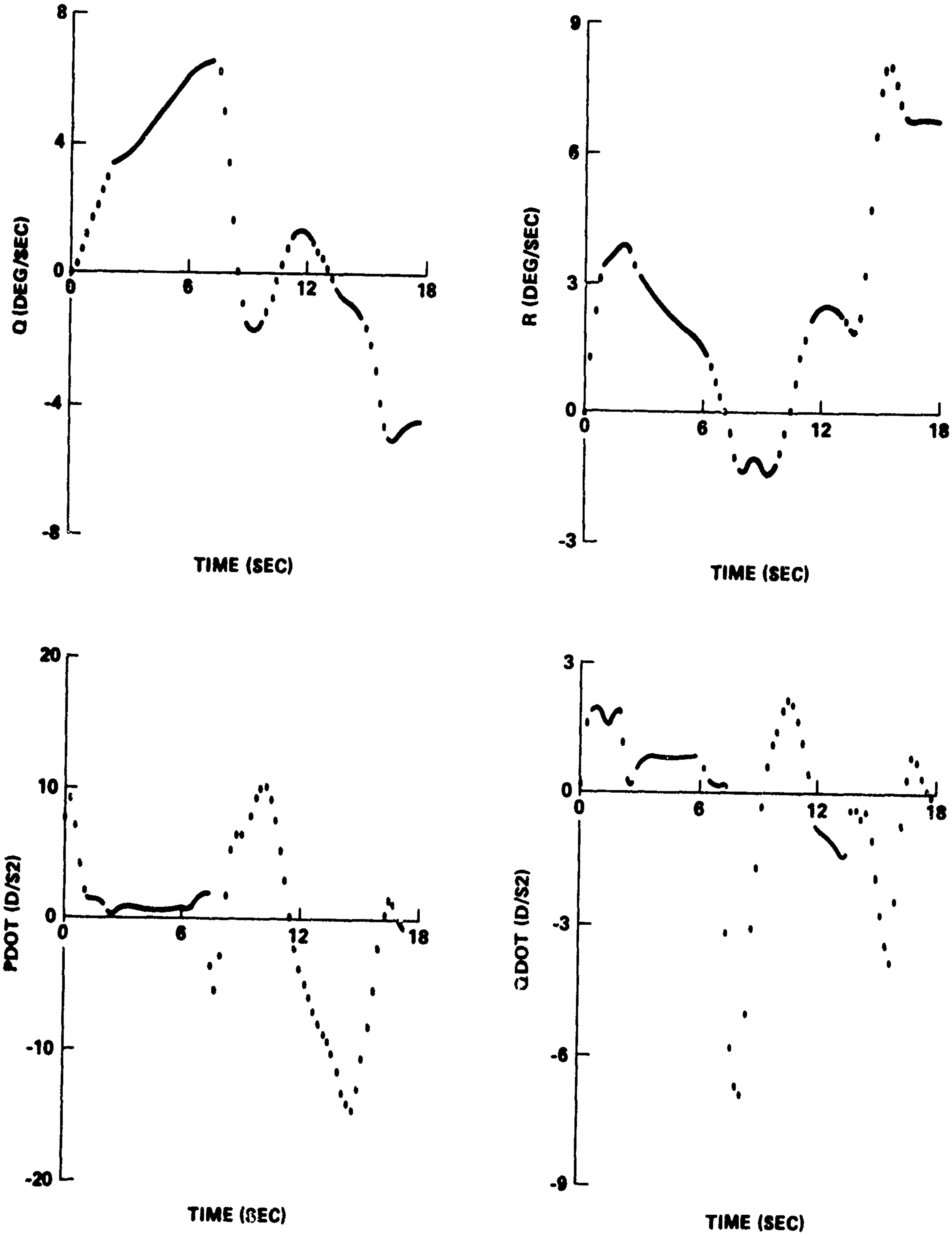

FIGURE B-3 ASCENT TRAJECTORY PARAMETERS FOR INTEGRATED VEHICLE WITH INADVERTENT RIGHT SRB SEPARATION AT LIFT-OFF

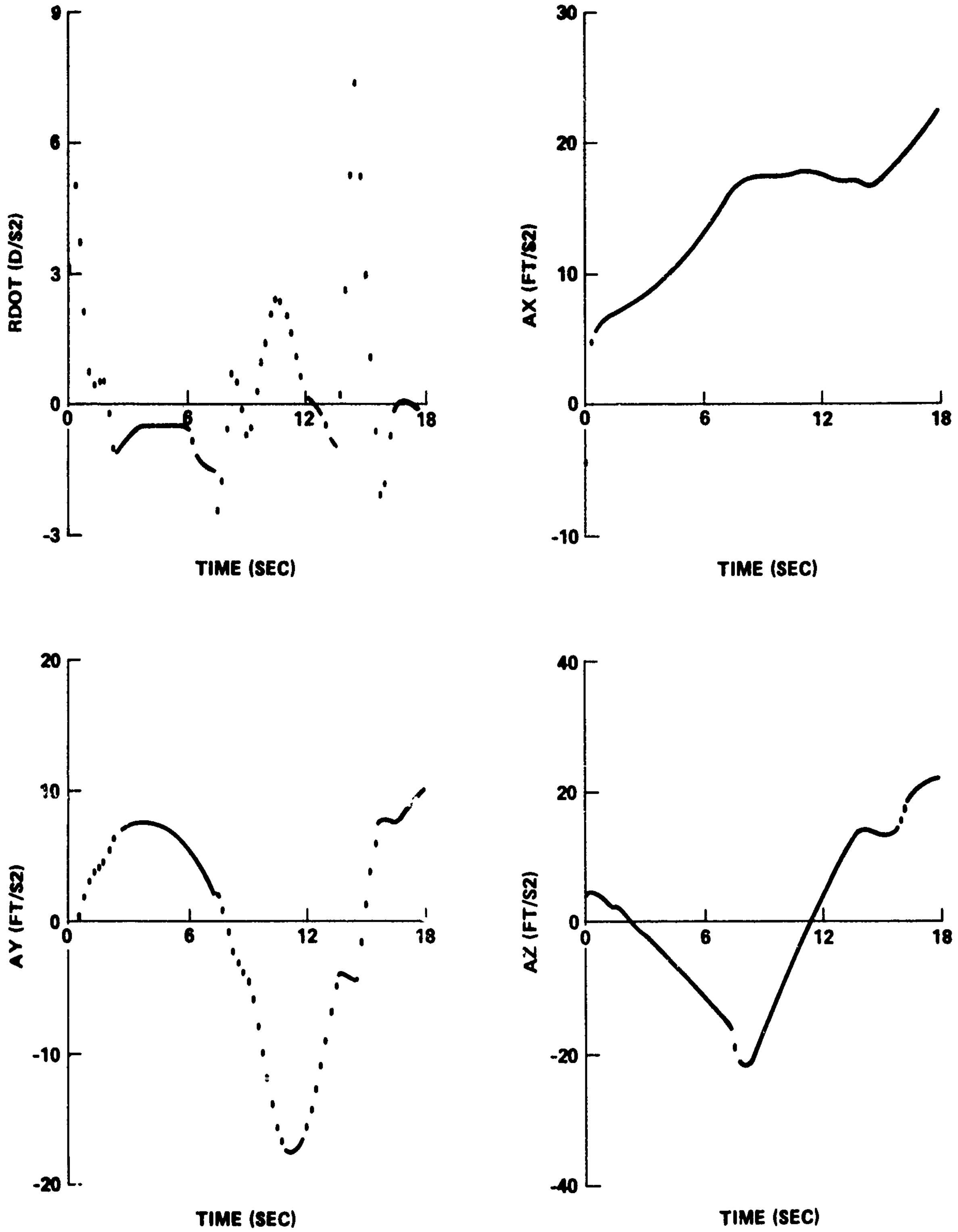

FIGURE B-4 ASCENT TRAJECTORY PARAMETERS FOR INTEGRATED VEHICLE WITH INADVERTENT RIGHT SRB SEPARATION AT LIFT-OFF

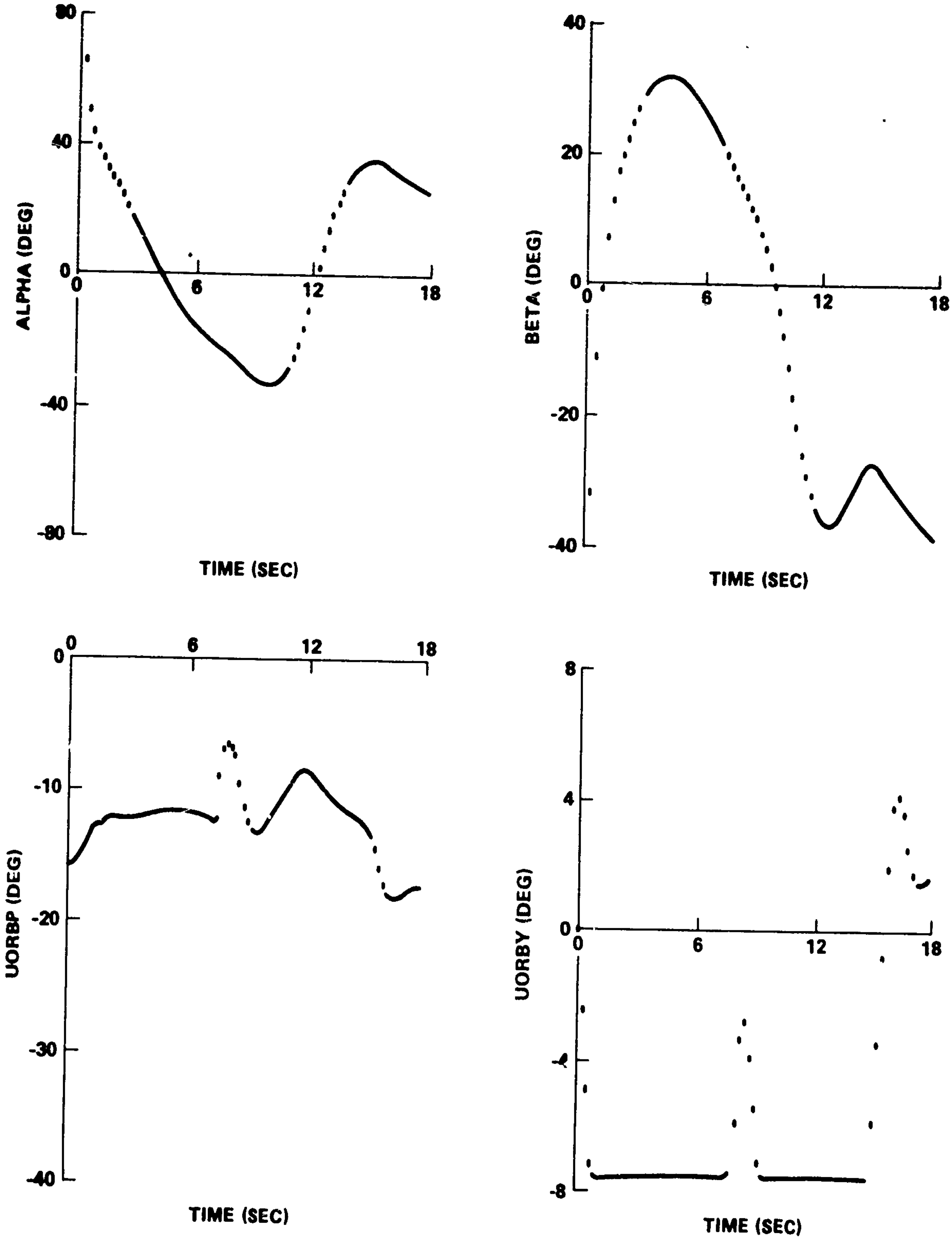

FIGURE B-5 ASCENT TRAJECTORY PARAMETERS FOR INTEGRATED VEHICLE WITH INADVERTENT RIGHT SRB SEPARATION AT LIFT-OFF

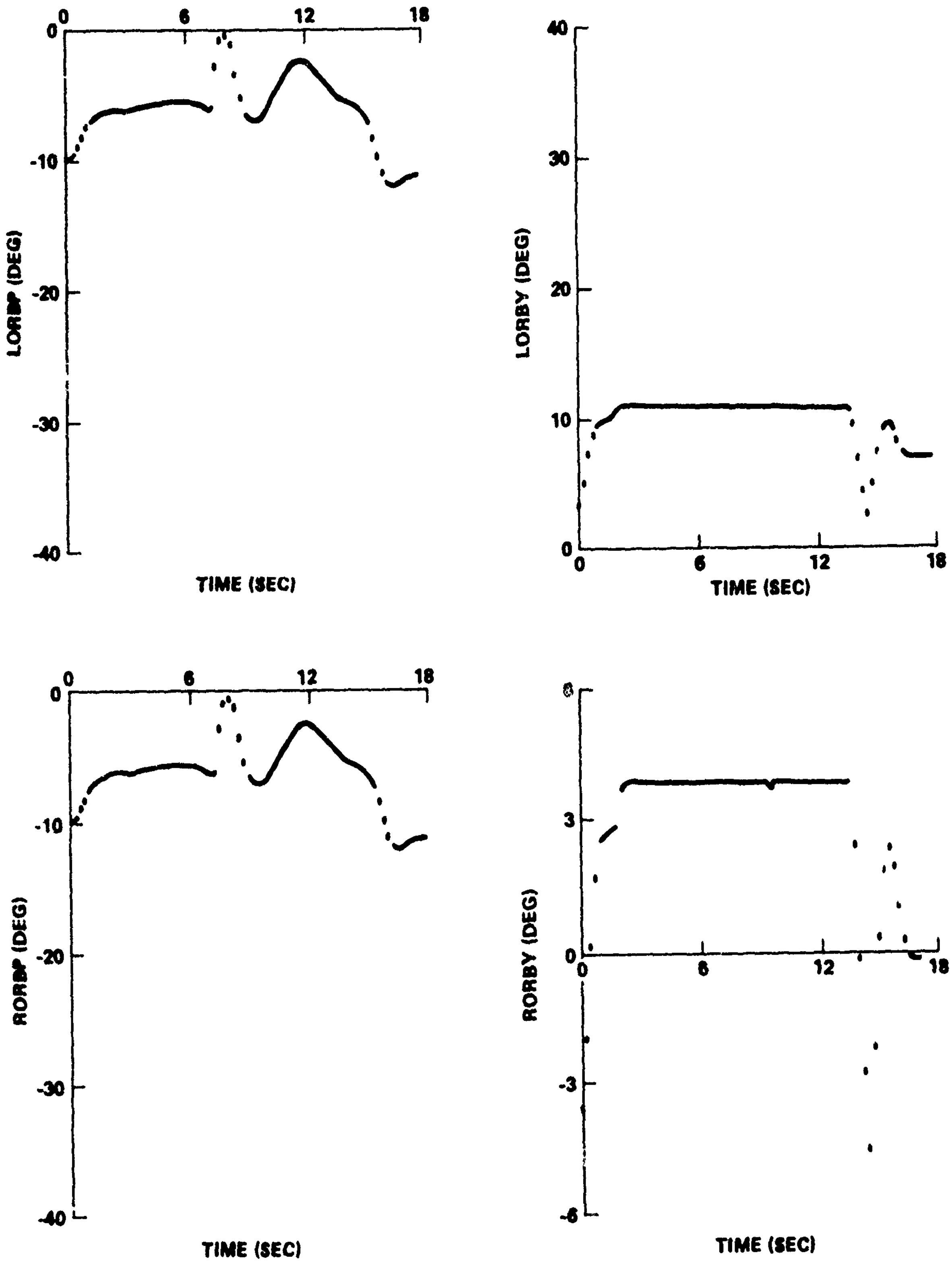

FIGURE B-6   ASCENT TRAJECTORY PARAMETERS FOR INTEGRATED VEHICLE WITH INADVERTENT RIGHT SRB SEPARATION AT LIFT-OFF

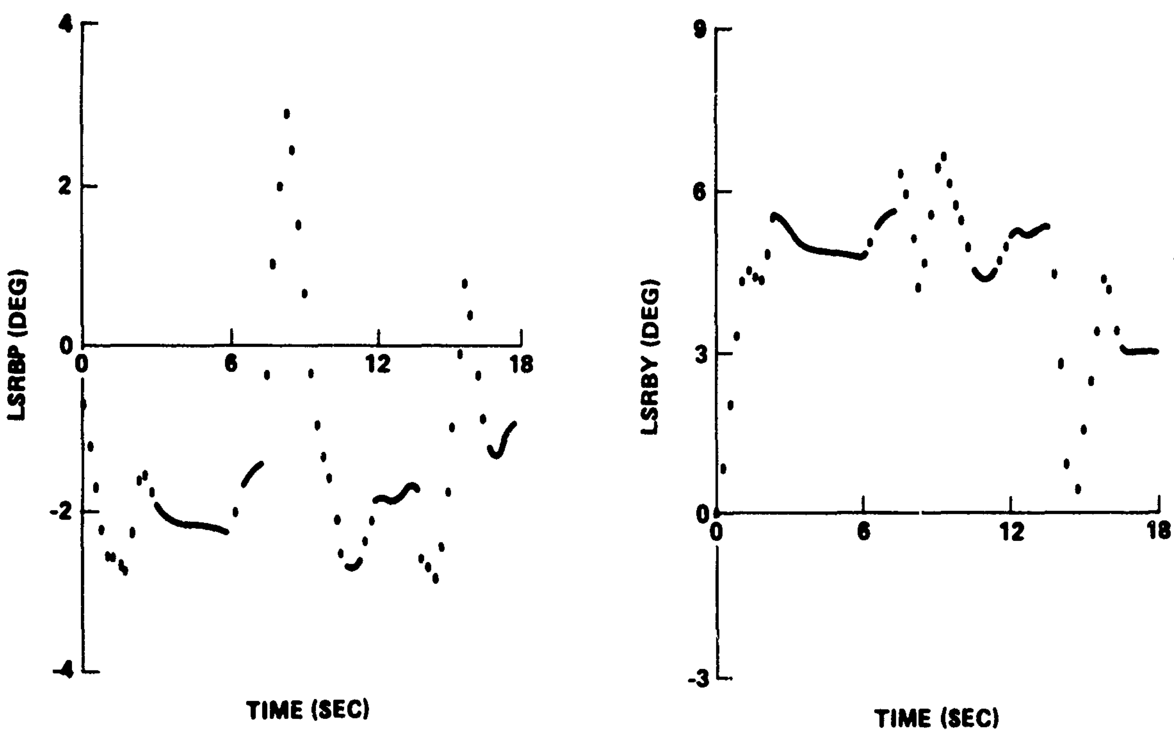

FIGURE B-7 ASCENT TRAJECTORY PARAMETERS FOR INTEGRATED VEHICLE WITH INADVERTENT RIGHT SRB SEPARATION AT LIFT-OFF

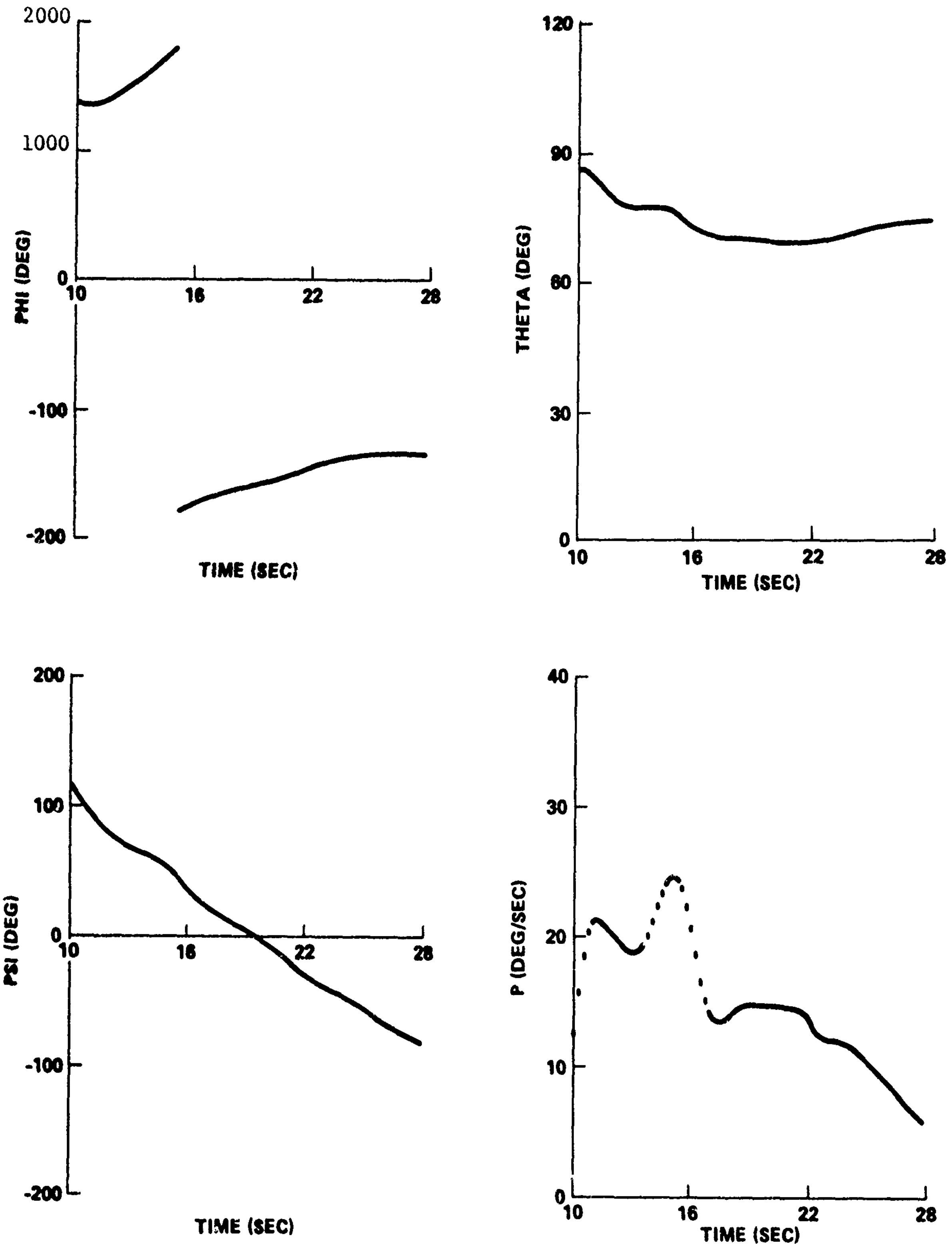

FIGURE B-8 ASCENT TRAJECTORY PARAMETERS FOR INTEGRATED VEHICLE WITH INADVERTENT RIGHT SRB SEPARATION 10 SECONDS AFTER LIFT-OFF

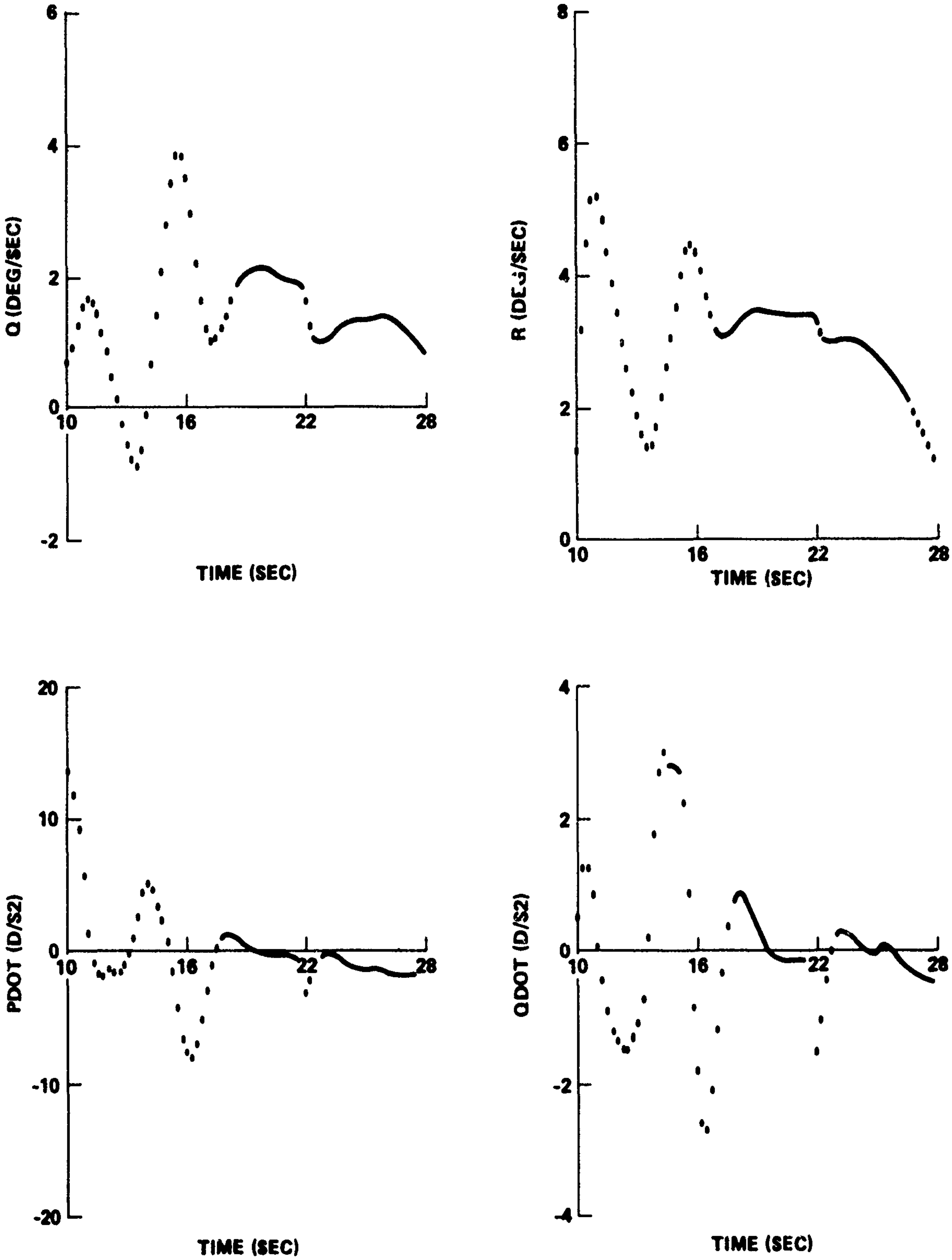

FIGURE B-9 ASCENT TRAJECTORY PARAMETERS FOR INTEGRATED VEHICLE WITH INADVERTENT RIGHT SRB SEPARATION 10 SECONDS AFTER LIFT-OFF

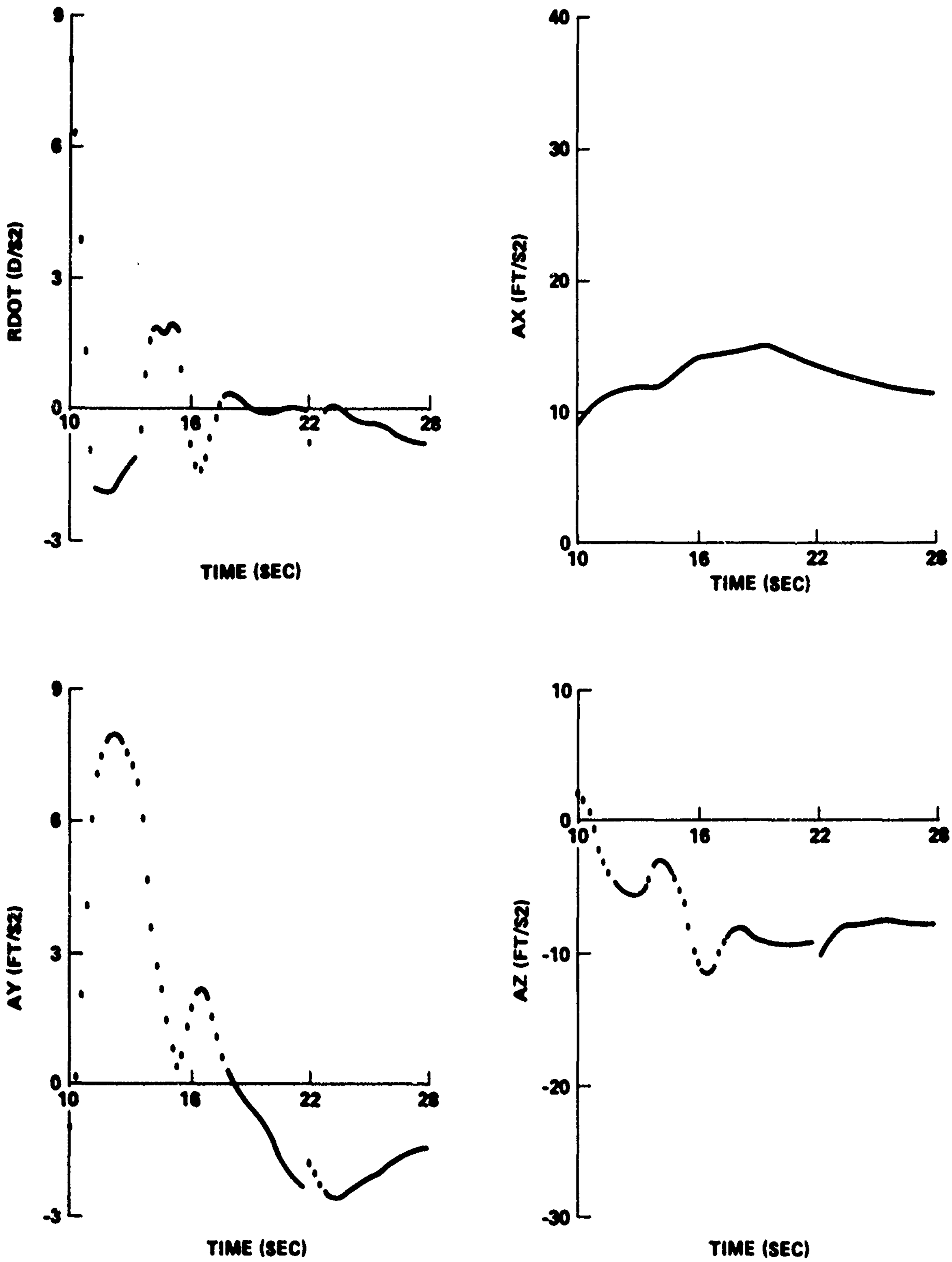

FIGURE B-10 ASCENT TRAJECTORY PARAMETERS FOR INTEGRATED VEHICLE WITH INADVERTENT RIGHT SRB SEPARATION 10 SECONDS AFTER LIFT-OFF

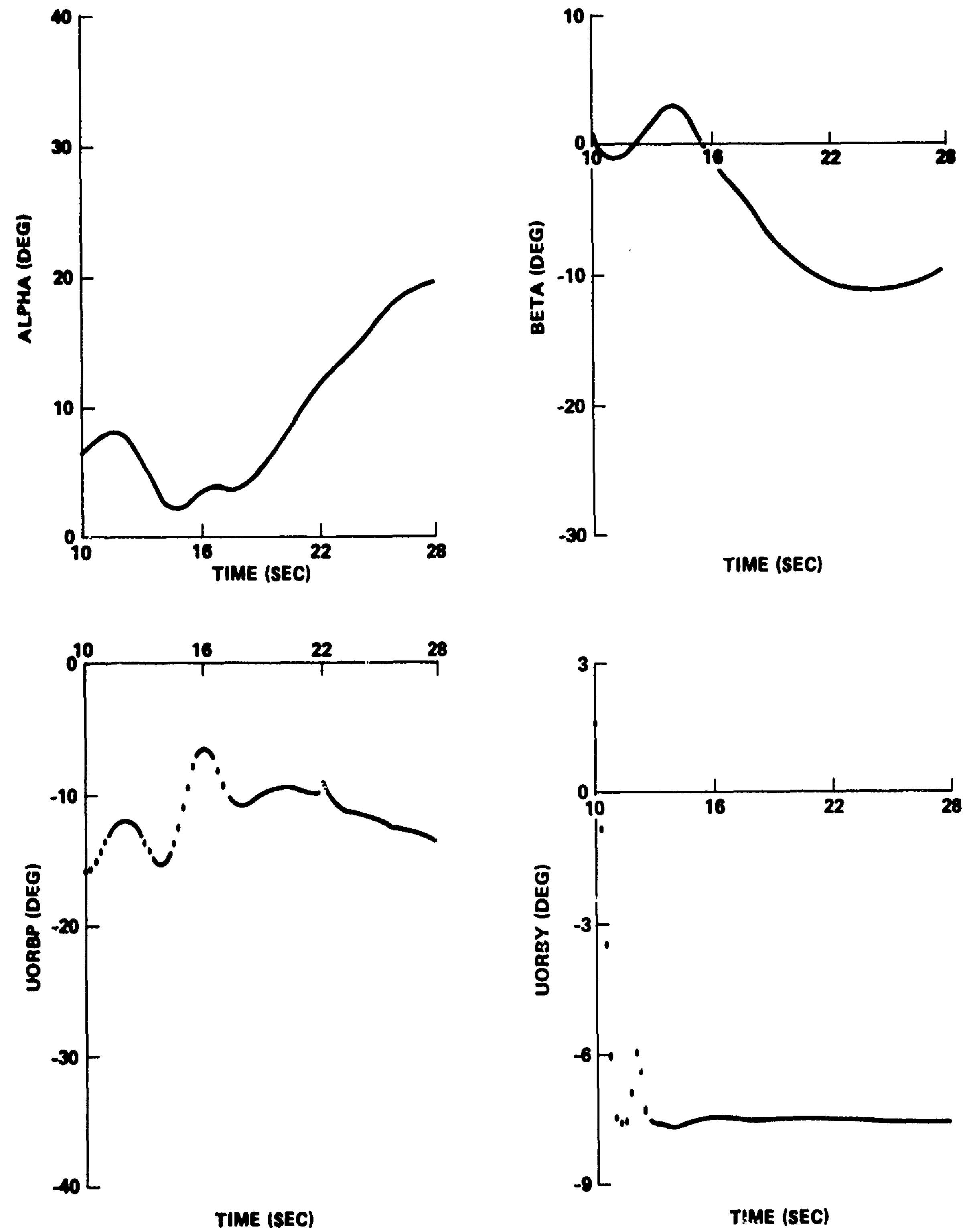

FIGURE B-11 ASCENT TRAJECTORY PARAMETERS FOR INTEGRATED VEHICLE WITH INADVERTENT RIGHT SRB SEPARATION 10 SECONDS AFTER LIFT-OFF

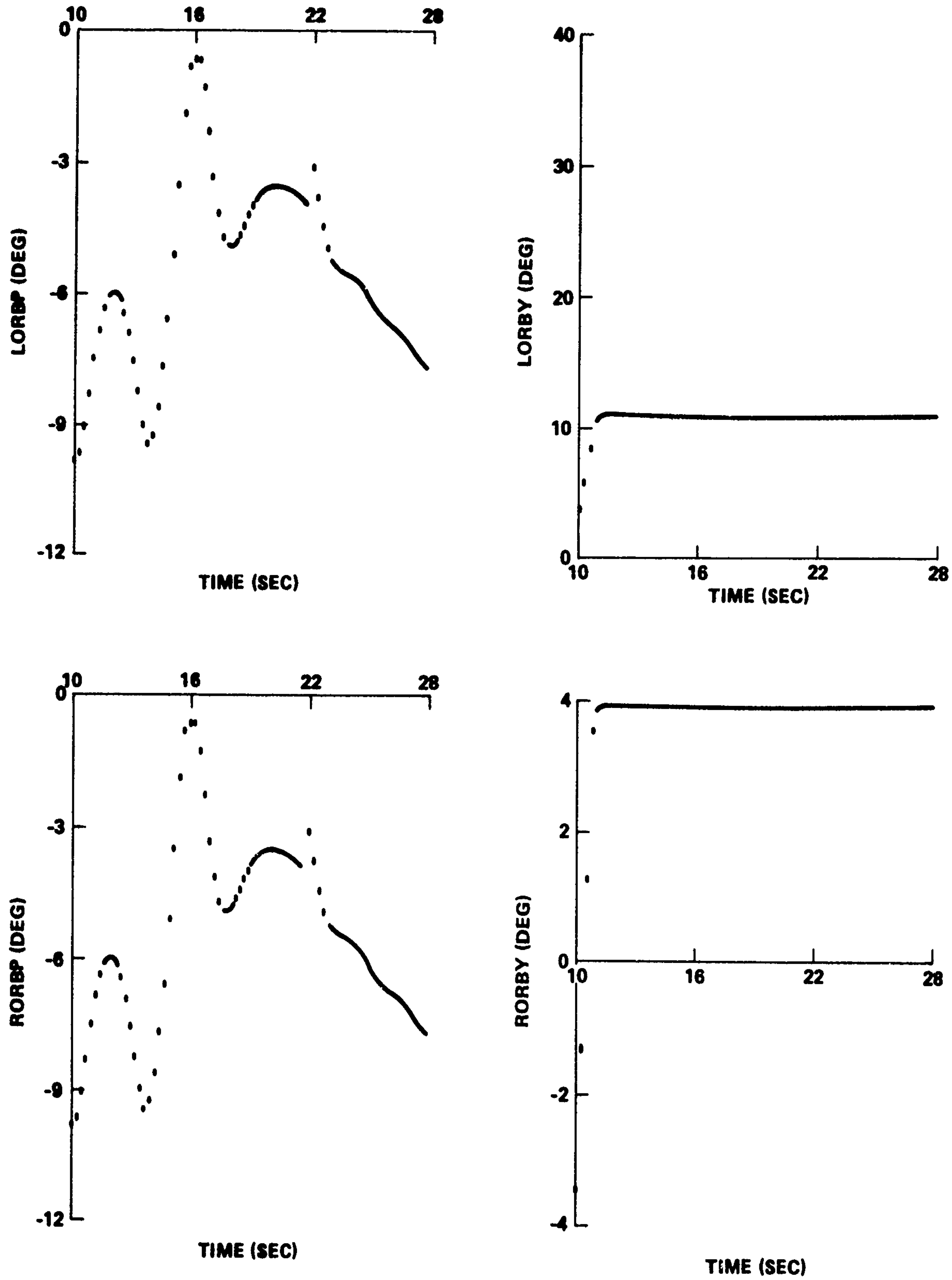

FIGURE B-12 ASCENT TRAJECTORY PARAMETERS FOR INTEGRATED VEHICLE WITH INADVERTENT RIGHT SRB SEPARATION 10 SECONDS AFTER LIFT-OFF

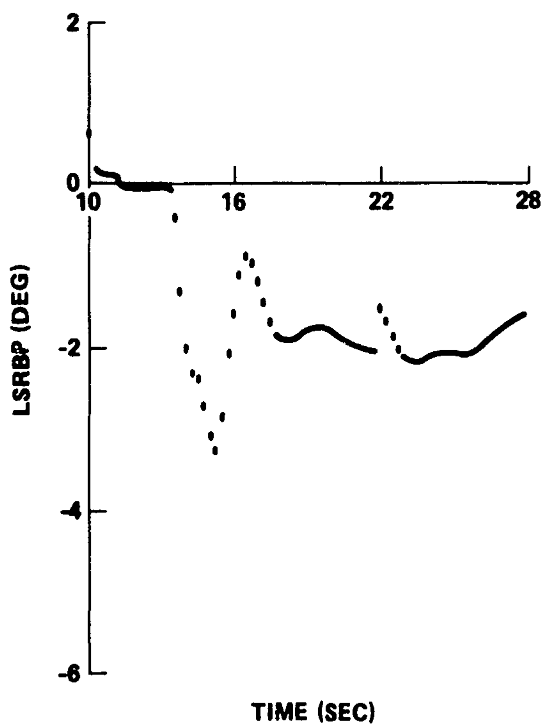

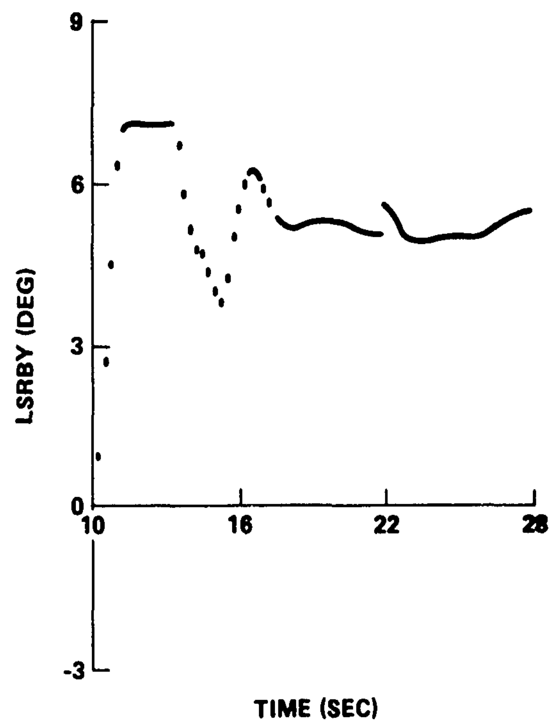

FIGURE B-13 ASCENT TRAJECTORY PARAMETERS FOR INTEGRATED VEHICLE WITH INADVERTENT RIGHT SRB SEPARATION 10 SECONDS AFTER LIFT-OFF

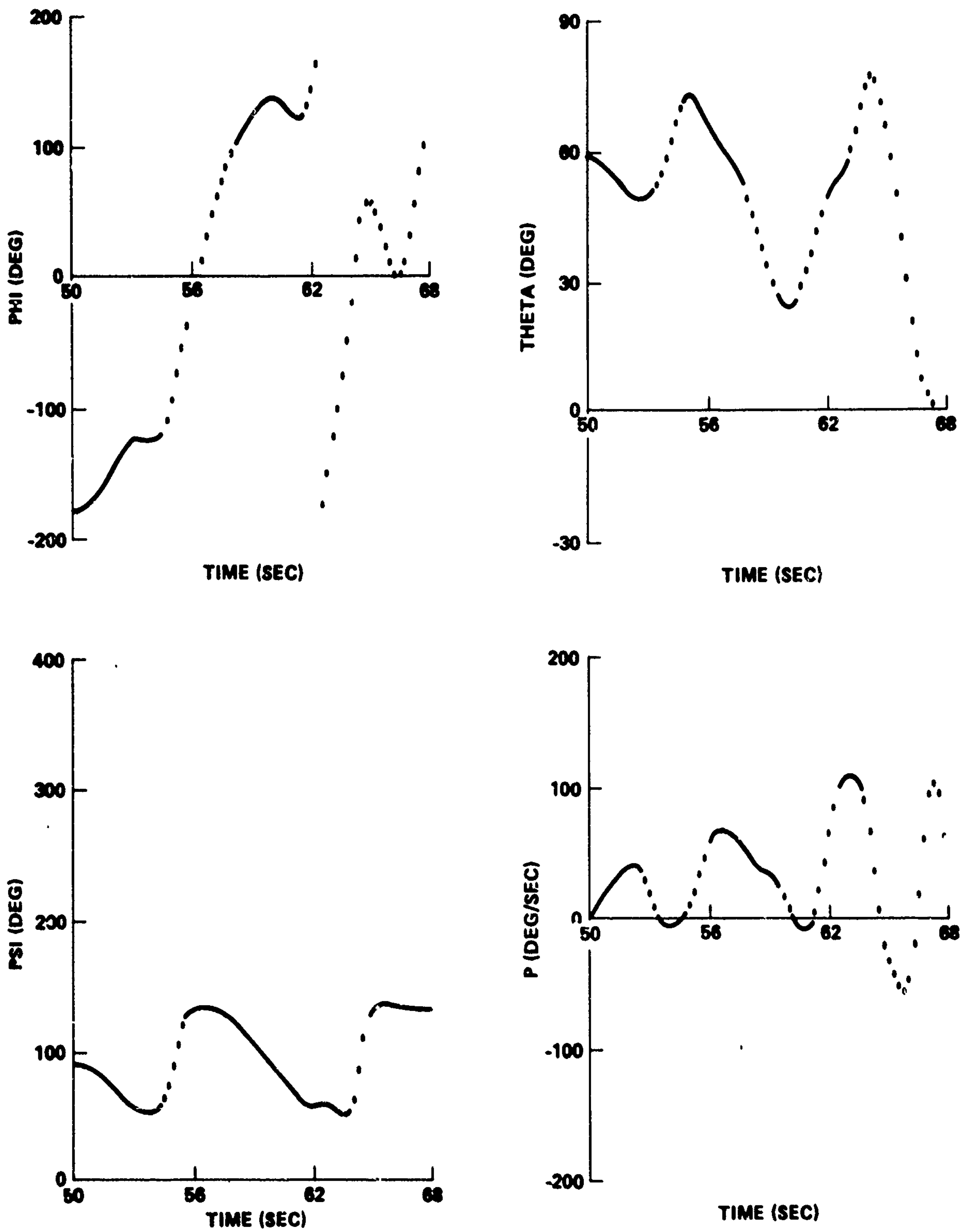

FIGURE B-14 ASCENT TRAJECTORY PARAMETERS FOR INTEGRATED VEHICLE WITH INADVERTENT RIGHT SRB SEPARATION 50 SECONDS AFTER LIFT-OFF

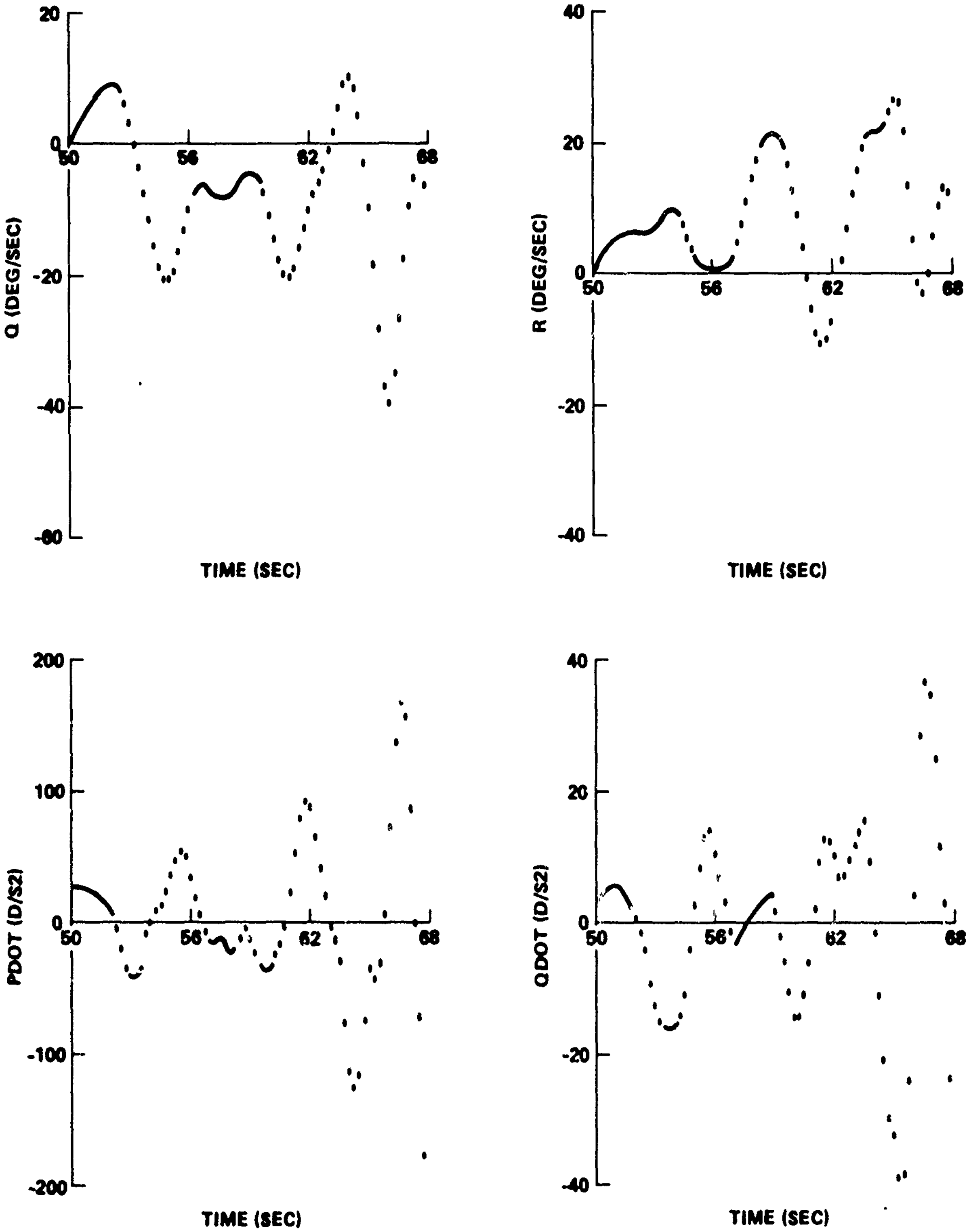

FIGURE B-15 ASCENT TRAJECTORY PARAMETERS FOR INTEGRATED VEHICLE WITH INADVERTENT RIGHT SRB SEPARATION 50 SECONDS AFTER LIFT-OFF

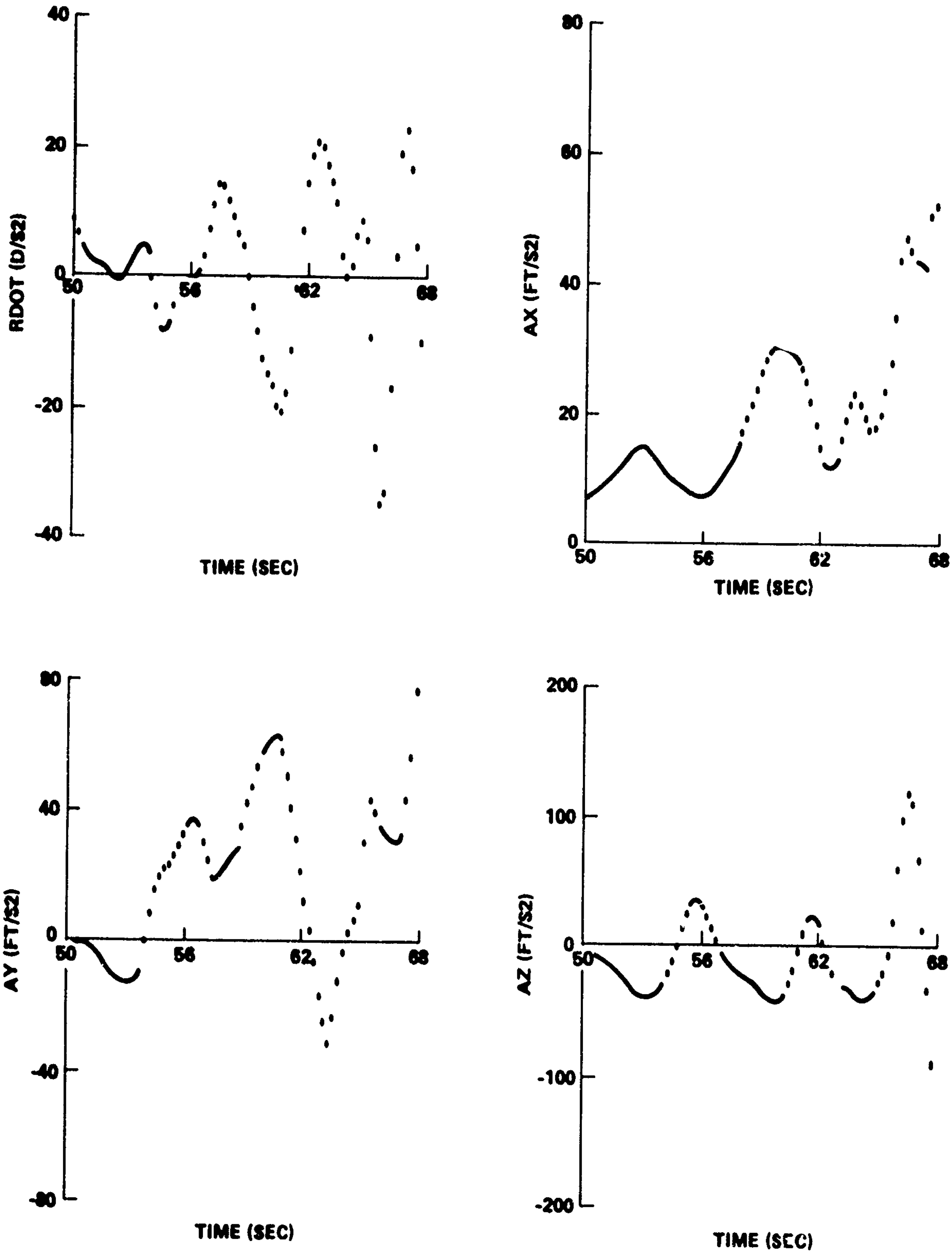

FIGURE B-16 ASCENT TRAJECTORY PARAMETEPS FOR INTEGRATED VEHICLE WITH INADVERTENT RIGHT SRB SEPARATION 50 SECONDS AFTER LIFT-OFF

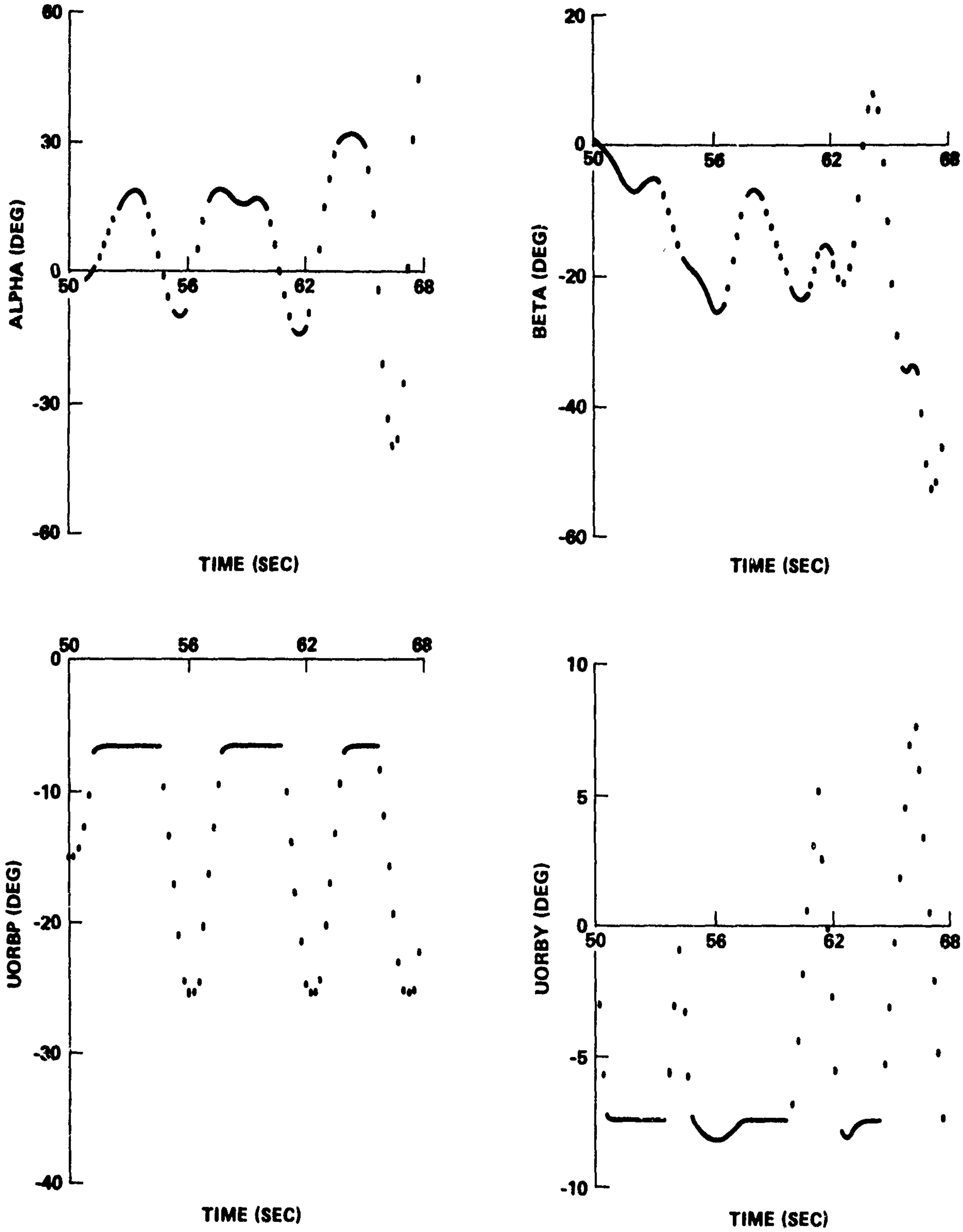

FIGURE B-17 ASCENT TRAJECTOR. PARAMETERS FOR INTEGRATED VEHICLE WITH INADVERTENT RIGHT SRB SEPARATION 50 SECONDS AFTER LIFT-OFF

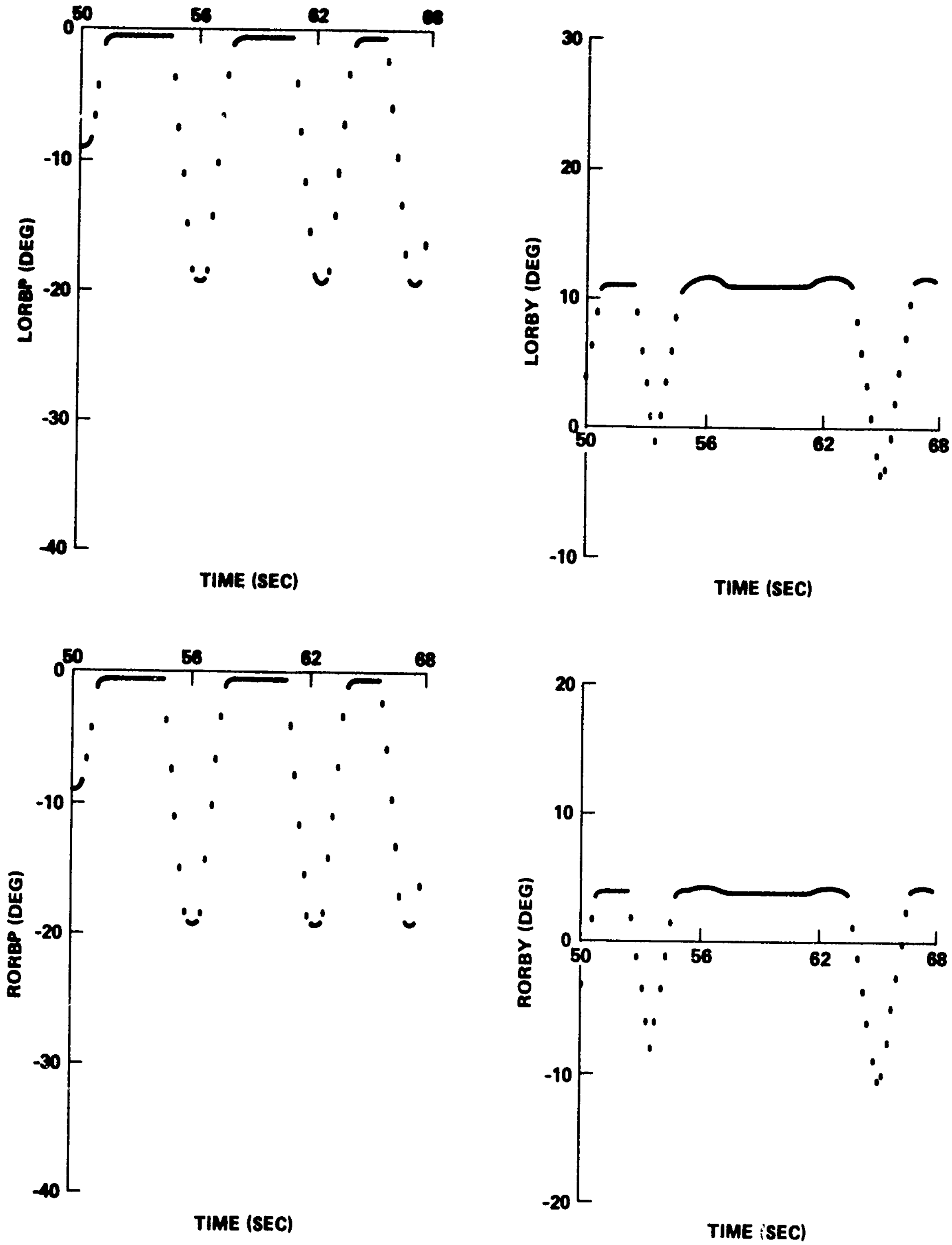

FIGURE B-18 ASCENT TRAJECTORY PARAMETERS FOR INTEGRATED VEHICLE WITH INADVERTENT RIGHT SRB SEPARATION 50 SECONDS AFTER LIFT-OFF

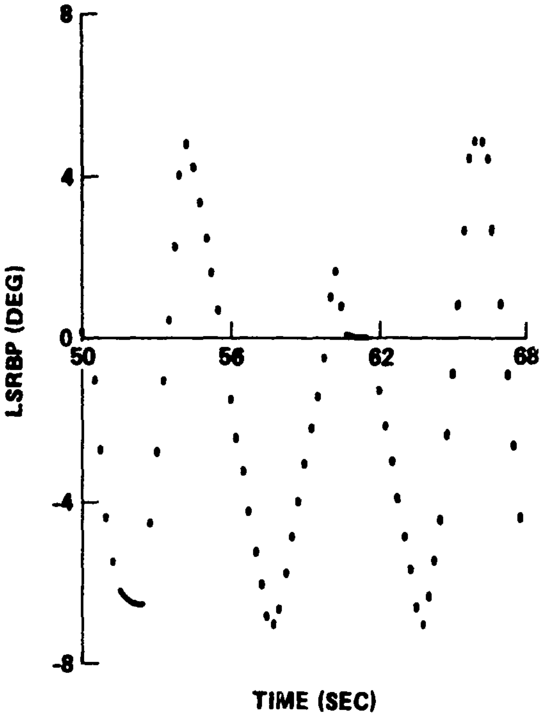

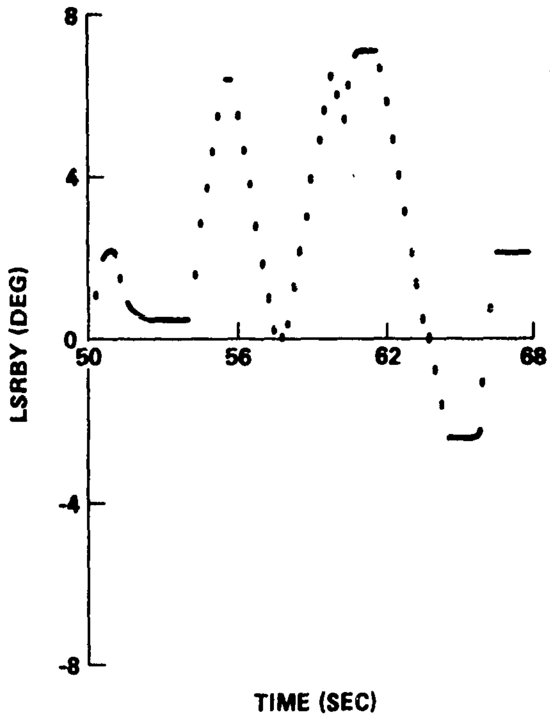

FIGURE B-19 ASCENT TRAJECTORY PARAMETERS FOR INTEGRATED VEHICLE WITH INADVERTENT RIGHT SRB SEPARATION 50 SECONDS AFTER LIFT-OFF

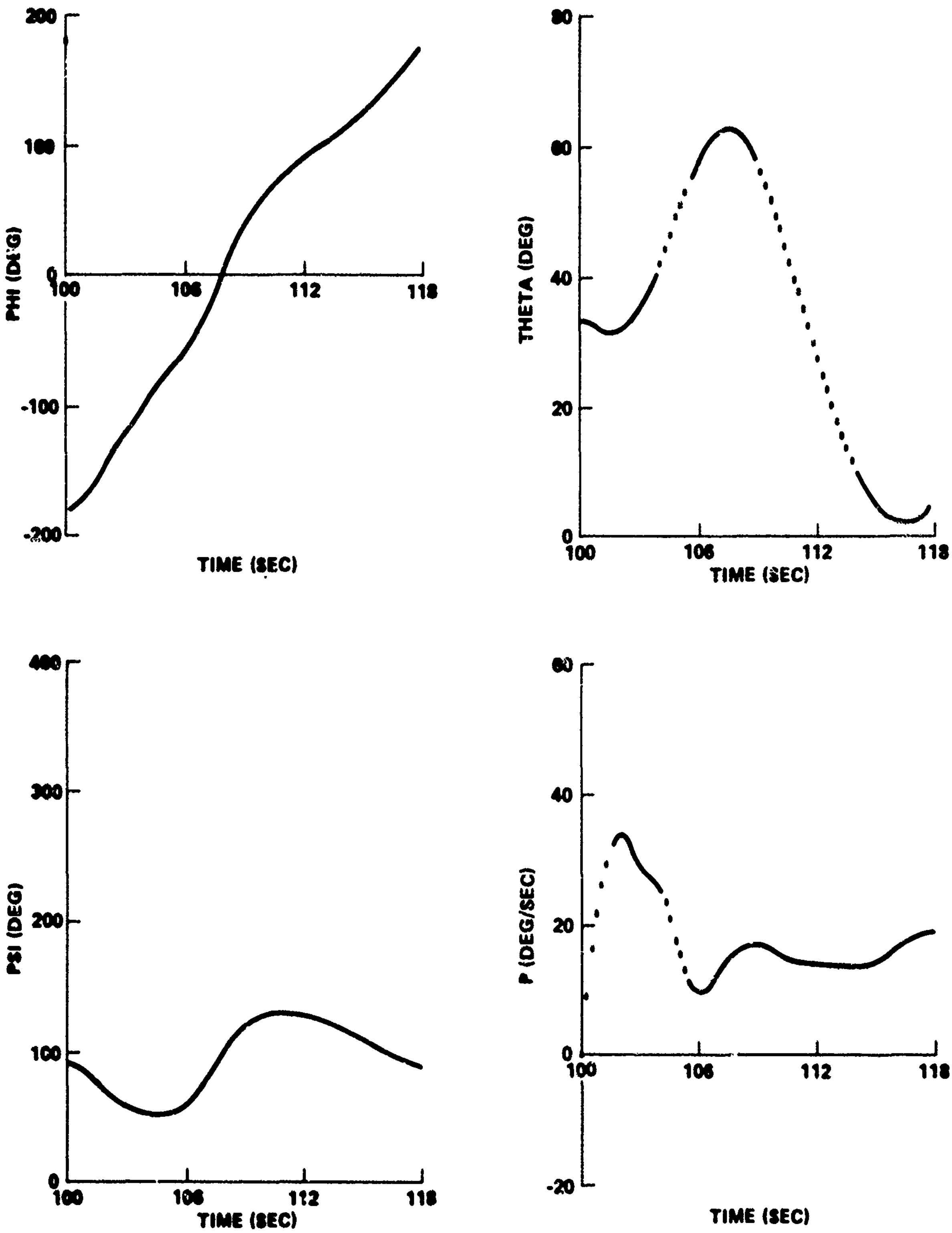

FIGURE B-20 ASCENT TRAJECTORY PARAMETERS FOR INTEGRATED VEHICLE WITH INADVERTENT RIGHT SRB SEPARATION 100 SECONDS AFTER LIFT-OFF

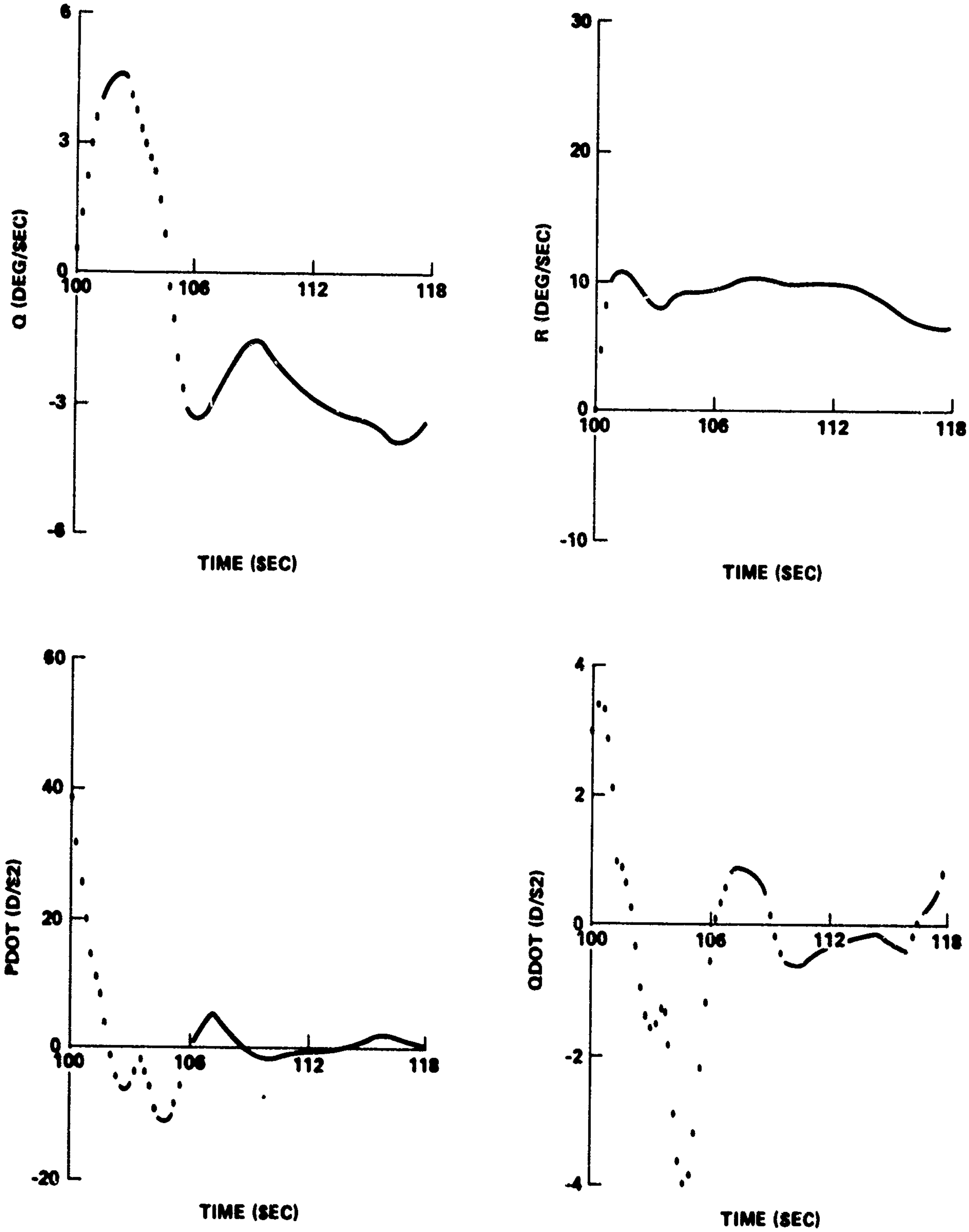

FIGURE B-21 ASCENT TRAJECTORY PARAMETERS FOR INTEGRATED VEHICLE WITH INADVERTENT RIGHT SRB SEPARATION 100 SECONDS AFTER LIFT-OFF

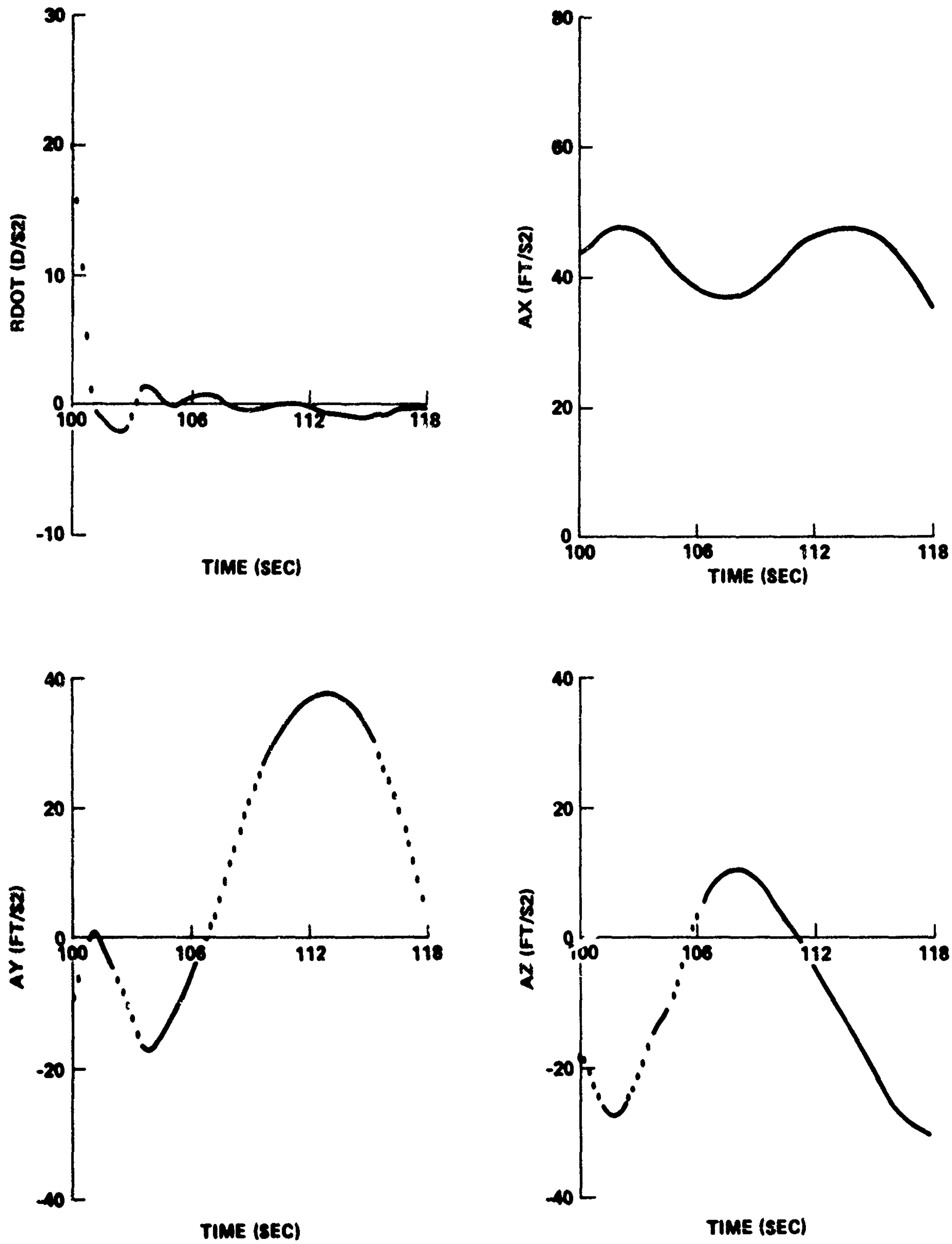

FIGURE B-22 ASCENT TRAJECTORY PARAMETERS FOR INTEGRATED VEHICLE WITH INADVERTENT RIGHT SRB SEPARATION 100 SECONDS AFTER LIFT-OFF

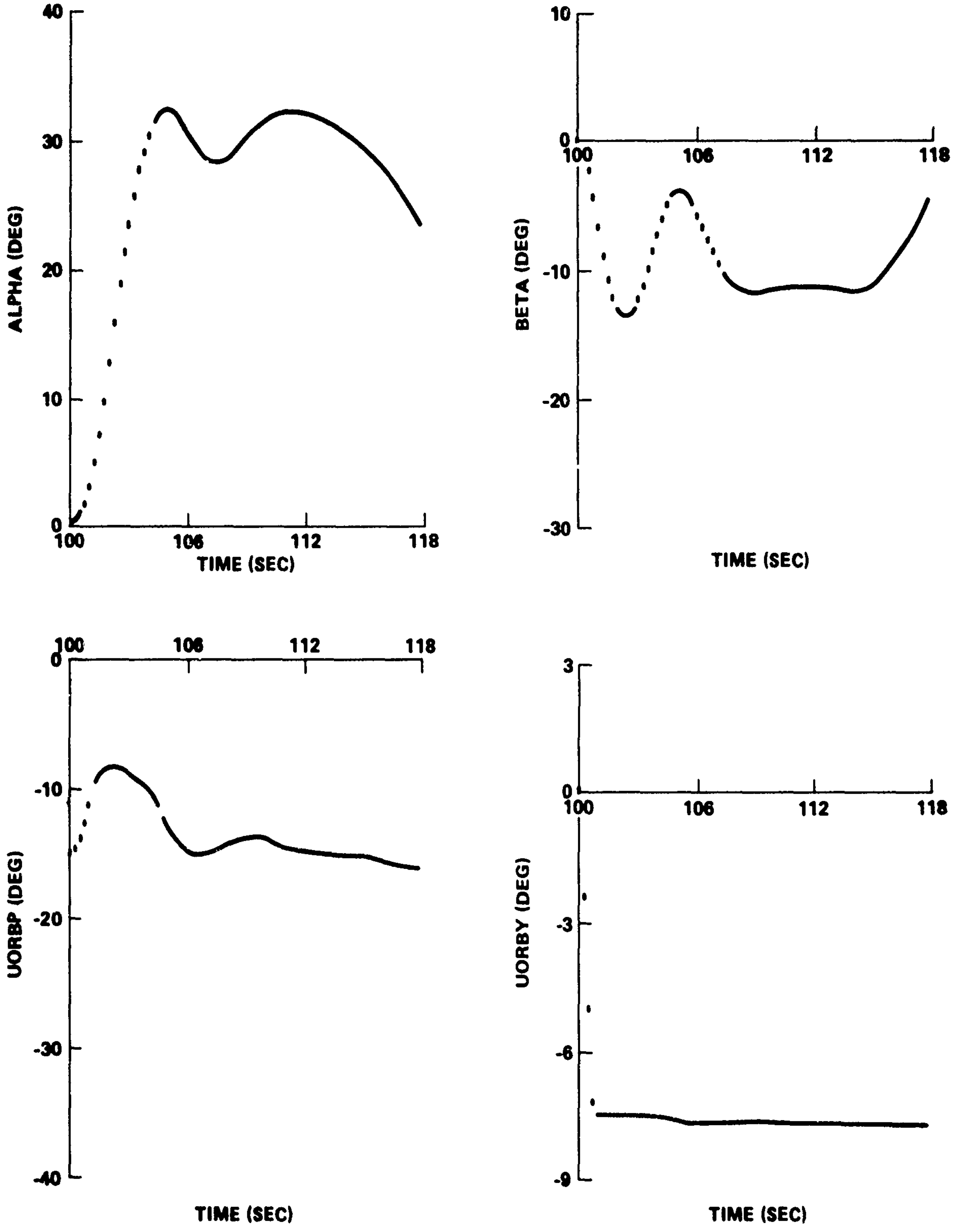

FIGURE B-23 ASCENT TRAJECTORY PARAMETERS FOR INTEGRATED VEHICLE WITH INADVERTENT RIGHT SRB SEPARATION 100 SECONDS AFTER LIFT-OFF

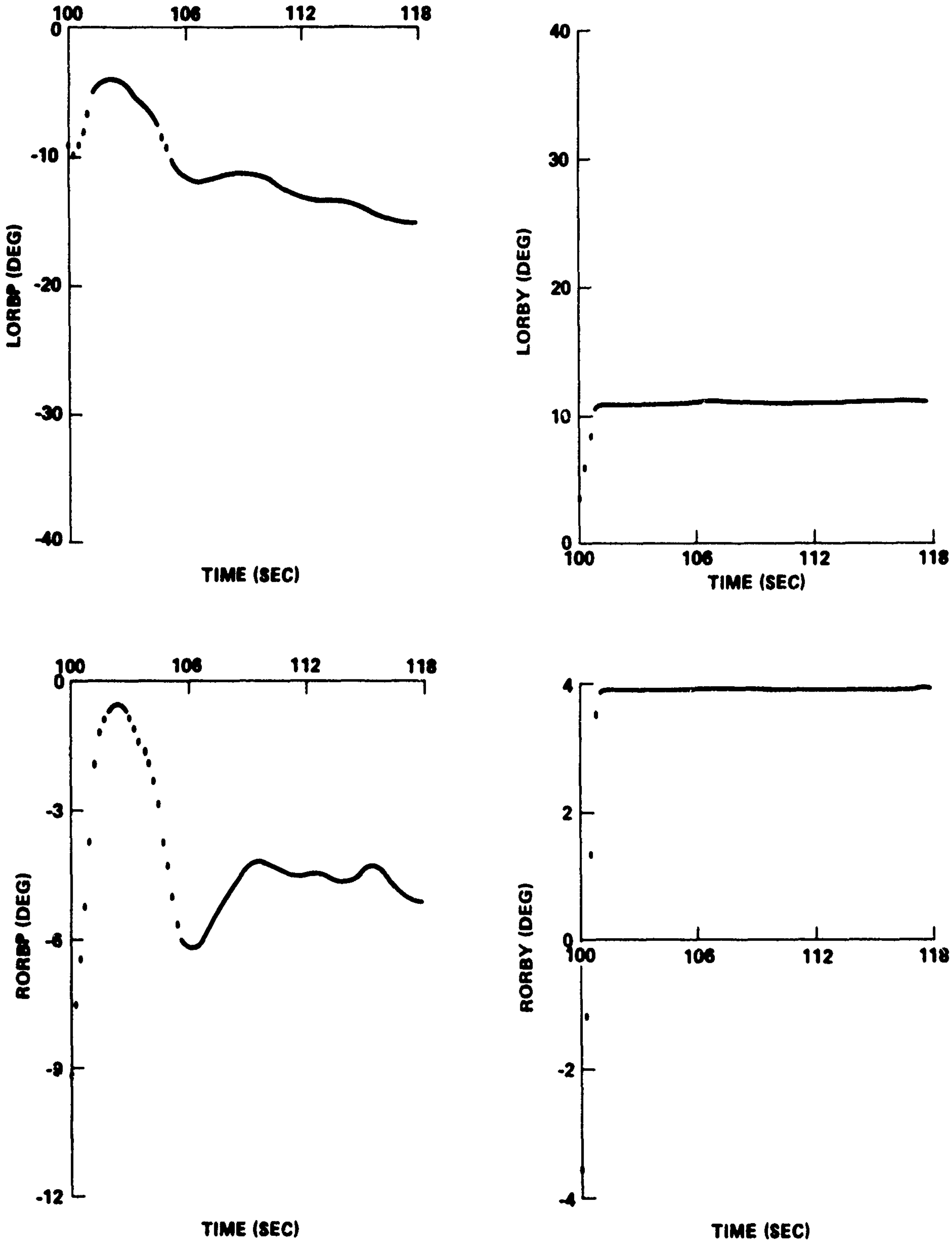

FIGURE B-24 ASCENT TRAJECTORY PARAMETERS FOR INTEGRATED VEHICLE WITH INADVERTENT RIGHT SRB SEPARATION 100 SECONDS AFTER LIFT-OFF

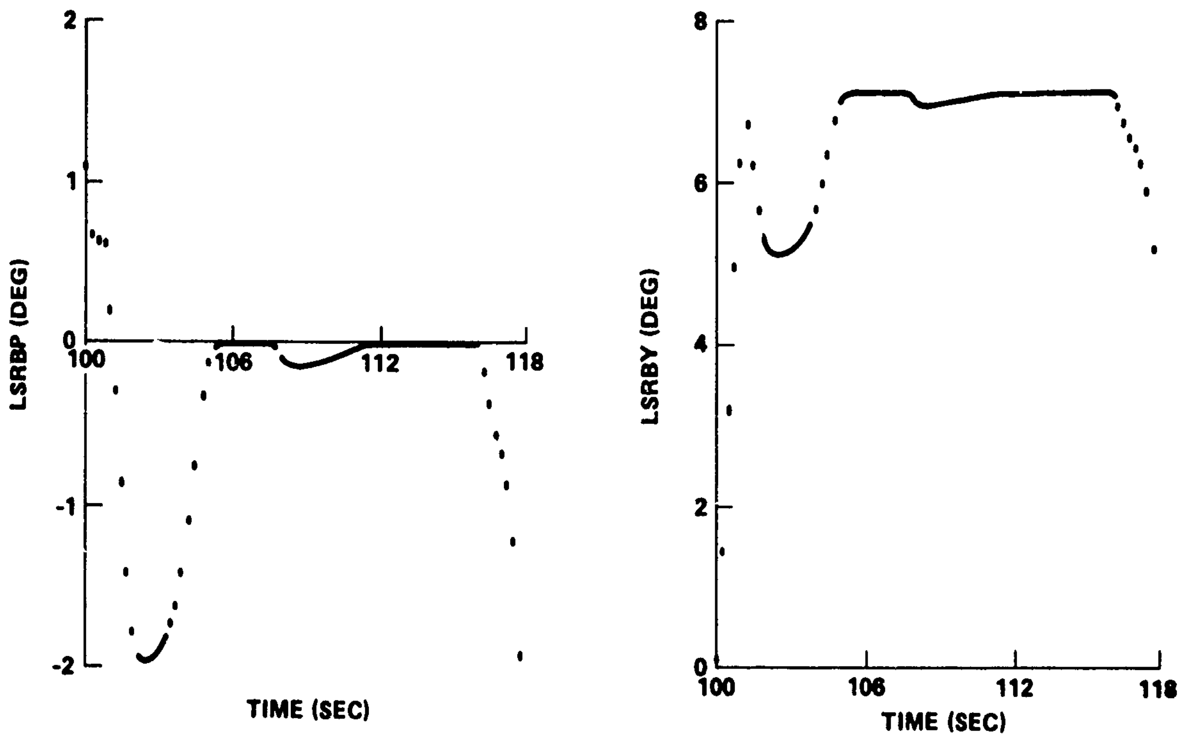

FIGURE B-25 ASCENT TRAJECTORY PARAMETERS FOR INTEGRATED VEHICLE WITH INADVERTENT RIGHT SRB SEPARATION 100 SECONDS AFTER LIFT-OFF

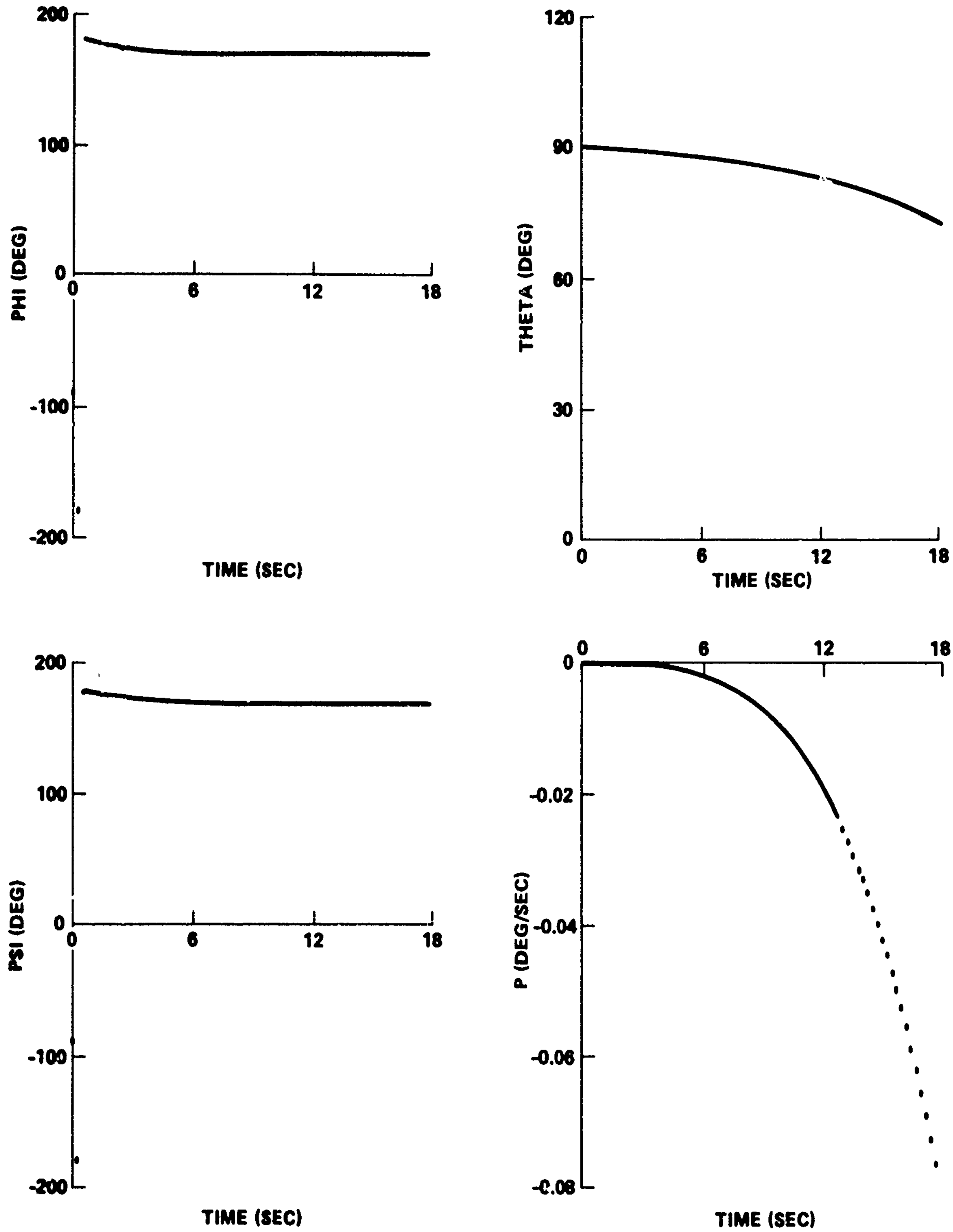

FIGURE B-26 ASCENT TRAJECTORY PARAMETERS FOR INTEGRATED VEHICLE WITH INADVERTENT ORBITER SEPARATION AT LIFT-OFF

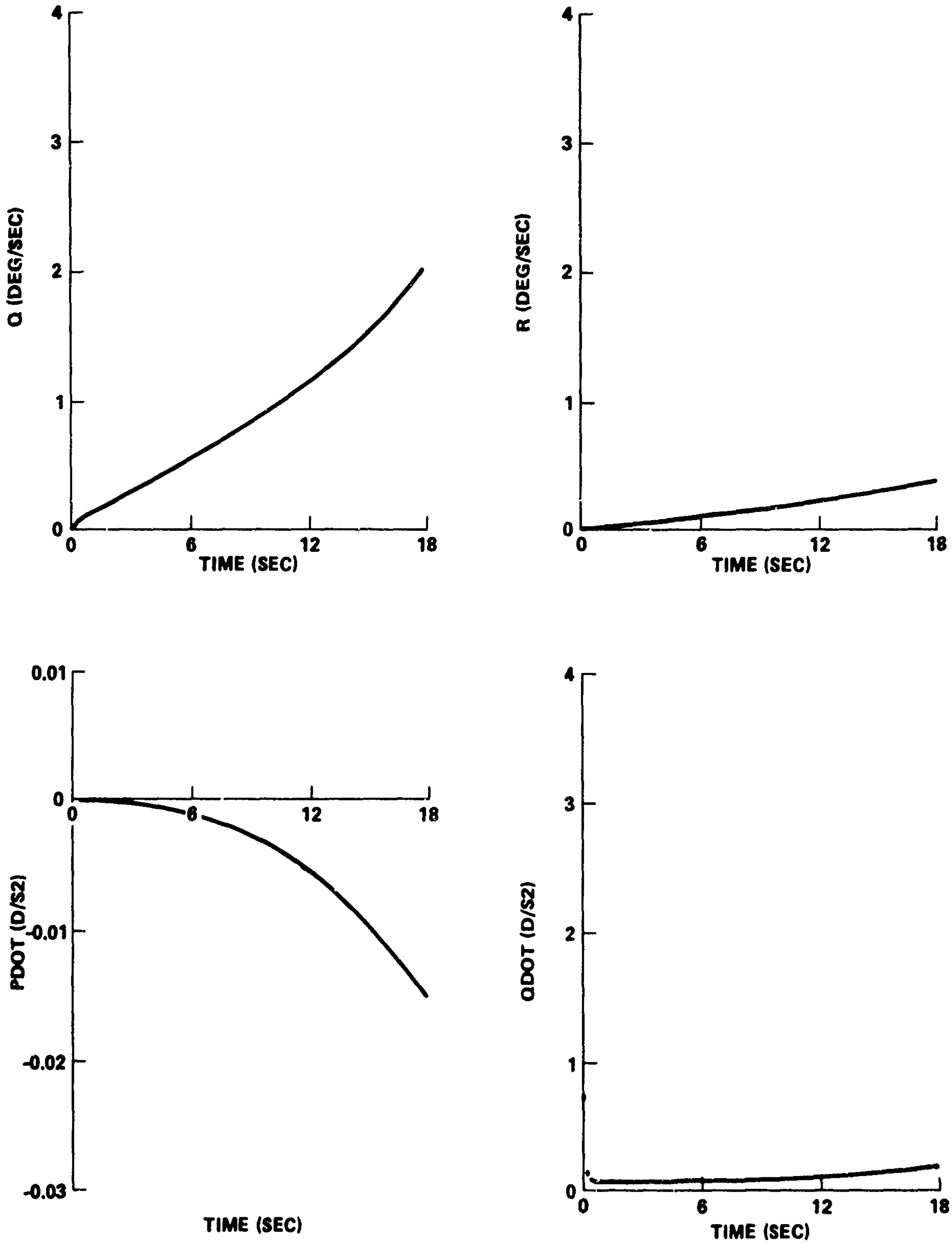

FIGURE B-27 ASCENT TRAJECTORY PARAMETERS FOR INTEGRATED VEHICLE WITH INADVERTENT ORBITER SEPARATION AT LIFT-OFF

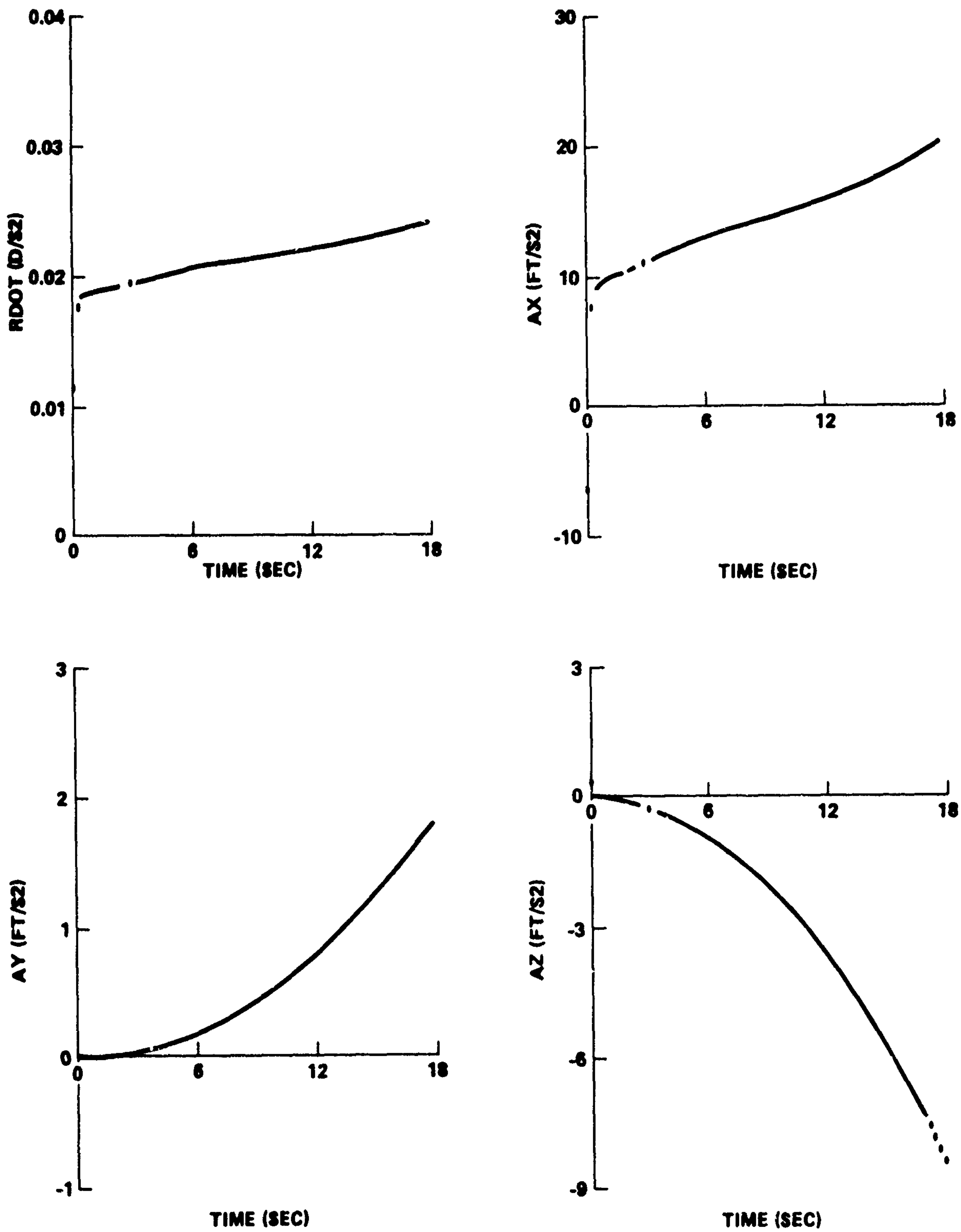

FIGURE B-28 ASCENT TRAJECTORY PARAMETERS FOR INTEGRATED VEHICLE WITH INADVERTENT ORBITER SEPARATION AT LIFT-OFF

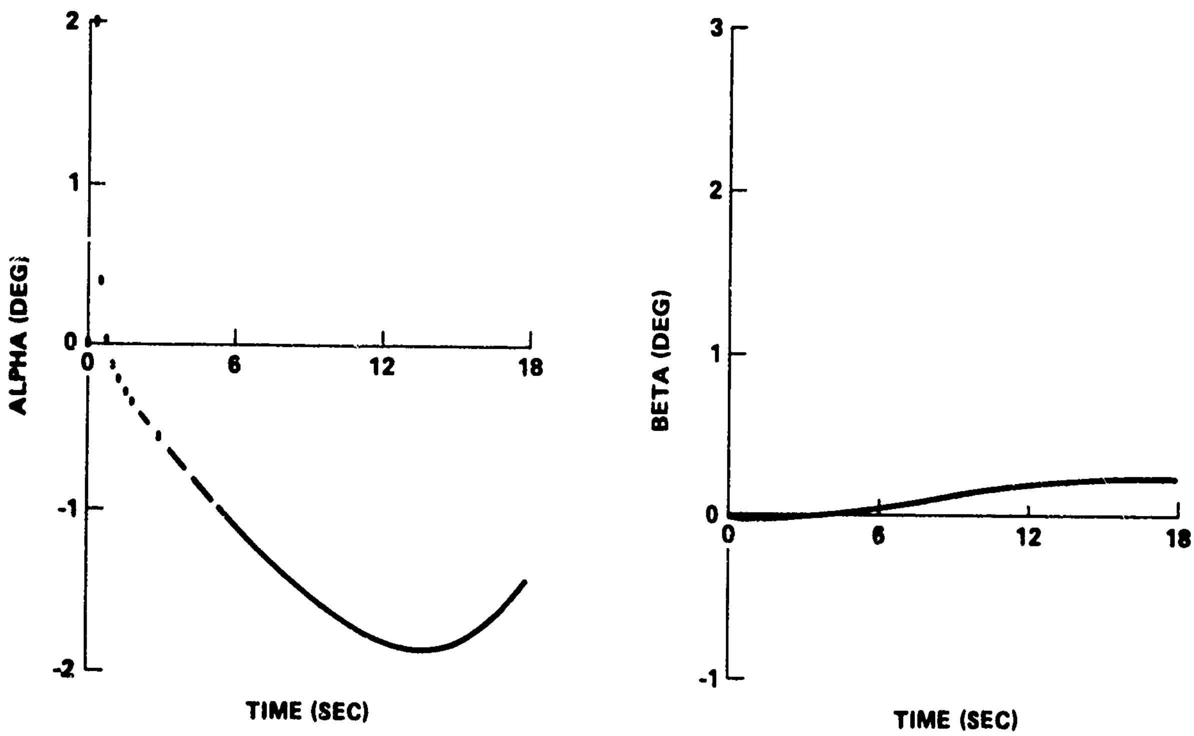

FIGURE B-29 ASCENT TRAJECTORY PARAMETERS FOR INTEGRATED VEHICLE WITH INADVERTENT ORBITER SEPARATION AT LIFT-OFF

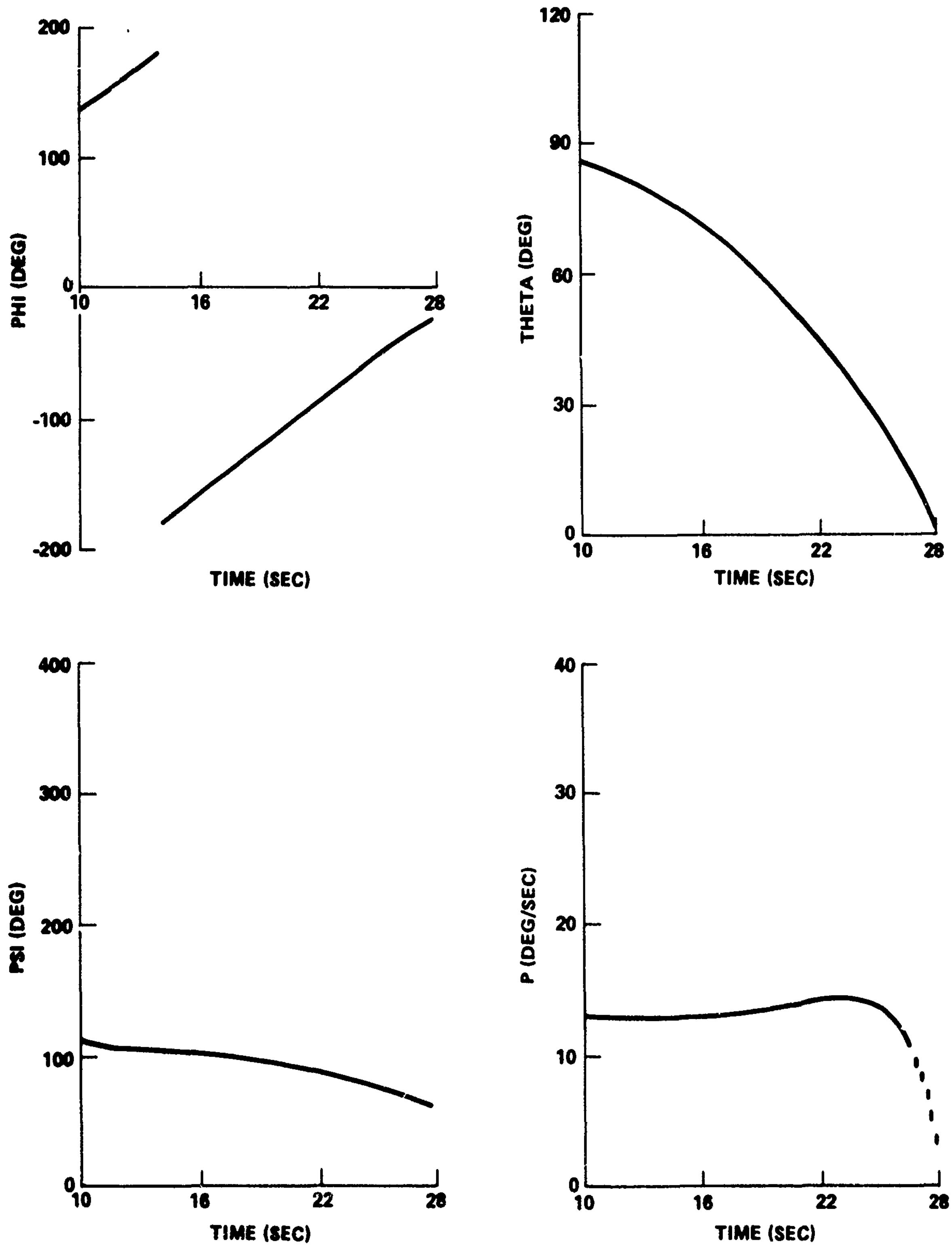

FIGURE B-30 ASCENT TRAJECTORY PARAMETERS FOR INTEGRATED VEHICLE WITH INADVERTENT ORBITER SEPARATION 10 SECONDS AFTER LIFT-OFF

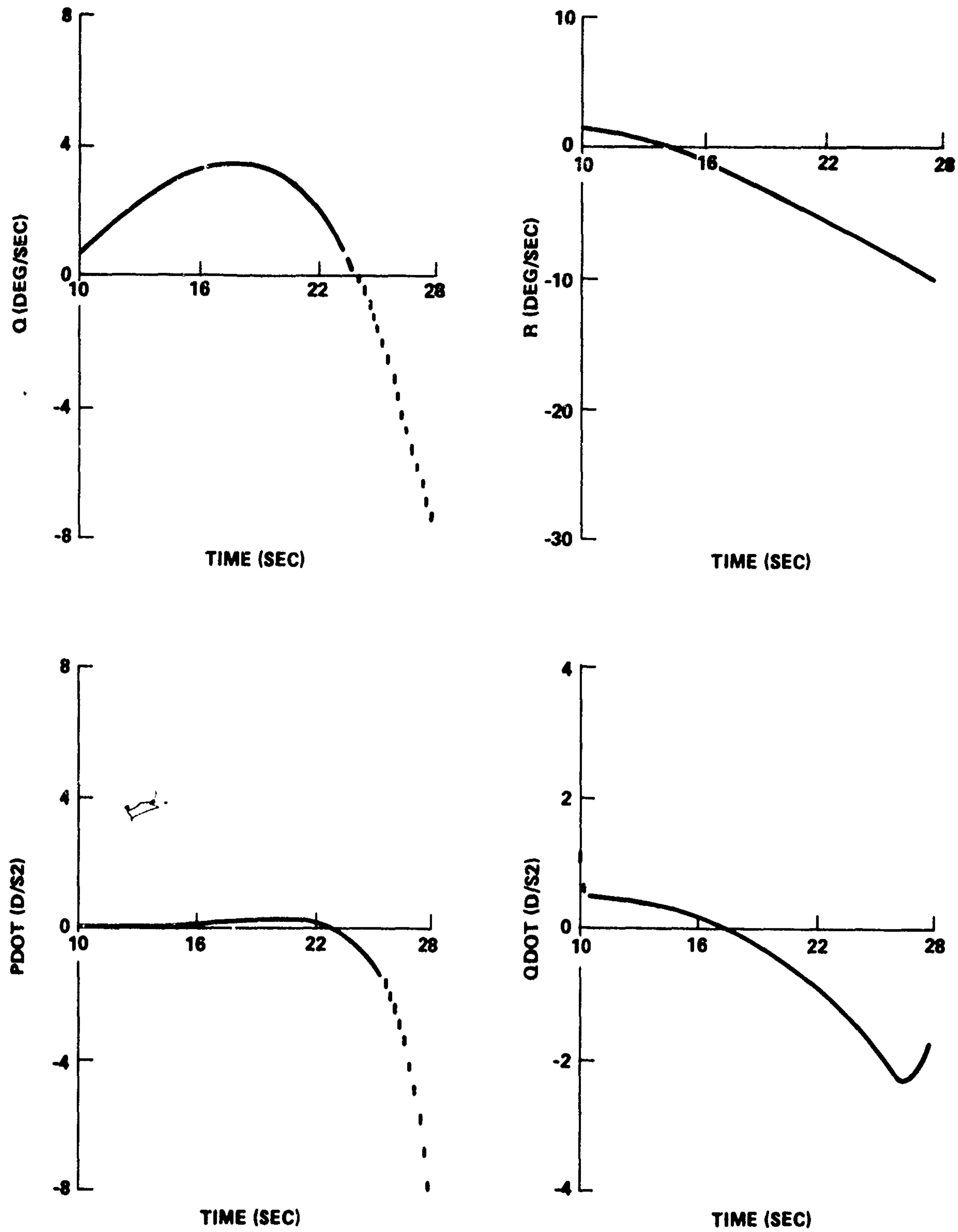

FIGURE B-31 ASCENT TRAJECTORY PARAMETERS FOR INTEGRATED VEHICLE WITH INADVERTENT ORBITER SEPARATION 10 SECONDS AFTER LIFT-OFF

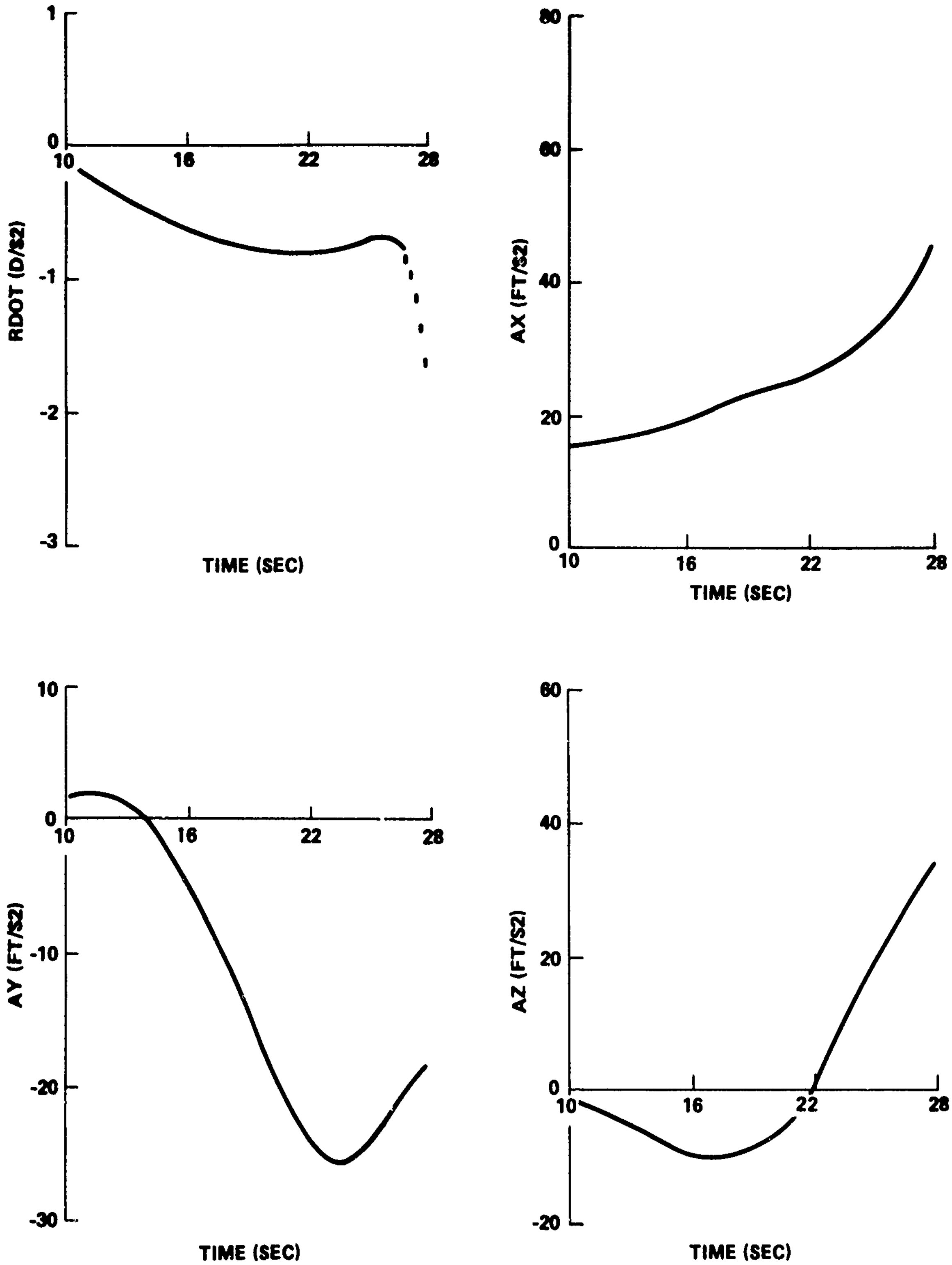

FIGURE B-32 ASCENT TRAJECTORY PARAMETERS FOR INTEGRATED VEHICLE WITH INADVERTENT ORBITER SEPARATION 10 SECONDS AFTER LIFT-OFF

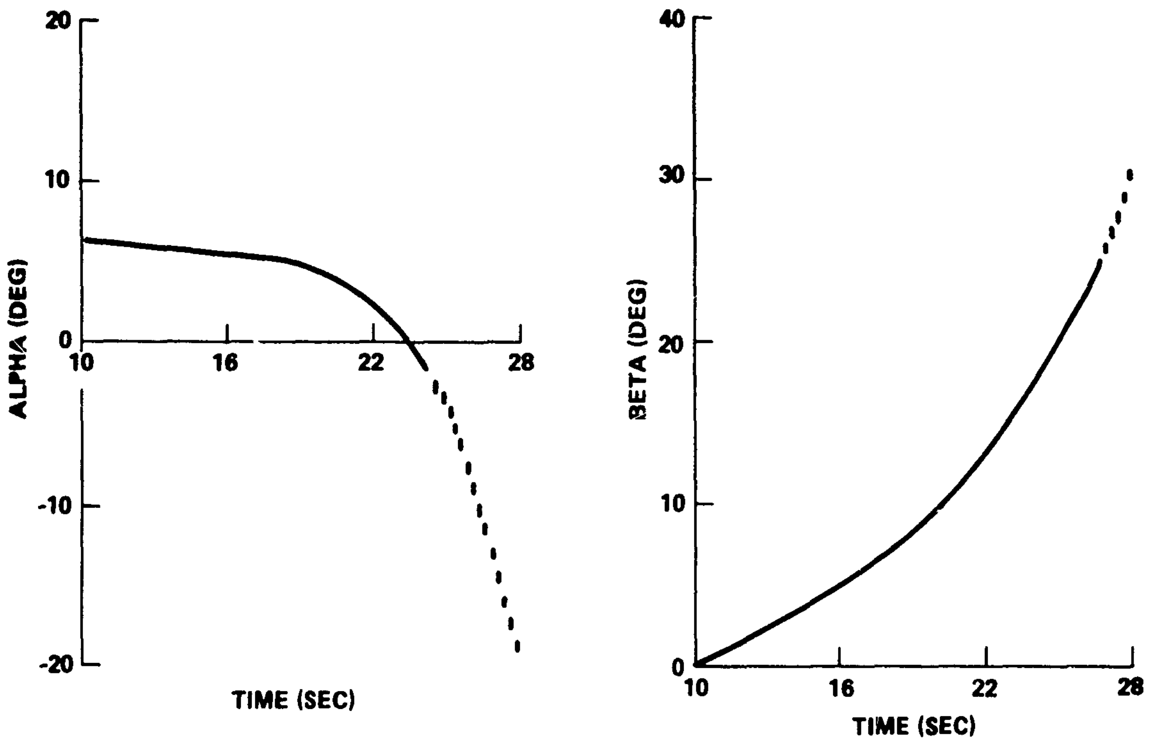

FIGURE B-33 ASCENT TRAJECTORY PARAMETERS FOR INTEGRATED VEHICLE WITH INADVERTENT ORBITER SEPARATION 10 SECONDS AFTER LIFT-OFF

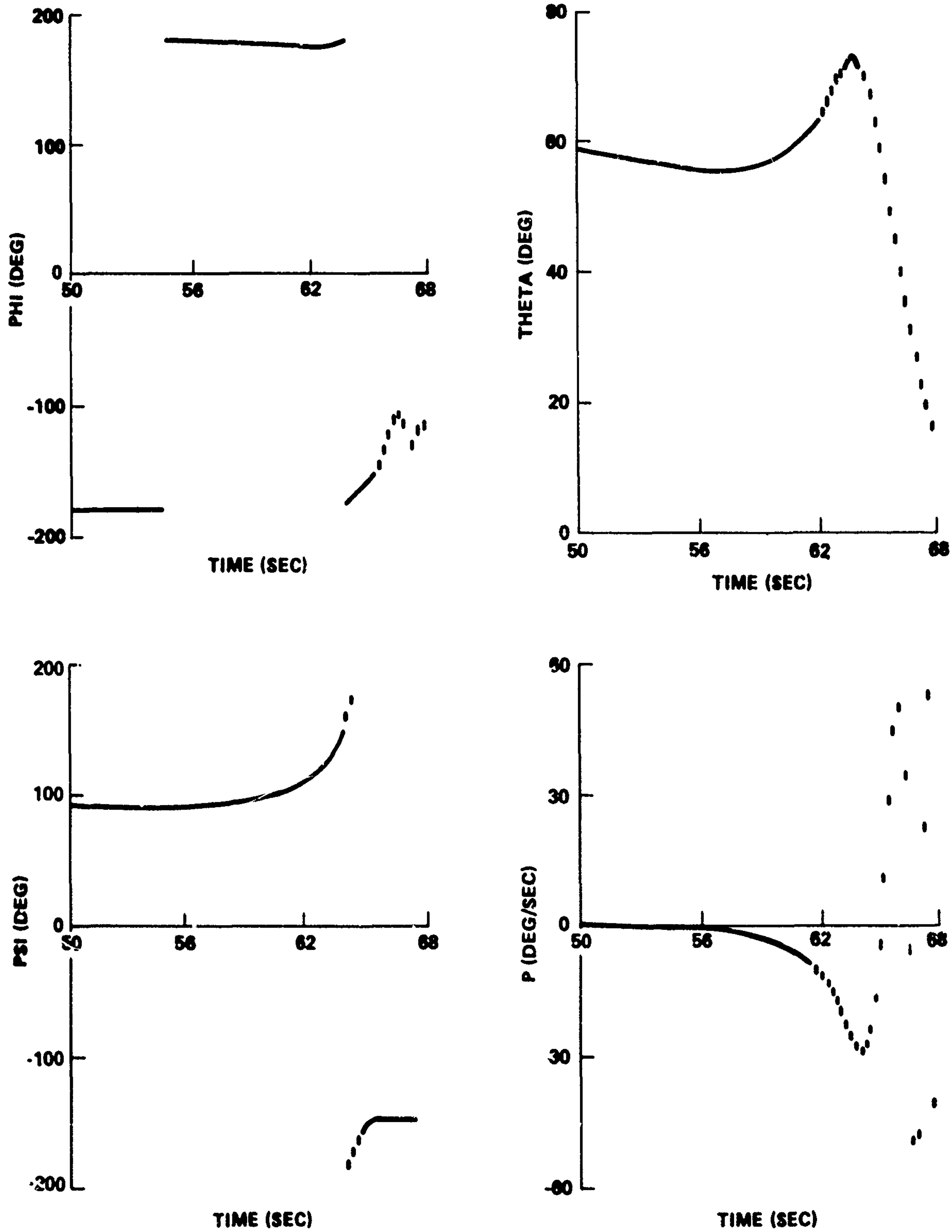

FIGURE B-34 ASCENT TRAJECTORY PARAMETERS FOR INTEGRATED VEHICLE WITH INADVERTENT ORBITER SEPARATION 50 SECONDS AFTER LIFT-OFF

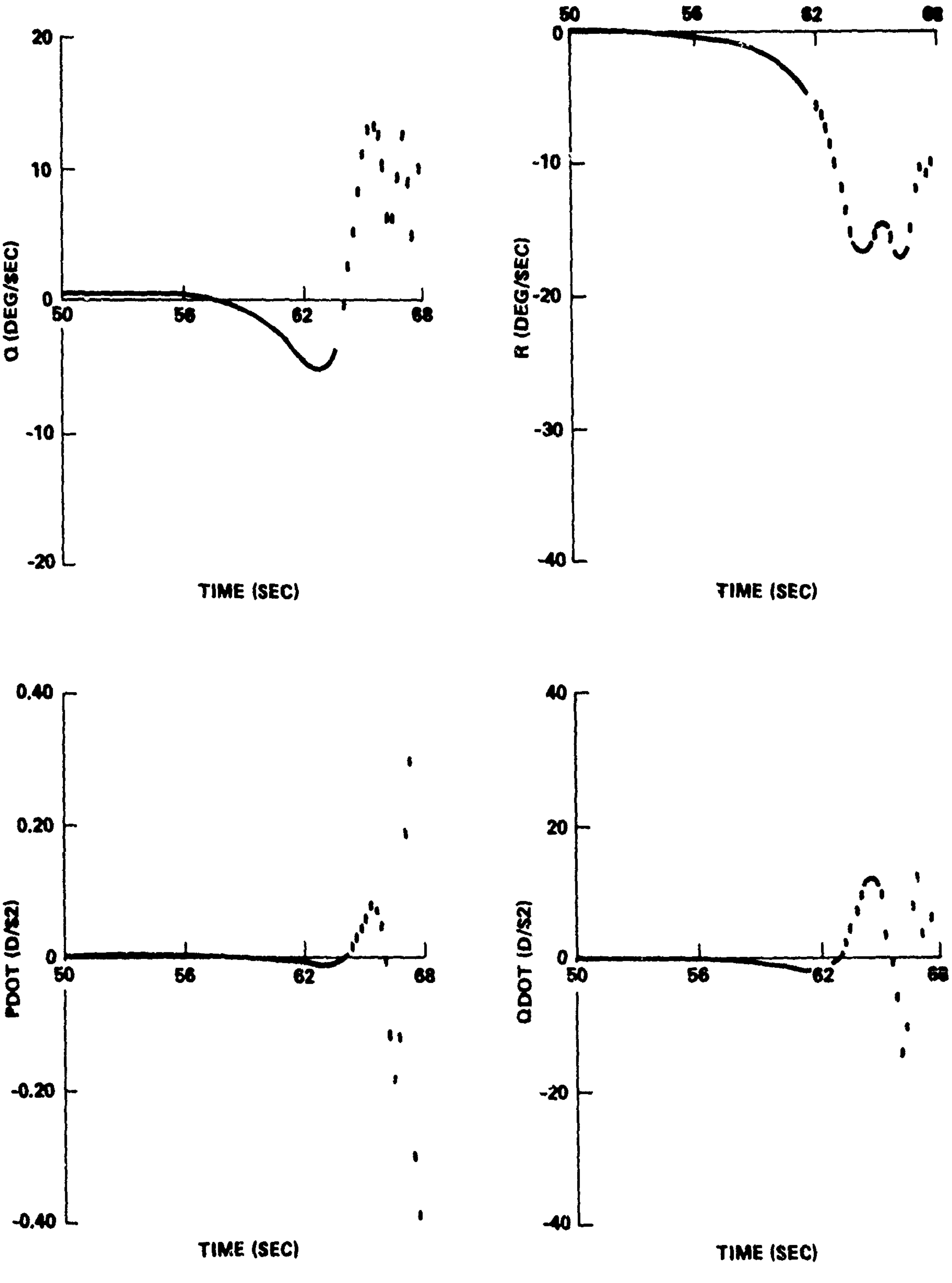

FIGURE B-35 ASCENT TRAJECTORY PARAMETERS FOR INTEGRATED VEHICLE WITH INADVERTENT ORBITER SEPARATION 50 SECONDS AFTER LIFT-OFF

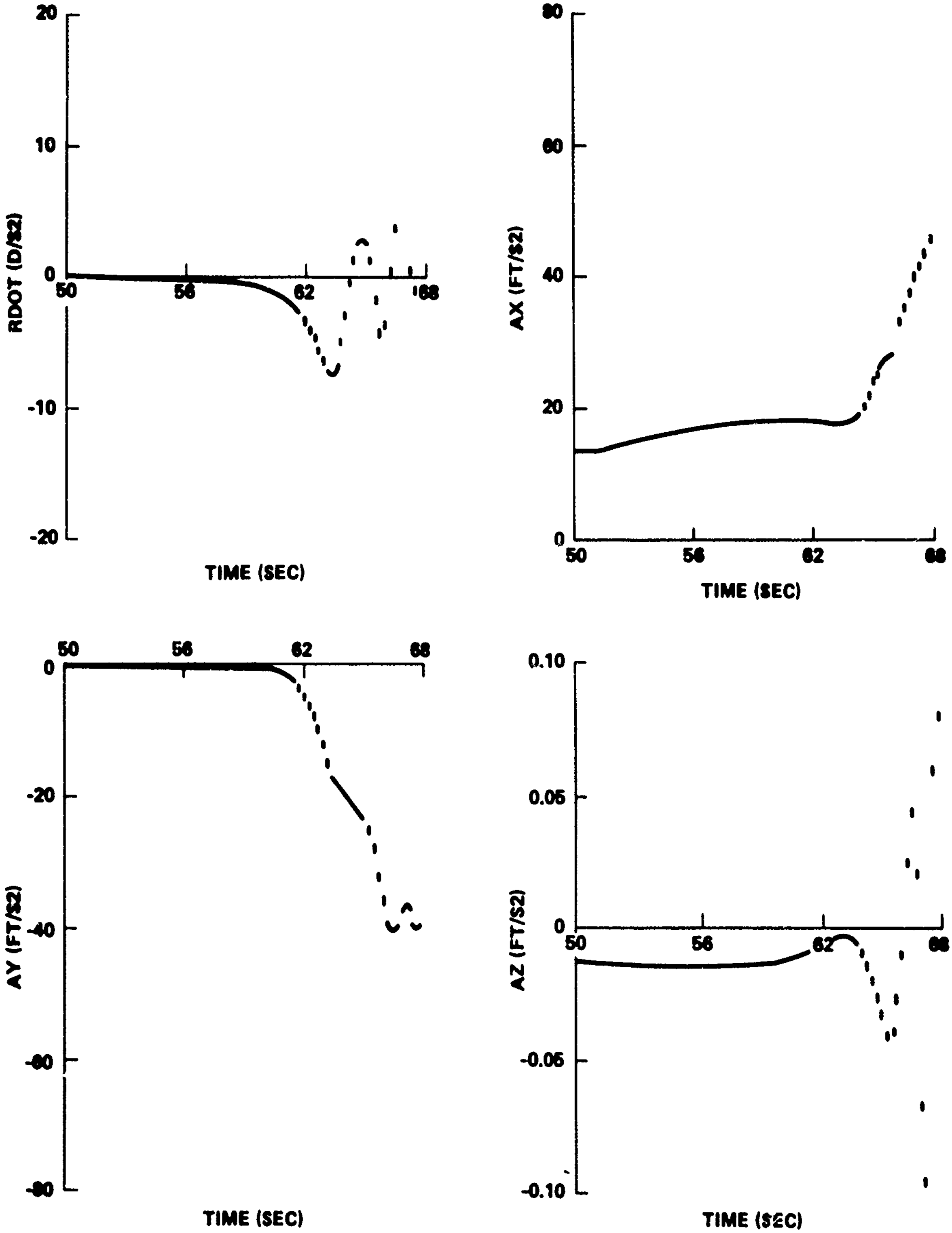

FIGURE B-36 ASCENT TRAJECTORY PARAMETERS FOR INTEGRATED VEHICLE WITH INADVERTENT ORBITER SEPARATION 50 SECONDS AFTER LIFT-OFF

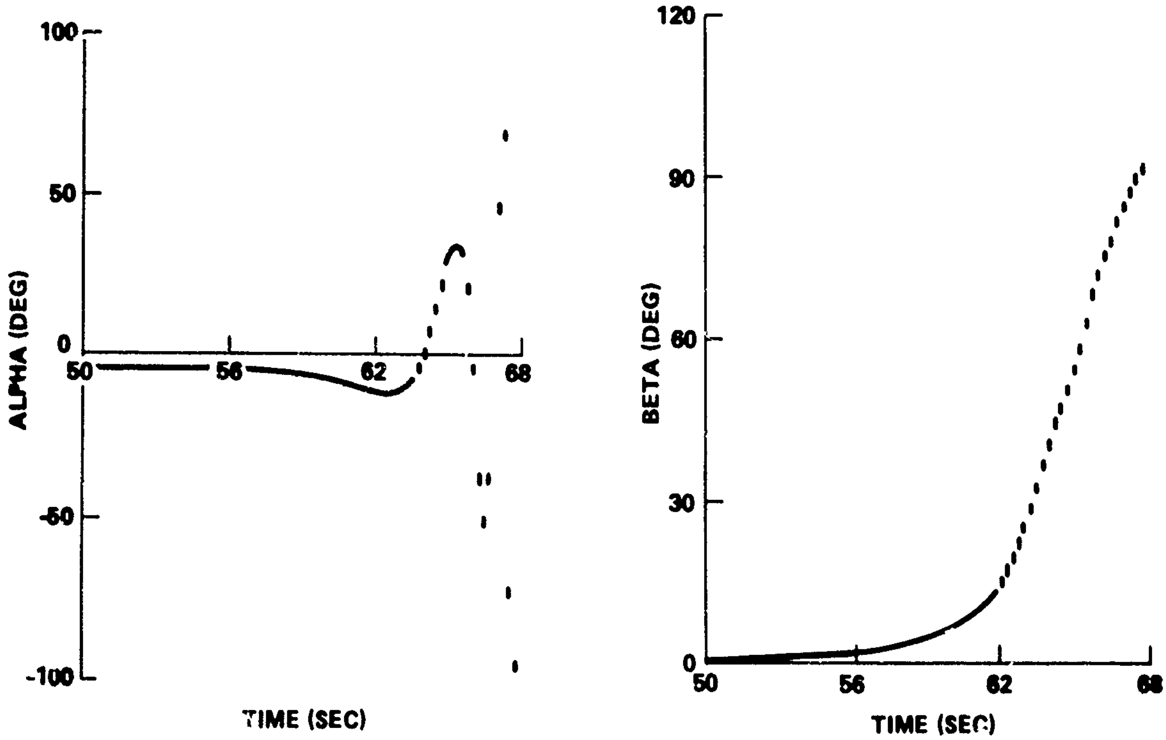

FIGURE B-37 ASCENT TRAJECTORY PARAMETERS FOR INTEGRATED VEHICLE WITH INADVERTENT ORBITER SEPARATION 50 SECONDS AFTER LIFT-OFF

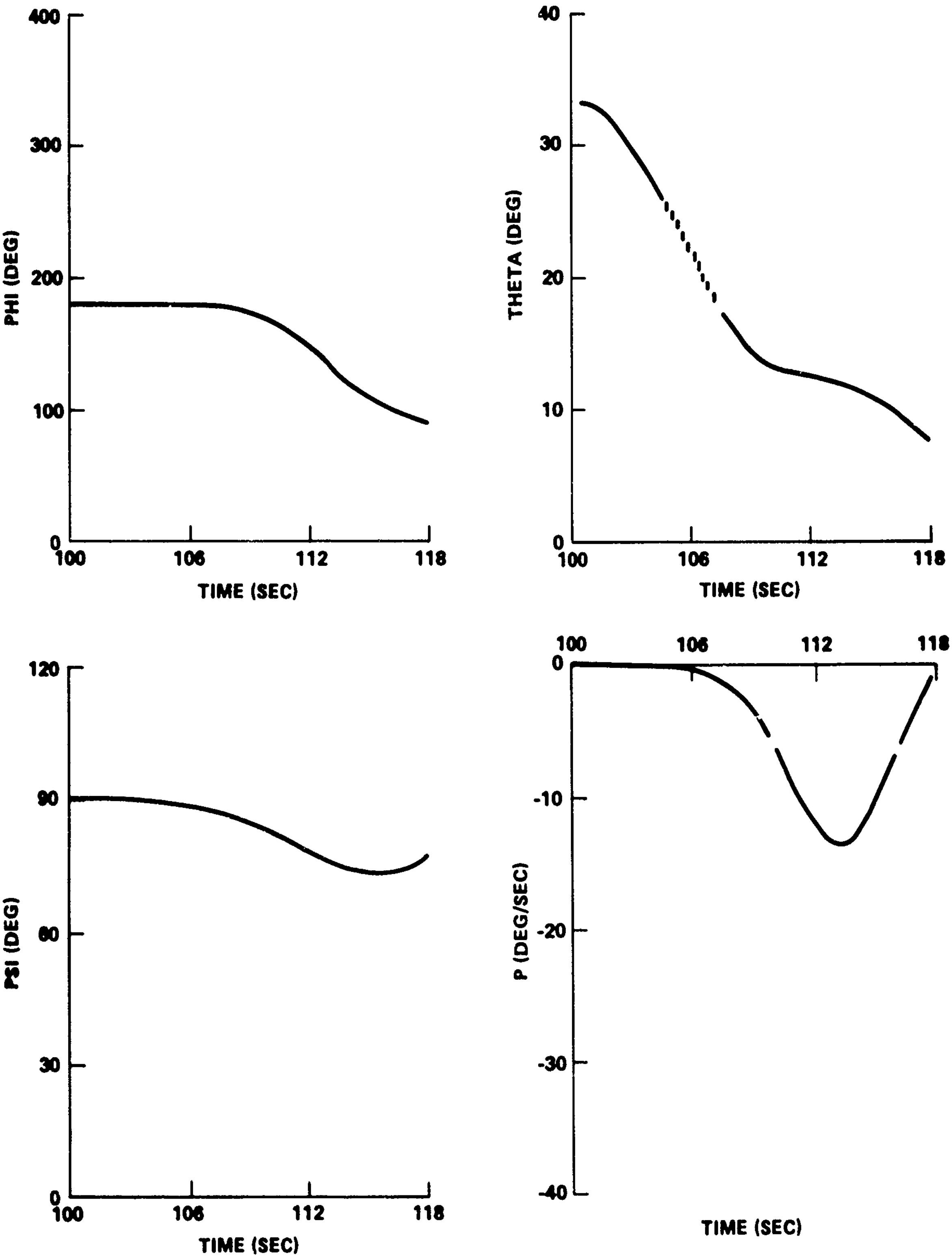

FIGURE B-38 ASCENT TRAJECTORY PARAMETERS FOR INTEGRATED VEHICLE WITH INADVERTENT ORBITER SEPARATION 100 SECONDS AFTER LIFT-OFF

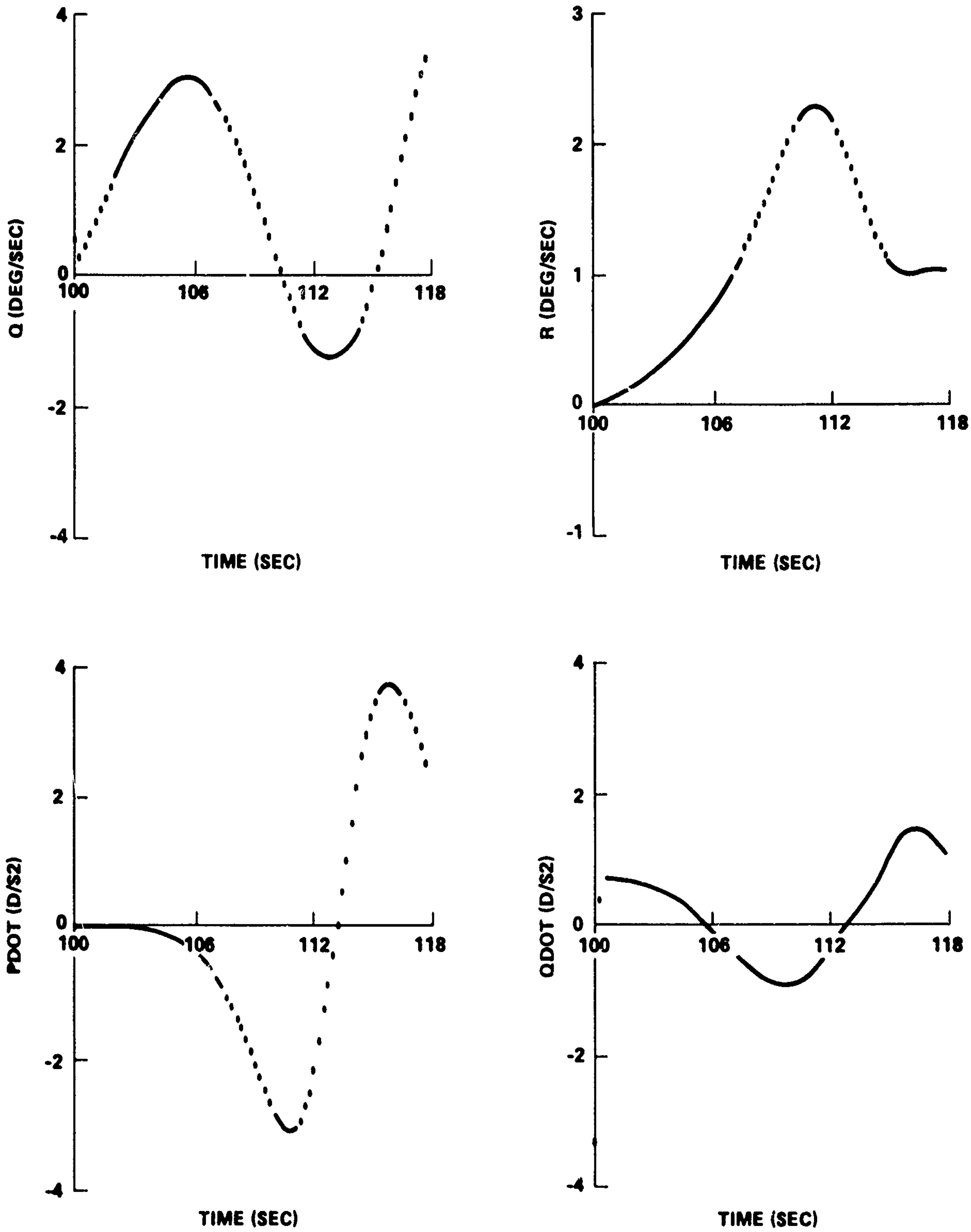

FIGURE B-39 ASCENT TRAJECTORY PARAMETERS FOR INTEGRATED VEHICLE WITH INADVERTENT ORBITER SEPARATION 100 SECONDS AFTER LIFT-OFF

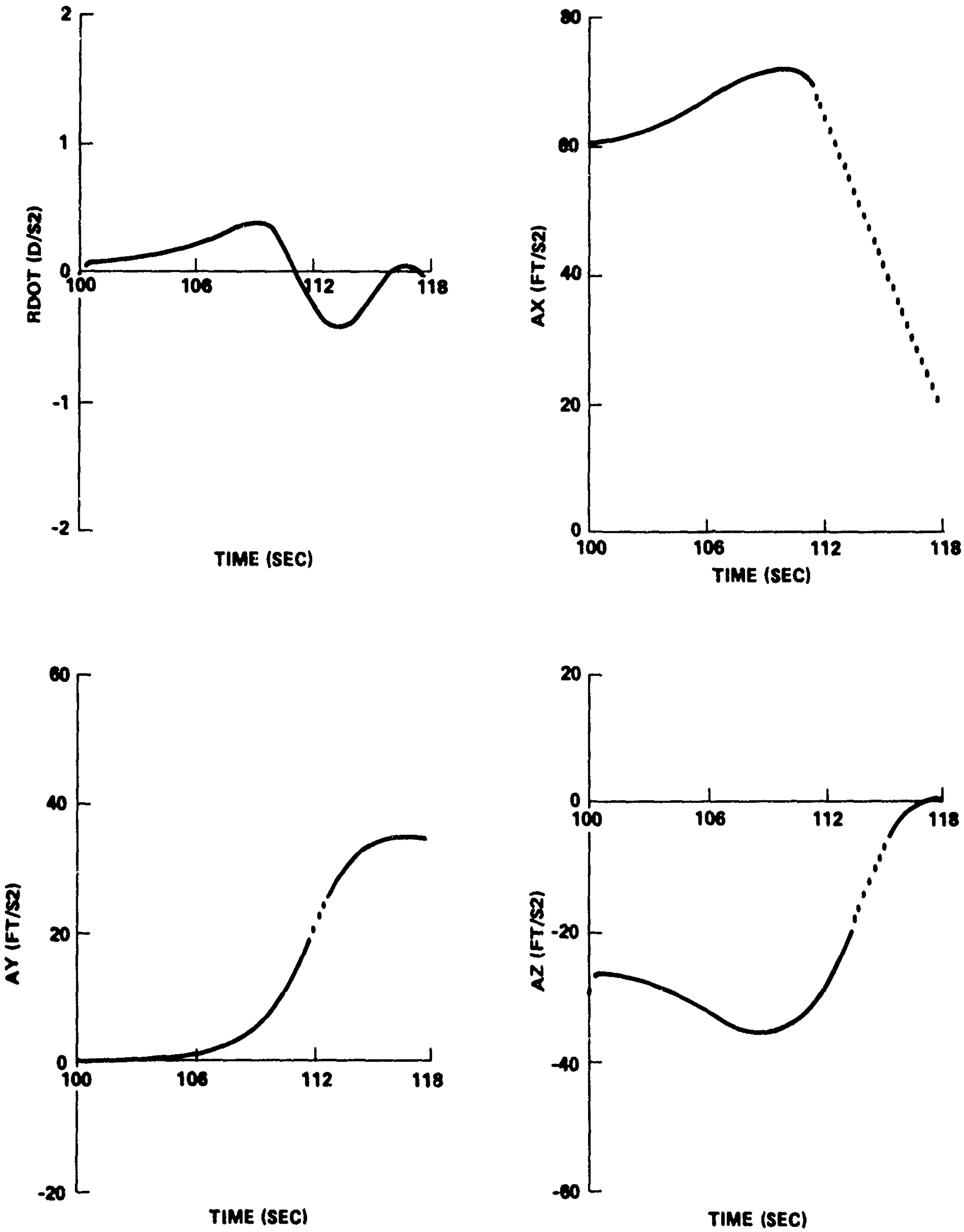

FIGURE B-40 ASCENT TRAJECTORY PARAMETERS FOR INTEGRATED VEHICLE WITH INADVERTENT ORBITER SEPARATION 100 SECONDS AFTER LIFT-OFF

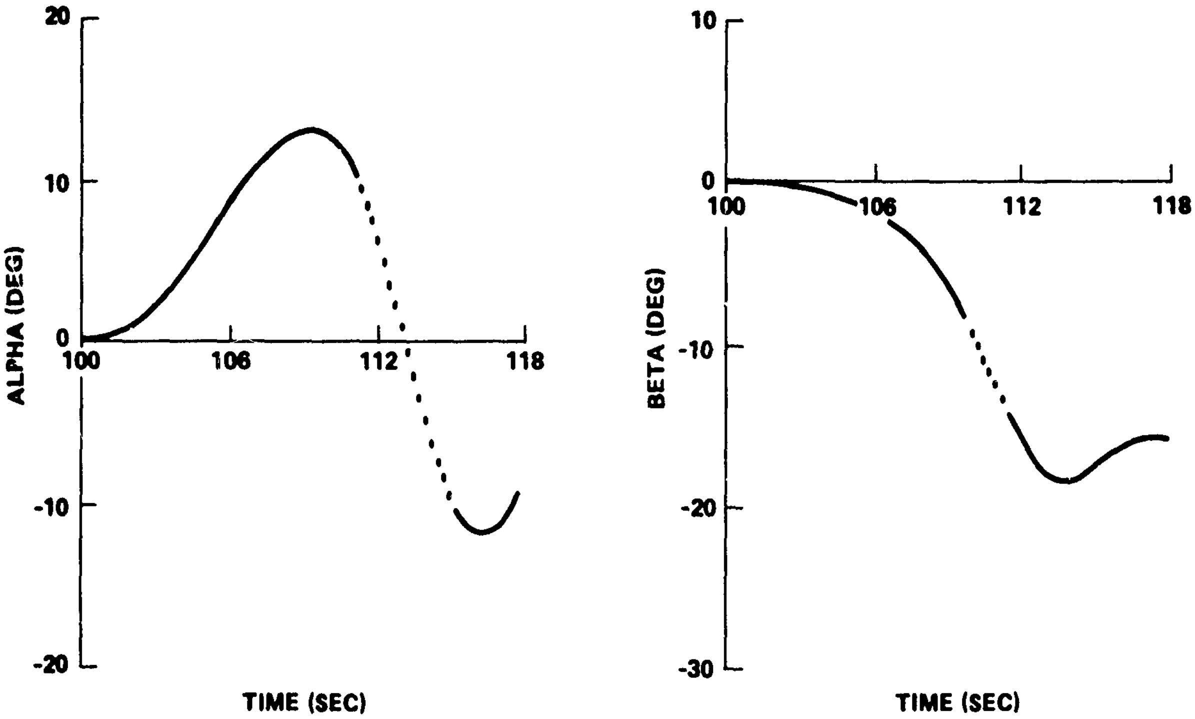

FIGURE B-41 ASCENT TRAJECTORY PARAMETERS FOR INTEGRATED VEHICLE WITH INADVERTENT ORBITER SEPARATION 100 SECONDS AFTER LIFT-OFF

APPENDIX C

FINITE ELEMENT MODEL OF ET FRAME X_T 2058

INTRODUCTION

The external tank (ET) aft ring frame (Fig. C-1), located at station X_T 2058, is designed to carry the solid rocket booster (SRB) and orbiter aft joint loads on the ET. In order to analyze the behavior of this ring frame during the destruct mode, a finite element model was constructed for use with the NASTRAN Computer Program. This model consists of the aft ET barrel section, the LH_2 dome, and all intrinsic ring frames and stringers.

FINITE ELEMENT MODEL

The finite element model is shown in Figure C-2. The model consists of 393 grid points connected by 729 triangular bending elements and 384 bar elements (not shown). The NASTRAN Bulk Data GRID, CTRIA2, and PTRIA2 cards were generated using the BING Computer Code.[C-1] The thickness of each plate element in the barrel section was determined from the shell thickness distribution shown in Figure C-3. The LH_2 dome was taken to be a constant thickness of 0.087 inch.

Three ring frames, in addition to the main ring frame at station X_T 2058, were modeled using NASTRAN CBAR elements offset from the shell meridian. These ring frames are located at stations 1888.28, 1973.50, and 2038.97. Representative cross sections of all ring frames and their positions relative to the shell model are shown in Figure C-4. The properties of the ring frames were computed using an in-house program, a typical result of which is shown in Figure C-5. The properties of the frame at station X_T 2058 were computed for angular increments averaging 15 degrees. The inertia of the radial stiffeners riveted to the basic web was ignored.

[C-1] Huang, P.C. and Matra, J. P., Jr., "Missile Body Input Generator (BING), A NASTRAN Pre-Processor, Theoretical Development, User's Manual, and Program Listing," NSWC/WOL/TR 75-9, Mar 1975.

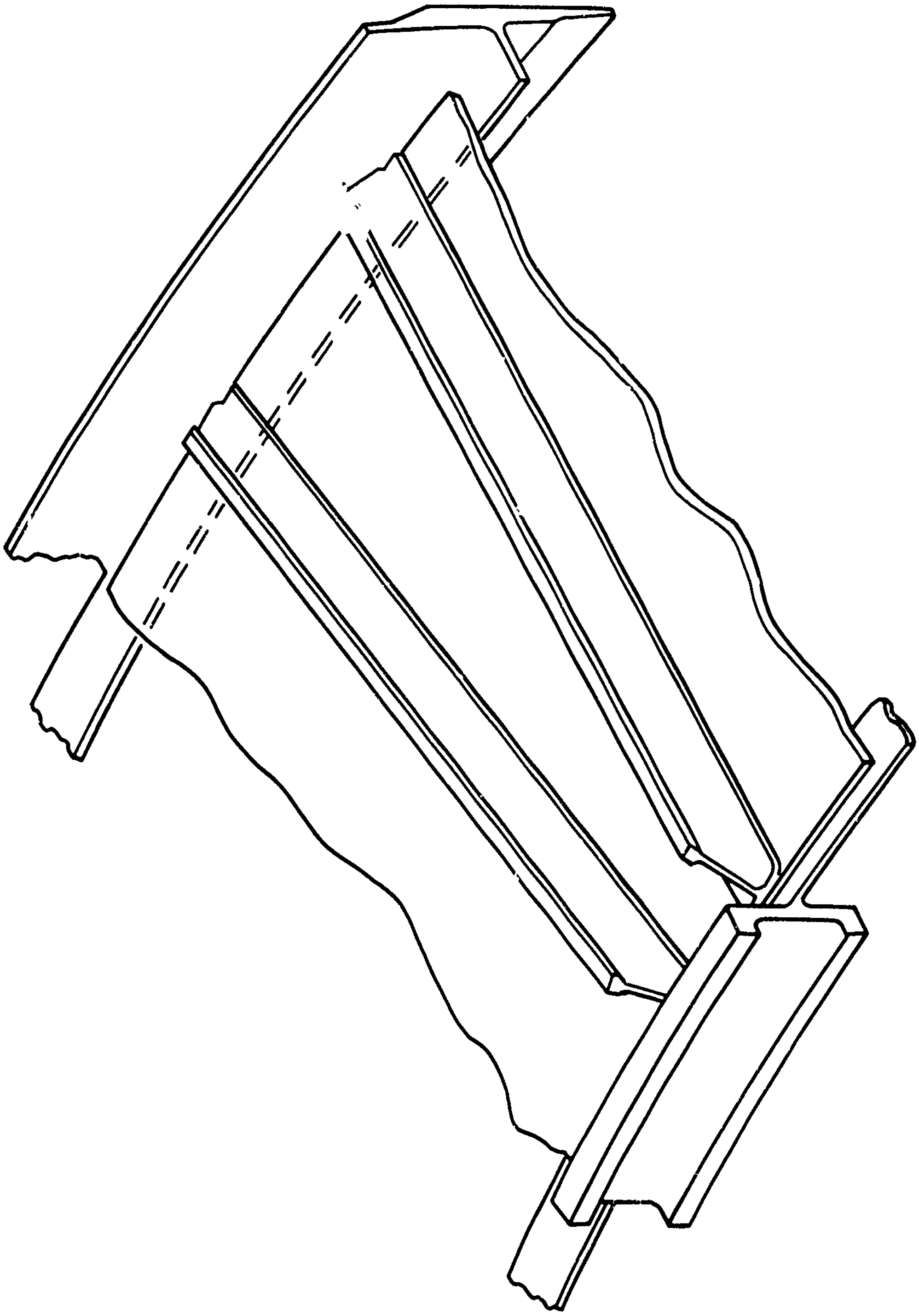

FIGURE C-1 ET RING FRAME AT STATION X_T 2058

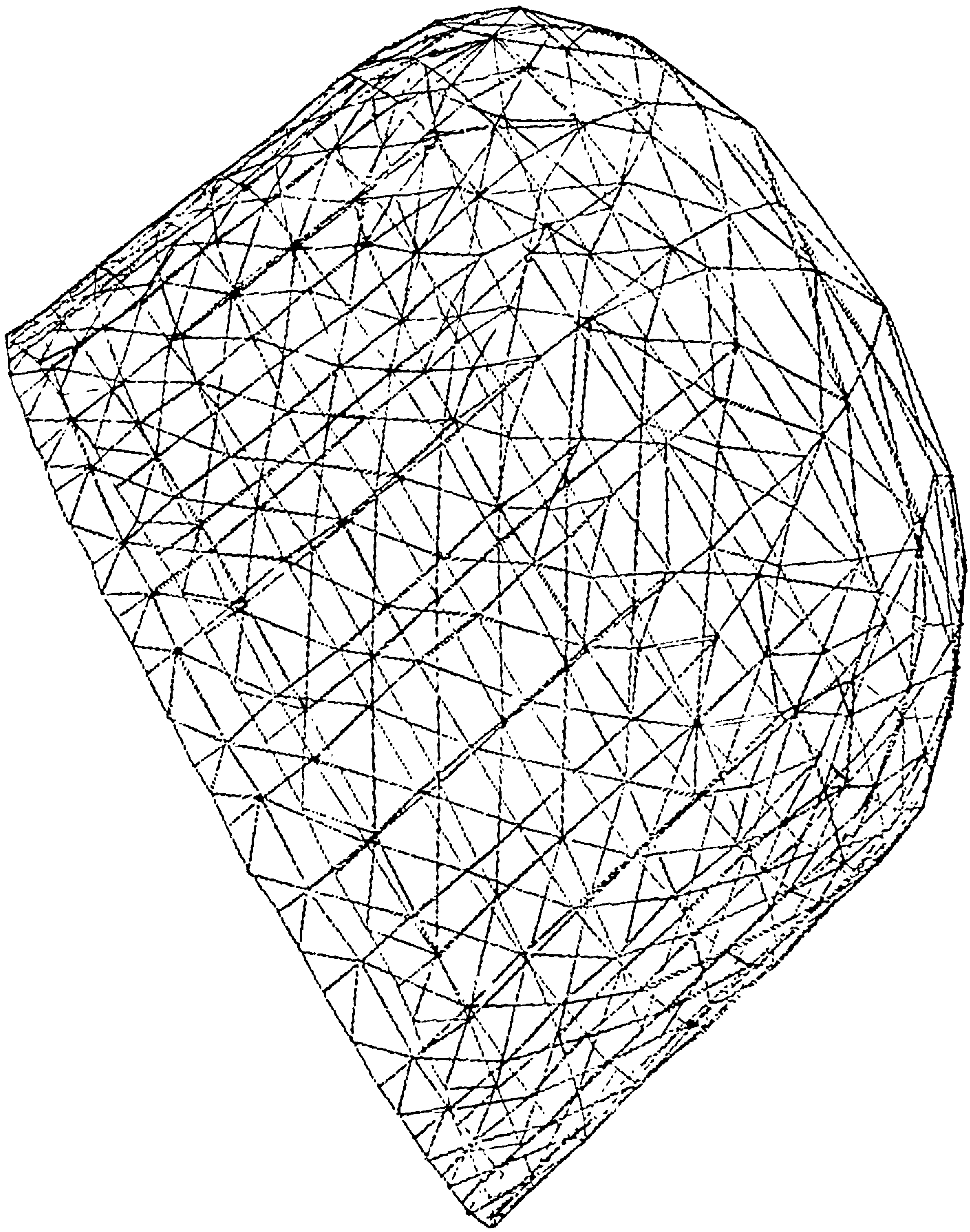

FIGURE C-2 FINITE ELEMENT MODEL

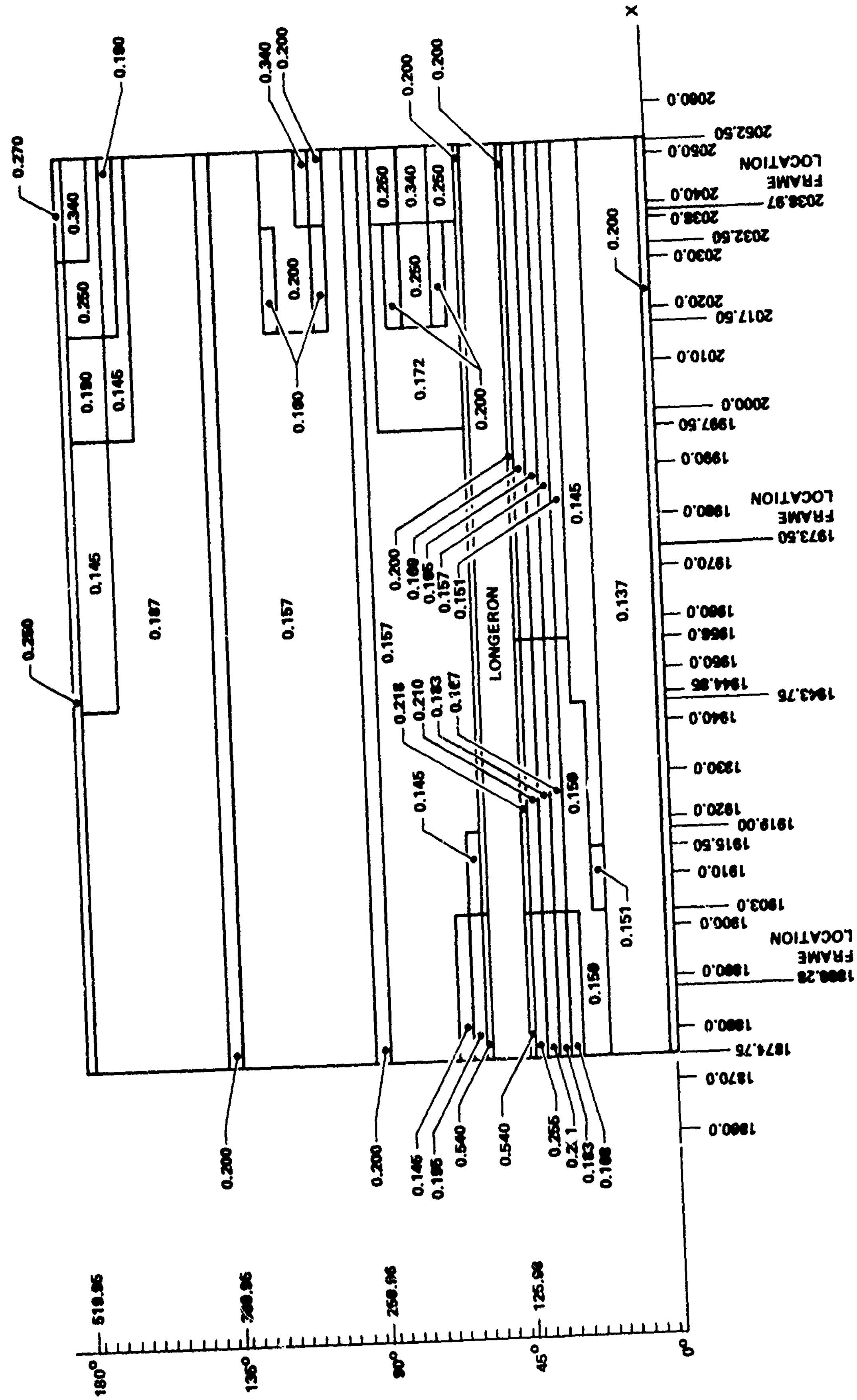

FIGURE C-3 ET SHELL THICKNESS VARIATION AT STATION X_T 2058

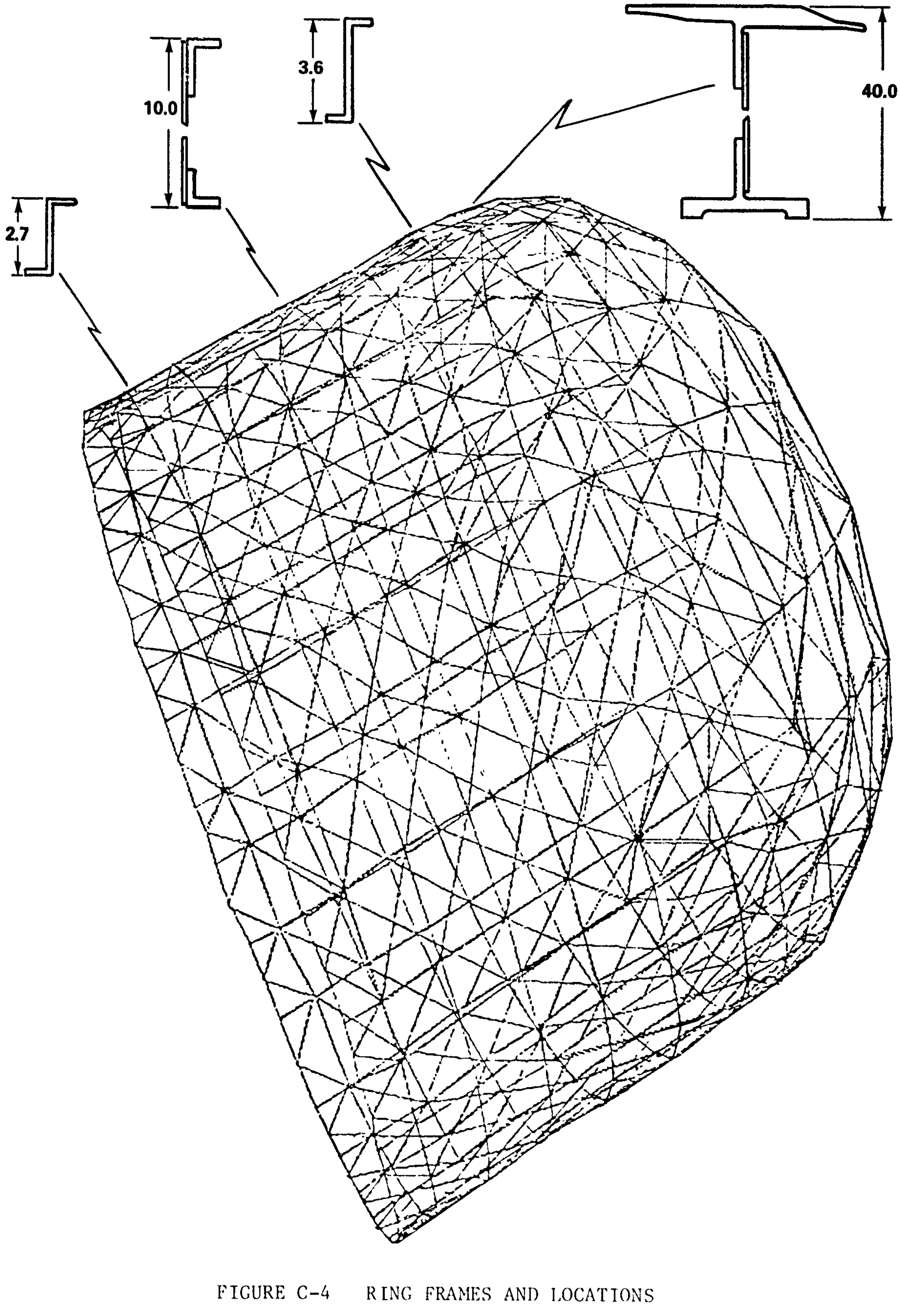

FIGURE C-4 RING FRAMES AND LOCATIONS

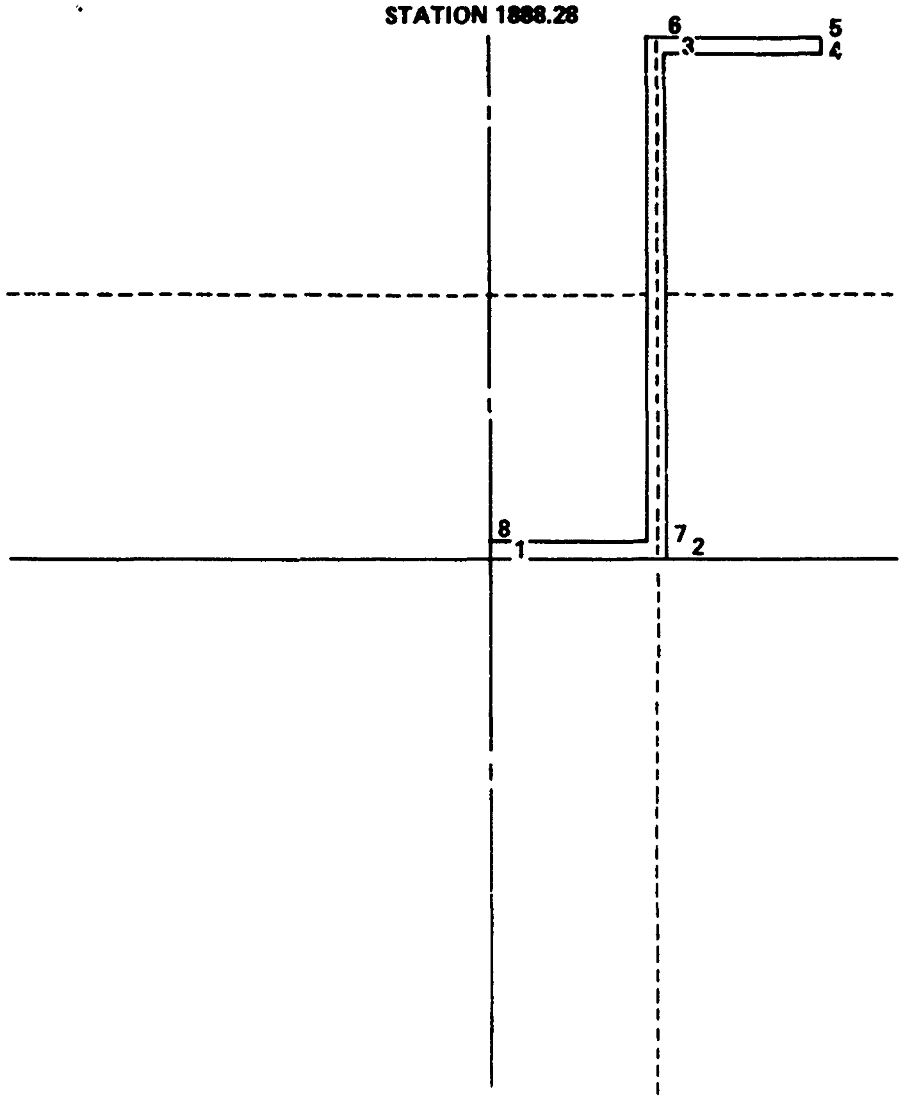

PROPERTIES WITH RESPECT TO

REFERENCE AXES	CENTER OF GRAVITY
I(XX) = 1.0458	I(XX) = 0.3899
I(YY) = 0.3820	I(YY) = 0.0479
I(XY) = 0.5671	I(XY) = 0.0964
I(P) = 1.4279	I(P) = 0.4312

COORDINATES OF CENTER OF GRAVITY: X-BAR (IN) = 0.9600
Y-BAR (IN) = 1.3500

AREA (IN^2) = 0.3632 **MINIMUM I = 0.0216**

ANGLE BETWEEN PRINCIPAL AND X-AXIS = 75.0966°

FIGURE C-5 TYPICAL FRAME PROPERTIES

The 96 integrally machined stringers in the ET shell were included in the model, using NASTRAN CBAR elements. Since the model did not include 96 circumferential grid points at any given longitudinal station, the properties of the stringers were smeared by "grid point averaging" over the arc length between grid points. It was felt that while this approximation may affect the shell deflections computed at any given point on the shell, the effect on the deflections and stresses computed for the ring frame at station X_T 2058 would be negligible.

TEST CASE

In order to verify the correctness of the model, a test case was run for comparison with the results given by NACA TN 1310. For this case, the thickness of all the triangular bending elements representing the aft ET barrel section were taken to be 0.137 inch. The ring was loaded by two diametrically opposed, one-kip radial loads located at the port and starboard sides of the ring. A comparison of the moment distributions is given in Figure C-6. It is felt that results obtained using NASTRAN are in very good agreement with those given by NACA TN 1310, especially in view of the inherent assumptions made in NACA TN 1310, such as the ring having a uniform cross section. Figure C-7 shows the deformed shape of the model for this test case. Figure C-8 gives the deflection vectors for the grid points to which the ring is attached.

RESULTS

The frame was analyzed for the loads occurring during destruct, as shown below:

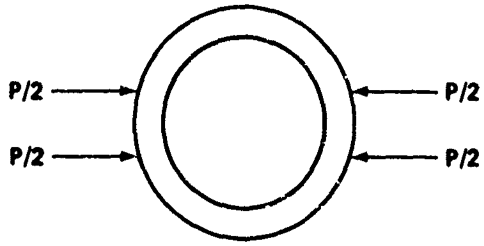

The critical stresses and deflections for a load $P = 1.42 \cdot 10^6$ lb are as follows:

$(f_b)_{frame} = 78{,}000$ psi

$M_{max} = 2.01 \times 10^7$ in-lb

$f_{skin} = 75{,}000$ psi

$\delta = 2.13$ in (vicinity of loads)

$$K = \frac{P}{\delta} = \frac{1.42 \times 10^6}{2.13} = 0.66 \times 10^6 \text{ lb-in}$$

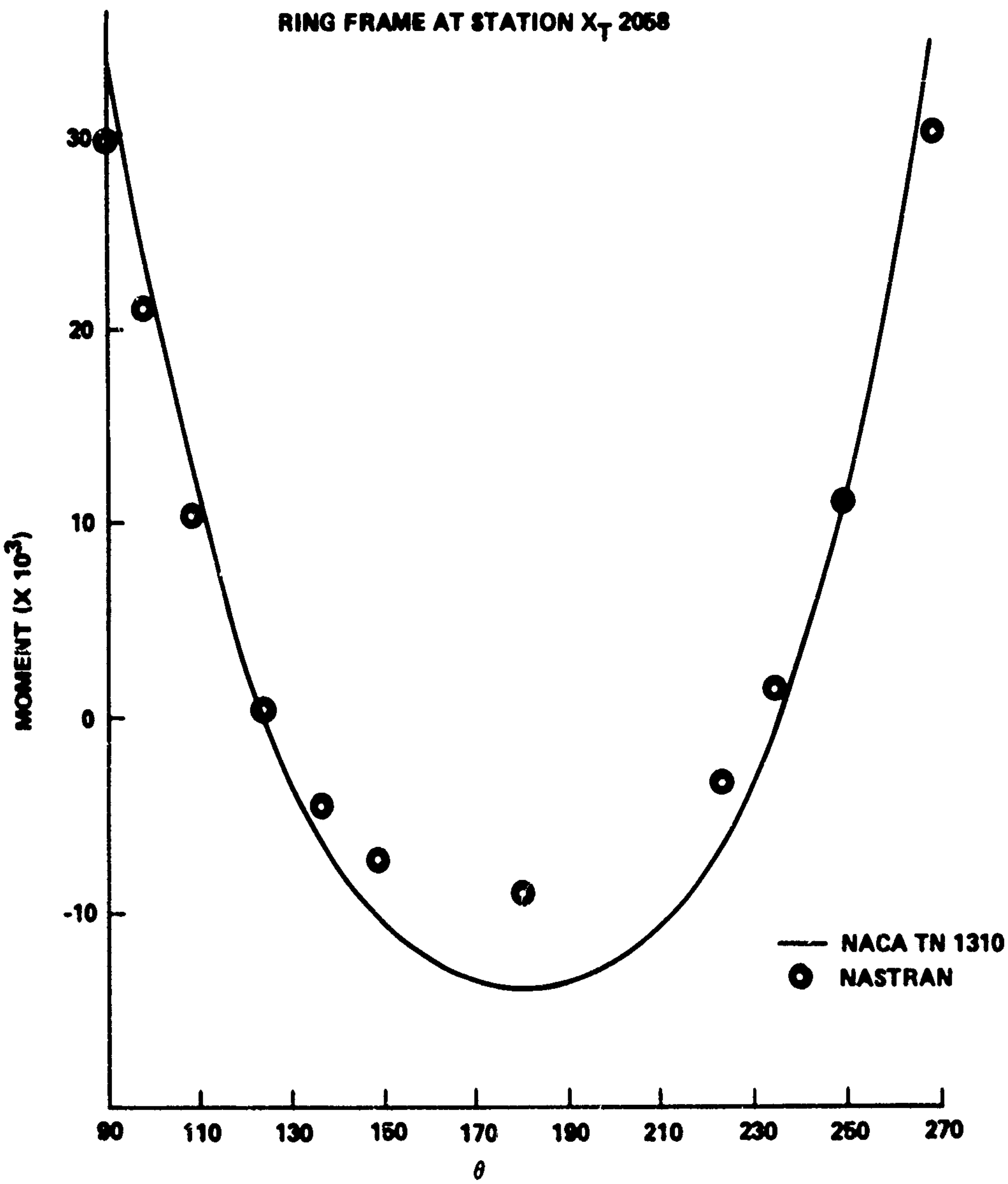

FIGURE C-6 TEST CASE — BENDING MOMENT DISTRIBUTION

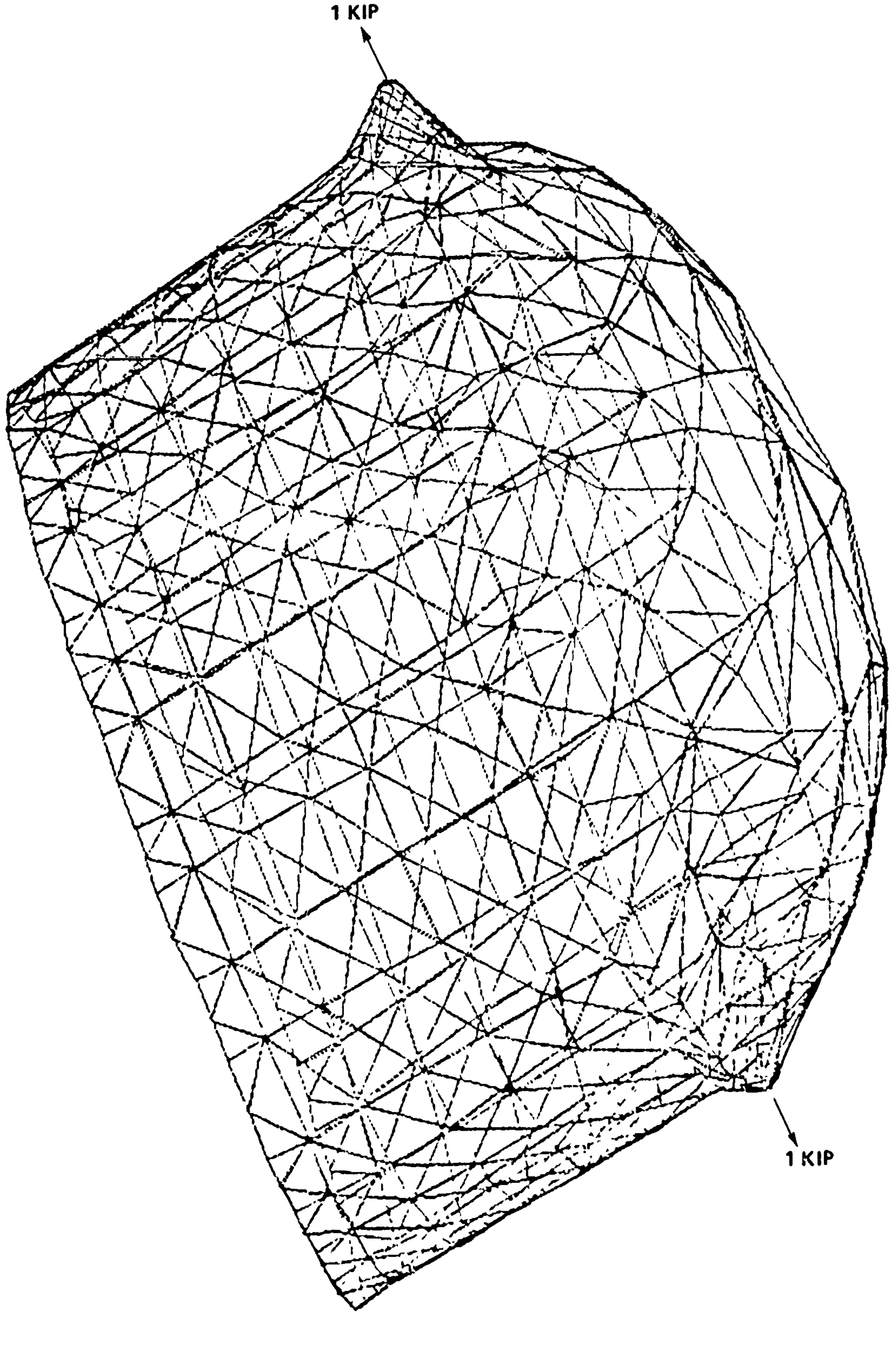

FIGURE C-7 STATIC ANALYSIS OF ET RING FRAME LOCATED AT STATION X_T 2058
TEST CASE ** 1-KIP RADIAL LOADS

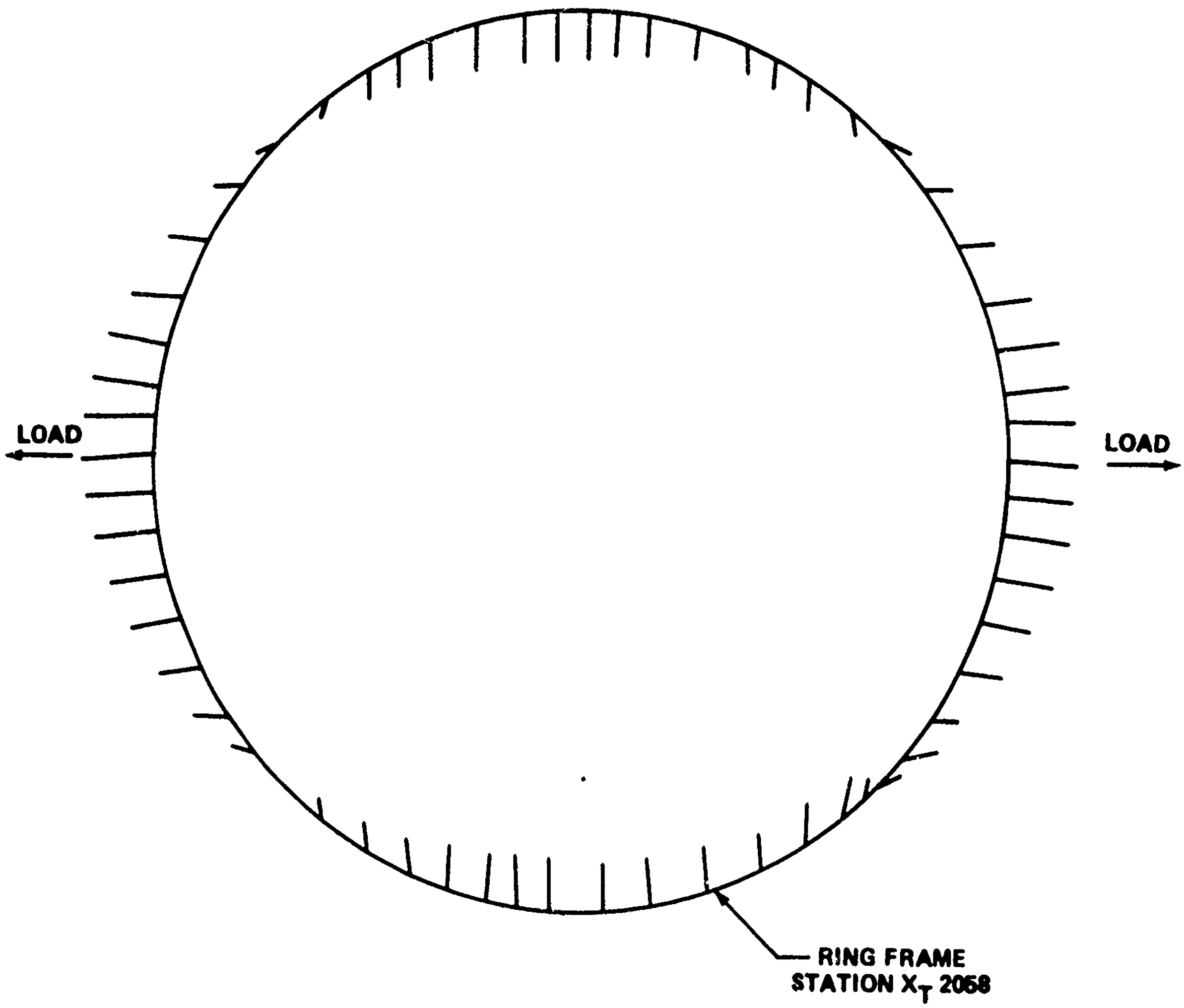

FIGURE C-8 DEFLECTION PATTERN — TEST CASE

The yield strength of the 2024 T 8511 AL inner chord is

$$F_{ty} = 78{,}000 \text{ psi}$$

Hence, a load of 1.42×10^6 lb is sufficient to initiate yielding.

The frame was also analyzed for just one SRB loading the frame.

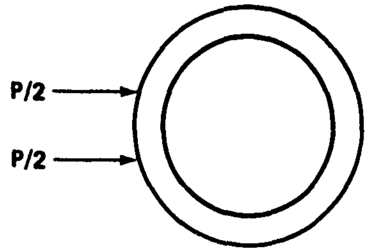

The maximum stresses and deflection for a load $P = 1.6 \times 10^6$ lb are as follows:

$$(f_b)_{frame} = 77{,}000 \text{ psi}$$

$$(M)_{frame} = 1.87 \times 10^7 \text{ in-lb}$$

$$\delta = 2.73 \text{ in}$$

$$K = \frac{P}{\delta} = \frac{1.6 \times 10^6}{2.73} = 0.58 \times 10^6 \text{ lb/in}$$

A load of 1.6×10^6 lb is sufficient to cause yielding in this case.

APPENDIX D

BOSOR4 MODEL OF AFT SRB FRAME

INTRODUCTION

The rear of the solid rocket booster (SRB) attaches to the external tank (ET) with a truss consisting of three struts which is capable of transferring a moment and loads in the plane of the cross section. No axial thrust loads are reacted at this joint. The rear attachment of the SRB to the ET is shown in Figure D-1. The ends of the struts consist of yokes which are pinned to a channel spanning the two external rings on the SRB. A meridional section of the rear SRB attachment ring and surrounding structure is shown in Figure D-2. The structure is axisymmetric except for channels tying the rings together at several circumferential locations. The rings are riveted to stubs protruding from a built-up section of skin and have angles riveted to their periphery for additional stiffness. The 1/8-inch thick rings are separated by 11.5 inches, and the skin is built up from 0.52 inch to 0.62 inch over a 22.25-inch length. A clevis joint for joining to another rocket motor casing section is located 19.52 inches forward of the ring frame's centerline. The material is D6AC steel with

$$F_{t_u} = 195{,}000 \text{ psi}$$

$$F_{t_y} = 185{,}000 \text{ psi}$$

$$F_{s_u} = 117{,}000 \text{ psi}$$

$$E = 30(10^6) \text{ psi}$$

$$\rho = 0.283 \text{ lb/in}^3$$

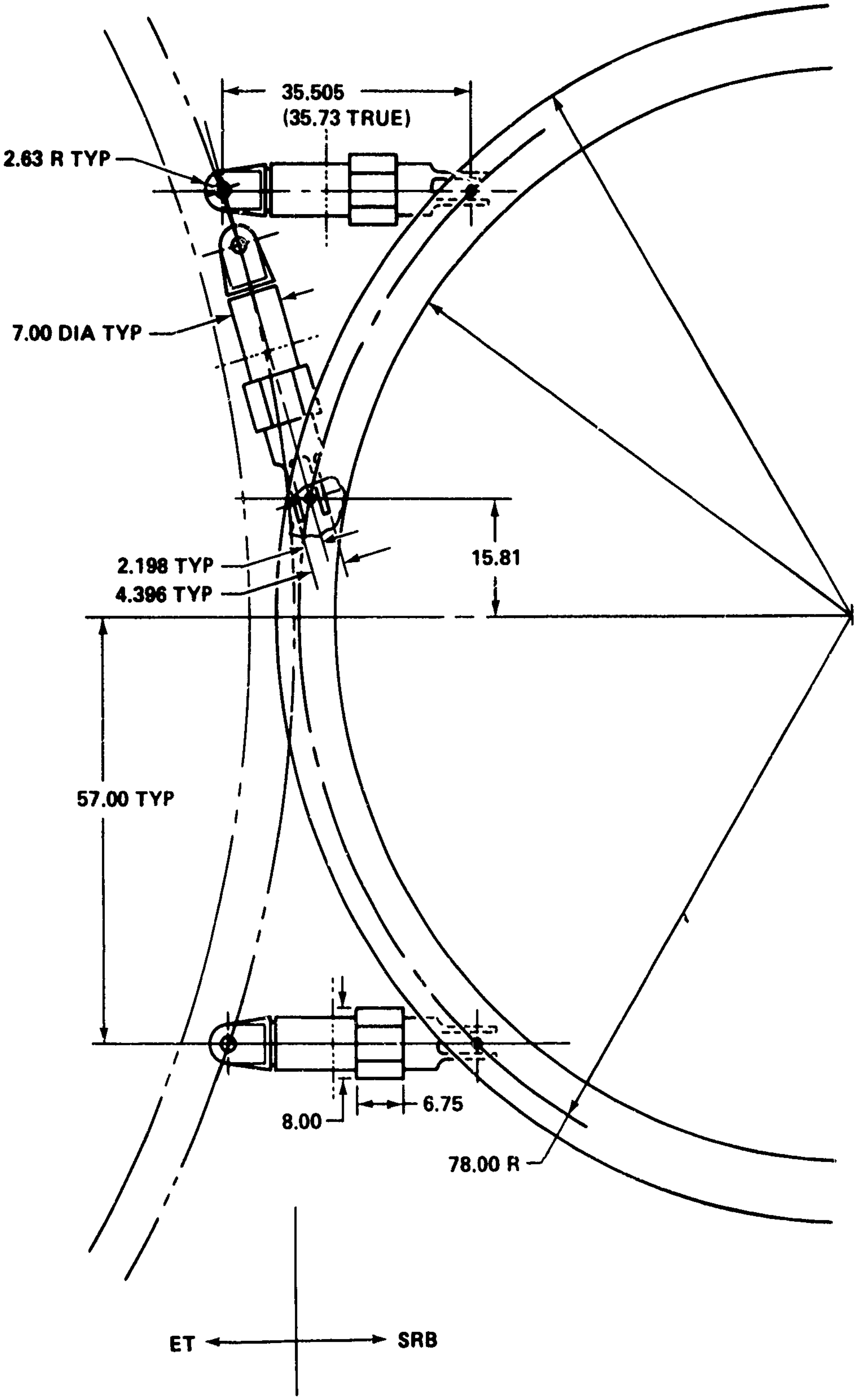

FIGURE D-1 SRB/ET AFT TRUSS

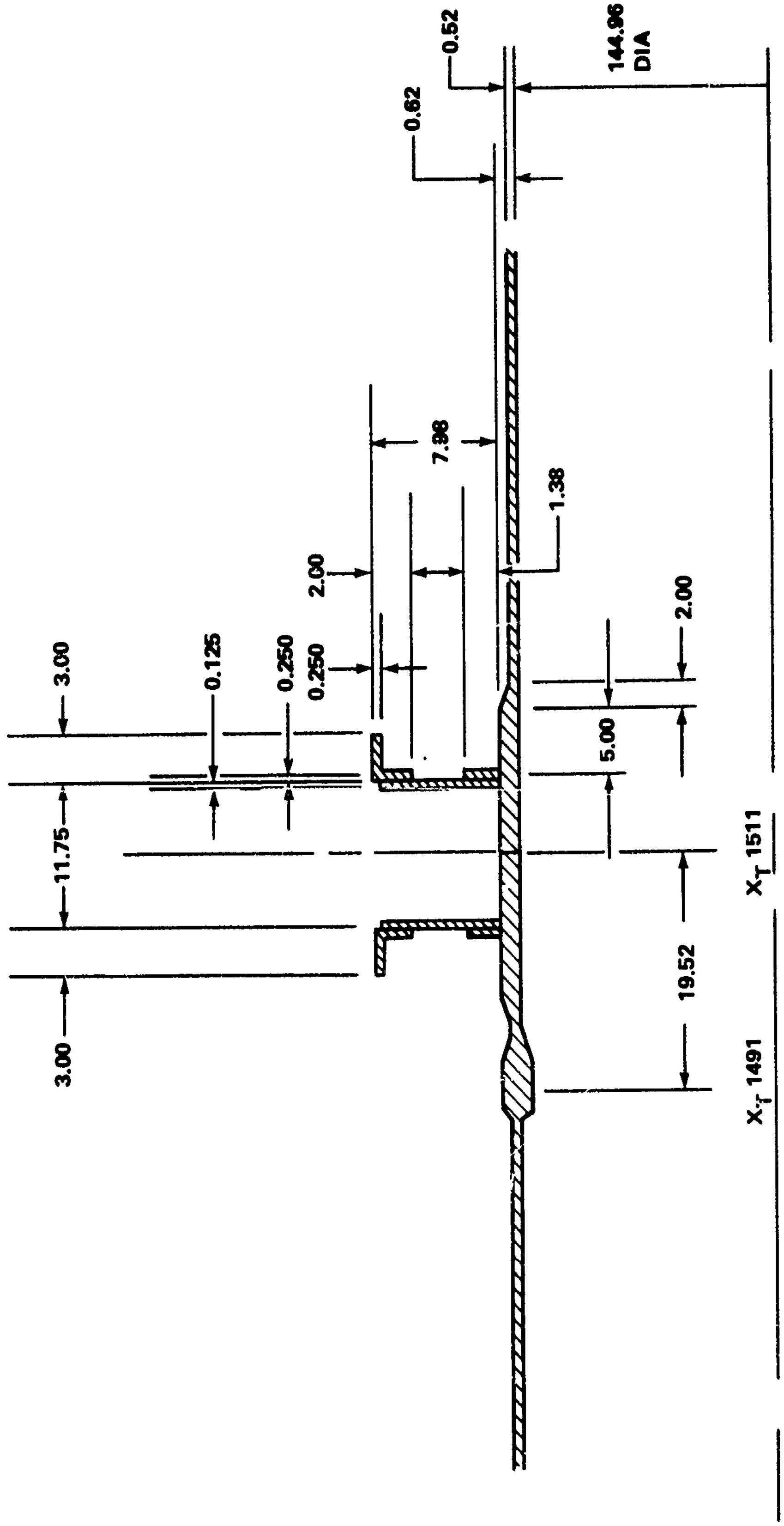

FIGURE D-2 AFT SRB ATTACHMENT RING

As mentioned on the previous page, the structure is essentially axisymmetric, the only exceptions being channels between rings at several circumferential locations. On the other hand, the loading consists of essentially point loading due to the attachment struts and internal pressure from the propellant gases. A number of computer codes were considered for the analysis, but it was felt that the best tradeoff between accuracy and computer running time would be obtained by using BOSOR4. This computer code treats shells of revolution with provisions for branched shells by a finite-difference-energy minimization method.[D-1] Although the structure must be symmetric, the loading may be asymmetric but expandable in a Fourier series. The asymmetric solution is then obtained as a superposition of linear analyses for each harmonic.

BOSOR4 MODEL

The BOSOR4 model for the aft SRB attachment frame is shown in Figure D-3 with the transverse displacement nodal points indicated with lines. The branched portion (ring frame) is treated as a shell of revolution. There are a total of 319 mesh points in the ten segments of the structure. The length of the skin was chosen to avoid introduction of "short shell" effects at the boundary; i.e., bending due to loading dampens out before reaching the boundary, thereby eliminating concern over the imposed boundary conditions. The boundary conditions imposed on the model are no in-plane displacements at the two ends of the structure. The restriction on circumferential displacement maximizes the shear stress in the motor casing.

The application of the attachment loads to the SRB involved a number of approximations. First, the point loading from the attachment strut had to be spread out circumferentially because of the harmonic analysis. Second, the channel between the rings could not be included in the BOSOR analysis because of their asymmetric locations. Therefore, the load at each circumferential location was divided equally between the two rings. Third, to accommodate loads at three circumferential locations within the restrictions of the BOSOR structure (harmonics and load function definition) the loads on the rings were applied as line loads in the circumferential direction. A typical circumferential distribution of the load is shown in Figure D-4. The radial location of the three attachment loads was nominally 78 inches.

[D-1] Bushnell, David, "Stress, Stability, and Vibration of Complex Branched Shells of Revolution: Analysis and User's Manual for BOSOR4," LMSC-D243605, Mar 1972.

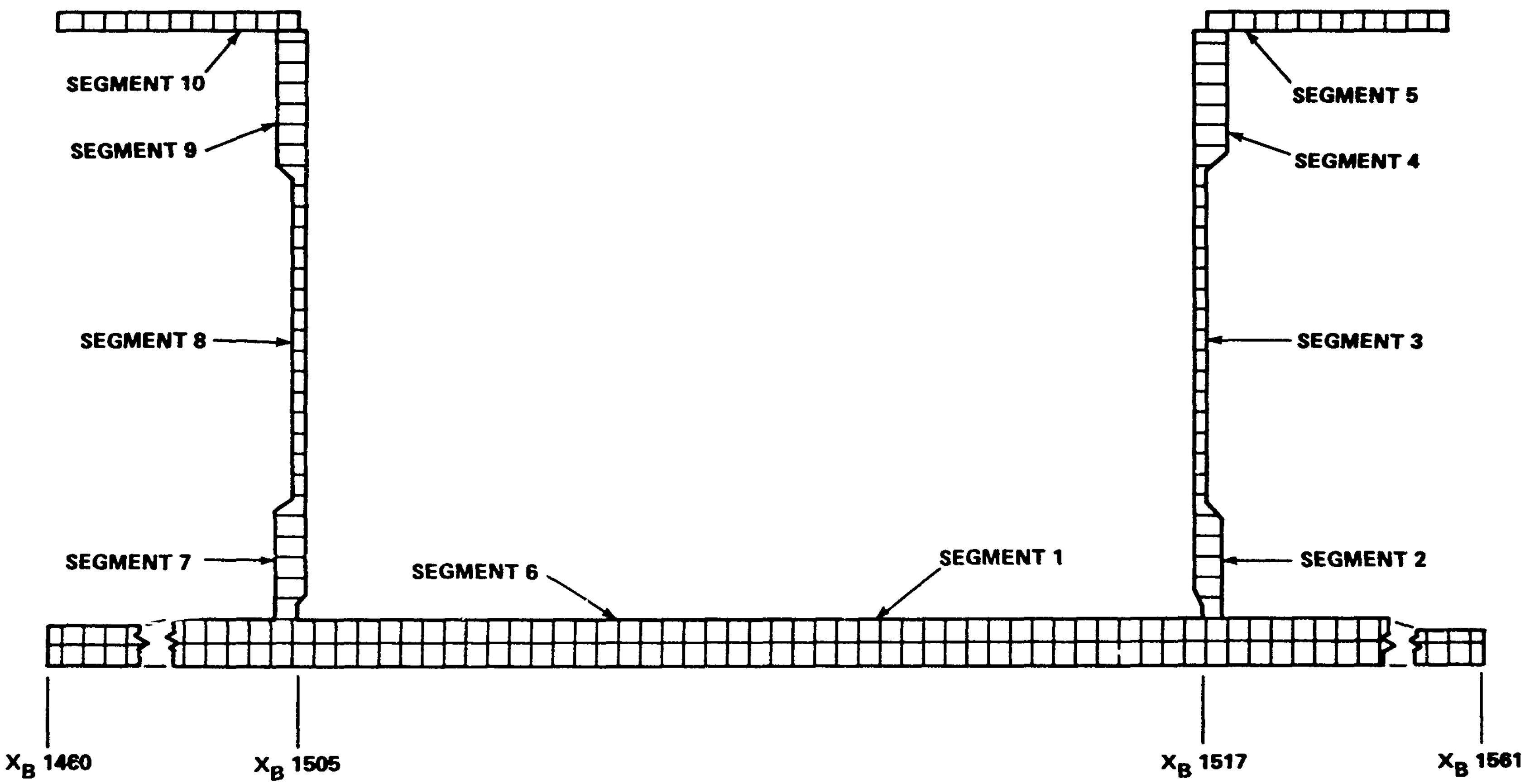

FIGURE D-3 BOSOR4 MODEL OF AFT SRB ATTACHMENT

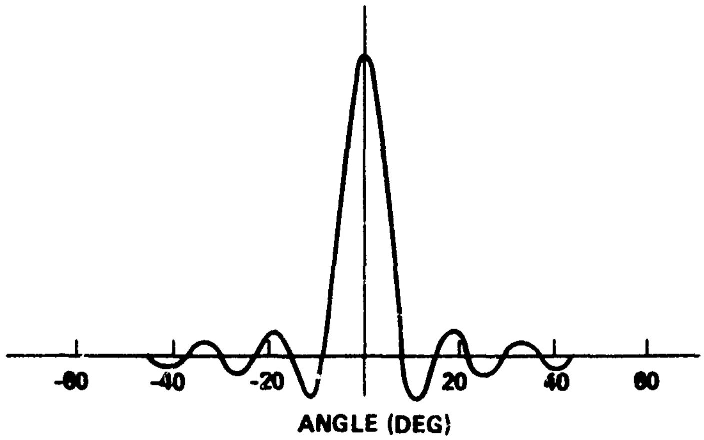

FIGURE D-4 LINE LOAD DISTRIBUTION APPROXIMATING 10-DEGREE TRIANGULAR DISTRIBUTION WITH 25 HARMONICS

CHECK CASE

As a check case for the structural model, the lift-off loads given in a Thiokol report were applied to the model and the results were compared.[D-2] The following loads were used:

$P_1 = 171,040$

$P_2 = 237,600$

$P_3 = 20,865$

where P_1, P_2, and P_3 are defined in Figure D-5. In addition, an internal pressure of 900 psi was applied. The comparison of outer hoop stress along a meridian intersecting the maximum load P_2 is quantitatively good, but Thiokol's results are larger in magnitude. Thiokol reports the maximum stress in the ring web as 185,000 psi, whereas the present analysis gives a 159,000 psi maximum stress. The load application method and number of harmonics used in the Thiokol analysis is unknown. Bushnell discusses the variation in stress due to insufficient harmonics.[D-3] Twenty-five harmonics were used to represent the triangular load of ten-degree circumferential span in this analysis.

[D-2] Kapp, J.R., Daines, J.V., and Anderson, E., "Stress Analysis Report for the Structural Elements of the SRM," Thiokol Chemical Corporation, Wasatch Division, Brigham City, Utah, TWR-10435, 18 Mar 1975.

[D-3] Bushnell, David, "Thin Shells," Structural Mechanics Computer Program, eds. Pilkey, W., Saczalski, K., and Schaeffer, H.. University of Virginia, 1974.

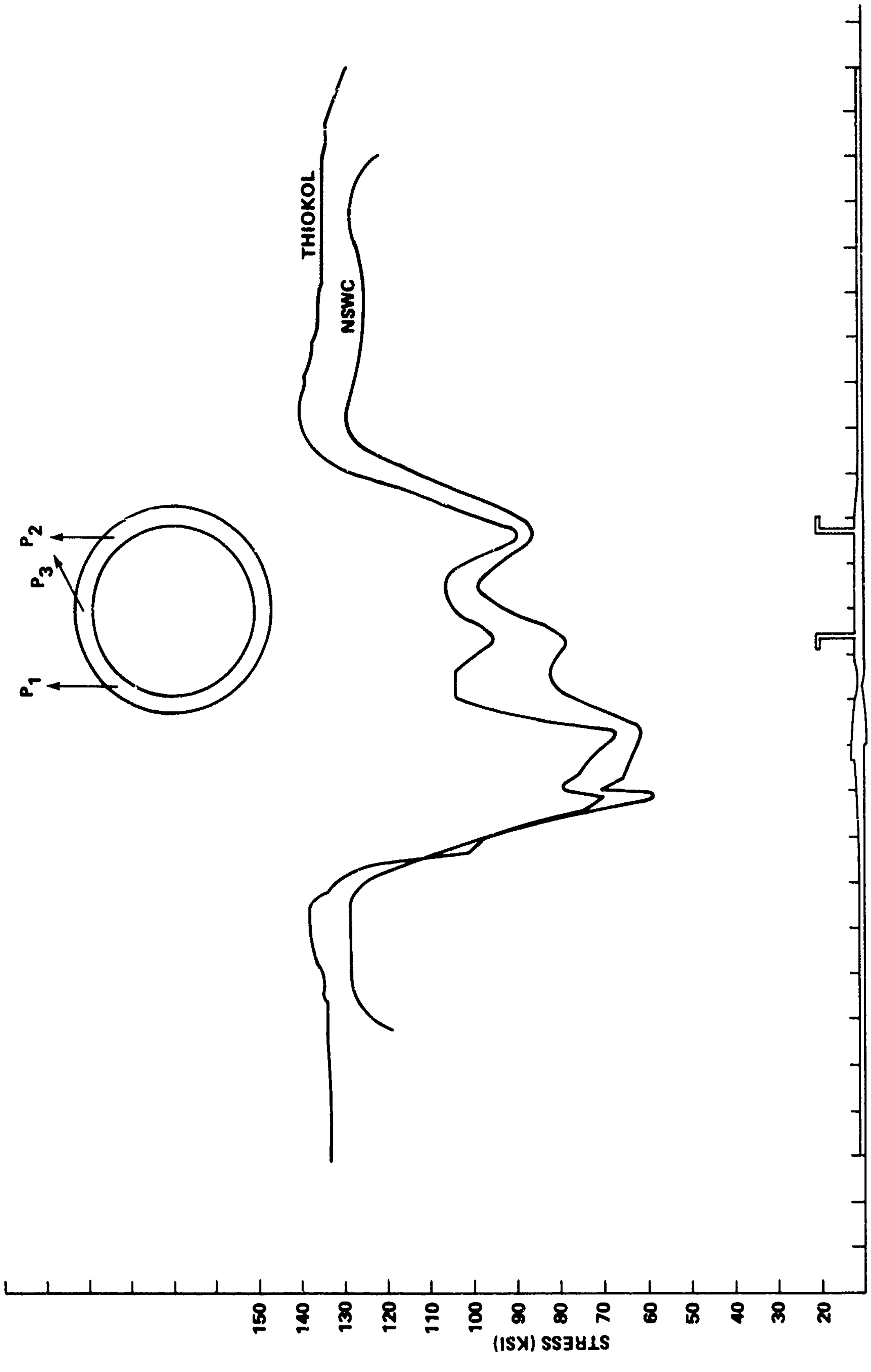

FIGURE I-5 HOOP STRESS DISTRIBUTION ALONG MERIDIAN INTERSECTING P2

APPENDIX E

FINITE ELEMENT MODEL OF ET INTERTANK

INTRODUCTION

A finite element model of the external tank (ET) intertank was formed using CTRIA2 plate elements containing membrane and bending stiffness to represent the skin, CBAR bar elements to represent the SRB beam, and CBAR offset bar elements to represent the stringers and ring frames. This intertank model, consisting of 1509 elements with 2788 degrees of freedom (DOF), was solved in Rigid Format 1 for various types of loadings to obtain the stresses, forces, deflections, and bending moments throughout the structure. A summary of results for the different destruct conditions is presented in Table E-1.

INTERTANK DESCRIPTION

The ET consists of three elements which can be physically separated, as schematically shown in Figure E-1. The forward element of the external tank is the liquid oxygen tank which is assembled to the intertank. The intertank provides the support points for the forward external tank (ET)/solid rocket booster (SRB) attach fittings.

The intertank is constructed of 7075 aluminum, consisting of a monocoque cylindrical shell 331 inches in diameter and 277.1 inches in length, supported by five ring frames and a cross beam (Fig. E-2). The shell varies in thickness. The heaviest regions are close to the SRB attachments, where the thickness is 2 inches. The shell thickness decreases to 0.071 inches in the sector located 90 degrees from this region, as indicated in Figure E-3. Five ring frames support the shell. The heaviest frame, a built-up I-section, is located at station X_T 985.70. This ring frame also couples to the cross beam extending between the SRB forward attach points (Fig. E-4). The cross beam carries the radial components of the loads applied by the SRB's. The four intermediate frames are located approximately equidistant along the length.

FINITE ELEMENT MODEL OF INTERTANK

The intertank model of the ET is shown in Figure E-5, a NASTRAN-generated plot of the shell and the cross beam. Plate elements (CTRIA2) containing membrane and bending stiffness are used to represent the outer skin. Bar elements (CBAR) are used to represent the cross beam, the ring frames, and the external stringers. The bar elements representing the ring frames (Fig. E-6) are offset from grid points in the shell. Similarly, the stringers (Fig. E-7) are offset from grid points in the shell. However, more stringers than grid points exist in the circumferential direction. Therefore, the properties of several stringers are lumped into each bar element.

TABLE E-1 SUMMARY OF RESULTS

Condition	F_{TB3}	F_{TB4}	F_{TB5}	F_{TB6}	Cross Beam		Frame		Skin	D_{max}	Applied Loading	K
					P_A	f_{max}	M_{max}	σ_{max}	f_{max}			
Nominal Destruct	550K (lb)	-550K (lb)	0 (lb)	0 (lb)	0 (lb)	0 (psi)	6.73 $(10)^6$ (in/lb)	16.7 $(10)^4$ (psi)	8.77 $(10)^4$ (psi)	4.0 (in)	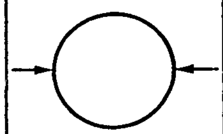	0.137×10^6
Nominal Destruct	550K	-550K	0	0	0.508 $(10)^6$	19,200	0.455 $(10)^6$	1.55 $(10)^4$	0.42 $(10)^4$	.273	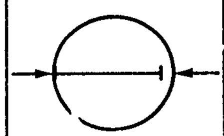	2.016×10^6
Nominal Destruct	550K	-550K	-350K	-350K	0.495 $(10)^6$	1.86 $(10)^4$	0.51 $(10)^6$	1.443 $(10)^4$	51.9 $(10)^4$	.2264	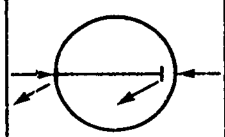	2.06×10^6
Destruct (Loss of one SRB)	0	-550K	0	-0.37 $(10)^6$	0.249 $(10)^6$	0.995 $(10)^4$	3.0 $(10)^6$	7.95 $(10)^4$	2.78 $(10)^4$	1.39	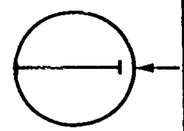	0.4×10^6

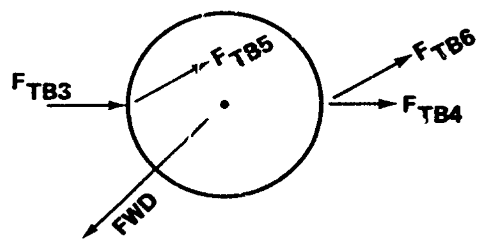

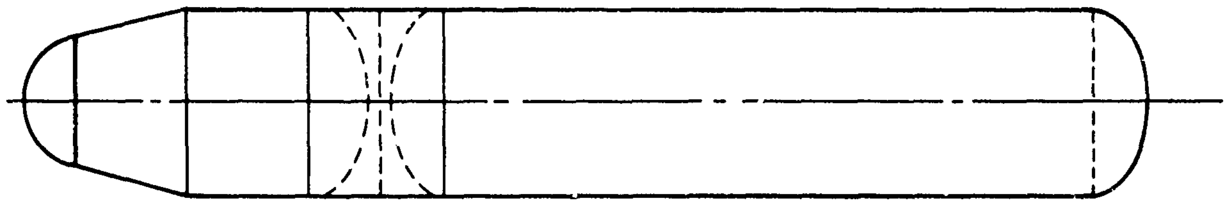

FIGURE E-1 ELEMENTS OF SPACE SHUTTLE ET

A NASTRAN preprocessor BINC (Missile Body Input Generator) was used to generate the finite element model of the outer shell.[E-1] This program generates axisymmetric shell models and punches NASTRAN bulk data cards. Minor changes were made in the model to adjust the thickness of the various elements.

The BANDIT computer program was used for the reduction of matrix bandwidth for NASTRAN.

The NASTRAN model was loaded for the following varying destruct conditions:

1. Nominal destruct without cross beam. Two radial loads, 550,000 pounds, equal in magnitude and opposite in direction were applied at the ET/SRB forward interface points.

2. Nominal destruct with cross beam.

   a. Two radial loads, 550,000 pounds, equal in magnitude and opposite in direction were applied at the interface points.

   b. Two axial loads, 350,000 pounds, equal in magnitude and in the forward direction were applied at the interface points together with the two radial loads in case 2a.

3. Destruct after the loss of one SRB, cross beam included. Axial and radial loads, 350,000 and 550,000 pounds, respectively, were applied at a single interface point.

[E-1] Huang, P.C., and Matra, J.P., Jr., "Missile Body Input Generator (BING), A NASTRAN Pre-Processor, Theoretical Development, User's Manual, and Program Listing," NSWC/WOL/TR 75-9, Mar 1975.

INTERTANK SUMMARY

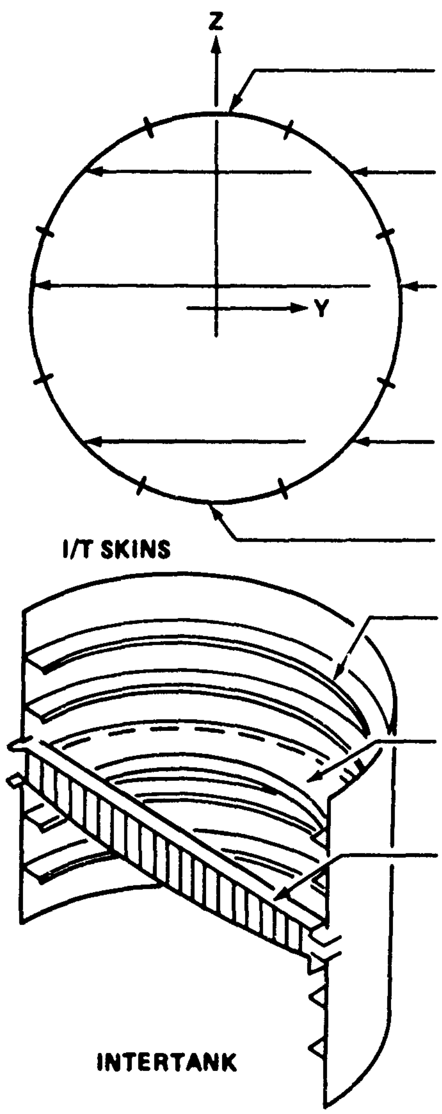

COMPONENT	DESIGN CONDITION
PANEL 1	LIFT-OFF
PANELS 2 AND 3	MAX SRB
PANELS 4 AND 5	MAX SRB (FWD) POST STAGING (AFT)
PANELS 6 AND 7	MAX SRB
PANEL 8	LIFT-OFF
INTERMEDIATE FRAMES	MAX SRB
985 RING	LIFT-OFF
SRB BEAM	1) MAX SRB 2) STIFFNESS CRITERIA – CLEARANCE WITH TANK BULKHEADS REQ'D

FIGURE E-2 INTERTANK CONSTRUCTION

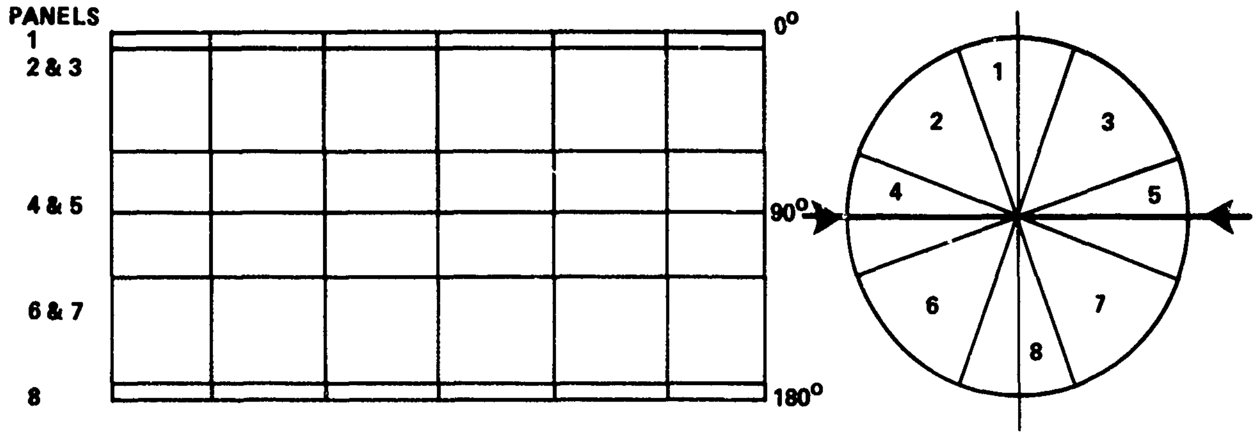

THICKNESS	PANEL
0.090	1
0.080	2 & 3
0.080	6 & 7
0.071	8

FWD ←

<table>
<tr><td rowspan="2">0.34</td><td rowspan="2">0.37</td><td rowspan="2">0.34</td><td>0.21</td><td>0.21</td><td>0.21</td><td>0.21</td><td rowspan="2">0.31</td><td rowspan="2">0.24</td><td rowspan="2">0.18</td></tr>
<tr><td>0.44</td><td>0.44</td><td>0.44</td><td>0.44</td></tr>
<tr><td rowspan="2">0.26</td><td rowspan="2">0.54</td><td rowspan="2">1.06</td><td>1.2</td><td>1.2</td><td>1.2</td><td>1.04</td><td rowspan="2">0.54</td><td rowspan="2">0.25</td><td rowspan="2">0.14</td></tr>
<tr><td>2.0</td><td>2.0</td><td>1.17</td><td>1.08</td></tr>
<tr><td rowspan="2">0.26</td><td rowspan="2">0.54</td><td rowspan="2">1.06</td><td>2.0</td><td>2.0</td><td>1.17</td><td>1.08</td><td rowspan="2">0.54</td><td rowspan="2">0.25</td><td rowspan="2">0.14</td></tr>
<tr><td>1.2</td><td>1.2</td><td>1.2</td><td>1.04</td></tr>
<tr><td rowspan="2">0.34</td><td rowspan="2">0.37</td><td rowspan="2">0.34</td><td>0.44</td><td>0.44</td><td>0.44</td><td>0.44</td><td rowspan="2">0.31</td><td rowspan="2">0.24</td><td rowspan="2">0.18</td></tr>
<tr><td>0.21</td><td>0.21</td><td>0.21</td><td>0.21</td></tr>
</table>

PANELS 4 AND 5 SKIN

FIGURE E-3 INTERTANK SKIRT SKIN THICKNESS

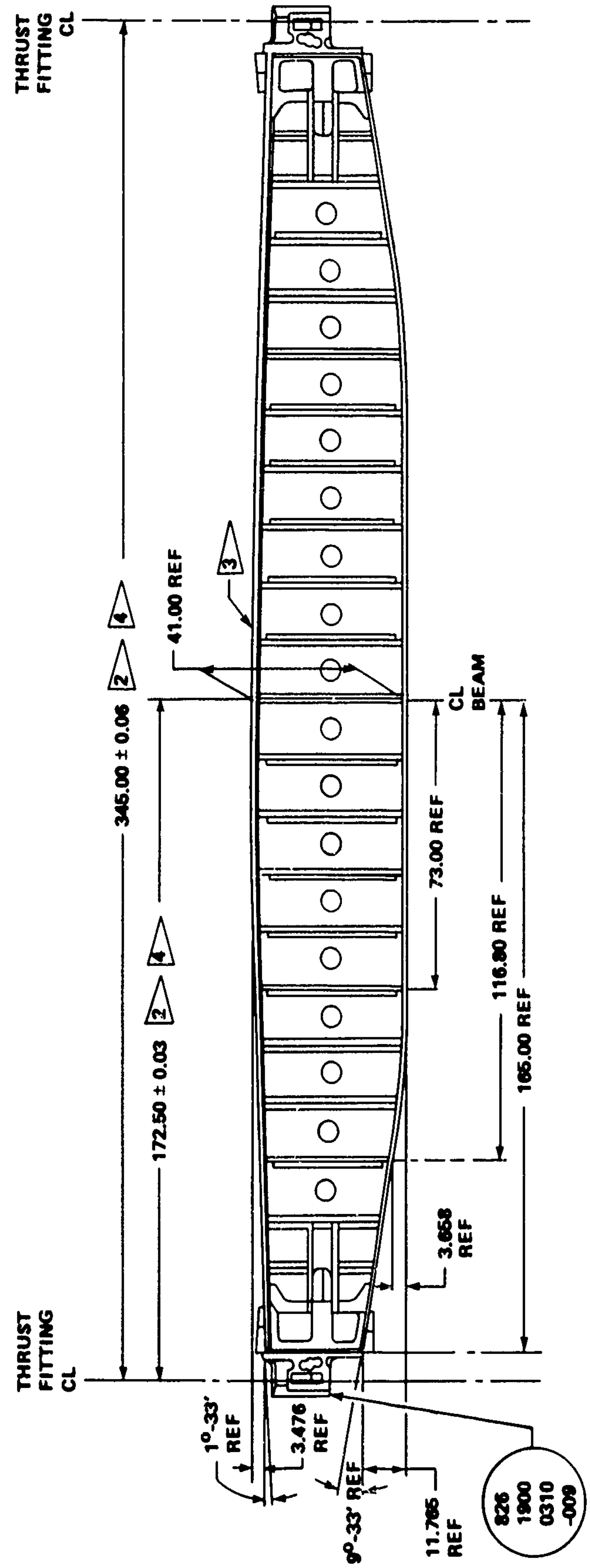

FIGURE E-4 INTERTANK CROSS BEAM

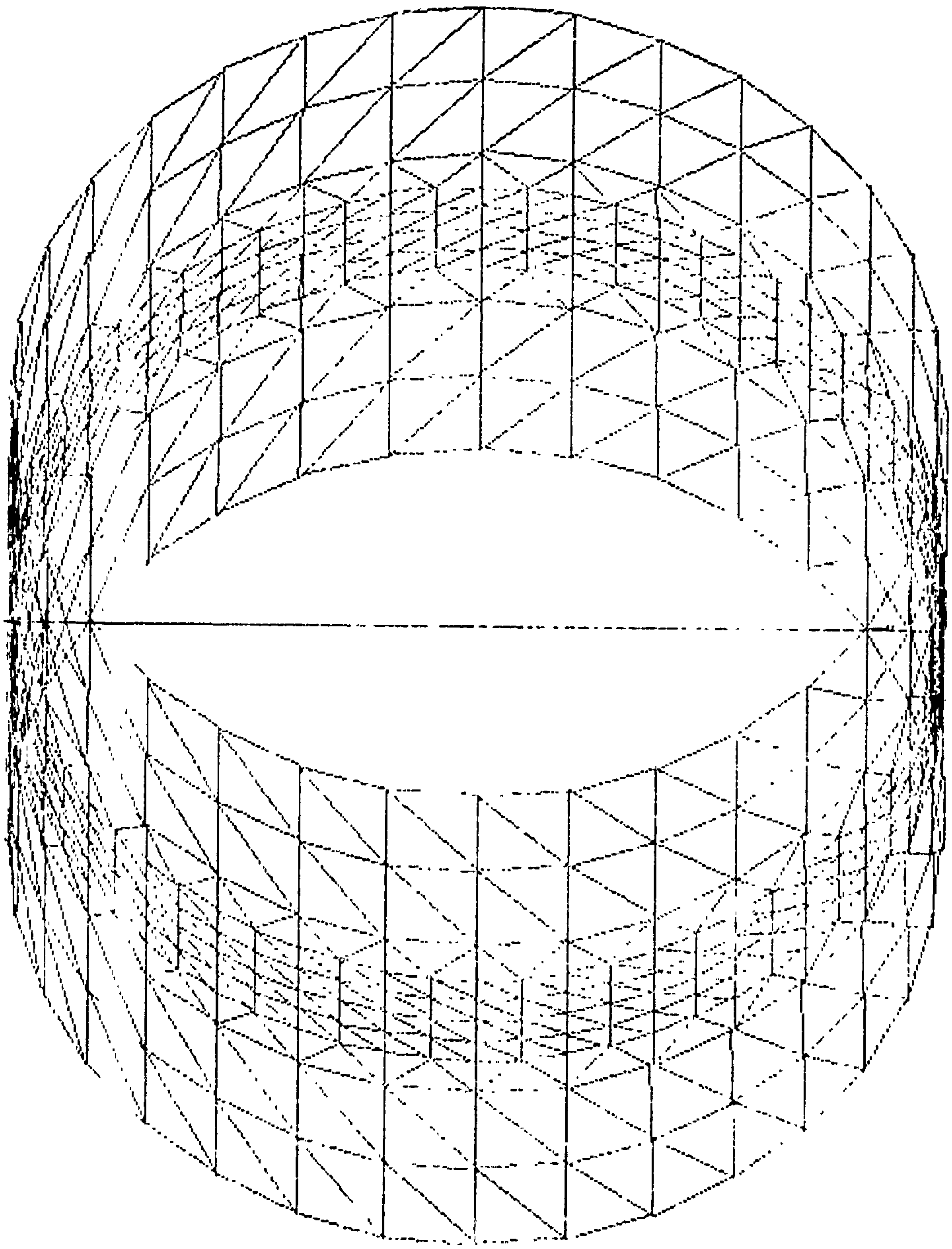

FIGURE E-5 FINITE ELEMENT MODEL OF INTERTANK

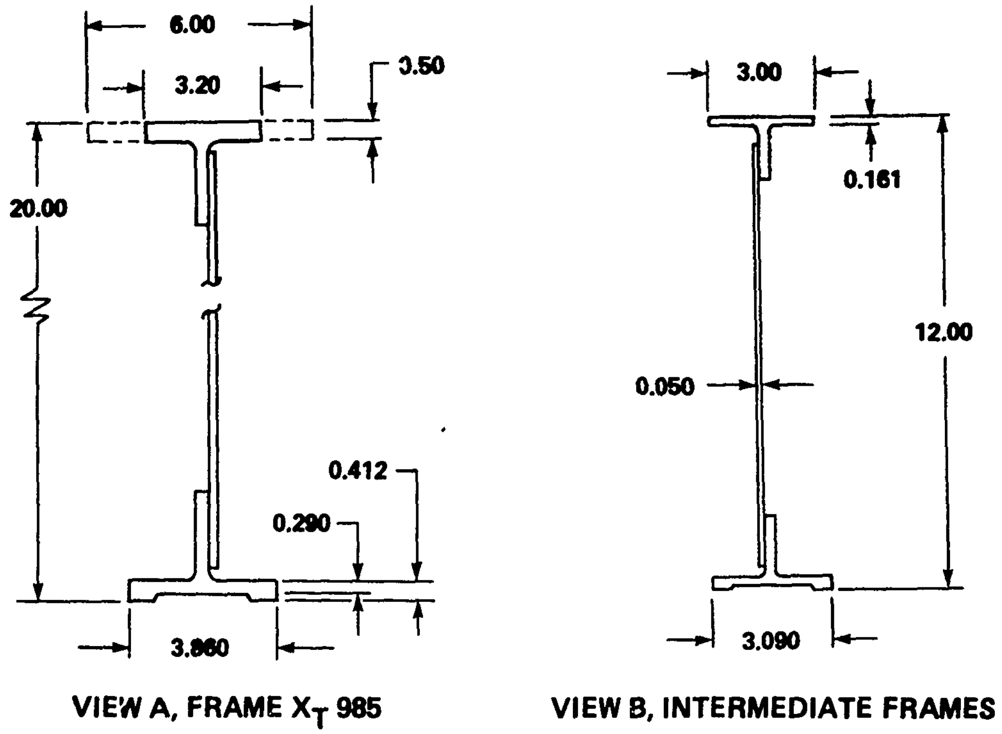

FIGURE E-6 INTERTANK RING FRAMES

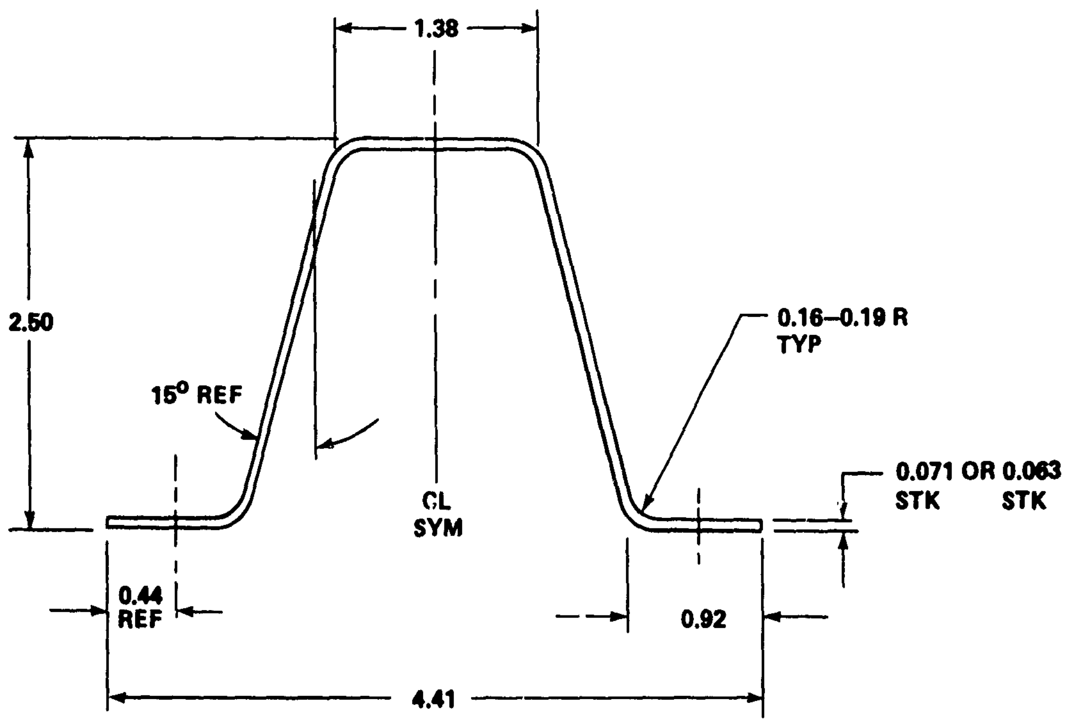

FIGURE E-7 TYPICAL INTERTANK STRINGER

DISCUSSION AND RESULTS

In order to obtain a guide for the accuracy of the NASTRAN program and the adequacy of the intertank finite element model, a check case was run to compare the NASTRAN results with the approximate solution from NACA TN 1310.[E-2] The results from the technical note are given in chart form so they can be obtained rather readily.

In the check case, it was assumed that the lateral strut buckled and the NASTRAN finite element model with the loading of Case 1 was applicable. The intertank was given fixed boundary conditions at both ends.

A comparison of results for the bending moment in the heavy ring frame located at station X_T 985.7 is presented in Figure E-8. The results compared very well. In addition, the comparison provided some results for the special case where the lateral strut had buckled.

The buckling strength of the cross beam was estimated as follows:

Average I about vertical neutral axis = 679.7 in^4

Average Cross Sectional Area = 26.8 in^2

$$\text{Average radius of gyration} = \frac{I}{A}$$

$$= 50.36 \text{ in}^2$$

$$\frac{L}{\rho\sqrt{c}} = \frac{345}{5.036} = 68.5$$

$$\sigma_{cr} = \frac{{}^2E}{\left(\frac{L}{\rho\sqrt{c}}\right)^2} = 21{,}000 \text{ psi}$$

$$P_{cr} = \sigma_{cr} A = 21{,}000 \times 26.8 \approx 560{,}000 \text{ lb}$$

NASTRAN runs were executed for Cases 2a, 2b, and 3. For these cases, the aft boundary was freed while the forward boundary remained fixed. Results are presented in the summary, Table E-1. Plots of the undeformed and deformed model are shown in Figures E-9 and E-10. A plot of the deformed ring frame directly under the applied loads is shown in Figure E-11.

[E-2] Kempner, J., and Duberg, J.E., "Charts for Stress Analysis of Reinforced Circular Cylinders Under Lateral Loads," NACA TN 1310, National Advisory Committee for Aeronautics, May 1947.

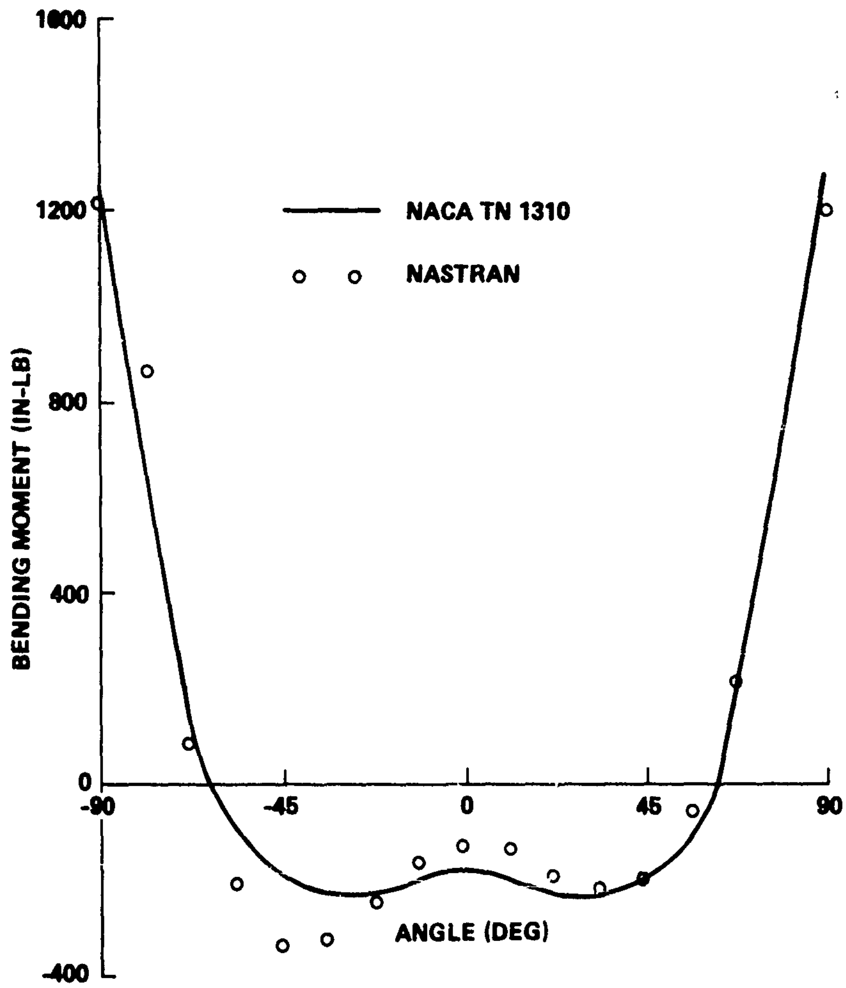

FIGURE E-8 TEST CASE — BENDING MOMENT IN FRAME X_T 985.7

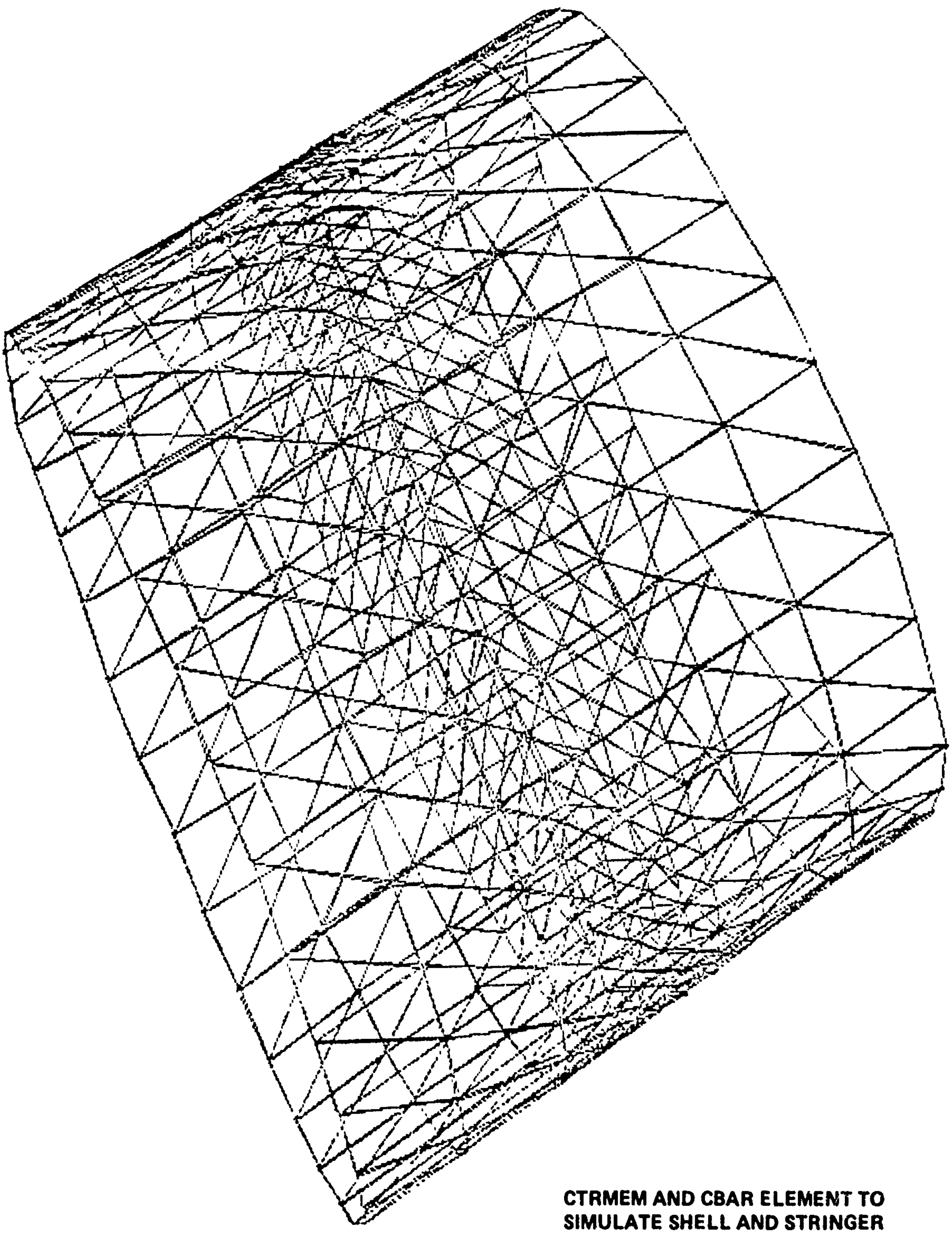

FIGURE E-9 UNDEFORMED SHAPE

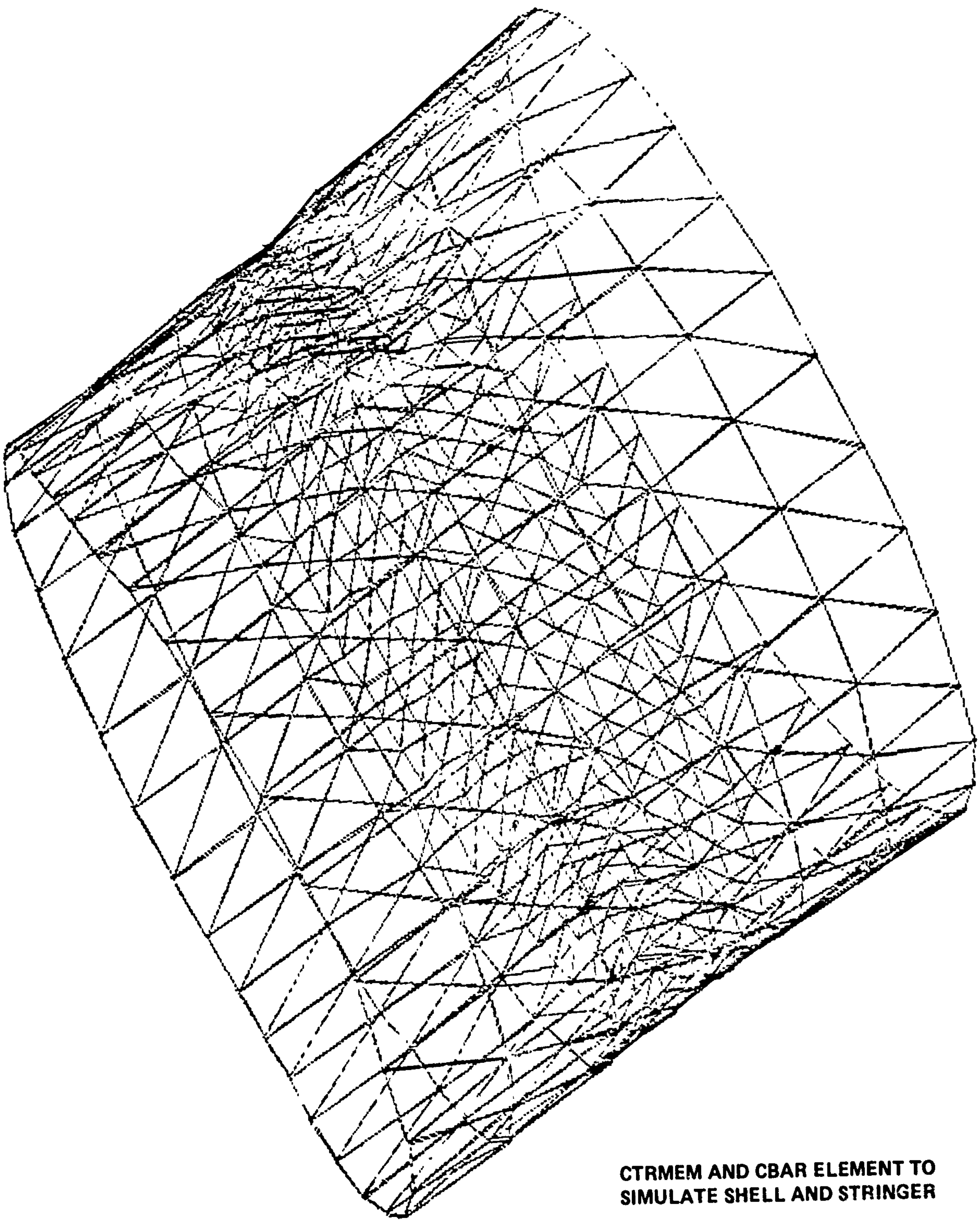

FIGURE E-10 STATIC DEFORMATION

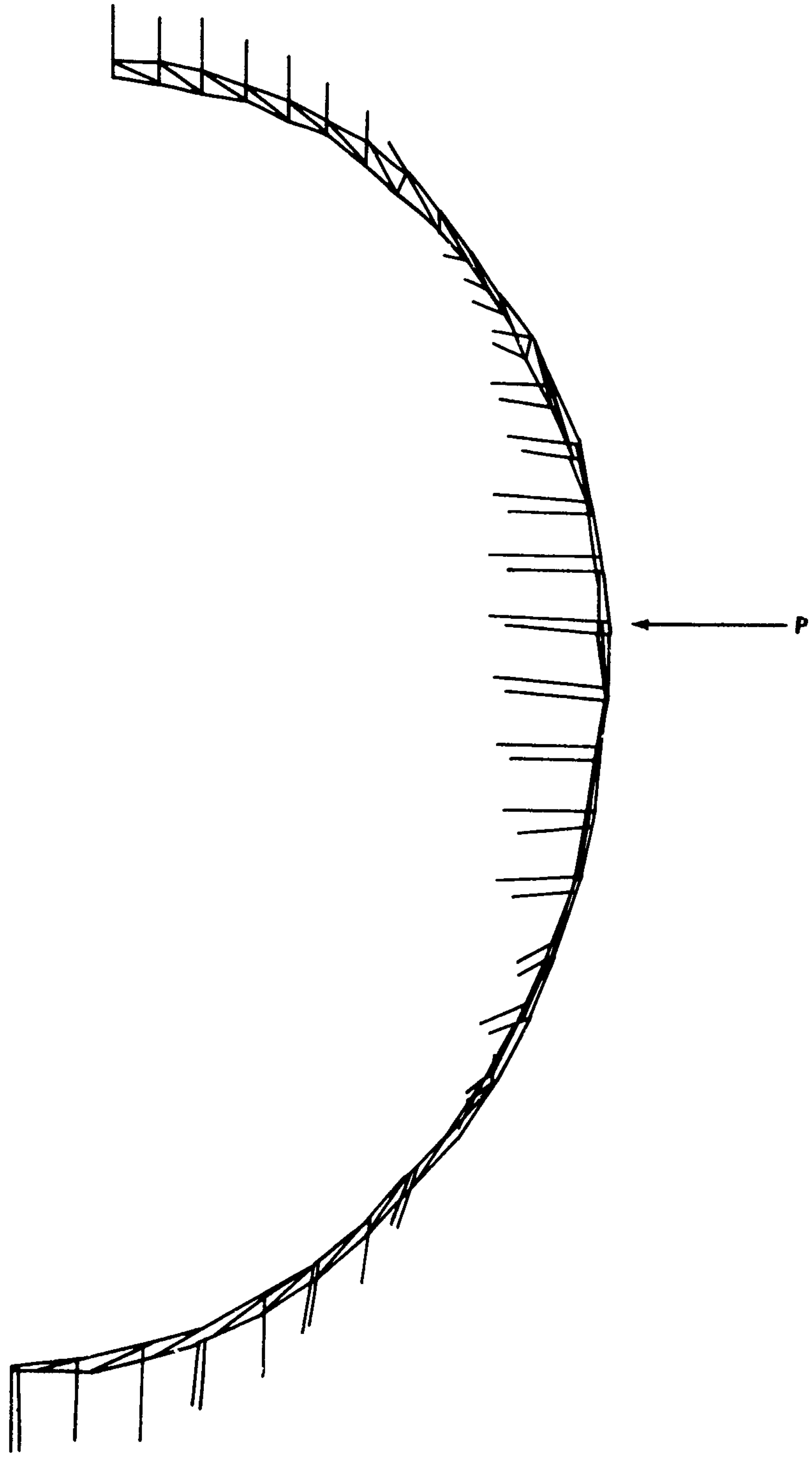

FIGURE E-11 DEFORMED SHAPE – FRAME X_T 985

APPENDIX F

FINITE ELEMENT MODEL OF SRB FORWARD SKIRT

INTRODUCTION

A finite element model of the forward skirt of the solid rocket booster (SRB) was formed using CTRIA2 plate elements containing membrane and bending stiffness and CBAR offset bar elements to represent the longerons and frames. Three layers of CIS3D8, three-dimensional, eight-node, isoparametric elements were used to model the SRB thrust past fitting. This model, consisting of 837 elements with 2058 degrees of freedom (DOF), was solved in Rigid Format 1 to obtain the stresses, forces, deflections and bending moments throughout the structure.

The following results were obtained for combined radial and axial forces of 550,000 and 350,000 pounds, respectively, applied at the thrust post fitting:

- Max frame stress 100,000 psi
- Max frame bending moment 438,000 in-lb
- Max skin stress 27,300 psi
- Max deformation 0.67 in

DESCRIPTION OF SRB FORWARD SKIRT

The SRB consists of four parts, schematically shown in Figure F-1: a nose frustum, a forward skirt, a propellant cylinder, and an aft skirt. The forward skirt is designed to carry the SRB/ET attach fitting loads. It is constructed of aluminum formed as a semi-monocoque cylindrical shell, 145 inches in diameter and 125 inches in length (Fig. F-2). The skin varies in thickness from the basic 0.25 to 0.8 inch in vicinity of the thrust post fitting. The thrust post fitting is supported by a built-up box beam (Fig. F-3) to distribute the axial and radial loads along the length of the skirt. Five ring frames tie into the box beam to carry the radial load (Fig. F-4).

Longerons tie frames A and B together. Frame C is interrupted at the access port. Longerons also tie frames B, C, and D together along the edges of the port. The access port cover and two smaller covers are securely fastened and assumed to be structurally equivalent to the skin.

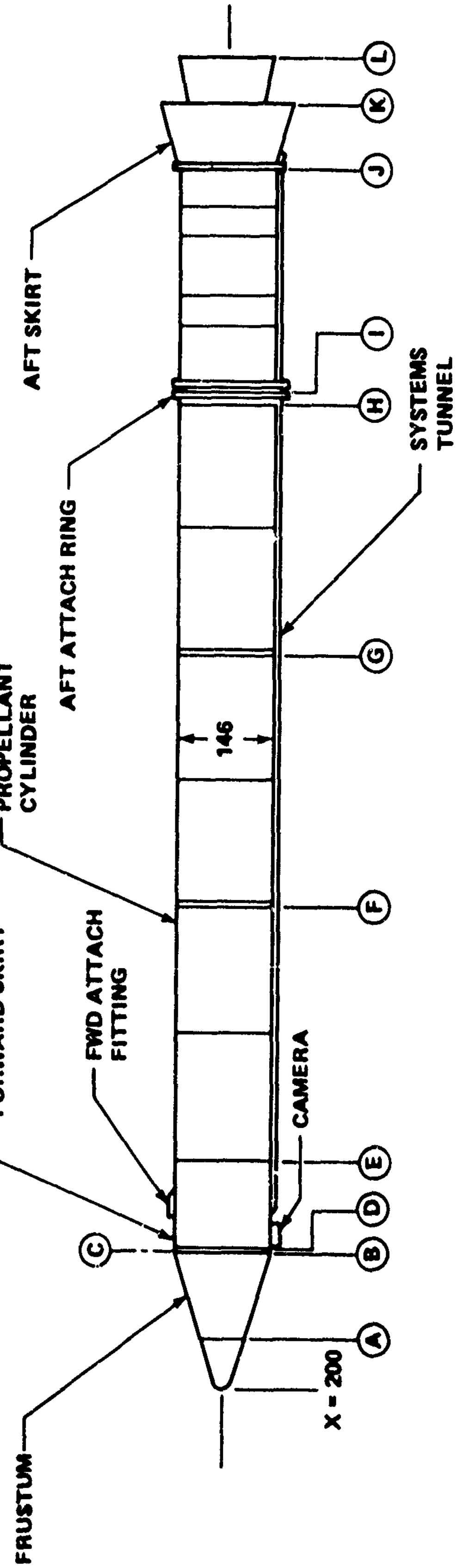

FIGURE F-1 COMPONENTS – SOLID ROCKET BOOSTER

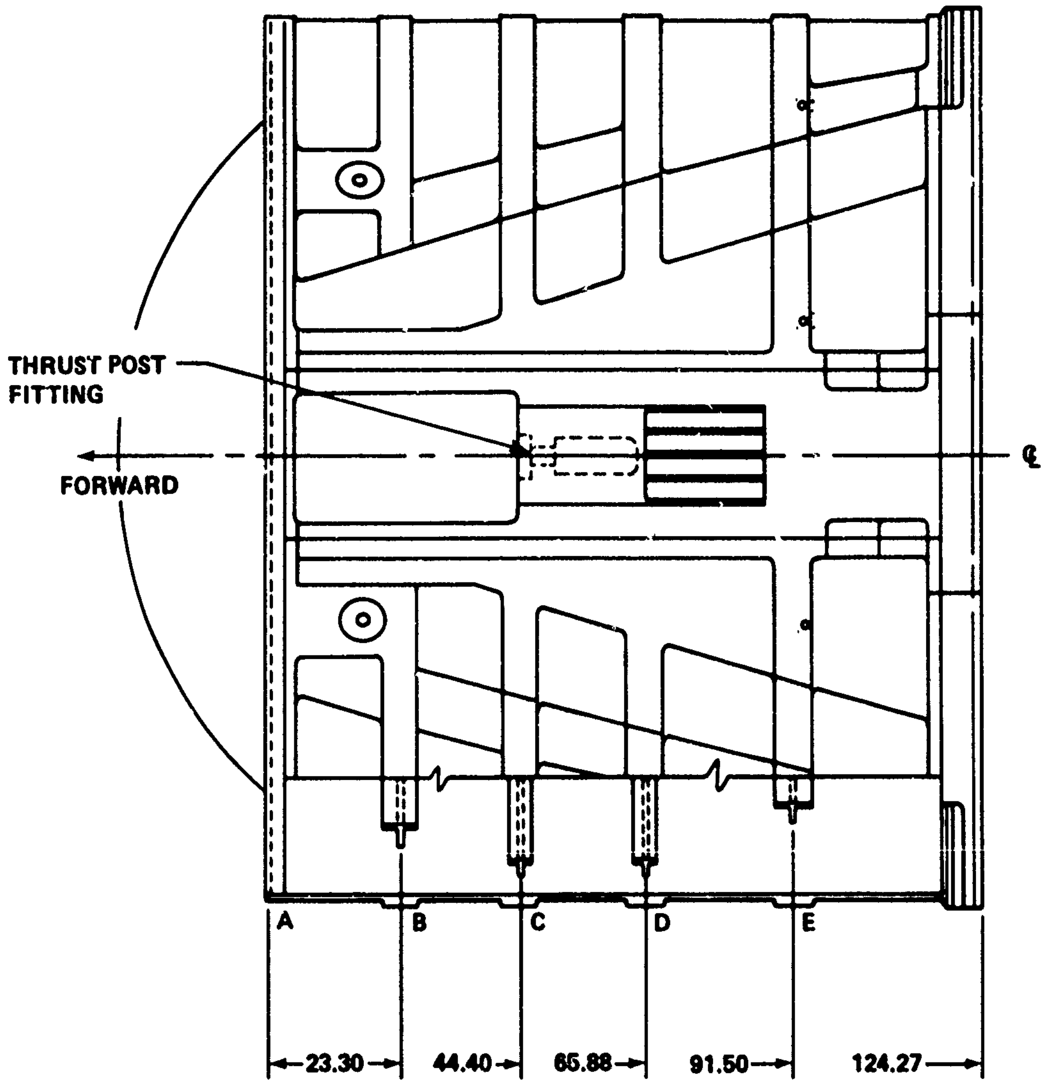

FIGURE F-2 SRB FORWARD SKIRT

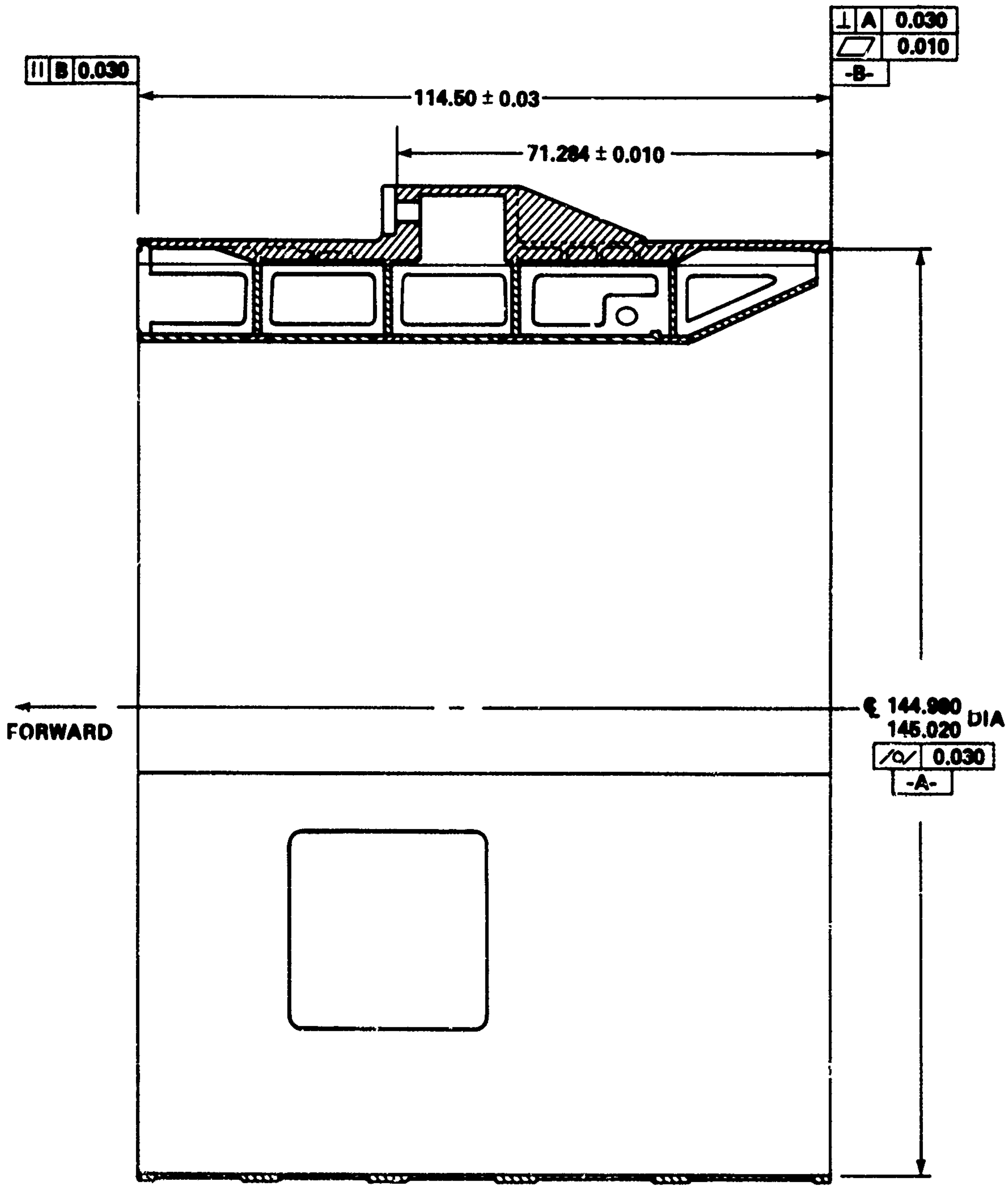

FIGURE F-3 THRUST POST FITTING AND BOX BEAM

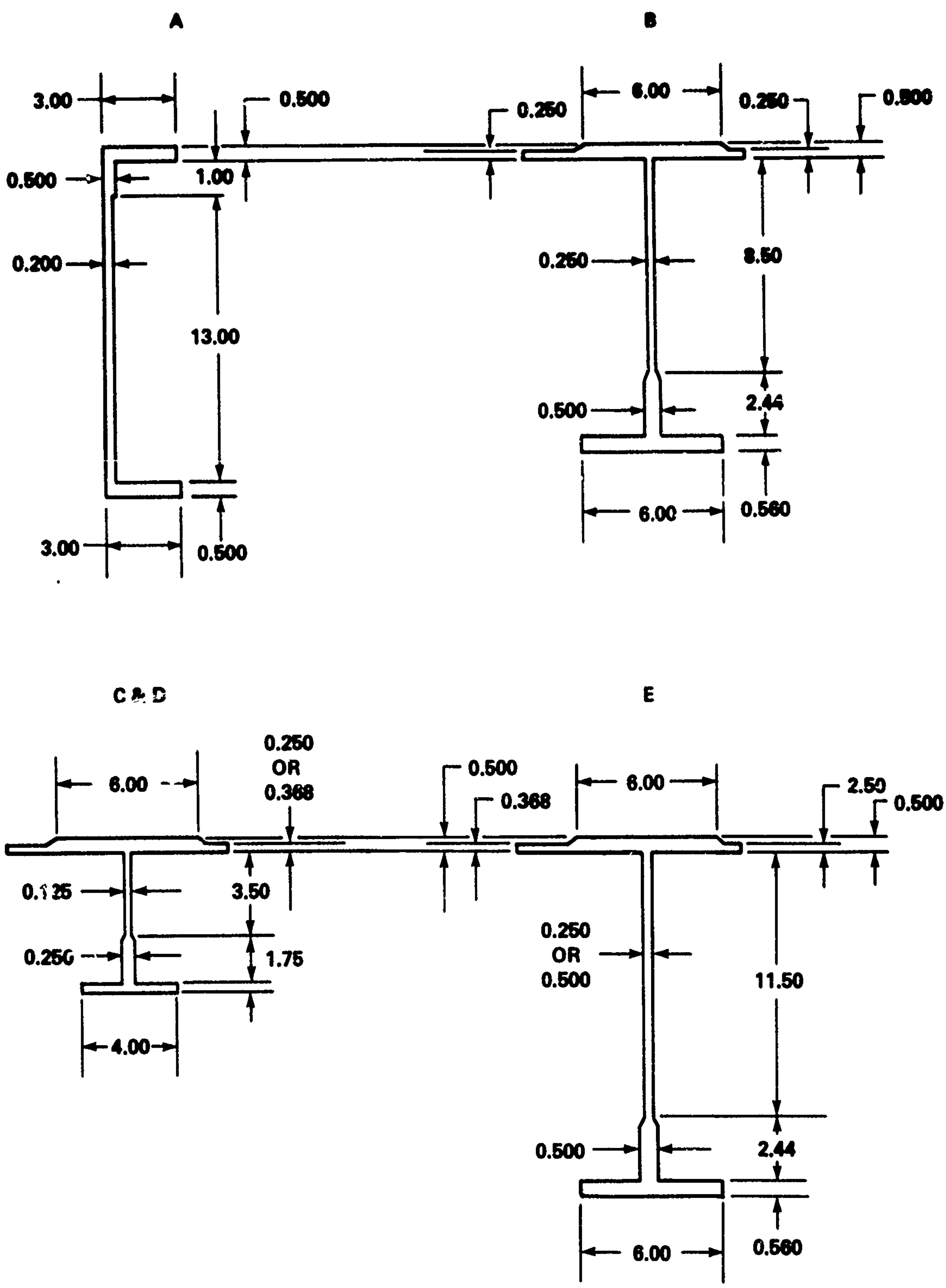

FIGURE F-4 RING FRAMES — FORWARD SKIRT

FINITE ELEMENT MODEL OF SRB

The forward skirt model of the SRB is shown in Figure F-5, a NASTRAN-generated plot of the outer shell and thrust post fitting. Plate elements (CTRIA2) containing membrane and bending stiffness are used to represent the outer skin. Offset bar elements (CBAR) are used to represent the frames and longerons. Figure F-6 presents a NASTRAN plot of the offset bar elements used. The dimensions used to model the frames and longerons are given in Figure F-4. Three-dimensional isoparametric elements (CIS3D8) and plate elements (CQUAD2 and CTRIA2) are used to model the thrust post fitting. The details of the thrust fitting are given in Figure F-7, and the corresponding finite element model is shown in Figure F-8. The primary purpose of using the 3-D isoparametric elements is proper distribution of the load to the remainder of the structure.

A NASTRAN preprocessor, Missile Body Input Generator (BING), was used to generate the finite element model of the outer shell. This program generates an axisymmetrical shell and punches NASTRAN bulk data cards. Minor changes were made in the shell model to adjust the thickness of the various elements. Since no attempt was made to number grid points in the most efficient sequence, the BANDIT Computer Program for the reduction of matrix bandwidth for NASTRAN was used for resequencing.

The NASTRAN model was loaded with radial and axial forces of 550,000 lb and 350,000 lb, respectively, applied at the thrust post fitting (Fig. F-5). The structure was given a free boundary condition at the forward end and a fixed boundary condition at the aft end. The undeformed model is shown in Figure F-5. The deformed model is shown in Figure F-9. A plot of the deformed ring frame at station X_B 445 is shown in Figure F-10.

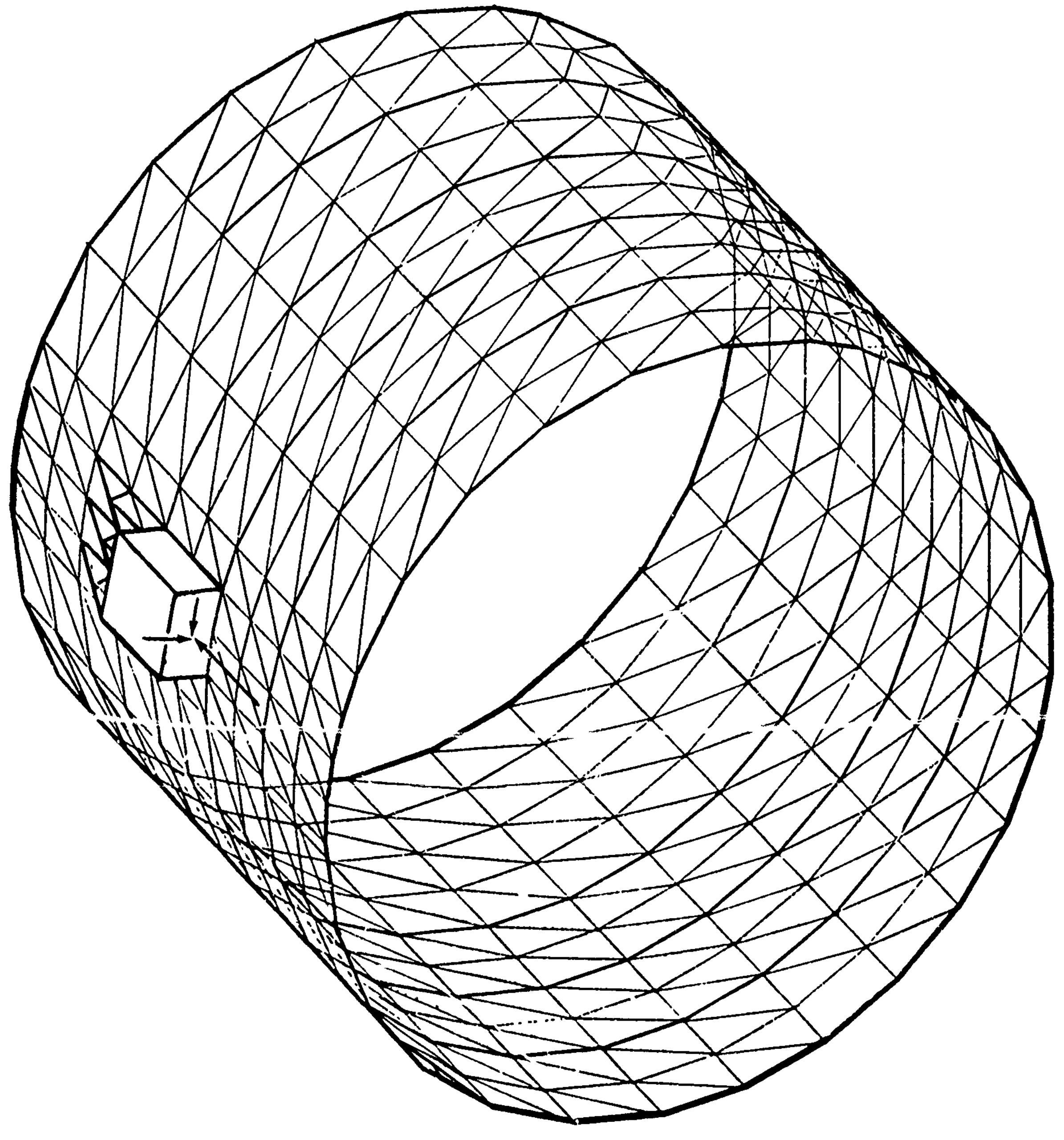

FIGURE F-5 FINITE ELEMENT MODEL OF FORWARD SKIRT

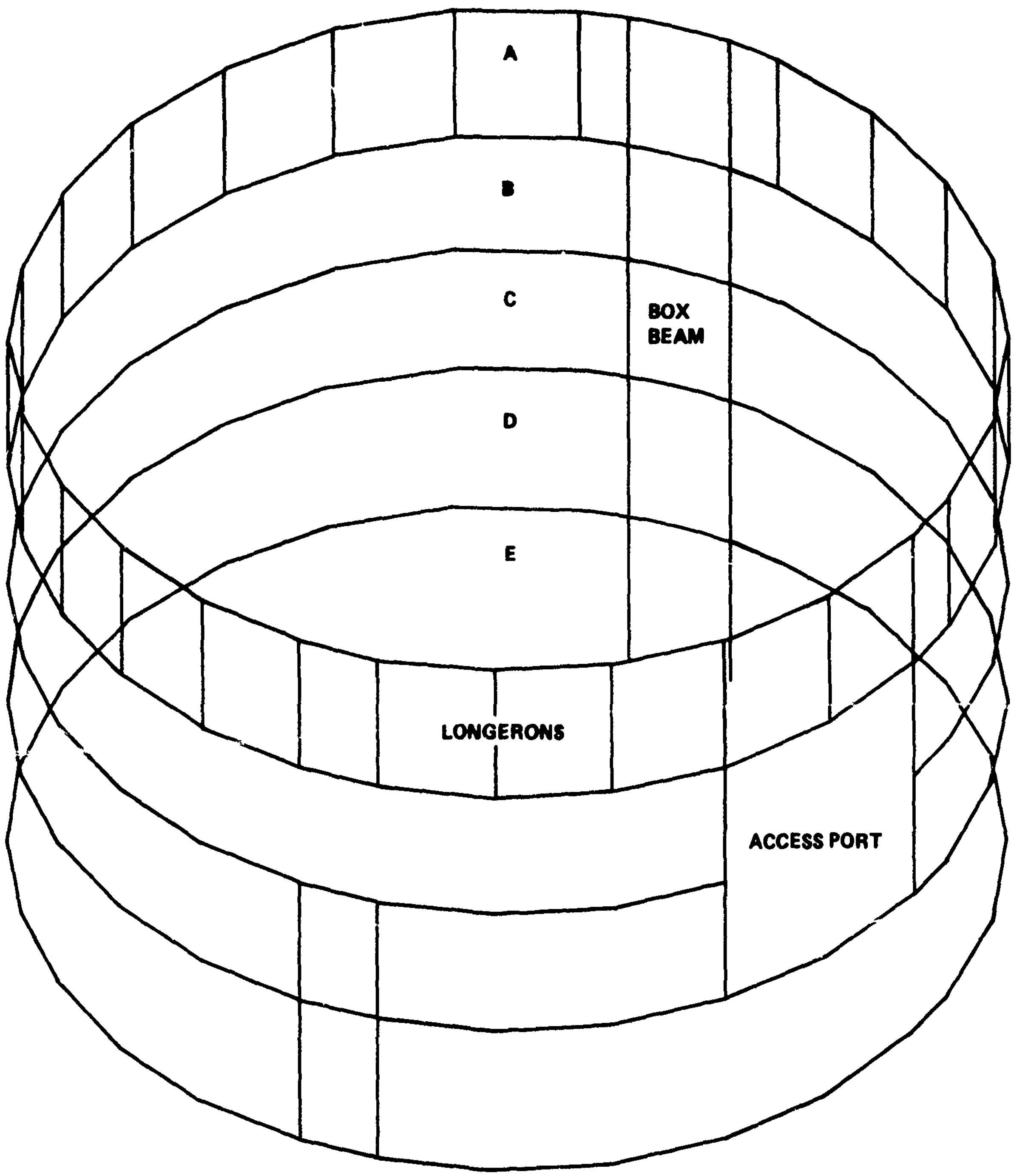

FIGURE F-6 FINITE ELEMENT MODEL OF RING FRAMES, BOX BEAM, AND LONGERONS

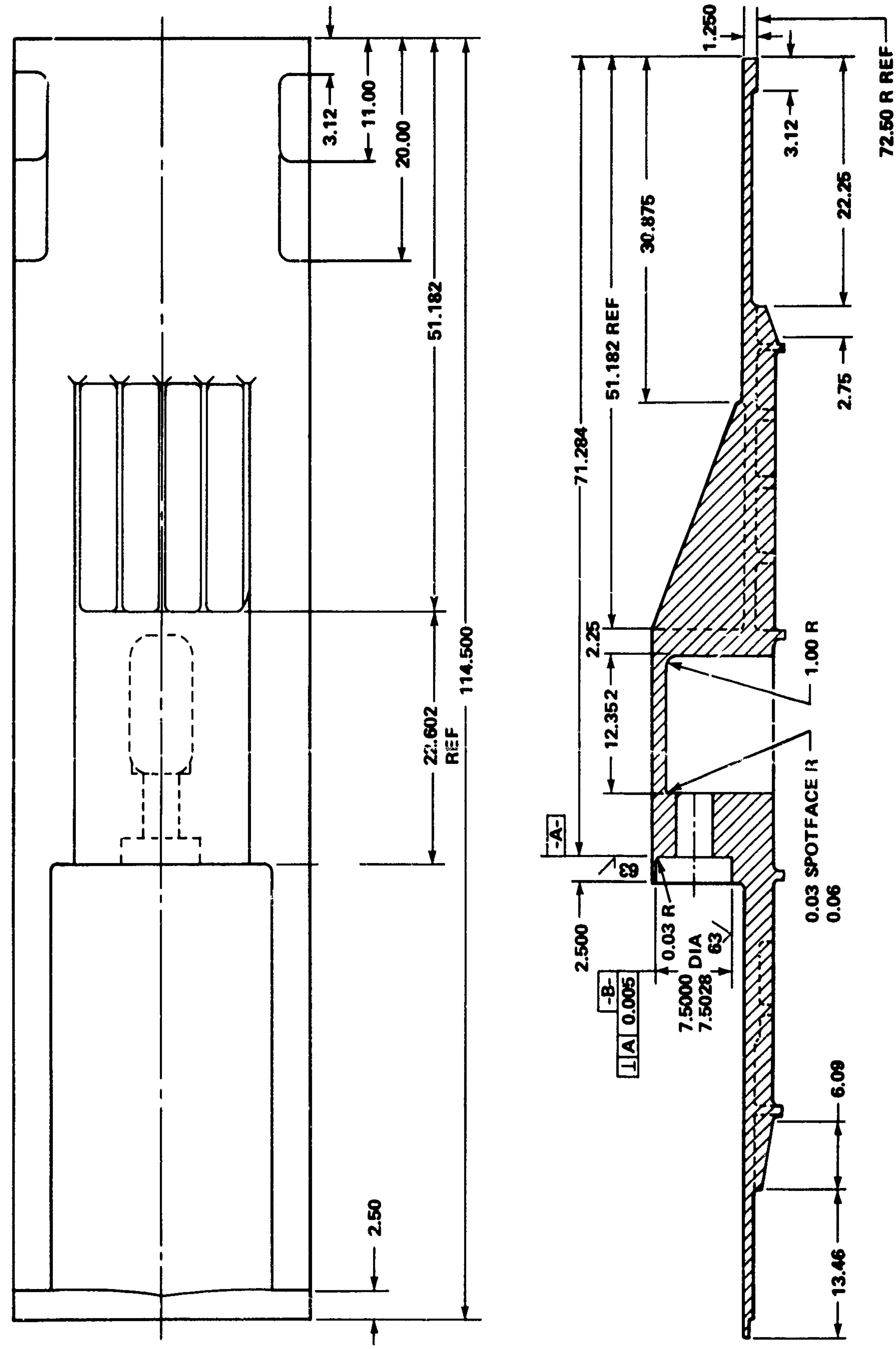

FIGURE F-7 THRUST POST FITTING

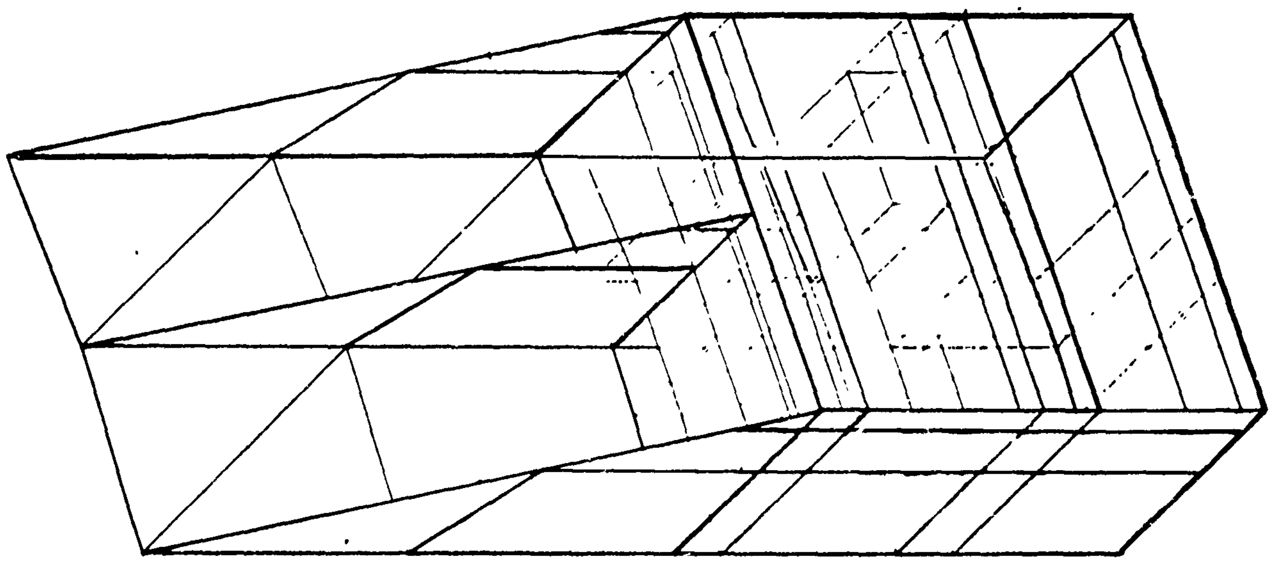

FIGURE F-8 FINITE ELEMENT MODEL OF THRUST POST FITTING

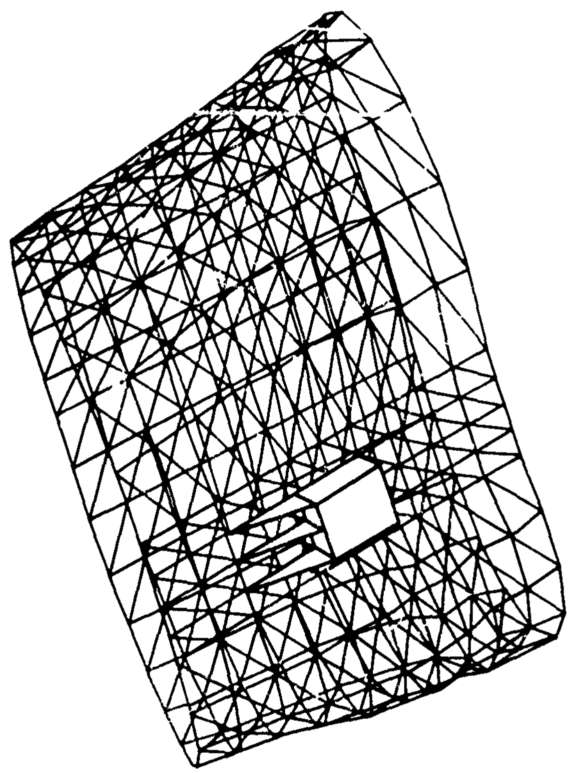

FIGURE F-9 DEFORMED SHAPE - AXIAL AND RADIAL LOADS

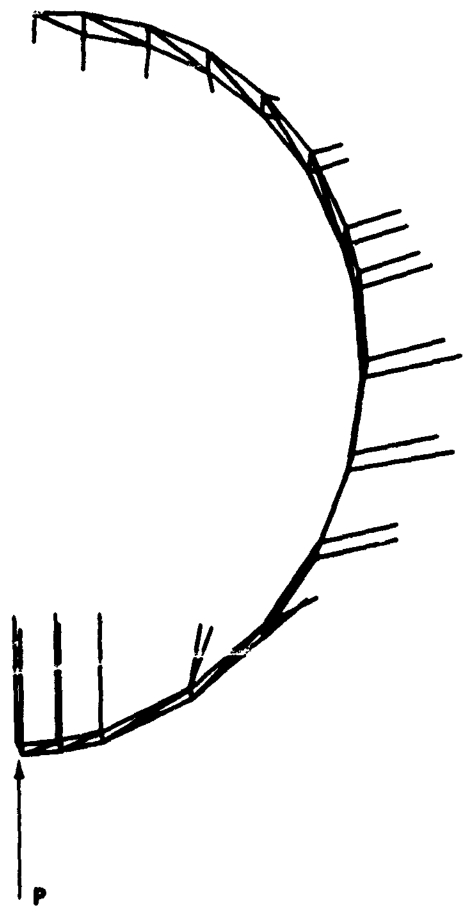

FIGURE F-10 DEFORMATION PATTERN — FRAME X_B 445

APPENDIX G

COLLAPSE OF A CIRCULAR FRAME DUE TO RADIAL LOADS

Several frames in the ET are loaded by equal and opposite radial loads, as shown below:

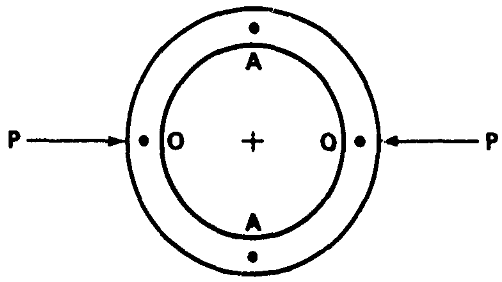

If we assume rigid plastic stress-strain behavior, an estimate of the collapse load can be made. Let us first compute the load P_y to yield the structure. By symmetry, we need only analyze 1/4 of the frame:

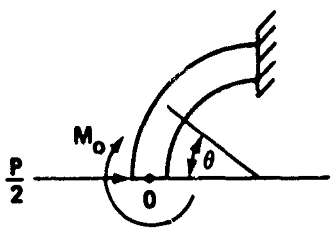

$$M = M_o \frac{P}{2} R (\sin \theta) \tag{G-1}$$

Using virtual work, the slope at the load is:

$$\theta = \int_0^{\pi/2} mM \frac{R d\theta}{EI} \tag{G-2}$$

where m is 1 in-lb couple. By symmetry, the slope at 0 must be zero. Hence,

$$\int_0^{\pi/2} \left(M_o - \frac{PR}{2} \sin \theta\right) d\theta = 0 \tag{G-3}$$

$$\left[M_o\theta + \frac{PR}{2}\cos\theta\right]_o^{\pi/2} = 0$$

$$M_o \frac{\pi}{2} - \frac{PR}{2} = 0$$

$$M_o = \frac{PR}{\pi} \simeq 0.318\ PR \tag{G-4}$$

The moment distribution is:

$$M = PR\left[\frac{1}{\pi} - \frac{\sin\theta}{2}\right] \tag{G-5}$$

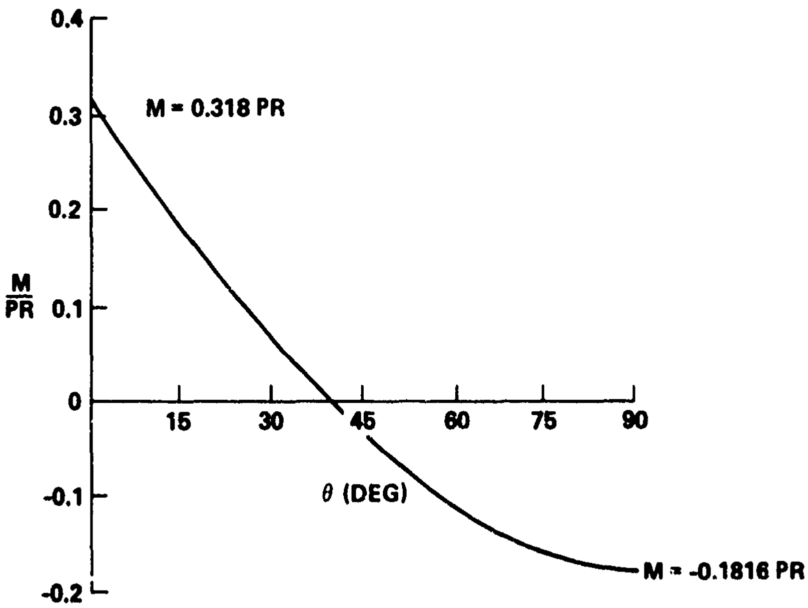

The maximum moment occurs at $\theta = 0$. This is where the plastic hinge forms. By limit analysis let M_p be the moment to make the cross section go completely plastic. Hence, the force to initiate a plastic hinge at point 0 is:

$$\frac{P_y R}{\pi} = M_p$$

$$P_y = \frac{\pi M_p}{R} \tag{G-6}$$

The collapse load P_c is the load required to form additional plastic hinges so that the frame behaves like a mechanism. Additional plastic hinges will form at point A. The moment at point A due to P_y is:

$$M_A = 0.1816\ PR = 0.5705\ M_p \tag{G-7}$$

If we had no redundancy, viz we had a beam as shown below

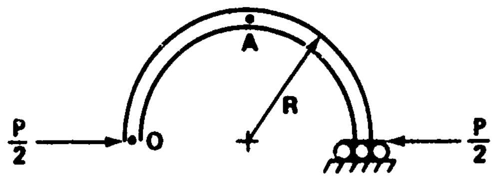

The moment at A would be

$$M_A = \frac{P}{2} R \tag{G-8}$$

We will use this later.

Now let us increase the force at O by ΔP. Since plastic hinges are formed at O, the moment distribution from ΔP is the same as for a beam with hinges. Plastic hinges are formed at point A when the moment builds up to M_p. Hence,

$$0.5705M_p + \frac{\Delta P}{2} R = M_p \tag{G-9}$$

or

$$\Delta P = \frac{M_p}{R} [1 - 0.5705]2$$

$$\Delta P = \frac{0.859M_p}{R} \tag{G-10}$$

The collapse load is then

$$P_c = P_y + \Delta P = \frac{\pi M_p}{R} + \frac{0.859}{R}$$

$$P_c = \frac{4M_p}{R} \tag{G-11}$$

The ratio of collapse load to yield load is

$$\alpha = \frac{P_c}{P_y} = \frac{4}{\pi} \tag{G-12}$$

PLASTIC STRAIN AS A FUNCTION OF DEFLECTION

During destruct, the frames in the ET will experience appreciable plastic strain. An estimate of the radial deflection needed to reach ultimate strain is required.

A crude estimate of the maximum displacement X_{max} corresponding to the development of the ultimate strain can be obtained as follows. Plastic hinges are formed at the points indicated.

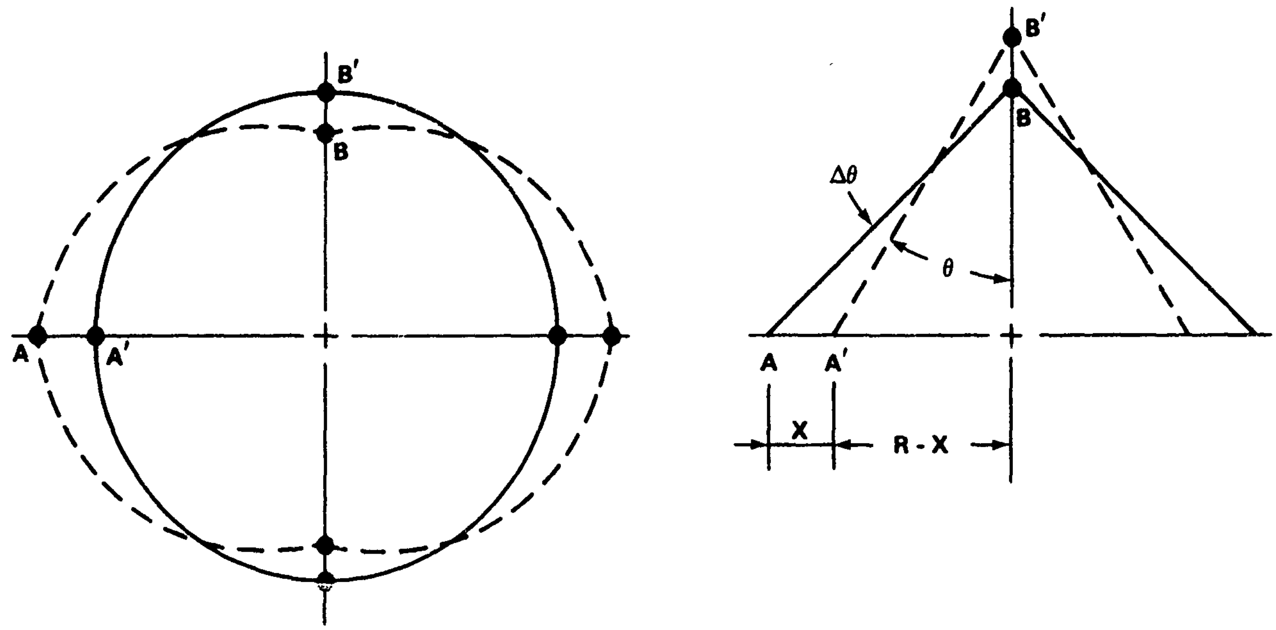

Assume the hinges rotate through an angle of $\Delta\theta$ as the frame deflects from A to A'. Further assume that the frame length AB = A'B' = $\sqrt{2}$ R. Then

$$\sin \theta = \frac{R - X}{\sqrt{2}\, R}$$

Taking the derivative

$$\cos \theta \frac{d\theta}{dx} = - \frac{1}{\sqrt{2}\, R}$$

or

$$d\theta = \frac{dX}{\sqrt{2}\, R \cos \theta} \approx \frac{dX}{R}$$

For small changes of X to ΔX, the hinge rotation is therefore approximately:

$$\Delta\theta = \frac{\Delta X}{R} \tag{G-13}$$

The problem now is to determine how much the hinge can rotate before the ultimate strain is exceeded. A good assumption is that plane sections remain plane during bending. Hence, for a section of plastic hinge

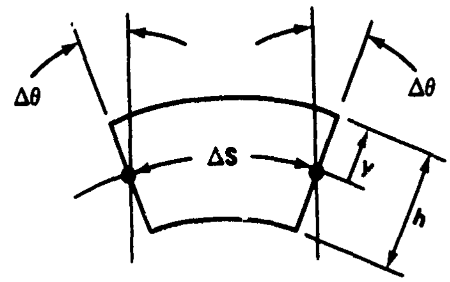

$$\epsilon = \frac{2Y\Delta\theta}{\Delta S} \tag{G-14}$$

where ΔS is the hinge length. Symonds indicates that for aluminum the hinge length is from 2h to 4h where h is the depth of the beam.[G-1] Hence, Equation G-14 can be written

$$\epsilon = \frac{2y\ \Delta\theta}{\zeta h} \tag{G-15}$$

where ζ is from 2 to 4.

From Equation G-13

$$\Delta X = \frac{R\zeta h\epsilon}{2y}$$

Using the average value of $\zeta = 3$ and $y = C_{max}$, where C_{max} is maximum distance from neutral axis, we get

$$X_{max} = \frac{3R\ h\ \epsilon_{ult}}{2\ C_{max}}$$

[G-1] Symonds, P.S., "Viscoplastic Behavior in Response of Structures to Dynamic Loading," Proceedings of Colloquium on Behavior of Materials Under Dynamic Loading, ASME, 1965, pp. 106-124.

For a symmetric beam $C_{max} = h/2$

$$\frac{X_{max}}{R} = 3\ \varepsilon_{ult}$$

For aluminum $\varepsilon_{ult} \approx 0.08$, then

$$\frac{X_{max}}{R} \approx 0.24$$

For steel ζ varies from 4 to 8 (see footnote G-1 on p. G-5).

APPENDIX H

REASSESSMENT OF DESTRUCT MECHANISM FOR CLAMSHELL-TYPE SRB BREAKUP

INTRODUCTION

The conclusions presented in Chapter 4, Sections I and II, of this study report Space Shuttle Range Safety Command Destruct System Analysis and Verification for destruct by clamshell-type solid rocket booster (SRB) breakup are predicated for a linear-shaped charge (LSC) length of 682 inches. The actual length of the LSC is 1032.6 inches, as indicated in Table 2-1. This appendix reassesses the destruct mechanism for the clamshell-type SRB breakup based on the actual LSC length and placement, as shown in Figure H-1. No change in the total force-time input to the analysis is required, but a change in the position and distribution of the lateral thrust load is in order. The correct distribution moves the thrust load aft, thereby exerting less load on the forward SRB/ET joint and a higher load on the aft joint. In fact, this was one recommendation expressed in the original report to increase effectiveness. However, as will be shown later, the dynamic response of the SRB shell results in reduced lateral velocity at the time of joint failure and subsequent reduced effectiveness in destructing the external tank (ET) at early times into the flight.

DYNAMIC RESPONSE OF SRB'S TO LATERAL THRUST

Paralleling the "Dynamic Elastic Response of SRB's to Lateral Thrust" analysis in Chapter 4, Section I, a dynamic response analysis of the SRB's has been made using the revised lateral thrust distribution. The lateral thrust-time curves for destruct at T = 0, 10, 50, and 100 seconds into flight remain as before (Fig. H-2). Figure H-3 shows the predicted forces (F1 and F2) and the velocities (V1 and V2) at the forward and aft joints (X_T 985 and X_T 2058) as a function of time during destruct at T = 0. As expected, the force on the forward joint decreased while that on the aft joint increased. However, the angular velocity of the SRB has been reduced, resulting in more uniform lateral translation and a lower average velocity in the portion of the SRB adjacent to the LH_2 tank. Similar results were obtained for T = 10, 50, and 100 seconds. The purpose of these calculations is, as before, to determine when the joints can be expected to fail, and to determine the corresponding SRB velocity at the joints (V_{R1} and V_{R2}) at the time of failure. In addition, the probability of SRB failure has been assessed through inspection of the maximum bending stresses generated during destruct (Fig. H-4). In all cases, the maximum bending stress calculated is less than the bending modulus of rupture for the SRB shell. However, at T = 100 seconds, the maximum bending stress approaches the rupture limit and may result in failure of the weakened shell.

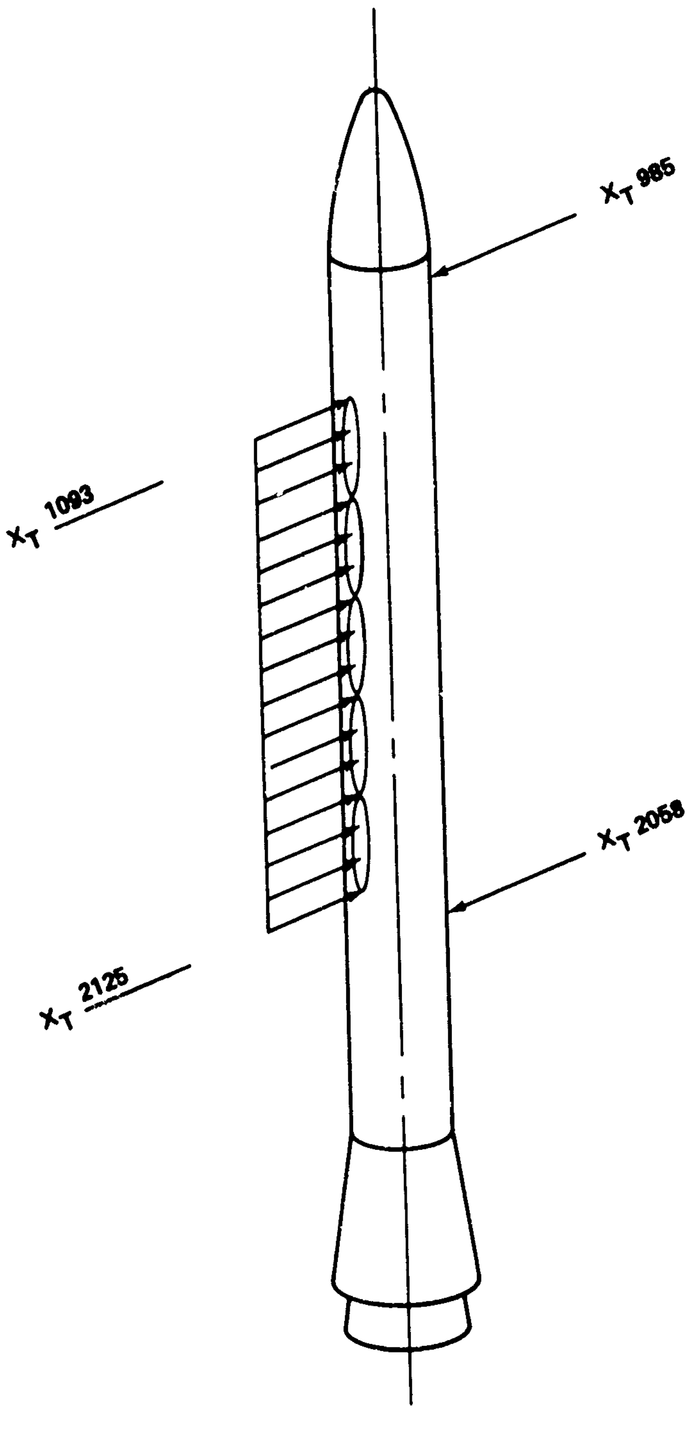

FIGURE H-1 THRUST FROM CLAMSHELL RUPTURE

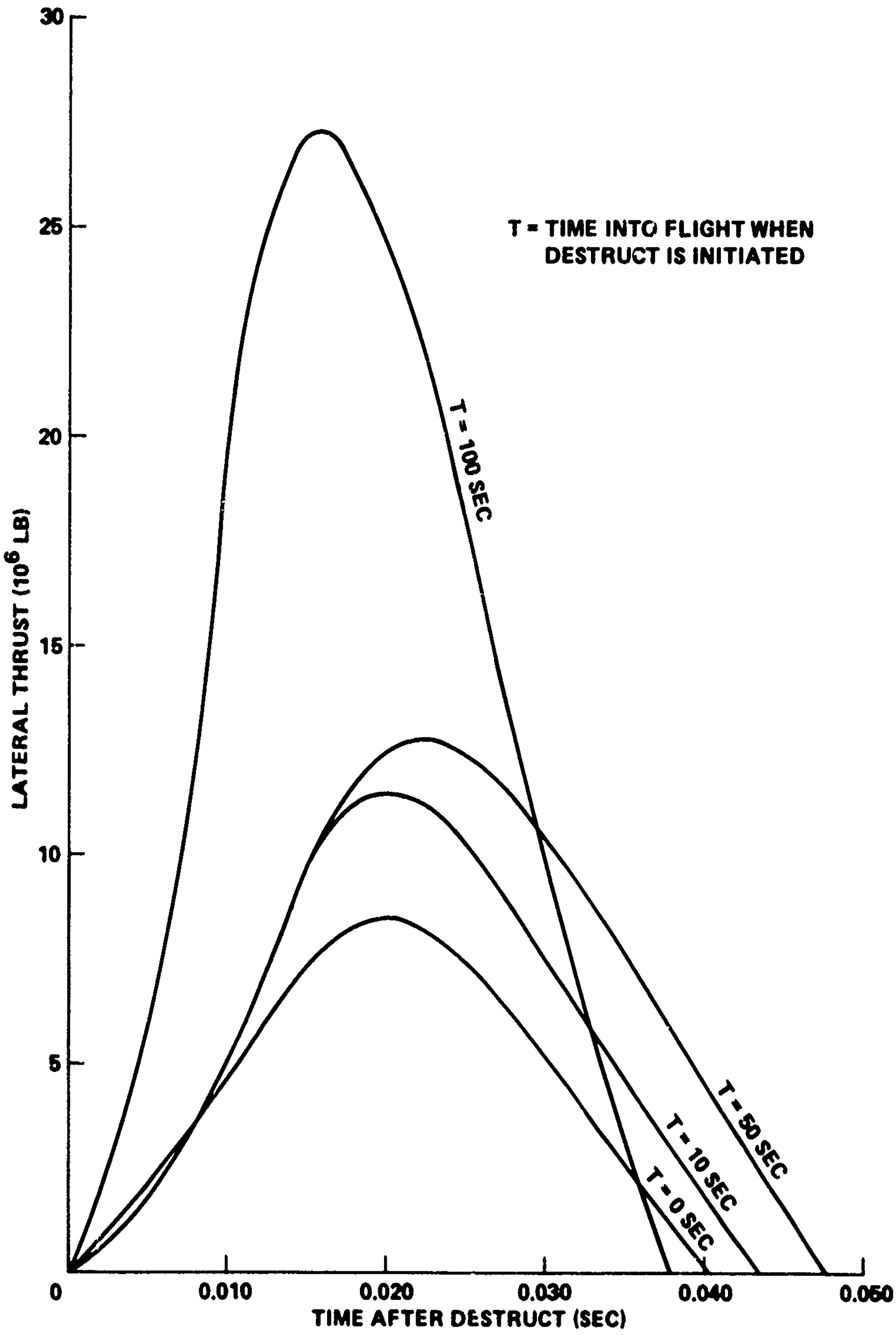

FIGURE H-2 LATERAL THRUST VS. TIME DUE TO CLAMSHELL RUPTURE OF SRB

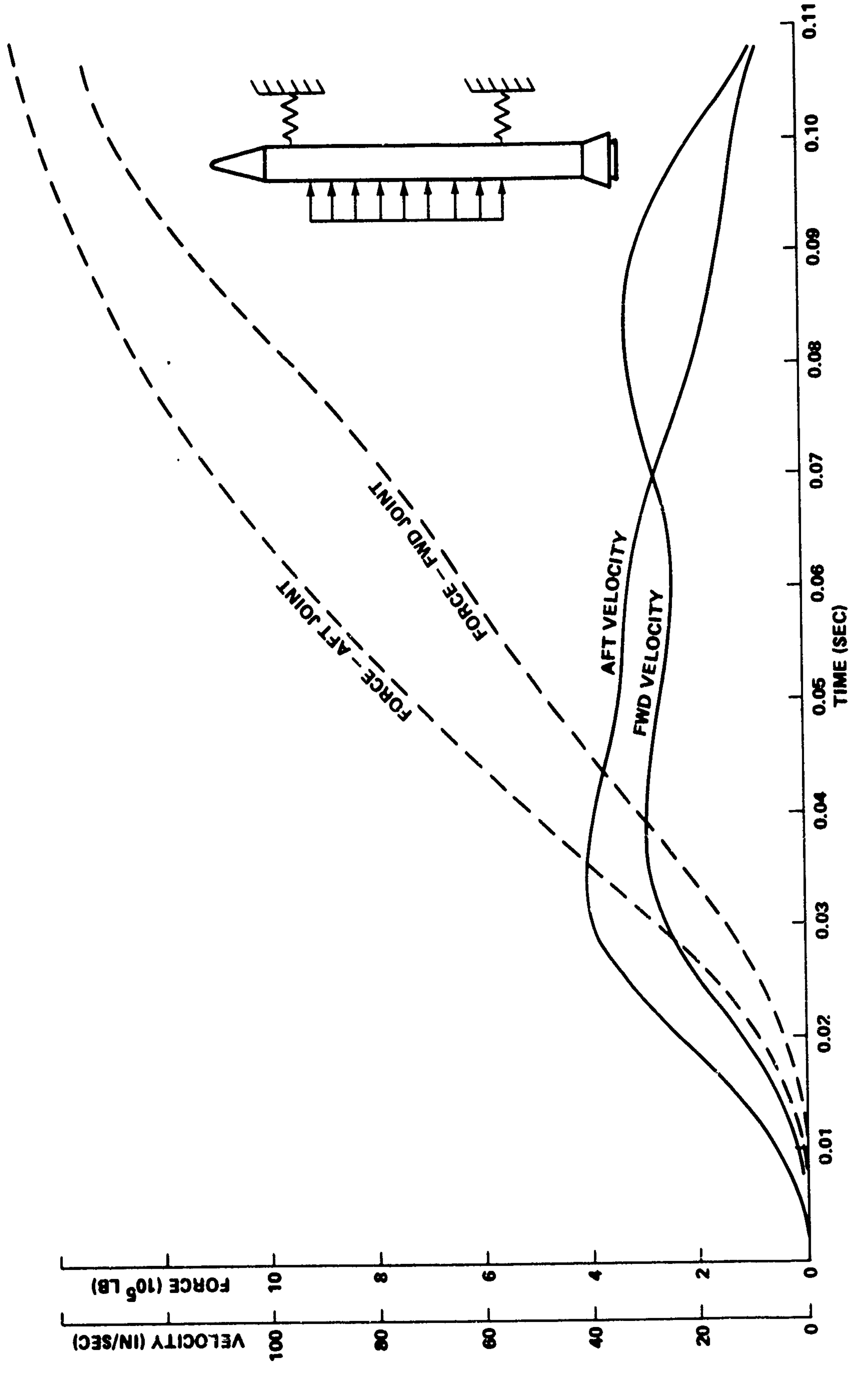

FIGURE H-3 FORCE AND VELOCITY AT FORWARD AND AFT JOINT VS. TIME AFTER DESTRUCT AT LIFT-OFF (T = 0)

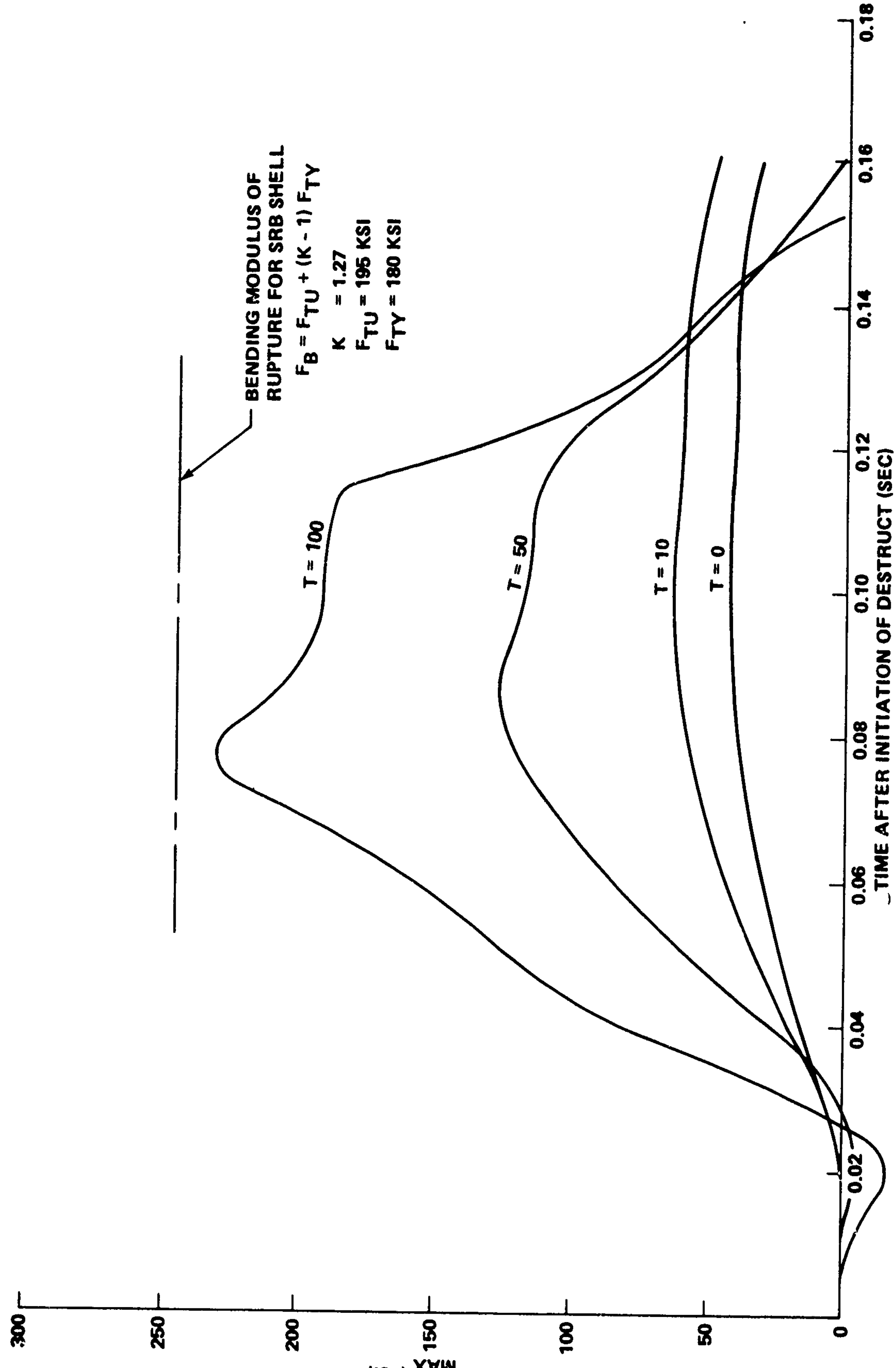

FIGURE H-4 MAXIMUM BENDING STRESS IN SRB VS. TIME FOLLOWING INITIATION OF DESTRUCT

CASE 1: MOTION OF SRB WITH NO RESISTANCE AT ET/SRB JOINT

"Static Analysis of Forward Joint," in Chapter 4, Section I, discusses two possible modes of joint failure. In Case 1 it was assumed that when the radial load on the joints reached a certain magnitude, the SRB was suddenly released with no further resistance. The velocity of the SRB at joint failure then goes into available kinetic energy for potential destruction of the LH_2 tank. Using the 550,000-pound and 850,000-pound failure loads for the forward and aft joints, respectively, failure of both joints occurs simultaneously at t = 0.056 seconds for T = 0 (Fig. H-3). The corresponding velocities, V_{R1} and V_{R2}, are 25 and 33 in/sec, respectively, yielding an average impact velocity of 29 in/sec. Similar calculations were made for T = 10, 50, and 100 seconds. A summary of the forces, velocities, deflections, and bending stresses from the above analyses is given in Table H-1.

CASE 2: MOTION OF SRB WITH RESISTANCE AT ET/SRB JOINTS

In Case 2, it was assumed that the frames at X_T 985 and X_T 2058 provide a constant resistance following joint failure equal to the respective failure loads. Elastic-perfectly plastic behavior is assumed for the force-displacement relationship. Table H-2 shows the velocity at the forward and aft supports after the SRB has traveled the 12-inch standoff distance. The results show that the 1.4×10^6 pound resistance from the support frames is sufficient to stop the SRB before it travels the 12-inch standoff distance for destruct at T = 0 and 10 seconds. For destruct at T = 50 and 100 seconds, the average impact velocity is quite low, since the lateral motion at the forward joint ends within the standoff distance. It will be seen later that for Case 2, the SRB's will not destruct the LH_2 tank if the frames do not rupture before the SRB's travel the 12-inch standoff distance. In Case 2, Chapter 4, it was shown that frame rupture could occur resulting in higher impact velocities.

TABLE H-1 SUMMARY OF FORCES, VELOCITIES, DEFLECTIONS, AND BENDING STRESS DURING DESTRUCT

Time of Destruct (sec)	Force at Failure		VR Velocity at Failure		XR Deflection at Failure		Average Impact Velocity (in/sec)	SRB Max Bending Stress (psi)
	Fwd (lb)	Aft (lb)	Fwd (in/sec)	Aft (in/sec)	Fwd (in)	Aft (in)		
0	550,000	850,000	25	33	1.0	1.5	29.0	43,000
10	550,000	850,000	43	56	1.0	1.5	49.5	64,000
50	550,000	850,000	105	92	1.0	1.5	125.0	127,000
100	550,000	850,000	177	155	1.0	1.5	367.0	231,000

TABLE H-2 SRB IMPACT VELOCITIES FOR CASE 2 ACCOUNTING FOR RESISTANCE FROM FRAMES AT X_T 985 AND X_T 2058

Time of Destruct (sec)	Total Impulse (lb-sec)	Weight of SRB (lb)	Net Resistance (lb)	Velocity After Moving 12-in Standoff		Average Velocity (in/sec)
				Fwd (in/sec)	Aft (in/sec)	
0	0.18×10^6	1.288×10^6	1.4×10^6	0	0	0
10	0.26×10^6	1.177×10^6	1.4×10^6	0	0	0
50	0.32×10^6	0.[illegible]7 $\times 10^6$	1.4×10^6	0	45	22.5
100	0.55×10^6	0.323×10^6	1.4×10^6	0	58	29.0

DYNAMIC PLASTIC DEFORMATION OF LH_2 TANK DURING DESTRUCT BY TWO SRB'S

Upon impact by the SRB's, the LH_2 tank is deformed (see "Dynamic Plastic Deformation of LH_2 Tank," Chapter 4). Typical computer results of the displacement at frame X_T 1624 as a function of time for destruct at T = 0, 10, 50, and 100 seconds are shown in Figure H-5. These results are for the initial velocities of Table 4-1 corresponding to Case 1. Frame failure, estimated to occur at a deflection of 44 inches, is seen to occur during destruct at T = 50 and 100 seconds. Figure H-6 shows the pressure buildup in the ullage volume for the "local crushing" mode of deformation. Again failure is predicted at T = 50 and 100 seconds due to pressure buildups which exceed the calculated 82.7 psi burst pressure. However, destruct of the LH_2 tank at T = 0 and 10 seconds is not predicted.

Given the low average impact velocities of Table H-2, and the results from Case 1 above, destruct of the LH_2 tank is not predicted for a purely Case-2-type response. However, should frame rupture occur before the SRB's travel the 12-inch standoff distance, destruct may be possible at the later times.

One possible mode of SRB failure, Case 3, not previously pursued, is breakup of the shell at the clevis joints. The immediate failure of the clevis joints at the instant of destruct initiation would eliminate the resistance at the joints. Table H-3 lists the resulting impact velocities, all of which are much higher than those of either Case 1 or Case 2. Corresponding frame displacement and ullage pressure buildups are plotted on Figures H-5 and H-6. Destruction of the LH_2 tank is now predicted at all times. In reality, clevis joint failure would probably not occur until some displacement of the SRB had taken place. Therefore, destruct by this mode at T = 0 should be viewed as marginal, at best.

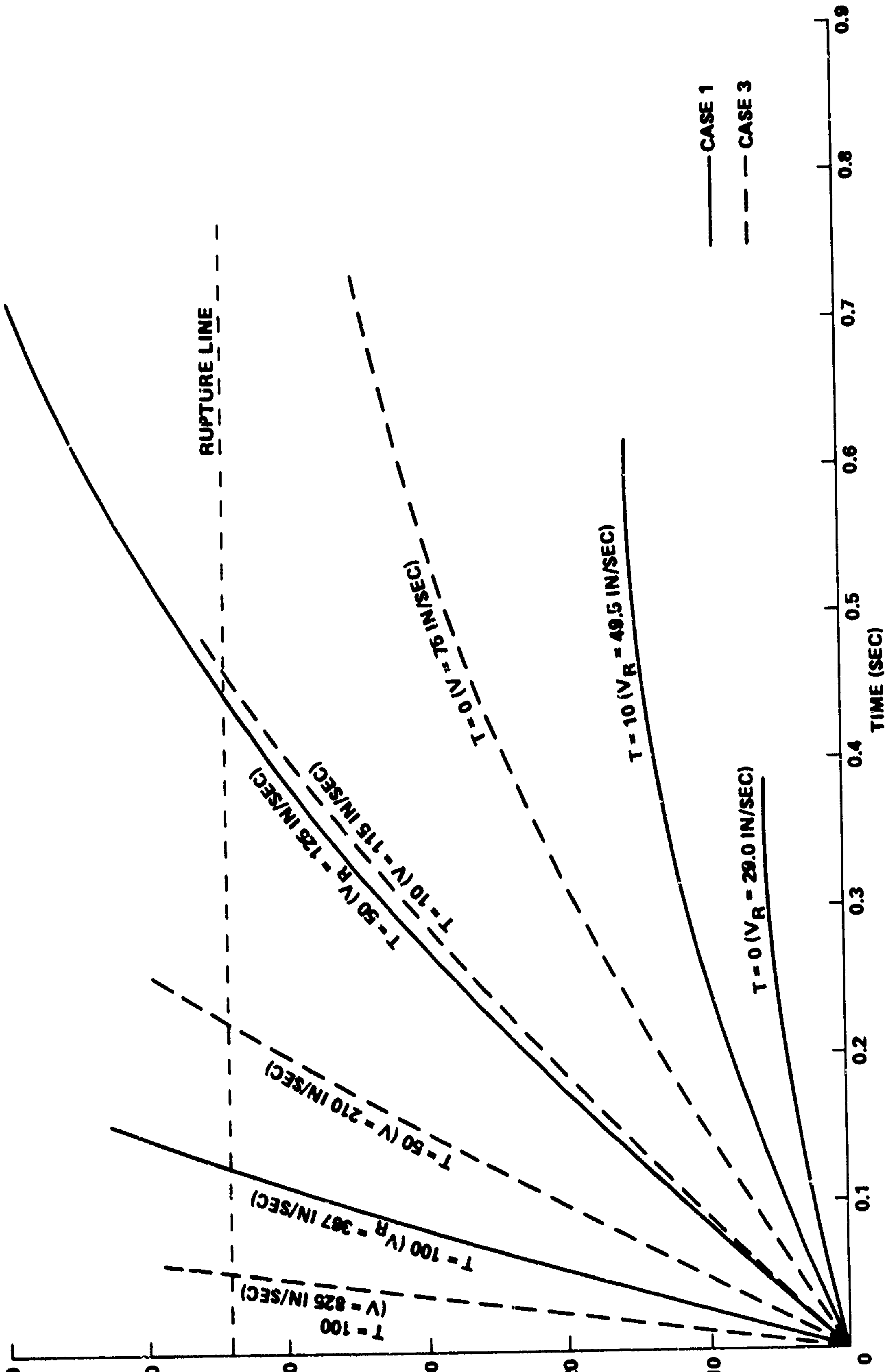

FIGURE H-5 LH_2 TANK FRAME DISPLACEMENT VS. TIME FOR DESTRUCT AT T = 0, 10, 50, 100 SECONDS

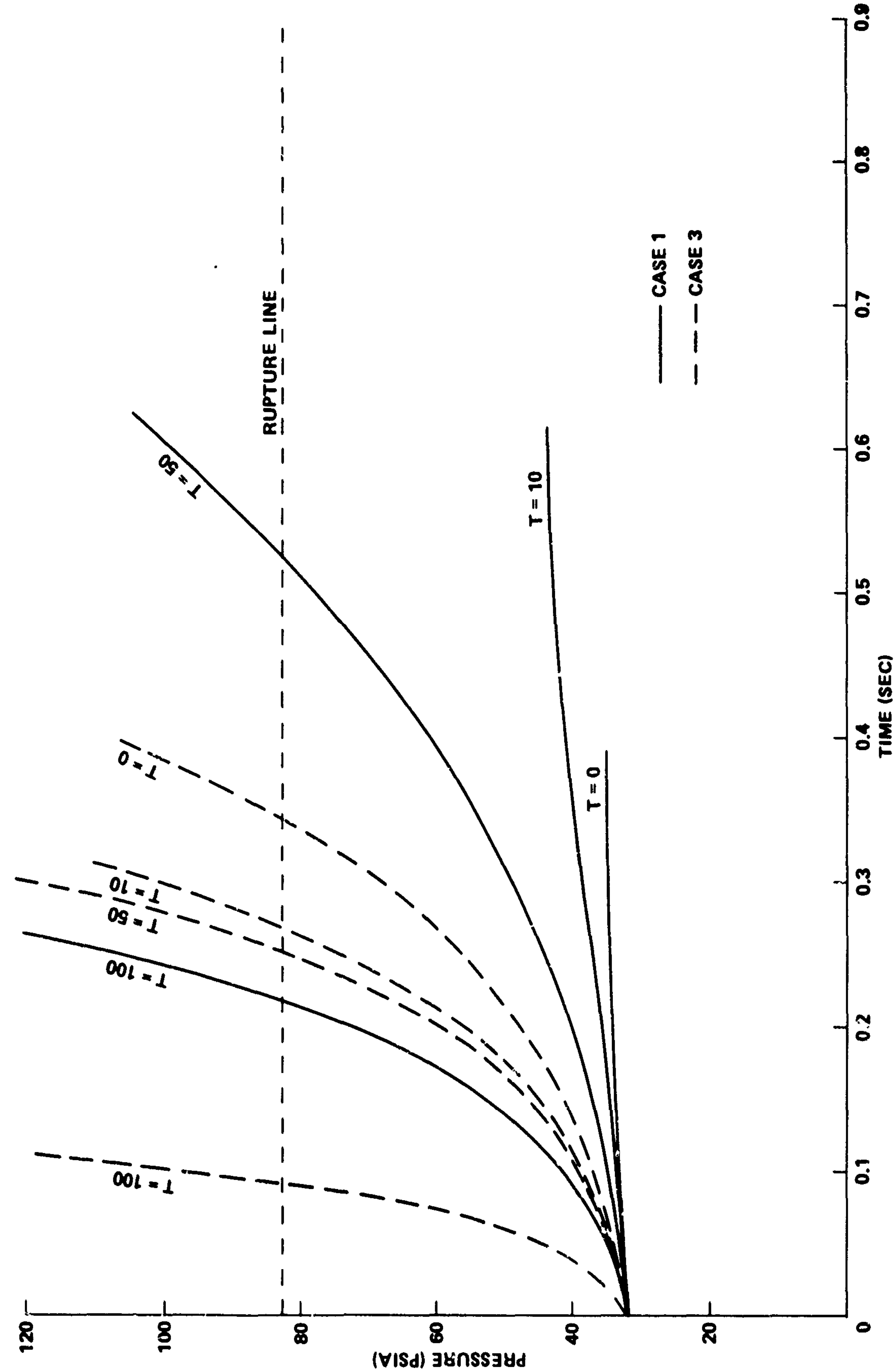

FIGURE H-6 PRESSURE IN ULLAGE VOLUME VS. TIME

TABLE H-3 SUMMARY OF SRB IMPACT VELOCITIES FOR DESTRUCT FOLLOWING BREAKUP OF SRB SHELL AT CLEVIS JOINTS (CASE-3)

Time of Destruct (sec)	Impulse (lb-sec/in)	Weight of SRB (lb/in)	Impact Velocity (in/sec)
0	174	925	75
10	252	850	115
50	310	575	210
100	533	250	825

DYNAMIC PLASTIC DEFORMATION OF LH_2 TANK DURING DESTRUCT BY ONE SRB

In Chapter 4, Section II, similar analyses were performed for destruct by one SRB. The ET can now move away resulting in lower average impact velocities at the corresponding times (Table H-4). For T = 0 and 10 seconds, the force at the aft joint never reaches the failure load. Hence, the average impact velocities are again low, and destruct of the LH_2 tank is not predicted. Plots of frame displacement and ullage pressure buildup are presented in Figures H-7 and H-8 for Cases-1- and -3 type responses. Destruct by frame rupture is the most probable mode at T = 50 and 100 seconds. Destruct by pressure buildup is a possible mode of destruct at T = 0 and 10 seconds for Case-3-type response only.

TABLE H-4 SUMMARY OF SRB IMPACT VELOCITIES FOR DESTRUCT FOLLOWING LOSS OF ONE SRB (CASE-1)

Time of Destruct (sec)	Impulse (lb/sec)	Weight of SRB (lb)	Weight of Orbiter plus ET (lb)	Velocities Fwd (in/sec)	Velocities Aft (in/sec)	Average Impact Velocity (in/sec)
0	0.18×10^6	1.28×10^6	1.895×10^6	47	0	23.5
10	0.26×10^6	1.177×10^6	1.861×10^5	59	0	29.5
50	0.32×10^6	0.767×10^6	1.733×10^6	172	57	120.0
100	0.55×10^6	0.323×10^6	1.57×10^6	252	132	329.0

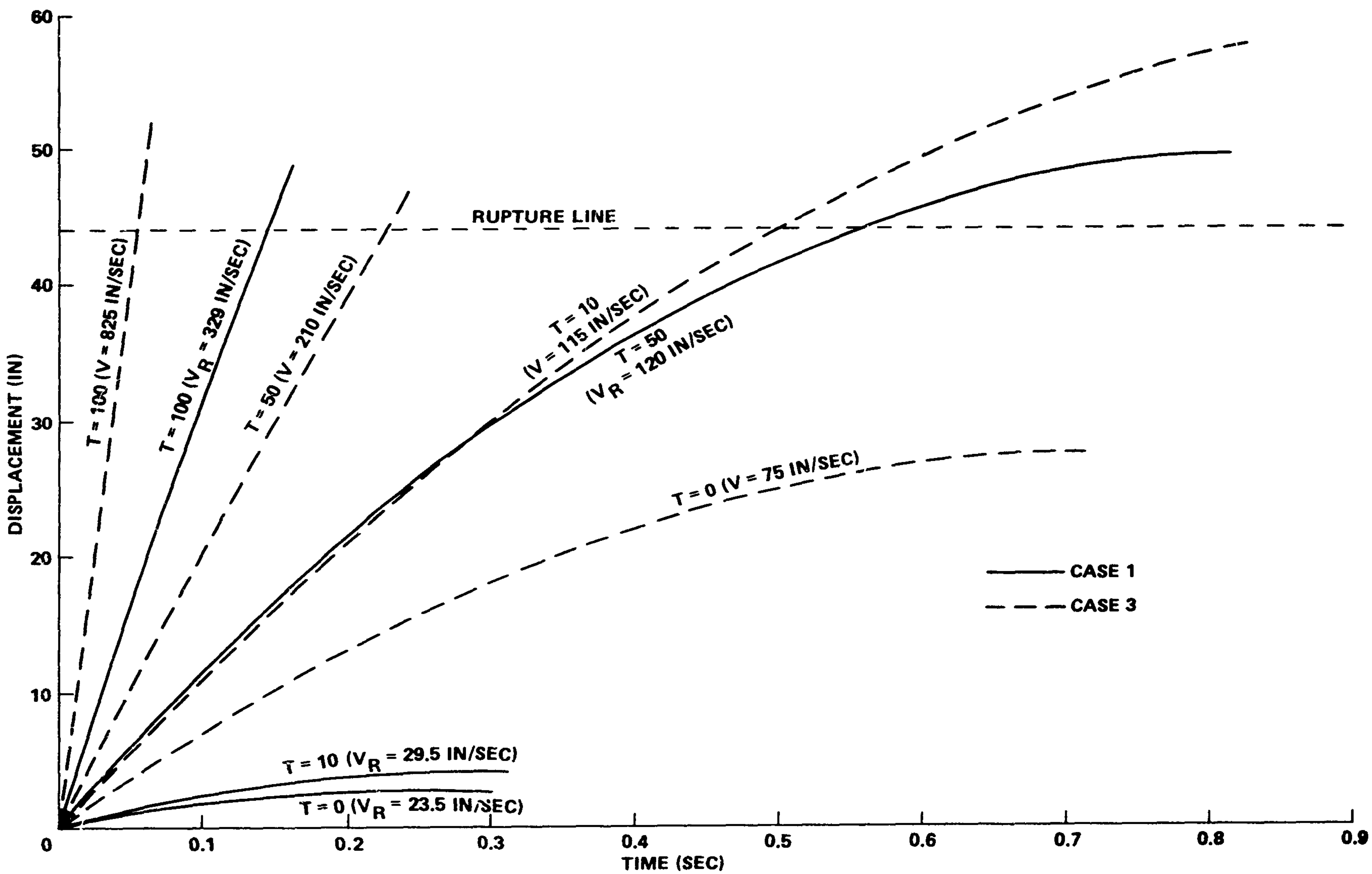

FIGURE H-7 LH_2 TANK FRAME DISPLACEMENT VS. TIME FOR DESTRUCT BY 1 SRB AT T = 0, 10, 50, 100 SECONDS

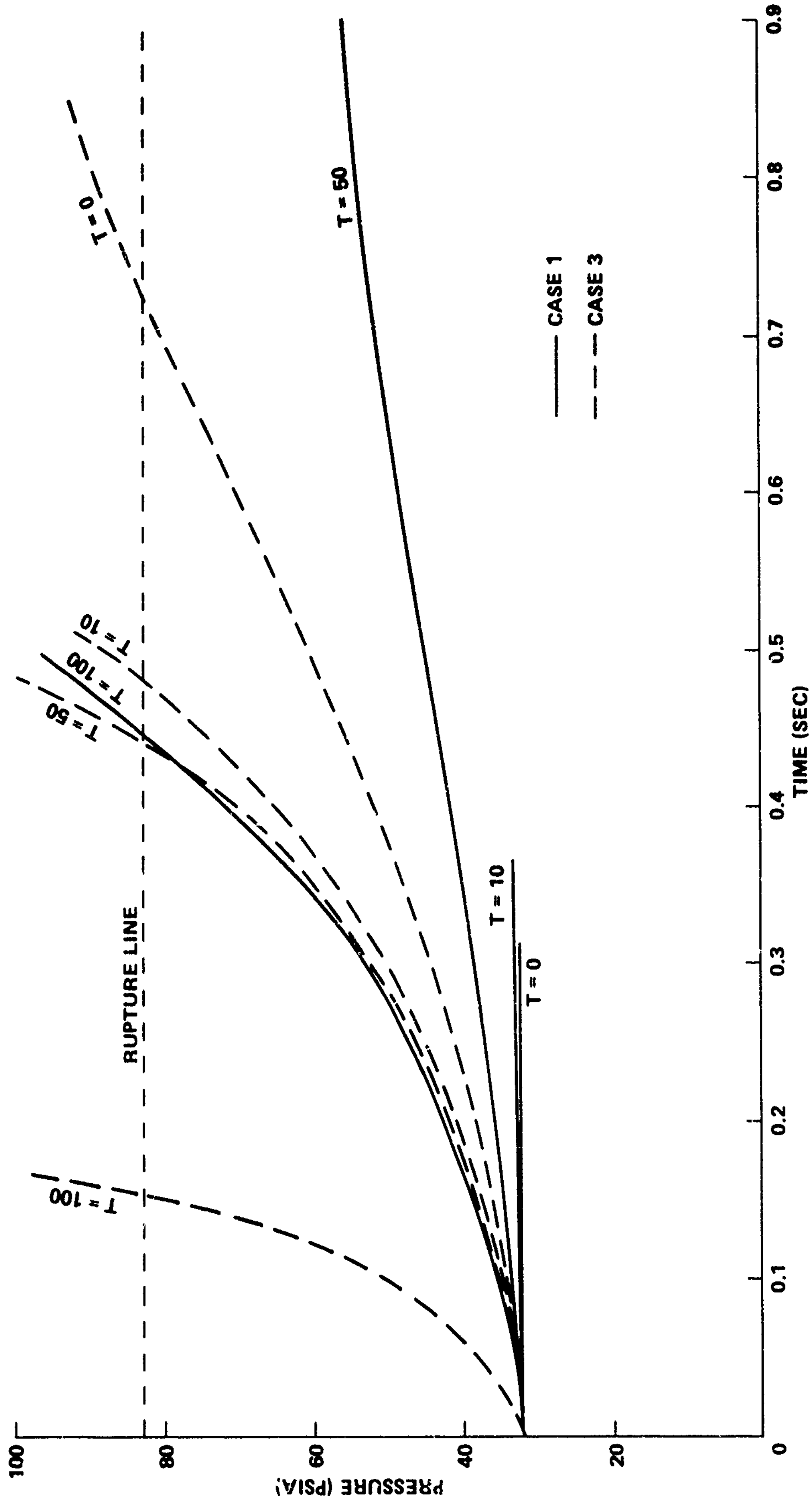

FIGURE H-8 PRESSURE IN ULLAGE TANK VS. TIME FOR DESTRUCT BY 1 SRB AT T = 0, 10, 50, 100 SECONDS

CONCLUSIONS

With the correct placement of the LSC, destruct of the LH_2 tank by one or two SRB's at T = 50 and 100 seconds is probable. Destruct is predicted for all but Case-2-type responses (sustained resistance at ET/SRB joints). It appears that destruct will be by gross deformation of the LH_2 tank frames.

For destruct at T = 0 and 10 seconds, destruct by excessive pressure buildup or frame deformation is unlikely. Only Case-3-typ response (breakup of SRB shell at clevis joints) gives a prediction of subsequent LH_2 tank destruct.

APPENDIX I

STRESS ANALYSIS OF FRAMES X_T 1377 AND X_T 1624

INTRODUCTION

During impact of the solid rocket booster (SRB) into the LH_2 tank, frames at stations X_T 1377 and X_T 1624 are loaded by radial loads. In order to estimate the load P_y to yield and the ultimate collapse load P_c, a static-elastic analysis must first be made. At a given time, the LH_2 tank will be loaded as shown in Figure I-1. In order to estimate the stresses in the skin and frames at stations X_T 1377 and X_T 1624, the method given in NACA TN 1310 will be used.[I-1] The skin bays to be analyzed are between stations X_T 1377 and X_T 1624, and between stations X_T 1624 and X_T 1871.

Once the SRB's begin to push on the LH_2 tank, the load will tend to peak at the frames, as illustrated by the probable load distribution in Figure I-2. This is assumed because the radial stiffness of the frames is considerably greater than the skin. Hence, an analysis based on a shell with concentrated loads at the frames should be reasonable.

FRAME ANALYSIS X_T 1624

Now consider frame X_T 1624 under a radial load of P_o, as illustrated in Figure I-3. The sign convention of the ring and skin stresses are illustrated. Even though the analytical model is based on an infinite cylinder, experimental results verify that the findings are accurate, provided the cylinder extends two bays on either side of the central ring (station 0 in Fig. I-3).

[I-1] Kempner, J., and Duberg, J.E., "Charts for Stress Analysis of Reinforced Circular Cylinders Under Lateral Loads," NACA TN 1310, National Advisory Committee for Aeronautics, May 1947.

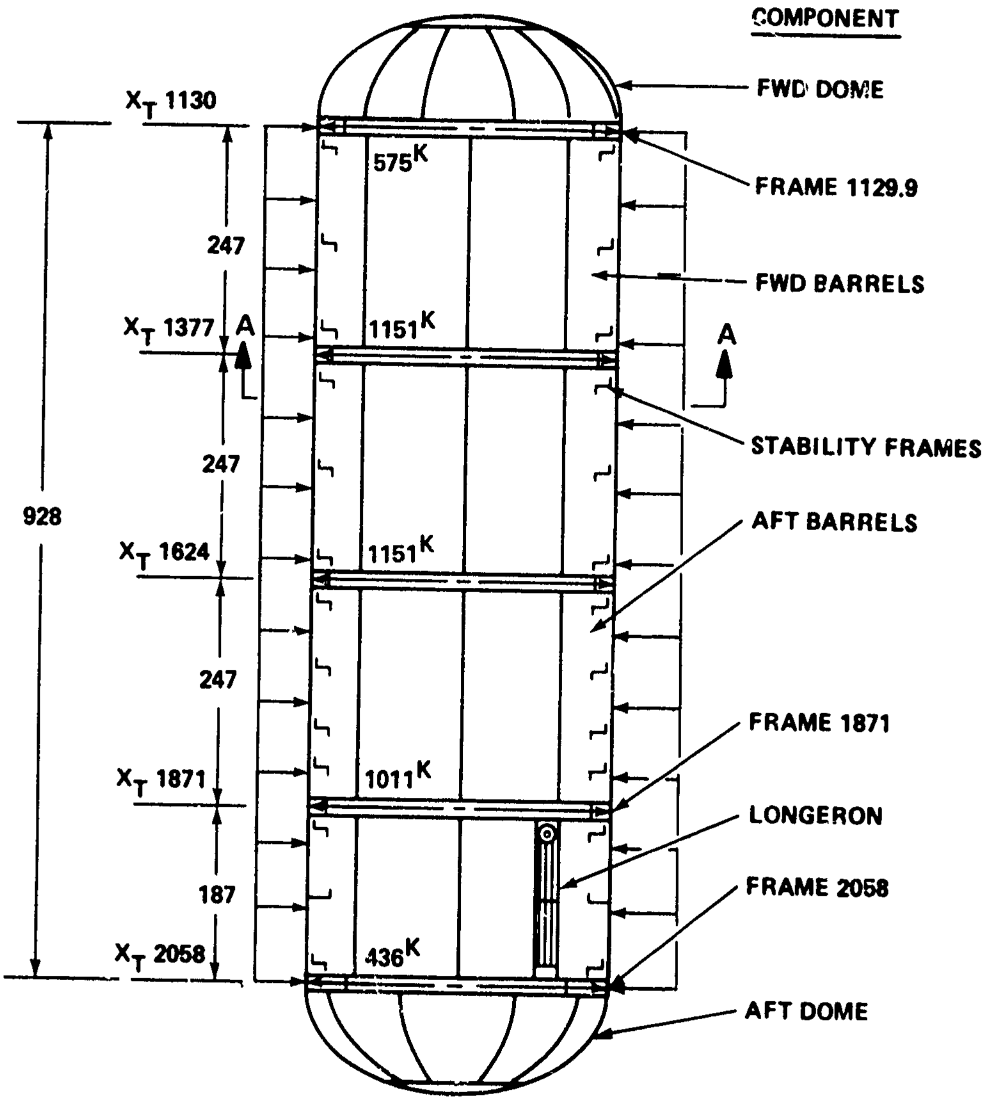

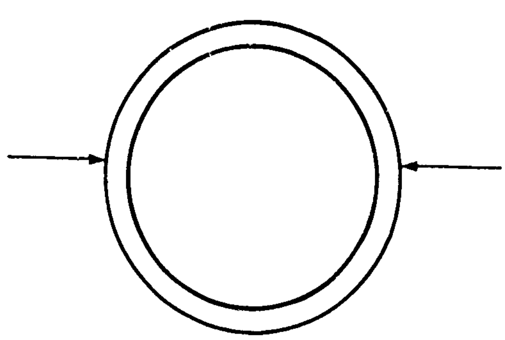

SECTION A-A

FIGURE I-1 LOADING ON LH_2 TANK

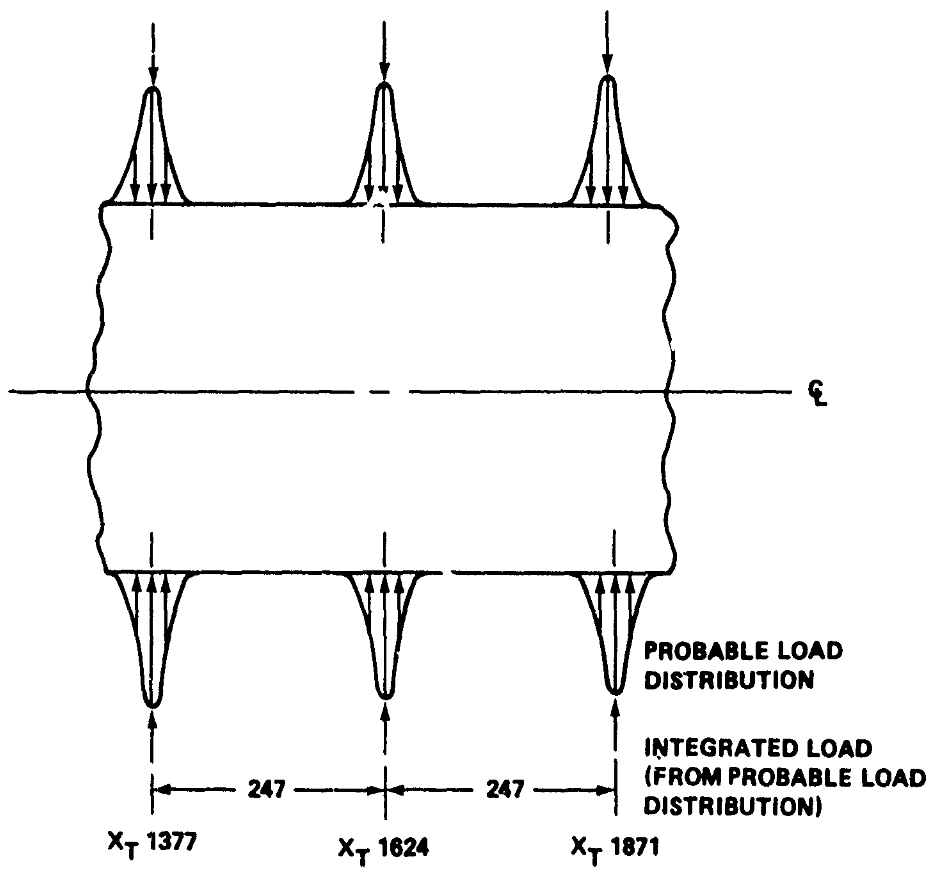

FIGURE I-2 STRUCTURAL MODEL FOR ET TANK (PLAN VIEW)

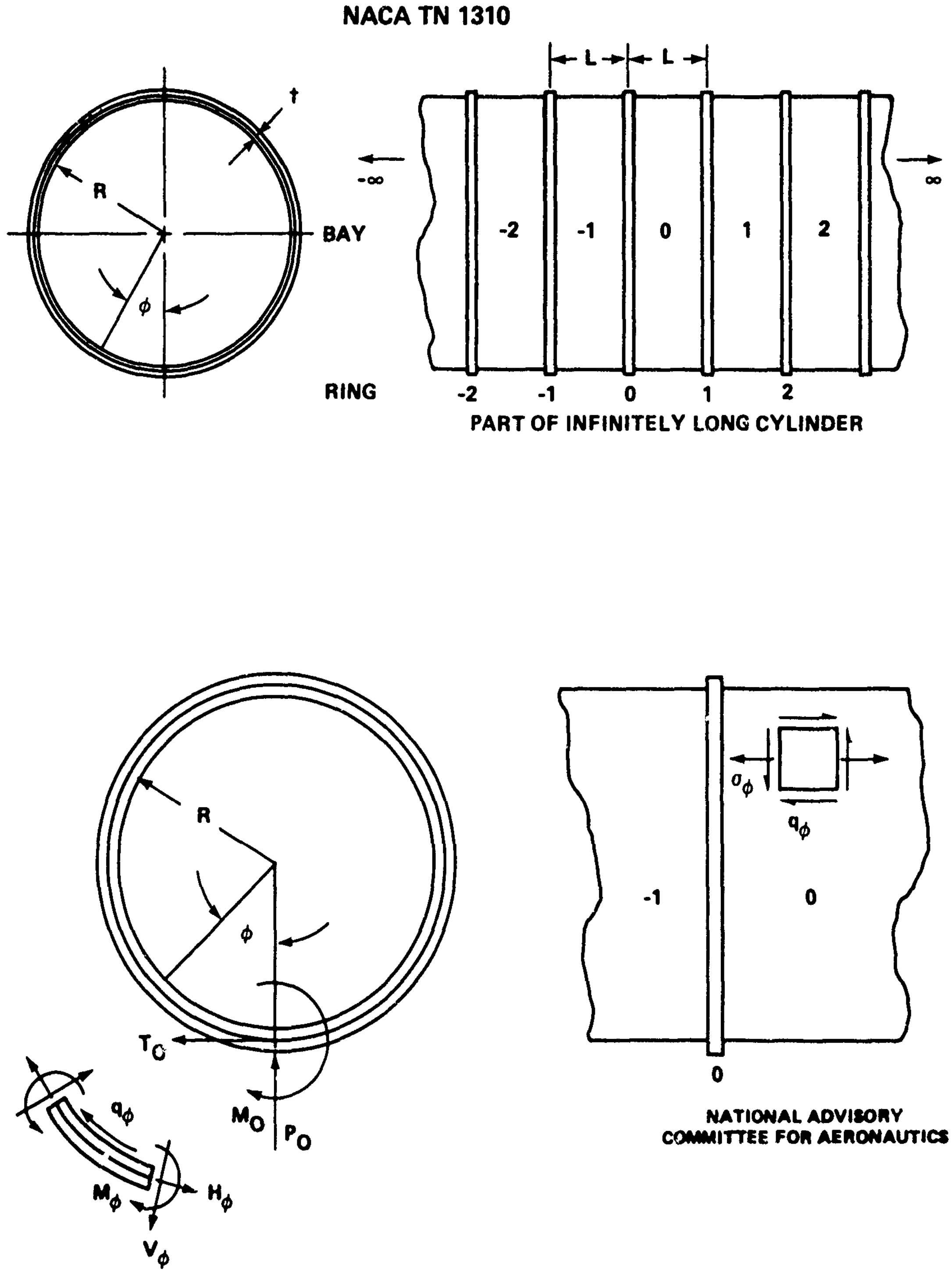

FIGURE I-3 STRUCTURAL MODEL FOR ET UNDER RADIAL LOADS
MODE 2 DESTRUCT

In order to account for the proximity effect of adjacent frames, various parameters from NACA TN 1310 must be calculated as follows:

$$A = \frac{R^6 t^1}{IL^3} = \frac{165.5^6 \times 0.164}{31.2 \times 247^3} = 7.1 \times 10^3 \tag{I-1}$$

$$B = \frac{Et^1 R^2}{GtL^2} = \frac{10.6 \times 10^6 \times 0.164 \times 165.5^2}{4 \times 10^6 \times 0.137 \times 247^2} = 1.42 \tag{I-2}$$

$$\frac{A}{B} = \frac{GtR^4}{EIL} = \frac{4 \times 10^6 \times 0.137 \times 165.5^4}{10.6 \times 10^6 \times 31.2 \times 247} = 5 \times 10^3 \tag{I-3}$$

$I_{avg} = 31.2$ in^4 (moment of inertia of ring)

$G = 4 \times 10^6$ psi

$E = 10.6 \times 10^6$ psi

$L = 247$ in

$R = 165.5$ in

$t^1 = 0.164$ in (effective skin thickness)

$t = 0.137$ in (actual skin thickness)

The skin thickness of the LH_2 tank varies along the length and circumference. A good average in the vicinity of frame X_T 1624 is $t = 0.137$ inch. The skin also has longitudinal stiffeners integrally machined at 96 locations equally spaced around the circumference. According to NACA TN 1310, the part of the skin sheet area which is considered to resist overall bending stresses is added to the stringer area, and the combination is uniformly distributed around the circumference of the cylinder. This resulting combination is the effective skin thickness t^1 which resists direct stresses. Hence,

$$t^1 = \frac{\overbrace{\pi \times 331 \times 0.137}^{\text{skin}} + \overbrace{96 \times 0.303}^{\text{stringers}}}{\pi \times 331} \tag{I-4}$$

$t^1 = 0.164$ in

The frame at X_T 1624 has a variable cross section. The method of NACA TN 1310 is based on uniform frame stiffness, but for the purpose of this analysis, the results from NACA TN 1310 should be sufficiently accurate at the point of maximum frame bending moment ($\phi = 0$). The average stiffness I_{avg} is used in the A and A/B. The maximum frame bending moment is relatively insensitive to these values and, hence, to I_{avg}. The maximum bending stress ($\phi = 0$) is computed using the section properties at $\phi = 0$.

The ring bending moment coefficients are given in Figure I-4 at ring 0 (X_T 1624). The maximum bending moment is

$$M_{\phi_o} = C_{Mr_o} P_o R \tag{I-5}$$

$$M_{\phi_o} = 0.14\ P_o R \qquad (\phi = 0)$$

The load at ring -1 (X_T 1377) also causes bending in the ring 0. Hence, from the bottom of Figure I-4

$$M_{\phi_{-1}} = C_{Mr_{-1}} P_o R \tag{I-6}$$

$$M_{\phi_{-1}} = 0.03\ P_o R \qquad (\phi = 0)$$

The total max bending in frame X_T 1624 is

$$M_{\phi_{tot}} = (0.14 + 0.03)\ P_o R \tag{I-7}$$

$$M_{\phi} = 0.17\ P_o R \qquad (\phi = 0)$$

Note that compared to the analysis of Appendix G, the skin effectively reduces the bending moment.

The direct skin stress can be obtained by superposition in a similar manner. Figure I-5 has a plot of direct stress skin coefficients. For the radial load at ring 0 (X_T 1624), the skin stress in the adjacent bay is

$$\sigma_{\phi_o} = C_{\sigma r_o} \frac{P_o L}{R^2 t^1} \tag{I-8}$$

$$\sigma_{\phi_o} = -4.2 \frac{P_o L}{R^2 t^1} \qquad (\phi = 0)$$

The additive skin stresses for load at X_T 1377 is

$$\sigma_{\phi-1} = C_{\sigma r_{-1}} \frac{P_o L}{R^2 t^1} \tag{I-9}$$

$$= -1.3 \frac{P_o L}{R^2 t^1}$$

The total skin stress is

$$\sigma = -5.5 \frac{P_o L}{R^2 t^1} \tag{I-10}$$

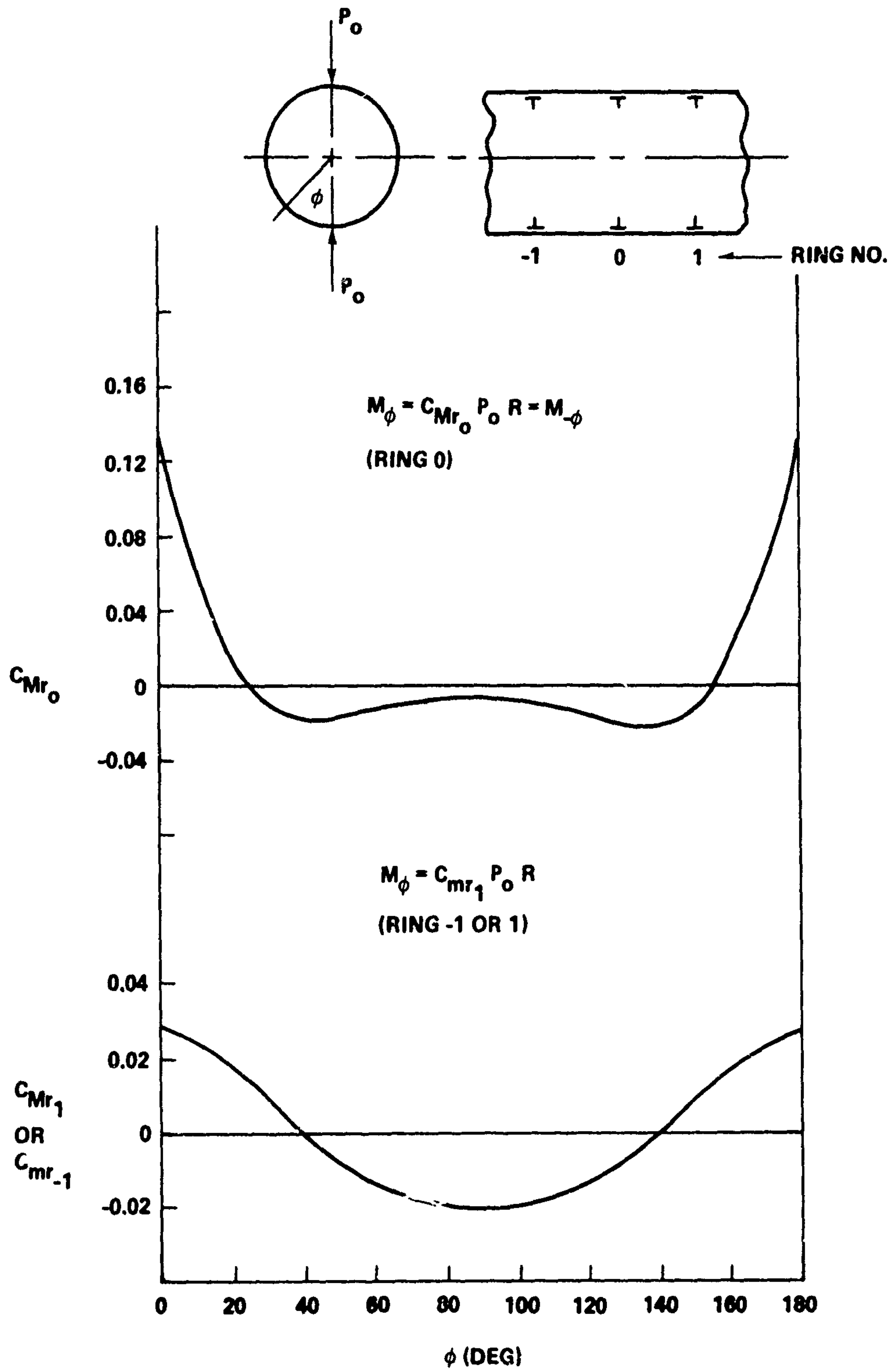

FIGURE I-4 RING-BENDING MOMENT COEFFICIENTS

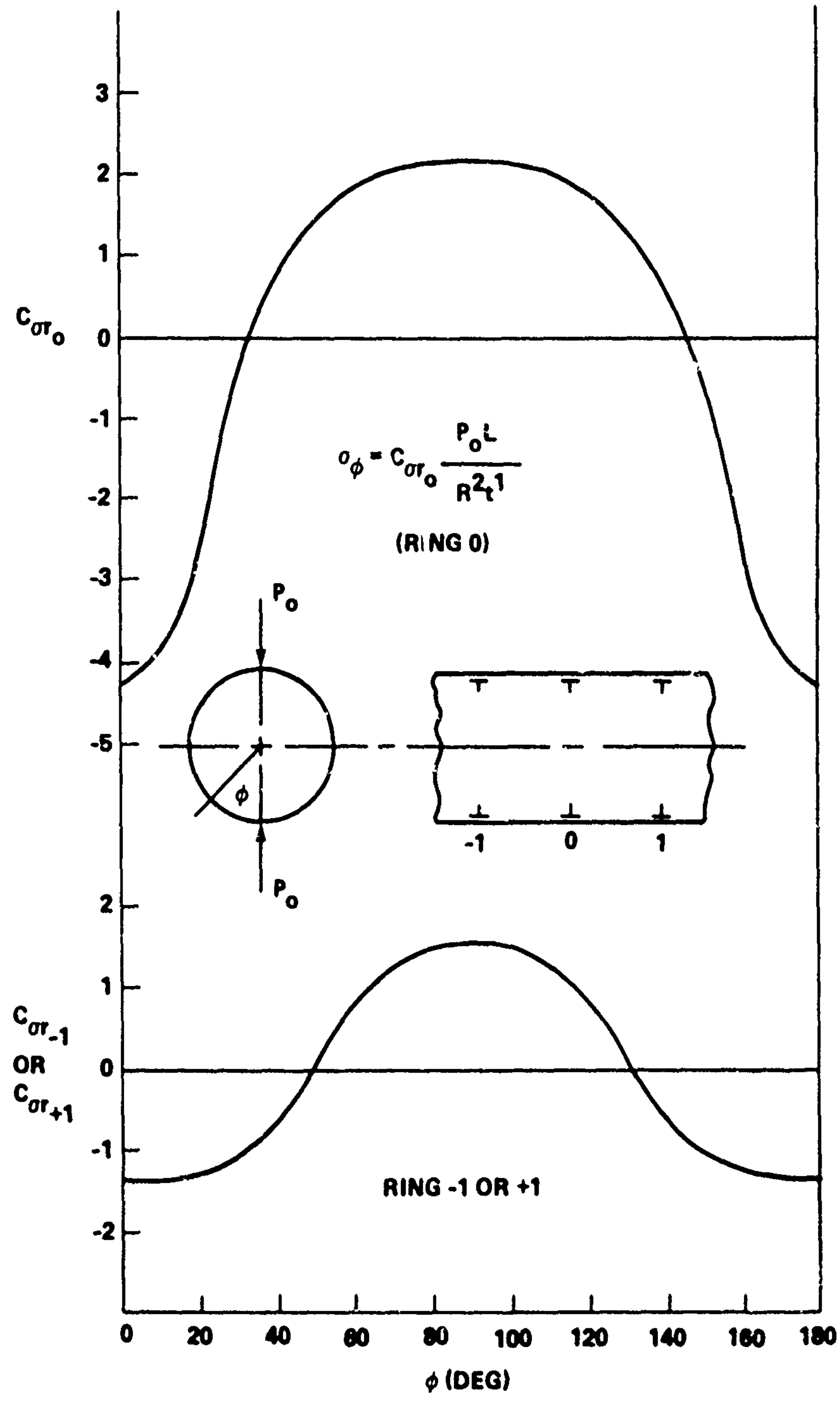

FIGURE I-5 SKIN-DIRECT STRESS COEFFICIENTS AT RINGS FOR RADIAL LOADS

APPENDIX J

ET BENDING MOMENT, SHEAR, AND END LOAD

Overall rigid-body bending moment, shear, and end load curves were determined for the external tank (ET) at selected times to check for shell failure at locations other than the solid rocket booster (SRB)/orbiter attachment joints. The general translational and rotational equations of motion were applied to the SRB's and, in turn, the ET to determine the forces and moments required to place the individual bodies in equilibrium. Aerodynamic, thrust, and body forces and moments were obtained from the trajectory calculations at the selected times. Cluster velocities and accelerations (given at the cluster reference point, station X_T 1440 on the ET centerline, in the trajectory calculations) yielded the inertial loads. The attach fitting loads, governed by structural geometry, became the only unknown forces and moments. A computer code was written to solve for these unknowns.

The program goes through a series of steps to put the bodies in dynamic equilibrium. First, locations of loading points, centers of gravity (CG's), and moments and products of inertia are defined for each body. The body forces used are calculated from the mass, the Eulerian angles, and the acceleration due to gravity and corrected with altitude. Next, the absolute accelerations of the CG's are calculated using the equations of motion for a rigid body fixed in a rotating coordinate system located on the centerline of the ET. The external moment of each body is found from the general equations of rotational motion which use the six components of inertia and the angular velocities and accelerations of the bodies. These equations use the centers of mass as reference points.

The loads at the forward and aft interfaces of each SRB to the ET are calculated by applying all external, body, and inertial forces to the SRB. The external forces include thrust and concentrated aerodynamic loads. With the SRB in static equilibrium, the unknown joint loads are solved for by summation of moments in two planes about a joint and then, a summation of forces in the three-body coordinate directions. The SRB joint loads are applied to the ET and a similar analysis is made to solve for the loads on the ET-orbiter joint loads. The rear loads on the ET are calculated at the aft interface (orbiter to ET separation plane) and then transferred through the rear truss to the ET body.

It was assumed that the axial loads at the two aft orbiter-ET attachment points were equal to eliminate the statically indeterminent equations. All moments about the Y-axis are thereby reacted by the forward and aft Y-forces. The accuracy of this assumption depends on the magnitude of angular acceleration in the heading plane, the offset of the CG of the orbiter to its centerline, and alignment of center of axial orbiter thrust to the centerline. The net tangential load at the aft orbiter/ET joint was reacted within the ET structure at station X_T 2058. If the axial load was divided unevenly between the two attachment points, a net tangential load would have been calculated at station X_T 1871. Given the load distribution on the ET, the end load, shear and bending moment solutions were programmed into the code in the manner described below.

Weight distribution data for the ET dry weight, liquid oxygen, and liquid hydrogen were incorporated into a CURVFIT program to obtain a cumulative weight distribution for each — the dry weight, the liquid oxygen, and the liquid hydrogen. A sixth order polynomial was obtained for each distribution, Figures J-1 through J-3. A total cumulative weight distribution is formed from the three distributions which is corrected for burned fuel and adjusted for altitude. The cumulative distribution was used to improve accuracy in finding the weight of a mass increment (a delta weight is calculated rather than a tabulated weight) and the elimination of the need to read in a long listing of data.

Since the inclusion of the inertia forces and accelerations of each mass increment is necessary to calculate end loads, shear, and moment diagrams, the accuracy of the results depends on how well the inherent inertia distributions in the CURVFIT description match the actual moments and products of ET inertia. In particular, the bending moments are most sensitive to the inertia distributions since each inertia term is multiplied by a moment arm, leaving room for a magnification of error. Therefore, an adjustment to the inertia distribution in the vicinity of the liquid oxygen and liquid hydrogen was made to compensate for the difference between the inertia of a cylinder with a large radius over the inertia of a slender rod.

Sample results are given in Figures J-4 through J-7. An obvious problem arises from the use of concentrated aerodynamic loads to calculate the shear and bending moments. The calculated peaks may be unrealistically high. However, further refinement is only necessary if the structural capabilities of the ET are exceeded.

Figure J-5 includes the end load envelope given in the Structural Design Loads Data Book along with the curve calculated for the sample case (T = 51.75 sec following loss of an SRB at T = 50 sec). The end load is within the envelope except near the nose where the aerodynamic drag has been applied. The drag force is not appreciably different from that encountered during normal flight and, therefore, presents no failure problem.

Conservative estimates of the shear strength of the ET structure are as follows: LOX tank barrel — 7.4×10^6 lb; intertank neglecting stringers — 3.3×10^6 lb; LH_2 tank neglecting stringers – 5.7×10^6 lb. The shear curves (Fig. J-6) do not exceed 2.6×10^6 lb. Therefore, failure in shear is not predicted.

Similarly, estimates of the bending moment capability of the ET structure based on stress are as follows: LOX tank barrel — 7.7×10^7 ft/lb; intertank — 6.8×10^7 ft/lb; LH_2 tank – 7.1×10^7 ft/lb. The bending moments curves (Fig. J-7) for the sample case do not exceed these values.

However, buckling of the compression side of the shell is possible at a lower value of the bending moment. The bending moment capability of the LH_2 tank, as given in the Structural Design Loads Data Book, is at least 1.2×10^7 ft/lb.

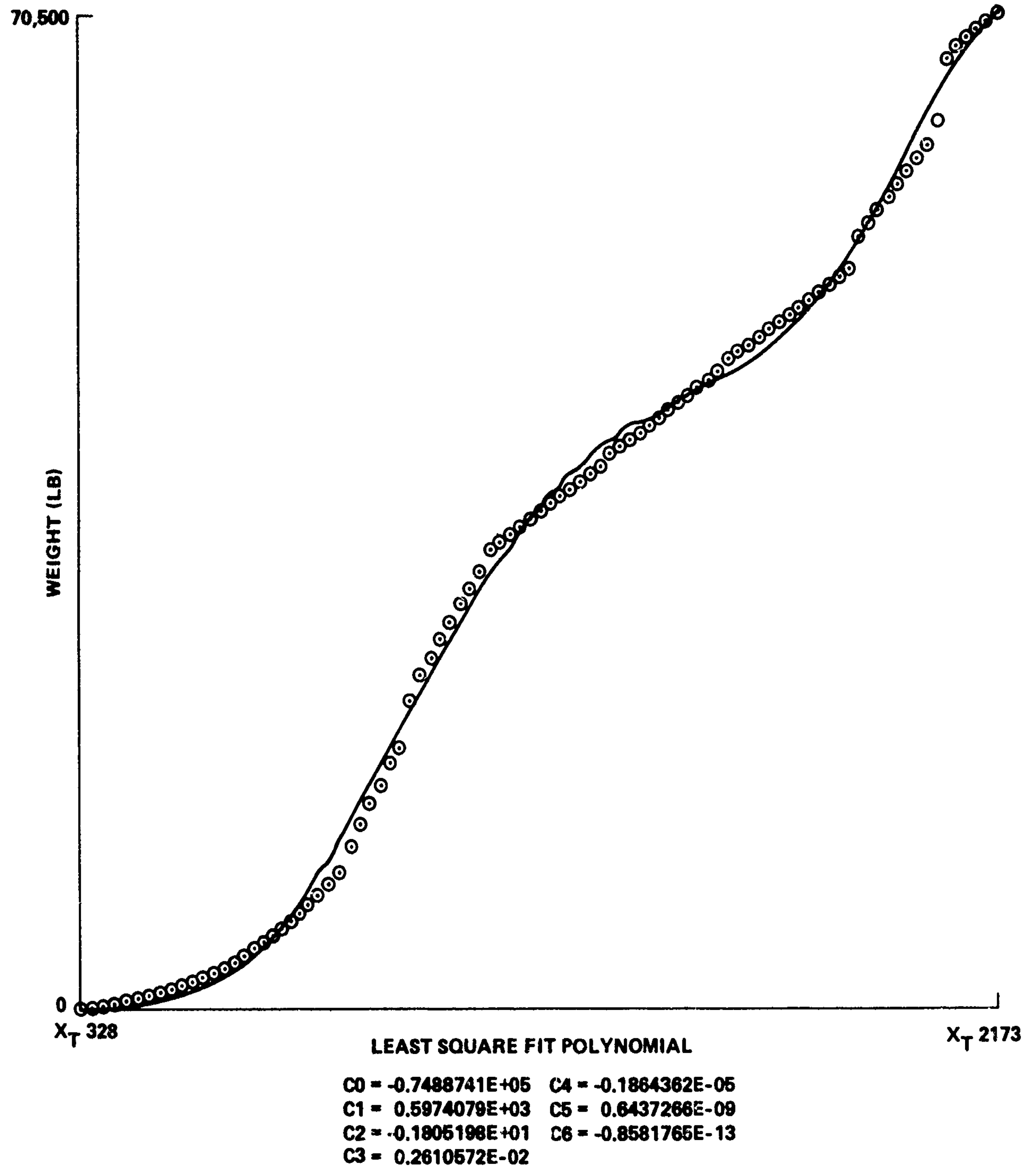

FIGURE J-1 ET DRY WEIGHT

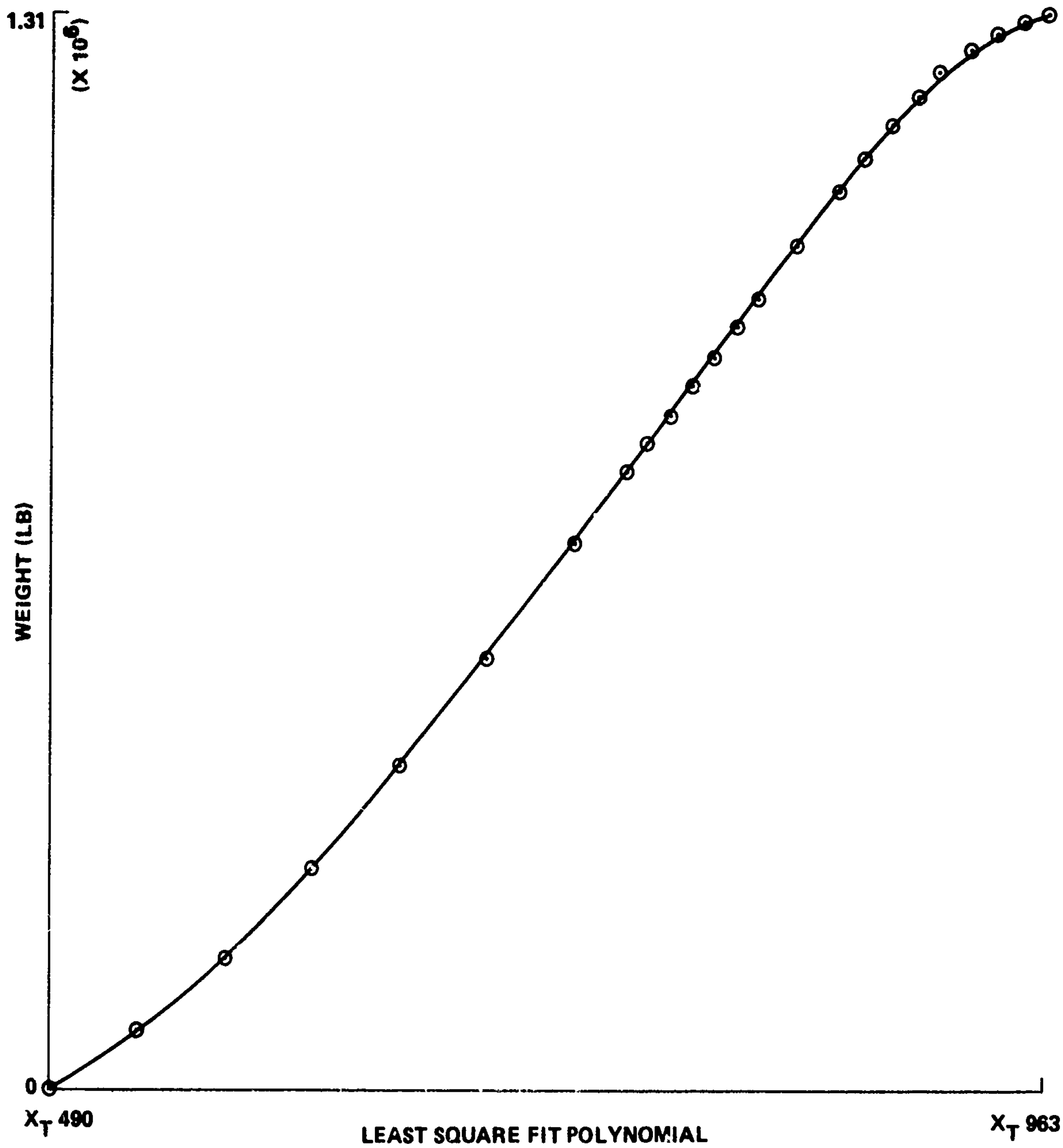

LEAST SQUARE FIT POLYNOMIAL

C0 = -0.5854180E+08   C4 = -0.4508475E- 02
C1 = 0.5383045E+06   C5 = 0.2633897E- 05
C2 = -0.2041607E+04   C6 = -0.6361152E- 09
C3 = 0.4073754E+01

FIGURE J-2 LOX WEIGHT

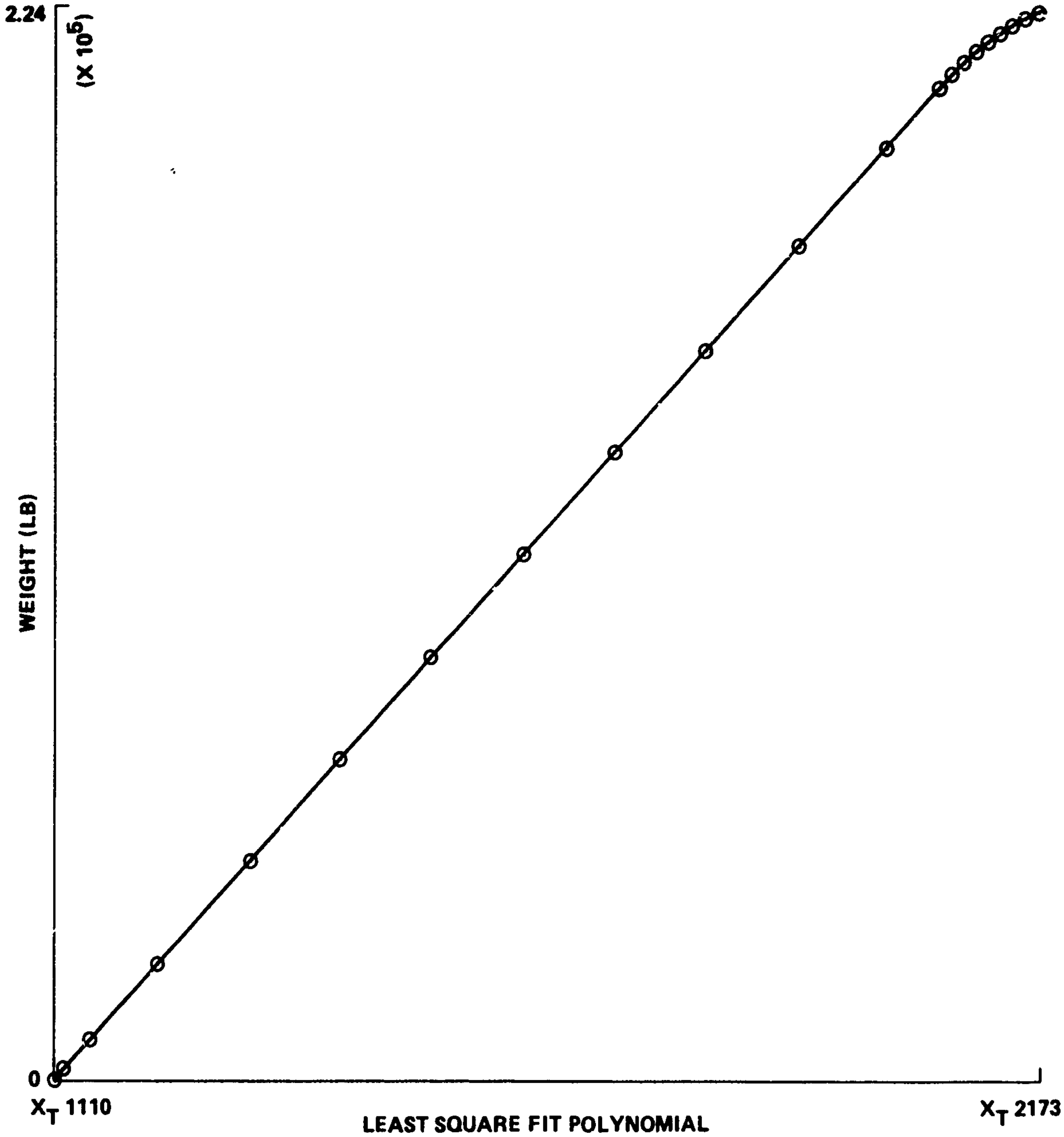

LEAST SQUARE FIT POLYNOMIAL

C0 = -0.1439360E+08	C4 = -0.3816631E-04
C1 = 0.5632506E+05	C5 = 0.9703449E-08
C2 = -0.9178488E+02	C6 = -0.1018322E-11
C3 = 0.7930016E-01	

FIGURE J-3 LH_2 WEIGHT

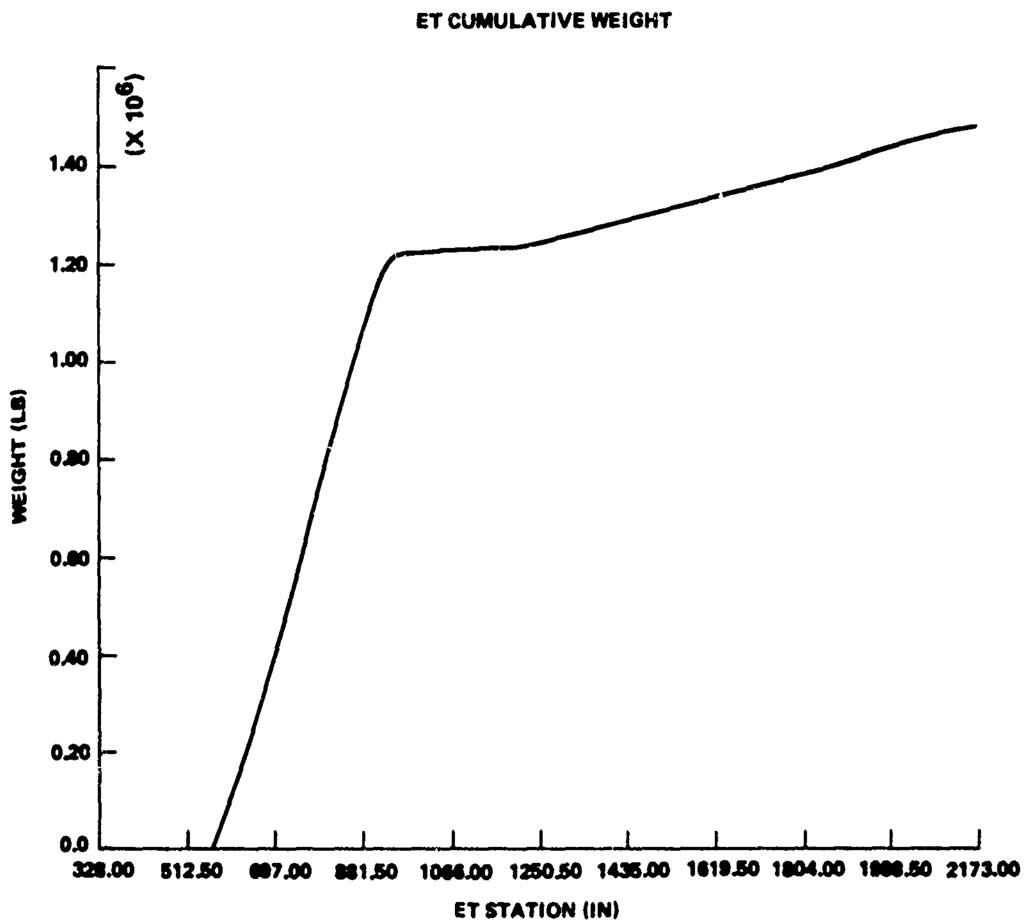

FIGURE J-4 ET CUMULATIVE WEIGHT (T = 51.75 SEC)

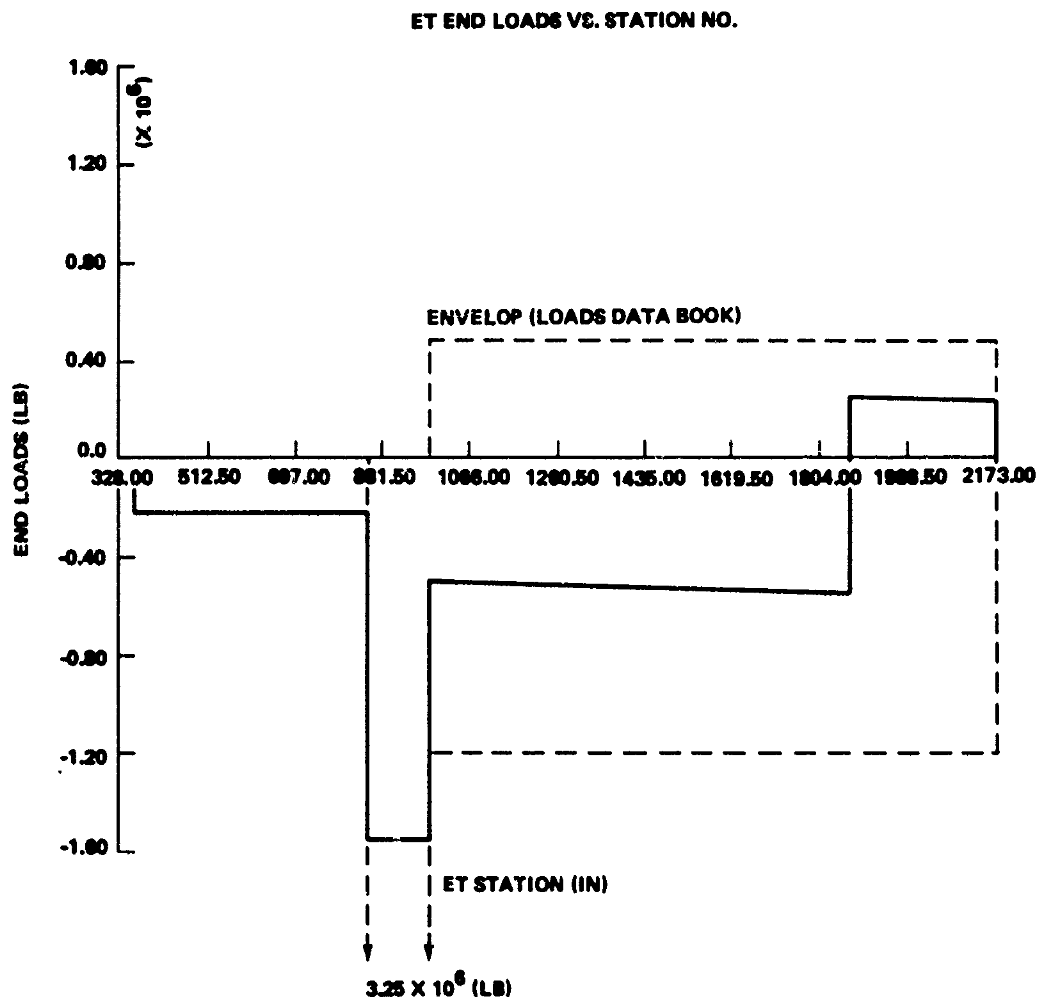

FIGURE J-5 ET END LOAD (T = 51.75 SEC) FOLLOWING LOSS OF SRB AT 50 SECONDS

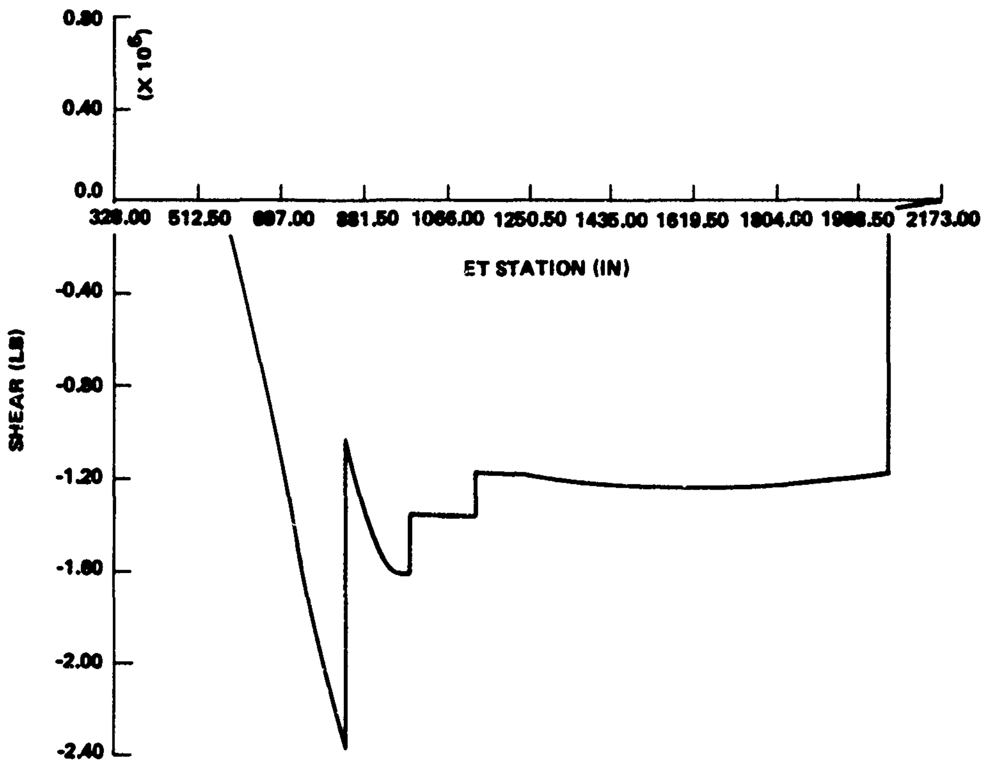

VIEW A, ET SHEAR, Y-DIRECTION

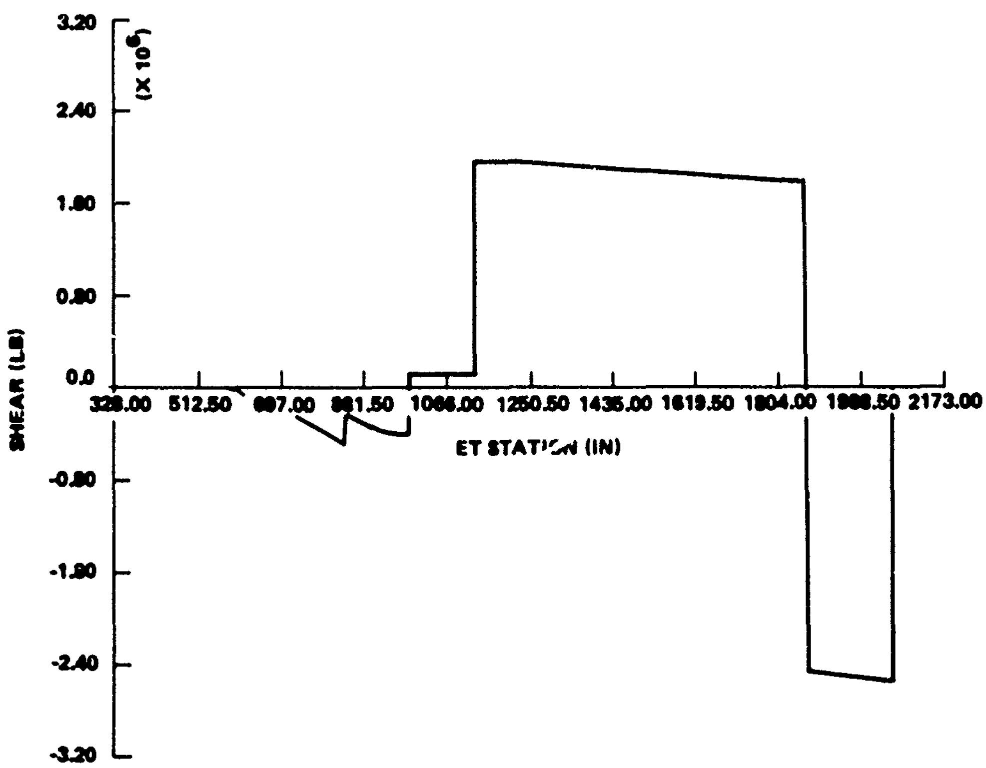

VIEW B, ET SHEAR, Z-DIRECTION

FIGURE J-6 ET SHEAR (T = 51.75 SEC) FOLLOWING LOSS OF SRB AT 50 SECONDS

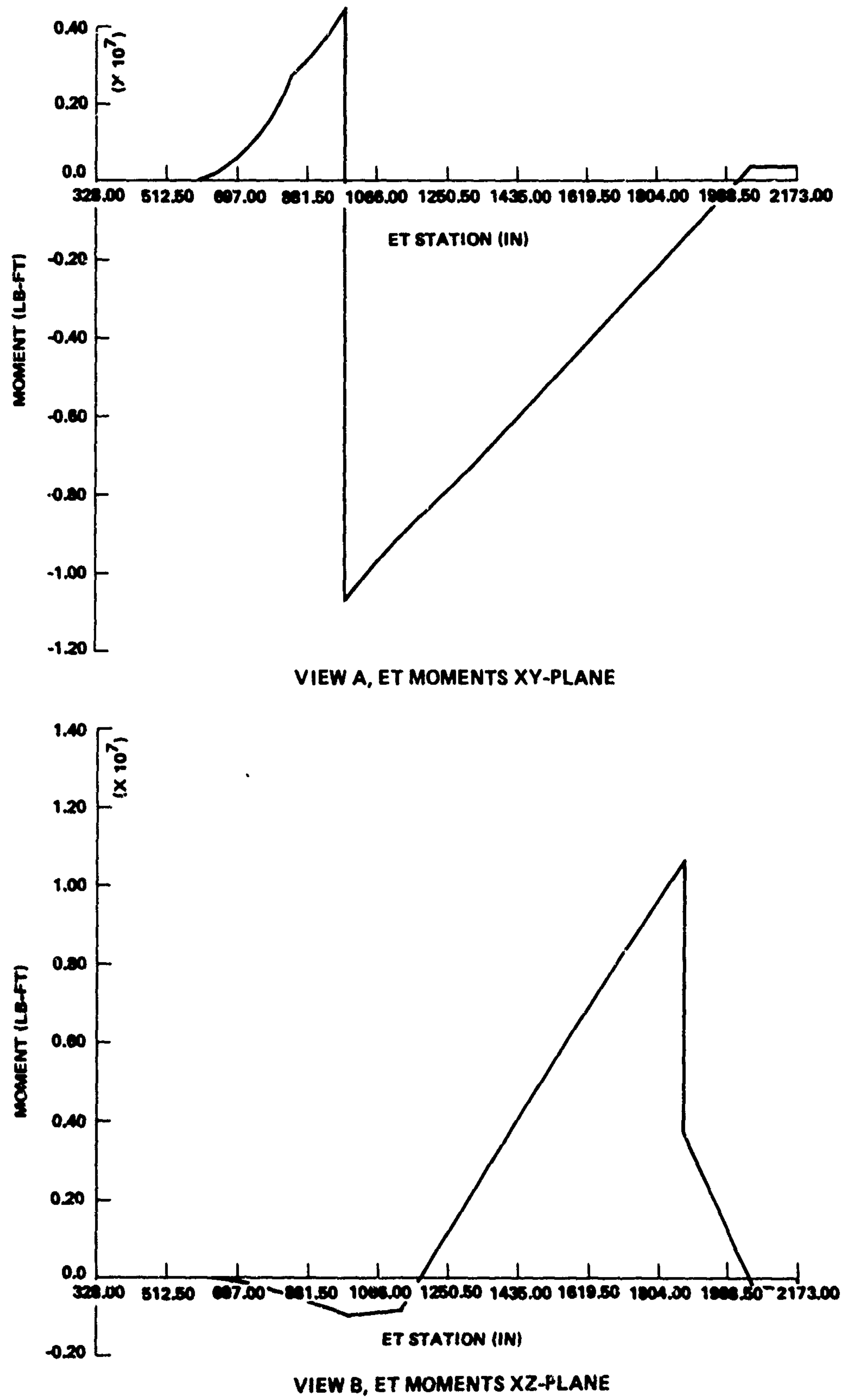

FIGURE J-7 ET BENDING MOMENTS (T = 51.75 SEC) FOLLOWING LOSS OF SRB AT 50 SECONDS

In the sample case, the calculated bending moments do not exceed the minimum allowable of 1.2×10^7 ft/lb. Therefore, no failure of the ET structure is expected due to bending.

APPENDIX K

STRESS ANALYSIS OF FRAME X_T 1129.9

During loss of one solid rocket booster (SRB) at 50 seconds, the load on frame X_T 1129.9 from the orbiter immediately exceeds the nominal design load. The loading on the frame at t = 50 sec is illustrated in Figure K-1. The frame will be analyzed using NACA TN 1310, recognizing that this analysis is approximate, as NACA TN 1310 applies to frames of uniform stiffness. Frame X_T 1129.9 has a varying cross section, as shown in Figure K-2.

The loads FT01 and FT02 must be resolved into radial and tangential components at locations A and B, Figure K-1. The static solution for the distribution of forces on the truss, all joints pinned, yields

$$P_A = 0.381 \text{ FT01} - 0.487 \text{ FT02} \tag{K-1}$$

$$T_A = 0.508 \text{ FT01} - 0.649 \text{ FT02} \tag{K-2}$$

$$P_B = 0.381 \text{ FT01} + 0.487 \text{ FT02} \tag{K-3}$$

$$T_B = 0.508 \text{ FT01} + 0.649 \text{ FT02} \tag{K-4}$$

Translating the tangential components to the neutral axis of the frame adds concentrated moments of

$$M_A = 12. \, T_A \tag{K-5}$$

$$M_B = 12. \, T_B \tag{K-6}$$

Figure K-3 shows a cross section of the outer chord and its attachment to the tank skin. The effective moment of inertia of the frame at the top was bounded between 824.4 in^4 and 761.43 in^4, depending on the amount of skin assumed (Figs. K-4 and K-5). The moment of inertia at the bottom of the frame was bounded between 97.4 in^4 and 91.3 in^4 (Figs. K-6 and K-7).

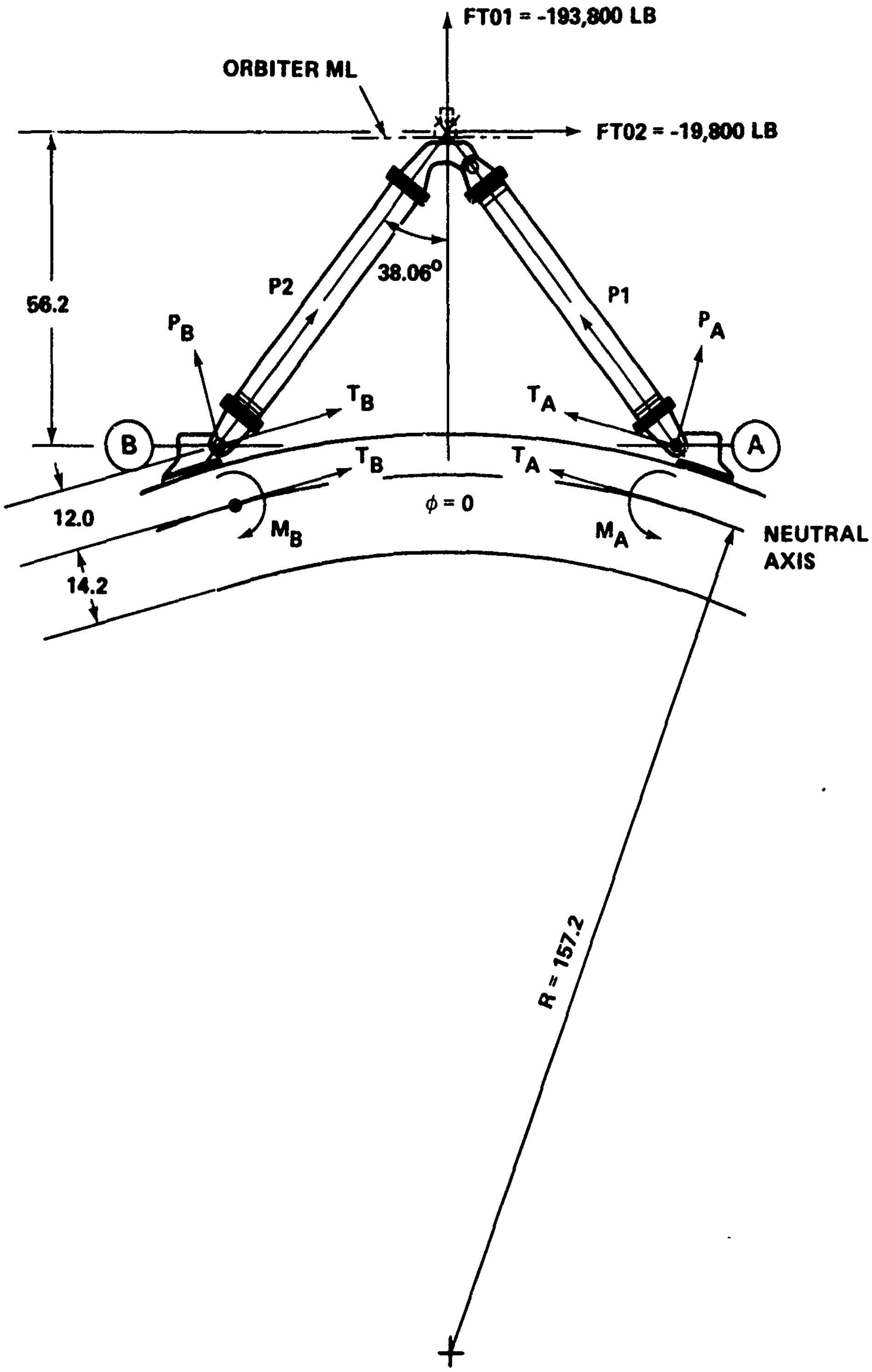

FIGURE K-1   FORWARD ORBITER/ET TRUSS LOADING

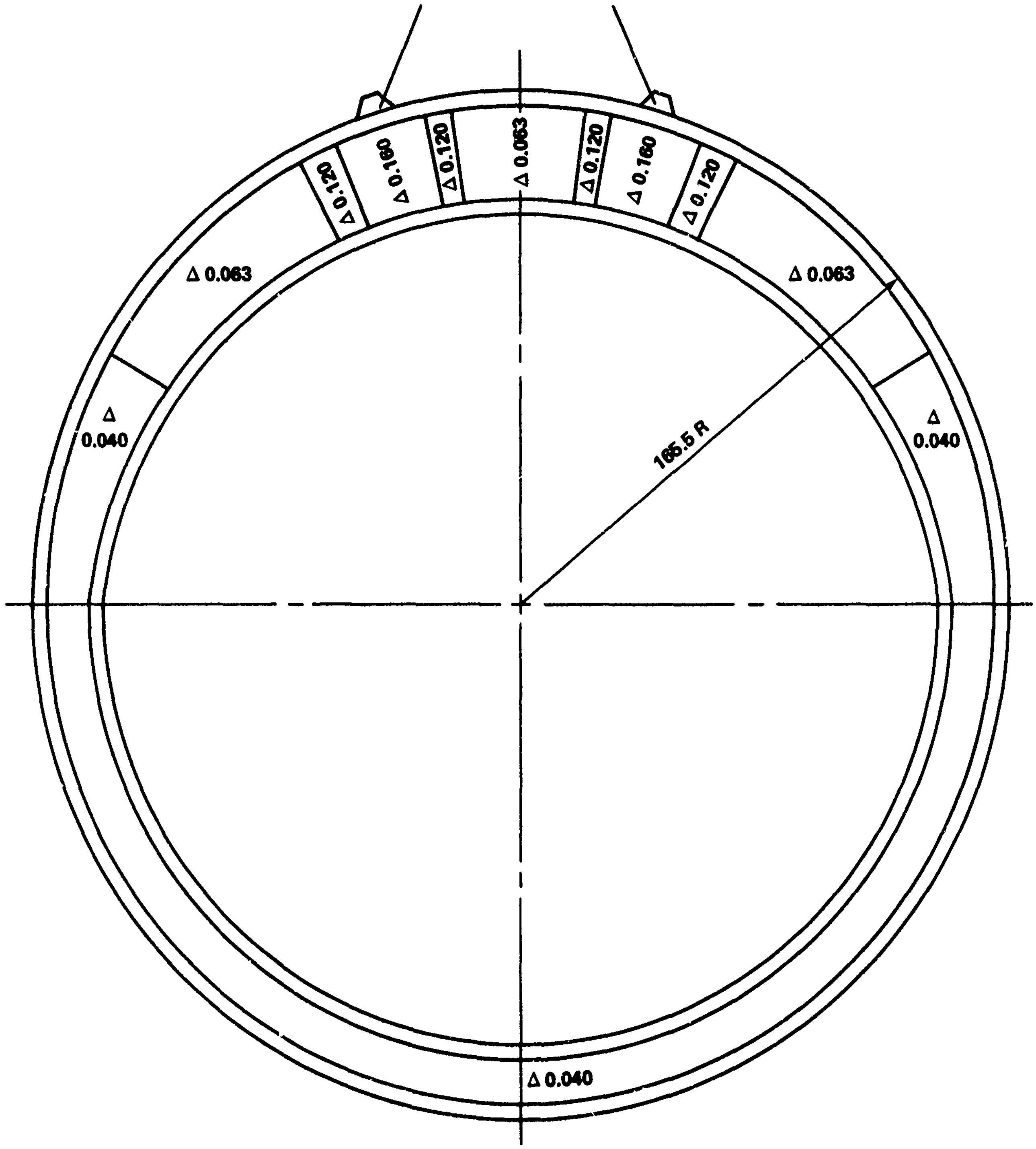

FIGURE K-2 RING FRAME X_T 1129.9

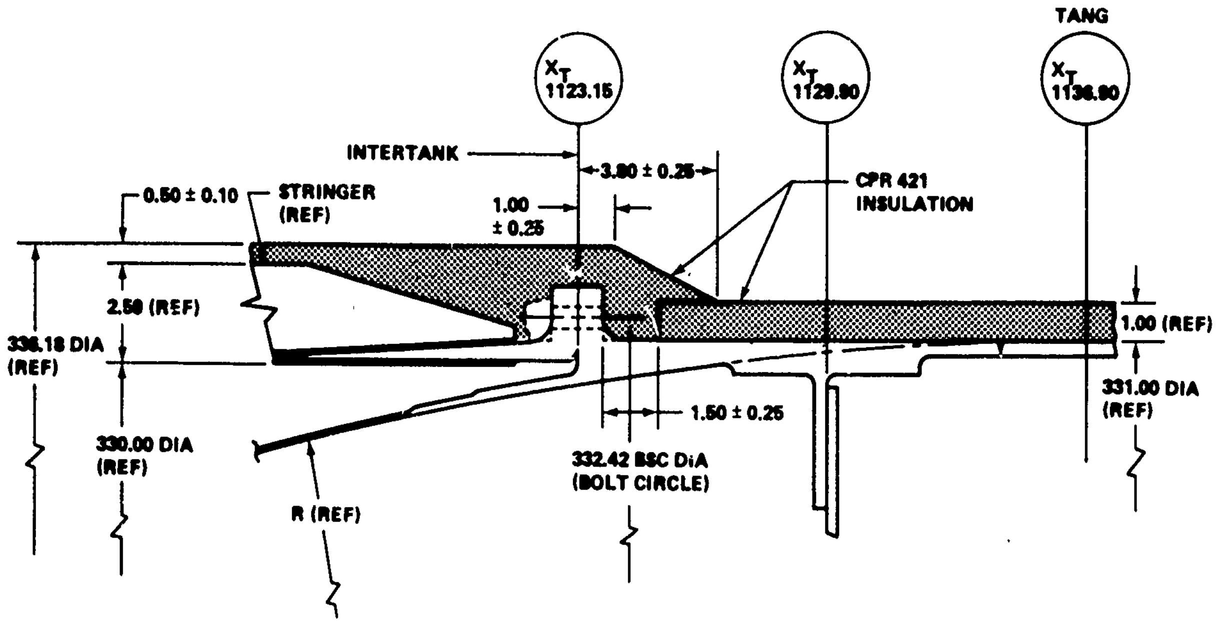

FIGURE K-3 OUTER CHORD — FRAME X_T 1129.9

The information required for analysis by NACA TN 1310 is as follows:

L = length of bay = 247 (1129.9 - 1377) in

I = moment of inertia of ring = 461 in^4 avg

t = thickness of skin = 0.137 in

t^1 = effective thickness of skin = 0.164 in

(See analysis of frame X_T 1624.)

R = 157.2 in

G = 4×10^6 psi

$$A = \frac{R^6 t^1}{IL^3} = \frac{157.2^6 \times 0.164}{461 \times 247^3} = 356 \qquad \text{(K-7)}$$

$$B = \frac{Et^1R^2}{GtL^2} = \frac{10.6 \times 10^6 \times 164 \times 157.2^2}{4 \times 10^6 \times 137 \times 247^2} = 1.28 \qquad \text{(K-8)}$$

$$\frac{A}{B} = \frac{GtR^4}{EIL} = \frac{4 \times 10^6 \times 0.137 \times 157.2^4}{10.6 \times 10^6 \times 461 \times 247} = 277.2 \qquad \text{(K-9)}$$

Use A = 200 and A/B = ∞ in the figures of NACA TN 1310.

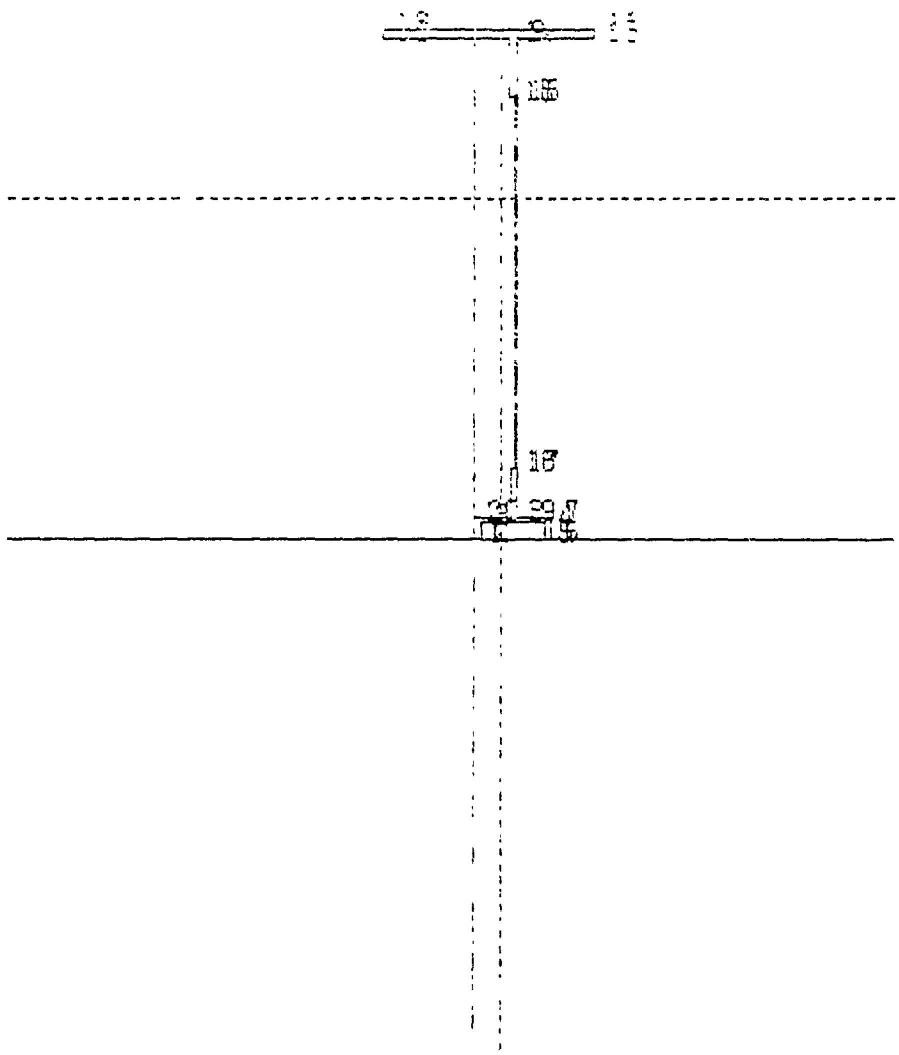

PROPERTIES WITH RESPECT TO

REFERENCE AXES	CENTER OF GRAVITY
I (XX) = 3001.0992	I (XX) = 824.4494
I (YY) = 67.2814	I (YY) = 49.5888
I (XY) = 154.2073	I (XY) = -41.9230
I (P) = 3068.3806	I (P) = 874.0382

COORDINATES OF CENTER OF GRAVITY: X-BAR (IN) = 1.4175
Y-BAR (IN) = 15.7318

AREA (IN^2) = 8.7948 MINIMUM I = 47.3272

ANGLE BETWEEN PRINCIPAL AND X-AXIS = -86.9122°

FIGURE K-4 MAXIMUM SECTION PROPERTIES AT TOP OF FRAME X_T 1129.9

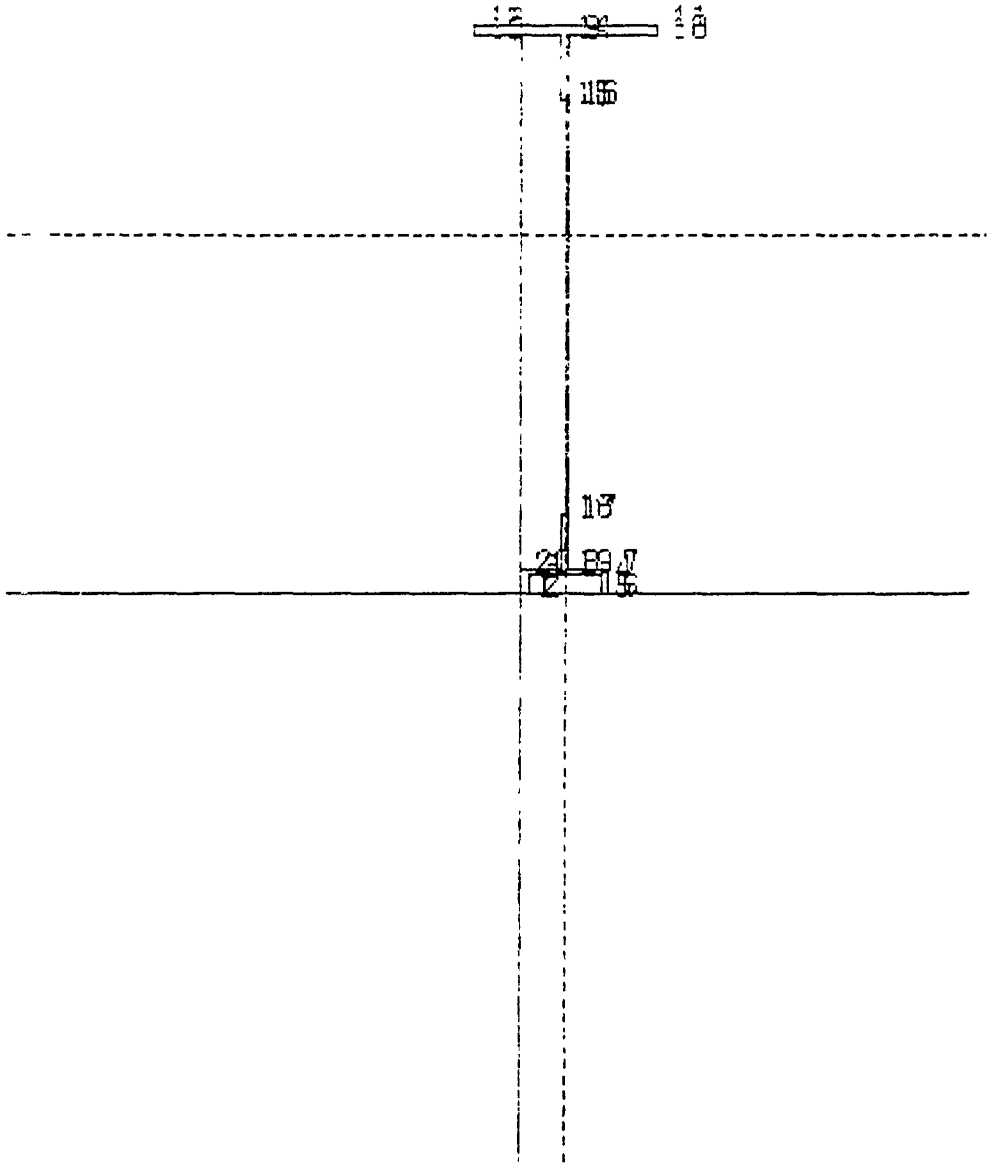

PROPERTIES WITH RESPECT TO

REFERENCE AXES	CENTER OF GRAVITY
I (XX) = 2461.1415	I (XX) = 761.4350
I (YY) = 55.2867	I (YY) = 23.0070
I (XY) = 232.8707	I (XY) = -1.3625
I (P) = 2516.4382	I (P) = 784.4420

COORDINATES OF CENTER OF GRAVITY: X-BAR (IN) = 2.0380
Y-BAR (IN) = 14.7700

AREA (IN^2) = 7.7904 **MINIMUM I = 23.0044**

ANGLE BETWEEN PRINCIPAL AND X-AXIS = -89.8626°

FIGURE K-5 MINIMUM SECTION PROPERTIES AT TOP OF FRAME X_T 1129.9

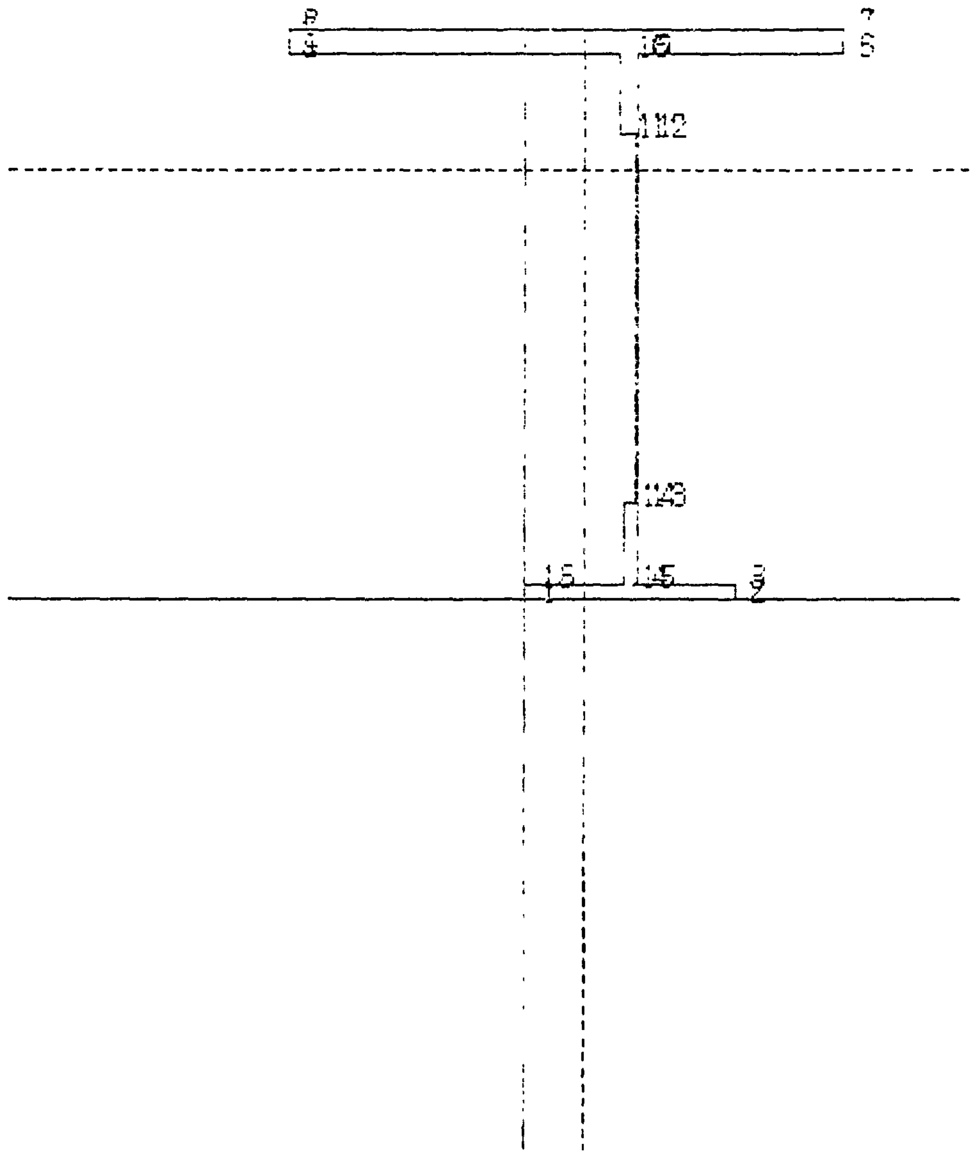

PROPERTIES WITH RESPECT TO

REFERENCE AXES	CENTER OF GRAVITY
I (XX) = 489.0878	I (XX) = 97.3886
I (YY) = 55.0408	I (YY) = 46.2086
I (XY) = 44.5275	I (XY) = - 12.7670
I (P) = 524.1284	I (P) = 143.5764

COORDINATES OF CENTER OF GRAVITY: X-BAR (IN) = 1.1633
Y-BAR (IN) = 7.5472

AREA (IN^2) = 6.5260 **MINIMUM I = 43.2005**

ANGLE BETWEEN PRINCIPAL AND X-AXIS = -76.7375°

FIGURE K-6 MAXIMUM SECTION PROPERTIES AT BOTTOM OF FRAME X_T 1129.9

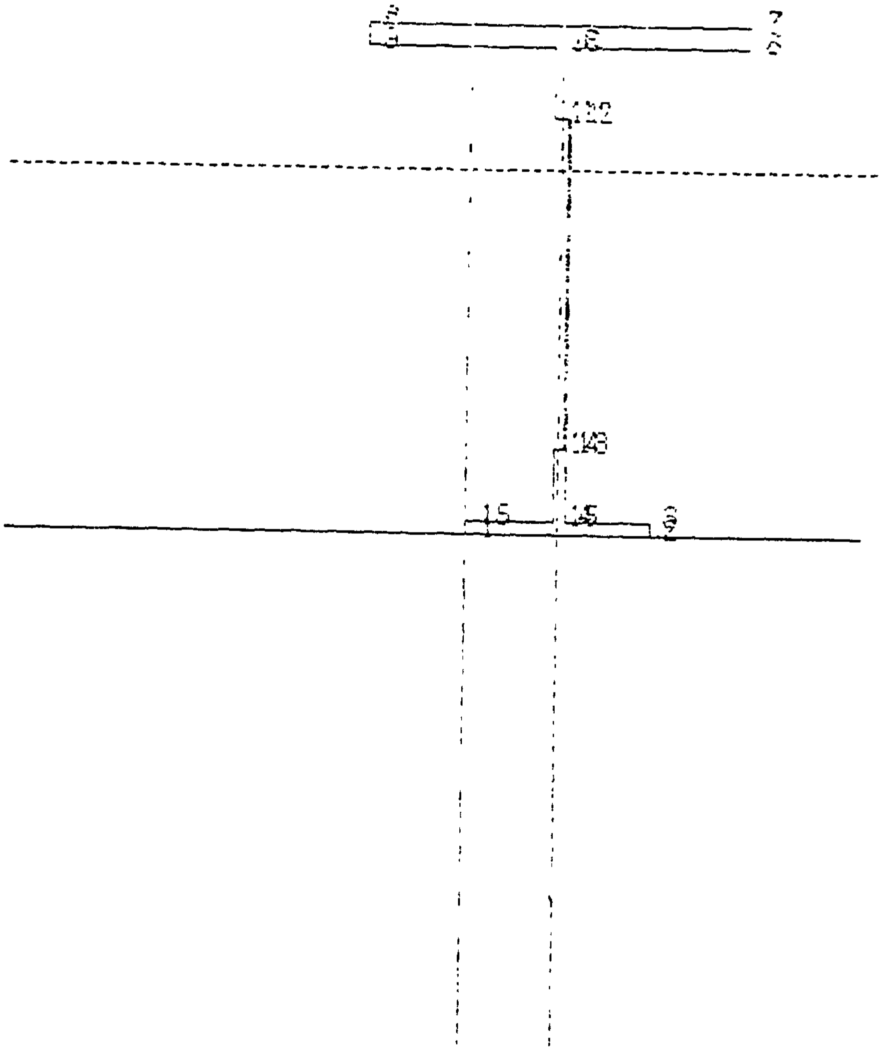

PROPERTIES WITH RESPECT TO

REFERENCE AXES	CENTER OF GRAVITY
I (XX) = 372.7034	I (XX) = 91.3524
I (YY) = 42.[illegible]	I (YY) = 20.9413
I (XY) = 78.0197	I (XY) = -0.5790
I (P) = 415.[illegible]022	I (P) = 112.2937

COORDINATES OF CENTER OF GRAVITY: **X-BAR (IN) = 1.[illegible]42**
Y-BAR (IN) = 7.13[illegible]3

AREA (IN^2) = 5.5215 **MINIMUM I = 20.[illegible]**

ANGLE BETWEEN PRINCIPAL AND X- AXIS = -[illegible].52[illegible]°

FIGURE K-7 MINIMUM SECTION PROPERTIES AT BOTTOM OF FRAME X_T 1129.9

Figure K-8 shows the moment distribution for a radial load ($-P_o$). Note that the max moment is relatively insensitive to A/B.

Figures K-9 and K-10 give similar curves for a tangential load (T_o) or a concentrated moment (Mo). The total moment at a given point on the frame is the algebraic sum of the individual moments resulting from all the forces acting on the frame.

As an example, consider the loading given in Figure K-1. The loads at A and B become

$$P_A = -64,200 \text{ lb}$$

$$T_A = -85,600 \text{ lb}$$

$$M_A = -1,027,000 \text{ in-lb}$$

$$P_B = -83,480 \text{ lb}$$

$$T_B = -111,300 \text{ lb}$$

$$M_B = -1,335,000 \text{ in-lb}$$

From Figures K-1, K-8, K-9, and K-10, the induced moments at B become

$$M_{B_{BR}} = (0.15)(83,480)(157.2) = 1,968,500 \text{ in-lb}$$

$$M_{B_{BT}} = 0$$

$$M_{B_{BM}} = \pm(0.50)(-1,336,000) = \pm 668,000 \text{ in-lb}$$

$$M_{B_{AR}} = (-0.016)(64,195)(157.2) = -161,500 \text{ in-lb}$$

$$M_{B_{AT}} = (-0.03)(-85,600)(157.2) = 403,700 \text{ in-lb}$$

$$M_{B_{AM}} = (0.13)(-1,027,000) = -133,500 \text{ in-lb}$$

where positive moments produce tension at the inner chord.

The total moment at B becomes

$$M_{TB} = 2.745 \times 10^6 \text{ in-lb}$$

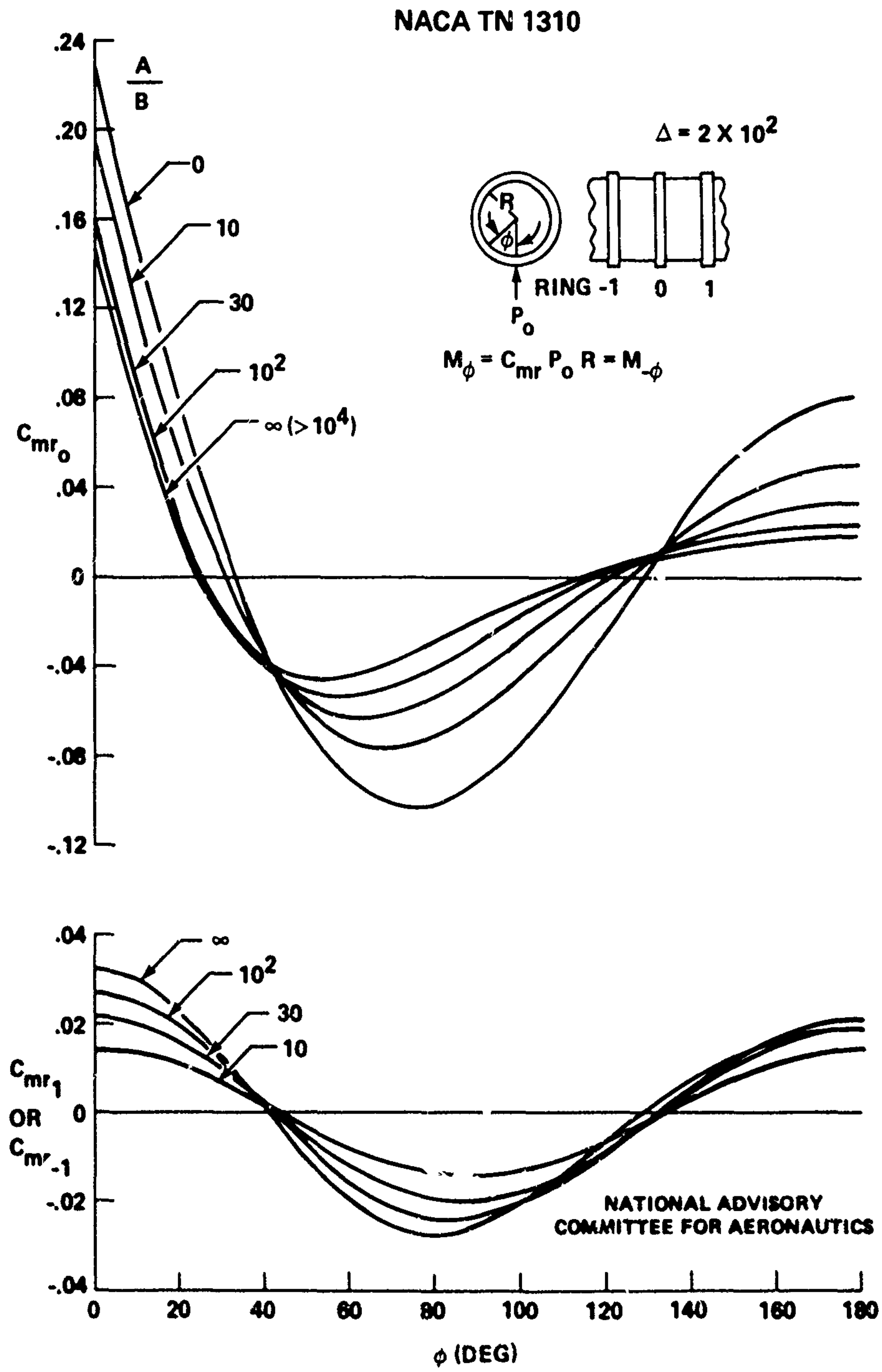

FIGURE K-8 RING BENDING-MOMENT COEFFICIENTS FOR RADIAL LOAD ($\Delta = 2 \times 10^2$)

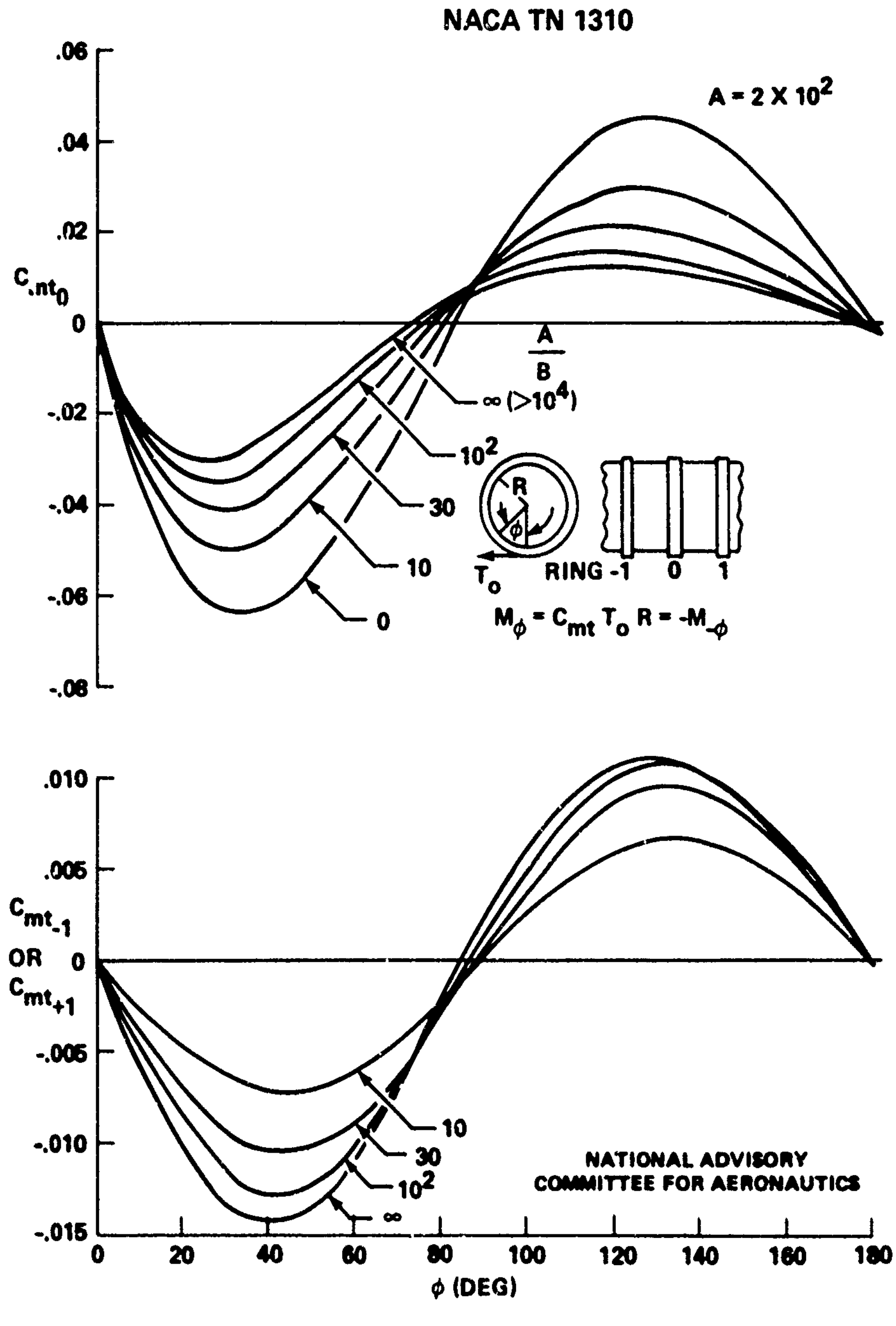

FIGURE K-9 RING BENDING-MOMENT COEFFICIENTS FOR TANGENTIAL LOAD ($A = 2 \times 10^2$)

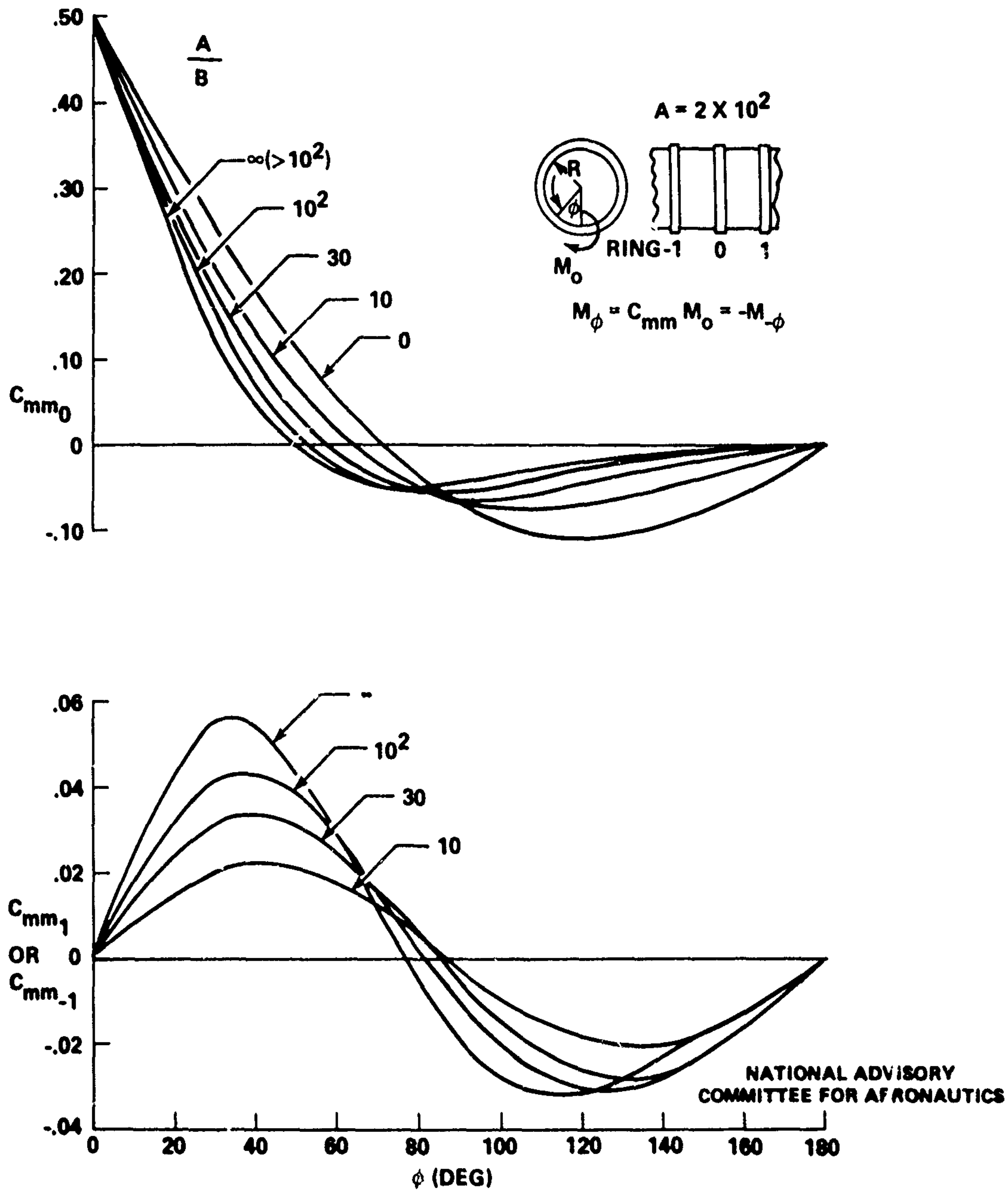

FIGURE K-10 RING BENDING-MOMENT COEFFICIENTS FOR MOMENT LOAD
($A = 2 \cdot 10^2$)

It can be shown that for this loading condition, the maximum bending moment occurs at B. Therefore, the maximum bending stress is

$$f_b = \frac{Mc}{I} = \frac{2.745 \times 10^6 \times 14.2}{824.44} = 47,300 \text{ psi} \tag{K-10}$$

(tension at inner chord). The minimum yield strength is above 57,000 psi. Frame X_T 1129.9 will not fail as a result of the initial overload at 50 seconds due to the loss of one SRB.

DISTRIBUTION

Copies

National Aeronautics and Space Administration
Marshall Space Flight Center
ATTN: J. A. Roach (EL-42) 40
Alabama 35812

National Aeronautics and Space Administration
Kennedy Space Center
ATTN: B. Rock (SF-ENG)
Florida 32899

National Aeronautics and Space Administration
Lyndon B. Johnson Space Center
ATTN: R. Rose
Houston, TX 77058

President
Naval War College
Newport, RI 02840

Superintendent
Naval Postgraduate School
ATTN: Library
Montery, CA 93940

Superintendent
Naval Academy
Annapolis, MD 21402

Commander
Harry Diamond Laboratories
2800 Powder Mill Road
ATTN: Technical Library
Adelphi, MD 20783

Commandant
Army War College
ATTN: Library
Carlisle Barracks, PA 17013

Commandant
Industrial College of the Armed Forces
Ft. Leslie J. McNair
ATTN: Document Control
Washington, DC 20315

Commandant
National War College
Ft. Leslie J. McNair
ATTN: Class. Rec. Library
Washington, DC 20315

Directorate of Safety Headquarters
Eastern Space and Missile Center
Patrick Air Force Base
ATTN: L. Ullian (SEM)
Florida 32925

SAMTEC/ROSF
ATTN: Colin Gardner
Vandenberg AFB, CA 93437

Commander
Air Force Weapons Laboratory
ATTN: Lt. N. Clemens (DYVS)
Kirtland Air Force Base, NM 87117

Air University Library
ATTN: Documents Section
Maxwell Air Force Base, AL 26112

Copies

Institute for Defense Analysis
400 Army-Navy Drive
ATTN: Library
Arlington, VA 22202

Chairman
Department of Defense Explosives
Safety Board
Room 856-C Hoffman Bldg. 1
2461 Eisenhower Avenue
ATTN: R. Perkins
R. Scott
T. Zaker
Alexandria, VA 22331

Director
Defense Nuclear Agency
ATTN: Technical Library
Washington, DC 20305

Commander
Field Command
Defense Nuclear Agency
ATTN: FCTA
Kirtland Air Force Base, NM 87115

Defense Technical Information Center
Cameron Station 12
Alexandria, VA 22314

Library of Congress
ATTN: Gift and Exchange Division
Washington, DC 20540

Thiokol/Wasatch Division
P. O. Box 524
ATTN: Technical Library
Brigham City, Utah 84302

Martin Marietta Corp.
Michoud Operations
ATTN: B. Elam
New Orleans, Louisiana

Rockwell International Space Division
12214 Lakewood Blvd.
ATTN: Technical Library
Downey, CA 90241

Battelle Memorial Institute
505 King Avenue
ATTN: E. Rice
Columbus, OH 43201

Denver Research Institute
Mechanical Sciences and
Environmental Engineering
University of Denver
ATTN: J. Wisotski
Denver, CO 80210

Falcon Research
ATTN: D. Parks
Denver, CO 80210

General American Transportation
Corporation
General American Research Div.
7449 North Natchez Avenue
ATTN: Technical Library
Niles, IL 60648

General Electric Company - TEMPO
816 State Street
ATTN: W. Chan/DASIAC
Santa Barbara, CA 93102

Hercules Incorporated
Box 98
ATTN: D. Richardson
Magna, UT 84044

IIT Research Institute
10 West 35th Street
ATTN: Technical Library
Chicago, IL 60616

Kaman Sciences Corp.
P. O. Box 7463
Colorado Springs, CO 80907

Los Alamos Scientific Laboratory
P. O. Box 1663
ATTN: LASL Library
Los Alamos, NM 87544

New Mexico Institute of Mining
and Technology
TERA
ATTN: M. L. Kempton
J. P. McLain
Socorro, NM 87801

Pacific Technology
P. O. Box 148
Del Mar, CA 92016

Physics International Company
2700 Merced Street
ATTN: Technical Library
San Leandro, CA 94577

R and D. Associates
P. O. Box 3580
ATTN: Technical Library
Santa Monica, CA 90403

Sandia Laboratories
P. O. Box 5800
ATTN: Library
J. Reed
L. Vortman
Albuquerque, NM 87115

Sandia Laboratories
Livermore Laboratory
P. O. Box 969
Livermore, CA 94550

Director
Scripps Institution of Oceanography
La Jolla, CA 92037

Shock Hydrodynamics Incorporated
15010 Ventura Boulevard
ATTN: Technical Library
Sherman Oaks, CA 91403

Southwest Research Institute
8500 Culebra Road
ATTN: W. Baker
San Antonio, TX 78206

Systems, Science and Software
P. O. Box 1620
La Jolla, CA 92037

Teledyne Energy Systems
110 W. Timonium Road
ATTN: T. Olsen
Lutherville, MD 21093

University of California
Lawrence Livermore Laboratory
ATTN: Technical Library
Livermore, CA 94550

URS Corporation
155 Bonet Road
ATTN: Document Control
San Mateo, CA 94402

Director
Woods Hole Oceanographic Institute
Woods Hole, MA 02543

J. H. Wiggins Corporation
1650 S. Pacific Coast Highway
ATTN: J. Baeker
Redonodo Beach, CA 90277